

Doped TiO_2 Nanomaterials and Applications

Guest Editors: M. S. A. Abdel-Mottaleb, V. Augugliaro, and L. Palmisano





Doped TiO₂ Nanomaterials and Applications

International Journal of Photoenergy

Doped TiO₂ Nanomaterials and Applications

Guest Editors: M. S. A. Abdel-Mottaleb,
V. Augugliaro, and L. Palmisano



Copyright © 2008 Hindawi Publishing Corporation. All rights reserved.

This is a special issue published in volume 2008 of “International Journal of Photoenergy.” All articles are open access articles distributed under the Creative Commons Attribution License, which permits unrestricted use, distribution, and reproduction in any medium, provided the original work is properly cited.

Editor-in-Chief

D. Bahnemann, Universität Hannover, Germany

Editor-in-Chief Emeritus

Mohamed Sabry Abdel-Mottaleb, Egypt

Associate Editors

M. A. Aegerter, Germany

Nicolas Alonso-Vante, France

Masakazu Anpo, Japan

Vincenzo Balzani, Italy

James Barber, UK

F. Barigelletti, Italy

Ignazio Renato Bellobono, Italy

F. Bordin, Italy

Dietrich Döepp, Germany

Abderrazek Douhal, Spain

Terry Egerton, UK

Mostafa El-Sayed, USA

Samy El-Shall, USA

Frederic Fages, France

P. Foggi, Italy

Peter Ford, USA

Karl-Heinz Funken, Germany

Julian Blanco Galvez, Spain

Beverley Glass, Australia

Anna Giardini Guidoni, Italy

A. Hagfeldt, Sweden

Kazuhito Hashimoto, Japan

H. Hidaka, Japan

Michael R. Hoffmann, USA

Prashant V. Kamat, USA

G. Kaupp, Germany

Jasper Knoester, Netherlands

C. Lévy-Clément, France

G. Li Puma, UK

Panagiotis Lianos, Greece

Stefan Lis, Poland

Gilles Mailhot, France

George Marston, UK

Ugo Mazzucato, Italy

Jacek Miller, Poland

Leonardo Palmisano, Italy

Onder Pekcan, Turkey

Ezio Pelizzetti, Italy

Peter Robertson, UK

Niyazi Serdar Sariciftci, Austria

Aldo Steinfeld, Switzerland

Masanori Tachiya, Japan

Anthony Testa, USA

Hanne Hjorth Tonnesen, Norway

Boris Uzhinov, Russia

Roel van De Krol, Netherlands

M. van Der Auweraer, Belgium

G. M. J. B. van Henegouwen, Netherlands

Jan W. Verhoeven, Netherlands

Han Vos, Ireland

David Worrall, UK

Fahrettin Yakuphanoglu, Turkey

J. Yu, Hong Kong

Klaas Zachariasse, Germany

J. Zhao, China

Contents

Doped TiO₂ Nanomaterials and Applications, M. S. A. Abdel-Mottaleb, V. Augugliaro, and L. Palmisano
Volume 2008, Article ID 419096, 1 page

Photocatalytic Degradation of Chlorobenzene by TiO₂ in High-Temperature and High-Pressure Water, N. Kometani, S. Inata, A. Shimokawa, and Y. Yonezawa
Volume 2008, Article ID 512170, 6 pages

Photocatalytic Degradation of Polynitrophenols on Various Commercial Suspended or Deposited Titania Catalysts Using Artificial and Solar Light, Hinda Lachheb, Ammar Houas, and Jean-Marie Herrmann
Volume 2008, Article ID 497895, 9 pages

Increase of the Photocatalytic Activity of TiO₂ by Carbon and Iron Modifications, Beata Tryba
Volume 2008, Article ID 721824, 15 pages

Visible-Light-Active Titania Photocatalysts: The Case of N-Doped TiO₂s—Properties and Some Fundamental Issues, Alexei V. Emeline, Vyacheslav N. Kuznetsov, Vladimir K. Rybchuk, and Nick Serpone
Volume 2008, Article ID 258394, 19 pages

Photocatalytic Hydrogen or Oxygen Evolution from Water over S- or N-Doped TiO₂ under Visible Light, Kazumoto Nishijima, Takaaki Kamai, Naoya Murakami, Toshiki Tsubota, and Teruhisa Ohno
Volume 2008, Article ID 173943, 7 pages

Thermal Behavior of TiO_{2-x}N_x Nanostructured Powder, Vladimír Balek, Jan Šubrt, Hiroshi Irie, and Kazuhito Hashimoto
Volume 2008, Article ID 267345, 7 pages

Hydrothermal Preparation of Visible-Light-Driven N-Br-Codoped TiO₂ Photocatalysts, Yonggang Sheng, Yao Xu, Dong Jiang, Liping Liang, Dong Wu, and Yuhan Sun
Volume 2008, Article ID 563949, 7 pages

Electrochemical Investigation of Doped Titanium Dioxide, J. W. J. Hamilton, J. A. Byrne, C. McCullagh, and P. S. M. Dunlop
Volume 2008, Article ID 631597, 8 pages

Preparation, Characterisation, and Photocatalytic Behaviour of Co-TiO₂ with Visible Light Response, Rossano Amadelli, Luca Samiolo, Andrea Maldotti, Alessandra Molinari, Mario Valigi, and Delia Gazzoli
Volume 2008, Article ID 853753, 9 pages

Preparation of Fluorine-Doped TiO₂ Photocatalysts with Controlled Crystalline Structure, N. Todorova, T. Giannakopoulou, G. Romanos, T. Vaimakis, Jiaguo Yu, and C. Trapalis
Volume 2008, Article ID 534038, 9 pages

Effect of Gold Dispersion on the Photocatalytic Activity of Mesoporous Titania for the Vapor-Phase Oxidation of Acetone, S. V. Awate, A. A. Belhekar, S. V. Bhagwat, R. Kumar, and N. M. Gupta
Volume 2008, Article ID 789149, 13 pages

The Effect of Transition Metal Doping on the Photooxidation Process of Titania-Clay Composites, Judit Ménesi, Renáta Kékesi, László Kőrösi, Volker Zöllmer, André Richardt, and Imre Dékány
Volume 2008, Article ID 846304, 9 pages

The Effect of Sulphate Doping on Nanosized TiO₂ and MoO_x/TiO₂ Catalysts in Cyclohexane Photooxidative Dehydrogenation, P. Ciambelli, D. Sannino, V. Palma, and V. Vaiano
Volume 2008, Article ID 258631, 8 pages

Silver Doped TiO₂ Nanostructure Composite Photocatalyst Film Synthesized by Sol-Gel Spin and Dip Coating Technique on Glass, Mojtaba Nasr-Esfahani and Mohammad Hossein Habibi
Volume 2008, Article ID 628713, 11 pages

Characterization and Evaluation of the Efficiency of TiO₂/Zinc Phthalocyanine Nanocomposites as Photocatalysts for Wastewater Treatment Using Solar Irradiation, Antonio E. H. Machado, Marcela D. França, Valdemir Velani, Gabriel A. Magnino, Hosana M. M. Velani, Flávio S. Freitas, Paulo S. Müller Jr., Christian Sattler, and Martin Schmücker
Volume 2008, Article ID 482373, 12 pages

The Function of TiO₂ with Respect to Sensitizer Stability in Nanocrystalline Dye Solar Cells, A. Barkschat, T. Moehl, B. Macht, and H. Tributsch
Volume 2008, Article ID 814951, 13 pages

Characterization of Conjugated Polymer Poly(fluorene-co-thiophene) and Its Application as Photosensitizer of TiO₂, Rongliang Qiu, Lin Song, Dongdong Zhang, Yueqi Mo, Eric Brewer, and Xiongfei Huang
Volume 2008, Article ID 164702, 5 pages

Influence of Irradiance, Flow Rate, Reactor Geometry, and Photopromoter Concentration in Mineralization Kinetics of Methane in Air and in Aqueous Solutions by Photocatalytic Membranes Immobilizing Titanium Dioxide, Ignazio Renato Bellobono, Mauro Rossi, Andrea Testino, Franca Morazzoni, Riccardo Bianchi, Giulia de Martini, Paola Maria Tozzi, Rodica Stanescu, Cristina Costache, Liliana Bobirica, Mauro Luigi Bonardi, and Flavia Groppi
Volume 2008, Article ID 283741, 14 pages

Editorial

Doped TiO₂ Nanomaterials and Applications

M. S. A. Abdel-Mottaleb,¹ V. Augugliaro,² and L. Palmisano²

¹ *Department of Chemistry, Faculty of Science, Ain Shams University, 11566 Abbassia, Cairo, Egypt*

² *Dipartimento di Ingegneria Chimica dei Processi e dei Materiali, Università di Palermo, 90128 Palermo, Italy*

Correspondence should be addressed to M. S. A. Abdel-Mottaleb, phochem08@photoenergy.org

Received 16 July 2008; Accepted 16 July 2008

Copyright © 2008 M. S. A. Abdel-Mottaleb et al. This is an open access article distributed under the Creative Commons Attribution License, which permits unrestricted use, distribution, and reproduction in any medium, provided the original work is properly cited.

This special issue briefly reviews some trends and factors that have impacted heterogeneous photocatalysis with next generation TiO₂ nanophotocatalysts that could absorb and make use of both UV (290–400 nm) and visible (400–700 nm) sunlight to enhance process efficiencies, along with some issues of current debate in the fundamental understanding of the science that underpins the field. Preparative methods and some characteristic features of doped TiO₂ as well as its environmental applications are presented and described. The next generation of doped TiO₂ photocatalysts should enhance overall process photoefficiencies in many cases, since doped TiO₂s absorb a greater quantity of solar radiation. The fundamental science that underpins heterogeneous photocatalysis with the next generation of photocatalysts is a rich playing field ripe for further exploration.

Different articles presented in this special issue have shown that modification of TiO₂ by doping of different atoms, both as cations and anions, can improve photoactivity of TiO₂. One reason is slowing down electron/hole recombination rate. The presence of certain dopants can increase the concentration of organic pollutants on the surface of TiO₂ facilitating the contact of the light-generated reactive species with the organic molecules. Doped TiO₂ can extend the absorption of the light to the visible region and makes the photocatalysts active under visible-light irradiation.

*M. S. A. Abdel-Mottaleb
V. Augugliaro
L. Palmisano*

Research Article

Photocatalytic Degradation of Chlorobenzene by TiO₂ in High-Temperature and High-Pressure Water

N. Kometani, S. Inata, A. Shimokawa, and Y. Yonezawa

Department of Applied Chemistry, Graduate School of Engineering, Osaka City University, 3-3-138 Sugimoto, Sumiyoshi-ku, Osaka 558-8585, Japan

Correspondence should be addressed to Y. Yonezawa, yonezawa@a-chem.eng.osaka-cu.ac.jp

Received 28 August 2007; Accepted 7 December 2007

Recommended by M. Sabry Abdel-Mottaleb

A fluidized-bed-type flow reactor available for the photocatalytic treatment of the suspension of model soil under high-temperature, high-pressure conditions was designed. An aqueous suspension containing hydrogen peroxide (H₂O₂) as an oxidizer and inorganic oxides as a model soil, titania (TiO₂), silica (SiO₂), or kaoline (Al₂Si₂O₅(OH)₄) was continuously fed into the reactor with the temperature and the pressure controlled to be $T = 20\text{--}400^\circ\text{C}$ and $P = 30\text{ MPa}$, respectively. The degradation of chlorobenzene (CB) in water was chosen as a model oxidation reaction. It appeared that most of the model soils are not so harmful to the SCWO treatment of CB in solutions. When the TiO₂ suspension containing H₂O₂ was irradiated with near-UV light, the promotion of the degradation caused by photocatalytic actions of TiO₂ was observed at all temperatures. Persistence of the photocatalytic activity in the oxidation reaction in high-temperature, high-pressure water would open up a possibility of the development of the hybrid process based on the combination of SCWO process and TiO₂ photocatalysis for the treatment of environmental pollutants in soil and water, which are difficult to handle by conventional SCWO process or catalytic SCWO process alone.

Copyright © 2008 N. Kometani et al. This is an open access article distributed under the Creative Commons Attribution License, which permits unrestricted use, distribution, and reproduction in any medium, provided the original work is properly cited.

1. INTRODUCTION

Since the discovery of the Becquerel effect in 1839, photochemistry and photocatalytic reactions of inorganic solids including semiconductors and photoconductors have been an important subject in solid-state photochemistry and catalytic chemistry. Focusing on electronic and ionic processes at the solid solution interface, the work by Brattain and Garrett on semiconductor electrochemistry of germanium (Ge) in 1955 pioneered a great deal of work in the United States, Germany, and Russia [1]. In 1972, Fujishima and Honda found that O₂ is produced without being accompanied with corrosion, when a titanium dioxide (TiO₂) single crystal electrode is illuminated with near-UV light, which triggered a lot of activities to find photoelectrochemical systems capable of splitting water into H₂ and O₂ [2, 3]. By virtue of high photocatalytic activity as well as chemical stability, TiO₂ photocatalyst is promising for a variety of applications such as solar energy conversion, treatments of organic-containing wastewater, recovery of natural resources [4, 5]. At the present time, TiO₂ is still efficient, practical, and the

most studied photocatalyst despite extensive efforts to find photocatalytic materials overcoming TiO₂. At the same time, numerous efforts have been devoted to the improvement of TiO₂ photocatalyst. However, those applications have been based on the premise that the photocatalyst is used under mild conditions near ambient temperature and pressure. On the other hand, from a wider viewpoint related to hydrothermal processes in geochemistry and earth sciences, it is of substantial interest how the photocatalytic actions of inorganic solids are influenced by the extreme conditions of the surroundings, particularly in the high-temperature, high-pressure water [6].

Supercritical water has been used as a reaction medium for chemical synthesis, fuel production, waste treatment by oxidation, and so on [7]. The supercritical water oxidation (SCWO) process for wastewater treatment has been extensively studied. Recently, there has been increasing interest in the use of heterogeneous catalysts in SCWO (catalytic SCWO) [8]. However, there has been no attempt to combine photocatalysis with SCWO. As a part of the project of extended applications of photocatalyst to environmental

problems, we have concentrated on the extensive use of photocatalytic reactions involving photoelectrons and photoholes under ambient ~ extreme conditions. An aqueous suspension of TiO_2 illuminated with near-UV light under ambient conditions has been known to oxidize many chlorinated hydrocarbons to carbon oxide under oxygenated or air-equilibrated conditions [9]. In this study, we chose chlorobenzene (CB) as a model compound for the photocatalytic oxidation as it is listed as a priority pollutant in water because of the low biodegradability and accumulation potential in soil and water [10]. Degradation of CB was undertaken in the aqueous suspension containing inorganic oxides: titania (TiO_2), colloidal silica (SiO_2), or kaoline ($\text{Al}_2\text{Si}_2\text{O}_5(\text{OH})_4$), which are regarded as the model soil contaminated with organochlorine compounds. To this end, we designed a fluidized-bed-type flow reactor available for the study of photocatalytic reactions of aqueous suspensions and slurry of inorganic oxides. A remarkable observation of this study is that TiO_2 can maintain the efficient photocatalytic activity even in high-temperature, high-pressure water up to $T = 400^\circ\text{C}$ and $P = 30\text{ MPa}$. A qualitative consideration of the reaction mechanism was discussed briefly.

2. EXPERIMENTAL METHODS

Inorganic oxides used in this study were TiO_2 powder (JRC-TIO-01) from Catalysis Society of Japan (Japan), SiO_2 from Nissan Chemical Industry Co. (Tokyo, Japan) and kaoline from Kishida Chemicals Co. (Osaka, Japan). CB, hydrogen peroxide (H_2O_2), and *n*-decane were of special grade purchased from Kishida Chemical Co. The photocatalytic activity of TiO_2 at room temperature in air was tested with respect to the photobleach of methylene blue (MB, Kishida Chemical Co.) in the TiO_2 suspension [11]. A 50 mL aqueous suspension containing TiO_2 and MB was illuminated with near-UV light from a 500 W high-pressure mercury lamp UI-501C (Ushio Denki Co., Tokyo, Japan) combined with a UV-D35 glass filter (Toshiba Co., Japan). The intensity of incident light was made almost equal to that used in the following experiments. The variations of the absorption spectrum were recorded on a V-560 spectrophotometer (JASCO Co., Tokyo, Japan). It appeared that about 90% of MB, existed at the beginning, was photobleached after 60 minutes irradiation, which ensured regular photocatalytic activity of the TiO_2 powder.

A fluidized-bed-type flow reactor equipped with sapphire windows was designed and tested. The schematic diagram of the reactor and the combination of experimental apparatus are illustrated in Figure 1. The basic structure of the reactor was the same as described in [12]. It was made of Hastelloy (inner volume $\sim 1.0\text{ cm}^3$) and was equipped with two sapphire windows whose diameter was 6.0 mm. The reactor could be heated at desired temperature $T = 20\text{--}400^\circ\text{C}$ by an electric furnace. Pressure was kept at $P = 30\text{ MPa}$ by a back pressure regulator (SCF-Bpg, JASCO Co., Tokyo, Japan). Typically, an aqueous suspension was composed of 1 mM CB and 0.1 wt% inorganic oxide in water, with or without 0.1 wt% H_2O_2 . The suspension was injected into the reactor by a slurry type HPLC pump PU-2086 Plus

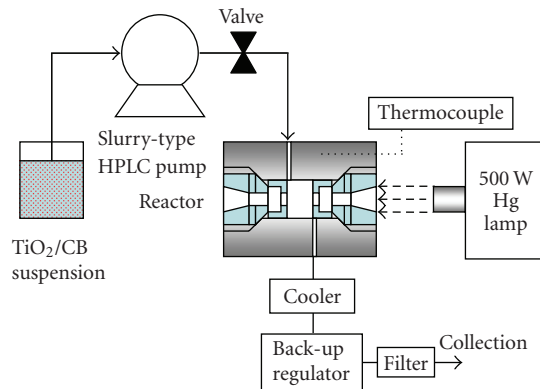


FIGURE 1: Schematic diagram of the fluidized-bed-type reactor designed for the study of photocatalytic reactions of TiO_2 suspension under high-temperature, high-pressure conditions.

(JASCO Co.) with the flow rate $0.2\text{--}1\text{ cm}^3\text{ min}^{-1}$, the average residence time being 1–5 minutes. To avoid the precipitation of inorganic oxides from the solution phase, the flow rate should be larger than $0.2\text{ cm}^3\text{ min}^{-1}$. The suspension was illuminated through the sapphire window with near-UV light ($\lambda = 300\text{--}400\text{ nm}$) from a 500 W high-pressure mercury lamp (USH-500D) with a Type HB-501A power supply (Ushio Denki Co.). Near-UV light was selected by the combination of a glass filter and a CuSO_4 solution filter. As the surface area of the window was small, the high-power lamp was used as the light source. The reaction mixture after cooling was first passed through a filter SS-4TF-0.5 (Swagelok Co., Ohio, USA) to remove TiO_2 powder larger than $0.5\text{ }\mu\text{m}$ in diameter before flowing into the back pressure regulator.

To trace the photocatalytic reactions, the reaction mixture was collected from the outlet of the back pressure regulator and then subjected to gas chromatographic analysis. Either a gas chromatograph mass spectrometer, GC/MS-QP 1000 (Shimadzu Co., Japan), or a G2800-F gas chromatograph (Yanagimoto Co., Koyto, Japan) was employed. CB was extracted from the reaction mixture with *n*-decane before being submitted to gas chromatograph mass spectrometer analysis.

3. RESULTS AND DISCUSSION

It has been reported that in the absence of suitable oxidants, some of the aromatic compounds like CB and phenol in water are tolerant to decomposition even under high-temperature, high-pressure conditions [13]. We at first tested the degradation of CB in aqueous suspensions containing model soils. The suspension containing 1 mM CB and model soil was supplied to the flow reactor with the rate $1\text{ cm}^3\text{ min}^{-1}$ at the temperature $T = 20\text{--}400^\circ\text{C}$. The fraction of residual CB collected at the outlet after passing through the reactor at each temperature is shown in Figure 2. The effects of the model soils on the degradation of CB were not straightforward. Kaoline promoted the reaction at all temperatures, while titania and silica suppressed the reaction at $T = 20\text{--}200^\circ\text{C}$. At the elevated temperature, certain promotion effect

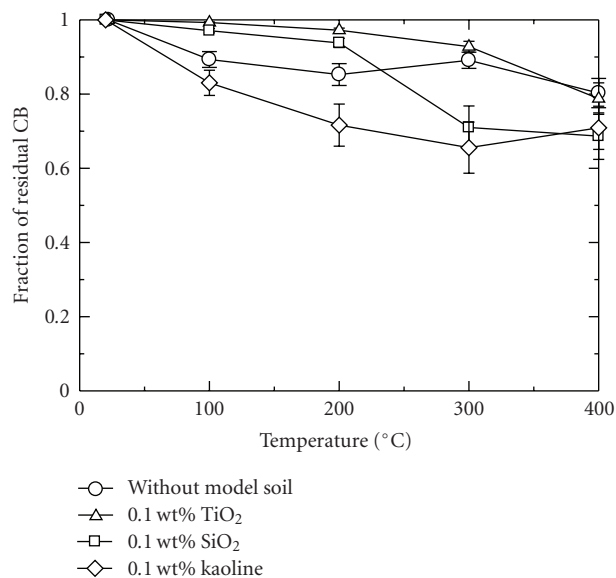


FIGURE 2: The fraction of residual chlorobenzene (CB) at different temperatures. Fluidized-bed-type reactor with the flow rate $1.0 \text{ cm}^3 \text{ min}^{-1}$ and $P = 30 \text{ MPa}$. $\text{CB} = 1 \text{ mM}$. ○: without model soil; △: 0.1 wt% TiO_2 ; □: 0.1 wt% SiO_2 ; ◇: 0.1 wt% kaoline.

was observed in the silica suspension. We next examined the influence of oxidant, H_2O_2 , on the degradation of CB. The fraction of residual CB in the aqueous solutions containing 1 mM CB and 0.1 wt% H_2O_2 , together with or without model soils at each temperature, is given in Figure 3. Despite the rather short residence time of about 1 minute in the reactor, more than 40% of CB disappeared at $T = 200\text{--}400^\circ\text{C}$, indicating the hydrothermal oxidation by H_2O_2 [14]. Although the reaction temperature (T) is not so much higher than critical temperature of water $T_c = 374.2^\circ\text{C}$, this is regarded as a kind of SCWO process. Yu and Savage chose several metal oxides, which are known to be active catalysts for aqueous-phase oxidation and examined catalytic activity during H_2O_2 oxidation of phenol in supercritical water [13]. Indeed they observed catalytic SCWO of phenol over bulk TiO_2 , but the reaction temperature, $T = 380\text{--}440^\circ\text{C}$, was somewhat higher than what we detected. It was observed that the presence of model soils has little effect on the SCWO process at all temperatures within the experimental errors. The observations in Figures 2 and 3 are summarized as follows: the addition of H_2O_2 brings about the degradation of CB at $T = 200\text{--}400^\circ\text{C}$. However, most of the model soils are not harmful to the SCWO treatment of CB at the temperature range studied here.

Considering the photocatalytic activity of TiO_2 , it is expected that titania is capable of decomposing CB on irradiation with near-UV light. We therefore focused on the influence of irradiation of near-UV light on the degradation of CB. We firstly examined the effects of irradiation under ambient conditions. The aqueous solution of 1 mM CB with or without 0.1 wt% titania was put in the quartz cell and irradiated with near-UV light, whose intensity was the same as that used in the photobleach of MB. The variations of the

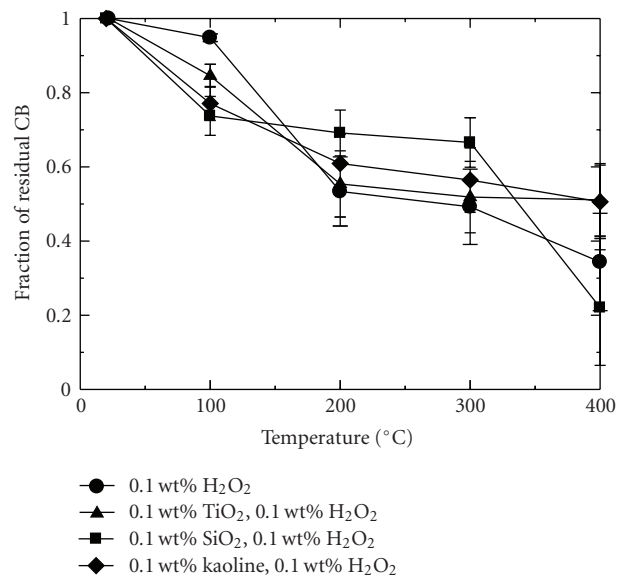


FIGURE 3: The fraction of residual chlorobenzene (CB) at different temperatures. Flow rate $1.0 \text{ cm}^3 \text{ min}^{-1}$ and $P = 30 \text{ MPa}$. $\text{CB} = 1 \text{ mM}$, $[\text{H}_2\text{O}_2] = 0.1 \text{ wt}\%$. ●: without model soil; ▲: 0.1 wt% TiO_2 ; ■: 0.1 wt% SiO_2 ; ◆: 0.1 wt% kaoline.

fraction of residual CB with irradiation time are shown in Figure 4. In the titania suspension, a rapid decrease of CB at the beginning was followed by a slower decrease with prolonged irradiation. About 25% of CB existed at the beginning disappeared after 1-minute irradiation. Photocatalytic degradation of CB under ambient conditions in Figure 4 is consistent with the works of Matthews [9] and Bhatkhande et al. [15]. On the other hand, degradation of CB did not proceed efficiently in the absence of titania. The fraction of CB disappeared after 60-minute irradiation was about 1/3 of that in the titania suspension. In view of the development of a hybrid process available for the extensive treatment of contaminated soil and water, the combination of the catalytic degradation by illuminated TiO_2 and SCWO process would attract much attention. The aqueous suspension comprising 1 mM CB, 0.1 wt% titania, and 0.1 wt% H_2O_2 was supplied to the flow reactor and irradiated with near-UV light through the sapphire window. The intensity of light incident to the reactor was managed to be nearly equal to that used in the photobleach of MB. The fraction of residual CB in the suspension at $T = 20\text{--}400^\circ\text{C}$ collected at the outlet is given in Figure 5. Irradiation of the suspension with near-UV light caused efficient degradation of CB at all temperatures. Even if the average reaction time was 1 minute, about 60% of CB disappeared at $T = 200\text{--}400^\circ\text{C}$. It is noted that the fraction of CB decomposed at $T = 20^\circ\text{C}$ and $P = 30 \text{ MPa}$ in Figure 5, about 25%, in which average reaction time is 1 minute, is not so much different from the corresponding value after 1-minute irradiation in ambient conditions (Figure 4). Accordingly, we may employ the fractional residues of CB at each temperature in Figure 5 as a measure of the rate of degradation of CB. This is a necessary approximation because it was difficult for us to trace ordinary kinetics curves, that is, variations of the

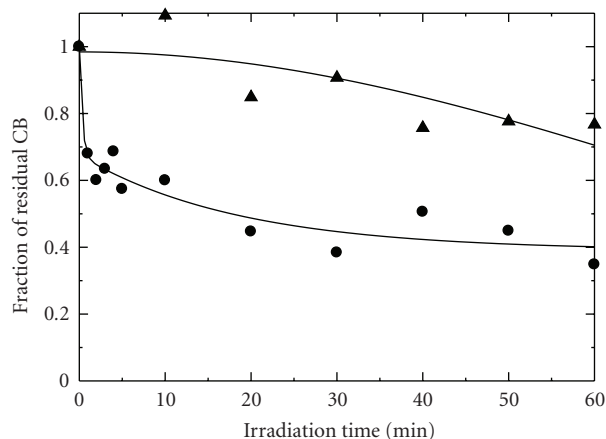
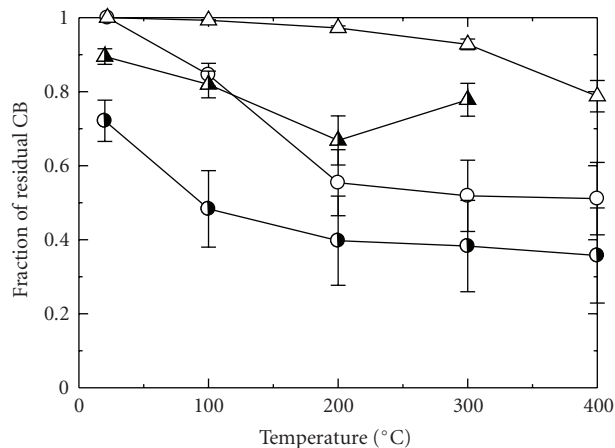


FIGURE 4: The time course of the fraction of residual chlorobenzene (CB) under near-UV irradiation at room temperature and atmospheric pressure. CB = 1 mM; ●: 0.1 wt% TiO₂; ▲: without TiO₂. The solid lines are drawn to guide the eyes.

concentration of CB as the continuous function of time, for catalytic/photocatalytic reactions in the high-temperature, high-pressure reactor. To examine the persistence of the photocatalytic activity of TiO₂ in the absence of H₂O₂, the aqueous suspension containing 1 mM CB and 0.1 wt% TiO₂ was fed to the reactor and irradiated with near-UV light. The fraction of residual CB for $T = 20\text{--}300^\circ\text{C}$ is added to Figure 5. We could confirm that photocatalytic degradation of CB proceeds in high-temperature, high-pressure water in the absence of H₂O₂, too. Judging from the dependence of the fractional residues of CB at each temperature in Figure 5, an ordinary Arrhenius-type relation between the rate of degradation and temperature does not seem to be realized in such complex reactions. We finally note that the near-UV irradiation of the aqueous solutions containing only 1 mM CB or 1 mM CB and 0.1 wt% H₂O₂ has practically no effect on the degradation of CB at all temperatures, and the results were almost identical to “○” in Figure 2 and “●” in Figure 3, respectively.

To obtain further evidence of the photocatalytic activity of TiO₂, we constructed a fixed-bed-type flow reactor having a holder of the inorganic powder [16]. A TiO₂ pellet was set in the holder and an aqueous solution, containing 1 mM CB, was injected into the reactor by an HPLC pump (PU-1580, JASCO Co.) at the flow rate of $0.2\text{ cm}^3\text{ min}^{-1}$ and the decomposition of CB by illumination with near-UV light was examined. It was found that near-UV irradiation surely promotes the reaction at $T = 20\text{--}400^\circ\text{C}$ in the absence of H₂O₂, that is, fractional residues of CB after average reaction time of 5 minutes were 0.9 ($T = 20^\circ\text{C}$), 0.8 (100°C), 0.4 (200°C), and 0.5 (300°C). These observations would reconfirm the photocatalytic activity of TiO₂ in the high-temperature, high-pressure water.

The photocatalytic reactions of TiO₂ are initiated by absorbing UV or near-UV light that can excite valence band electrons to the conduction band. Photoelectrons in conduction band and positive holes in valence band undergo subse-



—△— 0.1 wt% TiO₂ without irradiation
 —▲— 0.1 wt% TiO₂ with irradiation
 —○— 0.1 wt% TiO₂, 0.1 wt% H₂O₂ without irradiation
 —●— 0.1 wt% TiO₂, 0.1 wt% H₂O₂ with irradiation

FIGURE 5: The fraction of residual chlorobenzene (CB) with and without near-UV irradiation at different temperatures. Flow rate $1.0\text{ cm}^3\text{ min}^{-1}$ and $P = 30\text{ MPa}$. CB = 1 mM; △: 0.1 wt% TiO₂ without near-UV irradiation (taken from Figure 2); ▲: 0.1 wt% TiO₂ with near-UV irradiation; ○: 0.1 wt% TiO₂ + 0.1 wt% H₂O₂ without near-UV irradiation (taken from Figure 3); ●: 0.1 wt% TiO₂ + 0.1 wt% H₂O₂ with near-UV irradiation.

quent interfacial electron transfers and thermal reactions at the surface [17]. In a previous article [18], we have examined photocatalytic reduction of Ag⁺ ions by TiO₂ and observed that the photoreduction of Ag⁺ ions evident at room temperature is maintained in high-temperature, high-pressure water as well. Although reaction mechanism of the degradation of CB has not been well established, photoholes and OH radicals seem to be the oxidative species [9, 11, 15]. We have found for the first time that photocatalytic reactions of TiO₂, oxidation by holes and reduction by electrons, persist in subcritical ~ supercritical water, contrary to the conventional view that it should be depressed due to the preferred electron and hole recombination at higher temperatures. However, despite the important role of the structure and energy states at the semiconductor-solution interface [19], the nature of the TiO₂ surface and redox pairs in subcritical ~ supercritical water, for example, the energy band positions of TiO₂, electronic redox levels of redox pairs, as well as the structure of the electric double layer at the interface, are still beyond our scope. Concerning the properties of water, the ionic product of water is known to increase from $K_W = 10^{-14}$ at ambient conditions to about $K_W = 10^{-11}$ at $T = 200\text{--}300^\circ\text{C}$ and $P = 25\text{--}50\text{ MPa}$, and then it starts to decrease with increasing temperature higher than $T = 350^\circ\text{C}$ [20, 21]. The dielectric constant of water at $P = 30\text{ MPa}$ is a decreasing function of temperature from $T = 20^\circ\text{C}$ to 400°C , which may cause the decrease of the solvation energy for ionic species. Taking those features into consideration, we will make a speculative consideration of the persistence of the photocatalytic activity in high-temperature, high-pressure

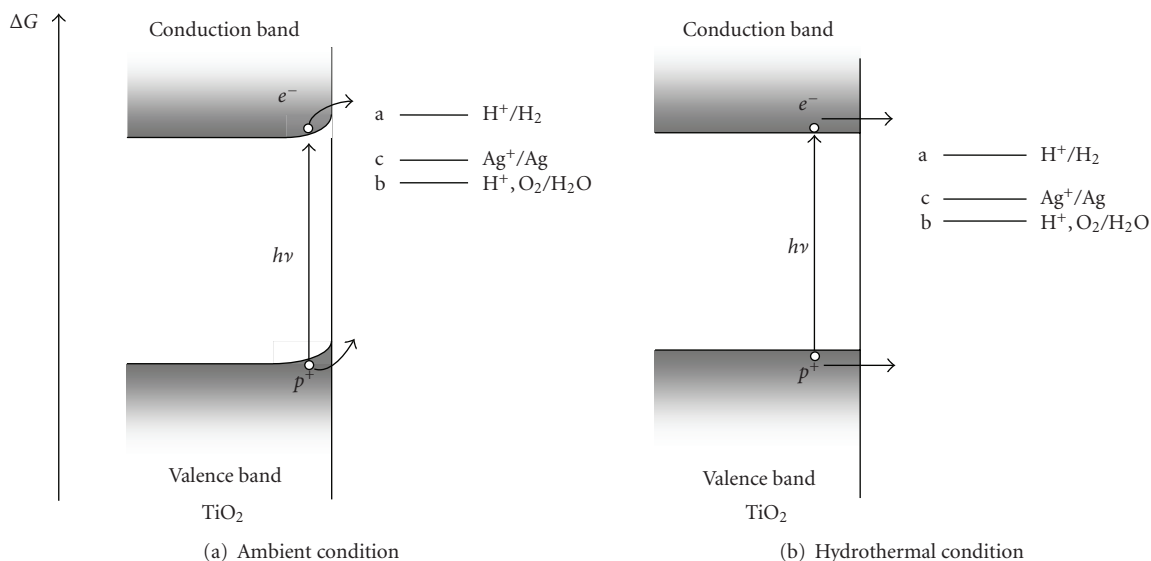


FIGURE 6: Schematic energy-level diagram showing photoreduction and photooxidation at the TiO_2 -aqueous solution interface. Symbols $h\nu$ denote the photon energy of near-UV light, e^- and p^+ the conduction-band electron and positive hole, respectively. a; H^+/H_2 , b; H^+ , $\text{O}_2/\text{H}_2\text{O}$, and c; Ag^+/Ag ; electronic redox levels. (a) Aqueous solution in ambient conditions; $T = 25^\circ\text{C}$, $P = 0.1$ MPa. (b) Aqueous solution in hydrothermal conditions; $T = 100\text{--}400^\circ\text{C}$, $P = 30$ MPa.

water. We sketch a schematic energy-level diagram at the TiO_2 -aqueous solution interface in hydrothermal conditions Figure 6(b) with reference to the conventional diagram in ambient conditions Figure 6(a) [22]. The reduced electric field in the space-charge layer at the TiO_2 surface due to high-temperature conditions and the positive shift of the electronic redox levels as a result of reduced solvation energy have been assumed. In Figure 6, some of the conduction-band electrons in TiO_2 , which are in contact with subcritical \sim supercritical water, can contribute to the reduction of, for example, Ag^+ and H^+ , while positive holes may contribute to the oxidation of certain molecular species like OH^- and H_2O . The higher concentration of OH^- ions may promote the consumption of positive holes. The increase in OH radicals would be a favorable condition for the oxidative degradation of CB. Furthermore, higher temperature in subcritical, supercritical water can in itself promote a variety of chemical reactions characterized by relatively large activation energy. However, to substantiate these considerations, further experimental and theoretical works are needed particularly on photochemistry and electrochemistry in high-temperature, high-pressure water [23].

In the last decade, much effort has been devoted to treat wastewater containing organic compounds such as aromatic compounds, chlorinated compounds. Conventional SCWO processes rely on free-radical reactions to convert organics to CO_2 and heteroatoms such as chlorine, sulfur to mineral acids with the help of concomitant oxygen or H_2O_2 and higher temperature $T > T_c$ [14, 24]. On the other hand, it was reported that the oxidation of a number of aromatic compounds to CO_2 takes place in aqueous suspensions of UV-irradiated TiO_2 at room temperature in air [9, 15]. In this study, we have observed that the addition of H_2O_2 to

the TiO_2 suspension promotes the degradation of CB at all temperatures. In certain temperature range, it looks as if a synergic effect comes out by the addition of H_2O_2 and the irradiation with near-UV light. However, due to experimental error, the detailed relation between the photocatalytic activities in the presence and absence of H_2O_2 has not been well established. According to the studies on the effect of H_2O_2 on the TiO_2 photocatalysis [25, 26], the combination of photocatalysis and SCWO would be attractive for the development of the innovated process capable of continuous treatment of wastewater at temperature $T < T_c$.

4. SUMMARY

An examination of inorganic semiconductors tolerant to corrosion under extreme conditions, irradiation with UV or near-UV light and contact to high-temperature, high-pressure water, is important to develop remediation processes for environmental and energy problems based on the photocatalysis in hydrothermal conditions. In this study, we constructed a fluidized-bed-type flow reactor available for the photocatalytic treatment of the model soil, titania, silica, or kaoline, contaminated with organochlorine compound, chlorobenzene (CB). We firstly examined the effect of the model soil on the SCWO treatment of CB with H_2O_2 and found that the presence of the model soils was not so harmful to this process. We next focused on the photocatalytic reaction of TiO_2 . The TiO_2 suspension containing CB and H_2O_2 was continuously fed to the reactor under high-temperature ($T = 20\text{--}400^\circ\text{C}$), high-pressure ($P = 30$ MPa) conditions and irradiated with near-UV light through the sapphire window installed to the reactor. It was observed that the degradation of CB was enhanced by irradiation at all temperatures.

Similar effects were observed in the absence of H_2O_2 or in case that the TiO_2 pellet was fixed inside the reactor. Based on these observations, we have concluded that the photocatalytic activity of TiO_2 persists in the high-temperature, high-pressure water. This finding is of great significance because the efficient photocatalytic activity of TiO_2 in the oxidation reaction in high-temperature, high-pressure water would open up a possibility of the development of the hybrid process based on the combination of SCWO process and TiO_2 photocatalysis for the treatment of environmental pollutants in soil and water, which are difficult to handle by conventional SCWO process or catalytic SCWO process alone.

ACKNOWLEDGMENT

This work was supported by the Sumitomo Foundation Grant for Environmental Research Projects 2003.

REFERENCES

- [1] V. A. Myamlin and Y. V. Plesov, *Electrochemistry of Semiconductors*, Plenum Press, New York, NY, USA, 1967.
- [2] A. Fujishima and K. Honda, "Electrochemical photolysis of water at a semiconductor electrode," *Nature*, vol. 238, pp. 37–38, 1972.
- [3] Y. V. Pleskov, *Semiconductor Photoelectrochemistry*, Consultants Bureau, Moscow, Russia, 1986.
- [4] M. R. Hoffmann, S. T. Martin, W. Y. Choi, and D. W. Bahnemann, "Environmental applications of semiconductor photocatalysis," *Chemical Reviews*, vol. 95, no. 1, pp. 69–96, 1996.
- [5] N. Serpone and E. Pelizzetti, *Photocatalyst: Fundamentals and Applications*, John Wiley & Sons, New York, NY, USA, 1989.
- [6] S. Horikoshi and H. Hidaka, "Non-degradable triazine substrates of atrazine and cyanuric acid hydrothermally and in supercritical water under the UV-illuminated photocatalytic cooperation," *Chemosphere*, vol. 51, no. 2, pp. 139–142, 2003.
- [7] P. E. Savage, "Organic chemical reactions in supercritical water," *Chemical Reviews*, vol. 99, no. 2, pp. 603–622, 1999.
- [8] J. Yu and P. E. Savage, "Kinetics of catalytic supercritical water oxidation of phenol over TiO_2 ," *Environmental Science & Technology*, vol. 34, no. 15, pp. 3191–3198, 2000.
- [9] R. W. Matthews, "Carbon dioxide formation from organic solutes in aqueous suspensions of ultraviolet-irradiated TiO_2 . Effect of solute concentration," *Australian Journal of Chemistry*, vol. 40, no. 4, pp. 667–675, 1987.
- [10] C. Stavarache, B. Yim, M. Vinatoru, and Y. Maeda, "Sonolysis of chlorobenzene in Fenton-type aqueous systems," *Ultrasonics Sonochemistry*, vol. 9, no. 6, pp. 291–296, 2002.
- [11] B. Ohtani, *Scientific Methods in Photocatalysis*, Tokyo Tosho, Tokyo, Japan, 2005.
- [12] F. Amita, K. Okada, H. Oka, and O. Kajimoto, "A high-temperature high-pressure optical cell for general-purpose spectrometers designed for supercritical water experiments," *Review of Scientific Instruments*, vol. 72, no. 9, pp. 3605–3609, 2001.
- [13] J. Yu and P. E. Savage, "Catalyst activity, stability, and transformations during oxidation in supercritical water," *Applied Catalysis B: Environmental*, vol. 31, no. 2, pp. 123–132, 2001.
- [14] J. R. Portela, E. Nebot, and E. M. de la Ossa, "Kinetic comparison between subcritical and supercritical water oxidation of phenol," *Chemical Engineering Journal*, vol. 81, no. 1–3, pp. 287–299, 2001.
- [15] D. S. Bhatkhande, S. B. Sawant, J. C. Schouten, and V. G. Pangarkar, "Photocatalytic degradation of chlorobenzene using solar and artificial UV radiation," *Journal of Chemical Technology & Biotechnology*, vol. 79, no. 4, pp. 354–360, 2004.
- [16] N. Kometani, S. Inata, K. Sugimoto, A. Shimokawa, and Y. Yonezawa, "Photocatalytic actions of TiO_2 in high-temperature and high-pressure water," in *Proceeding of Joint Meeting of 8th International Symposium on Hydrothermal Reactions & the 7th International Conference on Solvothermal Reactions (ISHR&ICSTR '06)*, p. 169, Sendai, Japan, August 2006.
- [17] Y. Yonezawa, N. Kometani, T. Sakaue, and A. Yano, "Photoreduction of silver ions in a colloidal titanium dioxide suspension," *Journal of Photochemistry and Photobiology A: Chemistry*, vol. 171, no. 1, pp. 1–8, 2005.
- [18] N. Kometani, K. Sugimoto, A. Fujita, and Y. Yonezawa, "Photocatalytic activity of TiO_2 nanoparticles in hydrothermal and supercritical water," *Journal of Chemical Engineering of Japan*, vol. 40, no. 6, pp. 463–467, 2007.
- [19] H. Gerischer, "Semiconductor electrochemistry," in *Physical Chemistry, An Advanced Treatise*, H. Eyring, D. Henderson, and W. Jost, Eds., vol. 9A, pp. 463–542, Academic Press, New York, NY, USA, 1970.
- [20] W. L. Marshall and E. U. Franck, "Ion product of water substance, 0–1000°C, 1–10,000 bars new international formulation and its background," *Journal of Physical and Chemical Reference Data*, vol. 10, no. 2, pp. 295–304, 1981.
- [21] T. Adschiri, et al., *Handbook of Hydrothermal Science*, Gihoudo Shuppan, Tokyo, Japan, 1997.
- [22] Y. Yonezawa, R. Hanawa, and H. Hada, "Application of a membrane cell to the study of photoelectrochemical processes at a TiO_2 solution interface," *Journal of Imaging Science*, vol. 29, no. 5, pp. 171–174, 1985.
- [23] A. C. McDonald, F. R. F. Fan, and A. J. Bard, "Electrochemistry in near-critical and supercritical fluids. 2. Water. Experimental techniques and the copper(II) system," *Journal of Physical Chemistry*, vol. 90, no. 1, pp. 196–202, 1986.
- [24] J. L. DiNaro, J. B. Howard, W. H. Green, J. W. Tester, and J. W. Bozzelli, "Elementary reaction mechanism for benzene oxidation in supercritical water," *Journal of Physical Chemistry A*, vol. 104, no. 45, pp. 10576–10586, 2000.
- [25] X. Li, C. Chen, and J. Zhao, "Mechanism of photodecomposition of H_2O_2 on TiO_2 surfaces under visible light irradiation," *Langmuir*, vol. 17, no. 13, pp. 4118–4122, 2001.
- [26] T. Hirakawa and Y. Nosaka, "Properties of $\text{O}_2^{\cdot-}$ and OH^{\cdot} formed in TiO_2 aqueous suspensions by photocatalytic reaction and the influence of H_2O_2 and some ions," *Langmuir*, vol. 18, no. 8, pp. 3247–3254, 2002.

Research Article

Photocatalytic Degradation of Polynitrophenols on Various Commercial Suspended or Deposited Titania Catalysts Using Artificial and Solar Light

Hinda Lachheb,¹ Ammar Houas,¹ and Jean-Marie Herrmann²

¹ *Equipe de Catalyse et Environnement, URECAP (99/UR/11-20) Ecole Nationale d'Ingénieurs de Gabès, Faculté des Sciences de Gabès, Campus Universitaire, 6072 Gabès, Tunisia*

² *Institut de Recherches sur la Catalyse et l'Environnement de Lyon (IRCELYON), (UMR CNRS5256), Université de Lyon, 2 Avenue Albert Einstein, F-69626 Villeurbanne Cedex, France*

Correspondence should be addressed to Hinda Lachheb, lachheb2001@yahoo.fr

Received 26 June 2007; Revised 10 October 2007; Accepted 27 January 2008

Recommended by Leonardo Palmisano

Phenol (PH) and three polynitrophenols (4-nitrophenol (PNP), 2,4-dinitrophenol (DNP), 2,4,6-trinitrophenol (TNP)) were photocatalytically degraded by using titania under either artificial or solar light. These four reactions were chosen as test reactions to compare the efficiencies of two suspended commercial titania photocatalysts (Degussa P-25 and Millennium PC-500). It appears that P-25 has a higher initial efficiency in all nitrophenol disappearance reactions. However, for the overall degradation rate, measured by the chemical oxygen demand (COD) disappearance, the performance of PC-500 was similar to that of P25. This was attributed to a favorable textural effect since PC-500 has a much higher surface area which facilitates the readsorption of intermediates. PC-500 was subsequently supported on a special photoinert paper provided by Ahlstrom Company (38-Pont Evêque, France). The influence of the silica binder used for sticking titania particles on the paper fibers was put in evidence as an inhibitor of the coulombic adsorption of anionic species, especially 2,4,6-trinitrophenol, because of the low pzc of silica. Once validated, this supported photocatalyst was introduced in an autonomous solar pilot photoreactor identical to the several prototypes built in the European AQUACAT program. It was demonstrated that the purification of water could be efficiently obtained in a larger scale without any final tedious filtration.

Copyright © 2008 Hinda Lachheb et al. This is an open access article distributed under the Creative Commons Attribution License, which permits unrestricted use, distribution, and reproduction in any medium, provided the original work is properly cited.

1. INTRODUCTION

The photocatalytic degradation of toxic compounds in aqueous medium provides a new opportunity for the treatment of urban and agricultural wastewater. Nitrophenols, for example, are released into the environment because of their wide use in syntheses of dyes, pesticides, plasticizers, and solvents. In addition, they are formed as degradation products of many chemicals such as herbicides (see for instance herbicides nitrofen [1] and parathion [2]) when they are exposed to sunlight [3]. The photocatalytic degradation rate of the different nitrophenols depends on various parameters, such as temperature [4], pH [4, 5], initial concentration of the pollutant [4–6], and light intensity. Various studies have shown that the number and positions of substituent in some aro-

matic compounds are widely linked to their photocatalytic reactivity [7–11].

Advanced oxidation processes (AOPs) have been proposed as an alternative for the treatment of wastewater containing nitrophenols. A lot of studies focused on these processes [12–16] have pointed out that, although the reacting systems were different [17, 18], they are all characterized by the same chemical feature, that is, the production of OH° radicals, which as the second best oxidant after fluorine, is the active species responsible for the destruction of organic pollutants [19, 20].

The objective of this study was the validation of the performances of two commercial catalysts using the photocatalytic degradation of polynitrophenols, (4-nitrophenol (PNP), 2,4-dinitrophenol (DNP), and 2,4,6-trinitrophenol

TABLE 1: Physicochemical characteristics of polynitrophenols.

| Compound | Mw (g/mol) | λ_{\max} (nm) | ϵ (L · mg ⁻¹ · cm ⁻¹) | pKa | pH |
|----------------------------|------------|-----------------------|---|------|-----|
| Phenol | 94.11 | 270 | 0.0153 | 9.20 | 6.7 |
| 4-nitrophenol (PNP) | 139.11 | 317 | 0.0623 | 7.16 | 5.8 |
| 2,4-dinitrophenol (DNP) | 184.11 | 260 | 0.0560 | 4.00 | 5.3 |
| 2,4,6-trinitrophenol (TNP) | 229.11 | 356 | 0.0461 | 0.80 | 4.0 |

TABLE 2: Langmuir parameters of phenolic compound adsorption.

| Reactants | Degussa P25 | | | PC500 | | | PC500/Paper 1048 | |
|----------------------------|-------------------|-------------------------|---|-------------------|-------------------------|---|-------------------|-------------------------|
| | q_{\max} (mg/g) | K_{ads} (L/mg) | n_{ads} (mol/nm ²) | q_{\max} (mg/g) | K_{ads} (L/mg) | n_{ads} (mol/nm ²) | q_{\max} (mg/g) | K_{ads} (L/mg) |
| Phenol | 4.87 | 0.031 | 0.62 | 6.27 | 0.136 | 0.125 | 10.44 | 0.290 |
| 4-nitrophenol (PNP) | 10.25 | 0.046 | 0.88 | 9.11 | 0.290 | 0.120 | 8.32 | 0.217 |
| 2,4-dinitrophenol (DNP) | 15.52 | 0.025 | 1.00 | 11.73 | 0.110 | 0.120 | 6.60 | 2.780 |
| 2,4,6-trinitrophenol (TNP) | 18.93 | 0.020 | 1.00 | 15.86 | 0.021 | 0.130 | 5.66 | 7.00 |

n_{ads} : area density of adsorbed phenol molecules (in molecules/nm²).

(TNP) or picric acid (TNP)) as test reactions. Such degradations are now well known [4–6, 17, 18, 21]. These reactions were performed in presence of powder or of supported TiO₂. In the last case, we used Millennium PC500 titania coated on an Ahlstrom nonwoven paper to validate its performances. Subsequently, this deposited photocatalyst was used in an “AQUACAT” pilot solar photoreactor to clean and reuse contaminated water in semiarid areas. This is in line with the pioneer works performed at Plataforma Solar de Almeria (PSA) on many pollutants [22–25].

2. EXPERIMENTAL

2.1. Materials and reagents

Titanium dioxide Degussa P-25 was used as the reference photocatalyst. It is constituted of 80% anatase and 20% rutile and its BET surface area is 50 m²/g, corresponding to a mean particle size of *ca.* 30 nm. Millennium PC500 titanium dioxide (100% anatase, specific surface area of 320 m²/g) was also used either as a powder in slurry or supported on a nonwoven paper (paper Ahlstrom 1048), offered by Mr. J. Dussaud from Ahlstrom Company. The area loading in TiO₂ was 18 g/m². Supported titania has been tested by using either UV artificial light in laboratory experiments or solar light for outside experiments in South Tunisia. The phenolic compounds were purchased from Aldrich (38-Ville D’Abeau, France) and used as received without further purification. Their solutions were prepared using twice-distilled water. Their physicochemical characteristics are given in Table 1.

2.2. Apparatus

A one-liter reactor was used in the laboratory experiments. It is equipped with a plunging tube in which a Philips HPK 125 W UV-lamp was placed vertically. To avoid the heating of the solution, water was circulated through a cylindrical jacket, made of Pyrex and located around the plunging tube.



FIGURE 1: Photograph of the autonomous AQUACAT solar pilot prototype.

The photon flux of the UV irradiation reaching the exposed inner part of the reactor at $\lambda > 290$ nm was measured to be around $6 \cdot 10^{-6}$ Einstein (mol of photons) per second. Another photoreactor was employed for solar experiments. It is an autonomous pilot scale prototype developed by the European Research Project AQUACAT using TiO₂ supported on Ahlstrom paper 1048 (Figure 1). This new photoreactor was employed for solar experiments and consists of one sun collector, one water tank, and one electrical circulating pump connected with a photovoltaic panel. The reactor itself consists of glass tubes connected in series and placed on a fixed platform inclined at a 37° angle corresponding to the local latitude for collecting a maximum solar irradiation around noon. The water circulating flow was fixed at 12 L/min. The total volume (V_T) of the water treated was 20 L and divided in 12 L in the irradiated glass tubes and 8 L in the tank. This pilot plant is a plug-flow reactor connected to a tank with recirculation. This ensemble corresponds to a batch reactor. During experiments, the temperature of the effluent varied in the range of 35–40°C, that is, close to the optimum for photocatalysis [19, 20].

TABLE 3: Kinetic data of the photocatalytic degradation of nitrophenols.

| | P25 | | | PC500 | | | Paper 1048 | | |
|-----|---------------------------------------|--|-----------------|---------------------------------------|--|-----------------|---------------------------------------|--|-----------------|
| | $K_{app} \cdot 10^2$ (mn^{-1}) | $K_{app}/g \cdot 10^2$ ($mn^{-1} \cdot g^{-1}$) | ro (ppm/min) | $K_{app} \cdot 10^2$ (mn^{-1}) | $K_{app}/g \cdot 10^2$ ($mn^{-1} \cdot g^{-1}$) | ro (ppm/min) | $K_{app} \cdot 10^2$ (mn^{-1}) | $K_{app} \cdot 10^2$ ($mn^{-1} \cdot g^{-1}$) | ro (ppm/min) |
| PH | 0.56 | 1.12 | 0.093 | 0.53 | 1.06 | 0.13 | 0.92 | 1.08 | 0.11 |
| PNP | 1.00 | 2.00 | 0.184 | 0.73 | 1.46 | 0.16 | 0.67 | 0.78 | 0.10 |
| DNP | 1.18 | 2.36 | 0.240 | 0.96 | 1.92 | 0.18 | 0.48 | 0.56 | 0.06 |
| TNP | 1.98 | 3.96 | 0.298 | 1.28 | 2.56 | 0.24 | 0.33 | 0.38 | 0.05 |

TABLE 4: Initial COD values in mgO_2/L for nitrophenols having the same initial ponderal concentration (30 mg/L). Apparent first-order rate constant K_{app} and corresponding specific one K_{app}/g_{cat} .

| | COD initial (mg/L) | P25 | | PC500 | | Paper 1048 | |
|----------------------------|--------------------|----------------------------|---|----------------------------|---|----------------------------|---|
| | | K_{app} (mn^{-1}) | K_{app}/g ($mn^{-1} \cdot g^{-1}$) | K_{app} (mn^{-1}) | K_{app}/g ($mn^{-1} \cdot g^{-1}$) | K_{app} (mn^{-1}) | K_{app}/g ($mn^{-1} \cdot g^{-1}$) |
| Phenol (PH) | 74 | 0.50 | 1.0 | 1.15 | 2.30 | 0.80 | 0.94 |
| 4-nitrophenol (PNP) | 50 | 0.80 | 1.6 | 1.73 | 3.46 | 1.12 | 1.31 |
| 2,4-dinitrophenol (DNP) | 45 | 1.28 | 2.5 | 2.19 | 4.38 | 1.66 | 1.95 |
| 2,4,6-trinitrophenol (TNP) | 30 | 1.84 | 3.7 | 3.14 | 6.28 | 3.62 | 4.25 |

TABLE 5: Solar degradation and mineralization kinetics (K_{app} , r_0) of phenolic compounds.

| | $K_{app} \cdot 10^2$ (mn^{-1}) | | r_0 (mol/L · min) | |
|----------------------------|------------------------------------|----------------|---------------------|----------------|
| | Degradation | Mineralization | Degradation | Mineralization |
| | Phenol | 0.17 | 0.15 | 0.068 |
| 4-nitrophenol (PNP) | 0.42 | 0.23 | 0.105 | 0.083 |
| 2,4-dinitrophenol (DNP) | 0.28 | 0.45 | 0.080 | 0.108 |
| 2,4,6-trinitrophenol (TNP) | 0.13 | 0.67 | 0.055 | 0.150 |

2.3. Procedure

2.3.1. Laboratory experiments

One liter of aqueous solution of each phenolic compound ($C_0 = 30$ mg/L) was introduced into the lab reactor and an amount of 500 mg of TiO_2 (P25 or PC500) was added to get a final concentration of 0.5 g/L. The same photoreactor was used with PC500- TiO_2 photocatalyst supported on Ahlstrom paper 1048. A sheet of this titania supporting paper was deposited on a glass cylinder of 12.5 cm in diameter and 12 cm high. The corresponding concentration of TiO_2 was about 850 mg/L. The degradation reactions were carried out at 293 K and at natural pH values (6.7, 5.8, 5.3, and 4.0, for phenol, PNP, DNP, and TNP, resp.). The suspension was first stirred in the dark for 90 minutes before irradiation in order to reach the adsorption equilibrium before starting the photocatalytic reaction.

2.3.2. Solar experiments

The total volume (V_T) treated was 20 L and the water flow rate was fixed at 12 L/min. The suspension was first stirred in the dark for 90 minutes before irradiation to reach equilibrated adsorption. Stirring was obtained by recirculating the total volume of 20 L at a flow rate of 12 L/min obtained by

the electrical pump run by the photovoltaic panel. As for laboratory experiments, the initial concentration of phenols was fixed at 30 mg/L.

2.4. Analyses

Before analysis, the aqueous samples were filtered through a $0.45 \mu m$ membrane filter to remove TiO_2 agglomerates in suspension. A Shimadzu-1700 UV-vis spectrophotometer was used to determine the concentration of the nitrophenols and to follow their kinetic disappearance. Calibration plots based on Beer-Lambert's law were established to relate the absorbance to the concentration. The molar extinction coefficients for phenol, 4-nitrophenol (PNP), 2,4-dinitrophenol (DNP), and 2,4,6-trinitrophenol (TNP) were estimated at 270, 317, 260, and 356 nm, respectively. Chemical oxygen demand (COD) was measured using the acidic dichromate method with a bioblock COD analyzer.

3. RESULTS AND DISCUSSION

3.1. Adsorption of phenolic compounds on titania

The adsorption of the different phenolic compounds is studied at room temperature ($20 \pm 2^\circ C$) and at natural pH. The

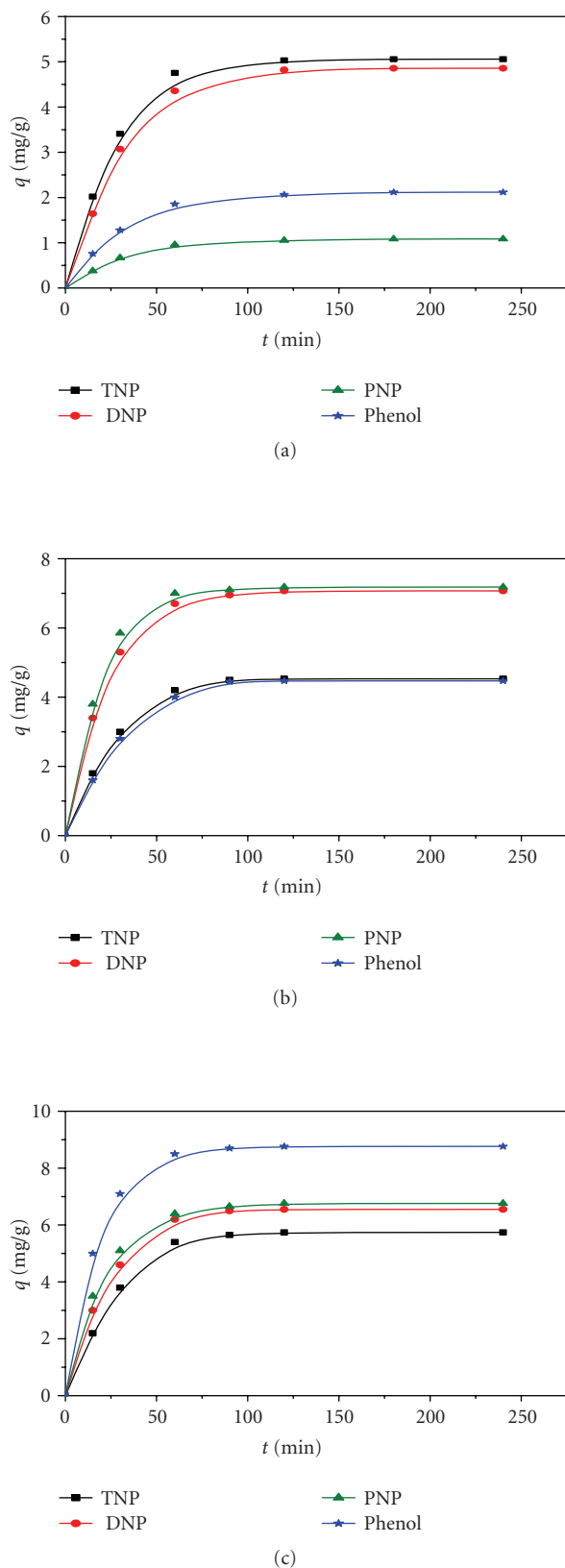


FIGURE 2: Kinetics of adsorption of phenolic compounds in presence of different catalysts (a). Degussa P25, (b) Millennium PC-500, and (c) Millennium PC-500 TiO₂ deposited on Ahlstrom paper 1048. Experimental conditions: $C_0 = 30$ mg/L, $[P25] = [PC500] = 2.5$ g/L, $V = 100$ mL, natural pH.

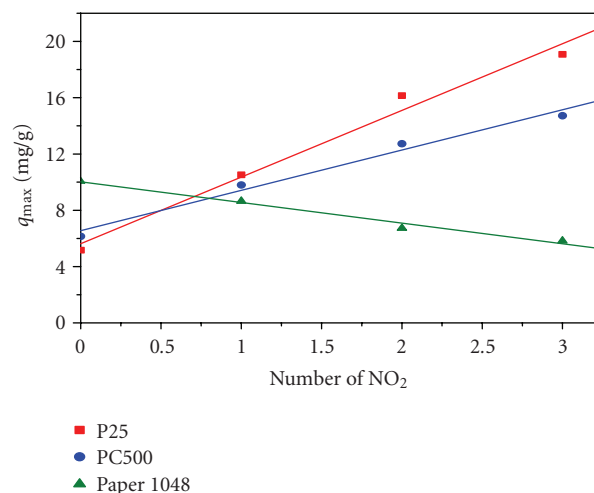


FIGURE 3: Linear variations between the maximum quantity of adsorbed polynitrophenols q_{\max} and the number of NO₂ substituent.

adsorption kinetic curves for the four phenolic compounds (phenol, PNP, DNP, and TNP) on different catalysts are represented in Figure 2. The initial concentration is fixed at 30 mg/L. For each phenolic compound, whatever the catalyst employed, the steady state of adsorption is reached within 90 minutes. Therefore, this time has been selected as the duration of the dark period previously to irradiation. The degradation initiates at the equilibrium of adsorption. The maximum absorbed quantities q_{\max} and the adsorption constants K_{ads} of phenols were determined at different initial concentrations varying between 5 and 30 mg/L using the linear transform of the Langmuir equation,

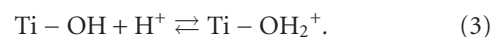
$$\frac{C_e}{q_e} = \frac{1}{Kq_{\max}} + \frac{C_e}{q_{\max}}, \quad (1)$$

where C_e is the equilibrium concentration of the phenolic compounds and q_e is the quantity of the adsorbed phenolic compounds at TiO₂ surface. The linearity of the curves clearly indicates that the Langmuir isotherm is correctly observed, implying a monolayer adsorption model. The calculated values are listed in Table 2.

The following general observations can be made. For both unsupported Degussa P25 and Millennium PC-500 photocatalysts, the maximum quantities of adsorbed phenolic compounds increase in the following order:

$$\text{Phenol} < \text{PNP} < \text{DNP} < \text{TNP}. \quad (2)$$

This is in line with an ionic type of adsorption. Because of their decreasing pKa's and of the resulting pH's of the solutions, the surface of titania samples gets positively charged according to



This favors the coulombic attraction and the related adsorbed quantities of the nitrophenols.

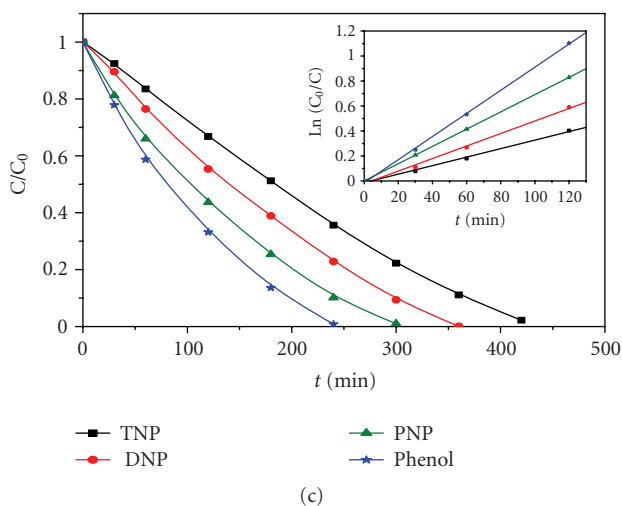
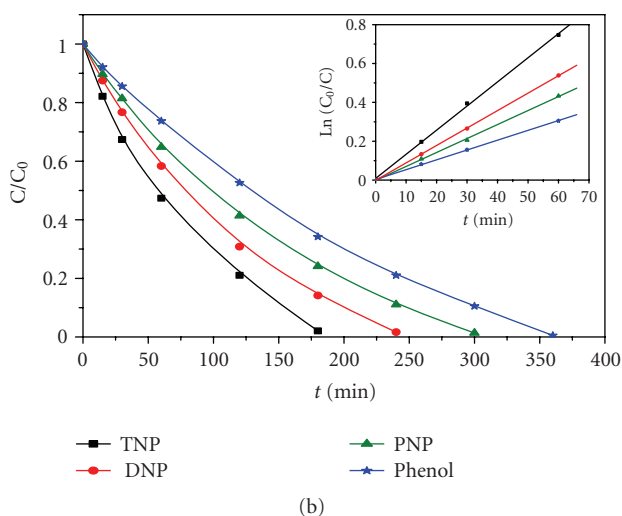
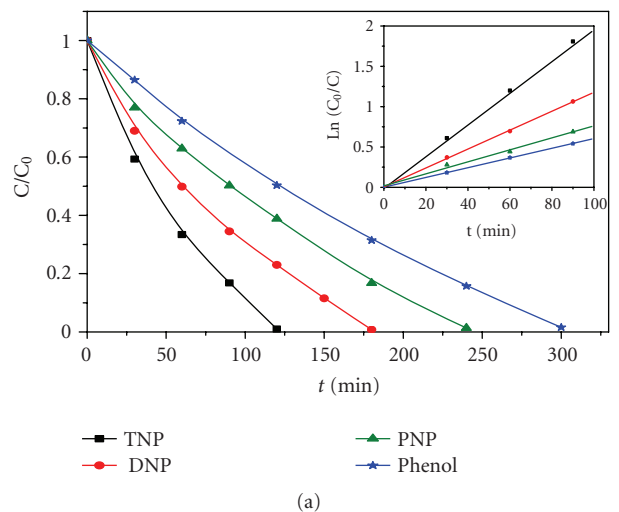


FIGURE 4: Kinetics of the photocatalytic degradation of phenols in presence of different catalysis ((a) P25, (b) PC500, and (c) supported TiO_2 (paper 1048)). In the insert, first-order linear transforms $\ln C_0/C = f(t)$. Experimental conditions: $C_0 = 30 \text{ mg/L}$, $[\text{P25}] = [\text{PC500}] = 0.5 \text{ g/L}$, $V = 1 \text{ L}$, natural pH.

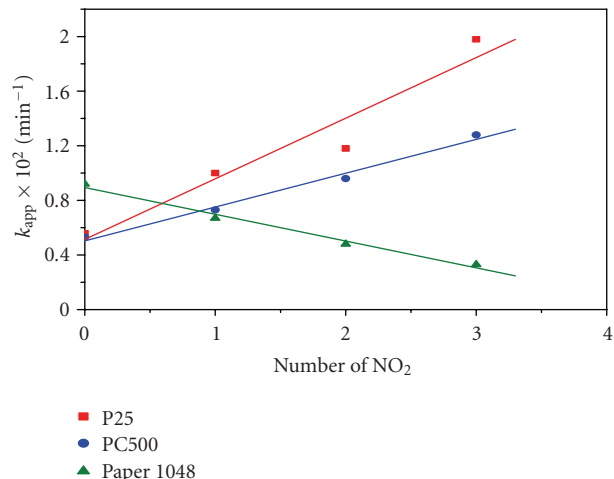


FIGURE 5: Linear variations of the rate constants with the number of NO_2 substituents.

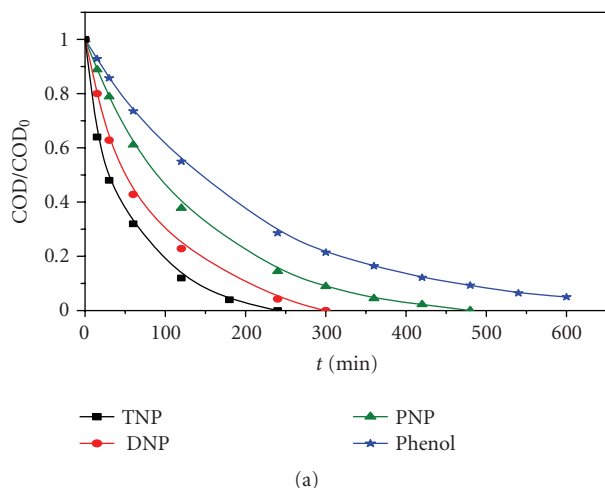
By contrast, the variations of q_{max} are opposite for PC-500/paper 1048. This is due to the presence of the amorphous silica binder. Since the pzc of silica is very low in comparison with that of titania (56), there is a coulombic repulsion of the anionic polynitrophenols by the negatively charged together (silica binder + titania catalyst). Surprisingly, there is a proportional variation between q_{max} and the number n of nitrosubstituents as illustrated in Figure 3.

3.2. Photocatalytic degradation of the polynitrophenols

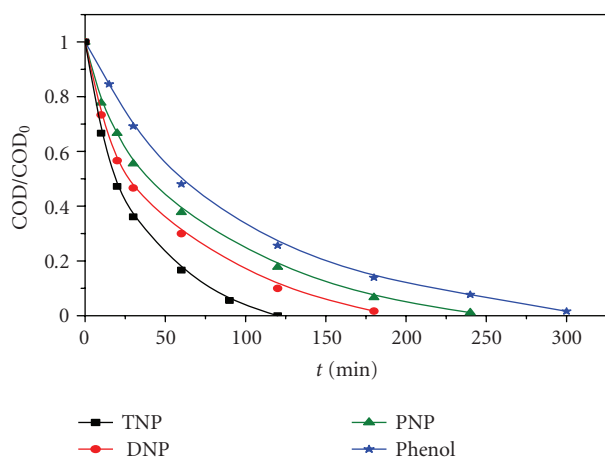
The disappearance rates of nitrophenolic compounds in contact with the three UV-irradiated photocatalysts are given in Figure 4. Starting with an initial concentration of 30 mg/L , the total disappearance of all nitrophenolic compounds is reached in between 2 and 7 hours.

All reactions followed an apparent first-order verified by the linear transforms $\ln(C_0/C) = f(t)$ illustrated in the insert in Figure 5. The slopes give the apparent rate constants listed in Table 3. The initial rates of disappearance in ppm/min are in the following order: $\text{TNP} > \text{DNP} > \text{PNP} > \text{phenol}$. It appears that PC500 is less efficient for the photocatalytic disappearance of nitrophenols than P25. This is also observed for specific activities, that is, rates per g of catalyst (see Table 3). For PC500 supported on Ahlstrom paper 1048, the order is different—phenol $<$ PNP $<$ DNP $<$ TNP.

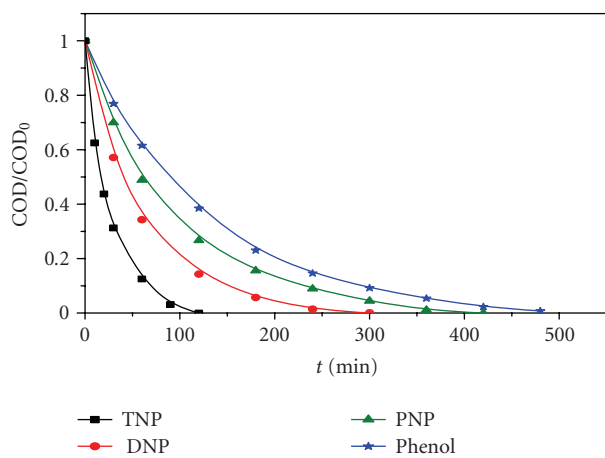
All these differences can be explained by considerations about adsorption. The rates of polynitrophenol disappearance vary in parallel with the quantities of adsorbed pollutants as indicated by the corresponding parameters indicated in Tables 2 and 3. In addition, this is confirmed by the parallel proportional variations of either the quantities of polynitrophenols adsorbed (Figure 3) or of the rate constants as function of the number of NO_2 groups (Figure 5). This confirms the Langmuir-Hinshelwood mechanism involved in these reactions.



(a)



(b)



(c)

FIGURE 6: Kinetics of COD disappearance of nitrophenols in presence of different catalysts ((a) Degussa P25, (b) Millennium PC-500, and (c) PC-500 supported on Ahlstrom paper 1048). Experimental conditions: $C_0 = 30$ mg/L, $[P25] = [PC500] = 0.5$ g/L, $V = 1$ L, natural pH.

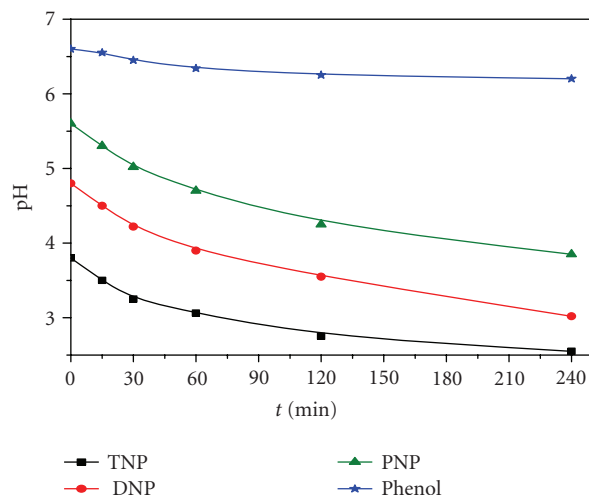


FIGURE 7: Kinetics of pH variations during the photocatalytic degradation of nitrophenols. Experimental conditions: $C_0 = 30$ mg/L, $[P25] = [PC500] = 0.5$ g/L, $V = 1$ L

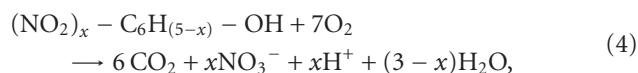
3.3. Kinetics of COD disappearance

The kinetics of the total mineralization of nitrophenols has been determined by following the disappearance of the chemical oxygen demand (COD). The kinetic isotherms are given in Figure 6. For all nitrophenols, COD reached 0 within 8 hours. The initial values of COD are in agreement with the chemical formulas and with the stoichiometries of all nitrophenols degradation reaction, TNP having the smallest COD.

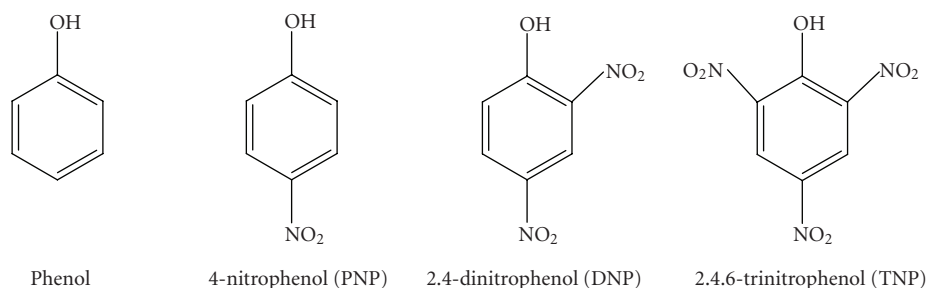
Although titania Degussa P-25 has the highest activity for nitrophenols disappearance, it clearly appears from Table 4 that PC-500 has an important efficiency in their total mineralization. This can be explained by a favorable textural effect. Since total degradation involves many consecutive reactions before reaching CO_2 , the readsorption of all the numerous intermediates is favored by catalyst having large surface areas, which is the case of PC-500. This advantage can be transposed to PC-500 supported on paper Ahlstrom 1048, as seen from data in Table 4. This underlines the interest of using supported catalyst to decontaminate wastewater by avoiding the tedious final filtration step, which strongly increases the overall cost of this potential treatment.

3.4. Kinetics of pH variations during the degradation of phenols

According to the stoichiometry of the total oxidation reaction,



the pH of the reaction medium is expected to decrease except for phenol ($x = 0$). This is actually observed with its temporal variations given in Figure 7. Therefore, the kinetics of pH variations is a good indicator of nitrophenols degradation or, at least, of their denitration. However, pH in the



SCHEME 1

UV-irradiated titania slurry is a rather important and complex parameter since it governs (i) water dissociation equilibrium, (ii) the surface charge of titania with respect to its pzc, and (iii) the ionization state of the organic reactants and of their intermediates. In addition, it also depends on the degradation of other pollutants present in the water to be treated. Nevertheless, in a batch photoreactor, its steady-state final value could be an easy and cheap indicator of the final reaching of total mineralization.

3.5. Solar experiments in the autonomous pilot plant

The polynitrophenol degradation reactions have been transposed to the solar pilot photoreactor and used to determine the efficiency of supported PC500 TiO₂ using solar energy in South Tunisia. This pilot plant is a plug-flow reactor connected to a tank with recirculation. This ensemble corresponds to a batch reactor. Because of the design of the reactor and of the varying solar radiant flux, a direct comparison with the results obtained in laboratory would not be correct. Only basic fundamental features are comparable for laboratory and pilot results. Actually, all reactions followed an apparent first-order kinetics, confirmed by the linear transforms $\ln C_0/C = f(t)$ in the inserts in Figure 8. The rate constants of the disappearance of nitrophenols are in a similar order of reactivity, PNP > DNP > phenol > TNP. The kinetic parameters of COD disappearance, which are illustrated by Figure 9 and listed in Table 5 show that TNP has the higher rate of COD disappearance as in laboratory experiments.

4. CONCLUSIONS

The photocatalytic degradation reactions of phenol and of mono-, di-, and trinitrophenol, chosen as test reactions to compare the efficiencies of two suspended commercial titania photocatalysts (Degussa P-25 and Millennium PC500), underlined the difficulty and complexity in objectively comparing two solids. If Degussa P-25 appeared easily as that having the higher initial efficiency in all nitrophenol disappearance reactions (as mostly observed in literature), however, for the overall degradation rate, measured by the chemical oxygen demand (COD) disappearance, the performances of PC-500 were similar to its own ones. This was attributed to

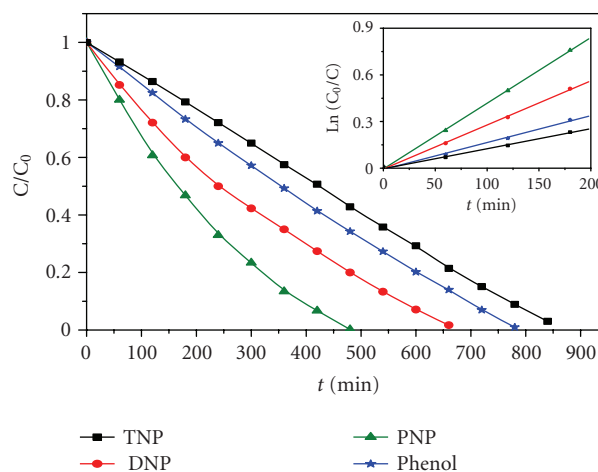


FIGURE 8: Experiments with pilot plant using solar energy, phenols disappearance. In the insert: first-order linear transforms $\ln C_0/C = f(t)$ of nitrophenols degradation. Experimental conditions: $C_0 = 30$ mg/L, $V = 20$ L, TiO₂ supported on Ahlstrom paper 1048, natural pH.

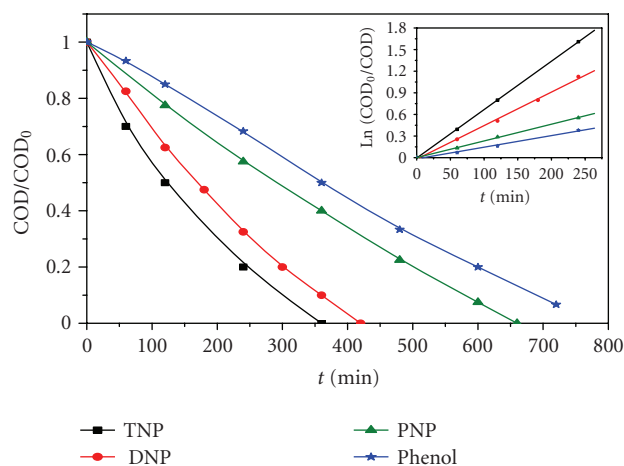


FIGURE 9: Experiments with pilot plant using solar energy, Kinetics of COD disappearance, in the insert: first-order linear transforms $\ln (COD_0)/COD = f(t)$ of nitrophenols mineralization. Experimental conditions: $C_0 = 30$ mg/L, $V = 20$ L, supported TiO₂ (paper 1048), natural pH.

a favorable textural effect since PC-500 has a much higher surface area, which facilitates the readsorption of the very large number of intermediates. When PC-500 was subsequently supported on a special photoinert paper provided by Ahlstrom Company, the presence of the silica binder, used for sticking titania particles on the paper fibers, perturbs several key parameters, principally the natural pH, because of the low pzc of silica. It acts as an inhibitor of the coulombic adsorption of anionic species, especially, 2,4,6-trinitrophenol. However, despite this negative influence, the supported photocatalyst when introduced in an autonomous AQUACAT solar pilot photoreactor clearly demonstrates that it can achieve purification of water with a reasonable efficiency, very compatible with the use of solar energy at a larger scale. In particular, it avoids the final tedious filtration necessary (i) to provide clean water and (ii) to recover and recycle the catalysts. Since filtration is declared as redhibitory by the chemical engineering point of view, this stresses the usefulness of such a material.

ACKNOWLEDGMENTS

The authors thank the European Commission (Research DG) for its financial support within confirming the international role of Community Research for Development (INCO-DEV). Project ICA3-CT2002-10016 "AQUACAT". The authors also wish to thank Dr J. Dussaud from Ahlstrom Research and Services for supplying the photocatalytic non-woven paper.

REFERENCES

- [1] M. Nakagawa and D. G. Crosby, "Photonucleophilic reactions of nitrofen," *Journal of Agricultural and Food Chemistry*, vol. 22, no. 6, pp. 930–933, 1974.
- [2] P. Méallier, J. Nury, B. Pouyet, C. Coste, and J. Bastide, "Photodegradation des molécules phytosanitaires II-cinetique et mecanisme de photodegradation du parathion," *Chemosphere*, vol. 6, no. 12, pp. 815–820, 1977.
- [3] S. Parra, J. Olivero, L. Pacheco, and C. Pulgarin, "Structural properties and photoreactivity relationships of substituted phenols in TiO₂ suspensions," *Applied Catalysis B*, vol. 43, no. 3, pp. 293–301, 2003.
- [4] D. Chen and A. K. Ray, "Photodegradation kinetics of 4-nitrophenol in TiO₂ suspension," *Water Research*, vol. 32, no. 11, pp. 3223–3234, 1998.
- [5] V. Augugliaro, M. J. López-Muñoz, L. Palmisano, and J. Soria, "Influence of pH on the degradation kinetics of nitrophenol isomers in a heterogeneous photocatalytic system," *Applied Catalysis A*, vol. 101, no. 1, pp. 7–13, 1993.
- [6] V. Augugliaro, L. Palmisano, M. Schiavello, et al., "Photocatalytic degradation of nitrophenols in aqueous titanium dioxide dispersion," *Applied Catalysis*, vol. 69, no. 1, pp. 323–340, 1991.
- [7] K. E. O'Shea and C. Cardona, "Hammett study on the TiO₂-catalyzed photooxidation of para-substituted phenols. A kinetic and mechanistic analysis," *Journal of Organic Chemistry*, vol. 59, no. 17, pp. 5005–5009, 1994.
- [8] S. Parra, J. Olivero, and C. Pulgarin, "Relationships between physicochemical properties and photoreactivity of four biorecalcitrant phenylurea herbicides in aqueous TiO₂ suspension," *Applied Catalysis B*, vol. 36, no. 1, pp. 75–85, 2002.
- [9] M. Salaces, B. Serrano, and H. I. de Lasa, "Photocatalytic conversion of phenolic compounds in slurry reactors," *Chemical Engineering Science*, vol. 59, no. 1, pp. 3–15, 2004.
- [10] A. Assabane, Y. A. Ichou, H. Tahiri, C. Guillard, and J.-M. Herrmann, "Photocatalytic degradation of polycarboxylic benzoic acids in UV-irradiated aqueous suspensions of titania. Identification of intermediates and reaction pathway of the photomineralization of trimellitic acid (1,2,4-benzene tricarboxylic acid)," *Applied Catalysis B*, vol. 24, no. 2, pp. 71–87, 2000.
- [11] E. Kusvuran, A. Samil, O. M. Atanur, and O. Erbatur, "Photocatalytic degradation kinetics of di- and tri-substituted phenolic compounds in aqueous solution by TiO₂/UV," *Applied Catalysis B*, vol. 58, no. 3-4, pp. 211–216, 2005.
- [12] S. Parra, C. Pulgarin, S. Malato, J. Blanco, and P. Peringer, "Concentrating vs. nonconcentrating reactor for solar photocatalytic degradation of p-nitrotoluene sulfonic acid," in *Proceeding of the 2nd International Conference on Oxidation Technologies for Water and Wastewater Treatment*, Cutec Institut GmbH, Clausthal-Zellerfeld, Germany, May 2000.
- [13] E. Kusvuran and O. Erbatur, "Degradation of aldrin in adsorbed system using advanced oxidation processes: comparison of the treatment methods," *Journal of Hazardous Materials*, vol. 106, no. 2-3, pp. 115–125, 2004.
- [14] F. J. Benitez, J. Beltrán-Heredia, J. L. Acero, and M. L. Pinilla, "Ozonation kinetics of phenolic acids present in industrial wastewaters from olive oil mills," *Industrial and Engineering Chemistry Research*, vol. 36, no. 3, pp. 638–644, 1997.
- [15] I. Casero, D. Silicia, S. Rubio, and D. Perez Bendito, "Chemical degradation of aromatic amines by Fenton's reagent," *Water Research*, vol. 31, no. 8, pp. 1985–1995, 1997.
- [16] O. Legrini, E. Oliveros, and A. M. Braun, "Photochemical processes for water treatment," *Chemical Reviews*, vol. 93, no. 2, pp. 671–698, 1993.
- [17] K. Tanaka, W. Luesaiwong, and T. Hisanaga, "Photocatalytic degradation of mono-, di- and trinitrophenol in aqueous TiO₂ suspension," *Journal of Molecular Catalysis A*, vol. 122, no. 1, pp. 67–74, 1997.
- [18] R. W. Matthews, "Kinetics of photocatalytic oxidation of organic solutes over titanium dioxide," *Journal of Catalysis*, vol. 111, pp. 264–272, 1988.
- [19] J.-M. Herrmann, "Heterogeneous photocatalysis: fundamentals and applications to the removal of various types of aqueous pollutants," *Catalysis Today*, vol. 53, no. 1, pp. 115–129, 1999.
- [20] J.-M. Herrmann, "Photocatalysis," in *Kirk-Othmer Encyclopedia of Chemical Technology*, vol. 19, pp. 73–115, Wiley-Interscience, New York, NY, USA, 5th edition, 2006.
- [21] A. Di Paola, V. Augugliaro, L. Palmisano, G. Pantaleo, and E. Savinov, "Heterogeneous photocatalytic degradation of nitrophenols," *Journal of Photochemistry and Photobiology A*, vol. 155, no. 1–3, pp. 207–214, 2003.
- [22] D. Curcó, S. Malato, J. Blanco, J. Giménez, and P. Marco, "Photocatalytic degradation of phenol: comparison between pilot-plant-scale and laboratory results," *Solar Energy*, vol. 56, no. 5, pp. 387–400, 1996.
- [23] C. Minero, E. Pelizzetti, S. Malato, and J. Blanco, "Large solar plant photocatalytic water decontamination: effect of operational parameters," *Solar Energy*, vol. 56, no. 5, pp. 421–428, 1996.

-
- [24] R. Goslich, D. Ralf, and D. Bahnemann, "Solar water treatment: principles and reactors," *Water Science and Technology*, vol. 35, no. 4, pp. 137–148, 1997.
- [25] J.-M. Herrmann, J. Disdier, P. Pichat, S. Malato, and J. Blanco, "TiO₂-based solar photocatalytic detoxification of water containing organic pollutants. Case studies of 2,4-dichlorophenoxyacetic acid (2,4-D) and of benzofuran," *Applied Catalysis B*, vol. 17, no. 1-2, pp. 15–23, 1998.

Review Article

Increase of the Photocatalytic Activity of TiO₂ by Carbon and Iron Modifications

Beata Tryba

Department of Chemical Technology and Engineering, Faculty of chemical Engineering, Szczecin University of Technology, ul. Pulaskiego 10, Szczecin 70-322, Poland

Correspondence should be addressed to Beata Tryba, beata.tryba@ps.pl

Received 27 August 2007; Accepted 23 November 2007

Recommended by M. Sabry A. Abdel-Mottaleb

Modification of TiO₂ by doping of a residue carbon and iron can give enhanced photoactivity of TiO₂. Iron adsorbed on the surface of TiO₂ can be an electron or hole scavenger and result in the improvement of the separation of free carriers. The presence of carbon can increase the concentration of organic pollutants on the surface of TiO₂ facilitating the contact of the reactive species with the organic molecules. Carbon-doped TiO₂ can extend the absorption of the light to the visible region and makes the photocatalysts active under visible-light irradiation. It was proved that TiO₂ modified by carbon and iron can work in both photocatalysis and photo-Fenton processes, when H₂O₂ is used, enhancing markedly the rate of the organic compounds decomposition such as phenol, humic acids and dyes. The photocatalytic decomposition of organic compounds on TiO₂ modified by iron and carbon is going by the complex reactions of iron with the intermediates, what significantly accelerates the process of their decomposition. The presence of carbon in such photocatalyst retards the inconvenient reaction of OH radicals scavenging by H₂O₂, which occurs when Fe-TiO₂ photocatalyst is used.

Copyright © 2008 Beata Tryba. This is an open access article distributed under the Creative Commons Attribution License, which permits unrestricted use, distribution, and reproduction in any medium, provided the original work is properly cited.

1. INTRODUCTION

The photocatalytic process with using TiO₂ photocatalyst is very promising for application in the water purification because many organic compounds can be decomposed and mineralized by the proceeding oxidation and reduction processes on TiO₂ surface. The most commonly tested compounds for decomposition through the photocatalysis are phenols, chlorophenols, pesticides, herbicides, benzenes, alcohols, dyes, pharmaceuticals, humic acids, organic acids, and others.

TiO₂ is the most commonly used photocatalyst, because it is nontoxic, chemically stable, cheap, and very efficient. However, it has some disadvantages: one of this is a relatively high value of the bandgap, around 3.2 eV, which limits its using to the UV light, high dispersion in the water which causes difficulties in sedimentation, and sensitivity to the recombination of photoinduced electrons and holes, which decreases its photocatalytic activity. Many efforts of researchers are focused on the enhancing the photoactivity of TiO₂ by improving the separation between free carriers, increasing the adsorption abilities of the photocatalyst surface, or charging

one photocatalyst by another when the mixture of two photocatalysts is used.

2. TiO₂ MODIFIED BY CARBON

2.1. Carbon-doped TiO₂ visible light-active photocatalysts

Recently, modification of TiO₂ by C doping towards obtaining the visible light-active photocatalyst has been reported [1–9]. The narrowing of the bandgap, the anodic shift of the quasi-Fermi potential, the visible-light absorption, and the transfer of photoexcited carriers to the reactive sites at the catalyst surface have been noticed as a result of nonmetal anion doping affecting its visible-light activity.

Sakthivel and Kisch [2] proved that prepared C/TiO₂ photocatalyst from TiCl₄ and tetrabutylammonium hydroxide was active under artificial solar light and could efficiently decompose tetrachlorophenol with the activity higher than TiO₂ and TiO₂ doped with nitrogen. In Figure 1, diffuse reflectance spectra of pure and carbon-doped TiO₂ are shown [2].

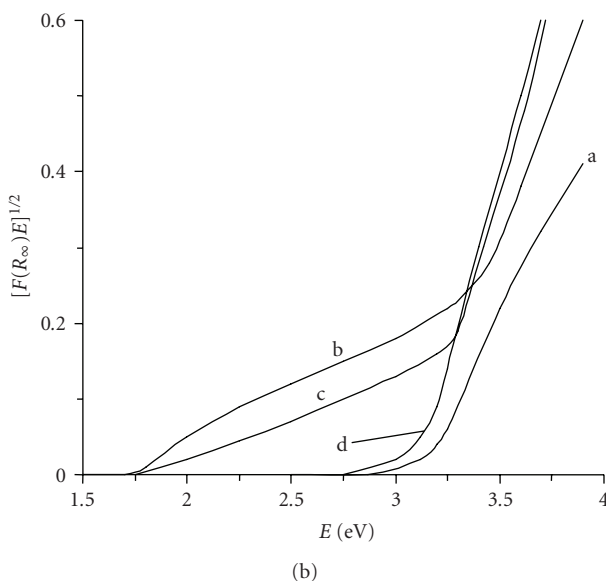
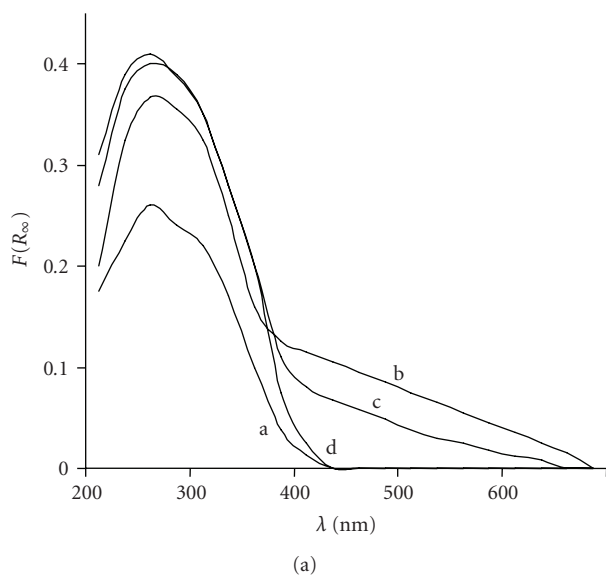


FIGURE 1: (A) Diffuse reflectance spectra of modified and pure TiO_2 , (B) plot of transformed Kubelka-Munk function versus the energy of the light absorbed; (a) TiO_2 , (b) TiO_2 -2.98%C, (c) TiO_2 -0.42%C, (d) TiO_2 -0.03%C.

Two absorption maxima on the UV-Vis spectra have been observed, in the range of UV and Vis, showing that these photocatalysts could be excited with the wavelengths in the visible region.

In Figure 2, the mineralisation of the tetrachlorophenol on these samples is presented.

Shen et al. [4] prepared C/ TiO_2 photocatalyst through calcination of TiCl_4 in air at 350°C and proved that such prepared photocatalyst was active for decomposition of trichloroacetic acid under visible light. Carbon-doped TiO_2 can be prepared also by hydrolysis and calcinations of TiCl_4 with tetra-*n*-butyl ammonium hydroxide [7], and by calci-

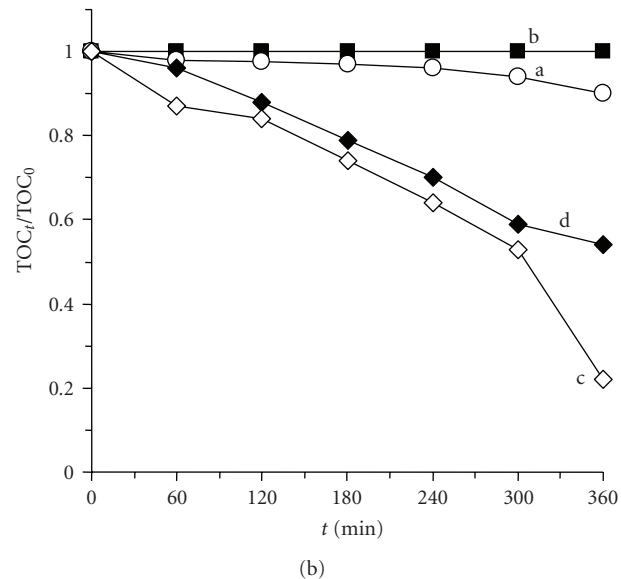
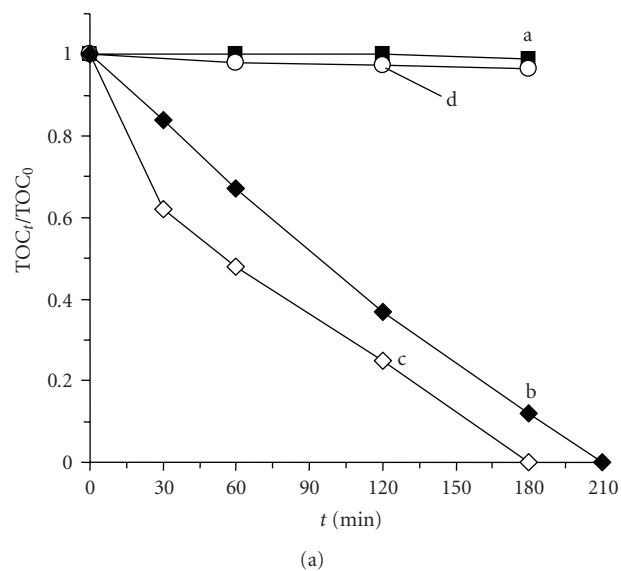


FIGURE 2: (A) Photomineralisation of 4-chlorophenol with artificial visible light ($\lambda = 455 \text{ nm}$; TOC_0 and TOC_t = total organic carbon content at times 0 and t); (B) diffuse indoor daylight degradation of 4-chlorophenol and remazol red on pure and modified TiO_2 ; (a) TiO_2 , (b) TiO_2 -2.98%C, (c) TiO_2 -0.42%C, (d) TiO_2 -0.03%C.

nations of TiO_2 with urea and thiourea [8] or oxidation of TiC at high temperatures [9]. Choi et al. [9] have investigated carbon-doped TiO_2 , and they claimed that substitution of C for O in the TiO_2 leads to a photocatalytic decomposition of methylene blue under visible-light irradiation. Di Valentin et al. [10] reported a theory of in-building of carbon atom in the structure of TiO_2 , and they showed that carbon atom could replace oxygen atom or titania atom depending on the concentration of oxygen in the structure of TiO_2 . Replacing of carbon atom with Ti conducts to form the new states in the bandgap. Some oxygen vacancies are formed, which could be responsible for the extending of the photocatalytic activity

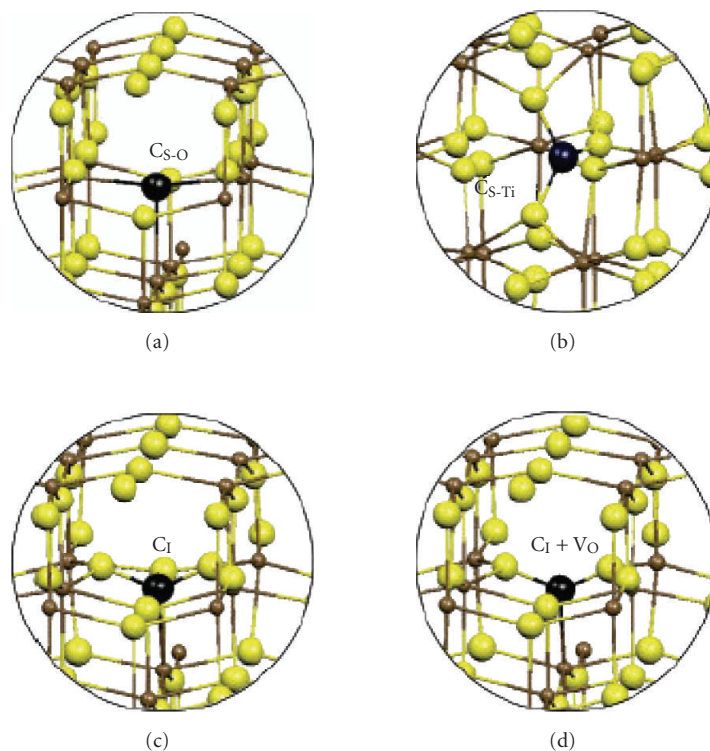


FIGURE 3: Partial geometry of the models for: (a) one substitutional C atom to O (C_{S-O}), (b) one substitutional C atom Ti (C_{S-Ti}), (c) one interstitial C atom (C_I), and (d) one interstitial C atom nearby an oxygen vacancy ($C_I + V_O$) in the anatase TiO_2 supercell; the yellow spheres represent O atoms, the small brown spheres represent Ti atoms, and the black represents the carbon impurity.

of C/TiO_2 to the visible range. The model proposed by Di Valentin et al. is presented in Figure 3 [10].

Preparation of C/TiO_2 photocatalyst by heating of TiO_2 with the vapours of n-hexane [11] and ethanol [12], and by mixing of TiO_2 with liquid ethanol and heating under pressure [13] has been also reported. Enhanced photoactivity of carbon-doped TiO_2 prepared under pressure has been noticed for decomposition of dyes under UV irradiation [13].

Carbon-doped TiO_2 electrodes have been prepared by modified sol-gel method from tetraisopropoxide, 2-propanol, and activated carbon at 600°C and were used for electrochemical photooxidation of sodium oxalate; the efficiency of electrode with 5% of doped activated carbon was two times higher than the electrode without carbon doping [14].

Effective photoresponse in the visible-light region was observed in carbon-doped TiO_2 [7, 15]. Carbon-doped TiO_2 nanotube arrays for efficient solar water splitting have been prepared by Park et al. [16]. The synthesised TiO_2-xC_x nanotube arrays showed much higher photocurrent densities and more efficient water splitting under visible-light illumination (>420 nm) than pure TiO_2 nanotube arrays.

2.2. TiO_2 and activated carbon (AC) composites

Herrmann et al. [17], Araña et al. [18, 19], and Liu et al. [20] have observed the synergistic effect for the mixture of TiO_2

with activated carbon (AC). Improving the photocatalytic properties of TiO_2/AC composite was explained by the high adsorption of the impurities on the surface of activated carbon and their transfer to TiO_2 surface. Carbon/ TiO_2 microsphere has been prepared by Nagaoka et al. [21], and it was successfully used for decomposition of acetaldehyde through the concentration of the pollutant around TiO_2 anchored on the composite surface. In Figure 4, the enhanced photoactivity with using TiO_2/AC composite is presented under both solar and UV irradiations, for photodecomposition of p-nitrophenol [19].

2.3. Carbon-coated TiO_2

Carbon-coated TiO_2 photocatalysts have been prepared by calcination of TiO_2 with carbon precursor such as (polyvinyl alcohol) (PVA), poly (terephthalate ethylene) (PET), or hydroxyl propyl cellulose (HPC) at high temperatures, 700–900°C [22–24], or impregnation of TiO_2 with saccharose 400–600°C [25]. Carbon coating TiO_2 retarded the phase transformation from anatase to rutile, which usually occurs during heating TiO_2 at 700°C and through that improved the crystallinity of anatase phase in TiO_2 , which was responsible for its high photoactivity. From the other hand, carbon coating reduced the amount of UV radiation reaching the surface of the TiO_2 particles. A balance among different factors controlled by the carbon layer on the TiO_2 particles was

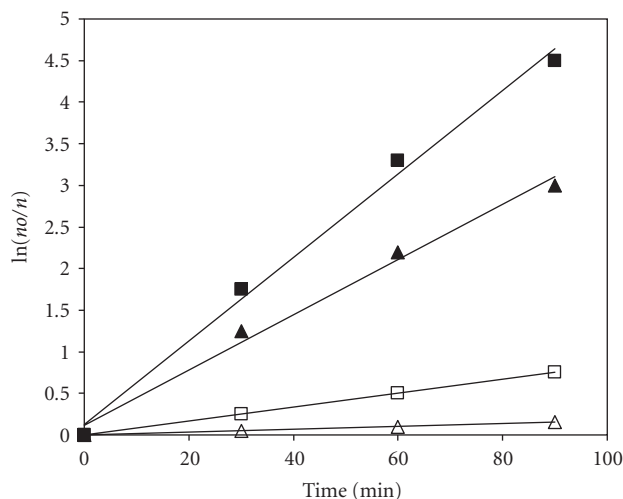


FIGURE 4: Apparent first-order linear transform $\ln(n_0/n) = f(t)$ of the p-nitrophenol concentration during its degradation; UV-light: (▲)—bare TiO₂, (■)—13% AC-TiO₂; solar light: (△)—bare TiO₂, (□)—13 % AC-TiO₂.

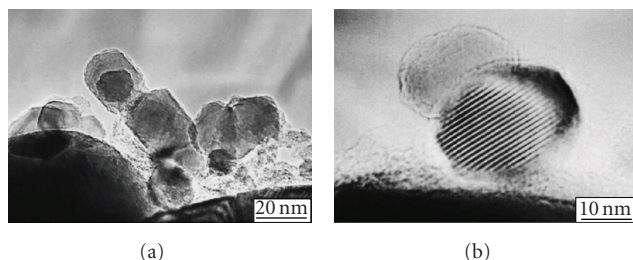


FIGURE 5: TEM images of carbon-coated TiO₂ prepared from TiO₂ and PVA.

required to get high-photocatalytic activity. On the sample prepared at 850°C with a carbon content of about 3.5 wt%, the highest rate constant for methylene blue decomposition was obtained, in which the transition from anatase to rutile was suppressed, and carbon layer was thin enough to transmit UV rays [24]. The TEM images of carbon-coated TiO₂ are presented in Figure 5 [23].

Carbon-coated TiO₂ samples showed high adsorption and high photoactivity towards methylene blue decomposition [22–25], however in case of phenol, reactive black 5 or iminocytidine triacetate decomposition was slower than on unmodified TiO₂ [23]. In Figure 6, there is shown a cycling decomposition of methylene blue on carbon-coated TiO₂ prepared from powders of TiO₂ and PVA at 900°C with ratio of TiO₂/PVA = 50/50 in weight [22].

Coating of carbon changes the nature of TiO₂ from hydrophilic to hydrophobic and results in lower adsorption of water on the photocatalyst surface and lower formation of OH radicals in comparison with TiO₂. Probably in case of methylene blue, decomposition is going by the direct oxidation pathway, therefore high adsorption of methylene blue on the carbon-coated TiO₂ improved its photocatalytic activity.

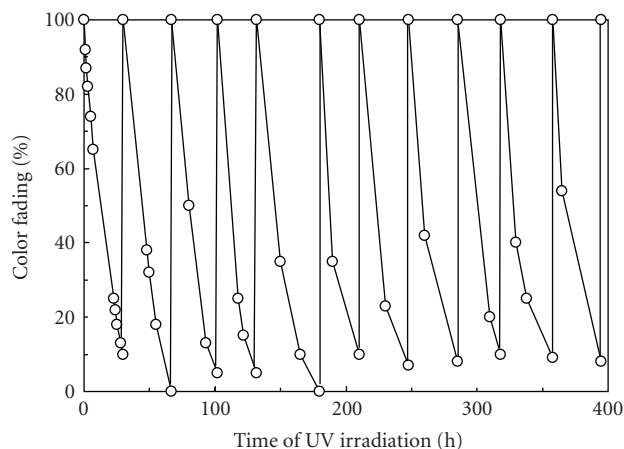


FIGURE 6: Color fading of MB solution under UV irradiation in the presence of carbon-coated TiO₂ sample (10 wt% of carbon) with cycling to use fresh MB solution, concentration of MB = 2.94×10^{-5} M.

2.4. TiO₂ loaded carbon

TiO₂ can be loaded on the activated carbon (AC) [26–35], carbon fibers [36], carbon nanotube [37], exfoliated graphite [38, 39] with efficient adsorption and decomposition of organic compounds such as phenol, 4-chlorophenol, methyl orange, methylene blue, iminocytidine triacetates, oils, dichloromethane, and so forth. In Figure 7, TiO₂ loaded on different carbon structures is presented.

TiO₂ loaded carbon spheres have been prepared by hydrolysis of TiOSO₄ under hydrothermal conditions. Adsorption and decomposition of methylene blue on TiO₂ loaded carbon spheres are presented in Figure 8 [28]. It can be observed saturation with methylene blue adsorption on carbon spheres (CS), and no change in methylene blue concentration with UV irradiation, whereas on anatase loaded carbon spheres (Ti/CS) methylene blue could be adsorbed in the dark and decomposed with UV irradiation in the cycles.

Tryba et al. [29] have reported preparation of TiO₂ loaded AC from the tetraorthotitanate solution. Higher removal of organic compounds has been achieved by combination of adsorption, which occurred in the pores of activated carbon, with decomposition on the anatase particles. Decrease in adsorption has been observed after TiO₂ mounting, because mounted TiO₂ particles blocked the entrance to the pores of AC, however these TiO₂ particles could decompose the adsorbed organic molecules in the pores of AC, enhancing the total removal of the pollutant [29].

El-Sheikh et al. [34] have prepared TiO₂ loaded AC by different methods: chemical vapour deposition (CVD), direct air-hydrolysis (DAH), and high-temperature impregnation (HTI), among those methods, CVD gave the best bonding of TiO₂ with the carbon surface; anatase particles were placed in the pores of activated carbon.

Tsumura et al. have mounted TiO₂ on the exfoliated graphite [38]. High sorption of oil and its decomposition under UV irradiation have been observed.

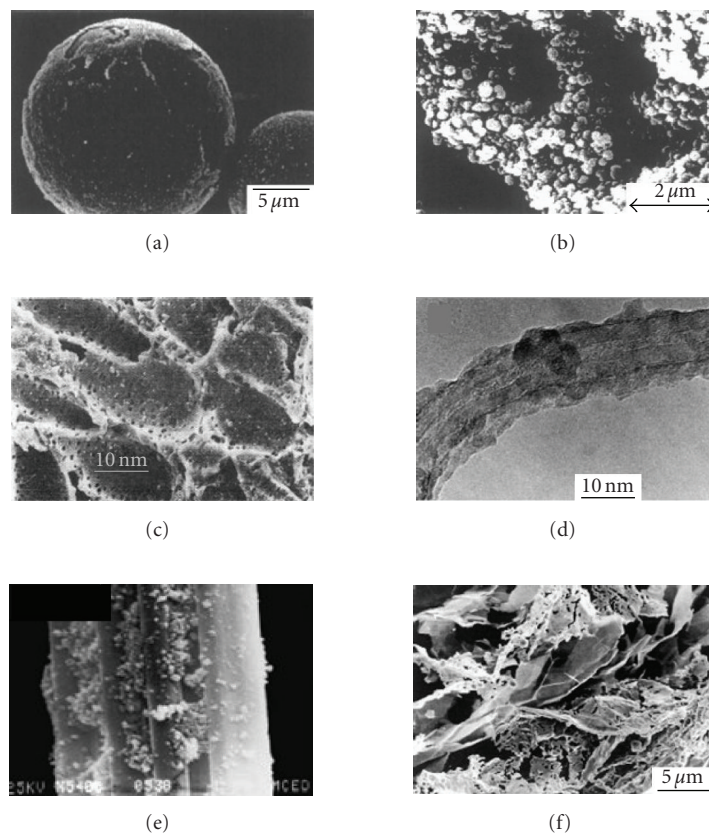


FIGURE 7: TiO_2 loaded on (a) carbon spheres [28], (b) activated carbon [28], (c) granular activated carbon [35], (d) carbon nanotubes [37], (e) carbon fibers [36], and (f) exfoliated graphite [38].

3. TiO_2 MODIFIED BY IRON

3.1. Preparation methods

There are few methods of Fe doping to TiO_2 . The sol-gel method has been widely used for preparation of Fe-doped TiO_2 from TiCl_4 or titania alkoxide and an iron precursor like FeCl_3 , $\text{Fe}(\text{NO}_3)_3 \cdot 9\text{H}_2\text{O}$, or $\text{Fe}(\text{III})$ -acetylacetonate [40–47]. Wang et al. [40] have reported that preferable preparation of Fe-doped TiO_2 to get the uniform distribution of the dopant ions on TiO_2 particles is hydrolysis of a homogeneous mixture of organic titanium and organic iron precursors in isopropyl alcohol. Preparation of Fe-doped TiO_2 by hydrolysis of TiCl_4 with FeCl_3 appeared to be less favourable than using $\text{Fe}(\text{III})$ -acetylacetonate as an iron precursor. Fe doping from microemulsion of Ti tetraisopropoxide with an aqueous solution of iron and further calcinations has been reported by Adán et al. [48], Fe-doped TiO_2 can be obtained also through the calcination of FeTiS_2 [49–51], plasma oxidative pyrolysis [52], one-step flame spray pyrolysis (FSP) [53], coprecipitation and immersion [46], and by the wet impregnation method from $\text{Fe}(\text{III})$ acetylacetonate [54] or $\text{Fe}(\text{NO}_3)_3 \cdot 9\text{H}_2\text{O}$ [42].

Navío has been reported that impregnation with $\text{Fe}(\text{III})$ -acetylacetonate gives more homogeneous distribution of iron for each mixed oxide sample on the particle surfaces but

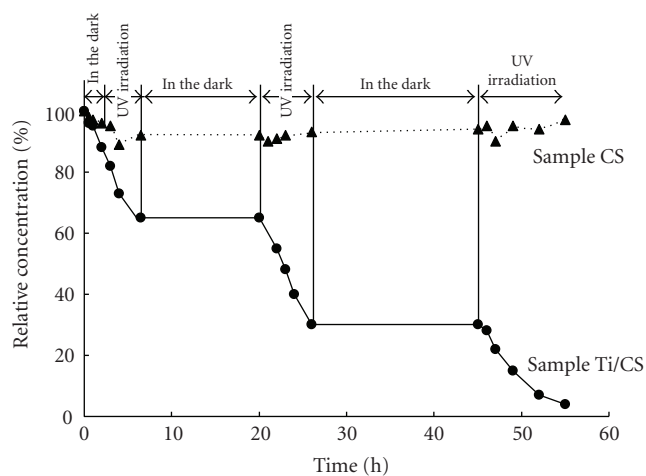


FIGURE 8: Changes in relative concentration of MB in the solution in which pristine carbon spheres (CS) and anatase loaded one (Ti/CS) were dispersed.

not between particles in comparison with impregnation with $\text{Fe}(\text{NO}_3)_3 \cdot 9\text{H}_2\text{O}$ [54].

Recently, doping of Fe to TiO_2 by the ultrasonic-induced hydrolysis reaction of tetrabutyl titanate ($\text{Ti}(\text{OC}_4\text{H}_9)_4$) in a ferric nitrate aqueous solution has been reported in [55].

The mechanical alloying on the solid state reaction of hematite, Fe_2O_3 , and titanium has been also sufficiently used for introducing of iron to TiO_2 lattice [56].

TiO_2/Fe thin film has been prepared by metal (Fe) plasma ion implantation [57, 58] and by magnetron sputtering method [59].

Using a simple sol-gel method, a novel magnetic photocatalyst was produced by immobilisation of TiO_2 nanocrystal on Fe-filled carbon nanocapsules. TiO_2 -coated Fe-CNC displayed good performance in the removal of NO gas under UV exposure [60].

Fe-doped TiO_2 nanotubes with small diameter of 10 nm were obtained by hydrothermal method [61].

3.2. Visible-light activity of Fe-doped TiO_2

It has been found that the addition of transition metals to TiO_2 can improve the photocatalytic activity of the photocatalyst by UV irradiation and extend its use in the visible region of the electromagnetic spectrum. It has been observed the red shift in the UV-Vis spectra due to the introduction of the 3d electron state of Fe^{3+} , $3d^5$, in the conduction band of TiO_2 [40, 44, 48, 49, 58, 59, 62–65].

The absorbance of visible light is higher for higher amount of doped iron, as it is presented in Figure 9 [48].

This implies that iron-doped TiO_2 may be photocatalytically reactive under visible-light irradiation. Navío et al. have reported that the photodegradation of oxalic acid under visible irradiation, not occurring with TiO_2 , could be observed for Fe-doped TiO_2 using 5% Fe-containing samples [54]. Nahar et al. reported that Fe-doped TiO_2 was responsive to the visible-light activity of phenol degradation [49]. Teoh et al. have reported that by flame spray pyrolysis a stable Fe- TiO_2 photocatalyst can be prepared and at the ratio of $\text{Fe}/\text{Ti} = 0.05$ it has high activity towards oxalic acid mineralisation under visible light [53]. Wang et al. have reported that for Fe(III) doping in $\text{TiO}_2 > 0.05$ at.%, decomposition of methyl orange under UV irradiation has been lower than on undoped TiO_2 , but under visible-light irradiation the Fe(III)-doped TiO_2 with an intermediate iron doping concentration of ≈ 1 at.% had the highest photocatalytic reactivity due to the narrowing of bandgap so that it could effectively absorb the light with longer wavelength [52]. Chen and Peng have reported the preparation of magnetic-nanometer titanium dioxide/ferriferous oxide ($\text{TiO}_2/\text{Fe}_3\text{O}_4$) composite photocatalyst with the particles size of 30–50 nm, which appeared to be very active under visible light and highly effective in discoloring of wastewater [66].

It has been investigated that Fe/TiO_2 particles had a higher hydrophilic property compared with TiO_2 [65, 67].

TiO_2/Fe thin film has been demonstrated to have antimicrobial activity after being irradiated with visible light [68].

3.3. Enhancement of photocatalytic activity of TiO_2 by iron doping

It is generally accepted that Fe(III) centres form shallow charge trapping sites within the TiO_2 matrix as well as on the particle surface through the replacement of Ti(IV) by Fe(III)

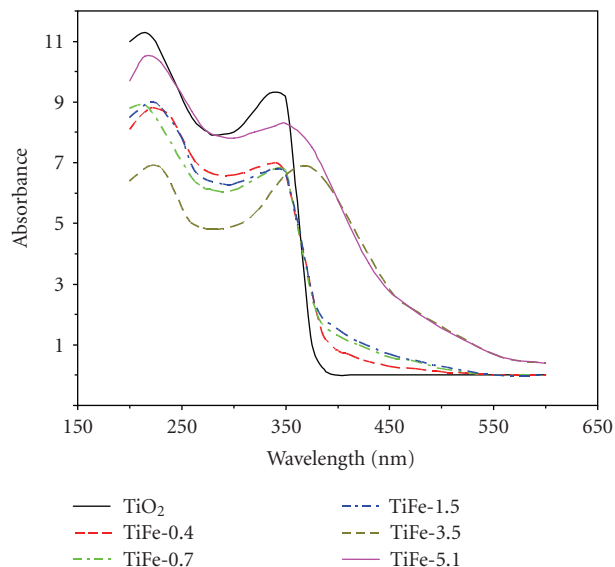


FIGURE 9: UV-Vis spectra of Fe-doped TiO_2 with different iron content.

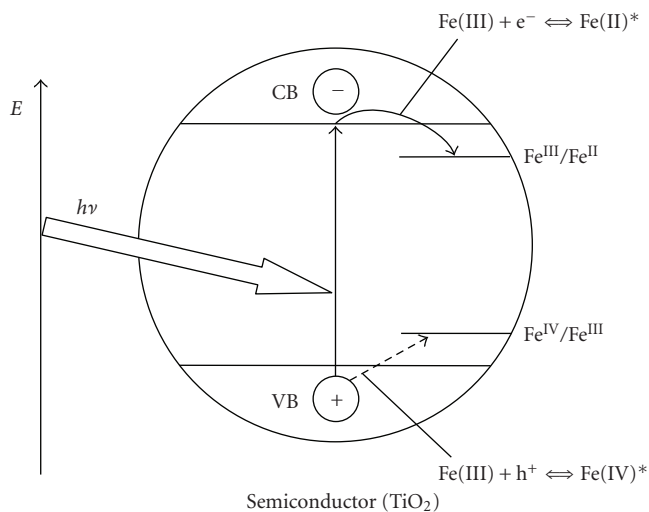


FIGURE 10: Scheme of mechanism of TiO_2 photocatalysis with modifications by Fe(III) ion doping (CB—conduction band, VB—valence band).

[69]. Based on the favourable energy levels, Fe(III) centres may act either as an electron or a hole trap (see Figure 10); so that photogenerated charge carriers are temporarily separated more effectively [40].

Wang et al. [40] have reported that enhancement of the quantum yield by Fe(III) doping TiO_2 can be explained by assuming that the Fe(III) centre acts predominately as a shallow electron trap from which the electron is transferred to molecular oxygen more rapidly than the undoped TiO_2 .

However, it was proved that the photoactivity of Fe/TiO_2 catalyst is dependent on the way of preparation and the amount and state of iron.

Wang et al. [40] have reported that the highest quantum yield has been obtained when Fe(III)-acetylacetonate precursor was used and for the optimal doping levels 0.25 and 0.5 atom %. They have also reported that above-mentioned optimal doping level, some of the Fe(III) dopants might act as shallow hole traps leading to an enhanced recombination of the trapped charge carriers.

Navío et al. [42] have also observed that at the some conditions and for the certain quantity of Fe(III), the dopant can be a center of recombination. They prepared Fe/TiO₂ by an impregnation of TiO₂ with Fe(NO₃)₃·9H₂O and by the sol-gel method from TiCl₄ and Fe(NO₃)₃·9H₂O. They have been reported that Fe/TiO₂ prepared by the sol-gel method was less active than TiO₂ due to the fact that dopants acted more as recombination centres than a trap sites for charge transfer and the obtained photocatalysts had the lower amount of surface hydroxyl groups and a lower anatase-to-rutile ratio compared with TiO₂ precursor sample. They proved that the existence of separated hematite or pseudobrookite (Fe₂TiO₅) phases in samples containing more than 2% iron could decrease the activity [42]. It has been also proved that the excess of deposited iron on TiO₂ can form Fe(OH)²⁺, which has the greater adsorption to the incidence light than TiO₂ in the range of 290–400 nm, and can cause decreasing of the Fe/TiO₂ photoactivity [69]. The low temperature of calcinations, such as 300°C in Fe/TiO₂ preparation appeared to be favoured taking into account its photoactivity [70].

Different amount of doped Fe(III) to TiO₂ has been reported to affect the enhanced photoactivity of photocatalyst, dependent on the way of preparation and degradation compound.

Adán et al. [48] reported the enhancement of photocatalytic activity of Fe-doped TiO₂ for doping levels up to ca. 1 wt%, which was attributable to the introduction of Fe³⁺ cations into the anatase structure. Nahar et al. [49] reported that the molar ratio of 0.005 Fe content in Fe-doped TiO₂ was the optimum for degradation rate of phenol under both the UV and visible-light irradiations. Hung et al. [44] also found that 0.005 mol% of iron ions can enhance the photocatalytic activity, while too great an amount will make the iron ions become recombination centres for the electron-hole pairs and reduce the photocatalytic activity. Chen et al. [47] and Feng et al. [71] have found the highest photocatalytic activity of Fe-doped TiO₂ for 0.05 at.% Fe(III). The photocatalytic decomposition of Rhodamine B. on the nanosize Fe(III)-doped TiO₂ catalysts prepared by the hydrothermal method with TiCl₄ as the precursor was higher than on TiO₂, and the optimal results have been obtained for the 0.1% Fe(III)-doped TiO₂ [72]. For photocatalytic oxidation of nitrite to nitrate, the most photoactive sample was found to be TiO₂ doped with 0.5 wt% of iron [73]. The mesoporous nanocrystalline Fe-doped TiO₂ samples prepared by ultrasonic method exhibited enhanced photocatalytic activity towards oxidation of acetone in air at a small amount of doped Fe³⁺ ions in TiO₂ particles. The found optimal atomic ratio of Fe to Ti was 0.25. The high activities of the Fe-doped TiO₂ powders could be attributed to the results of the synergistic effects of Fe-doping, large BET specific surface area, and small crystallite size [55]. Zhang et al. [74] reported that the

films with low-iron concentrations performed better photocatalytic activity than the pure TiO₂ film, and the best doped iron concentration was 0.58 at.-%.

Wang et al. have reported that the formation of surface defects in Fe-doped TiO₂ affects the high-photocatalytic activity of this photocatalyst [43, 75]. They reported that when the Fe content increased in Fe-doped TiO₂ prepared by the sol-gel method, the isolated Fe₂O₃, Fe₃O₄, and FeO species were observed and Ti-O-Fe species were formed, which increased the surface defects of the Ti/Fe particles and led to the higher activity of the catalyst than bare TiO₂ for the degradation of tetracycline [75]. They also reported that the concentration of titanium defects remained almost constant below 400°C but decreased as the calcination temperature was higher than 600°C due to the decrease of the hydroxyls in the crystalline structure. Below 400°C of calcination, all the samples had some brookite and a majority of anatase phase. when the temperature was 800°C, Fe₂TiO₅ was produced in the sample containing 5 wt% Fe by a reaction between interstitial iron ions and lattice titanium ions, and in the 10 wt% Fe sample through a reaction of hematite with titania phases. [43].

Egerton et al. have investigated that photoelectrocatalytic disinfection of Escherichia coli by an iron doped TiO₂ sol-gel electrode was more efficient than disinfection by the corresponding undoped electrode. The optimum disinfection rate corresponded to the replacement of ≈0.1% of the Ti atoms by Fe [76].

Some researchers have been observed that doping Fe to TiO₂ can be detrimental or not affect the enhancement activity of the photocatalysts [77, 78].

Fe₂O₃ can work as a photocatalyst and can decompose some organic compounds like aniline [79]. However, the mixture of Fe₂O₃ and TiO₂ has been reported to be less active than original TiO₂ [80, 81].

3.4. Mechanisms of organic compounds decomposition by Fe-doped TiO₂

Wang et al. [82] detected by cryo-TEM that Fe(III)-doped TiO₂ prepared by hydrolysis of TiCl₄ with Fe(III)-acetylacetonate as an iron precursor forms three-dimensional networks with nanoparticles of 2–4 nm, which act as antenna systems in photocatalysis, leading to an enhanced photocatalytic activity of the colloidal preparation. HRTEM image of such prepared particles is shown in Figure 11, and the scheme of this working system is presented in Figure 12 [82].

Once the energy has reached the particle with the adsorbed target molecule, the latter will act as a hole trap thus inducing the separation of the original excitation [82].

Araña et al. [83] have studied the photocatalytic degradation of maleic acid by using Fe-doped TiO₂ (0.15, 0.5, 2, and 5% w/w in Fe) catalysts. They observed that catalysts with the lowest Fe content (0.15 and 0.5%) showed a considerably better catalytic behaviour than nondoped TiO₂ and catalysts with higher Fe contents. Maleic acid molecules interacted with the surface of the lowest Fe-containing catalysts and as a consequence; iron atoms were extracted from the catalyst surface as photoactive Fe³⁺-maleic acid complexes.

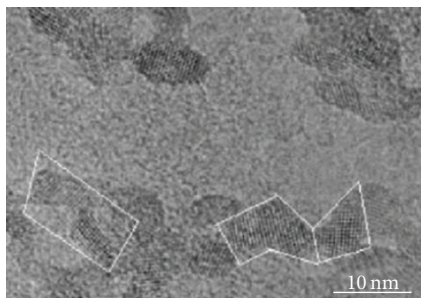


FIGURE 11: HRTEM image of 0.5 at % Fe(III)-doped TiO₂ nanoparticles.

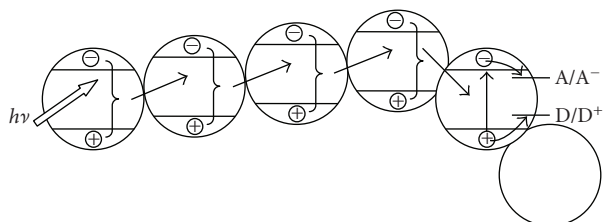


FIGURE 12: The scheme of increased photocatalytic activity through energy/exciton transfer in aggregated photocatalyst particles (antenna effect). A and D represent electron and hole scavengers, respectively.

When this complex was degraded, the resulting Fe²⁺ ions reacted with TiO₂ holes (h⁺) and the iron return to the catalyst surface as Fe₂O₃. In catalysts with low-Fe content (0.15 and 0.5% w/w in Fe), this process occurs in a fast way. On the contrary, in catalysts with high-Fe content (2 and 5% w/w in Fe), the formation of less photoactive complexes seems to predominate [83].

These authors have studied also the photocatalytic degradation of formic acid by Fe-doped TiO₂ calcined at 773 and 1073 K [84]. For 773 K calcined catalyst, results suggested that Fe was extracted through the formation of a [Fe-OOCH]²⁺ complex by which formic acid degrades. Fe²⁺ ions that remain in solution after formic acid degradation went back to the catalyst surface and were oxidised by photogenerated holes. In this way, the catalyst was reactivated becoming ready for a new degradation process. The formation of hydrogen-carbonates on the TiO₂ catalyst through OH radicals insertion was inhibited, and the formation of [Fe-OOCH]²⁺ complex was favoured. A markedly lower capacity for the formic acid degradation has been determined for the 1073 K calcined catalysts, because of its lower surface area and the major presence of lower-active phases such as rutile and Fe₂TiO₅ [84].

The formation of intermediate products over the photocatalytic decomposition was found to be important in the further oxidation processes.

Araña et al. [85] have proved that the mechanism of ethanol decomposition on Fe-TiO₂ was gone by the formation of ethoxides on the catalyst surface that were oxidised to acetate by radicals O^{2•-} and •OH. However, the forma-

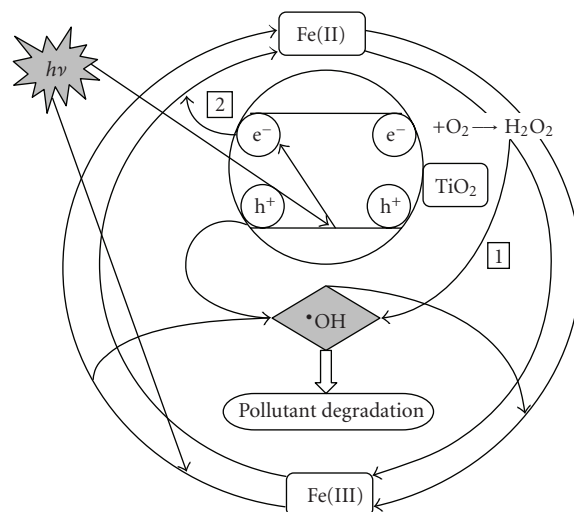


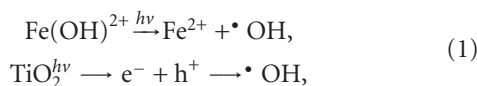
FIGURE 13: Photochemical cycle of combined system iron-TiO₂.

tion, an acetaldehyde as an intermediate product, caused that their catalytic activity progressively decreased over time, whereas on Pd-TiO₂ and Cu-TiO₂, formed ethyleneglycol caused faster degradation [85].

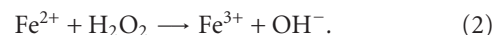
It has been also reported that the formation of a ternary compound HQ-Fe-H₂O₂ in phenol decomposition or formation of an intermediate, highly-oxidised and unstable form of Fe [Fe(IV)] in the case of chlorophenol decomposition were responsible for fast degradation of phenol and chlorophenol, respectively [86, 87].

The synergistic effect has been observed when a mixture of TiO₂ and iron has been used for oxidative photodegradation of monuron (3-(4-chlorophenyl)-1,1-dimethylurea). In a suspension of TiO₂ (24 mg L⁻¹) with addition of Fe(III) (3 × 10⁻⁴ mol L⁻¹), the measured rate constant was similar to that obtained in a suspension of TiO₂ with a concentration more than 20 times higher (500 mg L⁻¹). The optimisation of the photocatalytic systems was obtained when each photocatalyst plays a specific role: Fe(III) as a main OH radicals source and TiO₂ as an oxidizing agent of Fe(II) to Fe(III) favouring the photocatalytic cycle Fe(III)/Fe(II). This proposed mechanism is presented in Figure 13 [88].

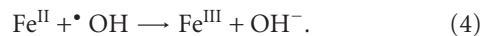
The following are photochemical reactions conducted to production of OH radicals:



and the reaction occurring in the dark (Fenton reaction):



It has been already established that the formation of H₂O₂ is negligible in homogeneous photocatalysis with Fe(III). The reactions between iron and TiO₂ appear to be essential:



The reaction (4) is detrimental for pollutant degradation. It has been reported that Fe(III) could easily adsorb on the surface of TiO₂, and Fe(II) cations were not adsorbed, therefore the reoxidation of Fe(II) by holes is unlikely. In the absence of oxygen Fe(III), cations react with the electron at the surface of TiO₂, allowing the formation of the active species h⁺ and •OH. However, it was proved that •OH radicals are more efficiently formed via the photodissociation of Fe(OH)²⁺, which was found to be responsible for fast degradation of monuron [88].

Ranjit and Viswanathan [45] reported that the photocatalytic activity of the iron-doped catalysts could be explained in terms of the heterojunction formed between the Fe/TiO₂ and α-Fe₂O₃ phases for the sol-gel-derived catalyst.

4. TiO₂ MODIFIED BY CARBON AND IRON

As it was described above, carbon-coated TiO₂ showed high photoactivity towards decomposition of methylene blue but the other organic compounds were poorly decomposed on these photocatalysts, therefore the preparation of carbon-coated TiO₂ has been modified to obtain carbon-coated TiO₂ with doped iron. For this purpose, poly(ethylene terephthalate) (PET) was impregnated with oxalic acid solution (FeC₂O₄) and then was mixed with powder TiO₂ and heat treated at different temperatures, 400–800°C, under flow of Ar [89]. The obtained samples are consisted from anatase phase, contained carbon from 7.5 to 15.5 wt%, and an iron from 0.34 to 0.67 wt%, mostly in the form of Fe(II) [89]. Such prepared samples did not show the enhanced photocatalytic activity towards phenol decomposition under UV irradiation, even though the sample prepared at 400°C exhibited high adsorption of phenol on its surface, around 30 · 10⁻⁵ mol/g, which was much higher than on the other samples, which showed adsorption of phenol in the range of 3–5 · 10⁻⁵ mol/g. However, high acceleration of the phenol decomposition has been observed on the sample prepared at 400°C, when 0.03 mol/L, H₂O₂ was added to the reaction mixture; see Figure 14 [89]. This could be caused by occurring photo-Fenton reactions, in which Fe²⁺ is oxidised to Fe³⁺ with H₂O₂ yielding in OH radicals. Increase of OH radicals production after H₂O₂ addition on samples contained iron was confirmed by OH radicals measurements [89–91].

The high-decomposition rate of phenol was obtained only on the sample, which showed high adsorption of phenol, although this sample contained the lowest content of Fe(II) in comparison with the other samples. Increase of OH radicals formation on samples with iron was not proportional to the decomposition rate of phenol under UV irradiation with H₂O₂. It has been proved that, in case of the sample prepared at 400°C, some complexes were formed, which were responsible for fast degradation of phenol [91]. The FTIR studies indicated that hydroquinone was more likely adsorbed on Fe-C-TiO₂ and could play a key role in the process of phenol decomposition, as reported by Chen and Pignatello [86] that some hydroquinones formed in the phenol decomposition could reduce iron and accelerate in this way the rate of phenol decomposition by the formation of a ternary HQ-Fe-H₂O₂ complex [93]. Cycling decomposi-

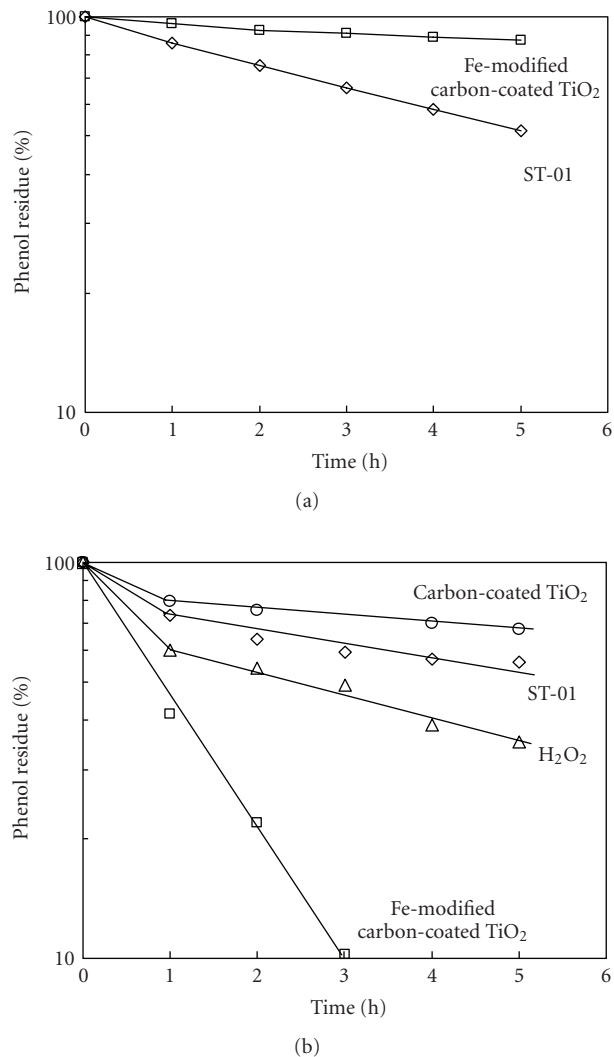


FIGURE 14: Phenol decomposition on commercial TiO₂-ST-01 and modified TiO₂ by carbon and iron at 400°C, (a) under UV irradiation and (b) under UV with addition of H₂O₂.

tion of phenol under UV and H₂O₂ was performed on Fe-modified carbon-coated TiO₂ photocatalyst heat treated at 400°C. For those measurements, photocatalyst was mounted on the adhesive tape and fixed to the metal grid, which was placed inside the reactor. For cycling performance, the metal grid with fixed photocatalyst each time was put to the fresh phenol solution with concentration of 2.1 · 10⁻⁴ mol/L; the results are presented in Figure 15.

A good performance of the phenol decomposition with cycling suggests that an iron present in the sample could follow the processes of oxidation and reduction, being reused in Fenton reactions and photodegradation of phenol. It is worth to add that in this case no pH adjustment was needed as it is usually applied in photo-Fenton process, and not any leaching of iron occurred.

In the further investigations on TiO₂ modified by carbon and iron photocatalysts, the preparation method was changed, the powder of TiO₂ was impregnated with FeC₂O₄

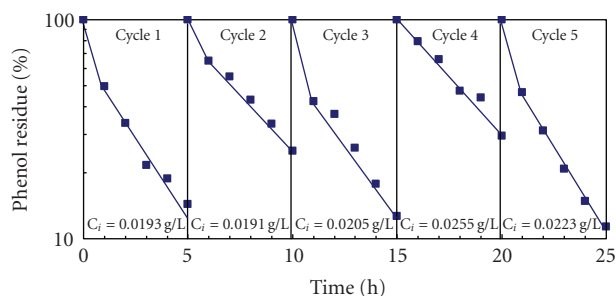
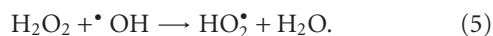


FIGURE 15: Cycling decomposition of phenol under UV irradiation and H_2O_2 on Fe-modified carbon-coated TiO_2 photocatalyst heat treated at 400°C .

solution and heated at $400\text{--}800^\circ\text{C}$ under flow of Ar, but not any polymer was added. The obtained Fe-C- TiO_2 samples contained a residue carbon, $0.2\text{--}3.3\text{ wt}\%$, which came from the carbonisation of oxalate [90]. A residue carbon did not prevent the transformation of anatase to rutile, which occurred at 700°C , with increasing the heat treatment temperature FeTiO_3 phase (ilmenite) appeared. The highest photoactivity for phenol decomposition under UV and H_2O_2 had the sample prepared at 500°C , which contained $2.4\text{ wt}\%$ of residue carbon, $0.70\text{ wt}\%$ of Fe(II), $0.96\text{ wt}\%$ of Fe(III), and did not have FeTiO_3 phase. The phenol decomposition on this sample was much faster than in the case of previous experiments, in which PET was used for preparation, phenol was decomposed after 2 hours of UV irradiation, and after 3 hours of UV irradiation not any ring products of phenol decomposition were detected [90, 91].

It was proved that in case of TiO_2 modified by FeC_2O_4 and heated at 550°C in air (Fe-TiO_2), FeTiO_3 phase is formed, which exhibits higher photocatalytic activity than pure TiO_2 for phenol decomposition under UV irradiation, but with H_2O_2 addition this activity decreases, proportional to the decreasing of OH radicals formation, due to the scavenging effect:

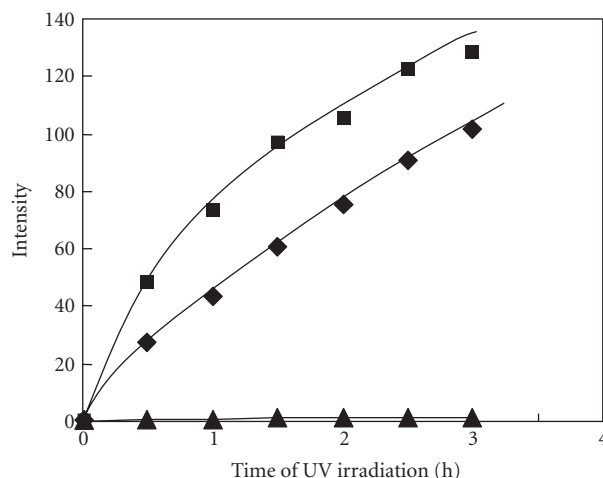


Formed in this reaction, $\text{HO}_2\cdot$ radicals are known to have lower potential of oxidation than $\cdot\text{OH}$ [91]. This scavenging effect has been observed to occur also on TiO_2 . In Figure 16, formation of OH radicals on TiO_2 , Fe-TiO_2 , and Fe-C-TiO_2 samples is presented [91].

In Figure 17, phenol decomposition on these samples is presented [91].

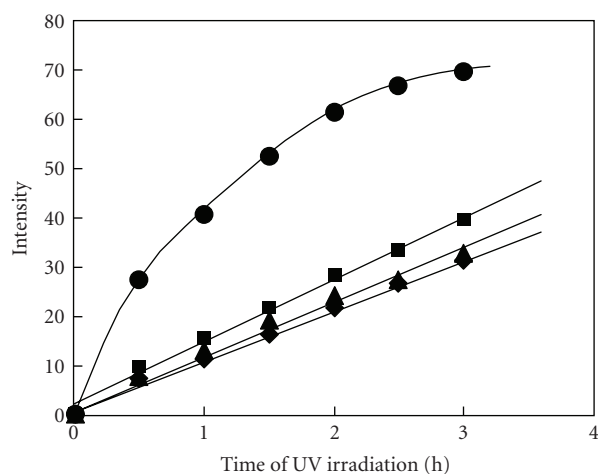
It can be observed that phenol decomposition is going through the radical reaction on TiO_2 and Fe-TiO_2 photocatalysts, whereas by the surface reactions on Fe-C-TiO_2 .

The cycling decomposition of phenol on Fe-C-TiO_2 sample prepared at 500°C has been performed in the circulated flow reactor [94]. For this purpose, the photocatalyst has been pasted on the cotton material with a suspension of the powdered photocatalyst with aqueous solution of sodium silicate (Na_2SiO_3) and was placed inside the reactor on the inner walls, along the UV lamp. Circulated phenol solution was



◆ TiO_2
 ■ Fe-TiO_2
 ▲ Fe-C-TiO_2

(a)



◆ $\text{TiO}_2 + \text{H}_2\text{O}_2$
 ■ $\text{Fe-TiO}_2 + \text{H}_2\text{O}_2$
 ▲ $\text{Fe-C-TiO}_2 + \text{H}_2\text{O}_2$
 ● H_2O_2

(b)

FIGURE 16: Formation of OH radicals on TiO_2 , Fe-TiO_2 , and Fe-C-TiO_2 prepared at 500°C , (a) under UV and (b) under UV with H_2O_2 .

irradiated with UV for some cycles, and with UV and H_2O_2 , as shown in Figure 18 [94].

Adsorption and following decomposition of phenol on immobilised Fe-C-TiO_2 photocatalyst can be observed under UV irradiation, but under UV with addition of H_2O_2 acceleration of phenol decomposition is observed with stable amount of decomposed phenol, over 90% and mineralisation degree around 50% [94].

It has been proved that preparation of Fe-C-TiO_2 from the other TiO_2 precursor of anatase structure at the same conditions as described above gives similar results; the highest photocatalytic activity under UV irradiation with H_2O_2

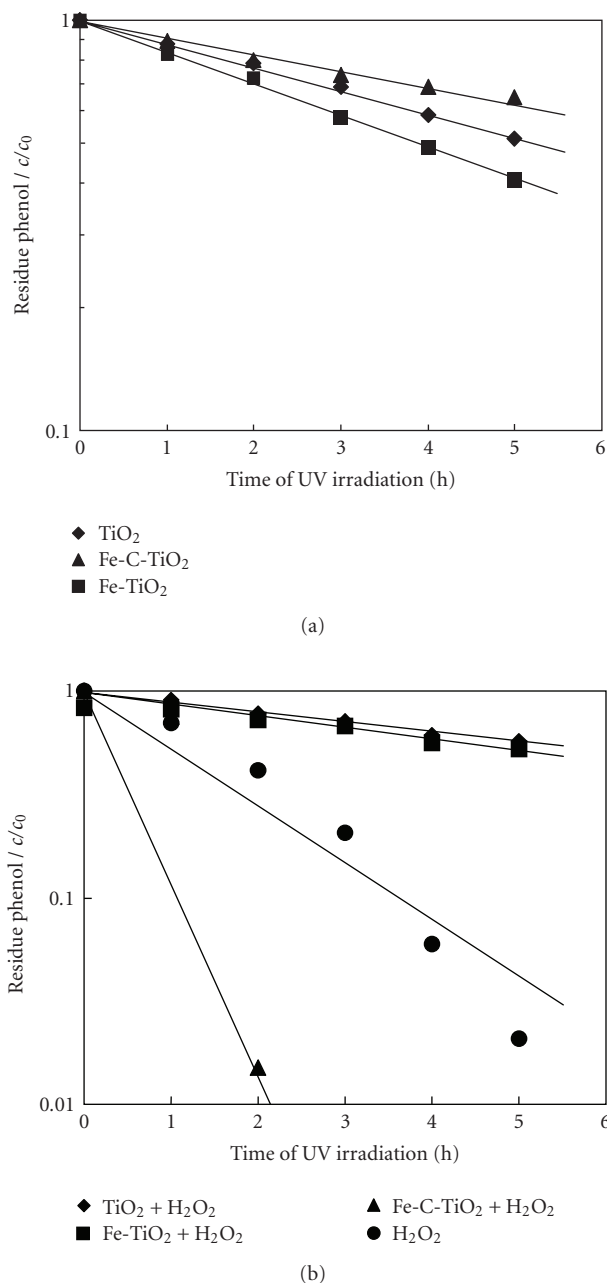


FIGURE 17: Phenol decomposition on TiO₂, Fe-TiO₂, and Fe-C-TiO₂ prepared at 500°C, (a) under UV and (b) under UV with H₂O₂.

has the sample prepared at 500°C [95]. The high photoactivity of Fe-C-TiO₂ sample prepared at 500°C has been found for decomposition of phenol, humic acids, and different dyes, like acid red, methylene blue, and reactive black 5. It has been found that FeTiO₃ phase is detrimental in photocatalytic activity of Fe-C-TiO₂ photocatalysts under UV with H₂O₂, and the low temperatures of preparation such as 500°C led to obtain the samples with high amount of paramagnetic iron on the surface, not built in TiO₂ lattice, which probably facilitates proceeding of the photo-Fenton reactions, in which iron is oxidised and reduced with cy-

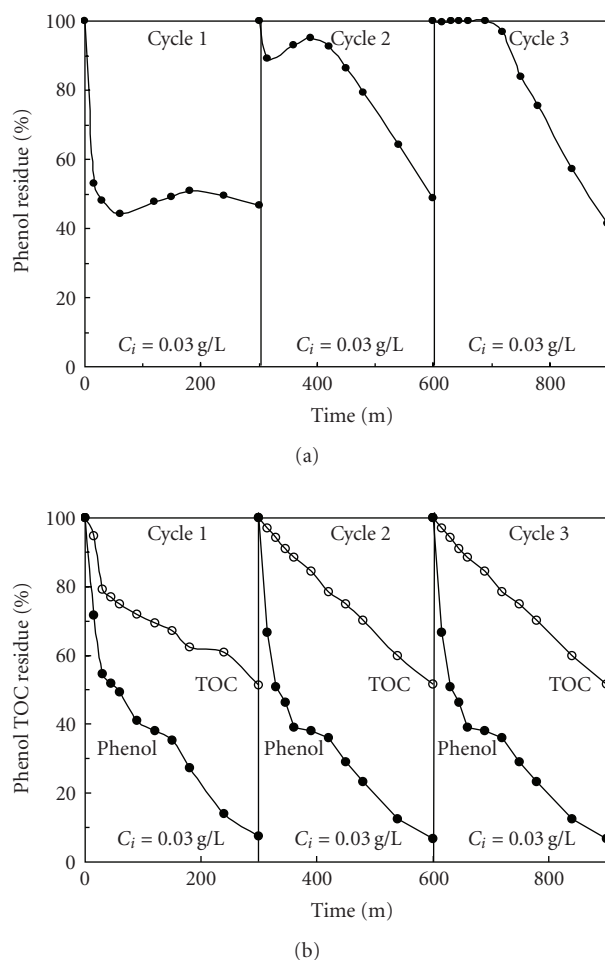


FIGURE 18: Cycling decomposition of phenol on immobilised Fe-C-TiO₂ prepared at 500°C. (a) under UV, (b) under UV with H₂O₂.

cling. The EPR spectra of Fe-C-TiO₂ samples prepared from anatase and FeC₂O₄ [95] are presented in Figure 19.

In obtained EPR spectra, some peaks can be observed, in anatase type TiO₂ a maximum at 344 MT, $g = 1.93$, which is assigned to Ti³⁺ ions associated to oxygen vacancies [96, 97], this peak was also observed in Fe-C-TiO₂ samples and was higher intensity in samples heated at higher temperatures. Some peaks assigned to Fe³⁺ ions were observed: in Fe-C-TiO₂ samples prepared from anatase at temperature 500 and 600°C, a broad peak with maximum at around 434 MT, $g = 1.53$ assigned to paramagnetic Fe³⁺ ions, peaks with maximum at around 330 and 310 M ($g \approx 2$) assigned to Fe³⁺ ions in octahedral symmetry in anatase [48, 96], and two broad peaks at the range of 133 to 272 MT assigned to Fe³⁺ ions substituting for Ti⁴⁺ in the TiO₂ rutile lattice [96].

5. SUMMARY

Modification of TiO₂ by carbon can enhance its photocatalytic activity: doped C can extend the light absorption to the visible range and give photocatalytic activity under visible light by the narrowing of the bandgap; carbon coated

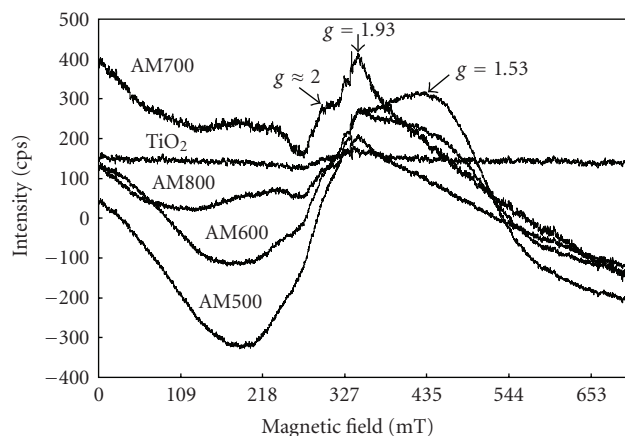


FIGURE 19: EPR spectra of TiO_2 and Fe-C- TiO_2 samples prepared from anatase and Fe- C_2O_4 at 500–800°C.

TiO_2 as well as TiO_2/AC composites can enhance the concentration of the organic compounds on the surface of the photocatalyst and accelerate the process of their decomposition through the transfer of the adsorbed molecules to the TiO_2 surface; TiO_2 loaded carbon can also work as a photocatalyst, on which the molecules are adsorbed in the pores of carbon and then they undergo the photocatalytic decomposition with UV irradiation.

Doping Fe(III) to TiO_2 causes formation of shallow charge trapping sites within the TiO_2 matrix and on the particle surface through the replacement of Ti(IV) by Fe(III). Fe(III) centres may act either as an electron or a hole trap. At high concentration of Fe(III) in Fe-doped TiO_2 Fe(III) ions can act as a recombination centres. The photocatalytic activity of Fe-doped TiO_2 has been found to depend strongly on the preparation method, iron precursor, and the amount and state of iron, generally insignificant amount of doped iron has a positive effect in the enhancement of the photocatalytic activity of Fe-doped TiO_2 , whereas amount of doped iron >2 wt% has been detrimental. It has been observed the red shift in the UV-Vis spectra of Fe-doped TiO_2 photocatalysts due to the introduction of the 3d electron state of Fe^{3+} , $3d^5$, in the conduction band of TiO_2 , what makes these photocatalysts active under visible light.

TiO_2 modified by carbon and iron can work in both photocatalysis and photo-Fenton processes, when H_2O_2 is used, enhancing markedly the rate of the organic compounds decomposition. The photocatalytic decomposition of organic compounds on TiO_2 modified by iron and carbon is going by the complex reactions of iron with the intermediates, what significantly accelerate the process of their decomposition. A good performance of cycling decomposition of phenol has been obtained on immobilised Fe-C- TiO_2 photocatalyst, what suggests that an iron present in the sample could follow the processes of oxidation and reduction, being reused in Fenton reactions and photodegradation of phenol. The additional advantage of using this photocatalyst for the decomposition of organic compounds is the fact that no pH adjustment is needed, and it was observed that there was not any leaching of iron from this photocatalyst.

ACKNOWLEDGMENT

This work was supported by the research Project no. 1T09D00730 for 2006–2009.

REFERENCES

- [1] S. U. M. Khan, M. Al-Shahry, and W. B. Ingler, "Efficient photochemical water splitting by a chemically modified n- TiO_2 ," *Science*, vol. 297, no. 5590, pp. 2243–2245, 2002.
- [2] S. Sakthivel and H. Kisch, "Daylight photocatalysis by carbon-modified titanium dioxide," *Angewandte Chemie International Edition*, vol. 42, no. 40, pp. 4908–4911, 2003.
- [3] C. Lettmann, K. Hildenbrand, H. Kisch, W. Macyk, and W. F. Maier, "Visible light photodegradation of 4-chlorophenol with a coke-containing titanium dioxide photocatalyst," *Applied Catalysis B*, vol. 32, no. 4, pp. 215–227, 2001.
- [4] M. Shen, Z. Wu, H. Huang, Y. Du, Z. Zou, and P. Yang, "Carbon-doped anatase TiO_2 obtained from TiC for photocatalysis under visible light irradiation," *Materials Letters*, vol. 60, no. 5, pp. 693–697, 2006.
- [5] H. Irie, Y. Watanabe, and K. Hashimoto, "Carbon-doped anatase TiO_2 powders as a visible-light sensitive photocatalyst," *Chemistry Letters*, vol. 32, no. 8, pp. 772–773, 2003.
- [6] J. Matos, J. Laine, and J.-M. Herrmann, "Effect of the type of activated carbons on the photocatalytic degradation of aqueous organic pollutants by UV-irradiated titania," *Journal of Catalysis*, vol. 200, no. 1, pp. 10–20, 2001.
- [7] K. M. Reddy, B. Baruwati, M. Jayalakshmi, M. M. Rao, and S. V. Manorama, "S-, N- and C-doped titanium dioxide nanoparticles: synthesis, characterization and redox charge transfer study," *Journal of Solid State Chemistry*, vol. 178, no. 11, pp. 3352–3358, 2005.
- [8] T. Tachikawa, S. Tojo, K. Kawai, et al., "Photocatalytic oxidation reactivity of holes in the sulfur- and carbon-doped TiO_2 powders studied by time-resolved diffuse reflectance spectroscopy," *Journal of Physical Chemistry B*, vol. 108, no. 50, pp. 19299–19306, 2004.
- [9] Y. Choi, T. Umehayashi, and M. Yoshikawa, "Fabrication and characterization of C-doped anatase TiO_2 photocatalysts," *Journal of Materials Science*, vol. 39, no. 5, pp. 1837–1839, 2004.
- [10] C. Di Valentin, G. Pacchioni, and A. Selloni, "Theory of carbon doping of titanium dioxide," *Chemistry of Materials*, vol. 17, no. 26, pp. 6656–6665, 2005.
- [11] M. Janus, B. Tryba, M. Inagaki, and A. W. Morawski, "New preparation of a carbon- TiO_2 photocatalyst by carbonization of n-hexane deposited on TiO_2 ," *Applied Catalysis B*, vol. 52, no. 1, pp. 61–67, 2004.
- [12] M. Janus, M. Inagaki, B. Tryba, M. Toyoda, and A. W. Morawski, "Carbon-modified TiO_2 photocatalyst by ethanol carbonisation," *Applied Catalysis B*, vol. 63, no. 3-4, pp. 272–276, 2006.
- [13] M. Janus, M. Toyoda, M. Inagaki, B. Tryba, and A. W. Morawski, "Preparation of TiO_2/C photocatalyst by ethanol modification of hydrolysed titania $\text{TiO}(\text{OH})_2$ in a pressure reactor," *Journal of Advanced Oxidation Technologies*, vol. 10, no. 2, pp. 1–7, 2007.
- [14] T. A. Egerton, M. Janus, and A. W. Morawski, "New TiO_2/C sol-gel electrodes for photoelectrocatalytic degradation of sodium oxalate," *Chemosphere*, vol. 63, no. 7, pp. 1203–1208, 2006.

- [15] H. Wang and J. P. Lewis, "Effects of dopant states on photoactivity in carbon-doped TiO₂," *Journal of Physics Condensed Matter*, vol. 17, no. 21, pp. L209–L213, 2005.
- [16] J. H. Park, S. Kim, and A. J. Bard, "Novel carbon-doped TiO₂ nanotube arrays with high aspect ratios for efficient solar water splitting," *Nano Letters*, vol. 6, no. 1, pp. 24–28, 2006.
- [17] J. Matos, J. Laine, and J.-M. Herrmann, "Association of activated carbons of different origins with titania in the photocatalytic purification of water," *Carbon*, vol. 37, no. 11, pp. 1870–1872, 1999.
- [18] J. Araña, J. M. Doña-Rodríguez, E. Tello Rendón, et al., "TiO₂ activation by using activated carbon as a support—part I. Surface characterisation and decantability study," *Applied Catalysis B*, vol. 44, no. 2, pp. 161–172, 2003.
- [19] J. Araña, J. M. Doña-Rodríguez, E. Tello Rendón, et al., "TiO₂ activation by using activated carbon as a support—part II. Photoreactivity and FTIR study," *Applied Catalysis B*, vol. 44, no. 2, pp. 153–160, 2003.
- [20] S. X. Liu, X. Y. Chen, and X. Chen, "A TiO₂/AC composite photocatalyst with high activity and easy separation prepared by a hydrothermal method," *Journal of Hazardous Materials*, vol. 143, no. 1-2, pp. 257–263, 2007.
- [21] S. Nagaoka, Y. Hamasaki, S.-I. Ishihara, et al., "Preparation of carbon/TiO₂ microsphere composites from cellulose/TiO₂ microsphere composites and their evaluation," *Journal of Molecular Catalysis A*, vol. 177, no. 2, pp. 255–263, 2002.
- [22] T. Tsumura, N. Kojitani, I. Izumi, N. Iwashita, M. Toyoda, and M. Inagaki, "Carbon coating of anatase-type TiO₂ and photoactivity," *Journal of Materials Chemistry*, vol. 12, no. 5, pp. 1391–1396, 2002.
- [23] B. Tryba, A. W. Morawski, T. Tsumura, M. Toyoda, and M. Inagaki, "Hybridization of adsorptivity with photocatalytic activity—carbon-coated anatase," *Journal of Photochemistry and Photobiology A*, vol. 167, no. 2-3, pp. 127–135, 2004.
- [24] M. Inagaki, F. Kojin, B. Tryba, and M. Toyoda, "Carbon-coated anatase: the role of the carbon layer for photocatalytic performance," *Carbon*, vol. 43, no. 8, pp. 1652–1659, 2005.
- [25] L. Lin, W. Lin, Y. X. Zhu, et al., "Uniform carbon-covered titania and its photocatalytic property," *Journal of Molecular Catalysis A*, vol. 236, no. 1-2, pp. 46–53, 2005.
- [26] X. Zhang, M. Zhou, and L. Lei, "Preparation of photocatalytic TiO₂ coatings of nanosized particles on activated carbon by AP-MOCVD," *Carbon*, vol. 43, no. 8, pp. 1700–1708, 2005.
- [27] Y. Li, X. Li, J. Li, and J. Yin, "Photocatalytic degradation of methyl orange by TiO₂-coated activated carbon and kinetic study," *Water Research*, vol. 40, no. 6, pp. 1119–1126, 2006.
- [28] M. Toyoda, Y. Nanbu, T. Kito, M. Hirano, and M. Inagaki, "Preparation and performance of anatase-loaded porous carbons for water purification," *Desalination*, vol. 159, no. 3, pp. 273–282, 2003.
- [29] B. Tryba, A. W. Morawski, and M. Inagaki, "Application of TiO₂-mounted activated carbon to the removal of phenol from water," *Applied Catalysis B*, vol. 41, no. 4, pp. 427–433, 2003.
- [30] T. Torimoto, Y. Okawa, N. Takeda, and H. Yoneyama, "Effect of activated carbon content in TiO₂-loaded activated carbon on photodegradation behaviors of dichloromethane," *Journal of Photochemistry and Photobiology A*, vol. 103, no. 1-2, pp. 153–157, 1997.
- [31] B. Tryba, A. W. Morawski, M. Toyoda, and M. Inagaki, "TiO₂-mounted activated carbon for the elimination of organic pollutants in water," *Water Research*, vol. 4, pp. 35–42, 2003.
- [32] Z. Ding, X. Hu, P. L. Yue, G. Q. Lu, and P. F. Greenfield, "Synthesis of anatase TiO₂ supported on porous solids by chemical vapor deposition," *Catalysis Today*, vol. 68, no. 1–3, pp. 173–182, 2001.
- [33] C. H. Ao and S. C. Lee, "Enhancement effect of TiO₂ immobilized on activated carbon filter for the photodegradation of pollutants at typical indoor air level," *Applied Catalysis B*, vol. 44, no. 3, pp. 191–205, 2003.
- [34] A. H. El-Sheikh, A. P. Newman, H. Al-Daffae, S. Phull, N. Cresswell, and S. York, "Deposition of anatase on the surface of activated carbon," *Surface and Coatings Technology*, vol. 187, no. 2-3, pp. 284–292, 2004.
- [35] D.-K. Lee, S.-C. Kim, I.-C. Cho, S.-J. Kim, and S.-W. Kim, "Photocatalytic oxidation of microcystin-LR in a fluidized bed reactor having TiO₂-coated activated carbon," *Separation and Purification Technology*, vol. 34, no. 1–3, pp. 59–66, 2004.
- [36] R. Yuan, J. Zheng, R. Guan, and Y. Zhao, "Surface characteristics and photocatalytic activity of TiO₂ loaded on activated carbon fibers," *Colloids and Surfaces A: Physicochemical and Engineering Aspects*, vol. 254, no. 1–3, pp. 131–136, 2005.
- [37] A. Jitianu, T. Cacciaguerra, R. Benoit, S. Delpeux, F. Béguin, and S. Bonnamy, "Synthesis and characterization of carbon nanotubes-TiO₂ nanocomposites," *Carbon*, vol. 42, no. 5-6, pp. 1147–1151, 2004.
- [38] T. Tsumura, N. Kojitani, H. Umemura, M. Toyoda, and M. Inagaki, "Composites between photoactive anatase-type TiO₂ and adsorptive carbon," *Applied Surface Science*, vol. 196, no. 1–4, pp. 429–436, 2002.
- [39] H. Yamashita, M. Harada, A. Tanii, J. Misaka, H. Nakao, and M. Anpo, "Design of TiO₂/activated carbon fiber systems by an ionized cluster beam method and their application for the photocatalytic water purification," *Molecular Crystals and Liquid Crystals*, vol. 388, no. 1, pp. 39–44, 2002.
- [40] C. Wang, C. Böttcher, D. W. Bahnemann, and J. K. Dohrmann, "A comparative study of nanometer sized Fe(III)-doped TiO₂ photocatalysts: synthesis, characterization and activity," *Journal of Materials Chemistry*, vol. 13, pp. 2322–2329, 2003.
- [41] J. A. Navío, G. Colón, M. Macías, C. Real, and M. I. Litter, "Iron-doped titania semiconductor powders prepared by a sol-gel method—part I: synthesis and characterization," *Applied Catalysis A*, vol. 177, no. 1, pp. 111–120, 1999.
- [42] J. A. Navío, J. J. Testa, P. Djedjeian, J. R. Padrón, D. Rodríguez, and M. I. Litter, "Iron-doped titania powders prepared by a sol-gel method—part II: photocatalytic properties," *Applied Catalysis A*, vol. 178, no. 2, pp. 191–203, 1999.
- [43] J. A. Wang, R. Limas-Ballesteros, T. López, et al., "Quantitative determination of titanium lattice defects and solid-state reaction mechanism in iron-doped TiO₂ photocatalysts," *Journal of Physical Chemistry B*, vol. 105, no. 40, pp. 9692–9698, 2001.
- [44] W.-C. Hung, S.-H. Fu, J.-J. Tseng, H. Chu, and T.-H. Ko, "Study on photocatalytic degradation of gaseous dichloromethane using pure and iron ion-doped TiO₂ prepared by the sol-gel method," *Chemosphere*, vol. 66, no. 11, pp. 2142–2151, 2007.
- [45] K. T. Ranjit and B. Viswanathan, "Synthesis, characterization and photocatalytic properties of iron-doped TiO₂ catalysts," *Journal of Photochemistry and Photobiology A*, vol. 108, no. 1, pp. 79–84, 1997.
- [46] M. Shui, L.-H. Yue, and Z.-D. Xu, "Photocatalytic activity of iron doping TiO₂ prepared by several methods," *Acta Physico-Chimica Sinica*, vol. 17, no. 3, p. 285, 2001.

- [47] X.-Q. Chen, J.-Y. Yang, and J.-S. Zhang, "Preparation and photocatalytic properties of Fe-doped TiO₂ nanoparticles," *Journal of Central South University of Technology*, vol. 11, no. 2, pp. 161–165, 2004.
- [48] C. Adán, A. Bahamonde, M. Fernández-García, and A. Martínez-Arias, "Structure and activity of nanosized iron-doped anatase TiO₂ catalysts for phenol photocatalytic degradation," *Applied Catalysis B*, vol. 72, no. 1-2, pp. 11–17, 2007.
- [49] M. S. Nahar, K. Hasegawa, and S. Kagaya, "Photocatalytic degradation of phenol by visible light-responsive iron-doped TiO₂ and spontaneous sedimentation of the TiO₂ particles," *Chemosphere*, vol. 65, no. 11, pp. 1976–1982, 2006.
- [50] M. S. Nahar, K. Hasegawa, S. Kagaya, and S. Kuroda, "Comparative assessment of the efficiency of Fe-doped TiO₂ prepared by two doping methods and photocatalytic degradation of phenol in domestic water suspensions," *Science and Technology of Advanced Materials*, vol. 8, no. 4, pp. 286–291, 2007.
- [51] N. Uekawa, Y. Kurashima, K. Kakegawa, and Y. Sasaki, "Preparation and nonstoichiometric property of wide compositional Fe(III)-doped TiO₂ (anatase)," *Journal of Materials Research*, vol. 15, no. 4, pp. 967–973, 2000.
- [52] X. H. Wang, J.-G. Li, H. Kamiyama, Y. Moriyoshi, and T. Ishigaki, "Wavelength-sensitive photocatalytic degradation of methyl orange in aqueous suspension over iron(III)-doped TiO₂ nanopowders under UV and visible light irradiation," *Journal of Physical Chemistry B*, vol. 110, no. 13, pp. 6804–6809, 2006.
- [53] W. Y. Teoh, R. Amal, L. Mädler, and S. E. Pratsinis, "Flame sprayed visible light-active Fe-TiO₂ for photomineralisation of oxalic acid," *Catalysis Today*, vol. 120, no. 2, pp. 203–213, 2007.
- [54] J. A. Navío, G. Colón, M. I. Litter, and G. N. Bianco, "Synthesis, characterization and photocatalytic properties of iron-doped titania semiconductors prepared from TiO₂ and iron (III) acetylacetonate," *Journal of Molecular Catalysis A*, vol. 106, no. 3, pp. 267–276, 1996.
- [55] M. Zhou, J. Yu, and B. Cheng, "Effects of Fe-doping on the photocatalytic activity of mesoporous TiO₂ powders prepared by an ultrasonic method," *Journal of Hazardous Materials*, vol. 137, no. 3, pp. 1838–1847, 2006.
- [56] C. H. Lee, S. H. Lee, S. J. Lee, J. S. Kim, and Y. S. Kwon, "Fabrication of Fe-TiO₂ nano-composite powders by mechanical alloying," *Journal of Ceramic Processing Research*, vol. 4, no. 3, pp. 122–125, 2003.
- [57] K. S. Yao, D. Y. Wang, J. J. Yan, L. Y. Yang, and W. S. Chen, "Photocatalytic effects of TiO₂/Fe thin film irradiated with visible light on cellular surface ultrastructure and genomic DNA of bacteria," *Surface and Coatings Technology*, vol. 201, no. 15, pp. 6882–6885, 2007.
- [58] H. Yamashita, M. Harada, J. Misaka, M. Takeuchi, B. Nepolian, and M. Anpo, "Photocatalytic degradation of organic compounds diluted in water using visible light-responsive metal ion-implanted TiO₂ catalysts: Fe ion-implanted TiO₂," *Catalysis Today*, vol. 84, no. 3-4, pp. 191–196, 2003.
- [59] J. O. Carneiro, V. Teixeira, A. Portinha, et al., "Iron-doped photocatalytic TiO₂ sputtered coatings on plastics for self-cleaning applications," *Materials Science and Engineering B*, vol. 138, no. 2, pp. 144–150, 2007.
- [60] H.-C. Huang, G.-L. Huang, H.-L. Chen, and Y.-D. Lee, "Immobilization of TiO₂ nanoparticles on Fe-filled carbon nanocapsules for photocatalytic applications," *Thin Solid Films*, vol. 515, no. 3, pp. 1033–1037, 2006.
- [61] X.-C. Song, L.-H. Yue, B. Liu, G. Han, W.-X. Chen, and Z.-D. Xu, "Preparation of Fe-doped TiO₂ nanotubes with small diameter by hydrothermal method," *Chinese Journal of Inorganic Chemistry*, vol. 19, no. 8, pp. 899–901, 2003.
- [62] C. Wang, Q. Li, and R. Wang, "Synthesis and characterization of mesoporous iron-doped TiO₂," *Journal of Materials Science*, vol. 39, no. 5, pp. 1899–1901, 2004.
- [63] D. H. Kim, H. S. Hong, S. J. Kim, J. S. Song, and K. S. Lee, "Photocatalytic behaviors and structural characterization of nanocrystalline Fe-doped TiO₂ synthesized by mechanical alloying," *Journal of Alloys and Compounds*, vol. 375, no. 1-2, pp. 259–264, 2004.
- [64] R. S. Sonawane, B. B. Kale, and M. K. Dongare, "Preparation and photo-catalytic activity of Fe-TiO₂ thin films prepared by sol-gel dip coating," *Materials Chemistry and Physics*, vol. 85, no. 1, pp. 52–57, 2004.
- [65] M. Kang, "Synthesis of Fe/TiO₂ photocatalyst with nanometer size by solvothermal method and the effect of H₂O addition on structural stability and photodecomposition of methanol," *Journal of Molecular Catalysis A*, vol. 197, no. 1-2, pp. 173–183, 2003.
- [66] J.-Y. Chen and T.-Z. Peng, "Preparation and properties of a magnetic-nanometer TiO₂/Fe₃O₄ composite photocatalyst," *Acta Chimica Sinica*, vol. 62, no. 20, pp. 2093–2097, 2004.
- [67] H. Jiang and L. Gao, "Enhancing the UV inducing hydrophilicity of TiO₂ thin film by doping Fe ions," *Materials Chemistry and Physics*, vol. 77, no. 3, pp. 878–881, 2003.
- [68] K. S. Yao, D. Y. Wang, J. J. Yan, L. Y. Yang, and W. S. Chen, "Photocatalytic effects of TiO₂/Fe thin film irradiated with visible light on cellular surface ultrastructure and genomic DNA of bacteria," *Surface and Coatings Technology*, vol. 201, no. 15, pp. 6882–6885, 2007.
- [69] M. I. Litter and J. A. Navío, "Photocatalytic properties of iron-doped titania semiconductors," *Journal of Photochemistry and Photobiology A*, vol. 98, no. 3, pp. 171–181, 1996.
- [70] X.-H. Qi, Z.-H. Wang, Y.-Y. Zhuang, Y. Yu, and J.-L. Li, "Study on the photocatalysis performance and degradation kinetics of X-3B over modified titanium dioxide," *Journal of Hazardous Materials*, vol. 118, no. 1–3, pp. 219–225, 2005.
- [71] J. Feng, R. S. K. Wong, X. Hu, and P. L. Yue, "Discoloration and mineralization of Orange II by using Fe³⁺-doped TiO₂ and bentonite clay-based Fe nanocatalysts," *Catalysis Today*, vol. 98, no. 3, pp. 441–446, 2004.
- [72] P.-F. Yan, D.-R. Zhou, J.-Q. Wang, L.-B. Yang, D. Zhang, and H.-G. Fu, "Preparation of iron-doped TiO₂ nanocrystal by hydrothermal method and its photocatalytic properties," *Chemical Journal of Chinese Universities*, vol. 23, no. 12, p. 2321, 2002.
- [73] A. Milis, J. Peral, X. Domenech, and J. A. Navío, "Heterogeneous photocatalytic oxidation of nitrite over iron-doped TiO₂ samples," *Journal of Molecular Catalysis*, vol. 87, no. 1, pp. 67–74, 1994.
- [74] W. Zhang, Y. Li, S. Zhu, and F. Wang, "Surface modification of TiO₂ film by iron doping using reactive magnetron sputtering," *Chemical Physics Letters*, vol. 373, no. 3-4, pp. 333–337, 2003.
- [75] X.-B. Yu, G.-H. Wang, and H.-X. Li, "The promoting effect on the activities of Fe doped TiO₂ photocatalysts," *Chemical Research in Chinese Universities*, vol. 17, no. 2, pp. 187–192, 2001.
- [76] T. A. Egerton, S. A. M. Kosa, and P. A. Christensen, "Photoelectrocatalytic disinfection of *E. coli* suspensions by iron doped TiO₂," *Physical Chemistry Chemical Physics*, vol. 8, no. 3, pp. 398–406, 2006.
- [77] L. Palmisano, M. Schiavello, A. Sclafani, C. Martin, I. Martin, and V. Rives, "Surface properties of iron-titania photocatalysts employed for 4-nitrophenol photodegradation in

- aqueous TiO₂ dispersion,” *Catalysis Letters*, vol. 24, no. 3-4, pp. 303–315, 1994.
- [78] E. Piera, M. I. Tejedor-Tejedor, M. E. Zorn, and M. A. Anderson, “Relationship concerning the nature and concentration of Fe(III) species on the surface of TiO₂ particles and photocatalytic activity of the catalyst,” *Applied Catalysis B*, vol. 46, no. 4, pp. 671–685, 2003.
- [79] C. Karunakaran and S. Senthilvelan, “Fe₂O₃-photocatalysis with sunlight and UV light: oxidation of aniline,” *Electrochemistry Communications*, vol. 8, no. 1, pp. 95–101, 2006.
- [80] M. Sadeghi, W. Liu, T.-G. Zhang, P. Stavropoulos, and B. Levy, “Role of photoinduced charge carrier separation distance in heterogeneous photocatalysis: oxidative degradation of CH₃OH vapor in contact with Pt/TiO₂ and cofumed TiO₂-Fe₂O₃,” *Journal of Physical Chemistry*, vol. 100, no. 50, pp. 19466–19474, 1996.
- [81] J. C. Crittenden, J. Liu, D. W. Hand, and D. L. Perram, “Photocatalytic oxidation of chlorinated hydrocarbons in water,” *Water Research*, vol. 31, no. 3, pp. 429–438, 1997.
- [82] C. Wang, C. Böttcher, D. Bahnemann, and J. Dohrmann, “In situ electron microscopy investigation of Fe(III)-doped TiO₂ nanoparticles in an aqueous environment,” *Journal of Nanoparticle Research*, vol. 6, no. 1, pp. 119–122, 2004.
- [83] J. Araña, O. González Díaz, M. Miranda Saracho, J. M. Doa Rodríguez, J. A. Herrera Melián, and J. Pérez Peña, “Maleic acid photocatalytic degradation using Fe-TiO₂ catalysts. Dependence of the degradation mechanism on the Fe catalysts content,” *Applied Catalysis B*, vol. 36, no. 2, pp. 113–124, 2002.
- [84] J. Araña, O. González Díaz, M. Miranda Saracho, J. M. Doa Rodríguez, J. A. Herrera Melián, and J. Pérez Peña, “Photocatalytic degradation of formic acid using Fe/TiO₂ catalysts: the role of Fe³⁺/Fe²⁺ ions in the degradation mechanism,” *Applied Catalysis B*, vol. 32, no. 1-2, pp. 49–61, 2001.
- [85] J. Araña, J. M. Doa Rodríguez, O. González Díaz, et al., “Gas-phase ethanol photocatalytic degradation study with TiO₂ doped with Fe, Pd and Cu,” *Journal of Molecular Catalysis A*, vol. 215, no. 1-2, pp. 153–160, 2004.
- [86] R. Chen and J. J. Pignatello, “Role of quinone intermediates as electron shuttles in fenton and photoassisted fenton oxidations of aromatic compounds,” *Environmental Science and Technology*, vol. 31, no. 8, pp. 2399–2406, 1997.
- [87] M. Pera-Titus, V. García-Molina, M. A. Baños, J. Giménez, and S. Esplugas, “Degradation of chlorophenols by means of advanced oxidation processes: a general review,” *Applied Catalysis B*, vol. 47, no. 4, pp. 219–256, 2004.
- [88] H. Měšťánková, G. Mailhot, J. Jirkový, J. Krýsa, and M. Bolte, “Mechanistic approach of the combined (iron-TiO₂) photocatalytic system for the degradation of pollutants in aqueous solution: an attempt of rationalisation,” *Applied Catalysis B*, vol. 57, no. 4, pp. 257–265, 2005.
- [89] B. Tryba, M. Toyoda, A. W. Morawski, and M. Inagaki, “Modification of carbon-coated TiO₂ by iron to increase adsorptivity and photoactivity for phenol,” *Chemosphere*, vol. 60, no. 4, pp. 477–484, 2005.
- [90] B. Tryba, A. W. Morawski, M. Inagaki, and M. Toyoda, “Effect of the carbon coating in Fe-C-TiO₂ photocatalyst on phenol decomposition under UV irradiation via photo-Fenton process,” *Chemosphere*, vol. 64, no. 7, pp. 1225–1232, 2006.
- [91] B. Tryba, A. W. Morawski, M. Inagaki, and M. Toyoda, “The kinetics of phenol decomposition under UV irradiation with and without H₂O₂ on TiO₂, Fe-TiO₂ and Fe-C-TiO₂ photocatalysts,” *Applied Catalysis B*, vol. 63, no. 3-4, pp. 215–221, 2006.
- [92] B. Tryba, A. W. Morawski, M. Inagaki, and M. Toyoda, “Mechanism of phenol decomposition on Fe-C-TiO₂ and Fe-TiO₂ photocatalysts via photo-Fenton process,” *Journal of Photochemistry and Photobiology A*, vol. 179, no. 1-2, pp. 224–228, 2006.
- [93] B. Tryba, M. Inagaki, M. Toyoda, and A. W. Morawski, “FTIR studies of the surface of TiO₂, Fe-TiO₂ and Fe-C-TiO₂ photocatalysts in phenol oxidation via the photo-fenton process,” *Journal of Advanced Oxidation Technologies*, vol. 10, no. 1, pp. 25–30, 2007.
- [94] B. Tryba, “Immobilization of TiO₂ and Fe-C-TiO₂ photocatalysts on the cotton material for application in a flow photocatalytic reactor for decomposition of phenol in water,” *Journal of Hazardous Materials*, vol. 151, no. 2-3, pp. 623–627, 2008.
- [95] B. Tryba, “Effect of TiO₂ precursor on the photoactivity of Fe-C-TiO₂ photocatalysts for Acid Red (AR) decomposition,” *Journal of Advanced Oxidation Technologies*, vol. 10, no. 2, pp. 267–272, 2007.
- [96] J. Soria, J. C. Conesa, V. Augugliaro, L. Palmisano, M. Schiavello, and A. Sclafani, “Dinitrogen photoreduction to ammonia over titanium dioxide powders doped with ferric ions,” *Journal of Physical Chemistry*, vol. 95, no. 1, pp. 274–282, 1991.
- [97] T. Berger, M. Sterrer, O. Diwald, et al., “Light-induced charge separation in anatase TiO₂ particles,” *Journal of Physical Chemistry*, vol. 109, no. 13, pp. 6061–6068, 2005.

Review Article

Visible-Light-Active Titania Photocatalysts: The Case of N-Doped TiO₂s—Properties and Some Fundamental Issues

Alexei V. Emeline,¹ Vyacheslav N. Kuznetsov,¹ Vladimir K. Rybchuk,¹ and Nick Serpone²

¹ Department of Photonics, Fock Research Institute of Physics, St. Petersburg State University, St. Petersburg, Russia

² Dipartimento di Chimica Organica, Università di Pavia, Via Taramelli 10, 27100 Pavia, Italy

Correspondence should be addressed to Nick Serpone, nick.serpone@unipv.it

Received 13 September 2007; Revised 14 October 2007; Accepted 12 November 2007

Recommended by M. Sabry A. Abdel-Mottaleb

This article briefly reviews some factors that have impacted heterogeneous photocatalysis with next generation TiO₂ photocatalysts, along with some issues of current debate in the fundamental understanding of the science that underpins the field. Preparative methods and some characteristic features of N-doped TiO₂ are presented and described briefly. At variance are experimental results and interpretations of X-ray photoelectron spectra (XPS) with regard to assignments of N 1s binding energies in N-doped TiO₂ systems. Relative to pristine nominally clean TiO₂ with absorption edges at 3.2 eV (anatase) and 3.0 eV (rutile), N-doped TiO₂s display red-shifted absorption edges into the visible spectral region. Several workers have surmised that the (*intrinsic*) band gap of TiO₂ is narrowed by coupling dopant energy states with valence band (VB) states, an inference based on DFT computations. With similar DFT computations, others concluded that red-shifted absorption edges originate from the presence of localized intragap dopant states above the upper level of the VB band. Recent analyses of absorption spectral features in the visible region for a large number of doped TiO₂ specimens, however, have suggested a common origin owing to the strong similarities of the absorption features, and this regardless of the preparative methods and the nature of the dopants. The next generation of (doped) TiO₂ photocatalysts should enhance overall process photoefficiencies (in some cases), since doped TiO₂s absorb a greater quantity of solar radiation. The fundamental science that underpins heterogeneous photocatalysis with the next generation of photocatalysts is a rich playing field ripe for further exploration.

Copyright © 2008 Alexei V. Emeline et al. This is an open access article distributed under the Creative Commons Attribution License, which permits unrestricted use, distribution, and reproduction in any medium, provided the original work is properly cited.

1. INTRODUCTION

As a first-generation material, pristine TiO₂ has served well in the photoassisted (often dubiously referred to as photocatalytic) disposition of contaminants in aqueous and atmospheric ecosystems. The science that underlies heterogeneous photocatalysis has shown that the lowest energy level of the bottom of the conduction band (CB) of TiO₂ is a measure of the reduction potential of the photogenerated electrons, whereas the higher energy level of the valence band (VB) is a measure of the oxidation potential of photogenerated holes. pH-dependent flatband potentials, V_{fb} , of the CB and VB bands of this metal oxide determine the energy of electrons and holes at the interface. Accordingly, reductive and oxidative processes of couples with redox potentials more positive and more negative than the V_{fb} of CB and VB, respectively, can be driven by surface trapped electrons (e^-) and

holes (h^+) that are poised to engage in various processes, the most important of which are photoreductions and photooxidations. An important issue regards the notion that once photogenerated, e^- and h^+ tend to recombine somewhat efficiently and rapidly relative to an otherwise slow redox chemistry at the TiO₂ surface. An additional, no less important issue is that TiO₂ absorbs a relatively small fraction (ca. 3–5%) of the solar radiation reaching the Earth's surface.

Of the two important polymorphs of TiO₂, anatase begins to absorb UV light around 387 nm (band gap energy, $E_{bg} \sim 3.2$ eV), whereas the absorption onset of rutile occurs around 413 nm ($E_{bg} \sim 3.0$ eV) increasing sharply to shorter wavelengths. Accordingly, in the late 1980s studies began to develop the next generation of titanium dioxides [1] that could absorb and make use of both UV (290–400 nm) and visible (400–700 nm) radiation to enhance process efficiencies. To achieve this feat required that the absorption edge

of TiO_2 be shifted to longer wavelengths (>400 nm). One way to accomplish this necessitated photosensitizing TiO_2 either with suitable dyes that unfortunately led to their own destruction, or with suitable metal-ion dopants that sometimes act as recombination centers of e^- and h^+ ; metal-ion dopants are often ineffective in aiding surface redox reactions, as appears to be the case when metal doping is achieved by wet impregnation [1]. However, metal-ion implantation methods have produced metal-doped TiO_2 specimens that enhance photoinduced surface processes even in the visible-light spectral region [2], where wet chemical methods failed.

First reports of anion-doped TiO_2 , began to appear in the early 1990s, although Sato [3] had earlier hinted at a N-doped TiO_2 . The 2001 study of Asahi and coworkers [4] on doping TiO_2 with various anions to prepare visible-light-active (VLA) N-doped TiO_2 s was the catalyst needed to produce second-generation TiO_2 materials that are photoactive over the UV and much of the visible-light region. Subsequent studies reported several other visible-light-active N-doped TiO_2 s, together with C-doped TiO_2 and S-doped TiO_2 . The reports by Asahi et al. [4, 5] has led to a lively debate on the causes that lead the absorption onset of TiO_2 to be red-shifted to the visible region. They proposed that N-doping of TiO_2 red-shifts the absorption edge of TiO_2 and increases photoactivity by a *narrowing of the TiO_2 band gap*. Carbon- and sulfur-doped TiO_2 displayed similar red-shifts accompanied by increased photoactivity. As we will see later, others have proposed that electronic transitions in N-doped TiO_2 systems activated by visible-light irradiation involve transitions from N 2p localized states to the CB of TiO_2 . Clearly, just as first-generation TiO_2 led to lively debates on the fundamental science that underpins TiO_2 -assisted photoredox surface processes following photo-activation, so are the second-generation VLA TiO_2 s generating enthusiastic discussions on the root cause that shifts the absorption onset to longer wavelengths. Three recent reviews have summarized some of the facets of first (undoped) and second generation (doped) titanias. [6–8].

This review article focuses briefly (a) on some preparative methods of visible-light-active N-doped TiO_2 materials and their XPS spectroscopic features, (b) on their visible absorption spectra that display the red-shift of the absorption edges, to terminate with (c) a brief visit into the lively debate concerning band gap narrowing.

2. NITROGEN-DOPED TiO_2 s– SYNTHESSES AND CHARACTERIZATION

Asahi et al. [4] initially set three requirements to achieve visible-light-activity for TiO_2 : (i) doping should produce states in the band gap of TiO_2 that absorb visible light; (ii) the CB minimum and the dopant states of doped TiO_2 should be as high as or higher than the $\text{H}_2/\text{H}_2\text{O}$ level to ensure photoreductive activity; and (iii) the intragap states should overlap sufficiently with the band states of TiO_2 to transfer photoexcited carriers to reactive sites at the TiO_2 surface within their lifetime. Metal dopants were undesirable because they did not meet conditions (ii) and (iii) as they produce localized d states deep in the band gap of TiO_2 and tend to act more

as e^-/h^+ recombination centers. Calculations of density of states (DOS) of substitutional doping with several nonmetals (C, N, F, P, or S) into O sites in anatase TiO_2 by the full-potential linearized augmented plane-wave (FLAPW) formalism in the framework of the local density approximation (LDA) led Asahi et al. [4, 5] to choose N since the 2p states apparently contribute to band gap narrowing through mixing with O 2p states in the valence band. On the other hand, Yates and coworkers [9] classified the methods of synthesizing N-doped TiO_2 s into (i) modification of existing TiO_2 by ion bombardment, (ii) modification of existing TiO_2 in powdered form, film, and single crystal, or else modify TiN by gas phase chemical impregnation, and (iii) grow $\text{TiO}_{2-x}\text{N}_x$ (crystals) from liquid or gaseous precursors.

Early on, Sato [3] had noted that calcination of $\text{Ti}(\text{OH})_4$ in the presence of NH_4Cl (or aqueous NH_3) led to photosensitization of TiO_2 when exposed to visible-light radiation. The powdered samples were deduced to be NO_x -doped TiO_2 with the NO_x impurity acting as the sensitizer. Noda et al. [10] reported a yellow-colored anatase TiO_2 powder obtained from aqueous hydrazine and TiCl_4 solutions, and deduced that visible-light absorption was due to the presence of oxygen vacancies V_{O} s.

In their 2001 seminal report, Asahi et al. [4] prepared crystalline $\text{TiO}_{2-x}\text{N}_x$ films by sputtering a TiO_2 target in a N_2/Ar gas mixture followed by annealing at 550 C in a N_2 atmosphere. The yellowish $\text{TiO}_{2-x}\text{N}_x$ films absorbed light below 500 nm. X-ray photoelectron N 1s spectra (XPS) of the N-doped TiO_2 showed bands at 402, 400 and 396 eV; the undoped TiO_2 film showed no 396 eV band. The latter was assigned to atomic β -N in $\text{TiO}_{2-x}\text{N}_x$, whereas the 402-eV and 400-eV bands were attributed to molecularly chemisorbed dinitrogen γ - N_2 [11]. Powdered samples prepared with NH_3/Ar as the source of N followed by calcination at 550–600 C produced a $\text{TiO}_{2-x}\text{N}_x$ systems that showed XPS peaks at 396 eV; these systems were photoactive toward the decomposition of methylene blue (optimal loading, ~ 0.25 at.% N). The sites for photoactivity under visible-light irradiation were those when N substitutionally replaced O, that is, sites associated with atomic β -N at 396 eV [4]. Lee et al. [12] fabricated N-doped TiO_2 anatase films by MOCVD using $\text{Ti}(\text{i-PrO})_4$ and N_2O at 420 C; XPS Ti 2p spectra showed N was incorporated into the TiO_2 lattice to form Ti–N bonds. Hydrolysis of $\text{Ti}(\text{SO}_4)_2$ with NH_3 in dry air at 400 C produced a visible-light-active anatase TiO_2 ($\lambda < 550$ nm) [13]; however, XPS spectra showed only trace amounts of N, with visible-light response due to an oxygen-deficient stoichiometry.

Pale yellow, yellow, and dark green $\text{TiO}_{2-x}\text{N}_x$ ($x = 0, 0.0050, 0.011, 0.019$) powdered samples can be prepared by annealing anatase TiO_2 powder (ST-01) in a flow of NH_3 at 550, 575, and 600 C, respectively [14]. XRD patterns indicated that the samples retain the anatase structure; no TiN phase was present. The XPS peak at 396 eV confirmed substitutional N doping of O sites yielding O–Ti–NO bonds. Noticeable shifts of the absorption edge into the visible spectral region were evident for $\text{TiO}_{2-x}\text{N}_x$. The feature at $\lambda > 550$ nm was attributed to Ti^{3+} since NH_3 decomposes into N_2 and H_2 at ca. 550 C, and H_2 reduces Ti^{4+} under these conditions.

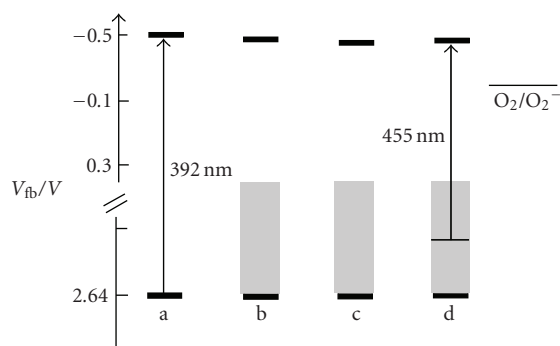


FIGURE 1: Electrochemical potentials (versus NHE) of band edges of three N-doped TiO_2 s: (a) TiO_2 , (b) $\text{TiO}_2\text{-N/1}$, (c) $\text{TiO}_2\text{-N/2}$, (d) $\text{TiO}_2\text{-N/3}$. Shaded areas denote surface states; the oxygen redox potential at pH 7 is also shown. Reproduced with permission from [16]. Copyright Wiley-VCH Verlag GmbH & Co. KGaA.

The band gap energy remained at 3.2 eV. Mineralization of isopropanol to CO_2 with UV-light and visible-light radiations resulted in different quantum yields, suggesting that N-doping forms a narrow N 2p band above the valence band of TiO_2 . Note that band gap narrowing in $\text{TiO}_{2-x}\text{N}_x$, as inferred by Asahi et al. [4], would have required identical quantum yields. On irradiating with visible light, the quantum yields decreased with increase in x of the dopant N because of the increase in oxygen vacancies, V_{O} , with increase of x in $\text{TiO}_{2-x}\text{N}_x$. In this case, V_{O} act as recombination centers for e^- and h^+ . Under UV irradiation, the quantum yields also decreased with increase in x , suggesting that the doping sites also act as recombination centers.

Nanocrystalline porous N-doped TiO_2 thin films, prepared by introducing N into anatase TiO_2 by means of DC magnetron sputtering in N_2 -containing plasma [15], displays new spectral features in the spectral range $410 < \lambda < 535$ nm at low N concentrations owing to excitation of e^- to unoccupied states from local states located slightly above the VB edge. N-doping had no effect on the conduction band edge. Band gap narrowing was deemed somewhat questionable by these authors [15]. Despite the intense recombination of charge carriers caused by N-doping, the new band gap states created by N-doping improved the visible-light photoresponse at the expense of some losses of the UV response.

Sakthivel and Kisch [16] prepared yellow N-doped anatase TiO_2 with various N loadings by hydrolysis of TiCl_4 with a N-containing base {aqueous NH_3 , $(\text{NH}_4)_2\text{CO}_3$ or NH_4HCO_3 } followed by calcination at 400 C. XPS spectra showed only a broad signal at ~ 404 eV (but no 396-eV peak) attributed to the hyponitrite (NO^-) species that was confirmed by infrared spectral techniques. No changes in the valence band edge occurred on N-doping, despite the red-shift of the TiO_2 absorption edge to ~ 250 nm. Contrary to the inference by Lindgren et al. [15], however, photoelectrochemical results [16] showed a slight change in the electrochemical potentials of the CB of TiO_2 (see Figure 1) for three of the specimens. According to the authors [16], N-doping led only to a “modest band gap narrowing.”

High-energy ball milling of P-25 TiO_2 (ca. 80% anatase and $\sim 20\%$ rutile) with various quantities of hexamethylenetetramine (HMT) at near-ambient temperatures yields yellowish N-doped rutile TiO_2 [17], which subsequent to calcination in air at 400 C gives an N-doped product that displays absorption edges at ~ 400 and 550 nm and a good visible-light photoresponse toward oxidation of NO.

Ion-assisted electron-beam evaporation of rutile titania powder and N_2 yields crystalline anatase $\text{TiO}_{2-x}\text{N}_x$ films with a considerable amount of substitutional N atoms (1.8 at.%) and chemisorbed molecular N_2 [18]. XPS spectra showed peaks at 402 and 396 eV assigned to molecularly chemisorbed $\gamma\text{-N}_2$ and atomic $\beta\text{-N}$, respectively; Ti 2p XPS spectra revealed $\text{Ti}^{4+} 2p_{3/2}$ and $\text{Ti}^{4+} 2p_{1/2}$ in the anatase TiO_2 film indicating that the majority of titanium in the $\text{TiO}_{2-x}\text{N}_x$ film consisted of Ti^{4+} , thus confirming the results of XRD patterns. N-doping caused no changes to the anatase TiO_2 structure as attested by Raman spectroscopy.

In a simplified synthesis, Gole and coworkers [19, 20] produced $\text{TiO}_{2-x}\text{N}_x$ samples at room temperature using direct nitridation of anatase TiO_2 with alkylammonium salts. The samples could be tuned to respond to wavelengths up to $\lambda \sim 550$ nm. The method first yielded metal-oxide colloids by the controlled hydrolysis of $\text{Ti}(\text{i-PrO})_4$ in aqueous/isopropanol media (pH 2; HNO_3), subsequent to which treatment in excess $(\text{C}_2\text{H}_5)_3\text{N}$ led to $\text{TiO}_{2-x}\text{N}_x$ nanocolloids. XRD and HRTEM results demonstrated that the treated $\text{TiO}_{2-x}\text{N}_x$ nanoparticles were predominantly anatase. Diffuse reflectance spectra (DRS) of the $\text{TiO}_{2-x}\text{N}_x$ crystallites rose sharply at ~ 450 nm; the corresponding DRS spectrum of nitrated $\text{TiO}_{2-x}\text{N}_x$ from partially agglomerated nanoparticles rose at ~ 550 nm. XPS analysis with Ar^+ -ion sputtering revealed the presence of N dopants at the surface and in the sub-layers of $\text{TiO}_{2-x}\text{N}_x$ agglomerates (N content, 3.6–5.1 at.%). No evidence was found for conversion of the anatase structure into rutile on N-doping for the initial TiO_2 nanocolloids and for the agglomerated gel solutions. Little if any XPS evidence of atomic $\beta\text{-N}$ binding at 396 eV was found in any of the $\text{TiO}_{2-x}\text{N}_x$ samples. Rather, the XPS results were consistent with nonstoichiometric surface-based Ti–O–N bonding.

In a later related detailed XPS study of a series of TiO_2 -based nanometer-sized photocatalysts that included nitrogen-doped TiO_2 nanoparticles, Chen and Burda [21] noted a broad N 1s binding energy peak of the nitrogen-doped TiO_2 nanoparticles that was centered at ca. 401.3 eV (see Figure 2) and extended from 397.4 eV to 403.7 eV, a range greater than the typical binding energy of 397.2 eV in titanium nitride, TiN . These findings were attributed to the formation of an O–Ti–N structure that was suggested as the chemical entity formed during the substitutional doping process and responsible for the significant increase in photocatalytic activity of synthesized nitrogen-doped nanoparticles. Moreover, the XPS observations reported by Chen and Burda [21] were not consistent with a Ti–N entity within the TiO_2 nanocolloid lattice [22]. The shift in the N 1s binding energy for the $\text{TiO}_{2-x}\text{N}_x$ nanocolloid to higher energies relative to TiN was likely due to a more positive oxidation state of nitrogen in relation to the N 1s binding energy in

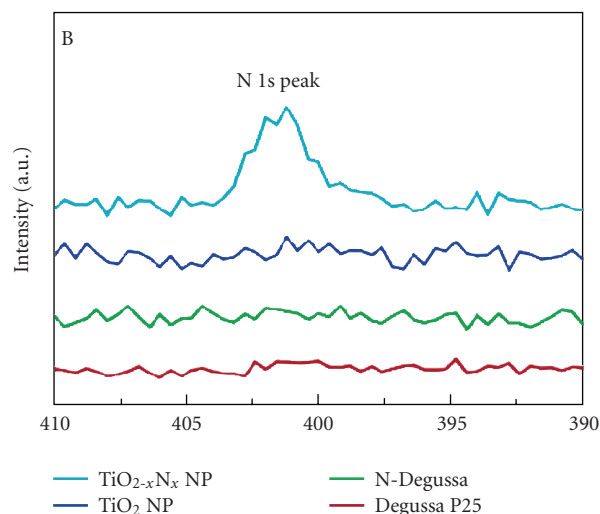


FIGURE 2: X-ray photoelectron spectra of various TiO_2 specimens; N-Degussa is nitrated P25 TiO_2 and $\text{TiO}_{2-x}\text{N}_x$ NP denotes $\text{TiO}_{2-x}\text{N}_x$ nanoparticles. Reproduced with permission from [21]. Copyright (2004) American Chemical Society.

NaNO_3 (408 eV), in NH_3 (398.8 eV) and adsorbed NO (400–401.5 eV) [23]. Attribution of the N 1s peak at 400 eV to $\gamma\text{-N}_2$ in N-doped titanias has been questioned by Chen et al. [23] in that N_2 is not chemisorbed on metal oxides such as TiO_2 at ambient temperature, preferring instead to assign the 400 eV peak to NO species consistent with the attendant heat release on the creation of these sites in the TiO_2 lattice.

Gopinath [24] recently questioned the validity of the conclusions reached by Chen and Burda [21] as not being consistent with the reported XPS observations, suggesting (among others) rather that there may have been surface contamination of the analyzed nanocolloidal N-doped TiO_2 material as a result of atmospheric degradation. Based on earlier studies of XPS spectra of NH_3 and primary alkyl/aromatic amines (398–399 eV), anionic N^{3-} in TiN (396–397 eV), adsorbed NO and NO_2 on ZnO (401 and 405 eV, resp.) and Sato and coworkers' [25] observation of the N 1s core level at 400 eV for N-doped TiO_2 prepared by a wet method and attributed to an impurity sensitization such as NO, Gopinath [24] argued that the 401.3-eV peak in the N- TiO_2 nanocolloid reported by Chen and Burda [21] was more likely due to oxidized nitrogen as in N-O-Ti-O or O-N-Ti-O, and that the high binding energy of 401.3 eV was associated with some partial positive charge on N as noted by György and coworkers [26] in the nitridation of titanium for the 400–401 eV peak attributed to an O-N-Ti structure. Also questioned by Gopinath [24] were the origins of the O 1s core levels at binding energies of 530 and 532 eV ascribed by Chen and Burda [21] to O-Ti-O and to N-Ti-O structural units, respectively. Gopinath [24] insisted that the 532-eV peak was likely due to surface contamination by some carbon oxide, such as CO_2 , and further claimed that the large level of N-doping in nanocolloids (ca. 4–8%) was rather unlikely. In an appropriate response, Burda and Gole [27] pointed out that Chen and Burda [21] used the shorthand notation N-Ti-O to mean

that N, Ti, and O were bound to next neighboring atoms (Ti or O) in the TiO_2 lattice and *not* to mean an isolated triatomic molecular species with a nonoxidized nitrogen, and were thus rather surprised by Gopinath's misinterpretation since such notation was chemically obvious even to others [28]—also see below. In fact, as clearly stated by the groups of Gole and Burda [19, 20, 22, 23] the discussion dealt with a minimal structure fragment within a doped TiO_2 lattice (characterized by NO sites), and *not* some species where the nitrogen was not oxidized. As well, the apparent discrepancy noted by Gopinath [24] in the XPS data reported earlier by others (see refs 13–20 in [27]) did not take into account that the data were taken under vastly different conditions across distinct physical entities that included films and undoped nanoparticles, not to mention the anatase and rutile structures. Burda and Gole [27] further noted that Gopinath's misinterpretation of their studies originated with the misconception that N, Ti, and O are isolated from their TiO_2 anatase environment, when in fact the XPS results reported by Chen and Burda [21] clearly demonstrated that nitrogen was partially oxidized and that the neighboring Ti was reduced relative to Ti in pure TiO_2 . The discussion concerning the valencies of the nitrogen had indeed attributed the 401-eV peak to an NO site [22, 23]; however, the precise location of the NO site within the titania lattice remains a subject yet to clarify. Finally, that the doping levels are as high as 4 to 8% in the N-doped TiO_2 colloids are not unusual based on nucleophilic substitution chemistry, as pointed out previously [23].

The above reports, misinterpretations and misunderstandings, together with other XPS results described below, clearly demonstrate that XPS results do not in themselves provide unequivocal understanding of the exact nature of N-doped titania specimens, not to mention the nature of other anion- and cation-doped TiO_2 s.

Nakamura and coworkers [29] produced anatase $\text{TiO}_{2-x}\text{N}_x$ materials by two methods: (a) in the dry method anatase ST-01 TiO_2 was heated to 550 C in a dry NH_3 flow and (b) in the wet method the $\text{Ti}(\text{i-PrO})_4$ precursor was hydrolyzed in aqueous NH_3 at 0 C followed by calcination at 400 C. Nitrogen-doped nanocrystalline TiO_2 (yellow) powders have also been synthesized by a procedure developed by Ma and coworkers [30]. Commercial anatase ST-01 TiO_2 heated at 500 C under a dry N_2 gas flow in the presence of a small quantity of carbon also yields N-doped yellow TiO_2 whose XRD patterns reveal the sample to have the anatase structure, even after annealing at 500 C. XPS spectra showed peaks at 396.2, 398.3, and 400.4-eV in the N 1s region, with the first two peaks attributed to chemically bound N-species and to O-Ti-N linkages within the crystalline TiO_2 lattice, respectively, whereas the 400.4-eV peak was ascribed to molecularly chemisorbed N_2 species.

Ion implantation of atomically clean TiO_2 (110) surfaces in single crystals with mixtures of N_2^+ and Ar^+ ions, followed by subsequent annealing under ultrahigh-vacuum conditions, led to incorporation of N into the TiO_2 lattice [31]. XPS spectra revealed only the N 1s feature at 396.6 eV attributed to substitutionally bound nitride nitrogen (O^{2-} ions substituted by N^{2-} anions). Contrary to expectations,

N-doped crystals containing only nitride ions exhibited a shift in the photothreshold energy of 0.2 eV to *higher* (shorter wavelengths) rather than *lower* (longer wavelengths) energy compared to undoped TiO₂ (110). N-doped TiO₂ (110) rutile single crystals previously treated in the presence of an NH₃/Ar gas mixture at ca 600 C exhibited photoactivity at the *lower photon energy* of 2.4 eV, that is, 0.6 eV below the band gap energy of rutile TiO₂ (3.0 eV) [32]. The active dopant state of the interstitial N responsible for this effect showed a N 1s binding energy at 399.6 eV attributed to a form of nitrogen likely bound to H. This is distinctively different from the substitutional nitride state, which displays a N 1s binding energy at 396.7 eV. Apparently a co-doping effect of N and H probably enhanced the visible-light photoactivity. Doped and undoped TiO₂ (110) samples also showed an impurity XPS feature at 399.6 eV, which on UV treatment in air and/or Ar⁺-ion sputtering led to extensive depletion of the signal indicating that traces of nitrogen may have contaminated the metal-oxide surface. Such inferences by the Yates group are in stark contrast to those of Asahi et al. [4] and those of others who claimed that nitridic nitrogens that substitute O²⁻ ions in the TiO₂ lattice are the necessary dopant species for TiO₂ photoactivity in the visible-light spectral region.

In a later study, Thompson and Yates [33] re-emphasized that the exclusive XPS N 1s signal at 396.7 eV attributed to substitutional β -N in ion-implanted N-doped TiO₂ does not account for the *decrease* in the photothreshold of TiO₂ (110), as observed for interstitially located N–H bound species. Rather, they pointed out that the 0.2-eV *increase* in photothreshold energy of N-doped TiO₂ systems arose from deposition of charge in the low levels of the CB (the band-filling mechanism). Although clear XPS evidence exists for the incorporation of β -substitutional N in N-doped TiO₂, there is no strong and firm evidence of any appreciable photoactivity when these doped systems are irradiated with visible light according to Yates et al. [9], a point also raised by Frach et al. [34] who further noted no improvement in visible-light activity on N-doping TiO₂, and by Li and coworkers [35] who reported that the nature and level of visible-light activity depended on the nitriding compound employed.

With TiCl₄, ethyl acetate and NH₃ as precursors and N₂ as the carrier gas, Yates and coworkers [9] used an atmospheric pressure thermal CVD coater to grow thin films of N-doped TiO₂ on glass substrates. Only three grown samples displayed the XPS N 1s peak at 396 eV of atomic β -substituted N. XPS N 1s spectra showed no evidence of the 397-eV signal typically due to the N³⁻ ion (TiN), but did reveal weak signals at 400 and 402 eV probably arising from molecularly chemisorbed N₂, or from NH_x species located at interstitial sites (399.6 eV), or from NO_x, or NH_x (400 eV), or from an oxynitride (399.3 eV) of stoichiometry equivalent to TiN_{0.5}O_{0.5}. Some of the films displayed visible spectral absorption features, but so did nominally undoped TiO₂ films indicating that N incorporation cannot be assumed on the basis of red-shifts of the absorption edge. Even though the N-doped TiO₂ specimens revealed the presence of β -N incorporation and absorption spectral features in the visible region, they were photo-inactive under visible light irradiation,

while the UV photoactivity was reduced considerably compared to films grown in the absence of NH₃. Clearly, the presence of β -nitrogen alone cannot be claimed to induce visible-light activity in N-doped TiO₂ films, a point also raised by Mrowetz and coworkers [36] who prepared two different yellow-colored N-doped TiO₂ samples: *sample A* prepared by the method of Gole et al. [19, 20] and *sample H* prepared by the high-temperature nitridation of commercial anatase TiO₂ at 550 C in a NH₃/Ar gas flow. XPS spectra of *sample A* surface revealed intense peaks at 399.6 and 404.5 eV in the N 1s region, whereas the peak at 396 eV in the XPS spectra of *sample H* powders was weak and diffuse, even after Ar⁺-ion sputtering. Despite these observations, the N-doped TiO₂ materials *failed to catalyze* the oxidation of HCOO⁻ to CO₂^{-*}, and NH₃–OH to NO₃⁻ under visible-light illumination.

The solvothermal process using a TiCl₃/HMT/alcohol (methanol or ethanol) mixed solution in an autoclave at 90 C and then at 190 C yields N-doped TiO₂ nanoparticles consisting of pure anatase (pH 9, methanol), rutile (pH 9, ethanol) and brookite (pH 1, methanol) phases, which showed good visible-light absorption and visible-light activity at $\lambda > 510$ nm [37]. The two-step absorption in the reported diffuse reflectance spectra (DRS) became apparent only after calcination at 400 C. The first absorption edge is related to the band structure of nondoped TiO₂, whereas the second absorption edge around 520–535 nm is due to the formation of a N 2p band located above the O 2p valence band in the TiO_{2-x}N_x specimen.

Electrochemical anodization of titanium in HF/H₂SO₄ electrolyte, followed by calcination at different temperatures (range 300–600 C) in pure NH₃, yields self-organized N-doped TiO₂ nanotubes [38]. The initial amorphous nanotubes were converted to anatase, with some rutile present depending on the heat-treatment temperature. Absorption spectra of the TiO_{2-x}N_x nanotubes displayed a sub-band gap energy of ~ 2.2 eV (that may be referred to as an *extrinsic band gap*) and the *intrinsic band gap* of anatase (~ 3.2 eV). The N 1s XPS spectrum showed two clear peaks, one at 400 eV, ascribed to molecularly chemisorbed dinitrogen (γ -N₂ state), and the other at 396 eV, attributed to the atomic β -N state.

The RF-MS deposition method produces N-substituted TiO₂{N–TiO₂(X)} photoactive thin films using various N₂/Ar mixtures as the sputtering gas (X = 2, 4, 10, 40) and a calcined TiO₂ plate as the source material [39]. The absorption edge of the films red-shifted to 550 nm, with the extent of the shift depending on the concentration of N(X) substituted within the TiO₂ lattice (range 2.0–16.5%). The specimen with 6.0% N exhibited the highest visible-light activity in the photooxidation of isopropanol (aqueous media; irradiation $\lambda \geq 450$ nm), and the photooxidation of H₂O (irradiation $\lambda \leq 550$ nm). XPS and XRD measurements showed significant substitution of lattice O atoms of TiO₂ by N atoms, which Kitano and coworkers [39] suggested as playing a crucial role in the *band gap narrowing* of the TiO₂ thin films (range 2.58–2.25 eV relative to 3.2 eV, depending on X) enabling the visible-light photoresponse. In samples with X > 4, the Ti³⁺ species formed in the N–TiO₂(X) samples

acted as recombination centers of e^- and h^+ and thus led to a decreased photoactivity.

Joung et al. [40] used the hydrolysis of $Ti(i-PrO)_4$ in anhydrous ethanol containing HCl, followed by treatment of the resulting colloids in an NH_3 stream at 400 C, 500 C and 600 C at various time intervals (5 to 60 min) to prepare visible-light-active N-doped TiO_2 materials. The highest photoactivities were seen for samples prepared at 400 C and 600 C and calcination times of 5 and 10 min, whereas for samples prepared at 500 C the highest photoactivity was observed for a calcination time of 60 min. XRD patterns of the TiO_2 powders before and after N-doping showed that N-doping caused no changes to the anatase phase. The N 1s XPS spectra of the $TiO_{2-x}N_x$ samples displayed a peak at 399.95 eV that was tentatively assigned to adsorbed NO or to N in Ti–O–N; however, no peak attributable to Ti–N bonding at 396 eV was observed. Band gap energies of N-doped TiO_2 inferred from absorption spectra ranged from 2.92 to 3.04 eV, for samples prepared at 400 C (5 min) and at 500 C (60 min), respectively. For samples prepared at 400 C (5 and 10 min), the active species were described as being NO, NO_2 , NO_2^- , NH_2 , whereas for samples prepared at 500 C (60 min) the active species was identified as doped atomic N; the active species for samples prepared at 600 C (5 and 10 min) were inferred to be doped atomic N along with NO, NO_2 , NO_2^- , and NH_2 species.

At this time, it is important to realize that visible-light photoactivity of N-doped TiO_2 materials appears to be highly sensitive to the preparative routes, because although such materials may absorb visible light, they are nonetheless frequently inactive in photooxidations. To the extent that photogenerated charge carriers in and by themselves do not impart photoactivity and that charge carrier recombination must be muted to allow the carriers to reach the metal-oxide surface, In and coworkers [41] prepared a series of $TiO_{2-x}N_x$ systems with nominal N loadings from 0.2 to 1.0 wt.% involving the sequential reaction of H_2O with a small known excess of $TiCl_4$ in toluene (step 1) under dry O_2 -free argon, followed by the stoichiometric reaction of the remaining $TiCl_4$ with a standard solution of NH_3 in dioxane (step 2). The resulting species were heat-treated in air at 400, 500, and 600 C. Tests of the $TiO_{2-x}N_x$ specimens for visible-light photoactivity revealed (i) that calcination at 400 C yields a solid with pronounced absorption in the visible spectral region but yet no visible-light photoactivity, (ii) that 500 C calcination produces an effective (yellow) visible-light-active sample, and (iii) that the heat treatment at 600 C results in an inactive white material.

In two extensive reports, Belver and coworkers [42, 43] prepared and characterized a series of nanosized N-doped TiO_2 -based materials by a reverse micelle microemulsion method using a $Ti(i-PrO)_4$ precursor and three N sources, for example, 2-methoxyethylamine, N,N,N',N'-tetramethylethylenediamine and 1,2-phenylenediamine, to produce Ti(IV) complexes in dry isopropanol under a N_2 atmosphere. Dropwise addition of the solution to the inverse microemulsion, that contained H_2O dispersed in n-heptane and Triton X-100 as the surfactant with hexanol as the cosurfactant, produced materials that were subsequently calcined at 200 C and

then at 450 C. A XANES examination confirmed the anatase structure of $TiO_{2-x}N_x$. XANES spectra also showed a lack of correlation between the number of oxygen vacancies (V_{OS}) and the N content in the samples. Above a certain limit, the association of point defects, such as V_{OS} and/or the presence of nonpoint extended defects, was detrimental to photoactivity. The distribution of defects and the nature of defects present in the N-doped samples were examined in a joint XANES/EXAFS investigation, which revealed that the distribution of defects was not simply related to the oxygen vacancies V_{OS} , since strong differences existed in the first cation-cation coordination shell that inferred the possible presence of nonpoint defects. The joint study also confirmed the point defects to be the V_{OS} ; no interstitial defects were seen and the O/Ti atom ratio was <2 . Evidently, there exists an optimal O/Ti ratio for maximum photoactivity achieved when oxygen vacancies are located in the bulk lattice that act as electron traps subsequent to visible-light photoactivation of the doped specimens. No apparent effect due to N-doping on the valence band edge was detected. Some localized states were, however, detected at the bottom of the conduction band with broad absorption around 500 nm. Results from DRIFT spectra indicated the presence of several anion-related impurities of a substitutional (N^{n-}) and interstitial (NO^+) nature. Although these species contributed to the absorption features, the authors [42, 43] found no clear correlation between any of these species and photoactivity. In fact, photoactivity best correlated with an optimal number of oxygen vacancies, above and below which a decrease of steady-state reaction rates occurred.

N-doped titania samples with high visible-light activity have been synthesized using a layered titania/isostearate nanocomposite from a sol-gel technique [44], with N-doping achieved by treating the composite with aqueous NH_3 followed by calcination either in an O_2/N_2 mixture or in pure N_2 at various temperatures (300, 350, 400, 450, and 500 C). The vivid yellow samples absorbed visible light in the 380–500 nm spectral region, and correlated with the extent of doped-N content in the samples. However, the visible-light photoactivity *did not correlate* with N content. The highest visible-light photoactivity was observed for the 400-C calcined sample. The quantity of N content in the sample decreased on increasing the calcination temperature, which was particularly significant between 300 and 350 C, with the decrease being more important for the sample calcined in O_2/N_2 than for the sample calcined in pure N_2 .

Thus far we have witnessed that visible-light-active (VLA) TiO_2 systems doped with nitrogen possess, in most cases, good attributes toward the photooxidation of organic and inorganic (e.g., NO_x) substrates. Of particular interest have been the materials doped with N whose preparative methods have been varied but otherwise simple in a large number of cases. Most important, however, although all the N-doped TiO_2 materials displayed absorption features and absorption edges red-shifted to the visible spectral region (at least to 550 nm), photoactivity of these systems under visible-light irradiation has not always correlated with these absorption features. In a recent study, Tachikawa and coworkers [45] addressed some of these issues and described

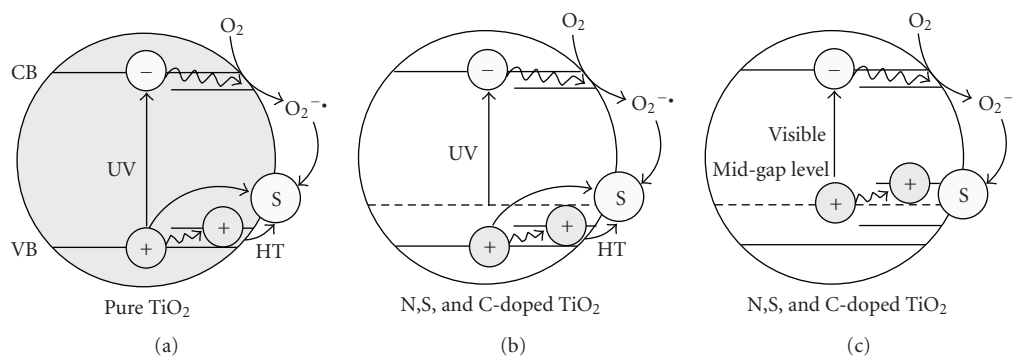


FIGURE 3: Cartoons illustrating possible photoassisted processes of a substrate adsorbed on the surfaces of pure, N-, S-, and C-doped TiO₂ nanoparticles. Reproduced with permission from [45]. Copyright (2007) American Chemical Society.

mechanisms of the photoactivity of VLA TiO₂ specimens. Using solid-state NMR measurements combined with transient diffuse reflectance (TDR) spectroscopy, these workers provided direct evidence of the degradation of ethylene glycol with VLA-active TiO_{2-x}N_x under visible-light irradiation. It appears that photoassisted oxidations of organic compounds on the surface of TiO_{2-x}N_x proceed by surface intermediates generated from oxygen reduction (the superoxide radical anion, O₂^{-•}) or otherwise water oxidation (the •OH radical) and not by direct reaction with h⁺ that may be trapped at the N-induced mid-gap level (see Figure 3). Based on their experimental results, it is rather evident that both an appropriate lower-energy photo-threshold for visible-light absorption and high carrier mobilities are needed for advanced visible light-active TiO₂-based photocatalysts.

3. DFT COMPUTATIONS OF BAND GAP ENERGIES IN N-DOPED TiO₂

Different preparative methods and strategies of N-doping TiO₂ as described above can lead to anion-doped metal-oxide materials with entirely different properties—these are the next generation TiO₂ photocatalysts. The key question that keeps recurring in the literature is the chemical nature and the location of the species that lead(s) the absorption edge of TiO₂ to be red-shifted and consequently to the visible-light activity of doped TiO₂. Species such as NO_x, NH_x, and N²⁻ have been proposed, not to mention NO⁻, NO₂⁻ and NO₃⁻ species that have been confirmed experimentally. Another key question regards the electronic structure(s) of the (anion)-doped materials and their fate when subjected to UV- and/or visible-light irradiation. Although, these questions have been addressed in several interesting computational studies, a consensual acceptance of the results has yet to be reached. Significant advances can be made in clarifying key questions by a combination of experimental and computational studies within the same laboratory or among collaborating laboratories.

Densities of states in anatase TiO₂ for substitutional doping of oxygen in the lattice by C, N, F, P, and S dopants were first reported by Asahi and coworkers [4, 46] using the full-potential linearized augmented plane-wave (FLAPW) for-

malism in the framework of the local density approximation (LDA). The calculations were carried out without geometry optimization for the five anion-dopings because the resulting atomic forces were apparently too large to obtain reasonable positions in the unit cell (eight TiO₂ units per cell). Three types of doping for N were considered in the computations: (a) substitutional N doping (N_S), (b) interstitial N doping (N_I), and (c) both types of doping (N_{S+I}) in the anatase TiO₂ architecture. Optimization of the N positions in the cell inferred molecularly bonding states (NO and N₂) for cases (b) and (c) with bond lengths (improved by the generalized gradient approximation GGA) in fair agreement with accepted values: 1.20 Å versus 1.15 Å (N–O) and 1.16 Å versus 1.10 Å (N₂). According to the authors [4], substitutional doping of N was the most effective because its 2p states contribute to band gap narrowing by mixing with O 2p states of the valence band. Calculated imaginary parts of the dielectric functions of TiO_{2-x}N_x showed a shift of the absorption edge to lower energy by N doping, with dominant transitions from N 2p_π → Ti d_{xy} rather than from O 2p_π as in TiO₂. However, the calculated band gap energies were considerably underestimated relative to the experimental value (e.g., E_{bg} = 2.0 eV versus 3.2 eV for anatase) attributed, in part, to the well-known shortcomings of the LDA approach. The underestimated band gap was corrected using a scissors operator (a sort of fudge factor) that displaces the empty and occupied bands relative to each other by a rigid shift of 1.14 eV to bring the minimum band gap in line with experiment for the band gap of anatase TiO₂ (corrected E_{bg} = 3.14 eV). Accordingly, the band gaps of N-doped TiO_{2-x}N_x systems were also adjusted by the factor 1.14 eV [4] on the assumption that the underestimated energy of the band gap in the LDA approach is not affected by N-doping because long-range screening properties in TiO_{2-x}N_x were likely similar to those in TiO₂.

The picture as to the exact cause of the red-shift of the absorption edge of TiO₂ in various N-doped TiO₂ (anatase) powders becomes somewhat confused with the report from Yates group [30] that the absorption edge of a N-doped TiO₂ rutile single crystal shifts to higher energy by 0.20 eV. Spin-polarized density functional theory (DFT) calculations within the GGA approximation by Di Valentin and coworkers [47] showed that whereas in anatase the localized N 2p

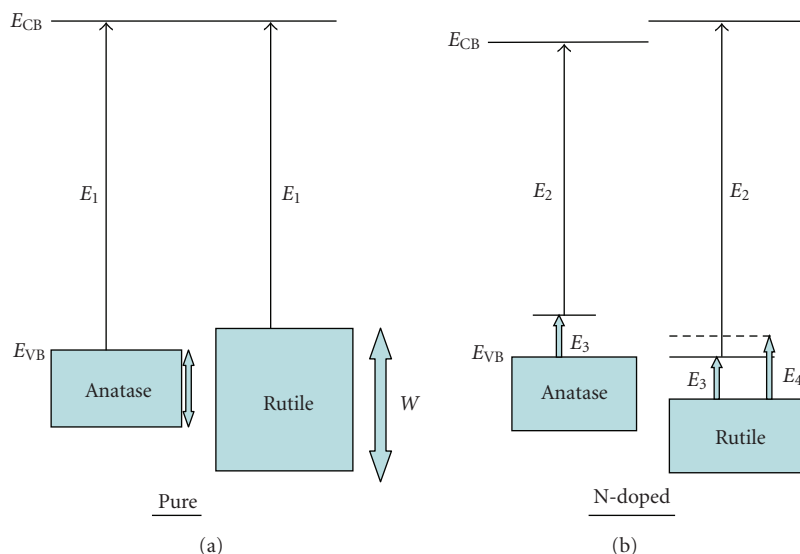
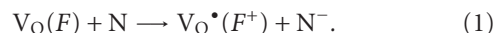


FIGURE 4: Schematic representation of the energy band structure of pure and N-doped anatase and rutile (energies not to scale). Note the modest shift of 0.03 eV in E_C of the conduction band to higher energies and the contraction energy E_4 in the N-doped rutile TiO_2 . E_3 represents the energy of the N dopant levels above the valence band. Higher levels of doping, for example, three N atoms per supercell, cause a small shift of ~ 0.05 eV to higher energies for E_C which is overcompensated by the presence of N-derived states just above VB, so that the excitation energy E_2 from these states to the conduction band is reduced by < 0.1 eV compared to pure anatase (W denotes the width of the valence bands). Adapted from results reported in [47].

states, located just above the O 2p states of the valence band, red-shift the absorption edge to lower energy, in rutile the tendency to red-shift the absorption edge is offset by a concomitant contraction of the O 2p valence band resulting in an overall increase in the optical transition energy by ca. 0.08 eV. Compared to anatase, rutile has a wider (W) O 2p band due to both its higher density and its different structure (see Figure 4). In this work [47], N-doping was modeled by replacing 1, 2, or 3 oxygen atoms in a 96-atom anatase supercell and 1 or 2 oxygen atoms in a 72-atom rutile supercell giving a stoichiometry comparable to that used in experiments for $\text{TiO}_{2-x}\text{N}_x$: $0.031 < x < 0.094$ for anatase and $0.042 < x < 0.084$ for rutile. Note that Asahi et al. [4, 46] used a higher level of N-doping, which yielded a stoichiometry of $\text{TiO}_{1.875}\text{N}_{0.125}$. Inclusion of more N atoms in the same supercell yielded more accurate results than using smaller supercells. Nonetheless, calculated band gaps [47] were still underestimated at 2.19 eV and 1.81 eV (at the Γ position) versus the experimental 3.2 eV and 3.0 eV, respectively, for pure undoped anatase and rutile TiO_2 , again because of the shortcomings of the DFT method. Analysis of the electronic energy levels (see Figure 4) shows that N-doping causes no shift of the position of both top and bottom of the O 2p VB band and of the CB band relative to pure undoped anatase TiO_2 , in significant contrast with the conclusions of Asahi and coworkers [4, 46] with respect to the undoped material. Structural variations in rutile TiO_2 subsequent to substitution of one O atom with N in the 72-atom supercell appear significant in rutile relative to anatase in which the variations were inconsequential. In any case, the N impurity states can act as deep electron traps in $\text{TiO}_{2-x}\text{N}_x$ systems (see Figure 4). Di Valentin et al. [47] also considered the contribution of

oxygen vacancies (V_{O}), estimated experimentally at 0.75 to 1.18 eV below the conduction band E_C (DFT calculations placed them at 0.3 eV below E_C), to the overall visible-light photoactivity of N-doped systems when V_{O} trap electrons to produce F -type color centers. The simultaneous presence of N dopants and V_{O} can also lead to charge transfer states (reaction 1) that can further contribute to the visible-light photoactivity,



In a later study that combined experiments (EPR, XPS) and DFT calculations performed using the plane-wave-pseudopotential approach, together with the Perdew-Burke-Ernzerhof (PBE) exchange correlation functional and ultrasoft pseudo-potentials, Di Valentin and coworkers [48] characterized the paramagnetic species present in N-doped anatase TiO_2 powders obtained by sol-gel synthesis, and unraveled some of the mechanistic details of the visible-light activity of N-doped TiO_2 as to whether photoactivity is due to NO_x or NH_x species or simply to substitutional N-doping. The $\text{TiO}_{2-x}\text{N}_x$ sample was obtained by hydrolysis of $\text{Ti}(\text{i-PrO})_4$ in isopropanol media in the presence of aqueous NH_4Cl as the N source, followed by calcinations of the N-doped specimen at ca. 500 C for 2 hrs. XPS N 1s spectra showed only a peak at ca. 400 eV attributed to interstitial N (without precluding others); no 396 eV peak was seen that might have originated from substitutional N-doping. EPR spectra indicated the presence of two different paramagnetic species that were attributed to substitutional and interstitial N species. These results led them to consider two structurally different locations for the N dopant in their DFT calculations: substitutional N(N_s) and interstitial N(N_i) atoms in

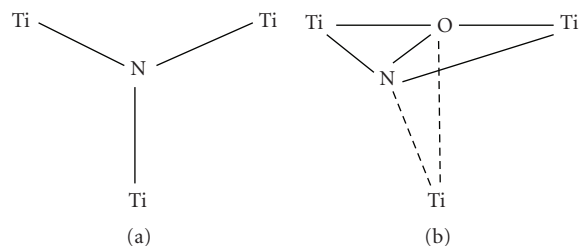


FIGURE 5

the TiO_2 anatase matrix. In the substitutional model, the N that replaces O in the TiO_2 lattice was taken to be bonded to three Ti atoms in the 96-atom supercell (a) so that the paramagnetic species is formally N^{2-} , whereas in the interstitial model N is added to the 96-atom supercell bonded to one or more O and thus is in a positive oxidation state as in NO^- , NO_2^- and/or NO_3^- (b) (see Figure 5). Figure 6 illustrates the DFT band structure of the N-doped TiO_2 and reports the calculated albeit still underestimated band gap energy of titania. The two bonding π states in Figure 6(b) for NO lie deep below the O 2p band but the two π^* still occupied states lie above (0.73 eV) the O 2p band and lie at higher energy than the 2p states of substitutional N (0.14 eV). A more interesting consequence of the picture of Figure 6 is that the two electrons left in the formation of an oxygen vacancy, which typically would form two Ti^{3+} color centers, may also be trapped by substitutional N_S and interstitial N_I yielding the azide species (N^{3-} denoted as N_S^-) and the hyponitrite species (NO^-). Another significant result deriving from the DFT calculations of Di Valentin and coworkers [48] is that N-doping leads to a substantially reduced energy of formation of V_OS (4.3 eV to 0.6 eV for anatase) with important consequences in the generation of F-type and Ti^{3+} color centers. Experimentally, which of the two types of N dopants predominates in the N-doped TiO_2 will depend on the experimental conditions, for example, nitrogen and oxygen concentrations, and calcination temperatures. What Figure 6 also implies is that moving from substitutional N to interstitial N is in fact an oxidative step, which according to DFT estimates is ca. 0.8 eV exothermic. Thus, there is a cost for the reverse, that is, interstitial N-doping is preferred when $\text{TiO}_{2-x}\text{N}_x$ systems are prepared in excess nitrogen and oxygen, whereas high-temperature calcination of N-doped systems, commonly done in most experiments, both substitutional N and formation of oxygen vacancies V_OS are likely the preferred occurrences.

The question on the blue-shift of the absorption edge of N-doped TiO_2 rutile single crystals contrasting the red-shifts in N-doped TiO_2 powders was also taken up in a DFT study by Yang and coworkers [49] using the plane-wave method. Results confirmed those of Di Valentin et al. [47] that some N 2p states lay above the O 2p valence band when N substitutes O in the TiO_2 lattice and when N is located at interstitial positions. However, *no band gap narrowing* was predicted by the calculations of Yang et al. [49]. When N substitutes Ti atoms in the rutile lattice, a band gap narrowing in the rutile crystal is apparently possible because the N dopant introduces some

energy states (the N 2p states) into the bottom of the conduction band [49]. The authors rationalized this inference by the fact that removal of electrons from the supercell on replacing one Ti with a N atom leads to a reduction of the Coulomb repulsion and thus to a shift of the energy band edges, that is, the band gap energy is reduced by ca. 0.25 eV relative to the undoped rutile supercell whose estimated band gap energy was calculated to be 1.88 eV. This is reminiscent of the assertion by Asahi et al. [4, 46] that N-doping TiO_2 causes band gap narrowing because the N 2p states mix with the O 2p states in the valence band, thereby widening the valence band and shrinking the band gap.

Substitutional N-doping can be stabilized by the presence of oxygen vacancies ($\text{N}_\text{S}\text{-O} + \text{V}_\text{O}$) under oxygen-poor experimental conditions, whereas under oxygen-rich conditions interstitial N species (N_I) become favored. The N-doped sample prepared by the sol-gel process of stoichiometry near $\text{TiO}_{1.907}\text{N}_{0.062}$, examined earlier by Di Valentin and coworkers [48], was re-examined more closely by Livraghi et al. [50] in a series of experiments and DFT calculations aimed at determining the fate of the doped specimen when irradiated at different wavelengths in the presence of adsorbates. The experiments asserted that N species were responsible for the absorption of visible-light radiation, and consequently for the visible-light activity, as well as for the photoinduced electron transfer from the solid to surface electron scavengers (adsorbates) such as molecular O_2 . The UV-visible diffuse reflectance spectrum of the sample (see Figure 7) is nearly identical to the many reported DRS spectra of N-doped TiO_2 specimens prepared in a variety of ways. However, as we will see below, this spectral behavior is identical to the spectral behavior of so many other doped TiO_2 samples that have been doped with different types of dopants (e.g., transition metal ions, C, S, and others) and synthesized by different methods. Previous EPR work (Di Valentin et al. [48]) had identified two distinct N-related paramagnetic species in N-doped TiO_2 , one of which was the molecular NO radical [51] located in closed pores within the crystals and thus had no influence on the electronic structure of the solid. No evidence of NH_x -type paramagnetic species was found as had been reported by Yates' group [31, 32]. Whatever the nature of the paramagnetic species, it was stable to washing and to calcination in air up to ca. 500 C. This was taken to mean that the nitrogen radical species, identified as $\text{N}_\text{b}^\bullet$ in Figure 8 interact strongly with the TiO_2 lattice. DFT calculations carried out on the 96-atom supercell involved two interstitial nitrogens ($\text{N}_\text{I}^\bullet$) or two substitutional nitrogen ($\text{N}_\text{S}^\bullet$) paramagnetic species plus an oxygen vacancy (V_O) located far away from these N-centers to avoid direct defect/impurity interactions. Note that removal of an O atom from the TiO_2 lattice leaves behind two electrons to form the *neutral* Fcenter (V_O in the Kroger-Vink notation), or they may be trapped by neighboring Ti^{4+} species to give two Ti^{3+} color centers, which Henderson et al. [52] positioned at 0.8 eV below the bottom of the conduction band. Other studies indicated otherwise, although there are electron traps around this energy. Ti^{3+} color centers certainly do exist as demonstrated by EPR measurements [53, 54]. One of the consequences of the high number of V_OS under oxygen-poor conditions in N-doped

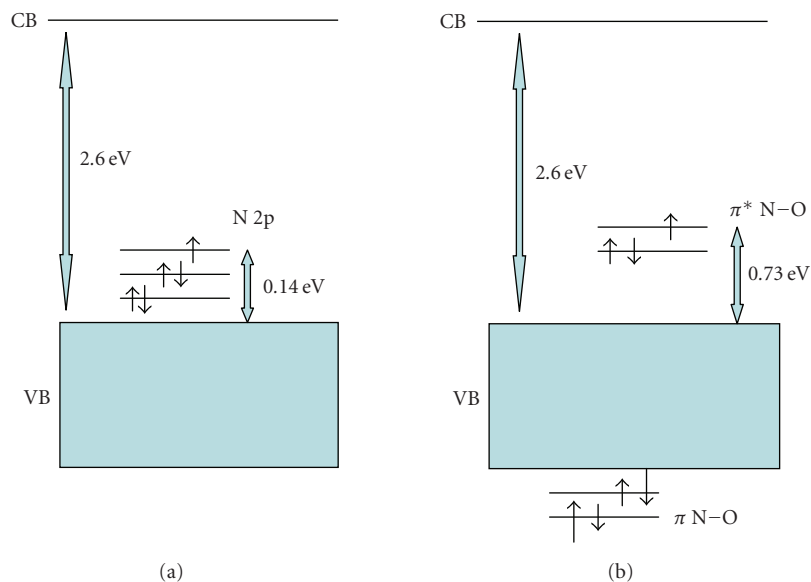


FIGURE 6: Electronic band structure for (a) substitutional and (b) interstitial N-doped anatase TiO_2 as given by PBE calculations at a low-symmetry k -point. In the former, the site contains the paramagnetic N^{2-} species making the site electrically neutral (replaced O^{2-}), whereas in the latter the site is occupied by the radical NO . The estimated band gap energy is also indicated. Reproduced with permission from [48]. Copyright (2005) American Chemical Society.

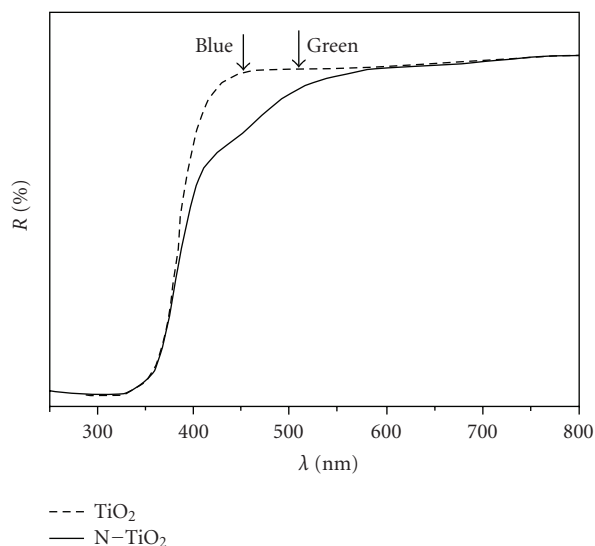


FIGURE 7: UV-visible diffuse reflectance spectra of undoped and N-doped TiO_2 . Reproduced with permission from [50]. Copyright (2006) American Chemical Society.

TiO_2 is the partial quenching of N_b^\bullet paramagnetic species, which are transformed [48] into N_b^- through reduction by Ti^{3+} color centers (see Figure 8). The energetically favored reduction of N_b^\bullet species may be the cause for the small energy cost in the formation of V_{O} in N-doped TiO_2 (see above). The EPR peaks attributed to N_b^\bullet centers disappeared on reduction of the sample (reaction (2)) whether by annealing in

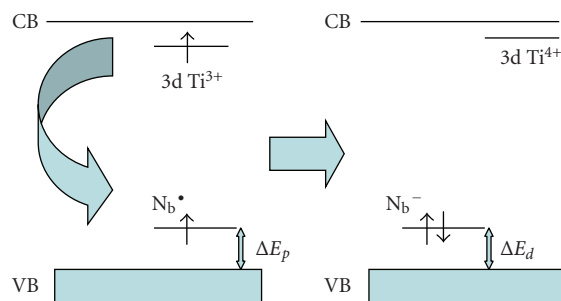
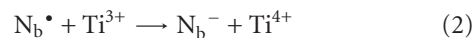


FIGURE 8: Electronic band structure changes from interactions between N_b^\bullet (N_s^\bullet or N_i^\bullet) and Ti^{3+} color centers. Reproduced with permission from [50]. Copyright (2006) American Chemical Society.

vacuo or by other means to then reappear on re-oxidation. Thus, the N-doped TiO_2 specimen (at least the one prepared



by the sol-gel method) contained paramagnetic N related species in the bulk lattice (N_b^\bullet) and a number of diamagnetic species (N_b^-), the presence of which depended on the oxygen content in the metal-oxide sample. The EPR signal due to N_b^\bullet increased on irradiating the doped sample at 437 nm in O_2 ($p_{\text{O}_2} = 5 \text{ kPa}$). A new EPR line appeared that was attributed to $\text{O}_2^{\bullet-}$ radical anions (reactions (3) and (4)). These anions are apparently stabilized on two different surface Ti^{4+} species, which Livraghi et al. [50] claimed could be typical of N-doped TiO_2 . Figure 9 illustrates the process embodied in the formation of the superoxide radical

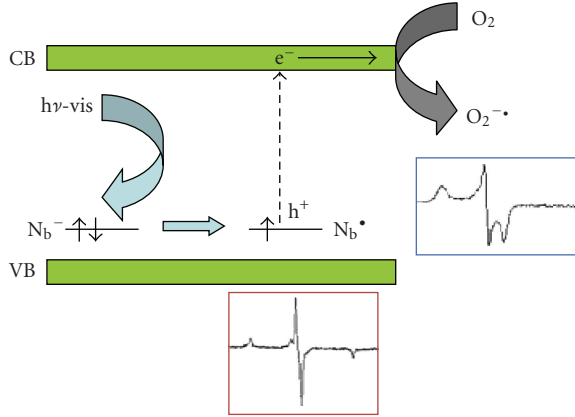
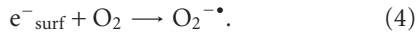
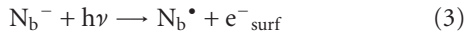


FIGURE 9: Sketch of the proposed mechanism for the processes induced by vis-light irradiation of the N-doped sample in O_2 atmosphere. Reproduced with permission from [50]. Copyright (2006) American Chemical Society.

anions



So far all the DFT-based calculations *have failed* to calculate experimentally commensurate band gap energies for undoped anatase and rutile TiO_2 , and consequently for all anion-doped TiO_2 systems unless, as some have done, one resorts to the scissor operator. In a comprehensive theoretical investigation of substitutional anion doping in TiO_2 , Wang and Lewis [55] explored the electronic properties of C-, N-, and S-doped TiO_2 materials using an *ab initio* tight-binding method (FIREBALL) based on density functional theory and a nonlocal pseudopotential scheme. The method uses confined atomic-like orbitals as the basis set, which led to a calculated direct band gap from Γ to Γ of 3.05 eV for rutile that accords with the experimental band gap of 3.06 eV [56]. The local density approximation (LDA) approach generally underestimates the experimental band gap for insulators and semiconductors; *ab initio* plane-wave calculations for TiO_2 also place the band gap at around 2.0 eV [57]. In their theoretical treatment, Wang and Lewis [55] compensated for the underestimation by the LDA approach. For anatase, the direct band gap from Γ to Γ of 3.26 eV accords with the experimentally observed 3.20 eV [58]—see Table 1. The upper valence bands are composed mainly of O 2p states, whereas the lower conduction bands consist primarily of unoccupied Ti 3d states.

In the computations of Wang and Lewis [55], two O atoms were replaced by one N because of the odd number of electrons in the N atom to yield an effective N-doping level of 0.52% in the low concentration case. The CB minimum remained unchanged. However, new states were introduced by N-doping just above the valence band edge of bulk TiO_2 , as well as states that penetrated into the upper valence band of the bulk states. No significant energy shift (<0.05 eV) in the VB edge was seen in N-doped *rutile* TiO_2 at the high N content of 5.2%, contrary to the significant shift observed for

TABLE 1: Comparison of calculated band gaps of undoped rutile and anatase TiO_2 with experimental and calculated values reported by others (E_{BG} is the direct band gap). From Wang and Lewis [55].

| Source | E_{BG} (rutile), eV | E_{BG} (anatase), eV |
|----------------|-----------------------|------------------------|
| Wang and Lewis | 3.05 | 3.26 |
| Experiments | 3.06 [56] | 3.20 [58], 3.42 [59] |
| Other calcns | 2.00 [57], 1.78 [60] | 2.22 [60], 2.00 [46] |

the low N-doping level of 0.52% which gave a narrowed band gap of 2.55 eV. Density-of states (DOS) calculations thus inferred that low doping N levels greatly improve the visible-light photoactivity. No significant overlap occurred between the N 2p states and the O 2p states for the 0.52%N-doping level. Moreover, at the low N concentration the valence band edge was more localized compared to the high N-doping level in N-doped *rutile* TiO_2 . Unlike N-doped *rutile* TiO_2 , however, identical shifts of ca. 0.44 eV were obtained in N-doped *anatase* TiO_2 at both high and low doping levels resulting in a band gap of ca. 2.82 eV (440 nm). DOS calculations indicated significant overlap between the N 2p states and O 2p states for the 5.2% N-doping. By contrast, at the low N-doping level of 0.52% N, the states introduced by N were distinct, highly localized on the single dopant state, and there was no significant overlap. A result of this is that the high N-doping level in N-doped *anatase* TiO_2 would lead to greater visible-light photoactivity.

The brief discussion above points to a lack of consensus on whether or not there is *band gap narrowing* in doped TiO_2 materials based on DFT calculations. Some of the theoretical studies have deduced from these calculations that there is a *rigid shift of the valence band edge* to higher energies, thus narrowing the *intrinsic band gap* of TiO_2 as a consequence of doping. The discrepancies cannot be attributed to a simple semantic problem. Experimentally, anion-doping and cation-doping of TiO_2 do red-shift the *absorption edge* of TiO_2 in the doped samples, thus yielding potentially visible-light photoactive materials that might prove useful in several important applications of surface processes occurring on the TiO_2 surface. In the past, we have referred to the longest visible-light wavelength at which photoactivity is seen as the *red limit of photocatalysis*. We wish to emphasize, however, that what does change is the lowest photo-threshold (i.e., *extrinsic* absorption edge) of the actinic light that can activate TiO_2 by introducing dopants into the metal-oxide lattice. When a N-doped TiO_2 system is photoactivated by visible light absorption, it also generates electrons and holes, although the latter carriers will have a decreased oxidative power (lower redox potential) *vis-a-vis* holes photogenerated from pristine TiO_2 (see, e.g., Figure 3). The *intrinsic* absorption edge of the metal oxide itself is not changed by the doping. In other words, the valence and conduction bands are not affected by the doping, *at least* at low doping levels and weak interactions. But if they were to be affected through strong coupling interactions between the dopant states and the O 2p states of the VB of TiO_2 , as some have surmised by DFT calculations, then we must face the inescapable conclusion that the material is no longer TiO_2 , but is some titanium

oxynitride material (for N-doped TiO_2) that possesses entirely different properties, not least of which are new electronic structures of their respective valence and conduction bands. In this regard, a recent study by Kim and coworkers [61] has demonstrated that a solid solution prepared from ZnO and ZnS, which could be referred to as S-doped $\text{ZnO}(\text{ZnO}_x\text{S}_{1-x})$ displays an absorption edge in the visible spectral region at 2.4 eV *vis-à-vis* the absorption edges of both ZnO (3.1 eV) and ZnS (3.5 eV). The XRD patterns indicated a new material, namely a zincoxysulfide phase, whose band gap is 2.4 eV, much narrower than either of the band gaps of the two initial substrates owing to strong coupling of the S 2p states with the O 2p states in the valence band of the *new* material. Note that in all the doped TiO_2 systems, XRD patterns showed that the doped TiO_2 retained the anatase (or rutile) structure; no new phase or new material could be ascertained.

4. OPTICAL PROPERTIES OF N-DOPED TiO_2

An examination of the optical properties of doped TiO_2 provides evidence based on the photobleaching phenomenon that the absorption bands observed in the visible spectral region for (any) doped TiO_2 material can be bleached. That is, the species that give rise to or that are responsible for the absorption bands in the visible spectral region of doped TiO_2 can be destroyed by irradiating with visible-light wavelengths corresponding to the absorption bands in the visible spectral region, or by a heat treatment. Under these conditions, it is important to recognize that neither the *intrinsic* VB nor the *intrinsic* CB can be destroyed.

Optical properties of doped TiO_2 specimens can be discussed in terms of difference diffuse reflectance spectra (ΔDRS) calculated from the DRS of various doped TiO_2 samples absorbing in the visible region [$\rho_{\text{abs}}(h\nu)$] and undoped TiO_2 samples that do not absorb in the visible spectral region [$\rho_{\text{non-abs}}(h\nu)$]. The latter is typically the DRS of a nominally clean TiO_2 sample or the DRS of the doped sample *prior* to any treatment that might induce visible-light absorption [62]. Where the transmittance spectrum of a thick sample is 0, the change in reflectance $\Delta\rho(h\nu)$, that is, [$\rho_{\text{non-abs}}(h\nu) - \rho_{\text{abs}}(h\nu)$] is then identical to the change in absorbance $\Delta A(h\nu)$. Moreover, where optical properties of doped specimens are characterized by absorption spectra $A(h\nu)$, the difference absorption spectra $\Delta A(h\nu)$ can be calculated in a manner similar to the difference DRS spectra, $\Delta\rho(h\nu)$. Usage of difference diffuse reflectance and/or difference absorption spectra provides a means for numerical analysis of the optical characteristics of the samples. The analysis typically involves (i) the characterization of each absorption spectrum by the position of the spectral maximum ($h\nu_{\text{max}}$), the intensity of this maximum ($\Delta\rho_{\text{max}}$, ΔA_{max}), and the spectral bandwidth at half-maximum amplitude, (ii) the comparison of the spectra of different samples after normalization by the $\Delta\rho_{\text{max}}/\Delta A_{\text{max}}$ factor, and (iii) the analysis of the shape of the absorption spectra to display the spectra as a sum of individual absorption bands.

Resulting absorption spectra of various nondoped TiO_2 specimens displaying maximal absorption around 3.0 eV and

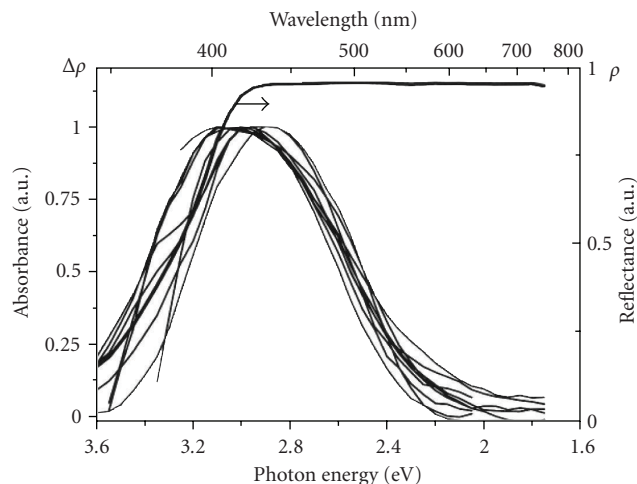


FIGURE 10: Absorption spectra of various anion-doped TiO_2 specimens before averaging (see text) and the diffuse reflectance spectrum (DRS) of Degussa P25 TiO_2 .

shown in Figure 10 are those of (i) mechanochemically activated N-doped TiO_2 [17], (ii) N-doped oxygen-deficient TiO_2 [13], (iii) N,F-codoped TiO_2 sample prepared by a spray pyrolytic method [63], (iv) N-doped *anatase* TiO_2 specimen prepared by a solvothermal process [37], (v) N-doped *rutile* TiO_2 sample also prepared by a solvothermal process [37], (vi) *yellow* N-doped TiO_2 specimen synthesized in short time at ambient temperatures using a nanoscale exclusive direct nitridation of TiO_2 nanocolloids with alkyl ammonium compounds [19, 20], (vii, viii) N-doped TiO_2 samples prepared by evaporation of the sol-gel with N-doping carried out under a stream of ammonia gas at different temperatures [40], and (ix) N-doped TiO_2 prepared via sol-gel by mixing a solution of titanium (IV) isopropoxide in isopropyl alcohol in the presence of an NH_4Cl solution [50].

Temperature and time of calcination are frequently reported as factors that affect the shape of the absorption spectra. For instance, an increase of temperature from 247 C to 347 C for 2 hrs [64], or prolonging the time of calcination from 5 min to 30 min at 400 C [40], decreased the absorption in the range $h\nu < 2.0$ eV, such that the absorption spectra then adopted a narrower shape. As an example, the broad absorption spectrum of the *orange* N-doped TiO_2 specimen, prepared in nearly the same manner as the *yellow* N-doped TiO_2 sample by Gole et al. [19, 20], showed a shoulder on the high-energy side at ca. 2.5 eV (see Figure 12, curve 3 below). Surprisingly, Figure 10 demonstrates a strong similarity between selected spectra in the visible region at energies $h\nu < 3.0$ eV, and noticeable differences in the range of *intrinsic* absorption at $h\nu > 3.0$ eV. Such differences are not surprising since the samples differed in phase composition (see, e.g., [37]) and sample thickness. Moreover, some workers often choose any available sample, for example, Degussa P25 TiO_2 , as the nonabsorbing specimen in the visible spectral region, rather than a specimen prepared in an otherwise identical fashion as the doped samples. Spectral similarities in Figure 10 afford averaging the spectra to obtain the mean

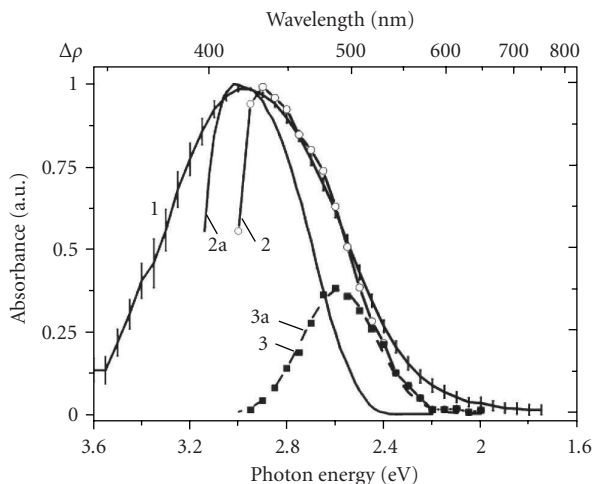


FIGURE 11: Average absorption spectrum of visible-light-active N-doped TiO_2 specimens (curve 1); difference absorption spectra of N-doped rutile crystal (curve 2) and of the color centers in the yellow anatase TiO_2 crystal (curve 2a). Curve 3 (solid squares) depicts the difference between curves 2 and 2a; curve 3a (line) is the Gaussian fit of curve 3 (see text for more details).

spectrum of visible-light-active N-doped TiO_2 samples illustrated in Figure 11 (curve 1; standard error of the mean spectrum was less than 2.3% at $h\nu < 3.0$ eV). Figure 11 also displays the absorption spectrum of the N-doped TiO_2 rutile crystal prepared by an NH_3 treatment at 597 C (curve 2) [21] and the absorption spectrum of the anatase crystal (curve 2a) reported by Sekiya and coworkers [65, 66].

The difference in spectra 2 and 2a in the region $h\nu > 3.0$ eV originates from the difference in the phase composition of the TiO_2 , whereas the difference between curves 2a and 2 at $h\nu < 3.0$ eV exhibits a single absorption band with $h\nu_{\text{max}} = 2.6$ eV, half-width of 0.35 eV and a near-Gaussian shape, that is, the band is very similar to the 2.55-eV AB2 band reported earlier by Kuznetsov and Serpone [62]. Sekiya and coworkers [65, 66] attributed the 3.0-eV band in the spectrum of anatase to oxygen vacancies that can trap electrons to yield *F*-type centers [66]. It should be emphasized that the AB1 absorption band with $h\nu_{\text{max}}$ at 3.0 eV can be obtained in a variety of ways: (i) by annealing the *as-grown* crystals under an oxygen atmosphere at $T > 374$ C [65, 66], and (ii) by annealing *colorless* crystals by subjecting them first to a reductive H_2 atmosphere at 647 C and then to an O_2 atmosphere at 497 C [66]. In both cases, only prolonged (ca. 60 hrs) annealing of the crystals at 797 C in an O_2 atmosphere (not inert or nitrogen atmosphere) transformed the yellow crystals displaying a band at 3.0 eV to a colorless state [66]. The origin of oxygen vacancies is associated with an uncontrolled reduction of TiO_2 assisted by impurities introduced into the crystal during its growth [65]. Absorption of N-doped rutile crystals in the visible spectral region is only partially associated with reduction of the TiO_2 bulk lattice [32]. According to Yates and coworkers [31–33] the red-shift in the photochemical threshold from 3.0 eV to 2.4 eV originates from the N dopant located in an interstitial site and

probably bonded to hydrogen. This suggestion contrasts the interpretation given by Sekiya and coworkers for the spectral features in the visible region [65, 66], by Di Valentin et al. from their EPR study [48], and with our assignments of absorption bands in the visible spectral region of various titania/polymer compositions [62].

The remarkable similarities in the absorption spectra of doped TiO_2 systems are displayed in Figure 12 as averaged spectra. Curve 1 depicts the average spectrum obtained from the absorption spectra (see [62] for details) of (i) Cr-implanted TiO_2 , (ii) Ce-doped TiO_2 , (iii) mechanochemically activated N-doped TiO_2 , (iv) N-doped oxygen-deficient TiO_2 , and (v) from $\text{Sr}_{0.95}\text{La}_{0.05}\text{TiO}_{3+\delta}$ treated with HNO_3 acid. Curve 2 represents the average spectrum obtained from the difference DRS's (absorption spectra) of various anion-doped titania specimens: (i) N,F-codoped TiO_2 , (ii) N-doped anatase TiO_2 , (iii) N-doped rutile TiO_2 , and (iv) yellow nitrided $\text{TiO}_{2-x}\text{N}_x$ nanocolloids. Curve 3 illustrates the averaged spectra of cation-doped TiO_2 , namely (i) Fe-doped TiO_2 nano-powders prepared by oxidative pyrolysis of organometallic precursors in an induction thermal plasma reactor, (ii) zinc-ferritedoped titania ($\text{TiO}_2/\text{ZnFe}_2\text{O}_4$) synthesized by sol-gel methods followed by calcinations at various temperatures, and (iii) the orange N-doped TiO_2 sample prepared by a procedure otherwise identical to that of yellow N-doped TiO_2 but with the former consisting of partially agglomerated nanocolloids (i.e., larger $\text{TiO}_{2-x}\text{N}_x$ clusters). Note the remarkable overlap of the relatively narrow average spectra 1 and 2 in Figure 12, which illustrates convincingly the independence of the spectra on the method of photocatalyst preparation. Such overlap features can only result from electronic and spectral features of color centers/defects in TiO_2 . Comparison of the broader mean spectrum 3 in Figure 12 with the narrower spectra 1 and 2 shows that broadening of the absorption spectrum of TiO_2 photocatalysts originates from the long-wavelength AB2 absorption band at 2.55 eV [62].

The remarkable coincidence of the absorption bands in the visible spectra of reduced TiO_2 with those of visible-light-active TiO_2 s infers that processes involved in the preparation of visible-light-active TiO_2 specimens (irrespective of the method) likely implicate a stage of TiO_2 reduction. Indeed, most of the syntheses included a heating stage at various temperatures. For example, the 3.0 eV absorption band of anatase crystals attributed to oxygen vacancies results from the removal of impurities introduced during the crystal growth at ca. 300 C [65]. Related to this, the visible-light absorption of metal-ion-implanted TiO_2 s was observed only after the samples had been calcined in the temperature range 450–550 C [2]. Accordingly, the absorption features displayed by TiO_2 specimens in the visible spectral region likely originate from the formation of color centers by reduction of TiO_2 after some form of heat treatment or some photostimulated process. Kuznetsov and Serpone [62] concluded that the visible absorption spectra of anion-doped (or otherwise) TiO_2 originated from color centers, and not from the narrowing of the intrinsic band gap of TiO_2 ($E_{\text{bg}} = 3.2$ eV; anatase), as originally proposed by Asahi et al. [4, 46] through mixing of oxygen and dopant states. True narrowing

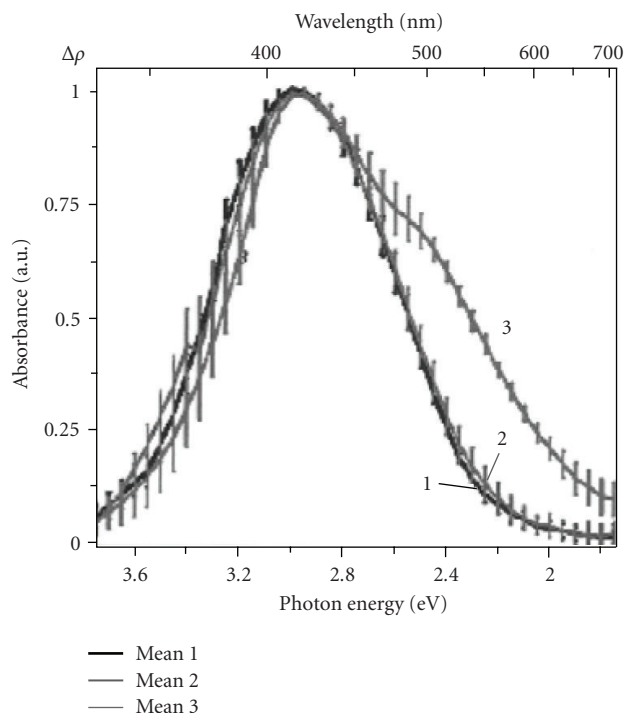


FIGURE 12: Average absorption spectra ($\Delta\rho$) of various titania systems. See text for details of the origins of these spectra. Reproduced with permission from [62]. Copyright (2006) American Chemical Society.

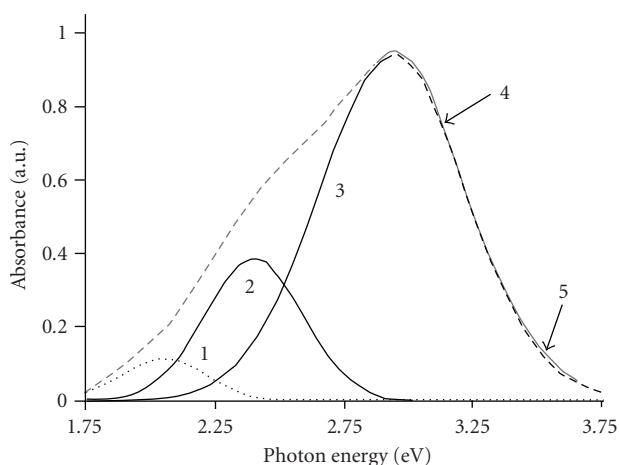
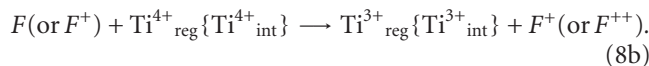
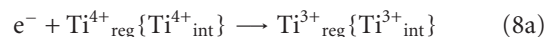
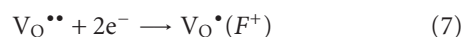
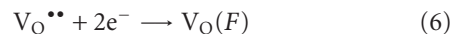
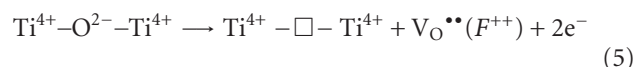


FIGURE 13: Deconvolution of spectrum 3 of Figure 12 (curve 5 herein). Band 4 represents the convolution sum of curves 1, 2, and 3. Reproduced with permission from [67]. Copyright (2006) American Chemical Society.

of the intrinsic band gap of a metal oxide such as TiO_2 would necessitate heavy anion or cation doping at high concentrations of dopants. In such case, however, one must question whether the metal oxide retains its original integrity. We think not as exemplified from the recent reported case of the zincoxysulfide [61].

The next question regards the nature of these color centers. Loss of an O atom in a metal oxide (reaction (5)), leaves behind an electron pair that is trapped in the V_O cavity (reaction (6)) giving rise to an F center; an F^+ center is equivalent to a single electron trapped in the oxygen vacancy, V_O^\bullet (reaction (7); Kroger-Vink notation). The electron-pair deficient oxygen vacancy, $V_O^{\bullet\bullet}$, also known as an anion vacancy, V_A , is a doubly charged F^{++} center (reaction (5)). Thus, color centers associated with oxygen vacancies imply F -type centers in TiO_2 and other metal oxides. In addition, electrons can also be trapped by Ti^{4+} ions in regular lattice sites ($\text{Ti}_{\text{reg}}^{4+}$) adjacent to V_O or in interstitial lattice sites ($\text{Ti}_{\text{int}}^{4+}$) to give $\text{Ti}_{\text{reg}}^{3+}$ and $\text{Ti}_{\text{int}}^{3+}$ color centers, respectively (reactions (8a)); F -type centers can also generate Ti^{3+} color centers through charge transfer (reaction (8b)),



Spectrum 3 of Figure 12 consists of three overlapping bands depicted in Figure 13 [67], one of which is centered at 2.1 eV (590 nm; band 1), another at ca. 2.40 eV (517 nm; band 2), and band 3 occurs around 2.93 eV (413 nm) in accord with band positions reported earlier by Kuznetsov and Serpone [62] for reduction of TiO_2 in polymeric media. The congruence of the bands in the absorption spectra of such disparate TiO_2 systems is remarkable when considering the large variations in the experimental conditions. This lends credence to the notion that the absorption bands likely share the same origins, namely electron transitions involving F -type centers and/or d-d transitions in Ti^{3+} color centers. Evidence for both has appeared in the literature (see references in [67]).

Using the embedded-cluster numerical discrete variational method, Chen et al. [68] estimated the band gap energy of rutile TiO_2 as 3.05 eV in good agreement with the experimental 3.0 eV for this polymorph. Calculations of energy levels of F -type centers gave energies for the F , F^+ and F^{2+} centers, respectively, of 0.87 eV, 1.78 eV and 0.20 eV below the bottom level of the CB band (see Figure 14). The band at 760 nm (1.61 eV) was ascribed to the electron transition $F^+ \rightarrow \text{CB}$ of TiO_2 .

Photoinduced detrapping of electrons from the F center to the conduction band followed by retrapping by the shallow F^{2+} centers can increase the number of F^+ centers. The deconvoluted bands 3 and 2 of Figure 13 at 2.9–3.0 eV (428–413 nm) and 2.4–2.6 eV (ca. 517–477 nm), respectively, have been attributed [67] to Jahn-Teller split ${}^2T_2 \rightarrow {}^2E$ transitions of Ti^{3+} centers. Existence of these centers has been confirmed by EPR examination of N-doped TiO_2 specimens calcined at various temperatures [40, 69]. Band 1 at 1.7–2.1 eV (729–590 nm) is likely due to the transition $F^+ \rightarrow F^{+*}$,

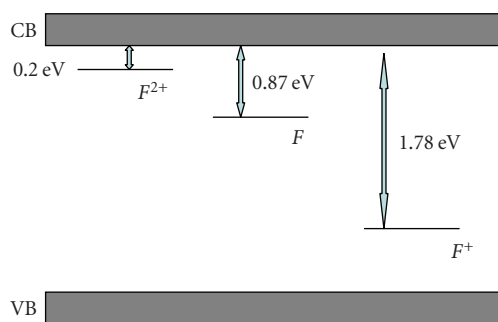


FIGURE 14

though the transition $F^+ \rightarrow \text{CB}$ is not precluded. The transition $S_0(F) \rightarrow S_1(F^*)$ or $S_0(F) \rightarrow \text{CB}$ of the F center likely occur at much lower energies (in the infrared). Rigorous systematic studies are needed to ascertain such assignments in anion- and cation-doped TiO_2 specimens examined by diffuse reflectance spectroscopy; additional EPR and photoconductivity studies should aid in such task.

5. IS THE (INTRINSIC) BAND GAP OF TiO_2 NARROWED IN N-DOPED TiO_2 ?

Taken literally, band gap narrowing in doped TiO_2 materials means that the *intrinsic* band gap energy of TiO_2 decreases in the presence of dopants. We re-emphasize that what does change is the energy phototreshold for activating doped titania specimens to carry out surface photoinduced redox processes. A better term to refer to the red-shift of the absorption edge might be (i) the *red-limit of TiO_2 photocatalysis*, used in the past to refer to redox processes occurring in the visible spectral region or (ii) the *extrinsic band gap(s)* of doped TiO_2 versus the term *intrinsic band gap* which for anatase is 3.2 eV and for rutile is 3.0 eV; the latter refer to pristine undoped titania. The term *band gap narrowing* used by Asahi et al. [4, 46] and others meant a rigid upward shift of the valence band edge toward the conduction band of TiO_2 . If the red-shift of the absorption edge were truly due to this rigid shift, then irradiation into the visible spectral bands of Figure 13 should cause no bleaching of the absorption bands. However, if the absorption features are due to the existence of color centers (F -type and/or Ti^{3+}), then bleaching of the spectral features should occur as observed in our recent studies on TiO_2 /polymer compositions [70] and on a N-doped TiO_2 system [71] that we now examine briefly.

The photocoloration of TiO_2 /polymers compositions and the photobleaching of color centers (see Figure 15) at various irradiation wavelengths (UV to near-IR region) were examined to probe the photoactivation of color centers on irradiating into the absorption bands at 2.90 eV (427 nm; AB1), 2.55 eV (486 nm; AB2) and 2.05 eV (604 nm; AB3). Such exercise should lead to two principal types of photostimulated absorbance changes: (i) increase in absorbance or (ii) decrease in absorbance. The decrease in absorbance (ii) is a direct experimental manifestation of the photobleaching phenomenon of colored TiO_2 /polymer

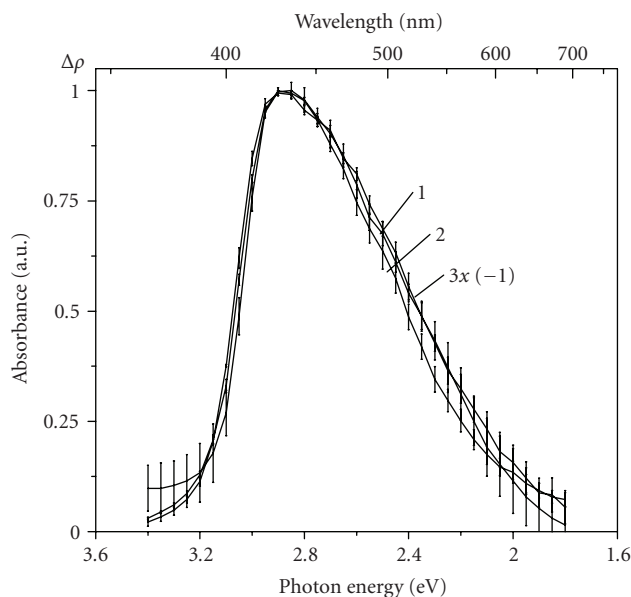


FIGURE 15: Averaged absorption spectra (1, 2) of various TiO_2 /polymer compositions normalized by $\Delta\rho_{\text{max}}$ and averaged bleaching spectrum (3) of the TiO_2 /[P(VDF-HFP)] composition irradiated at different wavelengths. Reproduced with permission from [70]. Copyright (2007) American Chemical Society.

compositions and would clearly demonstrate the presence and photoinduced disappearance/destruction of color centers in such TiO_2 /polymers systems. The average spectrum of the bleaching of the colored TiO_2 /[P(VDF-HFP)] composition {P(VDF-HFP) is poly(vinylidene fluoride/cohexafluoropropylene polymer)} is depicted as curve 3 in Figure 15 and is compared to the average heat-induced absorption spectrum (curve 1) and photoinduced absorption spectrum (curve 2) of several other TiO_2 /polymer compositions [70]. These observations confirm an earlier proposal [62] that absorption of light by various TiO_2 systems in the visible region originates *only* from color centers and *not* from a narrowing of the band gap of pristine TiO_2 . Results also indicate that photobleaching of colored TiO_2 /polymer compositions originates both from *intrinsic* absorption of light ($h\nu > 3.2$ eV, anatase) by TiO_2 and from (*extrinsic*) absorption of light by the color centers at wavelengths corresponding to their absorption spectral bands in the visible region. These bands are also active in the photodestruction of the color centers. Spectrum 3 in Figure 15 corresponds to the nearly complete discoloration of the compositions under irradiation mostly in the visible region. Hence, the total overlap of the absorption and bleaching spectra of Figure 15 demonstrate *unambiguously* that the *same* color centers are formed during the treatment that induced the absorption, and that they are subsequently destroyed on irradiation during the photobleaching process. These data conclusively negate any inference of broadening of the valence band of TiO_2 to account for the red-shifts of the absorption edges in doped visible-light-active TiO_2 systems. The VB and CB bands *can neither* be photodestroyed *nor* phototransformed,

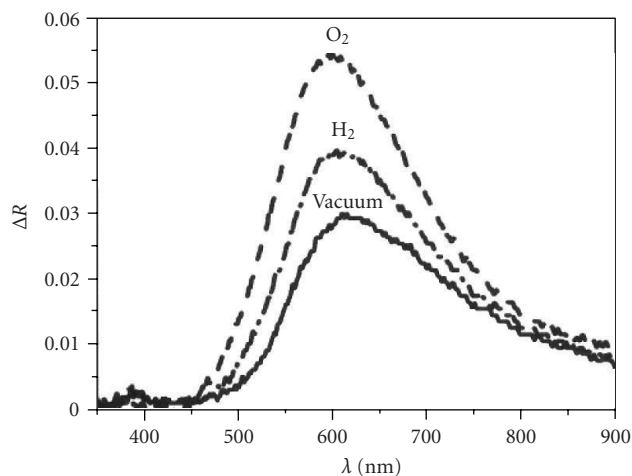


FIGURE 16: Absorption spectra of photoinduced color centers in N-doped TiO_2 obtained after pre-irradiation at 546 nm in vacuum, in the presence of O_2 and H_2 . Reproduced with permission from [71]. Copyright (2007) American Chemical Society.

contrary to the color centers. An additional study [71] examined the effect of molecular oxygen and hydrogen on the photostimulated formation of defects (color centers) on irradiation of $\text{TiO}_{2-x}\text{N}_x$ with visible light (546 nm). Results are displayed in Figure 16 as ΔR versus λ ; note that ΔR and $\Delta\rho$ have the same meaning, namely absorbance. A similar behavior was observed on irradiating at 436 nm and 578 nm. The influence of hydrogen on photocoloration on irradiation at 546 nm is nearly the same as on UV irradiation, in that the number of photoinduced defects increased, contrary to when O_2 is present for which the photoadsorption of O_2 is the exact opposite to that seen under UV irradiation. The ultimate level of photocoloration (increase in absorbance) in the presence of O_2 is considerably greater under 546-nm irradiation relative to the level in vacuum and relative to what is observed under UV irradiation. This inferred the mechanism of photoexcitation and surface photoreaction occurring under visible-light excitation of $\text{TiO}_{2-x}\text{N}_x$ in the presence of O_2 is different from the mechanism of UV-induced processes. Photobleaching of photoinduced color centers by red light at $\lambda > 610$ nm in vacuum and in the presence of oxygen and hydrogen is illustrated in Figure 17. No significant changes in absorption of photoinduced color centers occur during photoexcitation in vacuum and in the presence of H_2 . However, the presence of O_2 causes significant photo-bleaching (negative absorbance) of the UV-induced defects, a typical behavior of electron-type color centers (i.e., F -type and Ti^{3+} centers).

6. CONCLUDING REMARKS

In this survey, we have attempted to expose and explore some of the root causes that have had such impact and so changed the field of Heterogeneous Photocatalysis involving the next generation of TiO_2 photocatalysts. Preparative methods and

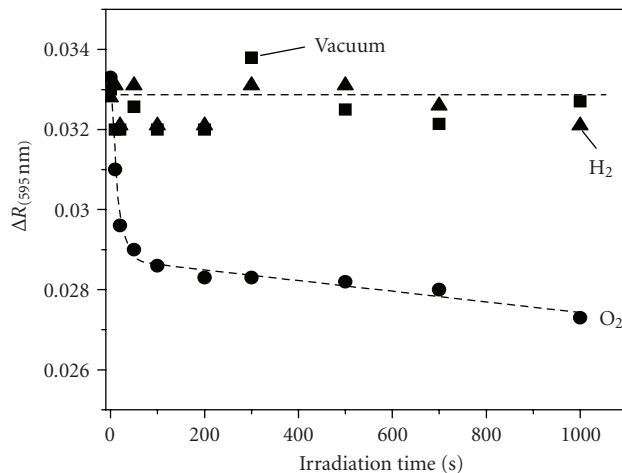


FIGURE 17: Kinetics of photobleaching (recorded at $\lambda = 595$ nm) of photoinduced color centers on irradiation of $\text{TiO}_{2-x}\text{N}_x$ at $\lambda > 610$ nm in vacuum, in the presence of oxygen and in the presence of hydrogen. Reproduced with permission from [71]. Copyright (2007) American Chemical Society.

some characteristic features of N-doped TiO_2 s have been described briefly. At variance are the experimental results and interpretations of X-ray photoelectron spectra with regard to assignments of binding energy peaks. Relative to pristine nominally clean TiO_2 , whose absorption edges are 3.2 eV (anatase) and 3.0 eV (rutile), N-doped TiO_2 specimens display red-shifted absorption edges into the visible spectral region. Several workers have surmised that the (*intrinsic*) band gap of TiO_2 is narrowed by the coupling of dopant energy states with the O 2p states in the VB band, an inference based on DFT computations of band gap energies, which are severely underestimated owing to the inherent faulty local density approximation (LDA). Using similar DFT calculations, others proposed that the red-shifted absorption edges originate from the presence of intragap dopant states above the upper level of the VB band. Analyses of spectral features in the visible region, however, inferred a common origin for the doped TiO_2 as deduced from the strong similarities of absorption features of a large number of TiO_2 specimens, regardless of the preparative methods employed and the nature of the dopants. This next generation of TiO_2 photocatalysts should enhance process engineering photoefficiencies, in some cases, since doped titania absorbs a greater quantity of sunlight radiation. The fundamental science that underscores Heterogeneous Photocatalysis with this new generation of photocatalysts is a rich playing field that is ripe for further exploration, limited only by one's imagination, creativity and resourcefulness.

REFERENCES

- [1] D. Lawless, *Photophysical studies on materials of interest to heterogeneous photocatalysis and to imaging science: CdS quantum dots, doped and undoped ultrasmall semiconductor TiO_2 particles, and silver halides*, Ph.D. thesis, Concordia University, Montreal, Canada, 1993.

- [2] M. Anpo and M. Takeuchi, "The design and development of highly reactive titanium oxide photocatalysts operating under visible light irradiation," *Journal of Catalysis*, vol. 216, no. 1-2, pp. 505–516, 2003.
- [3] S. Sato, "Photocatalytic activity of nitrogen oxide (No_x)-doped titanium dioxide in the visible light region," *Chemical Physics Letters*, vol. 123, pp. 126–128, 1986.
- [4] R. Asahi, T. Morikawa, T. Ohwaki, K. Aoki, and Y. Taga, "Visible-light photocatalysis in nitrogen-doped titanium oxides," *Science*, vol. 293, pp. 269–275, 2001.
- [5] T. Morikawa, R. Asahi, T. Ohwaki, K. Aoki, and Y. Taga, "Band-gap narrowing of titanium dioxide by nitrogen doping," *Japanese Journal of Applied Physics, Part 2: Letters*, vol. 40, no. 6 A, pp. L561–L563, 2001.
- [6] X. Chen and S. S. Mao, "Titanium dioxide nanomaterials: synthesis, properties, modifications and applications," *Chemical Reviews*, vol. 107, no. 7, pp. 2891–2959, 2007.
- [7] X. Chen, Y. Lou, S. Dayal, et al., "Doped semiconductor nanomaterials," *Journal of Nanoscience and Nanotechnology*, vol. 5, no. 9, pp. 1408–1420, 2005.
- [8] N. Serpone, A. V. Emeline, V. N. Kuznetsov, and V. K. Ryabchuk, "Second generation visible-light-active photocatalysts: preparation, optical properties and consequences of dopants on the band gap energy of TiO_2 ," in *Environmentally Benign Catalysts—Applications of Titanium Oxide-Based Photocatalysts*, M. Anpo and P. V. Kamat, Eds., Springer, New York, NY, USA, 2007.
- [9] H. M. Yates, M. G. Nolan, D. W. Sheel, and M. E. Pemble, "The role of nitrogen doping on the development of visible light-induced photocatalytic activity in thin TiO_2 films grown on glass by chemical vapour deposition," *Journal of Photochemistry and Photobiology A: Chemistry*, vol. 179, no. 1-2, pp. 213–223, 2006.
- [10] H. Noda, K. Oikawa, T. Ogata, K. Matsuki, and H. Kamata, "Preparation of titanium(IV) oxides and its characterization," *Bulletin of the Chemical Society of Japan*, pp. 1084–1090, 1986.
- [11] N. C. Saha and H. G. Tompkins, "Titanium nitride oxidation chemistry: an x-ray photoelectron spectroscopy study," *Journal of Applied Physics*, vol. 72, pp. 3072–3079, 1992.
- [12] D. H. Lee, Y. S. Cho, W. I. Yi, T. S. Kim, J. K. Lee, and H. J. Jung, "Metalorganic chemical vapor deposition of TiO_2 : N anatase thin film on Si substrate," *Applied physics letters*, vol. 66, pp. 815–816, 1995.
- [13] T. Ihara, M. Miyoshi, Y. Iriyama, O. Matsumoto, and S. Sugihara, "Visible-light-active titanium oxide photocatalyst realized by an oxygen-deficient structure and by nitrogen doping," *Applied Catalysis B: Environmental*, vol. 42, no. 4, pp. 403–409, 2003.
- [14] H. Irie, Y. Watanabe, and K. Hashimoto, "Nitrogen-concentration dependence on photocatalytic activity of $\text{TiO}_{2-x}\text{N}_x$ powders," *Journal of Physical Chemistry B*, vol. 107, no. 23, pp. 5483–5486, 2003.
- [15] T. Lindgren, J. M. Mwabora, E. Avandaño, et al., "Photoelectrochemical and optical properties of nitrogen doped titanium dioxide films prepared by reactive DC magnetron sputtering," *Journal of Physical Chemistry B*, vol. 107, no. 24, pp. 5709–5716, 2003.
- [16] S. Sakthivel and H. Kisch, "Photocatalytic and photoelectrochemical properties of nitrogen-doped titanium dioxide," *ChemPhysChem*, vol. 4, no. 5, pp. 487–490, 2003.
- [17] S. Yin, H. Yamaki, M. Komatsu, et al., "Preparation of nitrogen-doped titania with high visible light induced photocatalytic activity by mechanochemical reaction of titania and hexamethylenetetramine," *Journal of Materials Chemistry*, vol. 13, no. 12, pp. 2996–3001, 2003.
- [18] M.-C. Yang, T.-S. Yang, and M.-S. Wong, "Nitrogen-doped titanium oxide films as visible light photocatalyst by vapor deposition," *Thin Solid Films*, vol. 469–470, pp. 1–5, 2004.
- [19] C. Burda, Y. Lou, X. Chen, A. C. S. Samia, J. Stout, and J. L. Gole, "Enhanced nitrogen doping in TiO_2 nanoparticles," *Nano Letters*, vol. 3, no. 8, pp. 1049–1051, 2003.
- [20] J. L. Gole, J. D. Stout, C. Burda, Y. Lou, and X. Chen, "Highly efficient formation of visible light tunable $\text{TiO}_{2-x}\text{N}_x$ photocatalysts and their transformation at the nanoscale," *Journal of Physical Chemistry B*, vol. 108, no. 4, pp. 1230–1240, 2004.
- [21] X. Chen and C. Burda, "Photoelectron spectroscopic investigation of nitrogen-doped titania nanoparticles," *Journal of Physical Chemistry B*, vol. 108, no. 40, pp. 15446–15449, 2004.
- [22] S. M. Prokes, J. L. Gole, X. Chen, C. Burda, and W. E. Carlos, "Defect-related optical behavior in surface-modified TiO_2 nanostructures," *Advanced Functional Materials*, vol. 15, no. 1, pp. 161–167, 2005.
- [23] X. Chen, Y. Low, A. C. S. Samia, C. Burda, and J. L. Gole, "Formation of oxynitride as the photocatalytic enhancing site in nitrogen-doped titania nanocatalysts: comparison to a commercial nanopowder," *Advanced Functional Materials*, vol. 15, no. 1, pp. 41–49, 2005.
- [24] C. S. Gopinath, "Comment on 'photoelectron spectroscopic investigation of nitrogen-doped titania nanoparticles,'" *Journal of Physical Chemistry B*, vol. 110, no. 13, pp. 7079–7080, 2006.
- [25] S. Sato, R. Nakamura, and S. Abe, "Visible-light sensitization of TiO_2 photocatalysts by wet-method N doping," *Applied Catalysis A: General*, vol. 284, no. 1-2, pp. 131–137, 2005.
- [26] E. György, A. Pérez del Pino, P. Serra, and J. L. Morenza, "Depth profiling characterisation of the surface layer obtained by pulsed Nd:YAG laser irradiation of titanium in nitrogen," *Surface and Coatings Technology*, vol. 173, no. 2-3, pp. 265–270, 2003.
- [27] C. Burda and J. Gole, "Reply to comment on photoelectron spectroscopic investigation of nitrogen-doped titania nanoparticles," *Journal of Physical Chemistry B*, vol. 110, no. 13, pp. 7081–7082, 2006.
- [28] H. Irie, Y. Watanabe, and K. Hashimoto, "Nitrogen-concentration dependence on photocatalytic activity of $\text{TiO}_{2-x}\text{N}_x$ powders," *Journal of Physical Chemistry B*, vol. 107, no. 23, pp. 5483–5486, 2003.
- [29] R. Nakamura, T. Tanaka, and Y. Nakato, "Mechanism for visible light responses in anodic photocurrents at N-doped TiO_2 film electrodes," *Journal of Physical Chemistry B*, vol. 108, no. 30, pp. 10617–10620, 2004.
- [30] T. Ma, M. Akiyama, E. Abe, and I. Imai, "High-efficiency dye-sensitized solar cell based on a nitrogen-doped nanostructured titania electrode," *Nano Letters*, vol. 5, no. 12, pp. 2543–2547, 2005.
- [31] O. Diwald, T. L. Thompson, E. G. Goralski, S. D. Walck, and J. T. Yates Jr., "The effect of nitrogen ion implantation on the photoactivity of TiO_2 rutile single crystals," *Journal of Physical Chemistry B*, vol. 108, no. 1, pp. 52–57, 2004.
- [32] O. Diwald, T. L. Thompson, T. Zubkov, Ed. G. Goralski, S. D. Walck, and J. T. Yates Jr., "Photochemical activity of nitrogen-doped rutile $\text{TiO}_2(110)$ in visible light," *Journal of Physical Chemistry B*, vol. 108, no. 19, pp. 6004–6008, 2004.
- [33] T. L. Thompson and J. T. Yates Jr., " TiO_2 -based photocatalysis: surface defects, oxygen and charge transfer," *Topics in Catalysis*, vol. 35, no. 3-4, pp. 197–210, 2005.

- [34] P. Frach, D. Glöß, M. Vergöhl, F. Neumann, and K. Hund-Rinke, "Photocatalytic properties of titanium dioxide films prepared by reactive pulse magnetron sputtering," in *Proceeding of the 4th International Workshop on the Utilization and Commercialisation of Photocatalytic Systems (EJIPAC '04)*, Saarbrücken, Germany, October 2004.
- [35] D. Li, H. Haneda, S. Hishita, and N. Ohashi, "Visible-light-driven nitrogen-doped TiO₂ photocatalysts: effect of nitrogen precursors on their photocatalysis for decomposition of gas-phase organic pollutants," *Materials Science and Engineering B: Solid-State Materials for Advanced Technology*, vol. 117, no. 1, pp. 67–75, 2005.
- [36] M. Mrowetz, W. Balcerski, A. J. Colussi, and M. R. Hoffmann, "Oxidative power of nitrogen-doped TiO₂ photocatalysts under visible illumination," *Journal of Physical Chemistry B*, vol. 108, no. 45, pp. 17269–17273, 2004.
- [37] Y. Aita, M. Komatsu, S. Yin, and T. Sato, "Phase-compositional control and visible light photocatalytic activity of nitrogen-doped titania via solvothermal process," *Journal of Solid State Chemistry*, vol. 177, no. 9, pp. 3235–3238, 2004.
- [38] R. P. Vitiello, J. M. Macak, A. Ghicov, H. Tsuchiya, L. F. P. Dick, and P. Schmuki, "N-Doping of anodic TiO₂ nanotubes using heat treatment in ammonia," *Electrochemistry Communications*, vol. 8, no. 4, pp. 544–548, 2006.
- [39] M. Kitano, K. Funatsu, M. Matsuoka, M. Ueshima, and M. Anpo, "Preparation of nitrogen-substituted TiO₂ thin film photocatalysts by the radio frequency magnetron sputtering deposition method and their photocatalytic reactivity under visible light irradiation," *Journal of Physical Chemistry B*, vol. 110, no. 50, pp. 25266–25272, 2006.
- [40] S.-K. Joung, T. Amemiya, M. Murabayashi, and K. Itoh, "Relation between photocatalytic activity and preparation conditions for nitrogen-doped visible light-driven TiO₂ photocatalysts," *Applied Catalysis A: General*, vol. 312, no. 1-2, pp. 20–26, 2006.
- [41] S. In, A. Orlov, F. García, M. Tikhov, D. S. Wright, and R. M. Lambert, "Efficient visible light-active N-doped TiO₂ photocatalysts by a reproducible and controllable synthetic route," *Chemical Communications*, no. 40, pp. 4236–4238, 2006.
- [42] C. Belver, R. Bellod, A. Fuerte, and M. Fernández-García, "Nitrogen-containing TiO₂ photocatalysts. Part 1. Synthesis and solid characterization," *Applied Catalysis B: Environmental*, vol. 65, no. 3-4, pp. 301–308, 2006.
- [43] C. Belver, R. Bellod, S. J. Stewart, F. G. Requejo, and M. Fernández-García, "Nitrogen-containing TiO₂ photocatalysts. Part 2. Photocatalytic behavior under sunlight excitation," *Applied Catalysis B: Environmental*, vol. 65, no. 3-4, pp. 309–314, 2006.
- [44] T. Matsumoto, N. Iyi, Y. Kaneko, et al., "High visible-light photocatalytic activity of nitrogen-doped titania prepared from layered titania/isostearate nanocomposite," *Catalysis Today*, vol. 120, no. 2, pp. 226–232, 2007.
- [45] T. Tachikawa, M. Fujitsuka, and T. Majima, "Mechanistic insight into the TiO₂ photocatalytic reactions: design of new photocatalysts," *Journal of Physical Chemistry C*, vol. 111, no. 14, pp. 5259–5275, 2007.
- [46] R. Asahi, Y. Taga, W. Mannstadt, and A. J. Freeman, "Electronic and optical properties of anatase TiO₂," *Physical Review B—Condensed Matter and Materials Physics*, vol. 61, no. 11, pp. 7459–7465, 2000.
- [47] C. Di Valentin, G.-F. Pacchioni, and A. Selloni, "Origin of the different photoactivity of N-doped anatase and rutile TiO₂," *Physical Review B—Condensed Matter and Materials Physics*, vol. 70, no. 8, Article ID 085116, 2004.
- [48] C. Di Valentin, G.-F. Pacchioni, A. Selloni, S. Livraghi, and E. Giamello, "Characterization of paramagnetic species in N-doped TiO₂ powders by EPR spectroscopy and DFT calculations," *Journal of Physical Chemistry B*, vol. 109, no. 23, pp. 11414–11419, 2005.
- [49] K. Yang, Y. Dai, H. Baibiao, and H. Shenghao, "Theoretical study of N-doped TiO₂ rutile crystals," *Journal of Physical Chemistry B*, vol. 110, no. 47, pp. 24011–24014, 2006.
- [50] S. Livraghi, M. C. Paganini, E. Giamello, A. Selloni, C. Di Valentin, and G.-F. Pacchioni, "Origin of photoactivity of nitrogen-doped titanium dioxide under visible light," *Journal of the American Chemical Society*, vol. 128, no. 49, pp. 15666–15671, 2006.
- [51] S. Livraghi, A. Votta, M. C. Paganini, and E. Giamello, "The nature of paramagnetic species in nitrogen doped TiO₂ active in visible light photocatalysis," *Chemical Communications*, no. 4, pp. 498–500, 2005.
- [52] M. A. Henderson, W. S. Epling, C. H. F. Peden, and C. L. Perkins, "Insights into photoexcited electron scavenging processes on TiO₂ obtained from studies of the reaction of O₂ with OH groups adsorbed at electronic defects on TiO₂(110)," *Journal of Physical Chemistry B*, vol. 107, no. 2, pp. 534–545, 2003.
- [53] T. Berger, M. Sterrer, O. Diwald, et al., "Light-induced charge separation in anatase TiO₂ particles," *Journal of Physical Chemistry B*, vol. 109, no. 13, pp. 6061–6068, 2005.
- [54] D. C. Hurum, A. G. Agrios, K. A. Gray, T. Rajh, and M. C. Thurnauer, "Explaining the enhanced photocatalytic activity of degussa P25 mixed-phase TiO₂ using EPR," *Journal of Physical Chemistry B*, vol. 107, no. 19, pp. 4545–4549, 2003.
- [55] H. Wang and J. P. Lewis, "Second-generation photocatalytic materials: anion-doped TiO₂," *Journal of Physics Condensed Matter*, vol. 18, no. 2, pp. 421–434, 2006.
- [56] J. Pascual, J. Camassel, and H. Mathieu, "Fine structure in the intrinsic absorption edge of titanium dioxide," *Physical Review B*, vol. 18, pp. 5606–5614, 1978.
- [57] K. M. Glassford and J. R. Chelikowsky, "Structural and electronic properties of titanium dioxide," *Physical Review B*, vol. 46, pp. 1284–1298, 1992.
- [58] R. Sanjines, H. Tang, H. Berger, F. Gozzo, G. Margaritondo, and F. Levy, "Electronic structure of anatase TiO₂ oxide," *Journal of Applied Physics*, vol. 75, pp. 2945–2951, 1994.
- [59] H. Tang, F. Levy, H. Berger, and P. E. Schmid, "Urbach tail of anatase TiO₂," *Physical Review B*, vol. 52, pp. 7771–7774, 1995.
- [60] S. D. Mo and W. Y. Ching, "Electronic and optical properties of three phases of titanium dioxide: rutile, anatase, and brookite," *Physical Review B*, vol. 51, pp. 13023–13032, 1995.
- [61] C. Kim, S. J. Doh, S. G. Lee, S. J. Lee, and H. Y. Kim, "Visible-light absorptivity of a zincoxysulfide (ZnO_xS_{1-x}) composite semiconductor and its photocatalytic activities for degradation of organic pollutants under visible-light irradiation," *Applied Catalysis A: General*, vol. 330, no. 1-2, pp. 127–133, 2007.
- [62] V. N. Kuznetsov and N. Serpone, "Visible light absorption by various titanium dioxide specimens," *Journal of Physical Chemistry B*, vol. 110, no. 50, pp. 25203–25209, 2006.
- [63] D. Li, N. Ohashi, S. Hishita, T. Kolodiazny, and H. Haneda, "Origin of visible-light-driven photocatalysis: a comparative study on N/F-doped and N-F-codoped TiO₂ powders by means of experimental characterizations and theoretical calculations," *Journal of Solid State Chemistry*, vol. 178, no. 11, pp. 3293–3302, 2005.
- [64] J. Wang, W. Zhu, Y. Zhang, and S. Liu, "An efficient two-step technique for nitrogen-doped titanium dioxide synthesizing: visible-light-induced photodecomposition of methylene

- blue,” *The Journal of Physical Chemistry C*, vol. 111, pp. 1010–1014, 2007.
- [65] T. Sekiya, K. Ichimura, M. Igarashi, and S. Kurita, “Absorption spectra of anatase TiO₂ single crystals heat-treated under oxygen atmosphere,” *Journal of Physics and Chemistry of Solids*, vol. 61, no. 8, pp. 1237–1242, 2000.
- [66] T. Sekiya, T. Yagisawa, N. Kamiya, et al., “Defects in anatase TiO₂ single crystal controlled by heat treatments,” *Journal of the Physical Society of Japan*, vol. 73, no. 3, pp. 703–710, 2004.
- [67] N. Serpone, “Is the band gap of pristine TiO₂ narrowed by anion- and cation-doping of titanium dioxide in second-generation photocatalysts?” *Journal of Physical Chemistry B*, vol. 110, no. 48, pp. 24287–24293, 2006.
- [68] J. Chen, L.-B. Lin, and F.-Q. Jing, “Theoretical study of F-type color center in rutile TiO₂,” *Journal of Physics and Chemistry of Solids*, vol. 62, no. 7, pp. 1257–1262, 2001.
- [69] K. Suriye, P. Praserttham, and B. Jongsomjit, “Control of Ti³⁺ surface defect on TiO₂ nanocrystal using various calcination atmospheres as the first step for surface defect creation and its application in photocatalysis,” *Applied Surface Science*, vol. 253, no. 8, pp. 3849–3855, 2007.
- [70] V. N. Kuznetsov and N. Serpone, “Photo-induced coloration and photobleaching of titanium dioxide in TiO₂/polymer compositions on UV- and visible-light excitation into the color centers’ absorption bands. Direct experimental evidence negating band gap narrowing in anion-/cation-doped TiO₂,” *The Journal of Physical Chemistry C*, vol. 111, pp. 15277–15288, 2007.
- [71] A. V. Emeline, N. V. Sheremetyeva, N. V. Khomchenko, V. K. Ryabchuk, and N. Serpone, “Photoinduced formation of defects and nitrogen stabilization of color centers in N-doped titanium dioxide,” *Journal of Physical Chemistry C*, vol. 111, no. 30, pp. 11456–11462, 2007.

Research Article

Photocatalytic Hydrogen or Oxygen Evolution from Water over S- or N-Doped TiO₂ under Visible Light

Kazumoto Nishijima, Takaaki Kamai, Naoya Murakami, Toshiki Tsubota, and Teruhisa Ohno

Department of Material Science, Faculty of Engineering, Kyushu Institute of Technology, 1-1 Sensui-cho, Tobata-ku, Fukuoka 804-8550, Kitakyushu-shi, Japan

Correspondence should be addressed to Teruhisa Ohno, tohno@che.kyutech.ac.jp

Received 20 March 2007; Accepted 22 May 2007

Recommended by M. Sabry A. Abdel-Mottaleb

S- or N-doping of TiO₂ powder having an anatase or rutile phase extended the photocatalytic activity for water oxidation and reduction under UV light and visible light irradiation. For the reduction of water, anatase-doped TiO₂ showed higher level of activity than that of doped TiO₂ having a rutile phase using ethanol as an electron donor. Furthermore, the activity level of S-doped TiO₂ for hydrogen evolution was higher than that of N-doped TiO₂ photocatalysts under visible light. Photocatalytic oxidation of water on doped TiO₂ having a rutile phase proceeded with fairly high efficiency when Fe³⁺ ions were used as electron acceptors compared to that on doped TiO₂ having an anatase phase. In addition, water splitting under visible light irradiation was achieved by construction of a Z-scheme photocatalysis system employing the doped TiO₂ having anatase and rutile phases for H₂ and O₂ evolution and the I⁻/IO₃⁻ redox couple as an electron relay.

Copyright © 2008 Kazumoto Nishijima et al. This is an open access article distributed under the Creative Commons Attribution License, which permits unrestricted use, distribution, and reproduction in any medium, provided the original work is properly cited.

1. INTRODUCTION

Photocatalytic reactions on the surfaces of TiO₂ particles have been attracting much attention because of their possible application to the conversion of solar energy into chemical energy (water splitting) [1, 2] and to water purification from pollutants [3–5]. TiO₂ is chemically stable and nontoxic and it has a high oxidation power under photoirradiation. However, a high oxidation power of TiO₂ is only shown under UV light, which is a great disadvantage for practical application. Therefore, the development of a TiO₂ photocatalyst that shows a high level of activity under visible light is needed.

N, S, or C anion-doped TiO₂ photocatalysts having an anatase phase that shows a relatively high level of activity under visible light irradiation have been reported [6–9]. Sakthivel and Kisch succeeded in preparing TiO₂ photocatalysts containing some carbon species that show photocatalytic activity under visible light [10]. We have also reported the preparation of S cation-doped TiO₂ having anatase and rutile phases and its photocatalytic activity for oxidation of organic compounds [11, 12]. The absorbance of S cation-doped TiO₂ in the visible region is larger than that of N, C, or S anion-

doped TiO₂, and the photocatalytic activity level of S cation-doped TiO₂ for oxidation of organic compounds is relatively high under visible light compared to that of N, C, or S anion-doped TiO₂. It should be noted that S atoms were incorporated into the lattice of TiO₂ as cations and were thought to be replaced by Ti ions in the case of S cation-doped TiO₂.

Among the chemical reactions suitable for energy conversion is the decomposition of water, because the change in Gibbs energy is large. Hence, there have been many attempts to achieve photodecomposition of water using semiconductor particles such as TiO₂ [13], SrTiO₃ [14], and K₄Nb₆O₁₇ [15].

Abe et al. developed a water-splitting system by combining two photocatalytic systems including oxidation of water and reduction of water systems under visible light [16]. However, the efficiency of each system (hydrogen-evolving and oxygen-evolving systems) is not sufficient for application to a practical system. The aim of our study was to establish effective oxygen- and hydrogen-evolving systems. In this paper, we report the photocatalytic activities of S-doped or N-doped TiO₂ for reduction of water into molecular hydrogen and oxidation of water into molecular oxygen under visible

light using ethanol and Fe^{3+} ions as electron donors and electron acceptors, respectively.

2. EXPERIMENTAL

2.1. Materials and instruments

Various kinds of TiO_2 powders having anatase and rutile crystal structures were obtained from the Catalysis Society of Japan (TIO-3), Ishihara Sangyo (ST-01), TAYCA Corporation (MT-150A), and Toho Titanium Co. (NS-51). The contents of anatase and the surface areas of these powders were as follows: ST-01: 100%, 320.5 m^2/g ; MT-150A: 0%, 81.5 m^2/g ; TIO-3: 0%, 48.1 m^2/g ; NS-51: 1.0%, 6.5 m^2/g . Ethanol, FeCl_3 , thiourea, and urea were obtained from Wako Pure Chemical Industry. Other chemicals were obtained from commercial sources as guaranteed reagents and were used without further purification. The crystal structures of TiO_2 powders were determined from X-ray diffraction (XRD) patterns measured with an X-ray diffractometer (Philips, X'Pert-MRD) with a Cu target $K\alpha$ -ray ($\lambda = 1.5405 \text{ \AA}$). The relative surface areas of the powders were determined by N_2 adsorption/desorption isotherm analysis (BET method). The measurements were performed using Micromeritics FlowSorb II 2300. The absorption and diffuse reflection spectra were measured using a Shimadzu UV-2500PC spectrophotometer. X-ray photoelectron spectra (XPS) of the TiO_2 powders were measured using a JEOL JPS90SX photoelectron spectrometer with an Mg $K\alpha$ source (1253.6 eV). The shift of binding energy due to relative surface charging was corrected using the C 1s level at 284.6 eV as an internal standard. The XPS peaks were assumed to have Gaussian line shapes and were resolved into components by a nonlinear least-squares procedure after proper subtraction of the baseline.

2.2. Preparation of S- or N-doped TiO_2 powders

S- or N-doped TiO_2 powders were synthesized by previously reported methods [11, 12, 17–19].

S- or N-doped TiO_2 powders having a rutile or anatase phase were prepared as follows. Thiourea (for S doping) or urea (for N doping) was mixed with various kinds of TiO_2 powders having an anatase or rutile phase in an agate mortar. The mixed powder was packed in an alumina crucible and calcined at 400–600°C under air atmosphere for 3 hours. After calcination, the powder was washed with distilled water. The resulting samples were yellow in color and were found to have a homogenous anatase or rutile phase from XRD analysis. For TiO_2 powder calcined at a temperature higher than 600°C, no absorbance in the visible region was observed. The surface areas of S-doped and N-doped TiO_2 powders having an anatase phase (ST-01) calcined at 400°C were 120 m^2/g and 90 m^2/g , respectively. The surface areas of S-doped TiO_2 powders having a rutile phase (MT-150A, TIO-3, and NS-51) calcined at 500°C were 52.5 m^2/g , 32.2 m^2/g , and 5.4 m^2/g , respectively. The surface areas of N-doped TiO_2 powders having a rutile phase (TIO-3 and NS-51) calcined at 600°C were 26.3 m^2/g and 4.9 m^2/g , respectively. The relative sur-

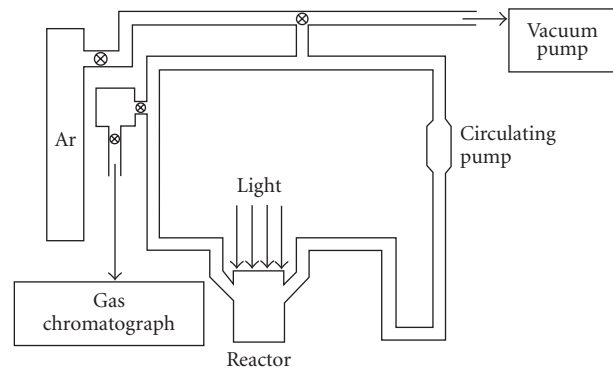


FIGURE 1: Schematic diagram of the closed gas circulating system.

face area decreased with increase in the calcination temperature.

2.3. Preparation of Pt-loaded TiO_2 photocatalysts for hydrogen evolution

Pt-loaded TiO_2 powders were prepared by a photochemical deposition method. The doped TiO_2 photocatalyst was stirred in a 5% ethanol aqueous solution containing H_2PtCl_6 and irradiated by a 500 W high-pressure Hg lamp ($2 \text{ mW}/\text{cm}^2$) for 12 hours. Photoreduction of H_2PtCl_6 took place, and highly dispersed Pt metal particles were deposited on the surface of the photocatalyst. After filtrating and washing by deionized water, the powder was dried at 100°C for 2 hours under reduced pressure to remove the ethanol adsorbed on the surface of the photocatalyst.

2.4. Photocatalytic reaction

The photocatalytic reactions were carried out using a closed gas-circulating system (Figure 1). The reaction under a wide range of incident light including UV and visible light was performed using a quartz glass-made outer irradiation type reactor. Irradiation to the aqueous suspension of a catalyst was carried out from outside the reactor using a 500 W xenon lamp (USHIO Co. Ltd., SXUI-501XQ) for H_2 evolution and O_2 evolution. To limit the irradiation wavelength, the light beam was passed through a UV-35, L-39, or L-42 filter (Kenko Co.) to cut off wavelengths shorter than 350, 390, or 420 nm, respectively. The irradiance of irradiation light was adjusted to 340 mW/cm^2 . The photocatalyst powder (0.3 g) was suspended in distilled water using a magnetic stirrer. S- or N-doped TiO_2 having anatase phase (ST-01) was used for hydrogen evolution, and S- or N-doped TiO_2 having rutile phase (NS-51) was used for oxygen evolution. The required amount of sacrificial reagent ethanol for hydrogen evolution and Fe^{3+} for oxygen evolution was added to the suspension. The pH of the solution containing Fe^{3+} ions was adjusted to 2.4 using 1 M HCl aqueous solution in order to prevent formation of $\text{Fe}(\text{OH})_3$.

In the case of water splitting in the two-step redox system, a 500 W high-pressure mercury lamp (USHIO Co. Ltd., SX-U1501HQ) was used as a light source. The Hg lamp has

emission line spectrum with peaks at 314, 365, 405, and 436 nm. To limit the irradiation wavelength, the light beam was passed through a UV-35 or L-39 filter (Kenko Co.) to cut off wavelengths shorter than 350 or 390 nm, respectively. A mixture (0.3 g) of S-doped TiO₂ powder having anatase phase (ST-01) and S-doped TiO₂ powder rutile phase (NS-51) which weight ratio was 1 : 1 was suspended in distilled water. The required amount of solute, such as NaI, was added to the suspension. I⁻/IO₃⁻ ions were used as a redox couple [16]. The pH of the solutions was adjusted to 9 using 1 M NaOH aqueous solution in order to prevent generation of I₃⁻ ions [16].

Finally, the suspension was thoroughly degassed and then argon gas (35 Torr) was introduced into the system and the system was exposed to irradiation. Evolved H₂ or O₂ gases were analyzed by online gas chromatography (TCD, molecular sieve 5 A).

3. RESULTS AND DISCUSSIONS

3.1. Physical properties of S-doped and N-doped TiO₂

Diffuse reflectance spectra for the obtained S-doped TiO₂ and N-doped TiO₂ are shown in Figure 2. All doped TiO₂ powders showed absorption in the visible region. Photoabsorption in the visible region of the doped TiO₂ having an anatase phase was stronger than that of the doped TiO₂ having a rutile phase. The TiO₂ having a rutile phase was hardly doped by S atoms or N atoms because the rutile phase has a smaller surface area and more stable crystal structure than those of the anatase phase. The absorption band edge of S-doped TiO₂ shifted to a longer wavelength than that of N-doped TiO₂. The band gap energies of S-doped TiO₂ and N-doped TiO₂ can be estimated from the tangent lines in the plot of the square root of the Kubelka-Munk functions against the photon energy [20], as shown in the insert to Figure 2. The band gap energies were estimated to be 2.28 eV (S-doped TiO₂ having an anatase phase), 2.58 eV (N-doped TiO₂ having an anatase phase), 2.34 eV (S-doped TiO₂ having a rutile phase), and 2.94 eV (N-doped TiO₂ having a rutile phase).

The chemical states of S atoms or N atoms incorporated into TiO₂ were studied by measuring the XPS spectra of the S-doped TiO₂ or N-doped TiO₂. Figure 3(a) shows the S2p_{3/2} spectrum of S-doped TiO₂. As shown in Figure 3(a), a strong peak around 168 eV was observed. This peak is thought to consist of several oxidation states of S atoms such as S⁶⁺ and S⁴⁺ states [11, 12]. Figure 3(b) shows the N 1s spectrum of N-doped TiO₂. Two peaks around 396 eV and 399 eV were observed. The peak around 396 eV was assigned to N atoms forming Ti–N bonds, and the peak around 399 eV was assigned to N₂ molecules adsorbed on the TiO₂ surface [17].

3.2. Selective water oxidation over doped TiO₂ photocatalysts in an aqueous solution containing Fe³⁺ ions

We investigated photocatalytic reduction of water into H₂ or oxidation of water into O₂ over various semiconductor

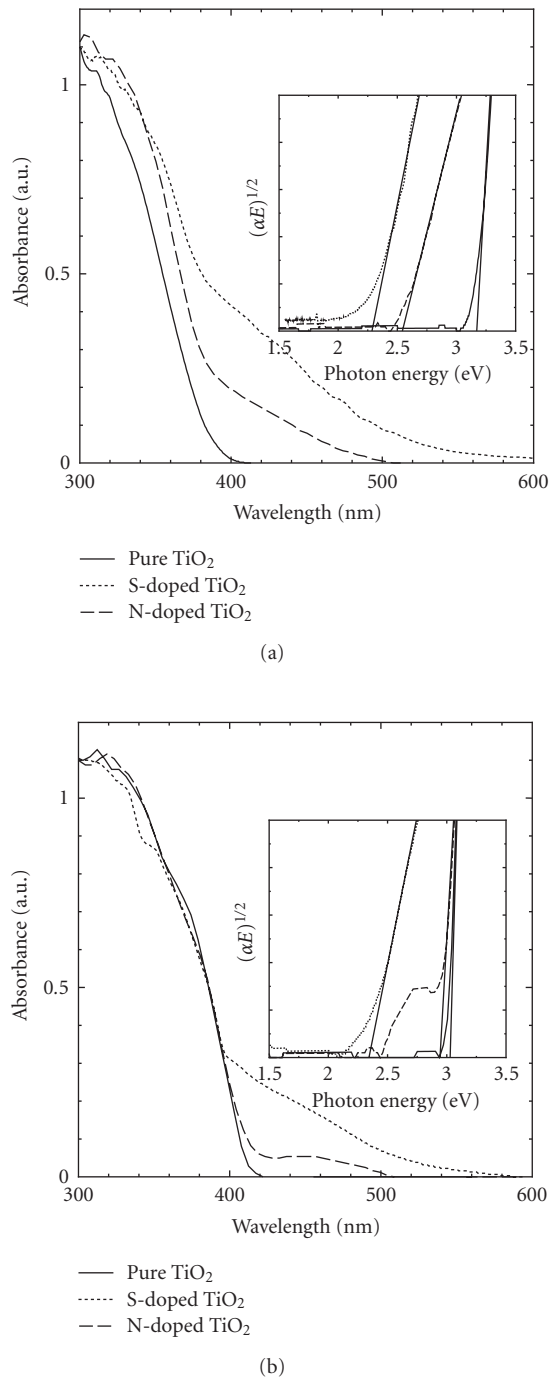
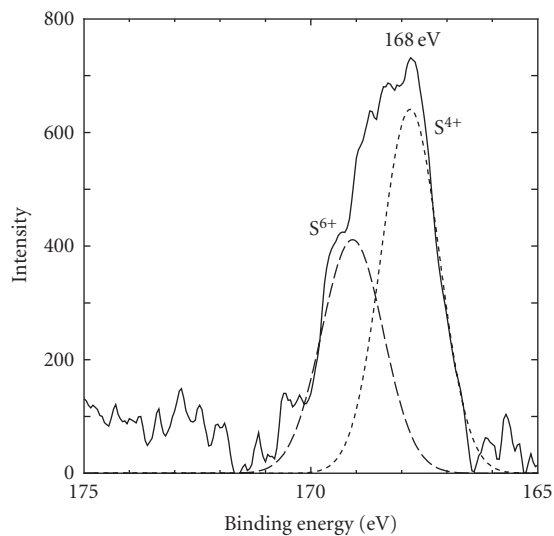
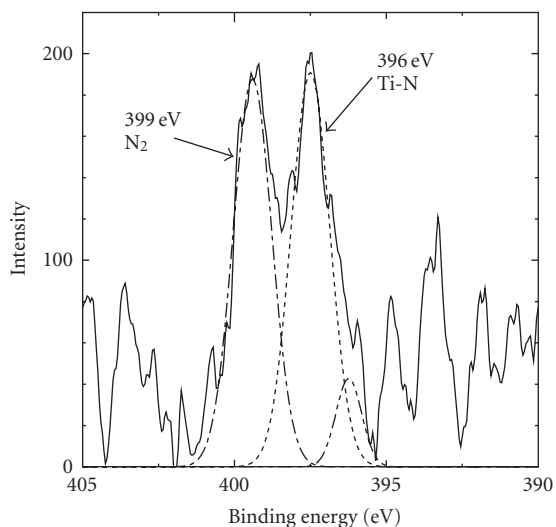


FIGURE 2: Diffuse reflectance spectra for the obtained S-doped TiO₂ and N-doped TiO₂ having an anatase or rutile phase. (a) TiO₂ having an anatase phase (ST-01), (b) TiO₂ having a rutile phase (NS-51).

photocatalysts in an aqueous solution containing an electron donor or an electron acceptor. In most cases, the reactions readily terminated when the concentration of the product in the solution reached a certain level because of the backward reactions. However, we found that efficient and selective O₂ evolution proceeded over TiO₂ photocatalysts having a rutile



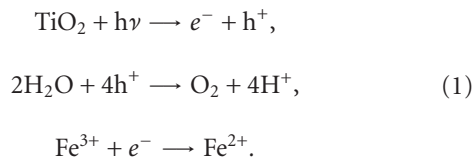
(a)



(b)

FIGURE 3: XPS spectra of S-doped TiO₂ and N-doped TiO₂. (a) S-doped TiO₂, (b) N-doped TiO₂.

phase in the aqueous solution (pH < 3) containing Fe³⁺ ions as electron acceptors with the following reactions [21]:



The optimized concentration of Fe³⁺ ions was 2 mmol/L. The rate of oxygen evolution was lowered by raising the concentrations of Fe³⁺ ions owing to a filter effect of the solution

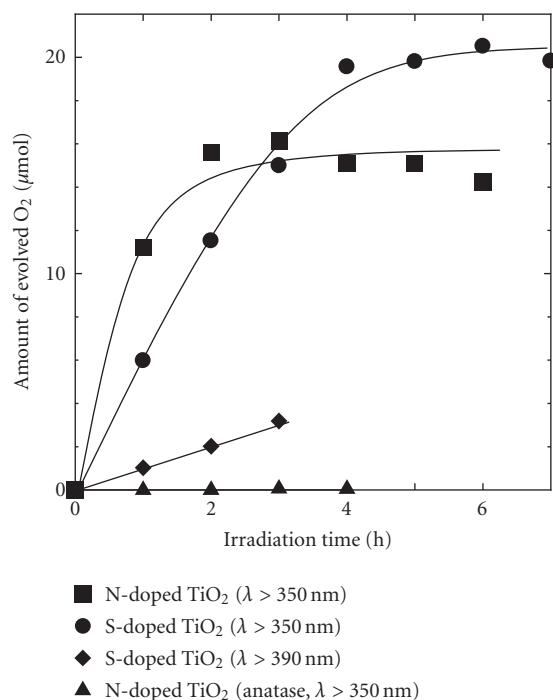


FIGURE 4: Amount of evolved O₂ from water containing Fe³⁺ ions as electron acceptors on S-doped TiO₂ having rutile phase (NS-51), N-doped TiO₂ having rutile phase (NS-51), and N-doped TiO₂ having anatase phase (ST-01).

at a high concentration [21]. Excess Fe³⁺ ions decreased rate of evolved oxygen because Fe³⁺ aqueous solution has absorption in visible light region. Figure 4 shows the amounts of evolved O₂ over S- or N-doped TiO₂ having rutile phase (NS-51) and N-doped TiO₂ having anatase phase (ST-01) from water containing Fe³⁺ ions as electron acceptors. The photocatalytic activity level of S-doped TiO₂ for water oxidation was higher than that of N-doped TiO₂. However, the amounts of evolved O₂ on S- or N-doped TiO₂ did not agree with concentration of Fe³⁺ ions. The backward reaction, oxidation of Fe²⁺ ions with holes, was thought to proceed. S-doped TiO₂ showed photoinduced oxidation of water under visible light irradiation at wavelengths longer than 390 nm. Photocatalytic oxidation of water on doped TiO₂ having a rutile phase proceeded with a fairly high efficiency compared to that on doped TiO₂ having an anatase phase as shown in Figure 4. This result suggested that the activity for the evolution of O₂ from H₂O is dependent on the particle size of doped TiO₂ powders. On anatase particles with a large surface area, decomposition of pollutants in air and water proceeds efficiently [4, 5]. In these reactions, the large surface area is especially important, because the concentrations of the pollutants are usually very low. On the other hand, for splitting water, which is an important reaction to convert light energy into chemical energy, rutile particles with a small surface area are efficient [21–23]. In this case, a band bending should be developed in each particle to oxidize water, and hence large particles are advantageous.

3.3. Selective water reduction over doped TiO₂ photocatalysts deposited with Pt in an aqueous solution containing ethanol

H₂ evolution from water containing ethanol as a sacrificial reagent proceeded over platinized TiO₂ having an anatase phase under UV and visible light irradiation. To improve the rate of H₂ evolution on doped TiO₂, Pt was deposited on the TiO₂ surface. The optimized amount of Pt deposited on the surface of TiO₂ was 0.5 wt%. Deposition of an excess amount of Pt (1.0 wt%) decreased photocatalytic activity because aggregated Pt particles on the TiO₂ surface prevented the TiO₂ photocatalyst from absorbing incident light or because TiO₂ surface active sites were covered with Pt particles. The reduction of water containing ethanol is as follows:

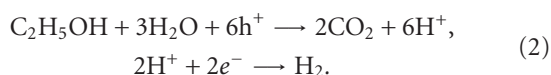


Figure 5 shows the amounts of evolved H₂ from water containing ethanol over S- or N-doped TiO₂ having anatase phase (ST-01) and S-doped TiO₂ having rutile phase (NS-51) under UV light irradiation. The amount of evolved H₂ on doped TiO₂ was smaller than that on pure TiO₂ because impurity level was formed by doping treatment. However, under visible light irradiation at wavelengths longer than 420 nm, the amount of evolved H₂ on doped TiO₂ was higher than that on pure TiO₂ as shown in Figure 5(b). S-doped TiO₂ showed a higher level of activity than that of N-doped TiO₂ for water reduction because S-doped TiO₂ showed higher photoabsorption than that of N-doped TiO₂ in the visible region as shown in Figure 2(a). Photocatalytic reduction of water on doped TiO₂ having an anatase phase proceeded with a fairly high efficiency compared to that on doped TiO₂ having a rutile phase as shown in Figure 5. This result suggested that the activity for the evolution of H₂ from H₂O is dependent on the surface area of doped TiO₂ powder. Potential of the conduction band of anatase phase is at a more negative position than that of rutile phase. Therefore, the excited electrons easily transfer H⁺ ions on the surface of TiO₂ having an anatase phase.

3.4. Water splitting over TiO₂ photocatalysts in an I⁻/IO₃⁻ shuttle redox-mediated system

Photocatalytic water splitting into H₂ and O₂ was observed in a two-step redox system using an iodate/iodide redox mediator. In this system, we used Pt-loaded S-doped TiO₂ having an anatase phase (ST-01) for H₂ evolution and S-doped TiO₂ having a rutile phase (NS-51) for O₂ evolution under incident light including UV and visible light. Figure 6 shows the mechanism of the two-step redox system. On TiO₂ having an anatase phase, water is reduced to H₂ by photoexcited electrons and the iodide ions are oxidized to iodate ions by holes. The iodate ions are reduced to generate iodide ions by photoexcited electrons at the same time as water is oxidized to O₂ by holes on TiO₂ having a rutile phase. The optimized concentration of I⁻ ions was 20 mmol/L. The oxidation products of I⁻ ions were IO₃⁻ and I₃⁻. An excess concentration of I⁻

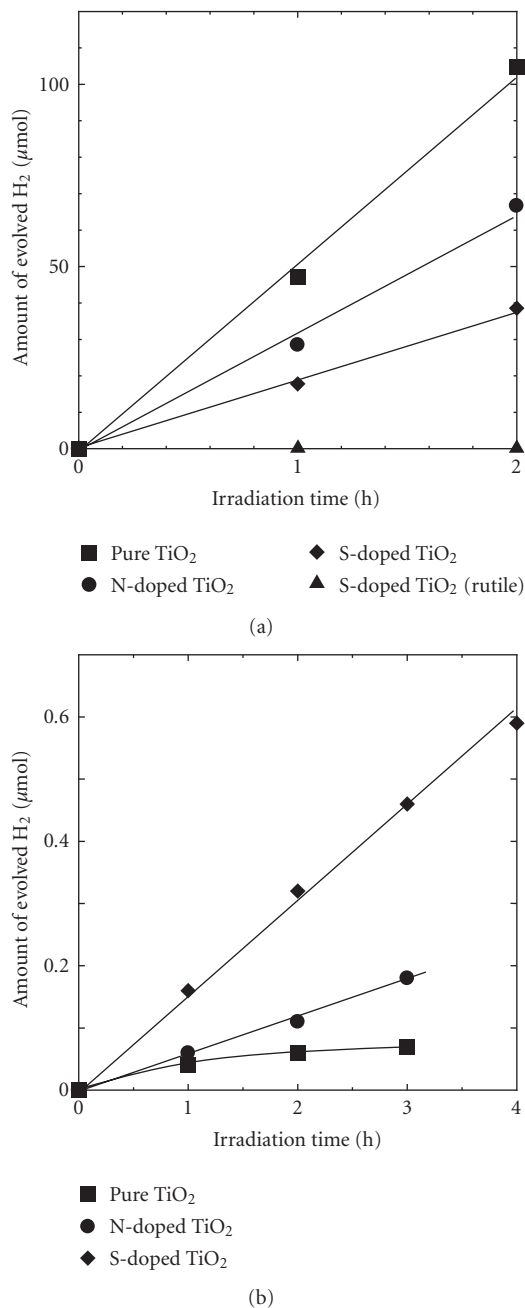
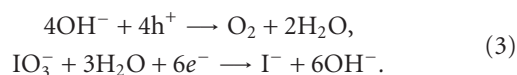


FIGURE 5: Amount of evolved H₂ from water containing ethanol as an electron donor on S- or N-doped TiO₂ (anatase phase: ST-01, rutile phase: NS-51) (a) under UV light irradiation at wavelengths longer than 350 nm or (b) under visible light irradiation at wavelengths longer than 420 nm.

ions resulted in I₃⁻ generation. The accumulation of I₃⁻ caused a light loss due to the strong absorption of I₃⁻ around 350 nm, resulting in a lower efficiency of the photocatalytic reaction [16]. Reactions over a rutile phase are as follows:



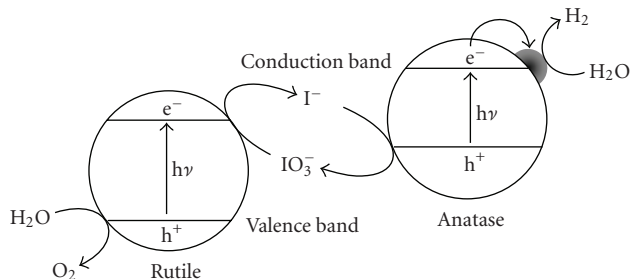


FIGURE 6: Mechanism for water splitting on TiO₂ with an I⁻/IO₃⁻ redox-mediator system.

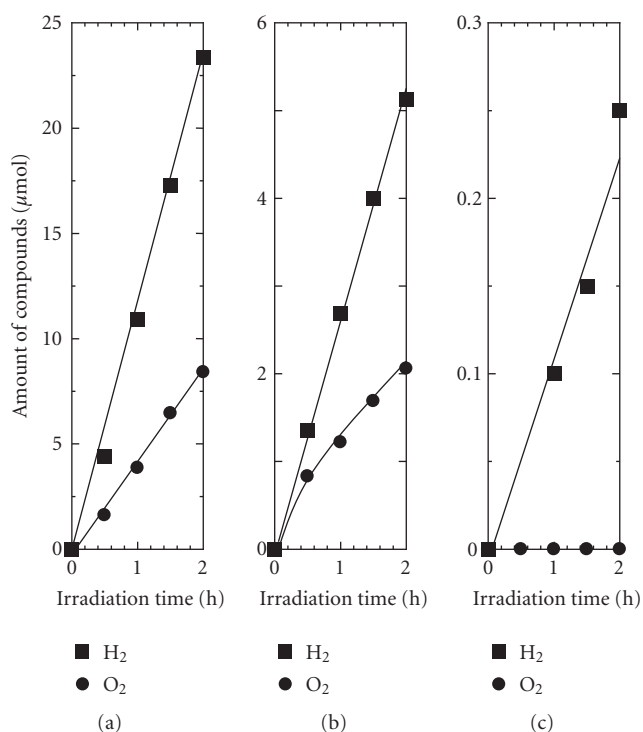
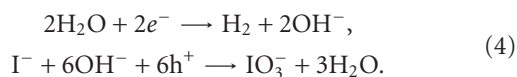


FIGURE 7: Amounts of evolved H₂ and O₂ from water containing I⁻/IO₃⁻ redox on S-doped TiO₂ powders having an anatase phase (ST-01) and a rutile phase (NS-51) under UV or visible light irradiation. (a) under UV light irradiation without a cutoff filter, (b) under UV light irradiation at wavelengths longer than 350 nm, (c) under visible light irradiation at wavelengths longer than 390 nm.

On the other hand, reactions over an anatase phase are as follows:



Amounts of evolved H₂ and O₂ in the two-step redox system under incident light including UV and visible light are shown in Figure 7. Under UV light irradiation without a cutoff filter and UV light irradiation at wavelengths longer 350 nm, both H₂ and O₂ evolved. However, the ratio of amount of evolved H₂ to amount of evolved O₂ was not 2 : 1. O₂ molecules generated from water oxidation were

thought to adsorb on the TiO₂ surface [24]. Under visible light irradiation at wavelengths longer than 390 nm, no O₂ evolution was observed because the number of holes is not sufficient for O₂ generation under low intensity of incident light. Under these circumstances, the intermediates generated by water oxidation were thought to be reduced by photoexcited electrons.

4. CONCLUSION

H₂ evolution from water containing ethanol as an electron donor was performed on N- or S-doped TiO₂ under visible light irradiation. An anatase TiO₂ powder showed a higher level of activity than that of a rutile TiO₂ powder. Oxidation of water containing Fe³⁺ ions as electron acceptors proceeded on doped TiO₂ under UV and visible light irradiation. Water splitting was performed in an I⁻/IO₃⁻ redox system on TiO₂ having an anatase phase for H₂ evolution and TiO₂ having a rutile phase for O₂ evolution. Under UV irradiation, both H₂ and O₂ were evolved, though the ratio of amount of evolved H₂ to amount of evolved O₂ was not 2 : 1.

ACKNOWLEDGMENTS

This work was supported by a Grant-in-Aid for Scientific Research on Priority Areas from the Ministry of Education, Culture, Science, and Technology (MEXT), Japan, and Nissan Science Foundation.

REFERENCES

- [1] A. Fujishima and K. Honda, "Electrochemical photolysis of water at a semiconductor electrode," *Nature*, vol. 238, no. 5358, pp. 37–38, 1972.
- [2] S. Sato and M. White, "Photodecomposition of water over Pt/TiO₂ catalysts," *Chemical Physics Letters*, vol. 72, no. 1, pp. 83–86, 1980.
- [3] M. R. Hoffmann, S. T. Martin, W. Choi, and D. W. Bahnemann, "Environmental applications of semiconductor photocatalysis," *Chemical Reviews*, vol. 95, no. 1, pp. 69–96, 1995.
- [4] M. V. Rao, K. Rajeshwar, V. R. Vernerker, and J. Kubow, "Photosynthetic production of hydrogen and hydrogen peroxide on semiconducting oxide grains in aqueous solutions," *Journal of Physical Chemistry*, vol. 84, no. 15, pp. 1987–1991, 1980.
- [5] S. Nishimoto, B. Ohtani, H. Kajiwara, and T. Kagiya, "Correlation of the crystal structure of titanium dioxide prepared from titanium tetra-2-propoxide with the photocatalytic activity for redox reactions in aqueous propan-2-ol and silver salt solutions," *Journal of the Chemical Society, Faraday Transactions 1*, vol. 81, no. 1, pp. 61–68, 1985.
- [6] S. Sato, "Photocatalytic activity of NO_x-doped TiO₂ in the visible light region," *Chemical Physics Letters*, vol. 123, no. 1-2, pp. 126–128, 1986.
- [7] R. Asahi, T. Morikawa, T. Ohwaki, K. Aoki, and Y. Taga, "Visible-light photocatalysis in nitrogen-doped titanium oxides," *Science*, vol. 293, no. 5528, pp. 269–271, 2001.
- [8] T. Umeybayashi, T. Yamaki, H. Itoh, and K. Asai, "Band gap narrowing of titanium dioxide by sulfur doping," *Applied Physics Letters*, vol. 81, no. 3, pp. 454–456, 2002.
- [9] H. Irie, Y. Watanabe, and K. Hashimoto, "Carbon-doped anatase TiO₂ powders as a visible-light sensitive photocatalyst," *Chemistry Letters*, vol. 32, no. 8, pp. 772–773, 2003.

- [10] S. Sakthivel and H. Kisch, "Daylight photocatalysis by carbon-modified titanium dioxide," *Angewandte Chemie*, vol. 42, no. 40, pp. 4908–4911, 2003.
- [11] T. Ohno, T. Mitsui, and M. Matsumura, "Photocatalytic activity of S-doped TiO₂ photocatalyst under visible light," *Chemistry Letters*, vol. 32, no. 4, pp. 364–365, 2003.
- [12] T. Ohno, M. Akiyoshi, T. Umebayashi, K. Asai, T. Mitsui, and M. Matsumura, "Preparation of S-doped TiO₂ photocatalysts and their photocatalytic activities under visible light," *Applied Catalysis A*, vol. 265, no. 1, pp. 115–121, 2004.
- [13] K. Yamaguchi and S. Sato, "Photolysis of water over metalized powdered TiO₂," *Journal of the Chemical Society, Faraday Transactions 1*, vol. 81, no. 5, pp. 1237–1246, 1985.
- [14] K. Domen, A. Kudo, and T. Onishi, "Mechanism of photocatalytic decomposition of water into H₂ and O₂ over NiO-SrTiO₃," *Journal of Catalysis*, vol. 102, no. 1, pp. 86–92, 1986.
- [15] K. Sayama, A. Tanaka, K. Domen, K. Maruya, and T. Onishi, "Photocatalytic decomposition of water over platinum-intercalated K₄Nb₆O₁₇," *Journal of Physical Chemistry*, vol. 95, no. 3, pp. 1345–1348, 1991.
- [16] R. Abe, K. Sayama, and H. Sugihara, "Development of new photocatalytic water splitting into H₂ and O₂ using two different semiconductor photocatalysts and a shuttle redox mediator IO₃⁻/I⁻," *Journal of Physical Chemistry B*, vol. 109, no. 33, pp. 16052–16061, 2005.
- [17] Y. Nosaka, M. Matsushita, J. Nishino, and A. Y. Nosaka, "Nitrogen-doped titanium dioxide photocatalysts for visible response prepared by using organic compounds," *Science and Technology of Advanced Materials*, vol. 6, no. 2, pp. 143–148, 2005.
- [18] T. Ohno, T. Tsubota, K. Nishijima, and Z. Miyamoto, "Degradation of methylene blue on carbonate species-doped TiO₂ photocatalysts under visible light," *Chemistry Letters*, vol. 33, no. 6, pp. 750–751, 2004.
- [19] T. Ohno, T. Tsubota, M. Toyofuku, and R. Inaba, "Photocatalytic activity of a TiO₂ photocatalyst doped with C⁴⁺ and S⁴⁺ ions having a rutile phase under visible light," *Catalysis Letters*, vol. 98, no. 4, pp. 255–258, 2004.
- [20] Y. I. Kim, S. J. Atherton, E. S. Brigham, and T. E. Mallouk, "Sensitized layered metal oxide semiconductor particles for photochemical hydrogen evolution from nonsacrificial electron donors," *Journal of Physical Chemistry*, vol. 97, no. 45, pp. 11802–11810, 1993.
- [21] T. Ohno, D. Haga, K. Fujihara, K. Kaizaki, and M. Matsumura, "Unique effects of iron(III) ions on photocatalytic and photoelectrochemical properties of titanium dioxide," *Journal of Physical Chemistry B*, vol. 101, no. 33, pp. 6415–6419, 1997.
- [22] K. Fujihara, T. Ohno, and M. Matsumura, "Splitting of water by electrochemical combination of two photocatalytic reactions on TiO₂ particles," *Journal of the Chemical Society, Faraday Transactions*, vol. 94, no. 24, pp. 3705–3709, 1998.
- [23] T. Ohno, K. Fujihara, K. Sarukawa, F. Tanigawa, and M. Matsumura, "Splitting of water by combining two photocatalytic reactions through a quinone compound dissolved in an oil phase," *Zeitschrift für Physikalische Chemie*, vol. 213, no. 2, pp. 165–174, 1999.
- [24] H. Luo, T. Takata, Y. Lee, J. Zhao, K. Domen, and Y. Yan, "Photocatalytic activity enhancing for titanium dioxide by copolymerizing with bromine and chlorine," *Chemistry of Materials*, vol. 16, no. 5, pp. 846–849, 2004.

Research Article

Thermal Behavior of $\text{TiO}_{2-x}\text{N}_x$ Nanostructured Powder

Vladimír Balek,¹ Jan Šubrt,² Hiroshi Irie,³ and Kazuhito Hashimoto^{3,4}

¹Nuclear Research Institute Řež, plc., 25068 Řež, Czech Republic

²Institute of Inorganic Chemistry, Academy of Sciences of the Czech Republic (AS CR), 25068 Řež, Czech Republic

³Graduate School of Engineering, The University of Tokyo, 7-3-1 Hongo, Bunkyo-ku, Tokyo 113-8656, Japan

⁴Research Center for Advanced Science and Technology, The University of Tokyo, 4-6-1 Komaba, Meguro-ku, Tokyo 153-8904, Japan

Correspondence should be addressed to Jan Šubrt, subrt@iic.cas.cz

Received 3 September 2007; Accepted 7 December 2007

Recommended by M. Sabry A. Abdel-Mottaleb

Diffusion structural analysis (DSA), based on the measurement of the release of radon previously incorporated into the samples, was used to characterize thermal behavior of N-doped titania powder prepared by heat treatment of anatase in gaseous ammonia at 575°C and the reference TiO_2 powder prepared from the ST-01 anatase titania powder (Ishihara Ltd., Japan). The results of DSA, surface area and porosity measurements by nitrogen adsorption, SEM micrographs, XPS, and XRD are presented and discussed. The results of DSA are in agreement with the results of other methods and indicated the annealing of the subsurface structure irregularities of the samples. Transport properties of the samples were determined from the mobility of radon atoms released on sample heating in air. The decrease of radon permeability in the porous titania powders in the temperature range 850–1000°C due to annealing of the subsurface structure irregularities, that served as radon diffusion paths in the samples, was evaluated from the DSA results.

Copyright © 2008 Vladimír Balek et al. This is an open access article distributed under the Creative Commons Attribution License, which permits unrestricted use, distribution, and reproduction in any medium, provided the original work is properly cited.

1. INTRODUCTION

Titanium dioxide attracted a great attention since Fujishima and Honda [1] discovered in 1972 the photocatalytic splitting of water on TiO_2 electrode. Recently, the application of TiO_2 focused on environmental remediation, especially water detoxification and air purification [2–4]. TiO_2 is an efficient photocatalyst, but UV light is necessary for its activation. Solar energy contains only about 4% UV light and much of the rest is visible light.

In order to utilize the visible (solar) light efficiently for the photocatalytic reactions, titanium dioxide has to be modified. There have been several approaches how to modify TiO_2 . Several authors [5–9] substituted Ti^{4+} in TiO_2 by Cr^{3+} or V^{3+} (V^{4+}) by metal ion implantation. It was demonstrated that the absorption band of Cr^{3+} -doped TiO_2 shifted and that NO_x decomposed giving rise to N_2 , O_2 , and N_2O as the result of the photocatalytic reaction under visible light irradiation with wavelength larger than 450 nm. It was reported [10–13] that it is possible to prepare the “oxygen-vacancy-based visible-light-sensitive titania” by the treatment of anatase under reductive hydrogen plasma.

N-doped titania photocatalyst sensitive to visible light irradiation was described in 2001 by Asahi et al. [14]. Since

then, various types of TiO_2 doped with anions but for nitrogen such as sulfur and carbon have been widely studied [15–23].

The purpose of this study is to characterize the thermal behavior of N-doped porous titania powder under in situ conditions of heating to 1050°C in air and to reveal differences in the annealing of porosity and subsurface structure defects. The diffusion structural analysis (DSA) [24, 25] was used to this aim. The DSA is based on the measurement of radon release rate from samples previously labelled, where radon atoms serve as a microstructure probe. In our previous studies, the DSA was already used to monitor the microstructure development of titania powders as well as titania gel layers [25] during heating of their precursors in various gas media.

2. EXPERIMENTAL

2.1. Preparation of samples

Two samples were investigated in this study: a reference sample of nondoped titania powder (called sample A) prepared by heating of anatase powder, type ST-01, Ishihara Sangyo Kaisha, Ltd., Japan, (surface area 311 m^2/g) at 550°C in air

for 3 hours, and N-doped titania (called sample B) prepared by heating of the anatase powder (sample A) under NH_3 gas flow at 575°C for 3 hours.

The chemical composition of the N-doped titania estimated by Irie et al. [23] was $\text{TiO}_{2-x}\text{N}_x$, where $x = 0.011$. The value of x was determined as the ratio of the XPS peak areas corresponding to 396 eV and 531 eV.

2.2. Methods

Scanning electron microscope (SEM) equipment by Philips, type XL 30CP, was used to characterize surface morphology.

Diffusion structural analysis (DSA) measurements were carried out by using the modified equipment NETZSCH DTA model 409 (NETZSCH, Selb, Germany) [26]. The radon-labelled titania powder (sample amount of 0.05 g) was situated in a corundum crucible and heated in air in the temperature range $20\text{--}1050^\circ\text{C}$ at the rate of $6^\circ\text{C}/\text{min}$. The constant air flow (flow rate 50 mL/min) took the radon released from the sample into the measuring chamber of radon radioactivity.

The DSA results are presented as temperature dependencies of radon release rate E (in relative units); $E = A_\alpha / A_{total}$, where A_α is α -radioactivity of radon released in unit time from the labelled sample and A_{total} is total γ -radioactivity of the labelled sample. The A_{total} value is proportional to the rate of radon formation in the sample. Semiconductor and NaI (Tl) detectors were used for the α - and γ -radioactivity measurements, respectively.

2.3. Labelling of samples for DSA measurements

Samples for DSA measurements were labelled by ^{220}Rn using recoil energy 85 keV/atom during spontaneous α -decay of radionuclides ^{228}Th and ^{224}Ra adsorbed as nitrates in trace amount on the sample surface from acetone solution. The specific activity of the sample was 10^5 Bq/gram. The depth of ^{220}Rn ions implantation by the recoil energy of 85 keV into the anatase was 60 nm from the surface of sample grains as calculated by means of Monte Carlo method using TRIM code [27]. It has been supposed that ^{220}Rn atoms formed by the spontaneous α -decay of ^{228}Th and ^{224}Ra were trapped in the subsurface layers of the sample and that structural irregularities served as diffusion paths for the radon atoms released by diffusion. The mechanisms of radon diffusion in open pores, intergranular space, or interface boundaries, respectively, were supposed to control the release of the radon from the sample.

In general, the increase in the radon release rate, E , may characterize an increase of the surface area of interfaces or porosity, whereas a decrease in E may reflect processes like closing up structure irregularities that serve as paths for radon migration, closing pores, and/or a decrease in the surface area of the interfaces.

The advantage of the DSA application consists in the possibility to characterize the microstructure changes under in situ conditions of sample heating in a selected gas environment and to bring about information about transport properties of the samples.

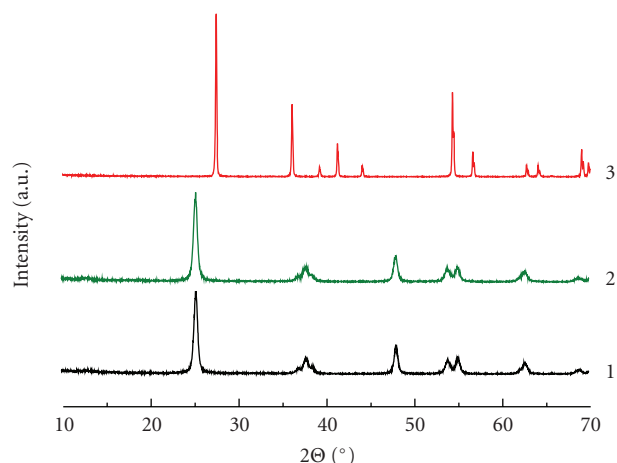


FIGURE 1: XRD patterns of the starting TiO_2 (sample A) and $\text{TiO}_{2-x}\text{N}_x$ (sample B) heated to various temperatures: (1) starting TiO_2 prepared from anatase ST 01, Ishihara Ltd., Japan (sample A), (2) $\text{TiO}_{2-x}\text{N}_x$ (sample B) prepared by heating sample A in a flow of NH_3 at $575^\circ\text{C}/3$ h, and (3) $\text{TiO}_{2-x}\text{N}_x$ (sample B) annealed at 950°C .

3. RESULTS AND DISCUSSION

3.1. Microstructure characterization

From the XRD pattern in Figure 1 (curve 2), it followed that the N-doped sample investigated in this study was homogeneous anatase, as no peaks of TiN were observed. It was found that values of BET surface area and porosity of sample B increased in comparison with sample A. The etching of nondoped titania powder at the temperature of 575°C with ammonia gas caused an increase of its surface area from 63 to $151\text{ m}^2/\text{g}$, and the total porosity volume increased from 0.36 to $0.84\text{ cm}^3/\text{g}$ (see Table 1).

SEM micrographs in Figure 2 characterized the surface morphology of samples A and B, respectively.

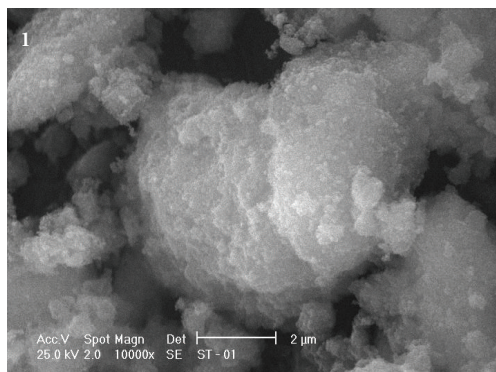
DSA results in Figure 3 were used to characterize the thermal behavior of the samples, their permeability for radon atoms, and microstructure changes on heating in air.

We assumed that the increase of the radon release rate, E , observed in Figure 3 in the temperature range $50\text{--}800^\circ\text{C}$ was due to the radon diffusion along structure irregularities in subsurface of the grains. The random “single-jump” diffusion mechanism of radon was supposed to control the release of radon in this temperature range.

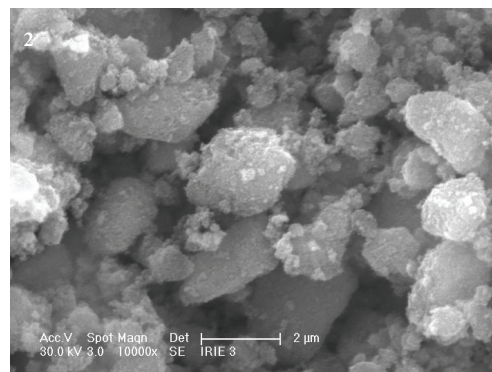
From Figure 3, it followed that the slope of the respective DSA curves slightly differed in this temperature range. The increased slope of the radon release rate, E , was observed with N-doped titania sample during air heating. It is in a good agreement with the higher values of total porosity and surface area found for sample B in comparison with reference sample A (see Table 1). From the observed decrease of the radon release rate, $E(T)$, it followed that annealing of microstructure irregularities took place with both samples A and B on heating in the temperature range $850\text{--}1000^\circ\text{C}$ accompanied by a decrease of surface area and porosity.

TABLE 1: Surface area and porosity of TiO_2 and $\text{TiO}_{2-x}\text{N}_x$ nanostructured powders.

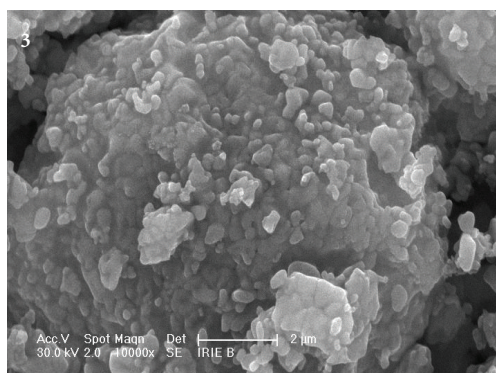
| Sample | Phases composition by XRD | Surface area by BET m^2/g | Total porosity volume cm^3/g |
|--|---------------------------|---|--|
| Starting TiO_2 -sample A | Anatase | 63.3 | 0.357 |
| $\text{TiO}_{2-x}\text{N}_x$ -sample B | Anatase | 151 | 0.839 |
| $\text{TiO}_{2-x}\text{N}_x$ -sample B annealed to 950°C | Rutile | 2.7 | 0.016 |



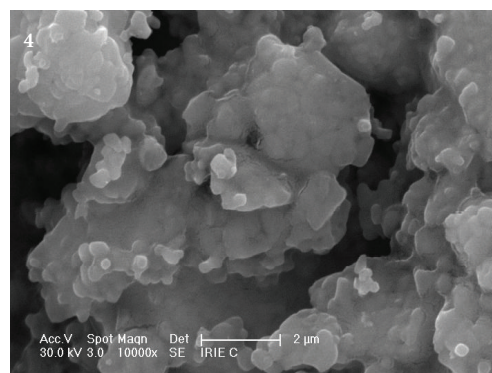
(a)



(b)



(c)



(d)

FIGURE 2: SEM micrographs of starting TiO_2 (sample A) and $\text{TiO}_{2-x}\text{N}_x$ (sample B) heated to various temperatures: (1) starting TiO_2 prepared from anatase ST 01, Ishihara Ltd., Japan, (2) $\text{TiO}_{2-x}\text{N}_x$ (sample B) prepared by heating sample A in a flow of NH_3 at $575^\circ\text{C}/3\text{ h}$, (3) $\text{TiO}_{2-x}\text{N}_x$ (sample B) annealed at 800°C , and (4) $\text{TiO}_{2-x}\text{N}_x$ (sample B) annealed at 950°C .

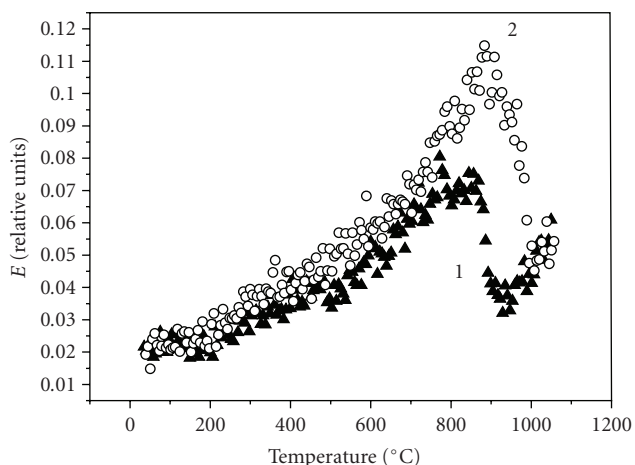


FIGURE 3: DSA results of sample A (curve 1) and sample B (curve 2) measured during heating in air at the rate of $6\text{ K}/\text{min}$.

The surface area and porosity values of sample B annealed to 950°C decreased to $2.7\text{ m}^2/\text{g}$ and $0.016\text{ cm}^3/\text{g}$, respectively.

Growth of crystallites of the samples on heating from 800 to 950°C was confirmed by the SEM micrographs (see Figure 2). Moreover, from the XRD pattern in Figure 1 (curve 3), it followed that in sample B annealed to 950°C the crystal transformation into rutile took place. In this respect, the DSA results (see Figure 3) monitored the anatase-rutile transition and the grain growth of the rutile particles during sample heating. The XRD and SEM micrographs confirmed the interpretation of the DSA results. From the XRD patterns presented in [28–30], it followed that the anatase-rutile transition took place on heating to the temperatures 800 – 900°C .

Figure 4 depicts XPS spectra of the N-doped titania heated to 800°C and 950°C , respectively. By means of X-ray photoelectron spectroscopy, it was demonstrated that the presence of the nitrogen atoms was no more indicated in the sample heated to 950°C .

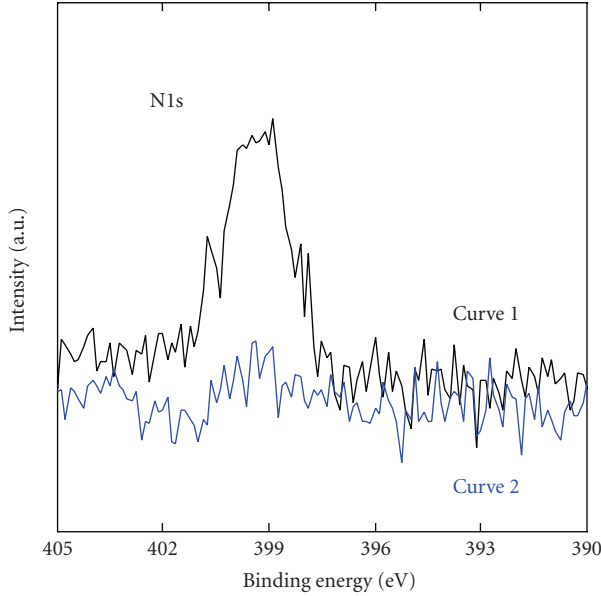


FIGURE 4: XPS spectra of the N-doped titania (sample B) heated to 800°C (curve 1) and 950°C (curve 2).

The microstructure development of the samples on heating was quantitatively described by the mathematical model [31, 32] supposing that pores and subsurface structure defects served as paths for radon diffusion. The application of the model enabled us to evaluate transport properties of the N-doped titania in comparison with the properties of the reference nondoped titania powder.

3.2. Transport properties of porous titania

It has been supposed that ^{220}Rn atoms were incorporated to the depth of 60 nm from the surface and trapped in the subsurface of the sample; the structural irregularities served as paths for the radon atoms released by diffusion. We assumed that the increase of the radon release rate, E , observed in the temperature range 50–800°C (see Figure 3) was due to the radon diffusion along structure irregularities in subsurface layers of the grains. The random “single-jump” diffusion mechanism of radon was supposed to control the release of radon in this temperature range.

The radon release rate, $E(T)$, can be written as [31]

$$E(T) = E_R + E_D(T) \cdot \Psi(T). \quad (1)$$

The term E_R is radon release rate due to recoil and the term E_D is radon release rate due to the diffusion, depending on the number of radon diffusion paths. The term E_D characterizes radon permeability along structure irregularities serving as diffusion paths, and $\Psi(T)$ is the function characterizing the decrease of the number of the radon diffusion paths. The advantage of the DSA application consists in the possibility to characterize microstructure changes under insitu conditions of sample heating in a selected gas environment and to bring about information about transport properties of the samples.

In the evaluation of the DSA results, it was supposed that radon atoms can migrate along several independent paths, such as micropores, intergranular space, as well as interface boundaries. Consequently, the mechanism of radon diffusion along two independent paths of the porous titania was considered. The following expression was used to describe the temperature dependence of the radon release rate E_D , due to diffusion:

$$E_D = \left(\frac{3}{y}\right) \left(\coth y - \left\{ \frac{1}{y} \right\} \right), \quad (2)$$

$$y(T) = \left(\frac{(S/M)\rho}{(D/\lambda)^{1/2}} \right),$$

where S/M is surface area of open pores, intergranular space, and interfaces serving as radon diffusion paths, ρ is density of the sample, $(D/\lambda)^{1/2}$ is average radon diffusion length, D is radon diffusion coefficient, and λ is radon decay constant ($\lambda = 0.00127 \text{ s}^{-1}$); $D = D_0 \exp(-Q_D/RT)$, where D_0 is the factor depending on the number of diffusion paths and their availability for radon atoms migration, Q_D is activation energy of the escape of radon atoms from the traps in the solid sample and that of the migration along diffusion paths in the solid.

In the mathematical model used in this study for the evaluation of DSA results, it was supposed that the decrease in the temperature dependence of the radon release rate, $E_D(T)$, reflected a decrease of the number of radon diffusion paths.

The following expression for $\Psi(T)$ functions was proposed [27] to describe the decrease of the number of radon diffusion paths due to changes of the microstructure:

$$\Psi(T) = 0.5 \left[1 + \operatorname{erf} \frac{1 - T_m/T}{\Delta T \sqrt{2}/T} \right], \quad (3)$$

where erf is the sign for the integral Gaussian function, T_m is the temperature of maximal rate of the annealing of the defects that serve as radon diffusion paths, and ΔT is the temperature interval of the respective solid state process.

3.3. Comparison of experimental DSA results with the model curves

It was demonstrated by DSA results (see Figures 5(a) and 5(b)) that the etching nondoped titania powder at the temperature of 575°C with ammonia gas caused changes in radon permeability in subsurface of samples. Radon diffusion parameters were calculated from the DSA results (see Table 2).

From Figures 5(a) and 5(b), it followed that experimental DSA results and model curves of the temperature dependences of the radon release rate are in a good agreement. The DSA results characterized differences in the annealing of subsurface structure irregularities, serving as radon diffusion paths in titania powders.

The experimental DSA results were evaluated by means of the mathematical model, supposing that nanopores and subsurface structure irregularities served as paths for radon

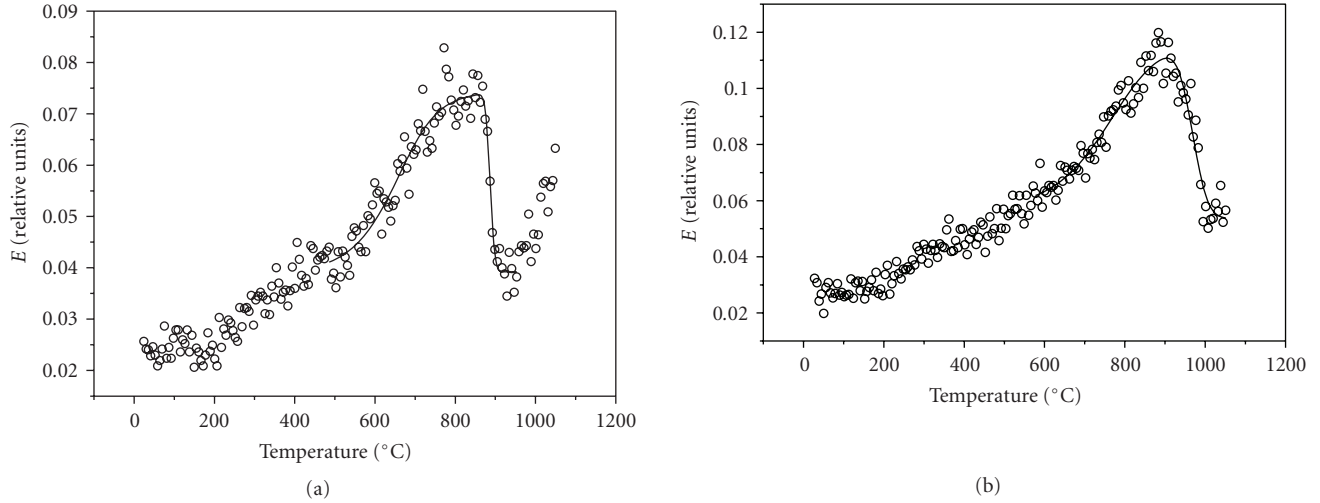


FIGURE 5: DSA experimental results (round points) and the results obtained by mathematical modeling and fitting with the experimental results (full lines) for the samples; (a) nondoped TiO_2 prepared from anatase ST 01, Ishihara Ltd., Japan, (b) sample B prepared by heating sample A in a flow of NH_3 at $575^\circ\text{C}/3\text{ h}$.

TABLE 2: Characteristics of radon permeability of TiO_2 and $\text{TiO}_{2-x}\text{N}_x$ evaluated from DSA results.

| Sample notation and preparation | Radon permeability characteristics Temperature range 20–450°C | |
|---|--|----------------|
| | D_0 (cm^2/s) | Q_D (kJ/mol) |
| Sample A: TiO_2 prepared from anatase ST 01 Ishihara Ltd. by heating at 550°C for 3 h in air | $8.4 \cdot 10^{-10}$ | 64 ± 5 |
| Sample B: $\text{TiO}_{2-x}\text{N}_x$ prepared by heating sample A in a flow of NH_3 at 575°C for 3 h | $1.8 \cdot 10^{-11}$ | 42 ± 5 |

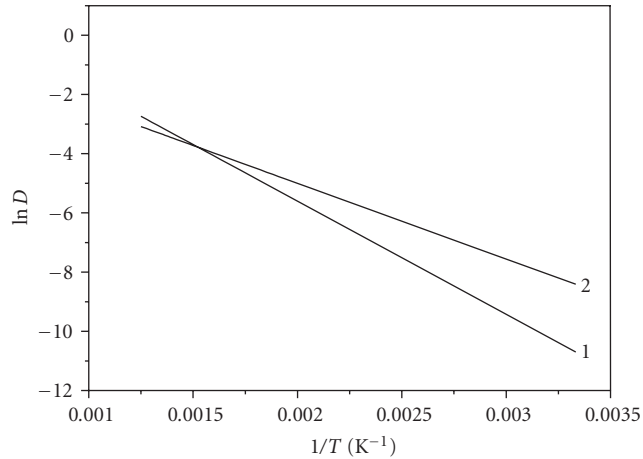


FIGURE 6: Temperature dependences of $\ln D$ versus $1/T$ for sample A (curve 1) and sample B (curve 2).

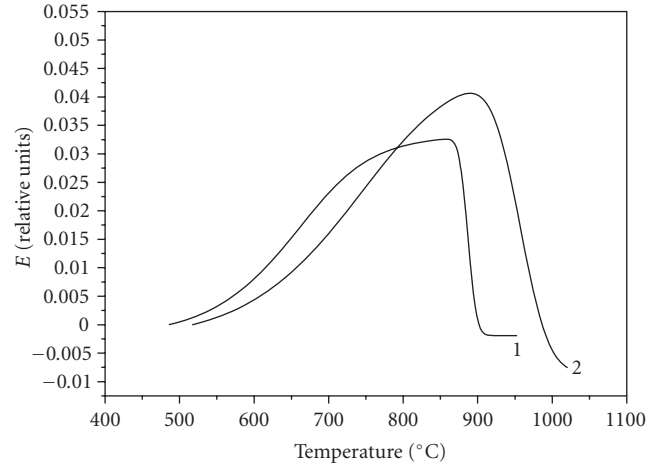


FIGURE 7: Model curves of the temperature dependences of the radon release rate $E(T)$ for sample A (curve 1) and sample B (curve 2).

diffusion. The temperature dependences of radon release rate, E_D due to diffusion, were calculated using (2). The temperature dependences of $\Psi(T)$ functions, that characterized the annealing of surface and subsurface structure irregularities, were calculated using (3).

Figure 6 depicts temperature dependences of $\ln D$ versus $1/T$ calculated from the DSA results measured on heating of sample A and sample B in the temperature range 50–450°C. The determined values of the radon permeability characteristics (activation energy Q_D of the radon diffusion) and the

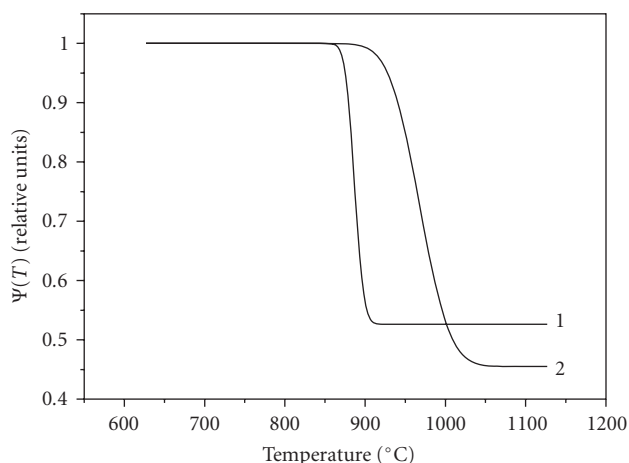


FIGURE 8: Temperature dependences of the functions $\Psi(T)$ for sample A (curve 1) and sample B (curve 2).

pre-exponential factor D_0 are presented in Table 2. Figure 7 depicts the model curves of the temperature dependences of the radon release rate $E(T)$ calculated from the DSA experimental results in the range 500–1050°C. The functions $\Psi(T)$ were used to characterize the annealing of subsurface structure irregularities in the titania powders (samples A and B) during heating in air. Figure 8 depicts the calculated temperature dependences of the functions $\Psi(T)$ for samples A and B. As it follows from Figure 8, the maximum rate of the radon release rate decrease due to annealing of subsurface structure irregularities was determined at 886°C for sample A and 997°C for sample B. Radon atoms have been used in this study as a probe of the nanostructure changes.

4. CONCLUSIONS

Thermal behavior of N-doped titania powders prepared by heat treatment of anatase in gaseous ammonia at 575°C was characterized by diffusion structural analysis (DSA). The radon permeability in the N-doped titania as well as in the reference nondoped titania powder was evaluated from the DSA results. The decrease of the radon release rate observed in the temperature range 850–1000°C made it possible to characterize annealing of microstructure irregularities.

ACKNOWLEDGMENTS

This work was supported in part by the Ministry of Education of the Czech Republic (Projects LA 292 and 1M4531433201) and Ministry for Science, Education, Sports and Culture of Japan.

REFERENCES

- [1] A. Fujishima and K. Honda, "Electrochemical photolysis of water at a semiconductor electrode," *Nature*, vol. 238, pp. 37–38, 1972.
- [2] A. Sobczyński and A. Dobosz, "Water purification by photocatalysis on semiconductors," *Polish Journal of Environmental Studies*, vol. 10, no. 4, pp. 195–205, 2001.
- [3] J. Peral, X. Domènech, and D. F. Ollis, "Heterogeneous photocatalysis for purification, decontamination and deodorization of air," *Journal of Chemical Technology and Biotechnology*, vol. 70, no. 2, pp. 117–140, 1997.
- [4] N. Getoff, "Purification of drinking-water by irradiation—a review," in *Proceedings of the Indian Academy of Sciences-Chemical Sciences*, vol. 105, pp. 373–391, Bangalore, India, January–December 1993.
- [5] T. Kudo, Y. Kudo, A. Ruike, A. Hasegawa, M. Kitano, and M. Anpo, "The design of highly active rectangular column-structured titanium oxide photocatalysts and their application in purification systems," *Catalysis Today*, vol. 122, no. 1–2, pp. 14–19, 2007.
- [6] Y. Cong, L. Xiao, J. Zhang, F. Chen, and M. Anpo, "Preparation and characterization of nitrogen-doped TiO₂ photocatalyst in different acid environments," *Research on Chemical Intermediates*, vol. 32, no. 8, pp. 717–724, 2006.
- [7] M. Kitano, K. Tsujimaru, and M. Anpo, "Decomposition of water in the separate evolution of hydrogen and oxygen using visible light-responsive TiO₂ thin film photocatalysts: effect of the work function of the substrates on the yield of the reaction," *Applied Catalysis A*, vol. 314, no. 2, pp. 179–183, 2006.
- [8] J. Zhu, F. Chen, J. Zhang, H. Chen, and M. Anpo, "Fe³⁺-TiO₂ photocatalysts prepared by combining sol-gel method with hydrothermal treatment and their characterization," *Journal of Photochemistry and Photobiology A*, vol. 180, no. 1–2, pp. 196–204, 2006.
- [9] M. Anpo and M. Takeuchi, "The design and development of highly reactive titanium oxide photocatalysts operating under visible light irradiation," *Journal of Catalysis*, vol. 216, no. 1–2, pp. 505–516, 2003.
- [10] T. Ihara, M. Miyoshi, M. Ando, S. Sugihara, and Y. Iriyama, "Preparation of a visible-light-active TiO₂ photocatalyst by RF plasma treatment," *Journal of Materials Science*, vol. 36, no. 17, pp. 4201–4207, 2001.
- [11] Y. Sakatani, H. Ando, K. Okusako, et al., "Metal ion and N co-doped TiO₂ as a visible-light photocatalyst," *Journal of Materials Research*, vol. 19, no. 7, pp. 2100–2108, 2004.
- [12] Y. Sakatani, J. Nunoshige, H. Ando, et al., "Photocatalytic decomposition of acetaldehyde under visible light irradiation over La³⁺ and N Co-doped TiO₂," *Chemistry Letters*, vol. 32, no. 12, pp. 1156–1157, 2003.
- [13] K. Takeuchi, I. Nakamura, O. Matsumoto, S. Sugihara, M. Ando, and T. Ihara, "Preparation of visible-light-responsive titanium oxide photocatalysts by plasma treatment," *Chemistry Letters*, no. 12, pp. 1354–1355, 2000.
- [14] R. Asahi, T. Morikawa, T. Ohwaki, K. Aoki, and Y. Taga, "Visible-light photocatalysis in nitrogen-doped titanium oxides," *Science*, vol. 293, no. 5528, pp. 269–271, 2001.
- [15] M. Mrowetz, W. Balcerski, A. J. Colussi, and M. R. Hoffmann, "Oxidative power of nitrogen-doped TiO₂ photocatalysts under visible illumination," *Journal of Physical Chemistry B*, vol. 108, no. 45, pp. 17269–17273, 2004.
- [16] T. Ohno, M. Akiyoshi, T. Umabayashi, K. Asai, T. Mitsui, and M. Matsumura, "Preparation of S-doped TiO₂ photocatalysts and their photocatalytic activities under visible light," *Applied Catalysis A*, vol. 265, no. 1, pp. 115–121, 2004.
- [17] T. Ohno, T. Mitsui, and M. Matsumura, "Photocatalytic activity of S-doped TiO₂ photocatalyst under visible light," *Chemistry Letters*, vol. 32, no. 4, pp. 364–365, 2003.
- [18] S. Sakthivel and H. Kisch, "Daylight photocatalysis by carbon-modified titanium dioxide," *Angewandte Chemie International Edition*, vol. 42, no. 40, pp. 4908–4911, 2003.

- [19] T. Umabayashi, T. Yamaki, H. Itoh, and K. Asai, "Band gap narrowing of titanium dioxide by sulfur doping," *Applied Physics Letters*, vol. 81, no. 3, p. 454, 2002.
- [20] T. Umabayashi, T. Yamaki, S. Tanaka, and K. Asai, "Visible light-induced degradation of methylene blue on S-doped TiO₂," *Chemistry Letters*, vol. 32, no. 4, pp. 330–331, 2003.
- [21] H. Irie, S. Washizuka, Y. Watanabe, T. Kako, and K. Hashimoto, "Photoinduced hydrophilic and electrochemical properties of nitrogen-doped TiO₂ films," *Journal of the Electrochemical Society*, vol. 152, no. 11, pp. E351–E356, 2005.
- [22] H. Irie, Y. Watanabe, and K. Hashimoto, "Carbon-doped anatase TiO₂ powders as a visible-light sensitive photocatalyst," *Chemistry Letters*, vol. 32, no. 8, pp. 772–773, 2003.
- [23] H. Irie, Y. Watanabe, and K. Hashimoto, "Nitrogen-concentration dependence on photocatalytic activity of TiO_{2-x}N_x powders," *Journal of Physical Chemistry B*, vol. 107, no. 23, pp. 5483–5486, 2003.
- [24] H. Hirashima, H. Imai, M. Y. Miah, I. M. Bountseva, I. N. Beckman, and V. Balek, "Preparation of mesoporous titania gel films and their characterization," *Journal of Non-Crystalline Solids*, vol. 350, pp. 266–270, 2004.
- [25] V. Balek, T. Mitsuhashi, I. M. Bountseva, H. Haneda, Z. Malek, and J. Šubrt, "Diffusion structural analysis study of titania films deposited by sol-gel technique on silica glass," *Journal of Sol-Gel Science and Technology*, vol. 26, no. 1–3, pp. 185–189, 2003.
- [26] V. Balek, J. Šubrt, T. Mitsuhashi, I. N. Beckman, and K. Györyová, "Emanation thermal analysis. Ready to fulfill the future needs of materials characterization," *Journal of Thermal Analysis and Calorimetry*, vol. 67, no. 1, pp. 15–35, 2002.
- [27] J. F. Ziegler and J. P. Biersack, *The stopping and range of ions in solids*, Pergamon, New York, NY, USA, 1985.
- [28] S. Bakardjieva, J. Šubrt, V. Štengl, M. J. Dianez, and M. J. Sayagues, "Photoactivity of anatase-rutile TiO₂ nanocrystalline mixtures obtained by heat treatment of homogeneously precipitated anatase," *Applied Catalysis B*, vol. 58, no. 3–4, pp. 193–202, 2005.
- [29] J. Krýsa, M. Keppert, J. Jirkovský, V. Štengl, and J. Šubrt, "The effect of thermal treatment on the properties of TiO₂ photocatalyst," *Materials Chemistry and Physics*, vol. 86, no. 2–3, pp. 333–339, 2004.
- [30] A. Daßler, A. Feltz, J. Jung, W. Ludwig, and E. Kaisersberger, "Characterization of rutile and anatase powders by thermal analysis," *Journal of Thermal Analysis*, vol. 33, no. 3, pp. 803–809, 1988.
- [31] V. Balek and I. N. Beckman, "Theory of emanation thermal analysis XII. Modelling of radon diffusion release from disordered solids on heating," *Journal of Thermal Analysis and Calorimetry*, vol. 82, no. 3, pp. 755–759, 2005.
- [32] I. N. Beckman and V. Balek, "Theory of emanation thermal analysis. XI. Radon diffusion as the probe of microstructure changes in solids," *Journal of Thermal Analysis and Calorimetry*, vol. 67, no. 1, pp. 49–61, 2002.

Research Article

Hydrothermal Preparation of Visible-Light-Driven N-Br-Codoped TiO₂ Photocatalysts

Yonggang Sheng,^{1,2} Yao Xu,¹ Dong Jiang,^{1,2} Liping Liang,^{1,2} Dong Wu,¹ and Yuhan Sun¹

¹ State Key Laboratory of Coal Conversion, Institute of Coal Chemistry, Chinese Academy of Sciences, Taiyuan 030001, China

² Graduate School of Chinese Academy of Sciences, Beijing 100049, China

Correspondence should be addressed to Yao Xu, xuyao@sxicc.ac.cn

Received 25 July 2007; Revised 14 November 2007; Accepted 20 January 2008

Recommended by Leonardo Palmisano

Using a facile hydrothermal method, N-Br-codoped TiO₂ photocatalyst that had intense absorption in visible region was prepared at low temperature (100°C), through a direct reaction between nanocrystalline anatase TiO₂ solution and cetyltrimethylammonium bromide (CTAB). The results of X-ray photoelectron spectroscopy (XPS) showed the existence of N-Ti-N, O-Ti-N-R, Ti³⁺ (attribute to the doped Br atoms by charge compensation), and TiO_xN_y species, indicating the successful codoping of N and Br atoms, which were substituted for lattice oxygen without any influence on the crystalline phase of TiO₂. In contrast to the N-doped sample, the N-Br-codoped TiO₂ photocatalyst could more readily photodegrade methylene blue (MB) under visible-light irradiation. The visible-light catalytic activity of thus-prepared photocatalyst resulted from the synergetic effect of the doped nitrogen and bromine, which not only gave high absorbance in the visible-light range, but also reduced electron-hole recombination rate.

Copyright © 2008 Yonggang Sheng et al. This is an open access article distributed under the Creative Commons Attribution License, which permits unrestricted use, distribution, and reproduction in any medium, provided the original work is properly cited.

1. INTRODUCTION

The development of photocatalysis has attracted much attention in the recent 30 years [1–3]. Of the materials being developed for photocatalytic applications, titanium dioxide (TiO₂) remains the most promising due to its high efficiency, low cost, chemical inertness, and photostability [4–6], and so forth. However, its wide-band gap (3.2 eV \equiv 380 nm for anatase) can only capture UV light, a small fraction (about 3–5%) of the solar irradiance at the earth surface, compared to the 45% of visible light [7]. Thus any red shift in the optical response of TiO₂ from the UV band to the visible band will have a profound positive effect on the photocatalytic efficiency of the materials [8, 9].

Doping TiO₂ with transition-metal elements was used as the initial approach to shift the optical response of TiO₂ from the UV band to the visible band [10–15]. However, these metal-doped TiO₂ materials suffered from thermal instability and low-quantum efficiency because of increased carrier trapping after doping, or require expensive facilities in the ion implantation case [8, 16, 17]. In contrast, better visible optical response of TiO₂ could be achieved by using nonmetal doping [8, 9, 18, 19]. Kinds of nonmetal elements, in-

cluding nitrogen [20–23], phosphor [24], carbon [25], sulfur [26, 27], boron [28], fluorine [18, 29], iodine [30], chlorine, and bromine [31], were found to be capable of making doped TiO₂ respond to visible light. In particular, the presence of substitutional N atoms in the TiO₂ matrix enhanced the absorption in the visible band and then led to a corresponding photocatalytic activity [32]. Moreover, doped halogen atoms into the oxygen sites should be accompanied by the formation of Ti³⁺ to maintain the overall electroneutrality of the crystal lattice, and a certain amount of Ti³⁺ reduced the electron-hole recombination rate and further enhanced the photocatalytic activity [18, 33]. Thus, one may want to know whether halogen atoms codoped in TiO₂ together with nitrogen have higher photocatalytic activity than that of N-doped TiO₂. To the best of our knowledge, there was no report on the visible-light-driven TiO₂ photocatalyst codoped by nitrogen and bromine.

Hereby, a simple process was utilized to prepare the N-Br-codoped TiO₂ nanocrystals via the direct reaction between nanocrystalline TiO₂ solution and cetyltrimethylammonium bromide (CTAB). Based upon the results of the present work, we found that the N-Br-codoped TiO₂ could be considered as an effective visible-light-driven photocatalyst.

2. EXPERIMENTAL

2.1. Materials preparation

All chemicals, including Titanium tetraisopropoxide (TTIP, Tianchang Chemical Co., Ltd., Tianchang, China), nitric acid (65–68%, Shanghai chemicals, Shanghai, China), CTAB (Tianjin Chemical International Trading Co., Ltd., Tianjin, China), and anhydrous ethanol (Tianjin Chemical International Trading Co., Ltd., China), were of reagent grade and were used without further purification. Water was doubly distilled and deionized.

2.1.1. Preparation of nanocrystalline TiO_2 solution

The preparation proceeded as follows: 15 mL of TTIP and 3 mL of ethanol were mixed and then added dropwise into 100 mL of water in a 200 mL beaker under continuous stirring. After 15 minutes ultrasonication, 2 mL of nitric acid were added to the mixture, and then the hydrothermal crystallization was carried out at 100°C for 5 hours to obtain a nanocrystalline TiO_2 blurry solution (denoted as TOS for convenience, the original solution for the following preparation).

2.1.2. Preparation of photocatalysts

For N-Br-codoped TiO_2 , 18.6 g of CTAB was added into TOS and was refluxed at 80°C for 3 hours under vigorous stirring, leading to a yellow milky solution. The product was then evaporated under low pressure (20-mmHg) to a yellow xerogel. Finally, the unreacted CTAB and other organic by-products were washed out with ethanol in a Soxhlet extractor and then the N-Br-codoped TiO_2 photocatalyst was obtained (denoted as TNB).

For comparison, N-doped TiO_2 photocatalyst (accordingly designed as TDN) was prepared by a direct reaction between TOS and triethylamine as the above process, and another undoped TiO_2 photocatalyst (denoted as TOX derived from TOS by a low-pressure evaporation) was also prepared.

2.2. Photocatalysts characterization

Several techniques were used to characterize the structure and properties of the above materials TDN and TNB. The X-ray diffraction (XRD) patterns were obtained on a D8 Advance diffractometer (Bruker AXS, GmbH, Karlsruhe, Germany) using Cu K α radiation. Line traces were collected over 2θ values ranging from 20° to 70°. The lattice spacing was observed by transmission electron microscopy (TEM, JEOL JEM-2010). Diffuse reflection absorption spectra (DRAS) of the samples were recorded using a UV-Vis-NIR spectrometer (UV-3150 spectrometer Shimadzu, Japan), and BaSO_4 was used as the reference sample. The DRAS spectra were used to evaluate the optical absorption properties of the samples [34]. The states of the charges were investigated by XPS (Mg K α as radiation source, PHI-5300X, Perkin-Elmer physics electronics), and all the bonding energies were calibrated to that of the adventitious C 1s peak fixed at 284.8 eV. In order to investigate the depth profile of N and Br atoms in

the lattice of TiO_2 particles, XPS analysis of sample TNB using Ar etching was performed.

For the undoped TiO_2 sample, TOX, XRD, and DRAS spectra were used to characterize the structure and properties.

2.3. Measurement of photocatalytic activity

2.3.1. Photoreactor

For UV-activity determination, the photocatalytic experiments were carried out on a photochemical reactor (SGY-1, Jiangsu Provincial Academy of Environmental Sciences) with a 300-W high-pressure mercury lamp as the light source, which provides a main irradiation wavelength about 365 nm.

For vis-activity determination, the light source was a 250 W metal halide lamp (Philips), which was positioned inside a cylindrical Pyrex vessel surrounded by a circulating water jacket to cool the lamp. A cutoff filter was also placed between lamp and the Pyrex jacket to remove the radiation below 420 nm, ensuring the reaction system to be irradiated only by visible light.

2.3.2. MB, photocatalytic activity determination

The photocatalytic experiments were carried out by adding 250 mg of samples into 250 mL of methylene blue (MB) solution (50 ppm). The suspension was stirred in dark for 30 minutes to obtain the saturated adsorption of MB before UV/visible light illumination. The concentration of MB at this point was used as the initial value for the further kinetic treatment of the photodecomposition process. At given irradiation time intervals, the dispersion was sampled (4 mL), centrifuged, and subsequently filtered through a millipore filter (pore size, 0.22 μm) to separate the catalyst particles. The concentration of MB was measured at 665 nm wavelength using UV-Visible spectrophotometer. Firstly, a series of standard MB solutions (2.5, 5, 10, 15, and 20 ppm) were prepared and measured using UV-Vis spectrophotometer. Then, a standard curve could be obtained. The concentration of MB during the degradation process could be obtained from the standard curve. Absorption spectra were recorded after 4-fold dilution.

3. RESULTS AND DISCUSSION

3.1. Crystal phase identification

Figure 1 shows the XRD patterns of samples, TOX, TDN, and TNB. The diffraction lines at $2\theta = 25.3^\circ, 37.8^\circ, 48.1^\circ, 53.9^\circ, 55.2^\circ,$ and 62.7° demonstrate that all the three samples are of the anatase phase. The average crystallite size, D_A , determined from the diffraction peak of the anatase (101) planes, is about 6.5 nm estimated from the Debye-Scherrer equation [35]. TEM (see Figure 2) of sample TDN and TNB clearly revealed the fringes of (101) planes of anatase with a lattice spacing of about 0.352 nm [36], which corresponds to the XRD patterns. Among the three main polymorphs, anatase TiO_2 is believed to exhibit the highest photocatalytic activity

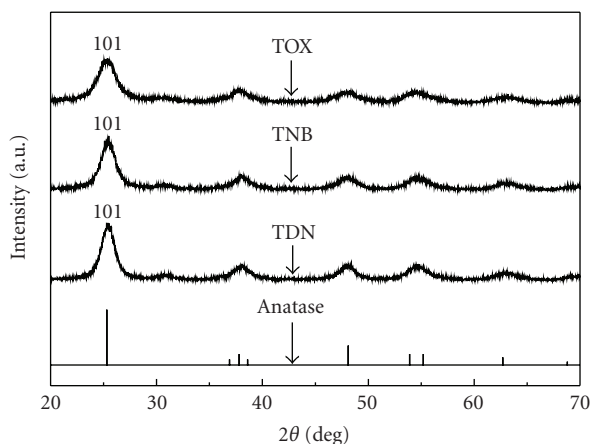


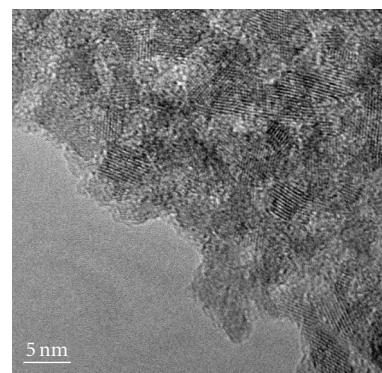
FIGURE 1: XRD patterns of samples, TOX, TDN, and TNB. Sample TOX was undoped TiO_2 , sample TDN was N-doped TiO_2 , and sample TNB was N, Br-codoped TiO_2 .

[31]. The anatase phase of the photocatalysts will contribute to a good photocatalytic activity.

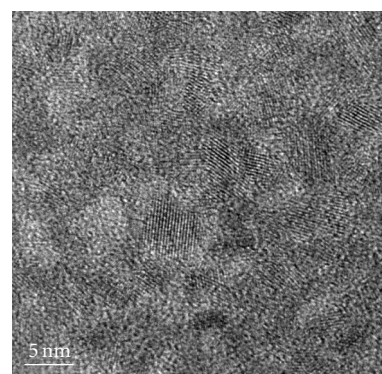
3.2. Optical properties and XPS analysis

The samples, TOX, TDN, and TNB show different color. TOX looks white, TDN yellow while TNB tan. From Figure 3 (DRAS of the samples), TOX have no absorption in the visible band; while the other two samples both have distinctly great absorption in the visible band. Compared to sample TDN, sample TNB showed obvious enhanced absorption in the visible range of 400–600 nm. The broad absorption below 500 nm is because the N 2p orbitals are localized above the top of the O 2p valence bands, whereas the absorption above 500 nm is mainly caused by oxygen vacancies [37]. The band gap energy of the synthesized samples was estimated to be about 3.12 eV for TOX, 2.03 eV for TDN, and 1.88 eV for TNB by the absorption edge. The band gap narrowing will result in the obvious red-shift in the optical response, which is helpful for visible photocatalytic activity.

The chemical composition of surface was determined by XPS (see Figure 4). The C 1s, O 1s, Ti 2p, and N 1s peaks components are discernible in the wide scan spectrum of the two samples, but obvious peaks of Br 3d can be found only for TNB. The N 1s core-level spectra of the two samples are showed in Figure 5. For TDN sample (Figure 5(a)), the feature at 396.7 eV is generally known as the “nitride” peak and can be assigned to the N^{2-} anions that replace oxygen atoms in the TiO_2 lattice to form N-Ti-N [38, 39]. N 1s peak of 399.3 eV can be attributed to the binding energy of the N atom in special environment of O-Ti-N-R (R: alkyl) [38–40]. The weak N 1s peak at 401.7 eV indicates the trace amount of nitrogen in the form of Ti-N-O [39]. For TNB sample, No N 1s peaks from N^+ of CTAB (at 402.3 eV) can be found in Figure 5(b) [38, 41], indicating that residual CTAB has been completely removed by the Soxhlet extracting method or at least the residual CTAB was too little to be detected. The two main N 1s peaks at 396.5 eV and 399.3 eV can be attributed to the binding energy of the N atom in special environment of N-Ti-N and O-Ti-N-R (R: alkyl) [38–40].



(a)



(b)

FIGURE 2: TEM images of samples, TDN (a) and TNB (b).

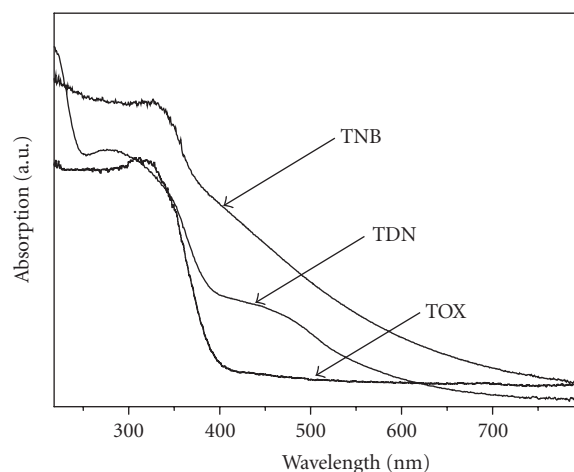


FIGURE 3: UV-Vis diffuse reflection absorption spectra of samples, TOX, TDN, and TNB.

Figure 6 showed Ti 2p core-level spectra of TDN and TNB. For TDN sample (Figure 6(a)), the deconvolution of Ti 2p bands yields two major doublets ($2p_{3/2}$ and $2p_{1/2}$) encompassing the set of two $2p_{3/2}$ peaks. The main Ti $2p_{3/2}$ peak at 458.6 eV is typical for pure TiO_2 [38, 42] and can be attributed to those unreacted TiO_2 , the other Ti $2p_{3/2}$ peak at 457.2 eV for TiO_xN_y [38, 42]. For TNB sample (Figure 6(b)), the deconvolution of the complex Ti 2p bands yields three major

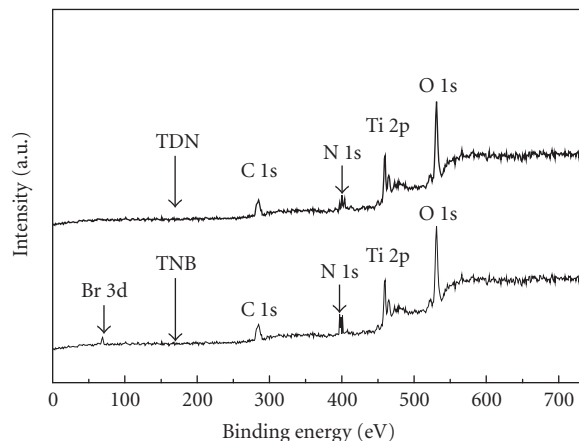


FIGURE 4: XPS wide scan spectra of samples, TDN and TNB.

TABLE 1: Results of XPS analysis using Ar etching, sample TNB.

| Name | Content/% | |
|----------------|-----------|------|
| | Br | N |
| Before etching | 0.31 | 3.68 |
| First etching | 0.11 | 1.81 |
| Second etching | 0 | 1.79 |
| Third etching | 0 | 1.17 |

doublets ($2p_{3/2}$ and $2p_{1/2}$) encompassing the set of three Ti $2p_{3/2}$ peaks. The strongest Ti $2p_{3/2}$ peak at 458.7 eV is typical for pure TiO_2 [38] and can be attributed to those unreacted TiO_2 , other peaks, at 455.7 eV typical for Ti^{3+} [38], and at 457.2 eV for TiO_xN_y [38, 42]. Doped nitrogen atoms result in the formation of TiO_xN_y [42], meanwhile, the formation of Ti^{3+} might attribute to the substitution of bromine atoms for oxygen just like the case of fluorine doping [33, 43].

From the results of the depth profile of N and Br atoms of sample TNB (see Table 1), we found that N and Br atoms were mainly at the surface of TiO_2 particles. Besides, the results of XPS indicate that N and Br atoms were actually existed in the lattice of the titania crystal.

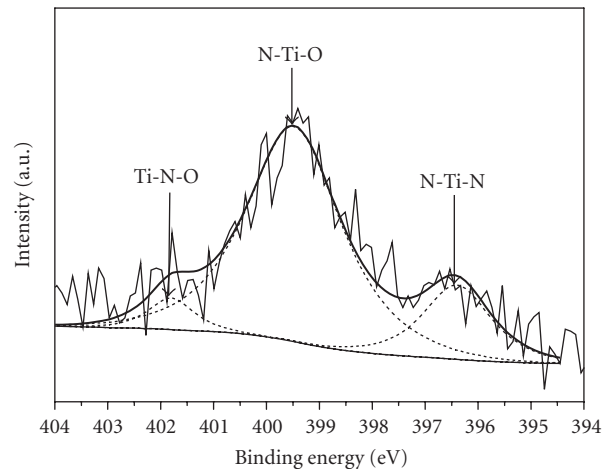
3.3. Photocatalytic activity

3.3.1. UV-activity

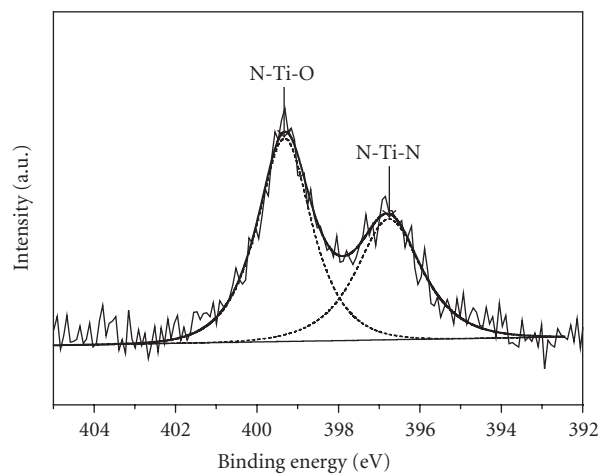
The photodecomposition of the MB in aqueous solution was carried out under UV light. The time-dependent concentration of MB is shown in Figure 7(a). With high crystallization, P25 can more readily photodegrade MB. The photocatalysts, TOX, TDN, and TNB, exhibit similar and good photocatalytic activity, which due to their similar crystallization and microstructure. Because the doping process was performed under low temperature, then there is little change of crystallization and microstructure.

3.3.2. Vis-activity

The photodecomposition of the MB in aqueous solution was carried out under visible light. The time-dependent concen-



(a)



(b)

FIGURE 5: (a) N 1s core-level spectrum (deconvolution of N 1s bands) of TDN. (b) N 1s core-level spectrum (deconvolution of N 1s bands) of TNB.

tration of MB in solution is shown in Figure 7(b). Compared with the visible-inactive P25 and TOX, both of TDN and TNB exhibit excellent photocatalytic activity, and obviously TNB can more readily photodegrade MB than TDN. One may raise the doubt of whether it is the photocatalyst that plays the key role in decomposing MB because MB can absorb visible light itself. This doubt, however, is not necessary considering the case using P25, TOX, TDN, or TNB as photocatalyst. If the decomposition of MB is due to the light absorbance itself, then the efficiency of the decomposition using a different photocatalyst may not vary so much as is shown in Figure 7(b). Also, one may consider such dyes degradation on photocatalysts surface under visible light to be a sensitization mechanism. If the decomposition of MB is due to a sensitization mechanism, then the efficiency of the decomposition using TOX may be similar to that of TDN and TNB due to their similar crystallization and microstructure.

The stability of the catalysts has been tested by using the photocatalysts repeatedly three times. No visible change of the photoactivity has been observed throughout these three

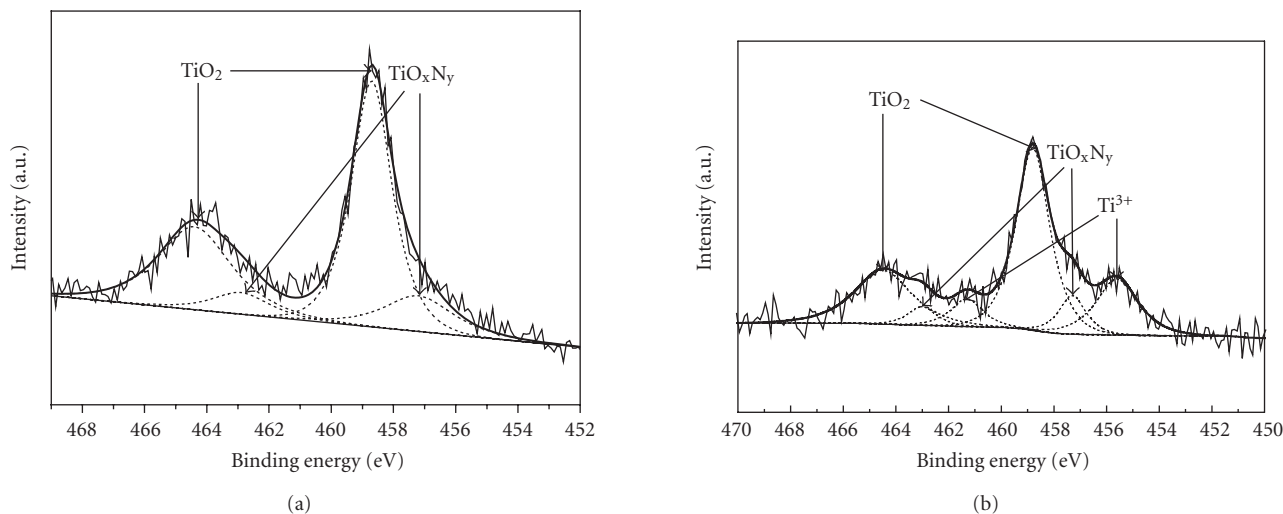


FIGURE 6: (a) Ti 2p core-level spectrum (deconvolution of Ti 2p bands) of TDN. (b) Ti 2p core-level spectrum (deconvolution of Ti 2p bands) of TNB.

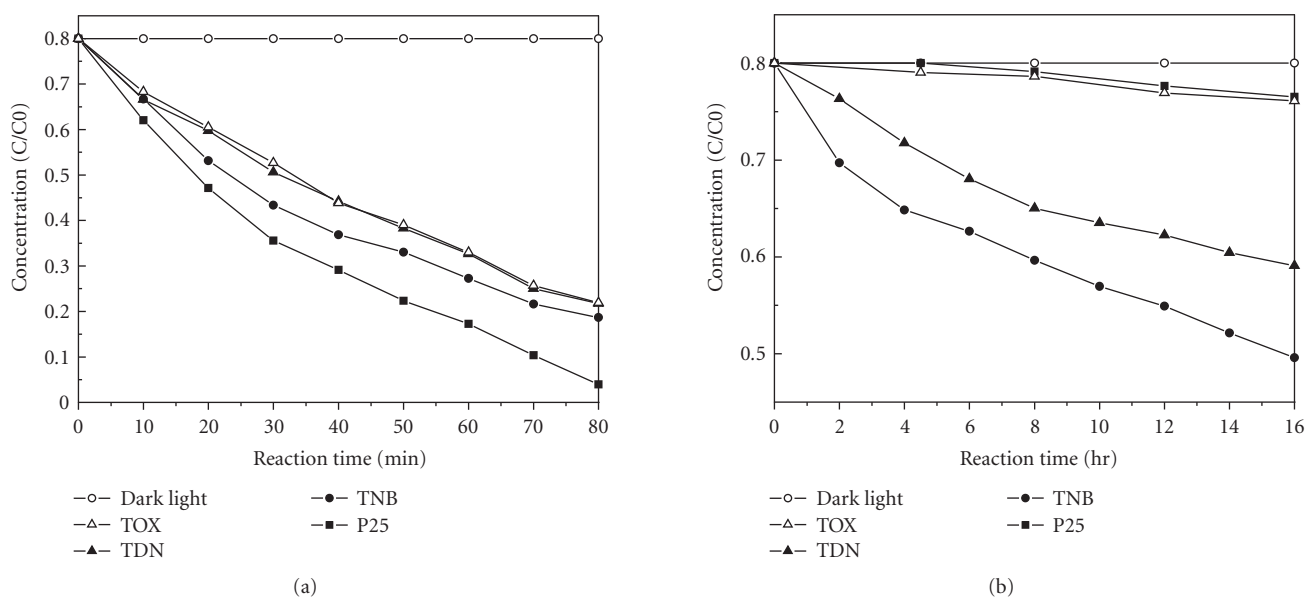


FIGURE 7: (a) Comparison of the UV photocatalytic activities of P25, TOX, TDN, and TNB on MB photodecomposition. Time-dependent concentration of MB in solution under UV light. (b) Comparison of the visible photocatalytic activities of P25, TOX, TDN, and TNB on MB photodecomposition. Time-dependent concentration of MB in solution under visible light.

runs. To ascertain the role of light radiation in the decomposition process, we have tested the effect of TNB without light radiation and the result is not unexpected (see Figures 7(a) and 7(b)). Without light, the decomposition process could hardly proceed.

Altogether, the excellent visible-light photoactivity of TDN and TNB can be explained by the doped microstructure. Because the N 2p orbitals are localized above the top of the O 2p valence bands, the doped N atoms will result in band gap narrowing and improve the visible light absorption of anatase TiO_2 . The improved visible light absorption can increase the number of photoinduced electrons. Undoubt-

edly, this can enhance the photocatalytic activity. Moreover, the N-doping is considered to have a contribution in the formation of oxygen vacancies [44–47]. Incorporation of two N atoms into the oxygen sites should be accompanied by the formation of one oxygen vacancy to maintain the overall electroneutrality of the crystal lattice. Many studies have confirmed that the formation of the superoxide ($\text{O}_2^{\cdot-}$) and hydroxyl radicals (OH^{\cdot}), two important active species for initiating a photocatalytic reaction [48–52], required oxygen vacancy sites [35, 53, 54]. For sample TNB, the contribution of the doped Br atoms to the visible photocatalytic activity is achieved mainly by the improvement of the quantum

efficiency. The doped Br atoms can convert Ti^{4+} to Ti^{3+} by charge compensation, and the existence of a certain amount of Ti^{3+} reduces the electron hole recombination rate and further enhanced the quantum efficiency and photocatalytic activity [43]. Moreover, halogen element, such as Br, Cl, F, doping for oxygen in TiO_2 can also cause the absorption edge of TiO_2 to shift to the lower energy region [31], though the red-shift is weak, which can enhance the photocatalytic activity too. Thus, the synergetic effect of doped N and Br atoms contributes to a higher visible photocatalytic activity of TNB.

4. CONCLUSIONS

In this paper, N-Br-codoped TiO_2 photocatalyst was prepared via a facile two-step homogeneous hydrothermal route at low temperature. As expected, the prepared photocatalyst showed a high-photocatalytic activity under visible irradiation, which was attributed to its anatase crystalline framework, low-electron hole recombination rate and high absorbance in the visible light range. A synergetic effect of both doped N atoms and Br atoms should be responsible for the enhanced visible photoactivity.

ACKNOWLEDGMENTS

The financial supports from the National Native Science Foundation (no. 20573128) and Shanxi Native Science Foundations (no. 20051025 and no. 2006021031) were acknowledged.

REFERENCES

- [1] A. Fujishima and K. Honda, "Electrochemical photolysis of water at a semiconductor electrode," *Nature*, vol. 238, no. 5358, pp. 37–38, 1972.
- [2] S. U. M. Khan and J. Akikusa, "Photoelectrochemical splitting of water at nanocrystalline $n-Fe_2O_3$ thin-film electrodes," *Journal of Physical Chemistry B*, vol. 103, no. 34, pp. 7184–7189, 1999.
- [3] S. Licht, B. Wang, S. Mukerji, T. Soga, M. Umeno, and H. Tributsch, "Efficient solar water splitting, exemplified by RuO_2 -catalyzed AlGaAs/Si photoelectrolysis," *Journal of Physical Chemistry B*, vol. 104, no. 38, pp. 8920–8924, 2000.
- [4] C. Burda, Y. Lou, X. Chen, A. C. S. Samia, J. Stout, and J. L. Gole, "Enhanced nitrogen doping in TiO_2 nanoparticles," *Nano Letters*, vol. 3, no. 8, pp. 1049–1051, 2003.
- [5] V. Kozhukharov, P. Vitanov, P. Stefchev, et al., " TiO_2 -photocatalyzed oxidative water pollutants degradation: a review of the state-of-art," *Journal of Environmental Protection and Ecology*, vol. 2, no. 1, pp. 107–111, 2001.
- [6] A. L. Linsebigler, G. Lu, and J. T. Yates Jr., "Photocatalysis on TiO_2 surfaces: principles, mechanisms, and selected results," *Chemical Reviews*, vol. 95, no. 3, pp. 735–758, 1995.
- [7] M. Mrowetz, W. Balcerski, A. J. Colussi, and M. R. Hoffmann, "Oxidative power of nitrogen-doped TiO_2 photocatalysts under visible illumination," *Journal of Physical Chemistry B*, vol. 108, no. 45, pp. 17269–17273, 2004.
- [8] R. Asahi, T. Morikawa, T. Ohwaki, K. Aoki, and Y. Taga, "Visible-light photocatalysis in nitrogen-doped titanium oxides," *Science*, vol. 293, no. 5528, pp. 269–271, 2001.
- [9] H. Irie, Y. Watanabe, and K. Hashimoto, "Nitrogen-concentration dependence on photocatalytic activity of $TiO_{2-x}N_x$ powders," *Journal of Physical Chemistry B*, vol. 107, no. 23, pp. 5483–5486, 2003.
- [10] S. I. Shah, W. Li, C.-P. Huang, O. Jung, and C. Ni, "Study of Nd^{3+} , Pd^{2+} , Pt^{4+} , and Fe^{3+} dopant effect on photoreactivity of TiO_2 nanoparticles," *Proceedings of the National Academy of Sciences of the United States of America*, vol. 99, 2, pp. 6482–6486, 2002.
- [11] A.-W. Xu, J.-Y. Zhu, Y. Gao, and H.-Q. Liu, "Iron-doped titania nanoparticles for the photocatalytic oxidative degradation of nitrite," *Chemical Research in Chinese Universities*, vol. 17, no. 3, pp. 281–286, 2001.
- [12] C. Wang, D. W. Bahnemann, and J. K. Dohrmann, "A novel preparation of iron-doped TiO_2 nanoparticles with enhanced photocatalytic activity," *Chemical Communications*, vol. 16, pp. 1539–1540, 2000.
- [13] Y. Wang, Y. Hao, H. Cheng, et al., "Photoelectrochemistry of transition metal-ion-doped TiO_2 nanocrystalline electrodes and higher solar cell conversion efficiency based on Zn^{2+} -doped TiO_2 electrode," *Journal of Materials Science*, vol. 34, no. 12, pp. 2773–2779, 1999.
- [14] A. A. Altyntnikov, G. A. Zenkovets, and V. F. Anufrienko, "ESR study of reduced vanadium-titanium oxide catalysts," *Reaction Kinetics and Catalysis Letters*, vol. 67, no. 2, pp. 273–279, 1999.
- [15] T. Umabayashi, T. Yamaki, H. Itoh, and K. Asai, "Analysis of electronic structures of 3d transition metal-doped TiO_2 based on band calculations," *Journal of Physics and Chemistry of Solids*, vol. 63, no. 10, pp. 1909–1920, 2002.
- [16] X. Chen, Y. Lou, A. C. S. Samia, C. Burda, and J. L. Gole, "Formation of oxynitride as the photocatalytic enhancing site in nitrogen-doped titania nanocatalysts: comparison to a commercial nanopowder," *Advanced Functional Materials*, vol. 15, no. 1, pp. 41–49, 2005.
- [17] H. Yamashita, M. Honda, M. Harada, et al., "Preparation of titanium oxide photocatalysts anchored on porous silica glass by a metal ion-implantation method and their photocatalytic reactivities for the degradation of 2-propanol diluted in water," *Journal of Physical Chemistry B*, vol. 102, no. 52, pp. 10707–10711, 1998.
- [18] J. C. Yu, J. Yu, W. Ho, Z. Jiang, and L. Zhang, "Effects of F^- doping on the photocatalytic activity and microstructures of nanocrystalline TiO_2 powders," *Chemistry of Materials*, vol. 14, no. 9, pp. 3808–3816, 2002.
- [19] S. U. M. Khan, M. Al-Shahry, and W. B. Ingler Jr., "Efficient photochemical water splitting by a chemically modified $n-TiO_2$," *Science*, vol. 297, no. 5590, pp. 2243–2245, 2002.
- [20] S. Sakthivel, M. Janczarek, and H. Kisch, "Visible light activity and photoelectrochemical properties of nitrogen-doped TiO_2 ," *Journal of Physical Chemistry B*, vol. 108, no. 50, pp. 19384–19387, 2004.
- [21] K. Kobayakawa, Y. Murakami, and Y. Sato, "Visible-light active N-doped TiO_2 prepared by heating of titanium hydroxide and urea," *Journal of Photochemistry and Photobiology A*, vol. 170, no. 2, pp. 177–179, 2005.
- [22] T. Ihara, M. Miyoshi, Y. Iriyama, O. Matsumoto, and S. Sugihara, "Visible-light-active titanium oxide photocatalyst realized by an oxygen-deficient structure and by nitrogen doping," *Applied Catalysis B*, vol. 42, no. 4, pp. 403–409, 2003.
- [23] S. Yin, H. Yamaki, M. Komatsu, et al., "Preparation of nitrogen-doped titania with high visible light induced photocatalytic activity by mechanochemical reaction of titania and hexamethylenetetramine," *Journal of Materials Chemistry*, vol. 13, no. 12, pp. 2996–3001, 2003.

- [24] L. Lin, W. Lin, Y. Zhu, B. Zhao, and Y. Xie, "Phosphor-doped titania - a novel photocatalyst active in visible light," *Chemistry Letters*, vol. 34, no. 3, pp. 284–285, 2005.
- [25] S. Sakthivel and H. Kisch, "Daylight photocatalysis by carbon-modified titanium dioxide," *Angewandte Chemie International Edition*, vol. 42, no. 40, pp. 4908–4911, 2003.
- [26] T. Ohno, T. Mitsui, and M. Matsumura, "Photocatalytic activity of S-doped TiO₂ photocatalyst under visible light," *Chemistry Letters*, vol. 32, no. 4, pp. 364–365, 2003.
- [27] T. Umebayashi, T. Yamaki, S. Tanaka, and K. Asai, "Visible light-induced degradation of methylene blue on S-doped TiO₂," *Chemistry Letters*, vol. 32, no. 4, pp. 330–331, 2003.
- [28] W. Zhao, W. Ma, C. Chen, J. Zhao, and Z. Shuai, "Efficient degradation of toxic organic pollutants with (Ni₂O₃)/(TiO_{2-x}B_x) under visible irradiation," *Journal of the American Chemical Society*, vol. 126, no. 15, pp. 4782–4783, 2004.
- [29] T. Yamaki, T. Umebayashi, T. Sumita, et al., "Fluorine-doping in titanium dioxide by ion implantation technique," *Nuclear Instruments and Methods in Physics Research, Section B*, vol. 206, pp. 254–258, 2003.
- [30] X. Hong, Z. Wang, W. Cai, et al., "Visible-light-activated nanoparticle photocatalyst of iodine-doped titanium dioxide," *Chemistry of Materials*, vol. 17, no. 6, pp. 1548–1552, 2005.
- [31] H. Luo, T. Takata, Y. Lee, J. Zhao, K. Domen, and Y. Yan, "Photocatalytic activity enhancing for titanium dioxide by co-doping with bromine and chlorine," *Chemistry of Materials*, vol. 16, no. 5, pp. 846–849, 2004.
- [32] C. Di Valentin, G. Pacchioni, and A. Selloni, "Origin of the different photoactivity of N-doped anatase and rutile TiO₂," *Physical Review B*, vol. 70, no. 8, Article ID 085116, 4 pages, 2004.
- [33] D. Li, H. Haneda, S. Hishita, and N. Ohashi, "Visible-light-driven N-F-codoped TiO₂ photocatalysts. 2. Optical characterization, photocatalysis, and potential application to air purification," *Chemistry of Materials*, vol. 17, no. 10, pp. 2596–2602, 2005.
- [34] H. Sun, Y. Bai, Y. Cheng, W. Jin, and N. Xu, "Preparation and characterization of visible-light-driven carbon-sulfur-codoped TiO₂ photocatalysts," *Industrial and Engineering Chemistry Research*, vol. 45, no. 14, pp. 4971–4976, 2006.
- [35] J. L. Gole, J. D. Stout, C. Burda, Y. Lou, and X. Chen, "Highly efficient formation of visible light tunable TiO_{2-x}N_x photocatalysts and their transformation at the nanoscale," *Journal of Physical Chemistry B*, vol. 108, no. 4, pp. 1230–1240, 2004.
- [36] H. Yu, J. Yu, and B. Cheng, "Preparation, characterization and photocatalytic activity of novel TiO₂ nanoparticle-coated titanate nanorods," *Journal of Molecular Catalysis A*, vol. 253, no. 1-2, pp. 99–106, 2006.
- [37] Z. Lin, A. Orlov, R. M. Lambert, and M. C. Payne, "New insights into the origin of visible light photocatalytic activity of nitrogen-doped and oxygen-deficient anatase TiO₂," *Journal of Physical Chemistry B*, vol. 109, no. 44, pp. 20948–20952, 2005.
- [38] J. Wang, W. Wu, and D. Feng, *XPS/AES/UPS*, National Defense Industry Press, Beijing, China, 1992.
- [39] J. Wang, W. Zhu, Y. Zhang, and S. Liu, "An efficient two-step technique for nitrogen-doped titanium dioxide synthesizing: visible-light-induced photodecomposition of methylene blue," *Journal of Physical Chemistry C*, vol. 111, no. 2, pp. 1010–1014, 2007.
- [40] O. Diwald, T. L. Thompson, T. Zubkov, E. G. Goralski, S. D. Walck, and J. T. Yates Jr., "Photochemical activity of nitrogen-doped rutile TiO₂(110) in visible light," *Journal of Physical Chemistry B*, vol. 108, no. 19, pp. 6004–6008, 2004.
- [41] X.-H. Liu, X.-H. Luo, S.-X. Lu, J.-C. Zhang, and W.-L. Cao, "A novel cetyltrimethyl ammonium silver bromide complex and silver bromide nanoparticles obtained by the surfactant counterion," *Journal of Colloid and Interface Science*, vol. 307, no. 1, pp. 94–100, 2007.
- [42] M. Drygaś, C. Czosnek, R. T. Paine, and J. F. Janik, "Two-stage aerosol synthesis of titanium nitride TiN and titanium oxynitride TiO_xN_y nanopowders of spherical particle morphology," *Chemistry of Materials*, vol. 18, no. 13, pp. 3122–3129, 2006.
- [43] J. C. Yu, J. Yu, W. Ho, Z. Jiang, and L. Zhang, "Effects of F⁻ doping on the photocatalytic activity and microstructures of nanocrystalline TiO₂ powders," *Chemistry of Materials*, vol. 14, no. 9, pp. 3808–3816, 2002.
- [44] I. Nakamura, N. Negishi, S. Kutsuna, T. Ihara, S. Sugihara, and K. Takeuchi, "Role of oxygen vacancy in the plasma-treated TiO₂ photocatalyst with visible light activity for NO removal," *Journal of Molecular Catalysis A*, vol. 161, no. 1-2, pp. 205–212, 2000.
- [45] T. Ihara, M. Miyoshi, M. Ando, S. Sugihara, and Y. Iriyama, "Preparation of a visible-light-active TiO₂ photocatalyst by RF plasma treatment," *Journal of Materials Science*, vol. 36, pp. 4201–4207, 2001.
- [46] I. Justicia, P. Ordejón, G. Canto, et al., "Designed self-doped titanium oxide thin films for efficient visible-light photocatalysis," *Advanced Materials*, vol. 14, no. 19, pp. 1399–1402, 2002.
- [47] T. Ihara, M. Miyoshi, Y. Iriyama, O. Matsumoto, and S. Sugihara, "Visible-light-active titanium oxide photocatalyst realized by an oxygen-deficient structure and by nitrogen doping," *Applied Catalysis B*, vol. 42, no. 4, pp. 403–409, 2003.
- [48] K.-L. Zhang, X.-P. Lin, F.-Q. Huang, and W.-D. Wang, "A novel photocatalyst PbSb₂O₆ for degradation of methylene blue," *Journal of Molecular Catalysis A*, vol. 258, no. 1-2, pp. 185–190, 2006.
- [49] M. M. Mohamed and M. M. Al-Esaimi, "Characterization, adsorption and photocatalytic activity of vanadium-doped TiO₂ and sulfated TiO₂ (rutile) catalysts: degradation of methylene blue dye," *Journal of Molecular Catalysis A*, vol. 255, no. 1-2, pp. 53–61, 2006.
- [50] J. Hong, C. Sun, S.-G. Yang, and Y.-Z. Liu, "Photocatalytic degradation of methylene blue in TiO₂ aqueous suspensions using microwave powered electrodeless discharge lamps," *Journal of Hazardous Materials*, vol. 133, no. 1–3, pp. 162–166, 2006.
- [51] A. Houas, H. Lachheb, M. Ksibi, E. Elaloui, C. Guillard, and J.-M. Herrmann, "Photocatalytic degradation pathway of methylene blue in water," *Applied Catalysis B*, vol. 31, no. 2, pp. 145–157, 2001.
- [52] S. Senthilkumar, K. Porkodi, R. Gomathi, A. Geetha Maheswari, and N. Manonmani, "Sol-gel derived silver doped nanocrystalline titania catalysed photodegradation of methylene blue from aqueous solution," *Dyes and Pigments*, vol. 69, no. 1-2, pp. 22–30, 2006.
- [53] M. A. Henderson, W. S. Epling, C. L. Perkins, C. H. F. Peden, and U. Diebold, "Interaction of molecular oxygen with the vacuum-annealed TiO₂(110) surface: molecular and dissociative channels," *Journal of Physical Chemistry B*, vol. 103, no. 25, pp. 5328–5337, 1999.
- [54] R. Schaub, P. Thostrup, N. Lopez, et al., "Oxygen vacancies as active sites for water dissociation on rutile TiO₂(110)," *Physical Review Letters*, vol. 87, no. 26, Article ID 266104, 4 pages, 2001.

Research Article

Electrochemical Investigation of Doped Titanium Dioxide

J. W. J. Hamilton,¹ J. A. Byrne,¹ C. McCullagh,² and P. S. M. Dunlop¹

¹Nanotechnology and Integrated BioEngineering Centre (NIBEC), University of Ulster, Jordanstown Campus, Newtownabbey, County Antrim BT37 0QB, Northern Ireland, UK

²The School of Resources and Environment Engineering (CREE), Faculty of Design and Technology, The Robert Gordon University, Clarke Building, Schoolhill, Aberdeen, AB10 1FR, UK

Correspondence should be addressed to J. W. J. Hamilton, jwj.hamilton@ulster.ac.uk

Received 30 August 2007; Revised 7 January 2008; Accepted 25 January 2008

Recommended by Vincenzo Augugliaro

Thin films of transition-metal doped (0.2, 1.0, and 5.0 atom%) TiO₂ were prepared on titanium foil using a sol-gel route catalyzed by ammonium acetate. Dopants investigated were the fourth-period transition metals. The prepared films were characterised by Raman spectroscopy, Auger electron spectroscopy, and photoelectrochemical methods. The films doped with transition metals showed a lower photocurrent response than undoped samples. No major red shift in the photocurrent response spectra of the doped films was observed. A photocurrent response was observed under visible light irradiation of the samples and was potential dependent peaking around -0.3 V (SCE), which is indicative of electron promotion from a filled defect level. Examination of the defect level potential dependence by analysis of the current-time response under chopped illumination at fixed potential (-0.8 V– $+1.07$ V) gave a good correlation with the potential dependence observed in the visible light irradiation studies.

Copyright © 2008 J. W. J. Hamilton et al. This is an open access article distributed under the Creative Commons Attribution License, which permits unrestricted use, distribution, and reproduction in any medium, provided the original work is properly cited.

1. INTRODUCTION

The photoactive properties of titanium dioxide (TiO₂) have been utilised for two main fields of application: (i) environmental remediation including water/air purification, and selfcleaning surfaces; (ii) solar energy conversion through photoelectrolytic water splitting to yield hydrogen and oxygen [1–4]. Nanoparticle TiO₂ electrodes have also found application in dye sensitised photovoltaic cells [5, 6]. The reported efficiency of TiO₂ for solar applications in (i) and (ii) above is low due to its wide band-gap (3.0–3.2 eV) requiring ultraviolet irradiation (UV). In attempts to increase the solar efficiency by utilising visible light, TiO₂ has been doped with other elements with the aim of producing a red shift in the absorbance spectrum. Transition metal ions are commonly employed dopants due to their strong absorption of visible light and their similar ionic radius to the parent titanium ion. However, studies into the effectiveness of transition metal ions as dopants to improve solar efficiency have reported conflicting results. For example, chromium doping of TiO₂ has been reported to yield both an increase in activity [7–10] and a decrease in activity [11–16]. The majority of dopant studies do report a red shift in the absorption spectra

of the doped material, however, this does not necessarily correlate with an increase in photoactivity [13, 17–20]. Unfortunately, there are few publications which report both the photocurrent response and absorption spectra for doped TiO₂. Where they exist, the results are conflicting, with some researchers reporting a good correlation between the photoactive spectrum and the absorption spectrum [8, 11, 17] while others have not found a correlation [21].

The direct comparison of published results for the efficiency of doped TiO₂ photocatalysts is not straightforward as reported materials have been produced using different methods and have been tested under different conditions. For example, if the photocatalytic degradation of a model pollutant is used as the measure of efficacy then changes in surface adsorption, due to changes in surface PZC resulting from doping, may result in an increase in photocatalytic degradation rate of certain organics but not others [15, 22].

Only a few papers discriminate between the effects of the dopant ion energy levels and the dopant ion-induced oxygen defect energy level within band structure. An oxygen defect level is introduced when the dopant has a lower valence than titanium thus leaving oxygen bonding unsatisfied and a new energy level is produced.

The effect of this induced defect level is difficult to study within a single dopant regime. Analysis of the dopant induced oxygen level within the band structure of platinised TiO_2 was studied by Karakitsou and Verekios using dopants of different valences to titanium [23]. Using hydrogen evolution as the measure of photoactivity, they reported that dopants with a valence greater than 4 gave higher activity, and dopants with valence less than 4 had a lower activity, as compared to the undoped TiO_2 . The decrease in the photoactivity with dopants of valence less than 4 was attributed to an increased rate of charge carrier recombination.

The effect of oxygen defect levels in the TiO_2 band structure have previously been reported in literature [24, 25]. Siripala and Tomkiewicz were the first to examine the effect of these defects on charge transfer at the TiO_2 electrolyte interface [26]. They reported that oxygen defect levels were responsible for observed photocurrent using sub-band gap illumination. The sub-band gap photocurrent was only observed between applied potentials of -0.6 V and $+0.6\text{ V}$ (SCE). Other workers have reported the generation of oxygen defect states via plasma modification of TiO_2 which yielded a visible photocurrent response [27].

In this work, we report the effect of doping with transition metal ions on changes in UV/Vis absorption spectra, crystal phase, current-potential response, and spectral photocurrent response.

2. EXPERIMENTAL

A sol gel procedure, adapted from the work of Murakami et al. [28] using ammonium acetate as a catalyst, was used to prepare TiO_2 films. A solution of 0.0973 g ammonium acetate, in 0.2 cm^3 water/ 15 cm^3 butan-1-ol, was added dropwise to solution of 0.377 g titanium (IV) butoxide in 10 cm^3 butan-1-ol. For doped samples, the relevant dopant acetate salt was added along with the ammonium acetate to give 0.2, 1.0, or 5.0 atom% (with respect to titanium). Dopants investigated were V, Cr, Mn, Fe, Co, Ni, and Cu. The resulting transparent sol gel was stirred for a further 1 hour before dip coating onto previously cleaned $2 \times 2\text{ cm}^2$ titanium foil coupons ($1.27 \times 10^{-2}\text{ cm}$ thick, Aldrich). Films were deposited in five coat cycles, drying between coats with an infrared lamp, before annealing at 500°C in air for 1 hour with a temperature ramp rate 1°C min^{-1} . Electrical contact was made to the coupons by attaching copper wire with conductive silver epoxy (Circuit Works, Chemtronics). The contact and coupons were painted with a negative photoresist (KPR resist, Casio Chemicals) and UV cured, leaving a defined area of TiO_2 exposed.

Electrochemical characterisation of samples was performed under potentiostatic control (Autolab PGSTAT30) in a one-compartment cell with quartz window, platinum basket counter electrode, and a saturated calomel reference electrode (SCE). The supporting electrolyte was 0.1 M sodium perchlorate, and irradiation was provided from a 1 kW Xe arc lamp (ss1000 Spears Robinson) either; unfiltered, with an AM1 filter (to simulate solar conditions) or with a sodium nitrite filter ($\lambda > 420\text{ nm}$) for high-intensity visible light. For monochromatic irradiation, a high-intensity monochro-

TABLE 1: Elemental analysis by AES for Cu and Cr doped TiO_2 films.

| Sample | Cu doped sample 1 atom% precursor | | | |
|-------------|-----------------------------------|--------|----------|----------|
| Element | Carbon | Oxygen | Titanium | Copper |
| Before etch | 8.65% | 75.17% | 15.79% | 0.39% |
| After etch | 22.86% | 52.42% | 24.64% | 0.09% |
| Sample | Cr doped sample 5 atom% precursor | | | |
| Element | Carbon | Oxygen | Titanium | Chromium |
| Before etch | 13.57% | 66.60% | 17.63% | 2.20% |
| After etch | 11.44% | 66.75% | 20.21% | 1.59% |

mator (GM252, set for 10 nm band pass) was positioned between the source and the photoreactor. Light intensity was measured using a calibrated spectral radiometer (Jobin Yvonne Gemini spectral radiometer). Linear sweep voltammetry (LSV) was carried scanning from -1.0 V to $+1.5\text{ V}$ with a scan rate of 10 mV s^{-1} . The current-time response was measured at fixed potentials using chopped irradiation (Uniblitz vmm-t1, Vincent Associates). The cell temperature was maintained at $25^\circ\text{C} \pm 2^\circ\text{C}$. The presence or absence of dissolved oxygen was controlled by sparging with air or oxygen free nitrogen (OFN), respectively. All potentials are reported versus SCE.

Elemental analysis was carried out by Auger electron spectroscopy (AES) (Kratos Φ 660) in a vacuum of 10^{-6} torr with electrons accelerated from a field-emission source at 4 kV accelerating voltage to give a beam current of $2\text{ }\mu\text{A}$. Depth profiling was achieved using an argon etch.

UV-Vis transmission spectra of films deposited on quartz were measured using a spectrophotometer (Lambda 11, Perkin Elmer). Optical band-gap values were calculated by extrapolation of the absorption band edge. Crystal phase was analysed by Raman spectroscopy (LabRam 300, ISA instruments) by comparing to commercial anatase (99.5%, Aldrich) and rutile (created from predominantly rutile sample (Aldrich) by heating to 800°C). The source was an argon laser $\lambda = 514\text{ nm}$. Optimum analysis was performed with an acquisition time of 5 seconds, averaged over 10 accumulations, with the neutral density filter set to 50%.

3. RESULTS AND DISCUSSION

AES measurements indicated that not all of the corresponding dopant was incorporated at the hydrolysis stage of sol-gel procedure. Determination of dopant concentrations at initial precursor levels below 1.0 atom% was not possible with the AES system used in this study. Analysis of doped samples containing 1.0 atom% and 5.0 atom%, as precursor, confirmed the presence of the dopants (Table 1), however, they were at much lower levels (ca. 40%) than that of the initial precursor dopant level.

For simplicity, we will continue to refer to percentage doping of samples as the initial concentration of dopant added to the sol precursor. Depth profiling of the thin films showed that the dopant species were preferentially located on the surface with lower concentrations present in the bulk. Additionally, a high proportion of carbon was measured

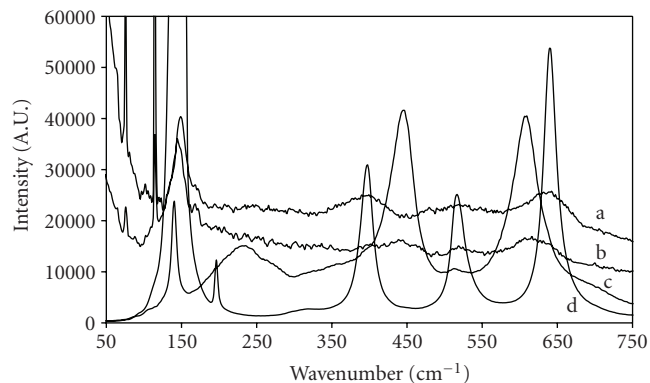


FIGURE 1: Raman spectra of (a) undoped TiO_2 film, (b) vanadium doped TiO_2 , (c) commercial anatase powder, (d) commercial rutile powder (following high-temperature anneal).

which originated from the alkoxide precursor used in the sol-gel process. Carbon was present in all samples including the undoped sample.

Figure 1 shows the Raman spectra obtained for a TiO_2 film and a $\text{TiO}_2:\text{V}$ film, compared with anatase and rutile powders. Analysis of the powder samples showed all relevant Raman vibration modes of anatase and rutile correlating with previous literature on Raman analysis of TiO_2 [29]. Comparison of the sol-gel derived thin films showed all samples to contain the E_g vibrational mode at 144 cm^{-1} common to both anatase and rutile. However, the rutile signal at 144 cm^{-1} is much weaker compared to the anatase signal. Since the sol-gel film shows a large peak at 144 cm^{-1} but no other rutile peaks, then we can assume it was predominantly anatase. The $\text{TiO}_2:\text{V}$ sample showed peaks present at 447 cm^{-1} (E_g) and 612 cm^{-1} (A_{1g}) representative of rutile and 519 cm^{-1} (B_{1g}) representative of an anatase crystal structure. The spectra of the undoped sample and all other doped samples were almost identical showing a predominantly anatase crystal phase, with the 399 cm^{-1} and 519 cm^{-1} B_{1g} peaks, along with the 639 cm^{-1} E_g peak associated with anatase.

UV-Vis absorption spectroscopy of the doped films, deposited on quartz, showed a minor red shift in the absorbance spectra as compared to the undoped film, however, this was mainly confined to the region from 250 nm to 350 nm (examples in Figure 2).

With all dopants investigated, an increase in the dopant concentration resulted in an increase in the absorbance between 290 nm and 350 nm with a small increase in absorbance at wavelengths greater than 350 nm. For example, the change in absorbance with concentration of dopant using $\text{TiO}_2:\text{Mn}$ is given in Figure 3. Changes in the absorption band edge, obtained by extrapolation of the UV/Vis absorption data, were in the range of 0.01–0.25 eV. The error in these calculations was not acceptable and therefore we do not report the band-gap values.

The photoelectrochemical characterisation of the films using linear sweep voltammetry (LSV) showed a typical n -type semiconductor response with negligible anodic current

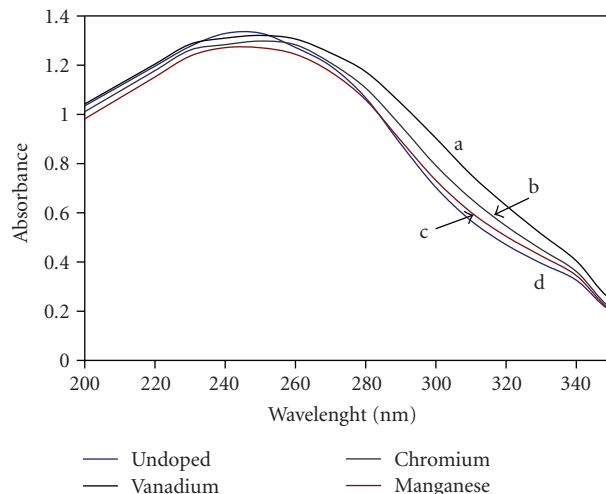


FIGURE 2: UV/Vis absorption spectra of doped TiO_2 films (a) V 0.2 atom%, (b) Cr 0.2 atom%, (c) Mn 0.2 atom%, (d) undoped TiO_2 .

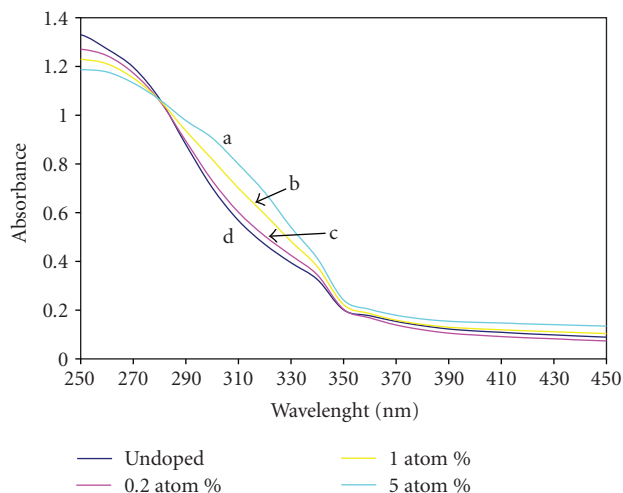


FIGURE 3: UV/Vis absorbance versus dopant concentration for $\text{TiO}_2:\text{Mn}$ (a) 5 atom%, (b) 1 atom%, (c) 0.2 atom%, (d) undoped.

in the dark and a significant increase in the anodic current under AM1 solar simulated irradiation (Figure 4).

The photocurrent was dependent on the applied potential, and the undoped TiO_2 sample showed a larger photocurrent response than any of the doped samples. Furthermore, a decrease in photocurrent with increasing dopant concentration was observed with all doped samples. Air sparging of the electrolyte prior to LSV resulted in a positive shift in the onset potential for anodic current (Figure 5 and Table 2).

The photocurrent response spectra of these films were obtained using chopped monochromatic illumination (10 nm band pass). The spectral current-time response for the undoped TiO_2 electrode is given in Figure 6. The incident photon conversion efficiency (IPCE) was calculated by

$$\%IPCE = \frac{J}{I_0 F} \times 100, \quad (1)$$

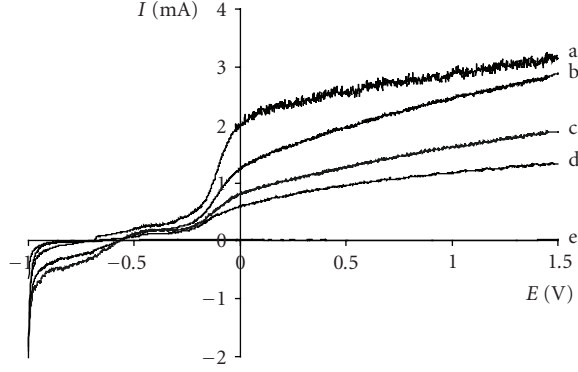


FIGURE 4: Linear sweep voltammograms under AM1 solar simulated irradiation for doped TiO_2 films (0.5 atom% dopant) (a) undoped, (b) Fe, (c) Co, (d) Ni, (e) dark response for undoped film.

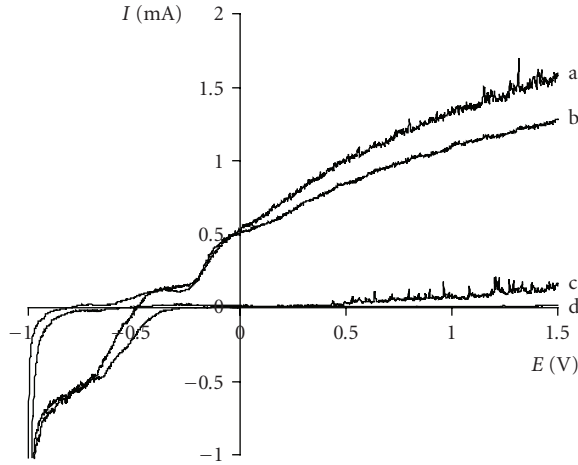


FIGURE 5: Effect of electrolyte air sparging on the I - E response for $\text{TiO}_2\text{:Cr}$ (0.2 atom%) under unfiltered irradiation (a) light, following air sparging, (b) light, following nitrogen sparging, (c) dark, following air sparging, (d) dark, following nitrogen sparging ($\text{SR} = 10 \text{ mV s}^{-1}$).

where J is the photocurrent density, I_0 is the incident light intensity, and F is Faraday's constant.

The %IPCE versus wavelength is given in Figure 7. The monochromatic light intensity was a limiting factor in these experiments yielding very low photocurrents. A small photocurrent response at wavelengths above 400 nm was observed for a number of samples (see Figure 6), however, a change in current less than three times the deviation of the background current (i.e., 30 nA) was not taken as significant. The doped samples exhibited no red shift in the %IPCE compared to the undoped TiO_2 .

To overcome the limitations of the low light intensity of the monochromatic source, the photocurrent response was measured under visible excitation using a NaNO_2 filter ($\lambda \geq 410 \text{ nm}$) with the Xe source. All samples showed a photocurrent response under sub-band gap irradiation which was dependent on applied potential with the photocurrent maxima observed between -0.5 and -0.1 V (see Figure 8).

TABLE 2: Anodic photocurrent onset potential for different preparations in the presence of oxygen (the undoped sample gave an onset potential of -0.8 V).

| Dopant | Onset potential (V) | | |
|-----------|---------------------|-----------|-----------|
| | 0.2 atom% | 1.0 atom% | 5.0 atom% |
| Vanadium | -0.49 | -0.47 | -0.46 |
| Chromium | -0.48 | -0.48 | -0.45 |
| Manganese | -0.47 | -0.45 | -0.41 |
| Iron | -0.56 | -0.45 | -0.49 |
| Cobalt | -0.58 | -0.44 | -0.45 |
| Nickel | -0.52 | -0.49 | -0.44 |
| Copper | -0.67 | -0.56 | -0.54 |

TABLE 3: Photoelectrochemical data for undoped and 0.5 atom% doped TiO_2 films under visible irradiation.

| Dopant | Onset potential for anodic current (V) | Peak potential (V) | Photocurrent at peak potential (mA) |
|-----------|--|--------------------|-------------------------------------|
| None | -0.71 | -0.19 | 0.038 |
| Vanadium | -0.51 | -0.24 | 0.049 |
| Chromium | -0.49 | -0.26 | 0.051 |
| Manganese | -0.53 | -0.30 | 0.070 |
| Iron | -0.51 | -0.22 | 0.044 |
| Cobalt | -0.60 | -0.31 | 0.076 |
| Nickel | -0.53 | -0.35 | 0.066 |
| Copper | -0.62 | -0.30 | 0.062 |

The peak potentials and onset potentials for anodic current are given in Table 3. AES analysis confirmed the presence of carbon impurities at high levels and this is common with sol-gel routes employing alkoxide precursors. It has been previously reported that carbon doped TiO_2 gives a visible response [30]. All samples contained carbon impurities and there was a small visible response observed for the *undoped* TiO_2 sample. This visible photocurrent for the *undoped* sample, which may be due to carbon impurities, is much less than that observed for the metal ion dopants (see Figure 8 and Table 3). Recently, Asahi et al. [31] reported the carbon defect level to be too low to give an optical transition in the visible. Changes in the optical or photoactive spectra of TiO_2 due carbon doping have been correlated to an increase in the concentration of Ti^{3+} stabilised by carbon impurities [32, 33].

The presence of metal ion dopants will result in oxygen vacancy states or single-bonded oxygen (possibly hydroxyl) due to the lower coordination of the dopant with respect to the parent Ti^{4+} . Nakamura et al. [27] reported that H_2 plasma treatment of TiO_2 resulted in the formation of oxygen vacancy states located around 2.02–2.45 eV above the valence band corresponding to a wavelength between 506 and 614 nm. Electrons may be promoted from the valence band to the vacancy states by visible light excitation. They

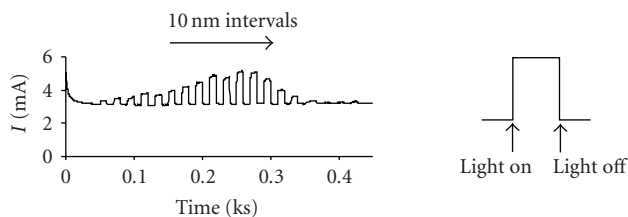


FIGURE 6: Current-time response under chopped irradiation for undoped sample as function of irradiation wavelength from 250 to 430 nm (left to right) in 10 nm intervals. Measured in a one-compartment cell with applied potential of +1.0 V and 0.1 M sodium perchlorate as a backing electrolyte with air sparging.

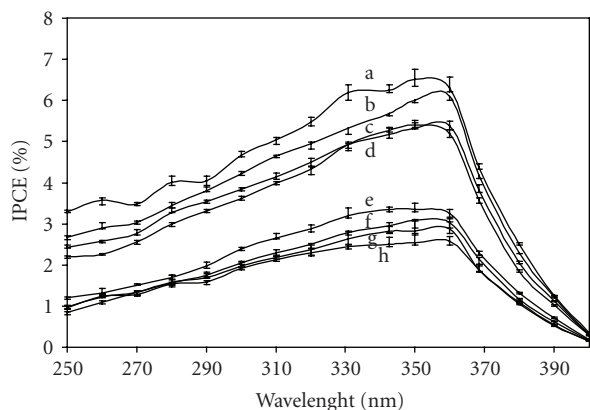


FIGURE 7: Incident photon to current efficiency for samples doped to 0.5 atom%. Dopant: (a) none, (b) Fe, (c) Cu, (d) V, (e) Co, (f) Cr, (g) Ni, (h) Mn (measured in a one-compartment cell at an applied potential of +1.0 V and 0.1 M sodium perchlorate electrolyte with air sparging).

reported that plasma modification of TiO_2 allowed visible-light-driven oxidation of NO.

Siripala and Tomkiewicz [26] investigated interactions between photoinduced and dark charge transfer at single crystal TiO_2 -aqueous electrolyte interfaces. They reported a sub-band gap irradiation resulted in electron injection from the valence band to states in the gap which lie around 0.6 eV below the bottom of the conduction band. Carrier excitation through such surface states should be much less potential dependent than carrier excitation through the bulk. Indeed they report that sub-band gap photocurrent is observed only between -0.5 and $+0.4$ V (SCE) at pH 6.5 (reported flat band potential was ca. -0.8 V). They proposed that the surface state was an intermediate of the dark reaction forming $\text{TiO}_2\text{-H}$, the energy for which lies within the band-gap.

The photocurrent under visible light excitation observed at negative potentials is consistent with previously published results which attribute this visible response to donor/acceptor energy levels below the conduction band caused by surface defects [24–27]. Photocurrent under sub-band gap illumination is only observed in the potential region where donor/acceptor energy levels are filled, that is, more negative than -0.1 V in this case. The presence

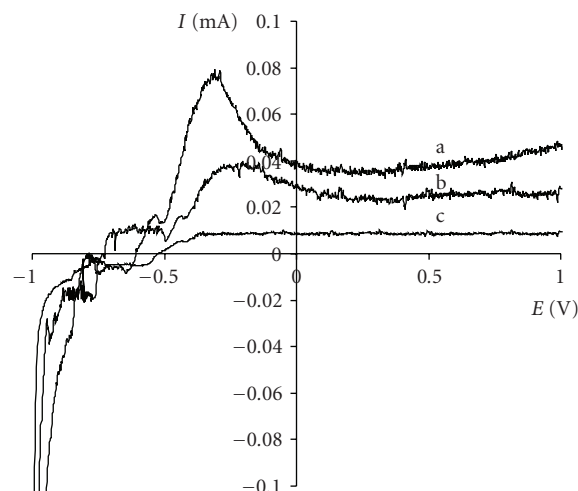


FIGURE 8: Visible ($\lambda > 410$ nm) photocurrent response (a) $\text{TiO}_2\text{:Co}$ 0.5 atom%, (b) undoped TiO_2 , and (c) dark current for undoped TiO_2 .

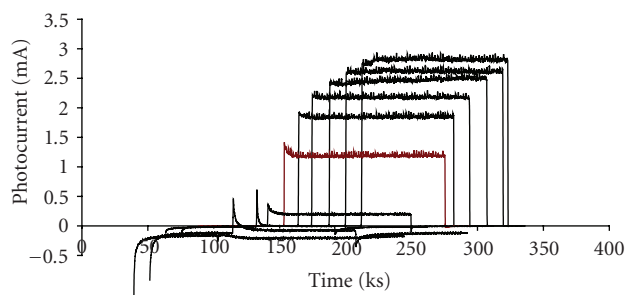


FIGURE 9: Changes in photocurrent transients as a function applied potential. Example of undoped sample under polychromatic illumination (applied bias from 1.0 V to -1.0 V in 0.2 V steps left to right).

of defect states is usually reported to have a negative effect on photoactivity because they act as recombination centres for charge carriers. However, under appropriate applied potential, these defect levels can act as electron donor states yielding a photocurrent response under sub-band gap irradiation.

To investigate the potential dependence of these defect levels, the current-time response of TiO_2 electrodes under chopped illumination was examined. Salvador [34] investigated the kinetics of recombination involving defects, surface groups, and absorbed species, by photocurrent transient measurements. Using single crystal TiO_2 electrodes, they reported that the initial photocurrent produced in the instant of illumination ($I_{\text{ph in}}$) decayed with time to a steady state ($I_{\text{ph st}}$) due to recombination on defects and surface states. By plotting the ratio of $I_{\text{ph st}}/I_{\text{ph in}}$ versus potential, the critical band bending was determined.

Figures 9 and 10 show examples of transients produced in this work for the undoped and doped samples, respectively. For the undoped samples, the initial photocurrent spike is

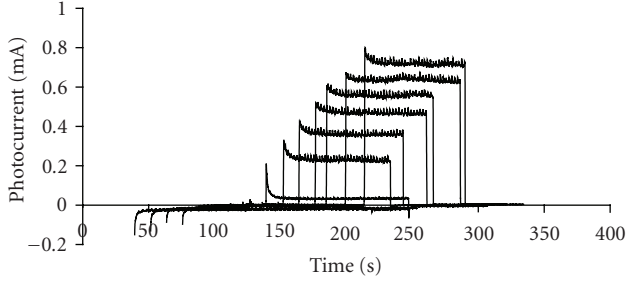


FIGURE 10: Changes in photocurrent transients as a function applied potential. Example of 0.2% chromium doped sample under polychromatic illumination (applied bias from +1.0 V to -1.0 V in 0.2 V steps left to right).

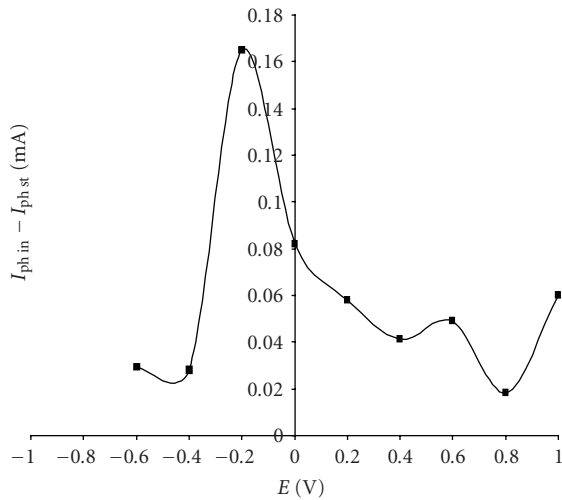


FIGURE 11: $I_{\text{ph in}} - I_{\text{ph st}}$ as a function of potential from 0.2 atom% chromium doped sample.

absent at potentials more positive than +0.6 V whilst for the doped samples, the initial spike was always present. Additionally, photocurrent showed n -type to p -type conversion at negative potentials close the E_{fb} . Matsumoto et al. [21] reported increasing p -type character at negative potentials following doping with transition metals which resulted in a lowering of the anodic photocurrent in comparison to the undoped sample, with higher p/n ratios correlating to higher defect densities.

The films used in this study were made using a sol-gel route which gave oxide films consisting of nanoparticles with a primary particle size around 38 nm [35]. For nanoparticles in this size range, band bending is not significant. However, initial and steady state photocurrent measurements can still be used to examine recombination as a function of potential by subtracting $I_{\text{ph st}}$ from $I_{\text{ph in}}$. Figure 11 shows the potential dependence of recombination in these electrodes. The peaks in recombination ($I_{\text{ph in}} - I_{\text{ph st}}$) with respect to potential are tabulated in Table 4.

The magnitude of $I_{\text{ph in}} - I_{\text{ph st}}$ is observed to follow the same potential dependence as the sub-band gap photocur-

TABLE 4: Potential dependence of recombination.

| Dopant | Peak in $I_{\text{ph in}} - I_{\text{ph st}}$ (V) |
|-----------|---|
| Undoped | 0.0 |
| Vanadium | -0.2 |
| Chromium | -0.2 |
| Manganese | -0.2 |
| Iron | -0.2 |
| Cobalt | -0.4 |
| Nickel | -0.4 |
| Copper | -0.4 |

rent response. Under band-gap irradiation, the defect states act as recombination centres lowering the photocurrent response at negative potentials; however, under sub-band gap irradiation, the defect states act as electron donors showing a visible photocurrent response. This is an agreement with other reported results [36].

There is a small visible photocurrent response is observed at potentials more positive than -0.6 V due to defect states. Nevertheless, it is clear that the primary band-gap photocurrent response is decreased by the addition of metal ion dopants, which act as charge-carrier recombination centres, and that the sub-band gap photocurrent is only a fraction of the band-gap photocurrent and, therefore, may not be relevant for practical applications including the photoelectrolytic splitting of water under solar irradiation.

4. CONCLUSIONS

Thin films of transition metal doped (0.2, 1.0, and 5.0 atom%) TiO_2 were prepared on titanium foil using a sol-gel route catalyzed by ammonium acetate. Raman spectroscopy confirmed anatase crystal phase in all samples except in the case of the $\text{TiO}_2:\text{V}$ sample where a mixture of anatase and rutile was obtained.

The films doped with transition metal ions showed lower photocurrent response than undoped samples under simulated solar irradiation. The photocurrent response spectra of the doped films were similar to the undoped sample with no major red shift. Sub-band gap irradiation of the samples gave a small photocurrent at negative potentials which is indicative of electron promotion from a filled defect level, the occupation of which is potential dependant. Examination of defect level potential dependence by analysis of photocurrent transients (from -0.8 to +1 V) showed a good correlation with the potential dependence in visible illumination studies.

The primary band-gap photocurrent response is decreased by the addition of metal ion dopants, which act as charge-carrier recombination centres, and the sub-band gap photocurrent is only a very small fraction of the band-gap photocurrent.

ACKNOWLEDGMENT

Department of Employment and Learning Northern Ireland for funding JWJ Hamilton.

REFERENCES

- [1] A. Mills, R. H. Davies, and D. Worsley, "Water purification by semiconductor photocatalysis," *Chemical Society Reviews*, vol. 22, no. 6, pp. 417–425, 1993.
- [2] R. J. Watts, S. Kong, M. P. Orr, G. C. Miller, and B. E. Henry, "Photocatalytic inactivation of coliform bacteria and viruses in secondary waste-water effluent," *Water Research*, vol. 29, no. 1, pp. 95–100, 1995.
- [3] O. Legrini, E. Oliveros, and A. M. Braun, "Photochemical processes for water treatment," *Chemical Reviews*, vol. 93, no. 2, pp. 671–698, 1993.
- [4] A. Mills, A. Lepre, N. Elliott, S. Bhopal, I. P. Parkin, and S. A. O'Neill, "Characterisation of the photocatalyst Pilkington Activ™: a reference film photocatalyst?" *Photochemistry and Photobiology A*, vol. 160, no. 3, pp. 213–244, 2003.
- [5] B. O'Regan and M. Grätzel, "A low cost, high efficiency solar cell based on dye sensitised colloidal TiO₂ films," *Nature*, vol. 353, no. 6346, pp. 737–740, 1991.
- [6] M. Grätzel, "Photovoltaic and photoelectrochemical conversion of solar energy," *Philosophical Transactions of the Royal Society A*, vol. 365, no. 1853, pp. 993–1005, 2007.
- [7] E. Borgarello, J. Kiwi, M. Grätzel, E. Pelizzetti, and M. Visca, "Visible light induced water cleavage in colloidal solutions of chromium-doped titanium dioxide particles," *Journal of the American Chemical Society*, vol. 104, no. 11, pp. 2996–3002, 1982.
- [8] M. Anpo, "Photocatalysis on titanium oxide catalysts: approaches in achieving highly efficient reactions and realizing the use of visible light," *Catalysis Surveys from Japan*, vol. 1, no. 2, pp. 169–179, 1997.
- [9] Y. Wang, H. Cheng, Y. Hao, J. Ma, W. Li, and S. Cai, "Photoelectrochemical properties of metal-ion-doped TiO₂ nanocrystalline electrodes," *Thin Solid Films*, vol. 349, no. 1–2, pp. 120–125, 1999.
- [10] W. Choi, A. Termin, and M. R. Hoffmann, "The role of metal-ion dopants in quantum-sized TiO₂: correlation between photoreactivity and charge carrier recombination dynamics," *Journal of Physical Chemistry*, vol. 98, no. 51, pp. 13669–13679, 1994.
- [11] A. Monnier and J. Augustynski, "Photoelectrolysis of water: photoresponses of nickel, chromium and zinc-doped polycrystalline TiO₂ electrodes," *Journal of the Electrochemical Society*, vol. 127, no. 7, pp. 1576–1579, 1980.
- [12] Z. H. Luo and Q.-H. Gao, "Decrease in the photoactivity of TiO₂ pigment on doping with transition-metals," *Journal of Photochemistry and Photobiology A*, vol. 63, no. 3, pp. 367–375, 1992.
- [13] H. Wittmer, St. Holten, H. Kliem, and H. D. Breuer, "Detection of space charge limited currents in nanoscaled titania," *Physica Status Solidi (A)*, vol. 181, no. 2, pp. 461–469, 2000.
- [14] V. Brezová, A. Blažková, L. Karpinsky, et al., "Phenol decomposition using Mⁿ⁺/TiO₂ photocatalysts supported by the sol-gel technique on glass fibres," *Journal of Photochemistry and Photobiology A*, vol. 109, no. 2, pp. 177–183, 1997.
- [15] A. Di Paola, E. García-López, S. Ikeda, G. Marci, B. Ohtani, and L. Palmisano, "Photocatalytic degradation of organic compounds in aqueous systems by transition metal doped polycrystalline TiO₂," *Catalysis Today*, vol. 75, no. 1–4, pp. 87–93, 2002.
- [16] J. A. Navío, J. J. Testa, P. Djedjeian, J. R. Padrón, D. Rodríguez, and M. I. Litter, "Iron-doped titania powders prepared by a sol-gel method—part II: photocatalytic properties," *Applied Catalysis A*, vol. 178, no. 2, pp. 191–203, 1999.
- [17] T. E. Phillips, K. Moorjani, J. C. Murphy, and T. O. Poehler, "TiO₂-VO₂ alloys—reduced bandgap effects in the photoelectrolysis of water," *Journal of the Electrochemical Society*, vol. 129, no. 6, pp. 1210–1215, 1982.
- [18] W. Choi, A. Termin, and M. R. Hoffmann, "Effects of metal-ion dopants on the photocatalytic reactivity of quantum-sized TiO₂ particles," *Angewandte Chemie International Edition in English*, vol. 33, no. 10, pp. 1091–1092, 1994.
- [19] A. Di Paola, G. Marci, L. Palmisano, et al., "Preparation of polycrystalline TiO₂ photocatalysts impregnated with various transition metal ions: characterization and photocatalytic activity for the degradation of 4-nitrophenol," *Journal of Physical Chemistry B*, vol. 106, no. 3, pp. 637–645, 2002.
- [20] D. Dvoranová, V. Brezová, M. Mazúr, and M. A. Malati, "Investigations of metal-doped titanium dioxide photocatalysts," *Applied Catalysis B*, vol. 37, no. 2, pp. 91–105, 2002.
- [21] Y. Matsumoto, J.-I. Kurimoto, T. Shimizu, and E.-I. Sato, "Photoelectrochemical properties of polycrystalline TiO₂ doped with 3d transition-metals," *Journal of the Electrochemical Society*, vol. 128, no. 5, pp. 1040–1044, 1981.
- [22] K. Wilke and H. D. Breuer, "The influence of transition metal doping on the physical and photocatalytic properties of titania," *Journal of Photochemistry and Photobiology A*, vol. 121, no. 1, pp. 49–53, 1999.
- [23] K. E. Karakitsou and X. E. Verykios, "Effects of altrivalent cation doping of TiO₂ on its performance as a photocatalyst for water cleavage," *Journal of Physical Chemistry*, vol. 97, no. 6, pp. 1184–1189, 1993.
- [24] V. N. Bogomolov, E. K. Kudinov, D. N. Merlin, and A. Y. Frisov, "Polaron mechanism of light absorption in rutile crystals," *Soviet Physics—Solid State*, vol. 9, pp. 1630–1639, 1963.
- [25] E. K. Kudinov, D. N. Mirlin, and A. Y. Firsov, "Polaron nature of the current carriers in rutile TiO₂," *Soviet Physics—Solid State*, vol. 11, pp. 2257–2266, 1970.
- [26] W. Siripala and M. Tomkiewicz, "Interactions between photoinduced and dark charge transfer across n-TiO₂-aqueous electrolyte interface," *Journal of the Electrochemical Society*, vol. 129, no. 6, pp. 1240–1245, 1982.
- [27] I. Nakamura, N. Negishi, S. Kutsuna, T. Ihara, S. Sugihara, and K. Takeuchi, "Role of oxygen vacancy in the plasma-treated TiO₂ photocatalyst with visible light activity for NO removal," *Journal of Molecular Catalysis A*, vol. 161, no. 1–2, pp. 205–212, 2000.
- [28] Y. Murakami, T. Matsumoto, and Y. Takasu, "Salt catalysts containing basic anions and acidic cations for the sol-gel process of titanium alkoxide: controlling the kinetics and dimensionality of the resultant titanium oxide," *Journal of Physical Chemistry B*, vol. 103, no. 11, pp. 1836–1840, 1999.
- [29] Y.-H. Zhang, C. K. Chan, J. F. Porter, and W. Guo, "Micro-Raman spectroscopic characterization of nanosized TiO₂ powders prepared by vapor hydrolysis," *Journal of Materials Research*, vol. 13, no. 9, pp. 2602–2609, 1998.
- [30] S. Sakthivel and H. Kisch, "Daylight photocatalysis by carbon-modified titanium dioxide," *Angewandte Chemie International Edition*, vol. 42, no. 40, pp. 4908–4911, 2003.
- [31] R. Asahi, T. Morikawa, T. Ohwaki, K. Aoki, and Y. Taga, "Visible-light photocatalysis in nitrogen-doped titanium oxides," *Science*, vol. 293, no. 5528, pp. 269–271, 2001.
- [32] Y. Li, D.-S. Hwang, N. H. Lee, and S.-J. Kim, "Synthesis and characterization of carbon-doped titania as an artificial solar light sensitive photocatalyst," *Chemical Physics Letters*, vol. 404, no. 1–3, pp. 25–29, 2005.

-
- [33] X.-Q. Chen, H.-B. Liu, and G.-B. Gu, "Preparation of nanometer crystalline TiO₂ with high photo-catalytic activity by pyrolysis of titanyl organic compounds and photo-catalytic mechanism," *Materials Chemistry and Physics*, vol. 91, no. 2-3, pp. 317–324, 2005.
- [34] P. Salvador, "Kinetic approach to the photocurrent transients in water photoelectrolysis at n-TiO₂ dioxide electrodes—1: analysis of the ratio of the instantaneous to steady-state photocurrent," *Journal of Physical Chemistry*, vol. 89, no. 18, pp. 3863–3869, 1985.
- [35] J. W. J. Hamilton, "Preparation and characterisation of photo-anode materials," Ph.D. thesis, Faculty of Engineering, University of Ulster, Northern Ireland, UK, 2004.
- [36] N. Beermann, G. Boschloo, and A. Hagfeldt, "Trapping of electrons in nanostructured TiO₂ studied by photocurrent transients," *Journal of Photochemistry and Photobiology A*, vol. 152, no. 1–3, pp. 213–218, 2002.

Research Article

Preparation, Characterisation, and Photocatalytic Behaviour of Co-TiO₂ with Visible Light Response

Rossano Amadelli,¹ Luca Samiolo,¹ Andrea Maldotti,² Alessandra Molinari,² Mario Valigi,³ and Delia Gazzoli³

¹ ISOF-CNR, Sezione di Ferrara, Dipartimento di Chimica, Università degli Studi di Ferrara, 44100 Ferrara, Italy

² Dipartimento di Chimica, Università degli Studi di Ferrara, 44100 Ferrara, Italy

³ Dipartimento di Chimica, Università di Roma "La Sapienza", 00185 Rome, Italy

Correspondence should be addressed to Rossano Amadelli, amr@unife.it

Received 1 August 2007; Revised 15 October 2007; Accepted 13 November 2007

Recommended by M. Sabry A. Abdel-Mottaleb

The preparation of cobalt-modified TiO₂ (Co-TiO₂) was carried out by the incipient impregnation method starting from commercial TiO₂ (Degussa, P-25) and cobalt acetate. XPS data show that cobalt is incorporated as divalent ion, and it is likely present within few subsurface layers. No appreciable change in structural-morphologic properties, such as surface area and anatase/rutile phase ratio, was observed. Conversely, Co addition brings about conspicuous changes in the point of zero charge and in surface polarity. Diffuse reflectance spectra feature a red shift in light absorption that is dependent on the amount of cobalt. The influence of cobalt addition on the performance of TiO₂ as a photocatalyst in the degradation of 4-chlorophenol and Bisphenol A is investigated. The results show that the modified oxide presents a higher photoactivity both for illumination with UV-visible ($\lambda > 360$ nm) and visible light ($\lambda > 420$ nm; $\lambda > 450$ nm), and that this enhancement depends on the amount of the added species and on the final thermal treatment in the preparation step. We also show that Co-TiO₂ is a more active catalyst than pure TiO₂ for the reduction of O₂ in the dark, which is an important reaction in the overall photocatalytic processes.

Copyright © 2008 Rossano Amadelli et al. This is an open access article distributed under the Creative Commons Attribution License, which permits unrestricted use, distribution, and reproduction in any medium, provided the original work is properly cited.

1. INTRODUCTION

Recent research in semiconductors photocatalysis is strongly oriented toward the preparation of functional materials that are able to meet specific requirements such as high efficiency and visible light response. These are important issues in the case, for example, of TiO₂ which is an attractive photocatalyst under many aspects but whose use is severely limited by the fact that it absorbs only a relatively small fraction of solar light. On the other hand, from the point of view of photocatalysis for fine chemicals production, illuminated TiO₂ is a too oxidizing system to expect selectivity. In this case, surface tailoring by molecular modification appears to be a viable direction [1].

Different investigations show that doping of TiO₂ by low amounts of foreign elements (both metals and nonmetals) sometimes leads to enhanced photocatalytic activity and to an increase of visible light absorption [2–6].

Metal-doped oxides are also extensively studied for the development of semiconductor nanomaterials with magnetic properties (diluted magnetic semiconductors). This field of research is only broadly related to application of semiconductors in heterogeneous photocatalysis. However, the two disciplines share the necessity of in-depth materials characterisation by a number of physical methods whose results are generally valid independently of the final application.

Among these studies, Co-doped anatase, in particular, is the object of a very large number of publications and review papers [7–14]. Although there seems to be no general consensus on results and interpretation, most authors agree on the fact that (i) Co is present as the divalent form; (ii) Co(II) states are located within the band gap; (iii) cobalt can be located in interstitial positions of the host oxide.

In this paper, we report on the characterisation and photocatalytic behaviour of Co-TiO₂ obtained by the impregnation method, using commercially available TiO₂ and cobalt

acetate as the precursor salt. We discuss, in particular, structural and interfacial properties such as the site occupation and valence state of the metal inside the host oxide, the degree of surface dispersion, changes in the polarity, and acid-basic properties of the surface.

We use the photodegradation of 4-chlorophenol and Bisphenol A to assess the photocatalytic activity of the Co-TiO₂ and TiO₂ and show that the activity of the former is higher, both under UV and visible light irradiation, depending on the degree of doping.

In previous literature work, authors mainly discuss Co-TiO₂ photocatalysts in the context of a more general examination of the effect of different metal dopants [15–20], and the doping degree is generally fixed at one value. Results on the influence of cobalt are contradictory: some authors report an altogether detrimental [15, 16] effect, while, in some cases, cobalt seems to improve photodegradation slightly [17] or selectively for some organic compounds as found by Di Paola et al. [18].

The valence state of Co is also a matter of debate. Thus Wang et al. [19] reach the conclusion that Co³⁺ is more active in bringing about a photoactivity enhancement, in contrast to the works of Choi et al. [15, 16] and of Iwasaki et al. [21]. The paper of the latter authors, on the photodegradation of acetaldehyde, is an interesting work that also examines the effect of the cobalt doping degree. However, neither that paper nor the other cited articles report on the problem of O₂ reduction activation which we deal with in the present publication and to which we attach a considerable importance for an evaluation of the overall activity of photocatalytic processes.

2. EXPERIMENTAL

2.1. Materials

Titanium dioxide P-25 from Degussa was employed in all experiments. The precursor salt used for TiO₂ modification was cobalt acetate obtained from Carlo Erba. The Reichardt reagent (used for measurements of the surface polarity) and all other chemicals were Aldrich pure reagents.

2.2. Apparatus and methods

X-ray diffraction (XRD) patterns in the 2θ angular range from 5° to 60° were obtained by a Philips PW 1729 diffractometer using Cu K α (Ni-filtered) radiation. UV-visible spectra of solutions were recorded on a Kontron spectrophotometer (Uvikon 943), while diffuse reflectance UV-visible spectra (DRS) were recorded in absorbance mode at room temperature in the range 200 nm–2500 nm on a Cary 5E spectrophotometer by Varian Win UV software. Halon was used as reference. The concentration of cobalt in the solution phase was determined by atomic spectroscopy using a Perkin-Elmer, Optica 3100 XL model, instrument.

XPS measurements were carried out with a Leybold-Heraeus LHS10 spectrometer using the Al K α (1486.6 eV) radiation on samples deposited on a gold sheet at a residual pressure in the chamber of 10⁻⁹ Torr. Differential thermal analysis (DTA) data were obtained on a Perkin Elmer

instrument, in the temperature interval from 30° to 800°C at a heating rate of 20°C/min in O₂ flow (50 mL/min), using α -Al₂O₃ as a reference.

Electrochemical experiments were carried out using an EG&G model 273A potentiostat-galvanostat using EG&G software. A conventional three-compartment glass cell was employed where the working electrode compartment had an optical window for illumination. The counter electrode was a Pt gauze and the reference electrode was SCE in all cases.

Photocatalytic experiments have been conducted on suspensions (2 g L⁻¹) or films of the semiconductor whose preparation is described in the following sections. A Helios Italquartz Q400 medium-pressure mercury lamp (15 mW cm⁻²), equipped with suitable cutoff filters, has been employed, and all experiments have been carried out at room temperature (298 ± 1 K) under an atmosphere of 101.3 kPa of O₂.

2.3. Preparation of Co-TiO₂

Cobalt-modified TiO₂ has been prepared by an incipient wetness impregnation method analogous to that described in the literature [22]. In a typical experiment, 0.5 g of TiO₂ (Degussa P-25) was dispersed in 10 mL H₂O that contained the necessary amount of cobalt acetate to obtain the desired percent of doping. The suspension is first sonicated for about 10 minutes to help particles dispersion, then stirred for 2 hours and finally dried in an oven at 100°C for 18 hours. The resulting powder was finely ground in a mortar and calcinated at different temperatures between 100° and 500°C for different times. For comparison, TiO₂ was also treated in the same way but in the absence of added cobalt. The modified oxide is henceforth written as Co-TiO₂ or as Co(*x*%)₂-TiO₂ when the percent (w/w Co/TiO₂) of the added metal needs to be specified. The final powder is greenish white, for comparison, Co-TiO₂ obtained by the hydrolysis of titanium tetraisopropoxide in the presence of cobalt has a yellow/orange colour.

2.4. Preparation of TiO₂ films

Films were prepared from the TiO₂ powders as described in the literature [23]. Pyrex glass was used as the support in photocatalytic experiments. Electrodes were obtained in the same way except that a titanium substrate was used as a support. This was pretreated in hot oxalic acid for 20 minutes before deposition of the TiO₂ films.

3. RESULTS AND DISCUSSION

3.1. Catalyst characterisation

3.1.1. General characterisation

Surface microstructure is highly dependent on the preparation conditions and on posttreatments. Small additions of various metal oxides can also greatly influence (alter) the crystalline morphology as well as the conductivity of the host matrix.

A general investigation of the materials characteristics includes measurements of surface area (BET method), X-ray

diffraction (XRD), and differential thermal analysis (DTA). Surface area measurements were carried out on TiO₂ samples doped with 0.2, 0.5, 1, and 2% w/w and the values obtained ranged from 47 to 49 m²g⁻¹, indicating that the adopted doping procedure does not bring about any surface area change with respect to the pristine oxide (~50 m²g⁻¹). Likewise, XRD spectra of samples with 0.2, 0.5, and 1% Co, collected in the 2θ range 5–60°, showed only peaks due to anatase and rutile, which is expected since the commercial TiO₂ used is well known to be a mixture of the two polymorphs. There is neither an evident change due to Co in the initial anatase/rutile phase distribution nor shift of the diffraction peaks, which can be due to the low resolution in the 5–60 angular range and to the low cobalt content.

DTA experiments gave no indication of phenomena associated with the combustion of organic species (Co acetate has been used as the precursor salt). On the other hand, an exothermic peak, attributable to anatase-rutile phase transformation, was evident in the range from 750° to 800°C.

Invariance of specific surface area facilitates a comparison of the photocatalytic properties of the different materials. More detailed analyses were carried out by XPS and DRS and will be discussed in some detail in the following section.

3.1.2. XPS and DRS measurements

The XPS investigation has provided us with information on both the valence state and the degree of dispersion of cobalt. The Co binding energy (BE) was determined with reference to the Ti2p(3/2) peak at 458.5 eV.

In presence of Co(II), the Co2p region feature two main peaks, Co2p(3/2)-Co2p(1/2), separated by 15.8 eV, and a Co2p(3/2)/Co2p(1/2) intensity ratio of 2. The peaks have shake-up satellites located at ~5.8 eV with higher BE than the main peaks which present a satellite-main peak ratio of about 0.8. Because of covalence and final state effects, the BE of Co(III) is lower than that of Co(II). The magnitude of the chemical shift between the two states is 1.0 eV at most [24]. Owing to the small BE difference and band broadening caused by “multiplet splitting,” the presence of Co(II) or Co(III), or both, cannot be established from the position of the Co2p components alone. A spectral feature that will distinguish between Co(II) and Co(III) is a decrease in the spin-orbit separation and the marked decrease of the satellites, because the main Co(II) peaks present a satellite, whereas the Co(III) peaks do not. As shown in Figure 1(a), in both the Co(1%)-TiO₂ and Co(2%)-TiO₂ samples, the Co2p(3/2) peak is accompanied by the shake-up signal characteristic of Co(II). In addition, for Co(1%)-TiO₂ (curve a), Co2p(3/2) is at 780.8 eV with a shake-up peak separated by 5.7 eV and a satellite-main peak ratio of about 0.8 which indicates the presence of divalent cobalt. For Co(2%)-TiO₂ (curve b) the Co2p(3/2) component is at 780.4 eV with a shake-up separation of 5.2 eV and a satellite-main peak ratio of about 0.45, indicating the presence of Co(II) and Co(III). It can be inferred that in the Co(1%)-TiO₂ sample cobalt is present as Co(II), whereas at increasing cobalt content both Co(II) and Co(III) states are present. The conclusion that Co is present

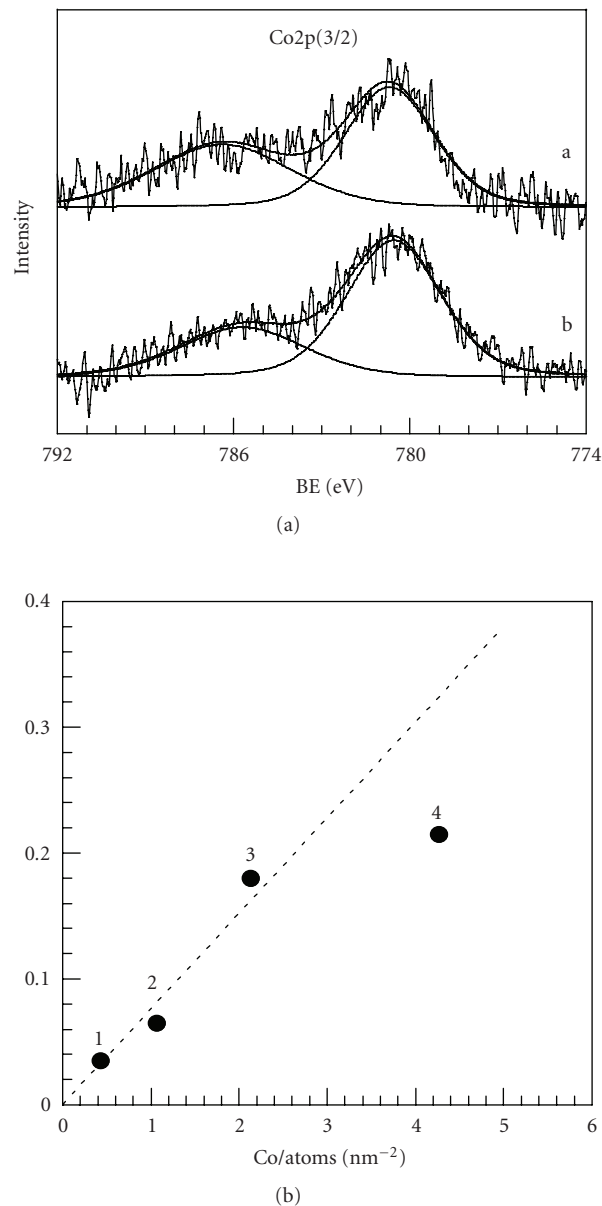


FIGURE 1: (a) XPS spectra in the Co2p(3/2) binding energy region for Co(1%)-TiO₂ (curve a) and Co(2%)-TiO₂ (curve b); (b) ratio of XPS peaks intensity, $I(\text{Co}2p)/I(\text{Ti}2p)$, as a function of the surface concentration of cobalt for Co($x\%$)-TiO₂ with (1) $x = 0.2\%$; (2) $x = 0.5\%$; (3) $x = 1\%$; (4) $x = 2\%$. Full circles are the experimental data and the dashed line refers to calculated values (see text). The final calcination temperature for all samples was 400°C.

in the divalent form is in accord with the above-cited literature [9].

The dispersion degree of cobalt on TiO₂ was determined from the (Co2p/Ti2p) intensity ratios. The plot of the intensity ratio as a function of the surface concentration of cobalt (see Figure 1(b)) shows a deviation from linearity as the content of cobalt increases. For a quantitative evaluation of the surface morphology, the experimental intensity ratios $I(\text{Co}2p)/I(\text{Ti}2p)$ were compared with the values predicted by two

models: the “nonattenuating overlayer over a semi-infinite support” and the “solid solution” models [25]. In the first model, the Co-TiO₂ system was represented as consisting of a nonattenuating dispersed layer of cobalt species on TiO₂ support with semi-infinite thickness:

$$\frac{I_{\text{Co}}}{I_{\text{Ti}}} = \frac{D_{\text{Co}} \sigma_{\text{Co}} s_{\text{Co}}}{D_{\text{Ti}} \sigma_{\text{Ti}} \rho_{\text{Ti}} \lambda_{\text{Ti}}}. \quad (1)$$

In the second model the Co species are considered homogeneously dispersed in the TiO₂ lattice:

$$\frac{I_{\text{Co}}}{I_{\text{Ti}}} = \frac{D_{\text{Co}} n_{\text{Co}} \sigma_{\text{Co}} \lambda_{\text{Co}}}{D_{\text{Ti}} n_{\text{Ti}} \sigma_{\text{Ti}} \lambda_{\text{Ti}}} \quad (2)$$

(ρ_{Ti} indicates the Ti atomic density in the support ($\rho_{\text{Ti}} = 0.29 \cdot 10^{23}$ atoms cm⁻³); D is the instrumental efficiency factor; σ_{Co} , σ_{Ti} are the cross-sections (σ_{Co} , 19.16; σ_{Ti} , 7.91); λ refers to the escape depth of electron (λ_{Ti} , 1.88 nm; λ_{Co} , 1.44 nm); s_{Co} is the Co atomic surface concentration (atoms nm⁻²); and $n_{\text{Co}}/n_{\text{Ti}}$ is the atomic concentration ratio).

The excellent agreement between experimental and calculated values in the Co concentration range 0.2%–1%, as in Figure 1(b), clearly indicates that cobalt is fully dispersed on the surface and within few subsurface layers. Conversely, the intensity ratios calculated by the solid solution model and the experimental ratios disagree (the calculated values are 3–4 times lower than the experimental ones).

The behaviour observed for the Co(2%) sample suggests an aggregation of the cobalt species, likely forming islands or small clusters of Co₃O₄. This is clearly evident in the diffuse reflectance data (see below).

The salient feature of the diffuse reflectance spectra (DRS) displayed in Figure 2 is that Co doping causes a shift of absorption to higher wavelengths (curves a–c). A more in-depth DRS analysis shows interesting details concerning absorption in the visible region (inset in Figure 2) that are useful in establishing the nature of sites occupied by cobalt within the TiO₂ host. For percentages of added Co from 0.2 to 1%, in the wavelength range from 500 to 1000 nm, one can identify three relatively broad peaks close to each other at approximately 530–550 nm, 600–620 nm, and 660–680 nm. For Co(2%)-TiO₂ the spectra (not shown) feature peaks, among others, at 450 nm and 730 nm which are typical of octahedrally coordinated Co(III) [26] indicating a separate phase formation at these degrees of doping, in keeping with the above discussed XPS results.

The pattern, shown in the inset of Figure 2, strongly suggests tetrahedrally coordinated Co and, in fact, the data are comparable with the diffuse reflectance spectra of several Co-modified inorganic materials [27, 28] and of Co-ZnO [29], for which it is well established that the doping metal is divalent and substitutionally occupies Zn tetrahedral sites. However, it is not possible to state that all Co are present in tetrahedral sites since the intensity of transitions attributed to octahedrally coordinated Co is reported to be about two orders of magnitude lower than that for the tetrahedral coordination [29].

The fact that at least a significant amount of Co has a tetrahedral coordination means that the added species which

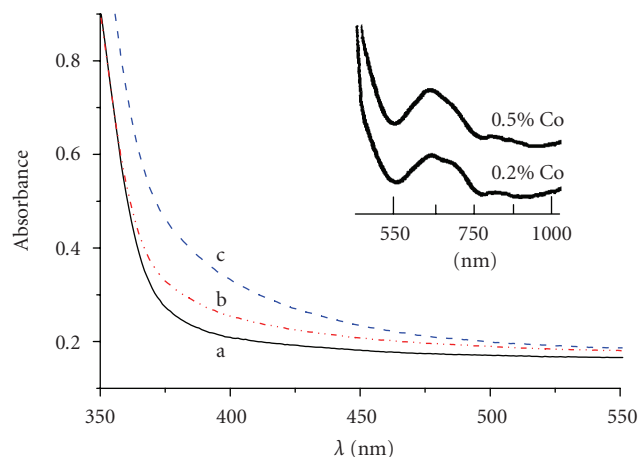


FIGURE 2: Diffuse reflectance spectra of TiO₂ (a); Co(0.2%)-TiO₂ (b); Co(0.5%)-TiO₂ (c). The inset shows measurements on an expanded scale. The final calcination temperature for all samples was 400°C.

entered the lattice, for a few layers, are occupying interstitial positions. This is probably not very surprising considering that our experimental conditions do not involve preparation of Co-TiO₂ by coprecipitation or calcination at high temperatures, which should favour the formation of a homogeneous solid solution with Co in octahedral sites. In this connection, it is interesting to note that among the vast literature on the structure and magnetic properties of Co-TiO₂ prepared by different methods, some studies [10] consider the presence of Co in interstitial tetrahedral sites as well as in octahedral ones plausible; in both cases, the dopant introduces states located about midway within the TiO₂ band gap and causes a raise in the Fermi level [10].

3.1.3. Point of zero charge (PZC) and surface polarity

Oxide surfaces can become charged as a consequence of the ability of coordinated OH groups to undergo hydrolysis. Thus negatively and positively charged surfaces are obtained by the dissociation of acid groups and protonation of basic groups, respectively. The point of zero charge (PZC), corresponding to the condition where no net charge is present on the surface, is an important factor that controls the adsorption of solution species and photocatalytic activity [18].

In the present work, the PZC has been determined by the powder titration method at various values of the solution ionic strength [30]. For undoped TiO₂ (P-25), the value of the PZC is 5.8 as often reported in the literature. In the case of the Co-doped oxide, the PZC is shifted to higher pH values: a value of 7.2 was obtained for TiO₂ doped with 1% Co, as reported earlier [18]. Thus the PZC seems to approach that of bulk Co₃O₄ [30], and one would be led to consider this as a possible cause; it can be ruled out, however, since our DRS and XPS measurements do not indicate the presence of Co³⁺ and of any separate phase formation for Co amounts ≤ 1%.

Quite obviously, the phenomenon we observed originates from changes in the surface properties that can be even

rather subtle, as pointed out in an illuminating work by Contescu et al. on heterogeneity of hydroxyl groups on TiO₂ polymorphs [31]. Among other factors, differences in coordination of –O– and –OH sites to cations, a different proportion of proton binding groups (oxo and hydroxo), variation of the proton-metal distances, and the contribution of different crystal planes (on different planes, terminal oxygen has different acidity) can bring about observable changes in the surface acid/basic behaviour. In contrast to relatively abundant information available for pure TiO₂, investigations on doped TiO₂ appear scanty [18].

From our X-ray data, we have neither evidence of changes in the crystallographic planes intensity upon Co incorporation nor evidence of changes in the TiO₂ unit cell parameters. In this regard, it is worth stressing that Geng and Kim [10] showed that the introduction of interstitial Co into Ti₁₆O₃₂ model clusters leads to volume expansion, and an increased Ti–O bond length can then possibly lead to a more basic behaviour of the surface as discussed by Contescu et al. [31].

In the present work, we also undertook the evaluation of surface polarity, which is an important parameter since changes in polarity (hydrophilicity), along with PZC, can strongly influence the adsorption/desorption equilibria of several compounds and can, consequently, affect the photocatalytic activity.

Experimentally, the quantification of surface polarity is based on suitable indicators which are employed to construct polarity scales. Among these, the $E_T^N(30)$ scale [32], based on the use of Reichardt's dye, is very well established and can be used to evaluate the polarity of surfaces [33].

Elaboration of our measurements are based on the dimensionless $E_T^N(30)$ scale [34] which ranges from 0 to 1 for nonpolar and very polar surfaces, respectively. The results yielded $E_T^N(30)$ values of 1 for undoped TiO₂ and 0.79 for the Co(0.5%)-doped oxide, clearly indicating a sensible decrease in the surface polarity.

The $E_T(30)$ parameter is correlated to the more accurate Kamlet-Taft scale [35, 36]:

$$E_T(30) = 301.1 + 12.99\pi^* - 2.74\delta + 14.45\alpha + 2.13\beta, \quad (3)$$

where α and β describe the hydrogen-bond acidity and the hydrogen-bond basicity, respectively; δ is a correction factor and π^* is a polarizability/polarity factor. The latter is clearly an important parameter whose evaluation needs separate experiments; however, based on the simple examination of the α parameter, the above-reported decreased acidity of Co-TiO₂ can provide one explanation of the decrease in the $E_T(30)$ or $E_T^N(30)$ compared to undoped TiO₂.

3.1.4. Photoelectrochemical measurements

Oxygen is the common electron acceptor in semiconductor photocatalysis and the study of its reduction bears a high relevance to the optimisation and elucidation of photocatalytic processes [37].

Our electrochemical measurements, in the pH range from 2 to 13, showed that cobalt brings about a shift of the onset of the O₂ reduction process (see Figure 3) toward

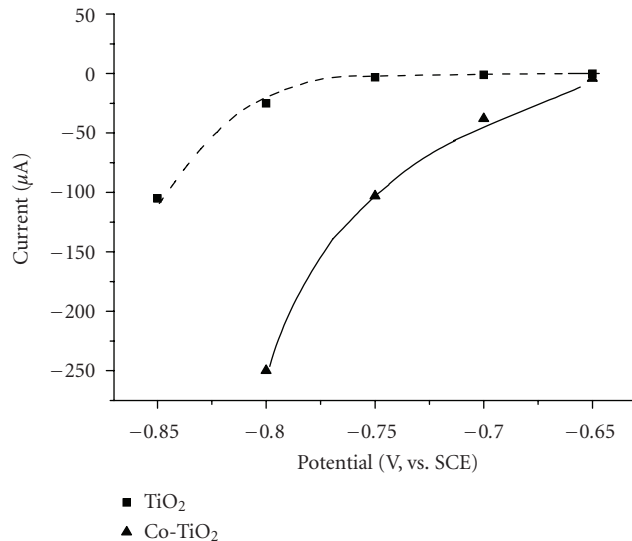


FIGURE 3: Cyclic voltammetry curves for O₂ reduction on TiO₂ and Co(0.5%)-TiO₂ in the dark. Sweep rate: 20 mV s⁻¹. Electrolyte: 0.1 M NaOH. Electrodes geometric area: 2 cm².

more positive potentials, which is ascribed to an electrocatalytic effect. On this basis, one can expect an improvement in the overall photocatalytic processes and, indeed, there is ample literature evidence confirming that coordinated cobalt is an efficient catalyst for oxygen and peroxides activation [38, 39], through pathways involving Co(II) and/or Co(I) species [40].

Our experimental evidence on the effect of added cobalt on peroxide formation during photooxidation processes will be discussed in a separate communication. The results of preliminary investigations show that during photocatalytic experiments, a relatively pronounced accumulation of peroxides in the solution phase is observed with Co-TiO₂ compared to the undoped TiO₂, and this can possibly correlate with the above-reported lower polarity of the former material.

In Figure 4, the photocurrent action spectra plots for TiO₂ and Co-TiO₂, are shown as IPCE (%) [41]:

$$\text{IPCE}(\%) = \frac{1240 \cdot i_{\text{ph}} (\text{mA/cm}^2)}{\lambda (\text{nm}) \cdot I (\text{mW/cm}^2)} * 100, \quad (4)$$

where i_{ph} is the photocurrent and I is the intensity of the light source. The data, obtained from photocurrent-time transients, show a clear response to visible light, in agreement with the DRS data of Figure 2. The lower UV response of Co-TiO₂ compared with TiO₂ (see Figure 4) has been frequently reported in the literature for doped TiO₂ [41, 42] and attributed to the presence of states in the band gap.

The possible charge transfer (CT) processes that occur upon visible light absorption include the dopant centred d-d (MMCT) electronic transitions. In principle, however, metal to ligand (MLCT) and ligand to metal (LMCT) excitation [43, 44] are possible. In our specific case, they would imply electron transfer from the TiO₂ valence band to

Co(II) ($L_{VB}MCT$) and from Co(II) to the conduction band ($ML_{CB}CT$), respectively.

There are investigations on the optical absorption by Co-TiO₂ [11]; however, we want to single out the related, elegant study by Liu et al. [45] because we think it is particularly detailed and informative, considering also that the band gap and band edge positions for ZnO and TiO₂ are similar. Two subbandgap transitions can lead to charge separation: a relatively weak $ML_{CB}CT$ at ~ 715 nm corresponding to Co³⁺ formation and a more intense $L_{VB}MCT$ at higher energy corresponding to Co⁺ formation. According to Schwarz and Gamelin, the Co⁺ state is located in the proximity of the ZnO CB [46].

3.2. Photocatalytic activity

An important goal of the present investigation is the assessment of the effect of cobalt addition on the photocatalytic activity of TiO₂ in the degradation of model organic pollutants. In the previous paragraph, we have drawn attention to the fact that the better catalytic activity of Co-TiO₂ for O₂ reduction, compared with the undoped oxide, offers one good reason to expect improvements in the efficiency of photocatalytic processes. In the following, we examine the photocatalytic activity, for irradiation with both UV and visible light, as a function of additional parameters in the Co-TiO₂ preparation method such as the amount of cobalt and the calcination temperature.

3.2.1. Optimisation of the photocatalytic activity of Co-TiO₂

We have discussed so far the effect of the degree of cobalt doping on the physical characteristics of TiO₂. In this section, we report on the influence of the amount of doping on the photoactivity of Co-TiO₂. Since the final treatment in the preparation of the photocatalysts is calcination, we also carried out a series of experiments aiming to determine the optimal calcination temperature. For this series of correlated experiments, we used 4-chlorophenol as a model substrate because its photodegradation has been extensively investigated and the reaction mechanism is well established [47].

The plots of Figure 5 illustrate the effect of calcination temperature on the time required for mineralization of 4-chlorophenol in suspensions of Co(0.2%)-TiO₂ and of TiO₂ for comparison. Examination of the results reveals that Co-TiO₂ is always more active than the original TiO₂ that was subjected to the same thermal treatment. The best result is obtained for heat treatment at 400 °C for 30 minutes: prolonged heating (>2 hours) at this temperature did not have appreciable effects.

It is important to point out, in this respect, that at this temperature no significant change in the morphology and phase composition is observed for the pure TiO₂ (P-25, Degussa). It is also noteworthy that a low-temperature treatment (100 °C), following TiO₂ impregnation with the cobalt salt, has a negligible influence on the photocatalytic activity (see Figure 5). Moreover, this temperature is not sufficiently high to drive the metal into the lattice, and hence it can be

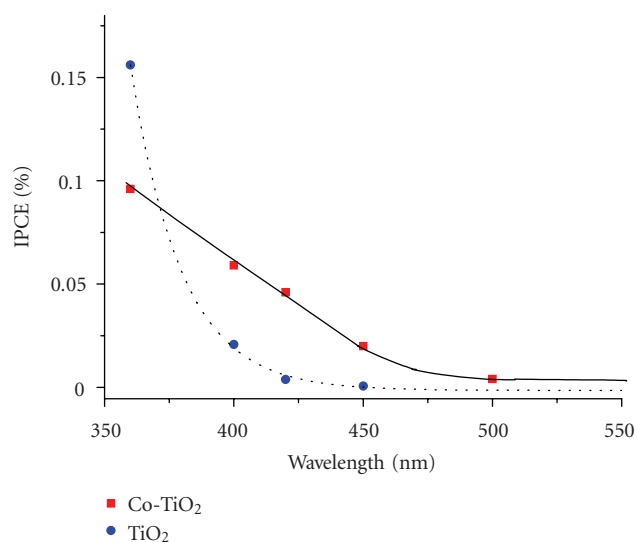


FIGURE 4: Photoaction spectra recorded from photocurrent-time transients using TiO₂ and Co(0.5%)-TiO₂ electrodes in 1M NaClO₄ solutions. Electrodes geometric area: 2 cm².

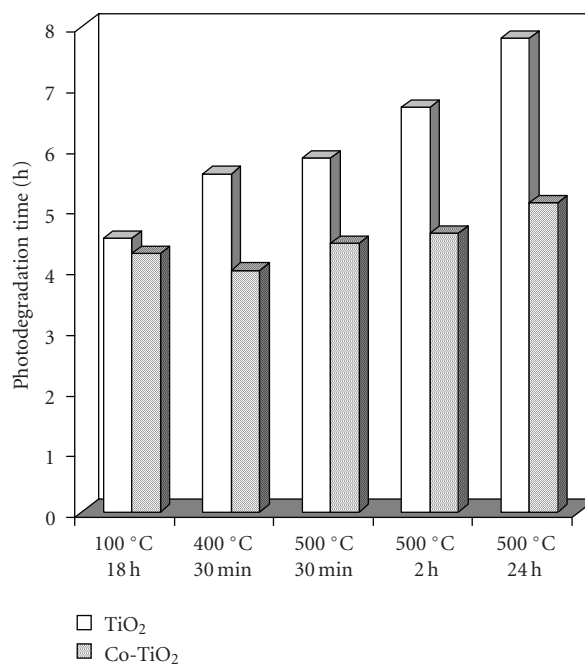


FIGURE 5: Effects of the calcination time and temperature on the time required for the photodegradation of 1 mM 4-chlorophenol in aqueous suspensions of TiO₂ and Co(x%)-TiO₂, where the degree of doping (x%) is 0.2.

concluded that adsorbed Co(II) does not provide active sites for improving the photocatalytic efficiency. This lack of effect is confirmed by photocatalytic experiments carried out in the presence of Co(NO₃)₂ added to the solution.

Experiments for the determination of the photodegradation efficiency of 4-chlorophenol in Co-TiO₂ suspensions were performed as a function of the amount of doping. The

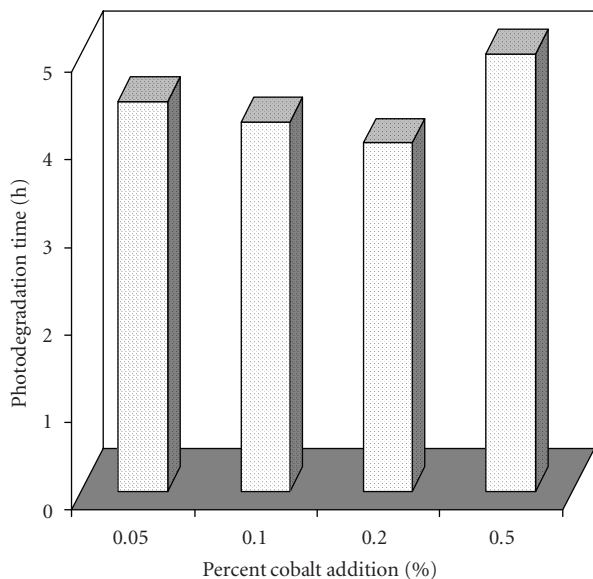


FIGURE 6: Time required for the photodegradation of 1 mM 4-chlorophenol in aqueous suspensions of $\text{Co}(x\%)\text{-TiO}_2$ as a function of the amount of cobalt ($x\%$). The final calcination temperature was 400°C for 30 minutes.

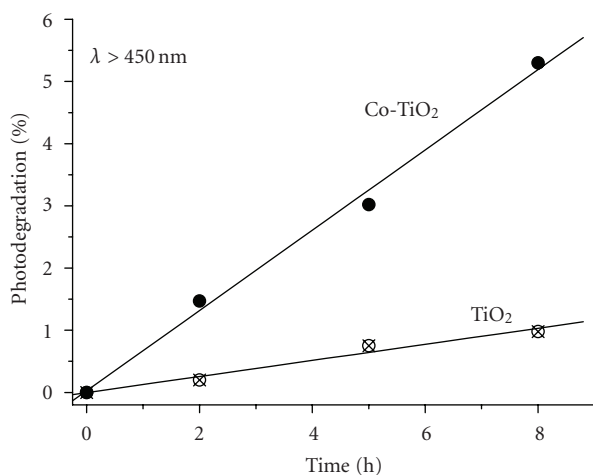


FIGURE 7: Visible light ($\lambda > 450\text{ nm}$) photodegradation of 1 mM 4-chlorophenol as a function of time in aqueous suspensions of TiO_2 and $\text{Co}(x\%)\text{-TiO}_2$, where the degree of doping ($x\%$) is 0.5. The final calcination temperature was 400°C for 30 minutes.

plots in Figure 6 show the effect of a different content in cobalt on the efficiency of 4-chlorophenol photodegradation in Co-TiO_2 suspensions. It is evident that the best results are obtained for a cobalt doping degree of 0.2%.

From the applied point of view, it is often more practical to use photocatalysts in the form of films supported on different substrates such as glass. This is mainly because the use of films avoids the separation of the solid by filtration at the end of experiments, which is a necessary procedure when one uses suspensions. For this reason, we made experiments

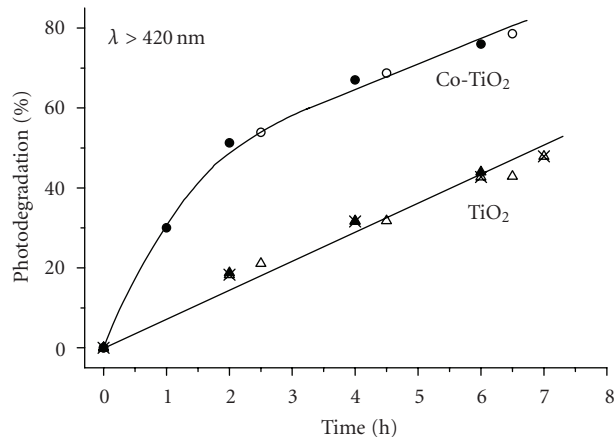


FIGURE 8: Visible light ($\lambda > 420\text{ nm}$) photodegradation of 0.8 mM 2,2'-bis(4'-hydroxyphenyl) propane (Bisphenol A), as a function of time in aqueous suspensions of TiO_2 and $\text{Co}(x\%)\text{-TiO}_2$, where the degree of doping $x\%$ is 0.5. The final calcination temperature was 400°C for 30 minutes.

using glass supported films of TiO_2 and Co-TiO_2 with a different percent of the doping element, again using the photodegradation of 4-chlorophenol as a model reaction. The results showed that in agreement with the reported data for suspensions, Co-TiO_2 is more active than the pristine oxide. Also in accordance with the results of Figure 6, there is an optimum degree of doping for which the photocatalytic activity reaches a maximum that, in this case, turns out to be around 0.5%.

Leaching of cobalt during photocatalytic measurements deserves to be mentioned. For the experimental conditions of Figures 5 and 6, that is, irradiation for ~ 6 hours at a pH close to neutrality, the loss of cobalt as soluble species from $\text{Co}(0.5\%)\text{-TiO}_2$ amounts to 1.44 mg L^{-1} which corresponds to 2.8% of the cobalt concentration that is impregnated into TiO_2 . Measurements at different pH values gave a leaching of 38% and 1.25% at $\text{pH} = 2$ and 10, respectively. It is evident that Co-TiO_2 is not a recommended photocatalyst for applications requiring acidic conditions. For a comparison with literature data, Tayade et al. [17] report a cobalt leaching of 4.6% at $\text{pH} = 5$.

3.2.2. Visible light photoactivity

Both the DRS data of Figure 2 and the photoaction spectra of Figure 4 show that Co-doping causes a red shift in the absorption of light, and in the discussion above we speculated on possible causes (*vide supra*). We thought it was meaningful to carry on experiments in which irradiation is restricted to the visible region ($\lambda > 420$ or 450 nm).

The photodegradation of 4-chlorophenol in Co-TiO_2 suspensions, illuminated with light of wavelength $\lambda > 420\text{ nm}$, confirmed that the doped photocatalyst responds to visible light in a way that depends on the amount of cobalt; the optimal doping degree was found to be 0.5%. The photocatalytic activity of Co-TiO_2 is still good at longer

wavelengths ($\lambda > 450$ nm), but it is interesting to note that undoped TiO₂ still shows residual, albeit low, activity even at these wavelengths (see Figure 7).

We extended our studies on the visible light response of Co-TiO₂ to the photodegradation of 2,2'-bis(4'-hydroxyphenyl) propane (Bisphenol A), a more complex chemical substrate than 4-chlorophenol, that is used for epoxy and polycarbonate resins and is well known to be an endocrine disrupting chemical [48, 49]. Typical results, obtained on irradiation of TiO₂ and Co(0.5%)-TiO₂ suspensions at $\lambda > 420$ nm, are shown in Figure 8. The data confirm the higher photocatalytic efficiency of Co-TiO₂, especially at short irradiation times. As noted for the case of 4-chlorophenol, undoped TiO₂ has an appreciable activity that, in our opinion, is not fully explained. Possible reasons are discussed in a recent paper by Kuznetsov and Serpone [50].

4. CONCLUSIONS

Cobalt-modified TiO₂ (Co-TiO₂) is able to bring about the photocatalytic degradation of pollutants such as 4-chlorophenol and Bisphenol A under both UV and visible light irradiation. The best photoactivity was observed for an amount of cobalt between 0.2% and 0.5% Co/TiO₂ w/w.

Diffuse reflectance measurements indicate that a substantial amount of incorporated Co is present in interstitial positions. XPS measurements show that Co enters the TiO₂ lattice as the divalent species, that it is well dispersed, and that there are no separate cobalt phase formation for percents of added Co < 1%. In this case, the foreign species are likely localized at the surface and within relatively few subsurface layers.

In comparison to pristine TiO₂, Co-TiO₂ features change in the point of zero charge (PZC) toward more basic values and a substantial decrease in the surface polarity. We also show that Co-TiO₂ is a more active catalyst than pure TiO₂ for the reduction of O₂ in the dark.

ACKNOWLEDGMENTS

The authors acknowledge the support of CTG-Italcementi, Gambarelli Group, MIUR, and CNR.

REFERENCES

- [1] R. Amadelli, A. Molinari, I. Vitali, L. Samiolo, G. M. Mura, and A. Maldotti, "Photo-electro-chemical properties of TiO₂ mediated by the enzyme glucose oxidase," *Catalysis Today*, vol. 101, no. 3-4, pp. 397-405, 2005.
- [2] K. Mizushima, M. Tanaka, A. Asai, S. Iida, and J. B. Goodenough, "Impurity levels of iron-group ions in TiO₂(II)," *Journal of Physics and Chemistry of Solids*, vol. 40, no. 12, pp. 1129-1140, 1979.
- [3] H. Kato and A. Kudo, "Visible-light-response and photocatalytic activities of TiO₂ and SrTiO₃ photocatalysts co-doped with antimony and chromium," *Journal of Physical Chemistry B*, vol. 106, no. 19, pp. 5029-5034, 2002.
- [4] O. Carp, C. L. Huisman, and A. Reller, "Photoinduced reactivity of titanium dioxide," *Progress in Solid State Chemistry*, vol. 32, no. 1-2, pp. 33-177, 2004.
- [5] M. Anpo, "Preparation, characterization, and reactivities of highly functional titanium oxide-based photocatalysts able to operate under UV-visible light irradiation: approaches in realizing high efficiency in the use of visible light," *Bulletin of the Chemical Society of Japan*, vol. 77, no. 8, pp. 1427-1442, 2004.
- [6] T. L. Thompson and J. T. Yates Jr., "Surface science studies of the photoactivation of TiO₂-new photochemical processes," *Chemical Reviews*, vol. 106, no. 10, pp. 4428-4453, 2006.
- [7] Y. Matsumoto, M. Murakami, T. Shono, et al., "Room-temperature ferromagnetism in transparent transition metal-doped titanium dioxide," *Science*, vol. 291, no. 5505, pp. 854-856, 2001.
- [8] J. M. Sullivan and S. C. Erwin, "Theory of dopants and defects in Co-doped TiO₂ anatase," *Physical Review B*, vol. 67, no. 14, Article ID 144415, 7 pages, 2003.
- [9] W. Prellier, A. Fouchet, and B. Mercey, "Oxide-diluted magnetic semiconductors: a review of the experimental status," *Journal of Physics: Condensed Matter*, vol. 15, no. 37, pp. R1583-R1601, 2003.
- [10] W. T. Geng and K. S. Kim, "Interplay of local structure and magnetism in Co-doped TiO₂ anatase," *Solid State Communications*, vol. 129, no. 11, pp. 741-746, 2004.
- [11] J. D. Bryan, S. M. Heald, S. A. Chambers, and D. R. Gamelin, "Strong room-temperature ferromagnetism in Co²⁺-doped TiO₂ made from colloidal nanocrystals," *Journal of the American Chemical Society*, vol. 126, no. 37, pp. 11640-11647, 2004.
- [12] J. R. Simpson, H. D. Drew, S. R. Shinde, R. J. Choudhary, S. B. Ogale, and T. Venkatesan, "Optical band-edge shift of anatase Ti_{1-x}Co_xO_{2-δ}," *Physical Review B*, vol. 69, no. 19, Article ID 193205, 4 pages, 2004.
- [13] J. M. D. Coey, "Dilute magnetic oxides," *Current Opinion in Solid State and Materials Science*, vol. 10, no. 2, pp. 83-92, 2006.
- [14] R. Janisch and N. A. Spaldin, "Understanding ferromagnetism in Co-doped TiO₂ anatase from first principles," *Physical Review B*, vol. 73, no. 3, Article ID 035201, 7 pages, 2006.
- [15] W. Choi, A. Termin, and M. R. Hoffmann, "Effects of metal-ion dopants on the photocatalytic reactivity of quantum-sized TiO₂ particles," *Angewandte Chemie International Edition*, vol. 33, no. 10, pp. 1091-1092, 1994.
- [16] W. Choi, A. Termin, and M. R. Hoffmann, "The role of metal ion dopants in quantum-sized TiO₂: correlation between photoreactivity and charge carrier recombination dynamics," *Journal of Physical Chemistry*, vol. 98, no. 51, pp. 13669-13679, 1994.
- [17] R. J. Tayade, R. G. Kulkarni, and R. V. Jasra, "Transition metal ion impregnated mesoporous TiO₂ for photocatalytic degradation of organic contaminants in water," *Industrial and Engineering Chemistry Research*, vol. 45, no. 15, pp. 5231-5238, 2006.
- [18] A. Di Paola, E. García-López, S. Ikeda, G. Marci, B. Ohtani, and L. Palmisano, "Photocatalytic degradation of organic compounds in aqueous systems by transition metal doped polycrystalline TiO₂," *Catalysis Today*, vol. 75, no. 1-4, pp. 87-93, 2002.
- [19] J. Wang, S. Uma, and K. J. Klabunde, "Visible light photocatalysis in transition metal incorporated titania-silica aerogels," *Applied Catalysis B: Environmental*, vol. 48, no. 2, pp. 151-154, 2004.
- [20] C. M. Whang, J. G. Kim, E. Y. Kim, Y. H. Kim, and W. I. Lee, "Effect of Co, Ga, and Nd additions on the photocatalytic properties of TiO₂ nanopowders," *Glass Physics and Chemistry*, vol. 31, no. 3, pp. 390-395, 2005.

- [21] M. Iwasaki, M. Hara, H. Kawada, H. Tada, and S. Ito, "Cobalt ion-doped TiO₂ photocatalyst response to visible light," *Journal of Colloid and Interface Science*, vol. 224, no. 1, pp. 202–204, 2000.
- [22] J. Araña, J. M. Doña-Rodríguez, O. González-Díaz, et al., "Gas-phase ethanol photocatalytic degradation study with TiO₂ doped with Fe, Pd and Cu," *Journal of Molecular Catalysis A: Chemical*, vol. 215, no. 1-2, pp. 153–160, 2004.
- [23] C. J. Barbé, F. Arendse, P. Comte, et al., "Nanocrystalline titanium oxide electrodes for photovoltaic applications," *Journal of the American Ceramic Society*, vol. 80, no. 12, pp. 3157–3171, 1997.
- [24] K. Wandelt, "Photoemission studies of adsorbed oxygen and oxide layers," *Surface Science Reports*, vol. 2, no. 1, pp. 1–121, 1982.
- [25] A. Cimino, D. Gazzoli, and M. Valigi, "XPS quantitative analysis and models of supported oxide catalysts," *Journal of Electron Spectroscopy and Related Phenomena*, vol. 104, no. 1, pp. 1–29, 1999.
- [26] Y. Brik, M. Kacimi, M. Ziyad, and F. Bozon-Verduraz, "Titania-supported Cobalt and cobalt-phosphorus catalysts: characterization and performances in ethane oxidative dehydrogenation," *Journal of Catalysis*, vol. 202, no. 1, pp. 118–128, 2001.
- [27] A. A. Verberckmoes, B. M. Weckhuysen, and R. A. Schoonheydt, "Spectroscopy and coordination chemistry of cobalt in molecular sieves," *Microporous and Mesoporous Materials*, vol. 22, no. 1–3, pp. 165–178, 1998.
- [28] H. Hoser, S. Krzyzanowski, and F. Trifiró, "Optical spectra of Co-zeolites," *Journal of the Chemical Society, Faraday Transactions 1*, vol. 71, pp. 665–669, 1975.
- [29] R. Pappalardo, D. L. Wood, and R. C. Linares Jr., "Optical absorption study of Co-doped oxide systems. II," *The Journal of Chemical Physics*, vol. 35, no. 6, pp. 2041–2059, 1961.
- [30] A. Daggetti, G. Lodi, and S. Trasatti, "Interfacial properties of oxides used as anodes in the electrochemical technology," *Materials Chemistry and Physics*, vol. 8, no. 1, pp. 1–90, 1983.
- [31] C. Contescu, V. T. Popa, and J. A. Schwarz, "Heterogeneity of hydroxyl and deuterioxy groups on the surface of TiO₂ polymorphs," *Journal of Colloid and Interface Science*, vol. 180, no. 1, pp. 149–161, 1996.
- [32] C. Reichardt, "Solvatochromic dyes as solvent polarity indicators," *Chemical Reviews*, vol. 94, no. 8, pp. 2319–2358, 1994.
- [33] D. J. Macquarrie, S. J. Tavener, G. W. Gray, et al., "The use of Reichardt's dye as an indicator of surface polarity," *New Journal of Chemistry*, vol. 23, no. 7, pp. 725–731, 1999.
- [34] S. Spange and A. Reuter, "Hydrogen-bond donating and dipolarity/polarizability properties of chemically functionalized silica particles," *Langmuir*, vol. 15, no. 1, pp. 141–150, 1999.
- [35] S. Spange, E. Vilsmeier, and Y. Zimmermann, "Probing the surface polarity of various silicas and other moderately strong solid acids by means of different genuine solvatochromic dyes," *Journal of Physical Chemistry B*, vol. 104, no. 27, pp. 6417–6428, 2000.
- [36] J. L. Jones and S. C. Rutan, "Solvatochromic studies of stationary phases on thin-layer chromatographic plates," *Analytical Chemistry*, vol. 63, no. 13, pp. 1318–1322, 1991.
- [37] A. Maldotti, A. Molinari, and R. Amadelli, "Photocatalysis with organized systems for the oxofunctionalization of hydrocarbons by O₂," *Chemical Reviews*, vol. 102, no. 10, pp. 3811–3836, 2002.
- [38] J. Premkumar and R. Ramaraj, "Photocatalytic reduction of dioxygen by colloidal semiconductors and macrocyclic cobalt(III) complexes in Nafion and cellulose matrices," *Journal of Molecular Catalysis A: Chemical*, vol. 132, no. 1, pp. 21–32, 1998.
- [39] R. S. Drago, "Homogeneous metal-catalyzed oxidations by O₂," *Coordination Chemistry Reviews*, vol. 117, pp. 185–213, 1992.
- [40] S. Leonard, P. M. Gannett, Y. Rojanasakul, et al., "Cobalt-mediated generation of reactive oxygen species and its possible mechanism," *Journal of Inorganic Biochemistry*, vol. 70, no. 3-4, pp. 239–244, 1998.
- [41] J. Y. Shi, W. H. Leng, W. C. Zhu, J. Q. Zhang, and C. N. Cao, "Electrochemically assisted photocatalytic oxidation of nitrite over Cr-Doped TiO₂ under visible light," *Chemical Engineering & Technology*, vol. 29, no. 1, pp. 146–154, 2006.
- [42] T. Lindgren, J. Lu, A. Hoel, C.-G. Granqvist, G. Romualdo Torres, and S.-E. Lindquist, "Photoelectrochemical study of sputtered nitrogen-doped titanium dioxide thin films in aqueous electrolyte," *Solar Energy Materials and Solar Cells*, vol. 84, no. 1–4, pp. 145–157, 2004.
- [43] G. Blaase, "Optical electron transfer between metal ions and its consequences," in *Structure & Bonding*, vol. 76, pp. 153–185, 1991.
- [44] D. A. Schwartz, N. S. Norberg, Q. P. Nguyen, J. M. Parker, and D. R. Gamelin, "Magnetic quantum dots: synthesis, spectroscopy, and magnetism of Co²⁺- and Ni²⁺-doped ZnO nanocrystals," *Journal of the American Chemical Society*, vol. 125, no. 43, pp. 13205–13218, 2003.
- [45] W. K. Liu, G. Mackay Salley, and D. R. Gamelin, "Spectroscopy of photovoltaic and photoconductive nanocrystalline Co²⁺-doped ZnO electrodes," *Journal of Physical Chemistry B*, vol. 109, no. 30, pp. 14486–14495, 2005.
- [46] D. A. Schwartz and D. R. Gamelin, "Reversible 300 K ferromagnetic ordering in a diluted magnetic semiconductor," *Advanced Materials*, vol. 16, no. 23–24, pp. 2115–2119, 2004.
- [47] M. R. Hoffmann, S. T. Martin, W. Choi, and D. W. Bahnemann, "Environmental applications of semiconductor photocatalysis," *Chemical Reviews*, vol. 95, no. 1, pp. 69–96, 1995.
- [48] A. Boscolo Boscoletto, F. Gottardi, L. Milan, et al., "Electrochemical treatment of bisphenol-A containing wastewaters," *Journal of Applied Electrochemistry*, vol. 24, no. 10, pp. 1052–1058, 1994.
- [49] Y. Ohko, I. Ando, C. Niwa, et al., "Degradation of bisphenol A in water by TiO₂ photocatalyst," *Environmental Science and Technology*, vol. 35, no. 11, pp. 2365–2368, 2001.
- [50] V. N. Kuznetsov and N. Serpone, "Visible light absorption by various titanium dioxide specimens," *Journal of Physical Chemistry B*, vol. 110, no. 50, pp. 25203–25209, 2006.

Research Article

Preparation of Fluorine-Doped TiO₂ Photocatalysts with Controlled Crystalline Structure

N. Todorova,¹ T. Giannakopoulou,¹ G. Romanos,² T. Vaimakis,³ Jiaguo Yu,⁴ and C. Trapalis¹

¹Institute of Materials Science, National Center for Scientific Research (NCSR) "Demokritos", 15310 Attica, Greece

²Institute of Physical Chemistry, National Center for Scientific Research (NCSR) "Demokritos", 15310 Attica, Greece

³Department of Chemistry, University of Ioannina, 45110 Ioannina, Greece

⁴State Key Laboratory of Advanced Technology for Materials Synthesis and Processing, Wuhan University of Technology, Wuhan 430070, China

Correspondence should be addressed to C. Trapalis, trapalis@ims.demokritos.gr

Received 1 September 2007; Accepted 13 December 2007

Recommended by M. Sabry Abdel-Mottaleb

Nanocrystalline F-doped TiO₂ powders were prepared by sol-gel route. The thermal behavior of the powders was recorded by DTA/TG technique. The crystalline phase of the fluorinated TiO₂ powders was determined by X-ray diffraction technique. It was demonstrated that F-doping using CF₃COOH favors the formation of rutile along with anatase phase even at low temperature. Moreover, the rutile's phase content increases with the increase of the quantity of the fluorine precursor in the starting solution. The surface area of the powders and the pore size distribution were studied by N₂ adsorption-desorption using BET and BJH methods. X-ray photoelectron spectroscopy (XPS) revealed that the fluorine is presented in the TiO₂ powders mainly as metal fluoride in quantities ~16 at %. The F-doped TiO₂ showed a red-shift absorption in UV-vis region which was attributed to the increased content of rutile phase in the powders. The powders exhibited enhanced photocatalytic activity in decomposition of acetone.

Copyright © 2008 N. Todorova et al. This is an open access article distributed under the Creative Commons Attribution License, which permits unrestricted use, distribution, and reproduction in any medium, provided the original work is properly cited.

1. INTRODUCTION

In the last decades, the TiO₂ is regarded as a promising material for organic pollutants remediation due to its properties [1]. Its wide application though is still retarded by the low efficiency of the photo-oxidative process. The development of titania-based photocatalysts activated by visible light ($\lambda \geq 385$ nm) remains a great challenge. Anion doping of TiO₂ films and powders with elements like nitrogen [2–5], sulfur [6, 7], carbon [8, 9], and fluorine [10–18] has been investigated in order to red-shift the absorbance to be achieved. Narrowing of the band gap of TiO₂ upon doping was often considered responsible for the enhanced visible light activity of these materials. Theoretical DOS calculations revealed intermediate energy levels available in the band gap of TiO₂ for most of the elements except fluorine [1]. Park and Choi [10] reported that surface fluorination (F-TiO₂) enhances the photocatalytic degradation of certain substrates due to the electron-trapping sites formation. The enhanced photocatalytic activity of F-doped powders has been attributed by

Li et al. [11–13] to several beneficial effects produced by F-doping and mainly to the creation of surface oxygen vacancies. Yu et al. [14] reported fluorine ions incorporation in the TiO₂ lattice using an NH₄F source. They attributed the stronger absorption in the UV-visible range to the presence of the F⁻ ions that favor anatase phase formation and improve the crystallinity of TiO₂. However, Yamaki et al. [15] claimed that F-doping causes a modification of the conduction band edge and introduction of impurity states near its bottom. Our recent study on fluorine-modified titania films [18] revealed improved anatase crystallinity upon fluorine doping without the effective band gap of TiO₂ to be affected.

Anatase is usually produced when TiO₂ is synthesized by sol-gel method [19]. Calcination of anatase at high temperatures is applied to obtain rutile phase. Mixtures of anatase and rutile (e.g., Degussa P25 consists of ~75% anatase and ~25% rutile) are reported to exhibit enhanced photocatalytic activity in degradation of organic pollutants as the electron-hole recombination rate is decreased in the composite system [20]. Cheng et al. [21] reported that rutile phase is developed

preferably from a solution with low pH. Klein et al. [22] produced rutile (100%) titania powders at low temperature using nitric and hydrochloric acids as catalysts.

In this work, we study the influence of CF_3COOH fluorine precursor on the structure and the properties of TiO_2 powders.

2. EXPERIMENTAL

Fluorine- (F-) doped TiO_2 powders have been prepared by sol-gel route. Tetraethyl orthotitanate (TEOTi) Merck was used as titanium source. Different amounts of fluoroacetic acid (Aldrich Chemical Co., Milwaukee, Wis, USA) (atomic ratios $\text{F}/\text{Ti} = 0, 10/90, 20/80$) were dissolved in deionized water (molar ratio $\text{H}_2\text{O}/\text{TEOTi} = 18$) under stirring at room temperature and the TEOTi was added to the solution dropwise. The sols were stirred in closed beakers at room temperature for 24 hours for completion of the hydrolysis process. Consequently, they were dried at 90°C in air for 12 hours for water and alcohol evaporation. The xerogels obtained were denoted as TF0, TF10, and TF20 for the undoped TiO_2 and the samples with $\text{F}/\text{Ti} = 10/90$ and $20/80$ atomic ratios, respectively. The as-prepared xerogels were calcinated at 400, 500, and 600°C for 1 hour in a Carbolite muffle furnace with heating rate of $5^\circ\text{C}/\text{min}$.

Differential thermal analysis (DTA) and thermogravimetry (TG) measurements were performed using NETZSCH equipment model STA 449. The samples with a mass ~ 14 mg were placed in alumina crucible and heated in air flow (30 mL/min) from room temperature up to 1000°C . The heating rate applied was $10^\circ\text{C}/\text{min}$.

The crystalline structure of the powders was investigated using X-ray diffraction (XRD) technique. SIEMENS D500 diffractometer with secondary graphite monochromator and $\text{CuK}\alpha$ radiation was used to obtain the X-ray diffraction patterns of the samples. The measurements were performed using the following combination of slits: $1.0^\circ/1.0^\circ/1.0^\circ$ as aperture diaphragms, 0.15° as detector diaphragm, and 0.25° as diffracted beam monochromator diaphragm. The measured 2θ range between 20° and 80° was scanned in steps of $0.03^\circ/2s$. The size of the crystallites responsible for the Bragg reflection was determined using the Scherrer equation

$$d = \frac{k\lambda}{b \cos \theta}, \quad (1)$$

where d is the crystallite diameter in \AA , k the shape constant (0.9), λ the wavelength in \AA , θ the Bragg angle in degrees, and b the observed peak width at half-maximum peak height in rad. The phase content (%) of the samples was calculated using the formula [14]

$$W_R = \frac{A_R}{K_A A_A + A_R}, \quad (2)$$

where W_R is the content of the rutile phase ($W_A = 100 - W_R$), A_A and A_R are the integrated intensities of anatase (101) and rutile (110) peaks, respectively, and K_A is a coefficient equal to 0.886.

The surface areas of the powders were determined by the Branauer-Emmet-Teller (BET) method. The equipment

COULTER 5200 USA was used for the nitrogen adsorption/desorption measurements at 77 K. All the samples were degassed at 573 K for 24 hours.

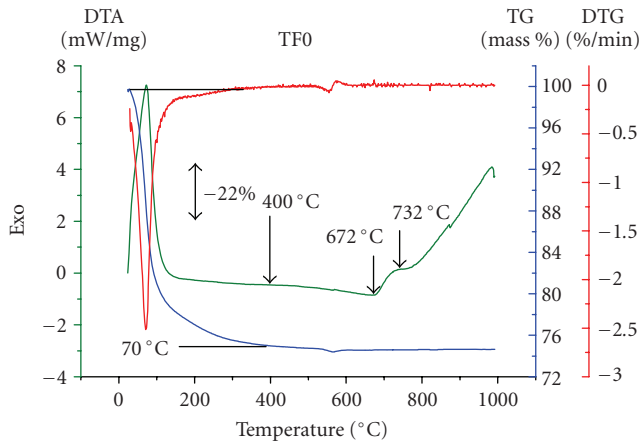
The presence of the fluorine in the TiO_2 , the valence state of the dopant, as well as the bonding element was analyzed by X-ray photoelectron spectroscopy (XPS). Non-monochromatized $\text{MgK}\alpha$ X-rays from a dual-anode VSW TA-10 source were used. The ultra-high vacuum (UHV) chamber was baked at 150°C for 12 hours to reach the 10^{-10} mbar pressure range. Measurements were performed for the samples without Ar ion sputtering (as received), as well as after a 45-minute light Ar^+ ion sputtering in order to remove most of the superficial carbon contamination.

UV-vis diffuse reflectance spectra of the samples in the wavelength range 200–900 nm were obtained using a UV-2100 Shimadzu instrument. The widths of the effective band gap of the samples were determined using Kubelka-Munk phenomenological theory [23].

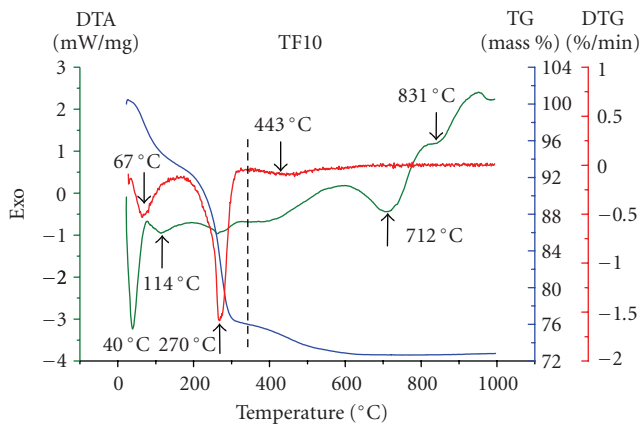
The photocatalytic activity of the powders was evaluated by photocatalytic oxidation of acetone (CH_3COCH_3) using a 7L reactor (INNOVA). An amount of 0.3 g of each powder was used for the preparation of aqueous suspensions which were placed in petri dishes and dried at 100°C for 2 hours. The samples were placed into the reactor where acetone was injected. The initial humidity in the reactor was controlled by dryer containing CaCl_2 . The acetone vapour was allowed to reach adsorption equilibrium with the photocatalyst prior measurements. Its initial concentration was about 400 ppm. A 15 W UV lamp (Cole Parmer Instr. Co., Chicago, Ill, USA) was used for illumination. The illumination time applied was 60 minutes. The amounts of acetone, carbon dioxide, and water vapour in the reactor were monitored. During the photocatalytic reaction, the acetone concentration decreased steadily. The photocatalytic activity of the powders was quantitatively evaluated by comparing the apparent reaction rate constants k_a of the decomposition reactions given that the degradation of acetone is known to be a reaction of pseudo first order [19].

3. RESULTS AND DISCUSSION

The TG, DTG, and DTA curves of undoped and F-doped TiO_2 powders are presented in Figure 1. For the undoped TiO_2 (Figure 1(a)), it can be observed that the total loss of weight ($\sim 25\%$) took place in three not well-defined steps. The first is the main loss of weight ($\sim 22.3\%$) that took place between ~ 30 and $\sim 180^\circ\text{C}$ and it was related to the evaporation of water and alcohol included in the xerogel. The second ($\sim 2.5\%$) and the third ($\sim 0.4\%$) weak losses took place between ~ 180 – 430°C and ~ 430 – 675°C , respectively, during which the remained water and organics ($\sim 2.9\%$) were gradually removed from the powders. The DTA curve reveals a weak exothermic phenomenon from 400°C to 672°C and it was connected to the process of crystallization of anatase. The endothermic effect after 670°C and the shoulder at 732°C were attributed to the process of anatase to rutile transformation. The DTA, TG, and DTG curves of the TF10 fluorinated xerogel are presented in Figure 1(b). It can be observed that the addition of fluorine containing substance



(a)

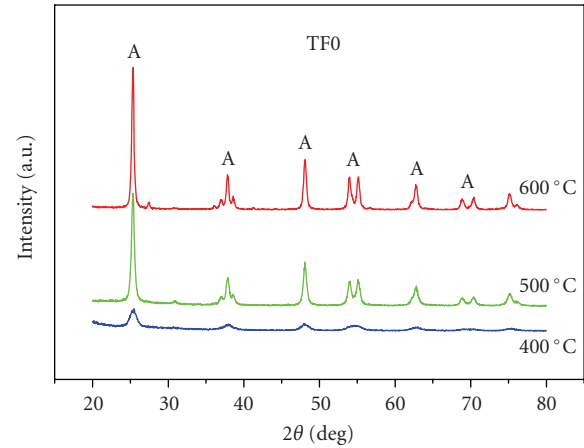


(b)

FIGURE 1: DTA, TG, DTG patterns of undoped (a) and fluorinated (b) titania powders.

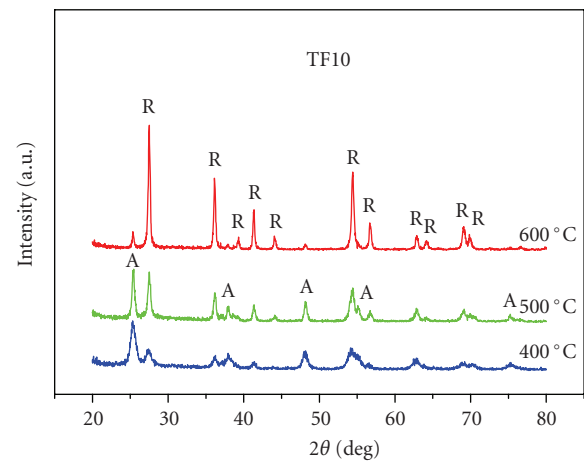
results in complication of TG and DTA curves in comparison with the undoped sample. The mass decrease of the samples TCF10 took place in three steps. The first step of about 7.3% took place in the range of 30 to 150°C and the second step of about 17% took place from 150 to 350°C. The latter was connected to the decomposition and removal of organic radicals (CF_3COO^-). In addition, in the range from about 390 to 700°C, mass loss of about 3% took place that can be ascribed to the release of less volatile components and reaction products. Beyond $\sim 700^\circ\text{C}$ the DTA curve exhibits endothermic tendency which might be attributed to the anatase to rutile transformation. The thermal behavior of TF20 xerogel (not given) was similar to the TF10 sample.

The X-ray diffraction patterns of the calcinated at 400, 500, and 600°C samples are presented in Figure 2. In our study, pure anatase was recorded for the undoped titania (Figure 2(a)) after thermal treatment at every temperature mentioned above. The XRD patterns of F-doped TiO_2 powders (Figures 2(b) and 2(c)) revealed that a second crystalline phase, that of rutile, was developed along with the anatase phase at temperatures as low as 400°C. The average sizes of

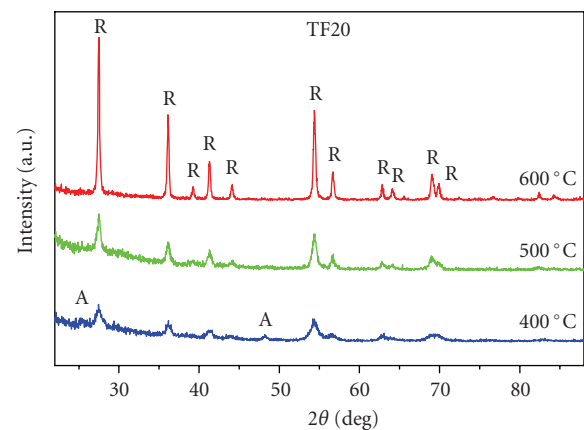


A: anatase

(a)

A: anatase
R: rutile

(b)

A: anatase
R: rutile

(c)

FIGURE 2: XRD patterns of undoped (a) and fluorinated TiO_2 powders with starting ratios $\text{F}/\text{Ti} = 10/90$ (b) and $\text{F}/\text{Ti} = 20/80$ (c).

TABLE 1: Phase content W (%) and average diameter d (nm) of the crystallites in the TiO_2 powders calcinated at different temperatures (A: Anatase, R: Rutile).

| Nominal name | Calcination temperatures | | | | | |
|----------------------|--------------------------|--------------|------------------|--------------|-----------------|--------------|
| | 400°C | | 500°C | | 600°C | |
| | W (%) | d (nm) | W (%) | d (nm) | W (%) | d (nm) |
| TF0 F/Ti = 0 | A:100 | 8.5 | A:100 | 12.0 | A:100 | 18.0 |
| TF10 F/Ti = 10/90 | A:72.5 R:27.4 | 10.5 10.6 | A:45.7 R:54.3 | 21.5 20.8 | A:9.3 R:90.7 | 15.5 20.8 |
| TF20 F/Ti = 20/80 | A:9.1 R:90.9 | 10.2 | R:100 | 14.1 | R:100 | 36.1 |

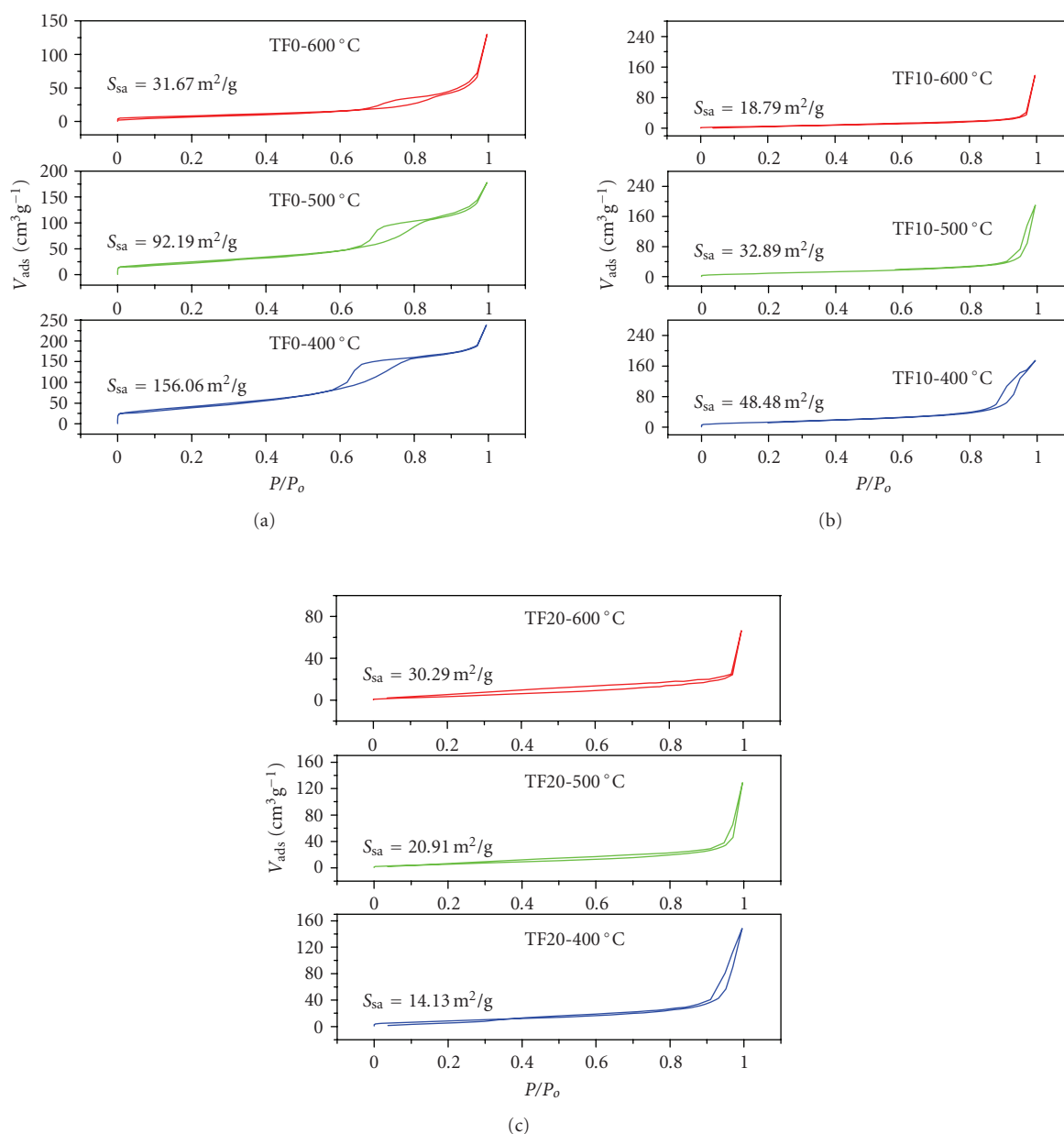


FIGURE 3: Nitrogen adsorption-desorption isotherms of undoped (a) and F-doped (b) and (c) powders calcinated at different temperatures.

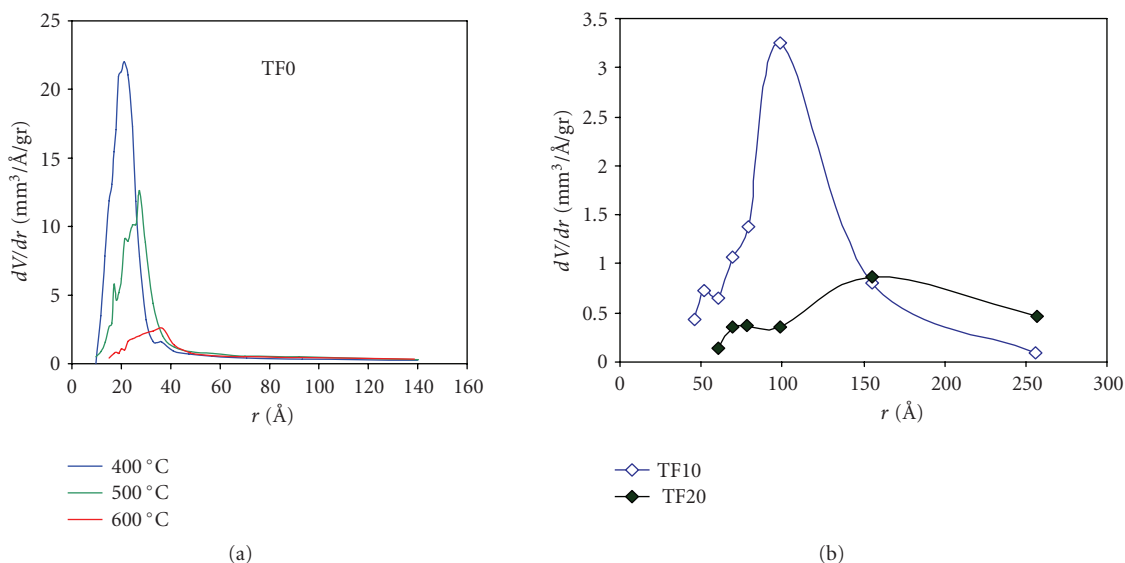


FIGURE 4: Pore size distribution in the undoped TiO_2 calcinated at different temperatures (a) and in the TF10 and TF20 powders calcinated at 400°C (b).

TABLE 2: BET surface area and porosity of TiO_2 powders calcinated at different temperatures.

| Nominal name | Calcination temperatures | | | | | |
|----------------------|--|--------------|--|--------------|--|--------------|
| | 400°C | | 500°C | | 600°C | |
| | BET _{SSA} (m^2/g) | Porosity (%) | BET _{SSA} (m^2/g) | Porosity (%) | BET _{SSA} (m^2/g) | Porosity (%) |
| TF0 F/Ti = 0 | 156.06 | 55.34 | 92.19 | 47.77 | 31.67 | 32.34 |
| TF10 F/Ti = 10/90 | 48.48 | 32.15 | 32.89 | 22.41 | 18.79 | 10.23 |
| TF20 F/Ti = 20/80 | 14.13 | 22.57 | 20.91 | 13.06 | 30.29 | 7.32 |

the crystallites (d , nm), as well as the anatase/rutile phase composition (W, %) of the powders are presented in Table 1. From the results displayed in Figure 2 and Table 1, it is evident that the crystallization process of TiO_2 depends on the presence and the quantity of the fluorine precursor, as well as the calcination temperature. The increase in the size of the crystallites with the increase of the calcination temperatures can be observed for all the samples. It is also evident that the polymorph phase composition is dependent on the quantity of the CF_3COOH in the starting solution. It can be deduced that fluorine-doped titania powders with controlled anatase/rutile phase composition can be synthesized by altering the molar ratio of $\text{CF}_3\text{COOH}/\text{TEOTi}$ in the starting solution and the calcination temperature.

The influence of the F^- ions on the crystallization process of TiO_2 has been studied and improved anatase crystallinity upon F-doping has been reported [14, 18]. Up to our knowledge, there is no report on direct synthesis and fluorination of TiO_2 powder with controlled anatase/rutile content. Moreover, the increase of the F/Ti molar ratio in the starting solution (sample TF20) leads to formation of pure

rutile even at 400°C . The crystallization of rutile alone or along with anatase phase at low temperatures is attributed to the acidic character of the fluorine precursor which provides low pH conditions during peptization. At these acidic conditions, the edge-shared bonding among the $[\text{TiO}_6]$ octahedrons which is responsible for anatase formation during calcination is suppressed, while the corner-shared bonding that is responsible for the rutile formation is favored [21].

Nitrogen adsorption-desorption isotherm measurements were performed to determine the specific surface area, the porosity, and the pore size distribution in the samples. The N_2 adsorption-desorption isotherms for the undoped TiO_2 and the fluorinated samples calcinated at 400°C clearly show a *hysteresis* in the desorption branch (Figure 3). These samples exhibited the highest BET surface area. Their pore size distribution curves obtained from the desorption branch are depicted in Figure 4. From the figures and the results presented in Table 2, it can be observed that the BET surface areas decrease significantly while the pore size distribution becomes wider with the increase of the calcination temperature for all samples. A decrease in the

porosity with the increase of the calcination temperature is also evident. The BET values for the fluorinated powders are much lower than those for the undoped TiO_2 powders when calcinated at the same temperatures. These findings are connected to the presence of fluorine containing organic precursor in the xerogels and the exothermic phenomena of its burning occurring during calcination. The heat release leads to the agglomeration of TiO_2 nanoparticles and to the decrease of the BET surface area. The process contributes to the improvement of the TiO_2 crystallinity as it was revealed by XRD results.

The chemical composition of the sample TF20 calcinated at 400°C was studied by XPS analysis. After the removal of the superficial carbon contaminant (3-4 monolayers), the elements detected were titanium, oxygen, and fluorine. The spectra obtained for Ti 2p, O 1s, and F 1s regions (Figure 5) revealed that the powder consists of TiO_2 , where titanium and oxygen are present as Ti^{4+} and O^{2-} . The valence states of the titanium and the oxygen were determined from the Ti 2p $_{3/2}$ -Ti 2p $_{1/2}$ splitting (~ 5.7 eV) and the difference of ~ 71.5 eV between the binding energies of the Ti 2p $_{3/2}$ peak (458.5 ± 0.1 eV) and the O 1s peak (530.0 ± 0.1 eV). The F 1s spectrum (Figure 5(c)) is nonsymmetric and the contribution near 684.3 eV indicates that the fluorine is presented in the sample mainly as TiF_4 [24] and/or to physically adsorbed F^- on TiO_2 [19]. The contribution near 685.4 eV could be related to TiOF_2 structures [12] and the tail near 688 eV to nonstoichiometric solid solution of F in TiO_2 of the $\text{TiO}_{2-x}\text{F}_x$ type [12, 19]. It can be also associated with C-F bonding in CF_3 residual groups [25]. The fluorine concentration was estimated as ~ 14 at % before and ~ 16 at % after the Ar^+ ions sputtering. This level of doping can be connected to the high temperature of decomposition of the fluorine precursor which is evident from the thermal analysis.

The diffuse reflectance spectra (R) of the samples were used to assess the absorption of the photocatalysts in the UV-vis region. The undoped TF0 sample and the TF20 samples revealed typical anatase and rutile spectra, respectively, and for this reason they are not shown. The absorption curves of the fluorinated TF10 samples with various anatase/rutile ratios are presented in Figure 6(a). The P25 absorption curve is also presented for comparison because of its mixed phase composition (anatase $\sim 75\%$ and rutile $\sim 25\%$). To determine the band gap of the powders, the Kubelka-Munk method based on the diffuse reflectance spectra was employed. The $(F(R)h\nu)^{1/2}$ versus $h\nu$ plots of the P25 and the TF10 samples are presented in Figure 6(b), where $F(R) = (1-R)/2R$. It can be observed that the band gap values obtained for the Degussa P-25 and the TF10 sample calcinated at 400°C are close (3.08 eV and 3.07 eV, resp.). This fact can be connected to the similar anatase/rutile phase content of the samples. This is also consistent with the literature [11, 12, 19] and support the conception that the fluorine doping does not affect the band gap of TiO_2 . With the increase of the calcination temperature, the widths of the band gap for the fluorinated samples decrease from 3.07 to 3.03 eV. This "narrowing" of the effective band gap is attributed to the increase of the rutile content in the powders which is in accordance with our XRD results.

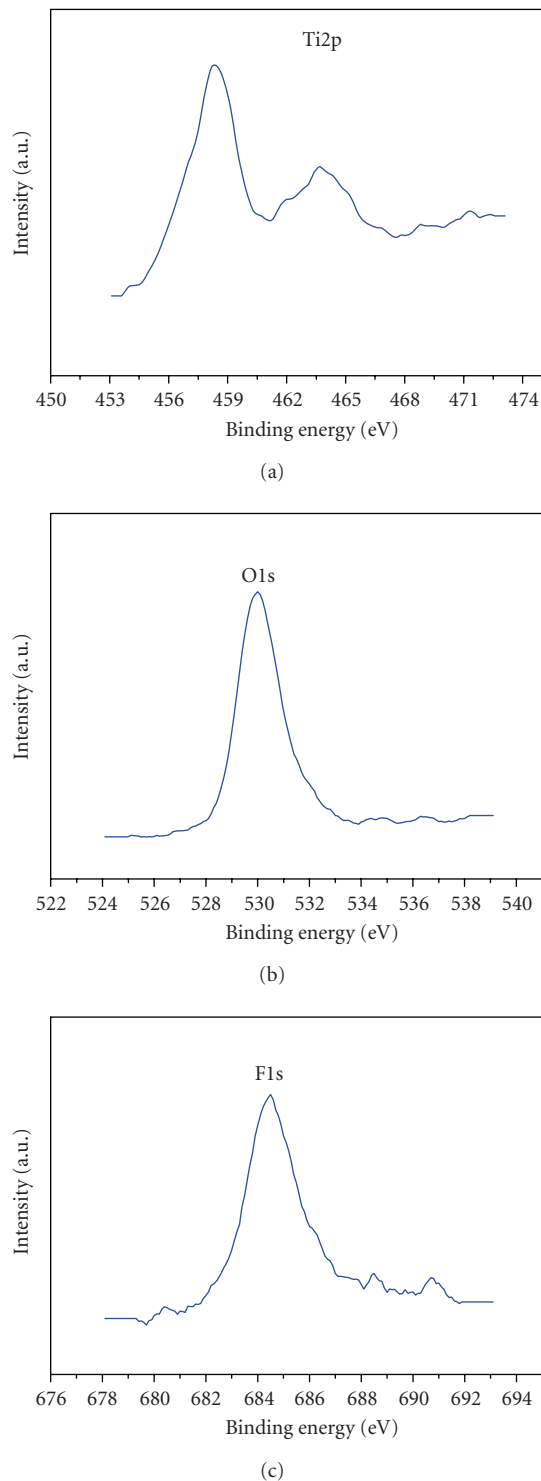


FIGURE 5: XPS spectra for Ti 2p (a), O 1s (b), and F 1s (c) regions of TF20 sample calcinated at 400°C .

The increase in the CO_2 concentration due to the decomposition of acetone and the calculated apparent rate constant of the photocatalytic reaction are presented in Figures 7 and 8, respectively. From our results, it can be concluded that the fluorinated TiO_2 powders exhibit enhanced activity in comparison to the reference photocatalyst Degussa P25.

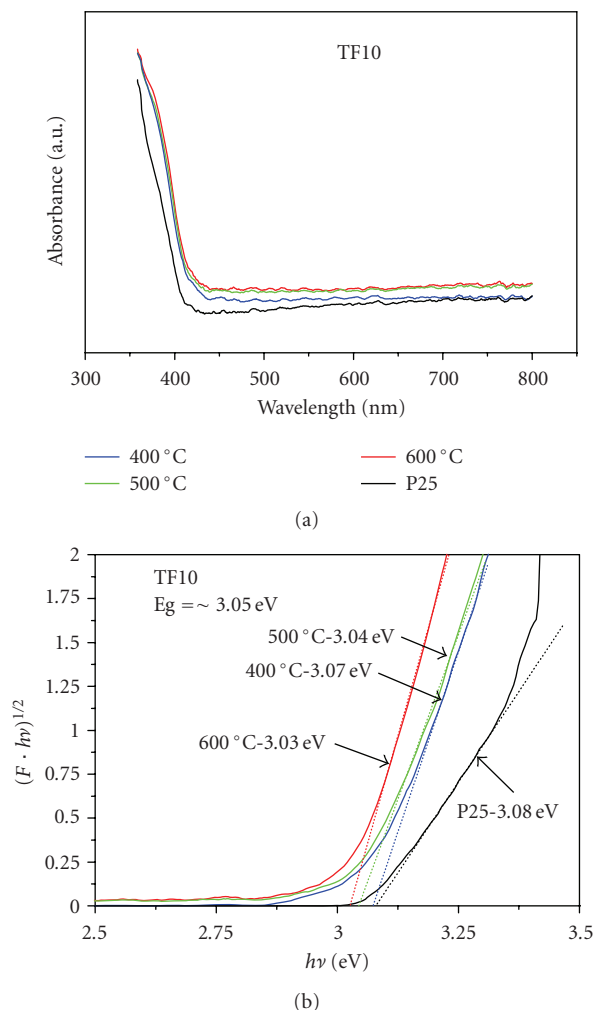


FIGURE 6: Absorbance spectra (a) and Kubelka-Munk plot for band gap evaluation (b) of fluorinated (TF10) TiO_2 and P25 powders.

The best results are recorded for the powders calcinated at 400°C which can be connected to the mixed anatase/rutile phase composition and the higher BET surface area in comparison to the samples calcinated at 500°C and 600°C . In addition, the activity of TF20 samples treated at 400°C and 500°C exceeds significantly the activity of the corresponding TF10 powders. This fact was attributed to the rutile rich composition of the powders and the higher level of fluorine doping. The drastic decrease in the activity of the treated at 600°C samples is attributed to the decrease of the BET surface area, as well as to the absence of anatase phase in the powders.

4. CONCLUSIONS

Simultaneous fluorination and controlled low-temperature anatase/rutile phase crystallization of nanosized TiO_2 powders were achieved using sol-gel route. It was found that the anatase/rutile crystalline ratio depends on the amount of fluorine precursor used for fluorination as well as on the temperature of thermal treatment.

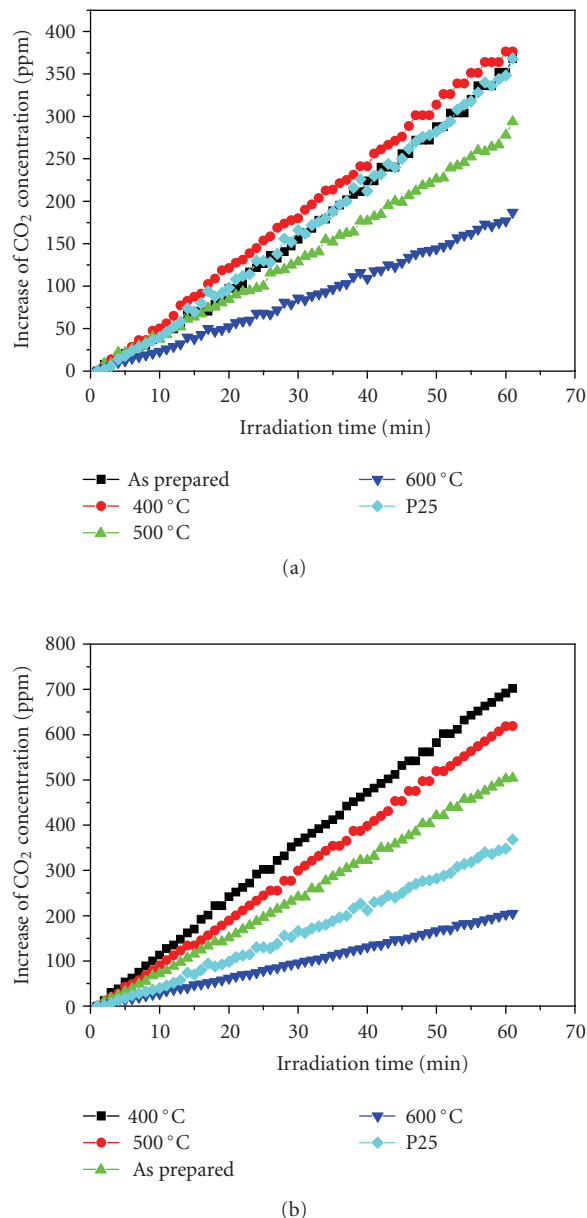


FIGURE 7: Increase of the CO_2 concentration due to decomposition of acetone for fluorinated TF10 (a) and TF20 (b) titania powders.

The crystallization of pure rutile or anatase/rutile mixture at low temperatures is attributed to the acidic character of the fluorine precursor. Improved crystallinity and enhanced absorbance of the powders in the UV-vis region are recorded upon F-doping. The fluorine is presented in the powders mainly as metal (Ti) fluoride.

The width of the TiO_2 band gap was not affected by the presence of fluorine. The red shift of the absorption edge is attributed to the increased rutile content in the fluorine doped TiO_2 powders. The prepared fluorine doped TiO_2 powders calcinated at 400°C exhibited higher photocatalytic activity than that of Degussa P-25 for decomposition of acetone under UV-vis illumination.

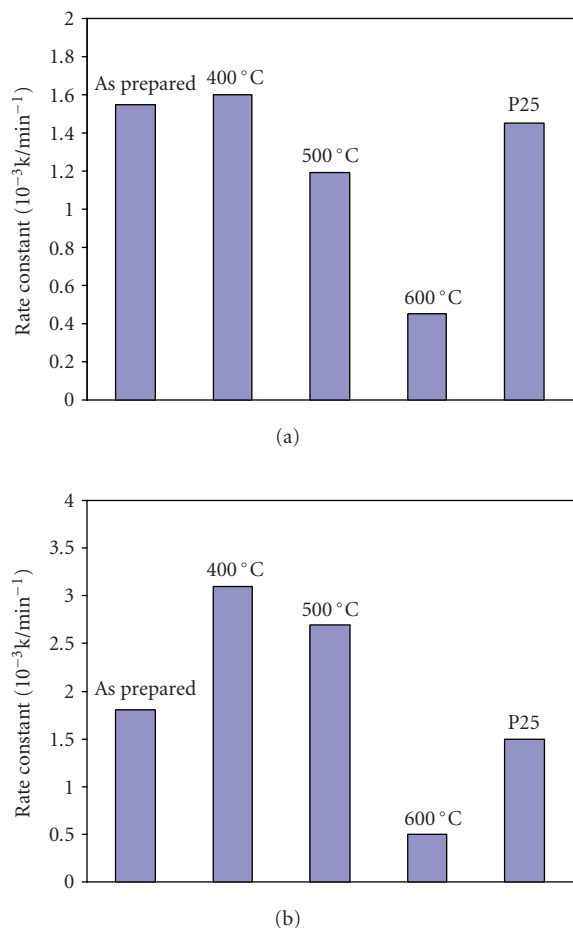


FIGURE 8: Photocatalytic activity of fluorinated TF10 (a) and TF20 (b) titania powders evaluated by decomposition of acetone.

ACKNOWLEDGMENTS

Financial support of National Secretariat for Research and Technology and the Ministry of Development, under Grant Non-EU 05 245 is gratefully acknowledged.

REFERENCES

- [1] R. Asahi, T. Morikawa, T. Ohwaki, K. Aoki, and Y. Taga, "Visible-light photocatalysis in nitrogen-doped titanium oxides," *Science*, vol. 293, no. 5528, pp. 269–271, 2001.
- [2] S. Sato, "Photocatalytic activity of NO_x -doped TiO_2 in the visible light region," *Chemical Physics Letters*, vol. 123, no. 1-2, pp. 126–128, 1986.
- [3] J. L. Gole, J. D. Stout, C. Burda, Y. Lou, and X. Chen, "Highly efficient formation of visible light tunable $\text{TiO}_{2-x}\text{N}_x$ photocatalysts and their transformation at the nanoscale," *Journal of Physical Chemistry B*, vol. 108, no. 4, pp. 1230–1240, 2004.
- [4] M. Batzill, E. H. Morales, and U. Diebold, "Influence of nitrogen doping on the defect formation and surface properties of TiO_2 rutile and anatase," *Physical Review Letters*, vol. 96, no. 2, Article ID 026103, 4 pages, 2006.
- [5] V. Balek, D. Li, J. Šubr, et al., "Characterization of nitrogen and fluorine co-doped titania photocatalyst: effect of temperature on microstructure and surface activity properties," *Journal of Physics and Chemistry of Solids*, vol. 68, no. 5-6, pp. 770–774, 2007.
- [6] T. Ohno, M. Akiyoshi, T. Umabayashi, K. Asai, T. Mitsui, and M. Matsumura, "Preparation of S-doped TiO_2 photocatalysts and their photocatalytic activities under visible light," *Applied Catalysis A*, vol. 265, no. 1, pp. 115–121, 2004.
- [7] T. Umabayashi, T. Yamaki, H. Itoh, and K. Asai, "Band gap narrowing of titanium dioxide by sulphur doping," *Applied Physics Letters*, vol. 81, no. 3, p. 454, 2002.
- [8] T. Tachikawa, S. Tojo, K. Kawai, et al., "Photocatalytic oxidation reactivity of holes in the sulphur- and carbon-doped TiO_2 powders studied by time-resolved diffuse reflectance spectroscopy," *Journal of Physical Chemistry B*, vol. 108, no. 50, pp. 19299–19306, 2004.
- [9] A. Hattori, K. Shimoda, H. Tada, and S. Ito, "Photoreactivity of sol-gel TiO_2 films formed on soda-lime glass substrates: effect of SiO_2 underlayer containing fluorine," *Langmuir*, vol. 15, no. 16, pp. 5422–5425, 1999.
- [10] H. Park and W. Choi, "Effects of TiO_2 surface fluorination on photocatalytic reactions and photoelectrochemical behaviors," *Journal of Physical Chemistry B*, vol. 108, no. 13, pp. 4086–4093, 2004.
- [11] D. Li, H. Haneda, S. Hishita, N. Ohashi, and N. K. Labhsetwar, "Fluorine-doped TiO_2 powders prepared by spray pyrolysis and their improved photocatalytic activity for decomposition of gas-phase acetaldehyde," *Journal of Fluorine Chemistry*, vol. 126, no. 1, pp. 69–77, 2005.
- [12] D. Li, H. Haneda, N. K. Labhsetwar, S. Hishita, and N. Ohashi, "Visible-light-driven photocatalysis on fluorine-doped TiO_2 powders by the creation of surface oxygen vacancies," *Chemical Physics Letters*, vol. 401, no. 4–6, pp. 579–584, 2005.
- [13] D. Li, N. Ohashi, S. Hishita, T. Kolodiazny, and H. Haneda, "Origin of visible-light-driven photocatalysis: a comparative study on N/F-doped and N-F-codoped TiO_2 powders by means of experimental characterizations and theoretical calculations," *Journal of Solid State Chemistry*, vol. 178, no. 11, pp. 3293–3302, 2005.
- [14] J. Yu, J. C. Yu, M. K.-P. Leung, et al., "Effects of acidic and basic hydrolysis catalysts on the photocatalytic activity and microstructures of bimodal mesoporous titania," *Journal of Catalysis*, vol. 217, no. 1, pp. 69–78, 2003.
- [15] T. Yamaki, T. Umabayashi, T. Sumita, et al., "Fluorine-doping in titanium dioxide by ion implantation technique," *Nuclear Instruments and Methods in Physics Research B*, vol. 206, pp. 254–258, 2003.
- [16] D. Huang, S. Liao, S. Quan, et al., "Preparation of anatase F-doped TiO_2 sol and its performance for photodegradation of formaldehyde," *Journal of Materials Science*, vol. 42, no. 19, pp. 8193–8202, 2007.
- [17] D. Huang, S. Liao, J.-M. Liu, Z. Dang, and L. Petrik, "Preparation of visible-light responsive N-F-codoped TiO_2 photocatalyst by a sol-gel-solvothermal method," *Journal of Photochemistry and Photobiology A*, vol. 184, no. 3, pp. 282–288, 2006.
- [18] T. Giannakopoulou, N. Todorova, C. Trapalis, and T. Vaimakis, "Effect of fluorine doping and SiO_2 under-layer on the optical properties of TiO_2 thin films," *Materials Letters*, vol. 61, no. 23-24, pp. 4474–4477, 2007.
- [19] J. C. Yu, J. Yu, W. Ho, Z. Jiang, and L. Zhang, "Effects of F-doping on the photocatalytic activity and microstructures of nanocrystalline TiO_2 powders," *Chemistry of Materials*, vol. 14, no. 9, pp. 3808–3816, 2002.

-
- [20] B. Sun and P. G. Smirniotis, "Interaction of anatase and rutile TiO_2 particles in aqueous photooxidation," *Catalysis Today*, vol. 88, no. 1-2, pp. 49–59, 2003.
- [21] H. Cheng, J. Ma, Z. Zhao, and L. Qi, "Hydrothermal preparation of uniform nanosize rutile and anatase particles," *Chemistry of Materials*, vol. 7, no. 4, pp. 663–671, 1995.
- [22] S. M. Klein, J. H. Choi, D. J. Pine, and F. F. Lange, "Synthesis of rutile titania powders: agglomeration, dissolution, and reprecipitation phenomena," *Journal of Materials Research*, vol. 18, no. 6, pp. 1457–1464, 2003.
- [23] E. L. Simmons, "Relation of the diffuse reflectance remission function to the fundamental optical parameters," *Journal of Modern Optics*, vol. 19, no. 10, pp. 845–851, 1972.
- [24] T. Yamaki, T. Sumita, and S. Yamamoto, "Formation of $\text{TiO}_{2-x}\text{F}_x$ compounds in fluorine-implanted TiO_2 ," *Journal of Materials Science Letters*, vol. 21, no. 1, pp. 33–35, 2002.
- [25] J. C. Yu, W. Ho, J. Yu, S. K. Hark, and K. Iu, "Effects of trifluoroacetic acid modification on the surface microstructures and photocatalytic activity of mesoporous TiO_2 thin films," *Langmuir*, vol. 19, no. 9, pp. 3889–3896, 2003.

Research Article

Effect of Gold Dispersion on the Photocatalytic Activity of Mesoporous Titania for the Vapor-Phase Oxidation of Acetone

S. V. Awate, A. A. Belhekar, S. V. Bhagwat, R. Kumar, and N. M. Gupta

Catalysis Division, National Chemical Laboratory, Dr. Homi Bhabha Road, Pune 411008, India

Correspondence should be addressed to N. M. Gupta, nm.gupta@ncl.res.in

Received 30 September 2007; Accepted 26 November 2007

Recommended by Vincenzo Augugliaro

Mesostructured titanium dioxide photocatalyst, having uniform crystallite size (6–12 nm) and average pore diameter of ~4.2 nm, was synthesized by using a low-temperature nonsurfactant hydrothermal route, employing tartaric acid as a templating agent. Gold additions from 0.5 to 2 wt% were incorporated, either during the hydrothermal process or by postsynthesis wet impregnation. Compared to the impregnation-prepared samples, the samples synthesized hydrothermally contained smaller-size (≤ 1 nm) gold clusters occluded in the pores of the host matrix. Whereas CO₂ and H₂O were the main reaction products in UV-assisted vapor-phase oxidation of acetone using these catalysts, C₂H₆ and HCO₂CH₃ were also produced for higher acetone concentrations in air. The conversion of acetone was found to increase with decrease in the size of both TiO₂ and gold particles. In situ IR spectroscopy revealed that titania and gold particles serve as independent adsorption and reaction sites for acetone and oxygen molecules. Acetone molecules adsorb exclusively at TiO₂ surface, giving rise to a strongly adsorbed (condensed) state as well as to the formation of formate- and methyl formate-type surface species. Hydroxyl groups at titania surface participate directly in these adsorption steps. Nanosize gold particles, on the other hand, were primarily responsible for the adsorption and activation of oxygen molecules. Mechanistic aspects of the photochemical processes are discussed on the basis of these observations.

Copyright © 2008 S. V. Awate et al. This is an open access article distributed under the Creative Commons Attribution License, which permits unrestricted use, distribution, and reproduction in any medium, provided the original work is properly cited.

1. INTRODUCTION

Concerted research has been devoted to oxidative degradation of volatile organic contaminants via photocatalytic route, with a view to find a viable solution to environmental pollution control [1–3]. Nevertheless, the low quantum yield and poor stability of presently available photocatalytic materials have posed limitations on the large-scale application of the above-mentioned process. These deficiencies arise mainly due to the following reasons: (i) dependence on UV radiation due to large band gap, (ii) a low rate of electron transfer to reactant molecules including oxygen, and (iii) a high rate of recombination of electron-hole pair resulting in low quantum yields. Various approaches have been attempted to enhance the efficiency of photocatalytic materials, either by bringing out certain structural and morphological modifications or by incorporation of certain cocatalysts. In the case of widely studied titanium dioxide photocatalyst, following general strategies have been adopted: (i) morphological changes in bulk TiO₂ [1–8], (ii) doping of TiO₂ with a group VIII metal or a noble metal to increase the lifetime

of electron-hole pair and extending the light absorption to visible region, [9–13], (iii) incorporation of TiO₂ in certain mesoporous materials in order to increase the exposed area [14–17], and (iv) chemical substitution at Ti or O sites, so as to modify the band characteristics and to shift the absorbance toward visible region [18–21]. In spite of these recent developments, detailed knowledge on the precise role of morphological properties of TiO₂, and also that of a metal cocatalyst, still eludes us.

In the recent studies reported by Bhattacharya et al. [14, 15], we demonstrated that the nanosize TiO₂ clusters dispersed in mesoporous MCM-41 silica matrix exhibited a microenvironment that was different from that of the bulk titania. The photocatalytic properties of these samples were found to exhibit direct relationship with the number of chemisorption sites rather than to the changes in electronic properties [15]. In the present study, we have adopted a hydrothermal route for the preparation of bulk titanium dioxide samples, comprised of nanosize crystallites that exhibit a mesoporous character. Gold additions from 0.5 to 2 wt% of gold were doped in these samples by adopting

two different approaches, namely inclusion of Au during the hydrothermal step or alternatively its dispersion over as-synthesized mesoporous TiO₂ by insipient wet impregnation. The samples were characterized for their structural and morphological properties by using the techniques of powder X-ray diffraction (XRD), diffuse reflectance UV-visible spectroscopy (DR UV-Vis), thermal analysis (TG/DTA), N₂ adsorption, and transmission electron microscopy (TEM). Vapor-phase photo-oxidation of acetone was employed as a representative and the reaction was carried out both under visible and UV irradiations. In situ diffuse reflectance infrared Fourier-transform (DRIFT) spectroscopy helped in probing the surface transient studies formed during the interaction of acetone alone or in the presence of oxygen. The role of these transient species in the overall photocatalytic process is elucidated on the basis of these experimental results.

2. EXPERIMENTAL

2.1. Sample preparation

The sample of mesoporous TiO₂ was synthesized by following a low-temperature nonsurfactant hydrothermal route, using tartaric acid as structure directing agent. In this method, about 10 mL of Ti(IV) isopropoxide (Aldrich Chemie, Steinheim, Germany) was added slowly to a mixture of 1N HCl and tartaric acid (3.6 g) under stirring, with the HCl/alkoxide ratio being ~1. The pH of the resultant mix was ~5. After complete hydrolysis of the alkoxide, the mixture was transferred into a Teflon-lined autoclave and heated at 403 K for 3 days followed by cooling to room temperature. The mass was centrifuged and washed several times with distilled water. The white precipitate thus achieved was dried at 373 K for 4–5 hours and then calcined at 623 K for 3 hours to get a sample denoted as T1.

The samples of mesoporous TiO₂ containing 0.5 to 2 wt% of gold were synthesized by following two different methods. In method I, a required amount of chloroauric acid (HAuCl₄, Loba Chemie, Mumbai, India) was added to the mixture of alkoxide and HCl during the hydrolysis step, as described above. After drying at 373 K, the samples were calcined at different temperatures in the range of 525–773 K and are denoted as H1–H6 in Table 1. In method II, hydrothermally prepared titania powder (sample T1) was impregnated with varying amounts of aqueous chloroauric acid solution, followed by drying and calcination at an optimized temperature of 623 K (samples denoted as I1–I3). For some comparative experiments, a sample of pure gold powder was prepared by hydrazine reduction of aqueous chloroauric acid solution, followed by filtration, drying at 370 K, and then heating under vacuum (520 K for 3 hours, 750 K for 2 hours).

2.2. Characterization

The gold content in the synthesized samples was estimated by energy dispersive analysis of X-rays (EDAX), using a PHOENIX stereoscan-440 accessory attached to a scanning electron microscope (Leica, Cambridge, UK). An Au–Cu

metal coupon was used for calibration purposes. The gold concentration in the samples, added initially and the analyzed value in the final product, is given in Table 1.

Powder XRD patterns were recorded in the wide-angle range on Rigaku, Miniflex (D Max III VC) XRD machine (CuK_α radiation) operated at 30 kV and 15 mA. Low-angle powder X-ray diffraction (LAXRD) patterns were recorded over the scan range $2\theta = 1.5$ to 5° using a Philips X'Pert Pro (M/S Panalytical) diffractometer using CuK_α radiation ($\lambda = 1.5406 \text{ \AA}$) operated at 40 kV and 30 mA.

TEM images were obtained on a JEOL-2010 CX microscope. The information about BET surface area and pore characteristics of different samples was derived from low-temperature nitrogen adsorption isotherms, recorded on a Quantachrome NOVA 1200 equipment, after pretreatment at 573 K under vacuum. The BJH formulation was employed to obtain the pore-size distribution data. The samples were further characterized by using DR UV-Vis spectroscopy (LAMBDA 650 spectrophotometer, Perkin-Elmer, Shelton, USA). About 3 wt% of a sample was mixed in barium sulfate for these absorbance measurements. The simultaneous TG/DTA scans were recorded in argon atmosphere for a representative sample H1, so as to monitor various steps involved in sample synthesis.

2.3. Catalytic activity

The experiments on photocatalytic oxidation of acetone were conducted both under UV radiation and also under visible light. A 400 W mercury vapor lamp (225–400 nm, peak at 365 nm) was employed for UV irradiation and a 500 W halogen lamp served as a visible light source. Both light sources were housed in water cooled jackets to cut off infrared radiation. An amount of 25 mg of a sample was charged in a pyrex glass photoreactor (100 mL capacity) for activity measurement where acetone vapor mixed in air (1–25 mol%) was introduced after a brief pumping. The experiments were conducted at room temperature under static condition, and the reaction products formed as a function of radiation exposure were analyzed on a gas chromatograph (Shimadzu model-R-15A, Porapaq-Q column, TCD detector). Qualitative analysis was also conducted on some of the representative samples using a GC-MS (Shimadzu model-R-15A) with a view to establish the identity of the reaction products formed.

2.4. IR study of transient surface species

The IR spectra of surface species formed during exposure of TiO₂ and Au/TiO₂ to acetone were recorded in DRIFT mode using a Shimadzu SSU-8000 spectrophotometer. About 14 mg catalyst powder packed in the sample holder was activated in situ at 625 K for ~3 hours in a flowing stream (40 mL min⁻¹) of pure N₂, followed by cooling to room temperature and recording of a background spectrum. The sample, maintained under nitrogen flow, was then exposed to several successive pulses of either pure acetone vapor or acetone (10 mol%) + air, and the IR spectra were recorded at each stage. The effect of raising the sample temperature subsequent to saturation coverage was also monitored.

TABLE 1: Physical properties of TiO₂ and Au/TiO₂ samples.

| Sample | Calcination Temp. (K) | Au content (wt%) | | Surface area (m ² g ⁻¹) | Average crystallite size ^(d) (nm) | Average gold particle size ^(e) (nm) | Average pore diameter ^(f) (nm) |
|-------------------|-----------------------|------------------|-------|--|--|--|---|
| | | Initial | Final | | | | |
| T1 ^(a) | 623 | — | — | 109 | 9.6 | — | 4.2 |
| H1 ^(b) | 375 | 1.0 | 0.6 | — | — | — | — |
| H2 ^(b) | 523 | 1.0 | 0.6 | 214.4 | 5.2 | ~1.0 | 3.5, 2.4 |
| H3 ^(b) | 623 | 1.0 | 0.6 | 157.0 | 4.4 | 1.0 | 3.3, 1.6 |
| H4 ^(b) | 773 | 1.0 | 0.6 | — | 10.8 | — | — |
| H5 ^(b) | 623 | 1.5 | 0.8 | 66.1 | 11.3 | 5.7 | 3.8 |
| H6 ^(b) | 623 | 2.0 | 1.3 | 65.0 | 8.7 | — | — |
| I1 ^(c) | 623 | 1.0 | 1.1 | 74.7 | 7.1 | 7.5 | 4.7 |
| I2 ^(c) | 623 | 1.5 | 1.7 | 35.7 | 7.0 | — | 4.5 |
| I3 ^(c) | 623 | 2.0 | 2.1 | 39.4 | 7.0 | 9.0 | 4.5 |

^(a)TiO₂ sample prepared by hydrothermal route.

^(b)Au/TiO₂ with gold incorporated during hydrothermal process.

^(c)Au/TiO₂ with gold dispersed over sample T1 by impregnation.

^(d)From XRD data using Scherrer's equation.

^(e)From TEM results.

^(f)From N₂ adsorption data.

200 scans were coadded at a resolution of 4 cm⁻¹ and the background spectrum of blank TiO₂ was compensated for recording of each plot.

3. RESULTS AND DISCUSSION

3.1. Morphological features

The notations and morphological properties of different samples are listed in Table 1. Figures 1(a)–1(c) provide TEM images of representative mesoporous TiO₂ and Au/TiO₂ samples. Comparative pore-size distribution in some of the samples, as measured by N₂-adsorption, is presented in Figures 2(a)–2(d). As seen in these data, the surface area, crystallite shape and size, and the pore characteristics of different samples depend considerably on the amount of gold present and the mode of its doping. The gold-free TiO₂ sample (T1), prepared by hydrothermal route and calcined at 623 K, is comprised of almost round shape crystallites, size varying from 6 to 12 nm and the majority being around 7.5 nm in cross-sectional diameter (Figure 1(a)). The pore-size distribution in this sample falls in a narrow range (3 to 5 nm), with the average pore-diameter being ~4.2 nm (Figure 2(a), Table 1). The inclusion of a small amount of gold (1 wt%) during hydrothermal synthesis resulted in more uniform and much smaller (1.5 to 3 nm) crystallites, as can be seen in Figure 1(b). The dark spots of high scattering contrast in the middle of these crystallites may be related to the presence of gold particles entrapped in the mesopores, the size of which is estimated at ≤1 nm. In addition to almost spherical-shape TiO₂ crystallites seen in Figure 1(b), the presence of titania nanotubes (cross-sectional diameter of around 6 nm and length varying from 15 to 70 nm) was also noticed in few TEM micrographs. No gold particles were, however, noticeable in the vicinity of these nanotubes.

The size of the gold particles increased considerably with the increase of gold loading and also when the samples were prepared by using method II. For instance, the TEM micrograph of sample H5 showed the presence of gold crystallites of size 3–8 nm, dispersed prominently at the extraneous host surface. The size of the gold crystallites was found to increase further in the samples synthesized by impregnation. Figure 1(c) exhibits the typical TEM micrograph of sample I1, containing 1 wt% of Au. Gold particles, having size in a wide range of 3 to 15 nm, are seen clearly in this picture.

The N₂-adsorption results reveal that the pore characteristics are affected considerably by the amount of gold present in a sample and the method of preparation. Thus, sample T1 consisted of uniform-size pores of average size 4.2 nm (Figure 2(a)), while samples H2 and H3 reveal the presence of a bimodal pore system (Figures 2(b), 2(c)). In the case of H2, the average size of mesopores is found to be ~3.5 nm instead of 4.2 nm and an equal number of pores in size range 1 to 3 nm are formed as a result of gold inclusion (Figure 2(b)). Increase in calcination temperature to 623 K for sample H3 resulted in further decrease in the size and number of larger-size pores whereas those of the smaller-size pores increased considerably (Figure 2(c)). For the samples containing higher loading of Au and also in case of the samples prepared by method II, the number of smaller-size pores is very small while the larger-size pores are affected only marginally. A typical pore-size distribution pattern for sample I3 is shown in Figure 2(d).

The results described above suggest that for the low loadings (≤1% Au), gold crystallites are very small in size (≤1 nm) and are located preferably within the mesopores of titania causing constriction, as is also indicated in the TEM picture of Figure 1(b). For the higher loadings and in the case when samples were synthesized by impregnation, the size of the gold particles increases considerably, and resultantly they

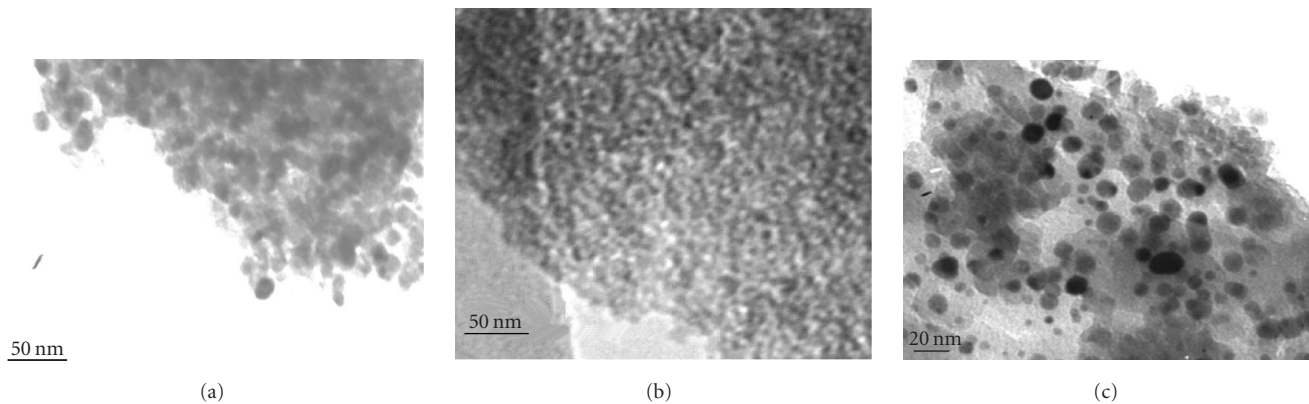


FIGURE 1: TEM micrographs of mesostructured titania and Au/TiO₂ samples: (a) mesoporous TiO₂ (T1), (b) Au/TiO₂ (H3), and (c) sample I1.

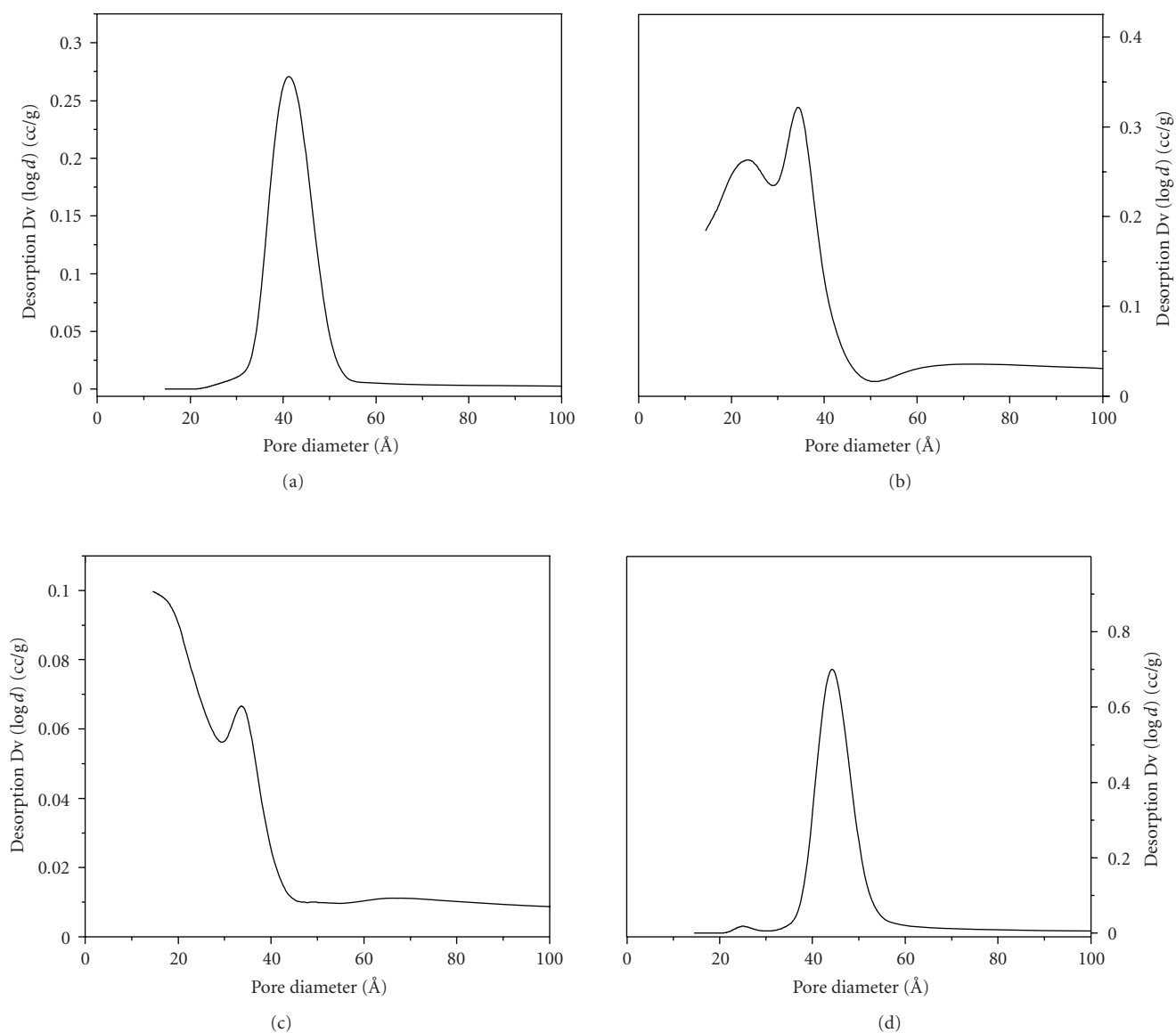


FIGURE 2: Pore-size distribution profiles in mesoporous TiO₂ and Au/TiO₂ samples: (a) T1, (b) H2, (c) H3, and (d) I3.

exist mainly at the extraneous surface of host titania matrix (Figure 1(c)). This may lead to complete or partial blockage of some of the pores while leaving others unaffected, as is indicated in the pore-size distribution data of Figure 2(d).

Our results also show that by adopting a nonsurfactant approach [22], and by using a small molecule such as tartaric acid for template, it is possible to synthesize physically stable, very small and uniform-size (6–12 nm) titania crystallites, as compared to several earlier attempts in this direction that employed large-size templating agents, such as dodecylamin and poly ethylene oxide (PEO) and obtained a material having a low surface area and a larger crystallite size [23–25].

3.2. Powder XRD

Curves (a)–(e) in Figure 3(a) show the wide-angle powder XRD patterns of gold-containing TiO₂ samples prepared by hydrothermal process followed by calcination under different conditions. Curve (f) in this figure is for corresponding gold-free titania sample T1. The prominent XRD lines appearing in curve (f) at 2θ values of 25.2, 36.8, 37.8, 48.1, 54.0, 55.1, and 62.7 degrees are the characteristic reflections of anatase-phase TiO₂ (JCPDS card 21-2172). A considerable increase in the line widths, particularly in curves (a)–(c), is a feature arising due to decrease in particle size. The size of crystallites in different samples, as calculated from the width of I₁₀₀ reflection by using Scherrer's equation, is given in Table 1. The presence of small amount of gold in our samples is indicated by a weak and broad XRD line appearing at 44.5° ($d = 2.04$) in curves (a)–(e), revealing again the small size of Au crystallites. The X-ray diffraction patterns of samples I1–I3 were found to be almost similar to those of sample T1, with no measurable change in 2θ value or in the line width (Figure 3(b)). A marginal change was, however, observed in the relative intensity of two main reflections appearing at 2θ values of 25.2 and 48.2 degrees.

Figure 4 presents the low-angle XRD patterns of some of the hydrothermally synthesized samples. Data in this figure reveal that an appropriate thermal treatment is vital for preparing a suitable mesoporous TiO₂ matrix. Figure 4 shows that no long-range mesoporous structure is formed at the stage of hydrothermal treatment (curve (a)) and also after subsequent calcination at a low temperature (~523 K) (curve (b)). This can be attributed to incomplete removal of condensed moieties from the pores. A well-ordered mesoporous structure is observed only on calcination of the sample at 623 K, as is reflected in the broad peak appearing at ~1.8° in curve (c) of Figure 4. A similar low-angle XRD pattern has been reported earlier for mesoporous titania [1]. At the same time, the break down of this ordered structure is observed for the further increase in calcination temperature, as is evident from the LAXRD pattern of sample H4, shown in curve (d) of Figure 4.

3.3. TG/DTA studies

TG/DTA curves in Figure 5 correspond to as-synthesized Au (1%)/TiO₂ (sample H1), where after hydrothermal treatment the sample was subjected to drying in air at 375 K with-

out further calcination. The differential TG scan (curve (b)) indicates weight loss in two major steps: at 400 K due to release of adsorbed water and at 510 K because of the decomposition of tartaric acid used as a templating agent. These assignments were validated by independently recording the thermal data for pure tartaric acid. Closely spaced dual endotherms appearing at 510 K and 525 K in DTA plot (curve (c)) suggest that the decomposition of tartaric acid and the release of the reaction products may occur in two different steps. A small TG peak appearing at 645 K (curve (b)) and the corresponding endotherms in curve (c) are related to conversion of gold to its metallic state.

The data of thermal analyses presented above in conjunction with low-angle XRD results of Figure 4 help us to demonstrate that the removal of tartaric acid at an appropriate temperature subsequent to hydrothermal treatment and drying of gel is a vital step for preparing mesoporous titania. Thus, no N₂ adsorption or mesoporosity are observed in sample H1, dried at 375 K (Table 1) but subjected to no further calcination. Removal of tartaric acid begins at 470 K but remains incomplete on calcination at 523 K (Figure 5, curve (b)), and the sample H2 therefore exhibits nitrogen adsorption corresponding to mesoporous materials (Figure 2(b)), but no long-range mesoporous network is formed yet (Figure 4, curve (b)). Calcination at 623 K enables complete removal of tartaric acid and thus gives rise to a long-range mesoporous network (Figure 4, curve (c)). Further, calcination at 750 K or above resulted in the collapse of porous titania network, as is revealed in curve (d) of Figure 4, recorded for sample H4.

3.4. DR UV-Vis spectra

The presence of gold was found to have a considerable influence on the DR UV-Vis spectrum of TiO₂, depending upon its amount and the method of sample preparation. Figures 6(a) and 6(b) exhibit these data for Au/TiO₂ samples synthesized by using methods I and II, respectively. Comparative data on sample T1 are given in curve (e) of Figure 6(a). As is noticed in Figure 6(a), absorbance in UV region increases considerably in case of Au/TiO₂ samples synthesized by method I, as compared to sample T1 (curve (e)). The intensity of this absorbance band, however, decreases progressively on calcination at higher temperatures (curve (c)), and also for higher loadings of Au (curve (d)). We also observe a broad absorption band in the entire visible region of spectrum in the case of samples containing gold (cf. Figure 6(a), curve (e)). The intensity of the visible region absorbance (400–800 nm) is also found to decrease marginally with the increasing gold content.

The intensity of UV-region absorbance band for samples I1–I3, synthesized by impregnation, was found to be almost similar to that of T1. However, the visible region absorbance was much higher for these samples, which may be attributed to the absorbance by the gold crystallites existing at the external surface (Figure 6(b)).

The results presented above thus clearly reveal a direct relationship between the intensity of absorbance bands, both

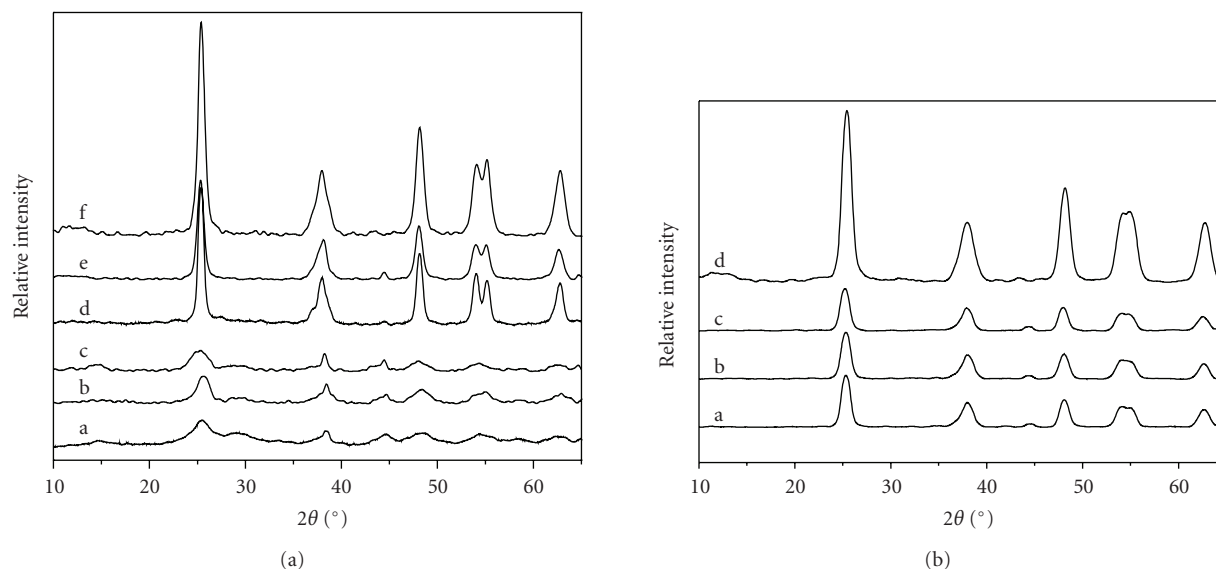


FIGURE 3: (a) Wide-angle powder XRD patterns of mesoporous TiO_2 and hydrothermally synthesized Au/TiO_2 samples: (a) H1, (b) H2, (c) H3, (d) H4, (e) H5, and (f) T1. (b) Comparative wide-angle powder XRD patterns of impregnation-prepared Au/TiO_2 and gold-free TiO_2 samples: (a) I1, (b) I2, (c) I3, and (d) T1.

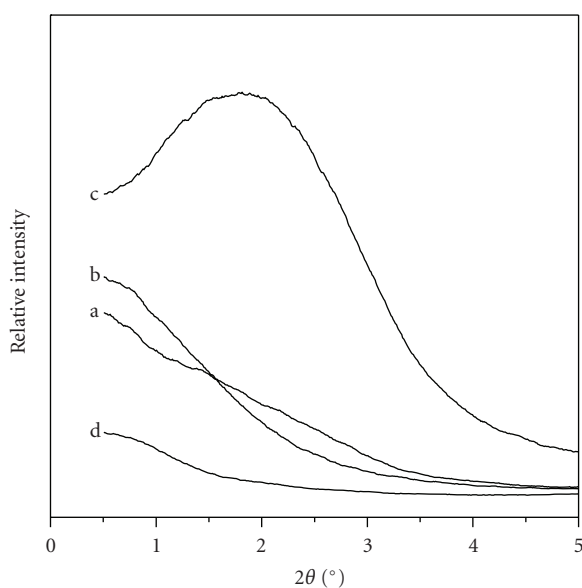


FIGURE 4: Low-angle powder XRD patterns of mesoporous Au/TiO_2 samples synthesized by hydrothermal route and calcined at different temperatures: (a) H1, (b) H2, (c) H3, and (d) H4.

in UV and visible regions, and the crystallite size of titania as well as that of the dispersed gold. In both cases, the higher the crystallite size is, the lower the value of the absorbance will be. The visible region absorbance in Figures 6(a), 6(b) is a characteristic feature associated with the nanostructured gold where the weak and broad band appearing at 550–600 nm is a well-reported phenomenon arising due to plasmon resonance [26].

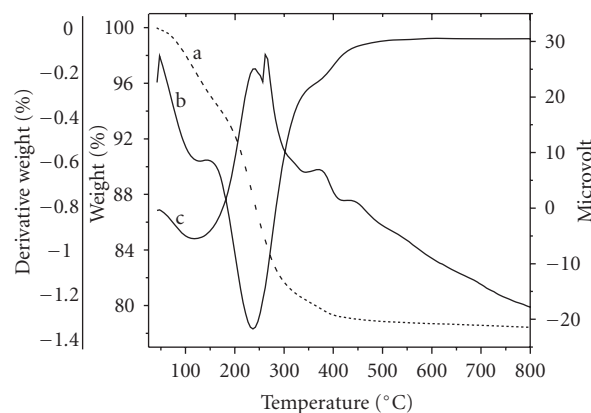


FIGURE 5: Thermal analysis data on hydrothermally prepared uncalcined Au/TiO_2 gel (sample H1): (a) TG, (b) DTG, and (c) DTA.

3.5. Photocatalytic activity

When acetone vapor + air were fed to the reactor at room temperature and in the absence of radiation, no reaction occurred over mesoporous TiO_2 (sample T1) as well as over Au/TiO_2 samples prepared by the two methods described above. Similarly, no products were formed in the presence of visible light.

The reaction products formed during photo-oxidation of acetone under UV irradiation were mainly carbon dioxide and water. Small quantities of ethane and methyl formate ($\text{H}-\text{COO}-\text{CH}_3$, IUPAC name methyl methanoate) were produced only for higher concentrations of acetone in air. The catalytic activity and yield of these products depended on various factors, such as radiation dose, concentration of

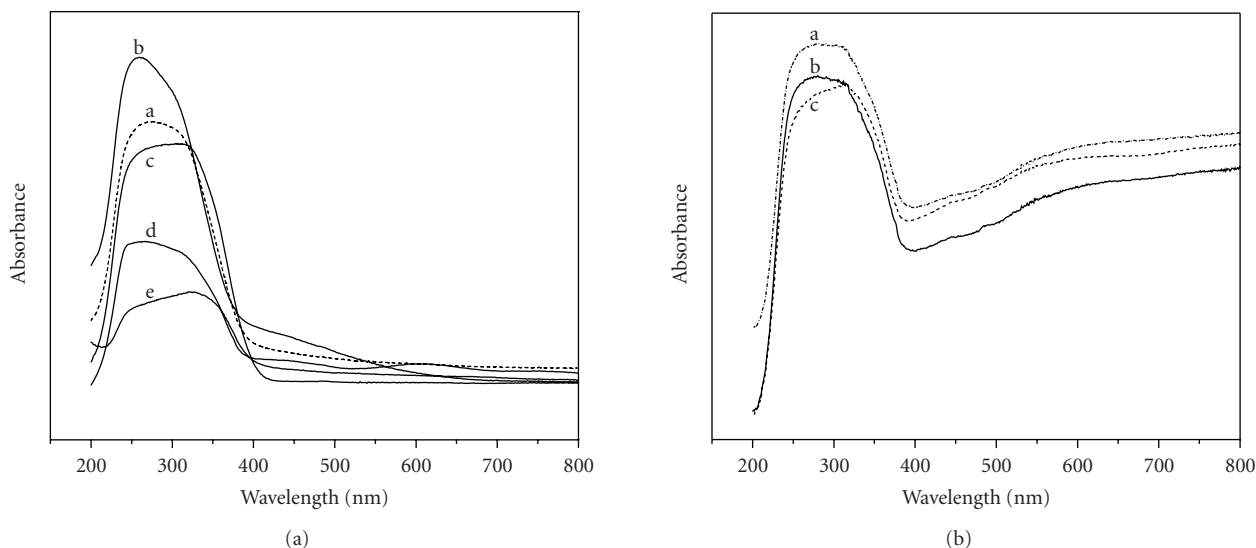


FIGURE 6: Diffuse reflectance UV-Vis spectra of (a) hydrothermally prepared Au/TiO₂ and TiO₂ samples: (a) H2, (b) H3, (c) H4, (d) H6, and (e) T1, and (b) impregnation-prepared Au/TiO₂ samples: (a) I1, (b) I2, and (c) I3.

acetone in reactant mixture, and the pore characteristics of the catalyst samples. The presence of gold also resulted in considerable enhancement of the activity of a catalyst, where both the content and the size of Au particles played an important role. The highlights of these results are presented below.

3.5.1. TiO₂

Curves (a)–(c) in Figure 7 show the yield of CO₂ as a function of UV irradiation, when a mixture of acetone and air, containing varying concentrations of acetone, was reacted over mesoporous TiO₂ (sample T1). As seen in these data, yield of CO₂ corresponds to 100% conversion for acetone concentration of 2.7 mol% or less, the value of $t_{1/2}$ (time taken for 50% conversion of acetone) being around 30 minutes (curve (a)). The yield of CO₂ decreased progressively along with the simultaneous formation of other reaction products for increasing acetone: air mol ratios in the reaction mixture. For instance, in the case of acetone concentration at 10 mol%, conversion to CO₂ was limited to ~25% even after ~2 hours of reaction time (curve (c)). As mentioned above, ethane and methyl formate were the other reaction products formed for higher molar concentrations of acetone in air, as detected in the GC-MS analysis of reaction products. Curve (d) in Figure 7 shows the representative data on ethane yield for the experiment carried out with 13 mol% of acetone in air. The yields of methyl formate and water formed in the reaction were not very reproducible because of their condensing nature, and no attempt is therefore made to compile the quantitative data on these products.

3.5.2. Au/TiO₂

The reaction rate was much higher in the case of gold containing TiO₂ samples, with the activity depending upon the

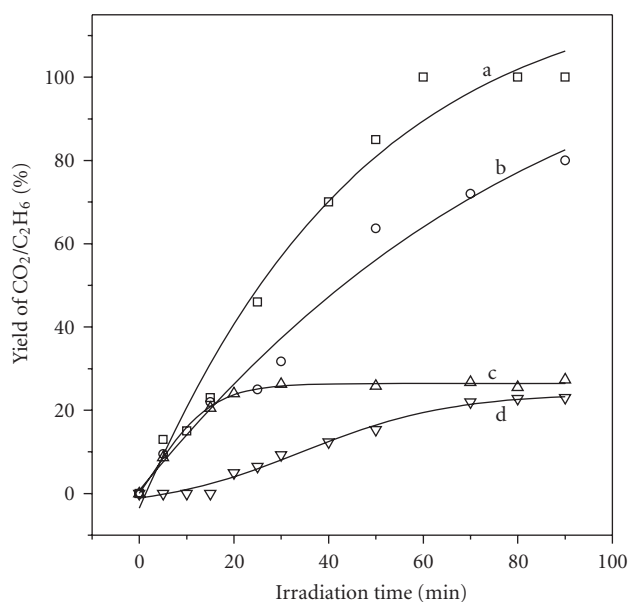


FIGURE 7: Yield of CO₂ (curves (a)–(c)) and C₂H₆ (curve (d)) as a function of time, when mesoporous TiO₂ (sample T1) was used for the UV-induced vapor-phase photocatalytic oxidation of acetone present at varying concentrations in air. (a) 2.7, (b) 5.3, (c) 10, and (d) 13 mol%.

gold content and the morphology of TiO₂. Figure 8 presents the yield of CO₂ during photo-oxidation of acetone as a function of irradiation time for the experiments conducted on hydrothermally prepared sample H3 and for the different compositions of reactant mixture. As seen in the results of curves (a)–(c) in Figure 8, not only the conversion but the rate of the reaction also depended upon acetone concentration, the lower the concentration the faster being the reaction, as expected. Lower conversions were observed for the

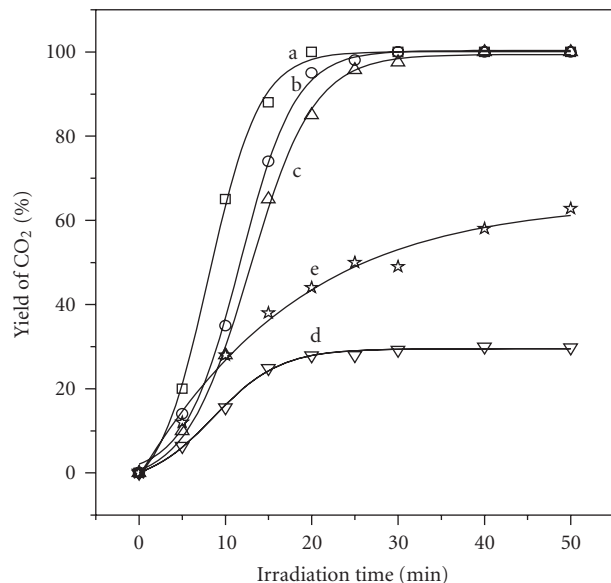


FIGURE 8: Yield of CO₂ as a function of UV-radiation dose when hydrothermally synthesized Au/TiO₂ catalyst H3 (curves (a)–(d)) and H4 (curve (e)) were employed for vapor-phase photo-oxidation of acetone present at different concentrations in air. (a) 1.1, (b) 2.5, (c) 4.8, (d) 13, and (e) 3.9 mol%.

reaction mixture containing a higher concentration of acetone (Figure 8, curve (d)), along with the formation of other reaction products as in the case of TiO₂.

Calcination of a sample at higher temperatures resulted in considerable loss of catalytic activity. Comparative data on reaction of acetone (3.9 mol%) + air over sample H4, that is sample calcined at 773 K instead of 623 K (sample H3), are shown in curve (e) of Figure 8. As seen in Figure 8 curve (e), less than 60% of acetone gets converted to CO₂ in this case, even for a lower concentration of acetone in air. These results show a strong relationship between the catalytic activity, surface area, and the size of gold particles, which are affected considerably on calcination.

Au/TiO₂ samples H5 and H6, with a higher gold content of 0.8 and 1.3 wt%, respectively (see Table 1), showed lower catalytic activity as compared to sample H3 containing ~0.6 wt% Au. For instance, samples H5 and H6 gave rise to a maximum yield of CO₂ at ca. 70% and 80%, respectively, during the reaction of acetone (3.5 mol%) + air for about 80 minutes. Similarly, the samples synthesized by impregnation (I1–I3) showed lower catalytic activity in terms of reaction rate as compared to the corresponding hydrothermally synthesized samples. Figure 9 presents typical results on dose-dependent CO₂ yields for reaction of acetone (~3.4 mol%) + air over samples I1–I3. A progressive increase in activity is observed as a function of gold content in these data. Thus, while almost 100% conversion of acetone was observed in case of samples containing 1.5 or 2 wt% of Au (curves (b) and (c)), sample I1 gave only ca. 60% conversion even after two hours of reaction time. At the same time, the value of $t_{1/2}$ is about 20 to 30 minutes in case of data in Figure 9 curves

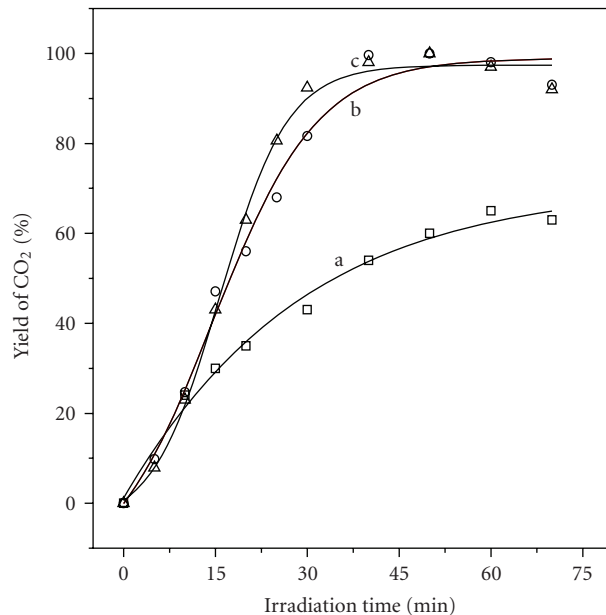


FIGURE 9: Yield of CO₂ as a function of UV-radiation dose during the vapor-phase photo-oxidation of acetone, (3.2–3.5 mol% in air) at room temperature over impregnation-prepared Au/TiO₂ samples I1 (curve (a)), I2 (curve (b)), and I3 (curve (c)).

(b) and (c), as compared to 8 to 13 minutes in case of sample H3 having lower gold content (Figure 8).

These results thus provide evidence that the activity of a catalyst is governed by multiple factors. In addition to surface area and gold content, morphology of TiO₂ and the size of the gold particles also contribute significantly to the overall catalytic activity. The poorer activity of samples H5 and H6 as compared to H3 may be attributed to the increase in gold crystallite size with increasing gold content (TEM evidence). The extraordinary catalytic and optical properties of smaller-size (<2 nm) gold particles are now a well-reported phenomenon [27, 28]. It is known that the gold catalysts are structure sensitive and the binding states of reactant molecules over Au nanoparticles dispersed over metal oxide supports are found to be different than those over bulk gold or gold films. It is suggested that the gold-metal oxide interfaces act as sites for the activation of molecules such as O₂, CO, hydrocarbons, and so forth [27]. In some of the studies, these unique properties of gold nanoparticles are attributed to their electronic structure [29]. We have demonstrated earlier that even a marginal increase in gold particle size as a result of high-temperature calcination may lead to a considerable decrease in the adsorption and catalytic activity of Au/Fe₂O₃ catalysts [30].

3.6. Infrared spectroscopy

The results of our in situ DRIFT spectroscopy studies, where pure acetone vapor or acetone + air was dosed over representative catalyst samples after appropriate pretreatment, are presented in the following subsections.

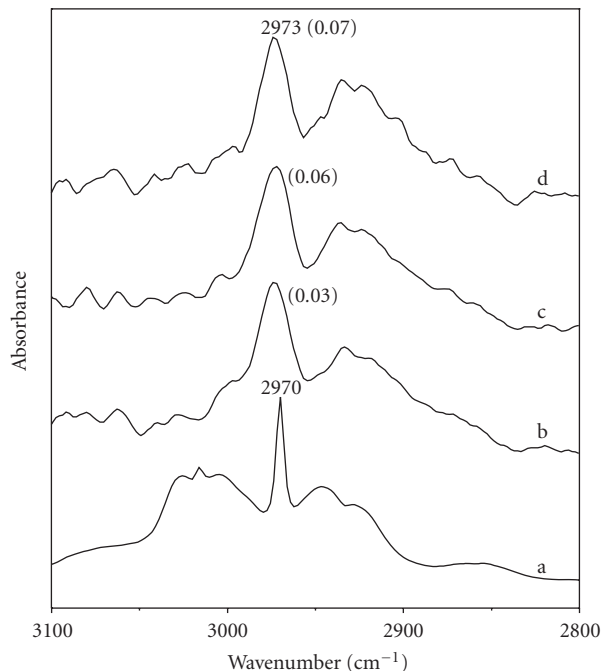


FIGURE 10: C–H stretching region infrared spectra of sample H3 (hydrothermally synthesized Au/TiO₂), exposed to 0.2 μmol of acetone vapor and recorded after the lapse of 10 minutes (curve (b)) and subsequent heating at 320 K (curve (c)) and 360 K (curve (d)). Curve (a) shows corresponding vibrational bands of acetone vapor. The numbers given in the parentheses indicate the absorbance value of the particular IR band.

3.6.1. Adsorption of acetone

Curve (b) in Figure 10 exhibits the C–H stretching (3100–2800 cm^{-1}) vibrational bands formed over hydrothermally prepared Au/TiO₂ sample H3 on exposure to 0.2 $\mu\text{mol g}^{-1}$ of acetone at room temperature and recorded after the lapse of ~ 10 minutes. The intensity of this band remained unchanged when more amount of acetone (up to $\sim 1 \mu\text{mol g}^{-1}$) was dosed over the sample in form of successive pulses. Comparative IR spectrum recorded for acetone vapor in this region is shown in curve (a) of this figure. The $\nu(\text{C–H})$ bands of Figure 10(b) show the absence of Q-branch splitting of vibrational-rotational bands associated with acetone vapor (curve (a)). Also, instead of a sharp band at 2970 cm^{-1} (band width $\sim 5 \text{ cm}^{-1}$) in case of acetone vapor (curve (a)), we observe a considerably broadened band at 2973 cm^{-1} , the corresponding value of band width (full width at half maximum, FWHM) being $\sim 18 \text{ cm}^{-1}$ for acetone in its adsorbed state (curve (b)). This band was found to be quite stable on thermal activation, as seen from the relative absorbance values in spectra (c) and (d) of Figure 10, recorded on rise in sample temperature to 320 K and 360 K subsequent to saturation coverage. The intensity of this band decreased only marginally even after raising the sample temperature to 470 K.

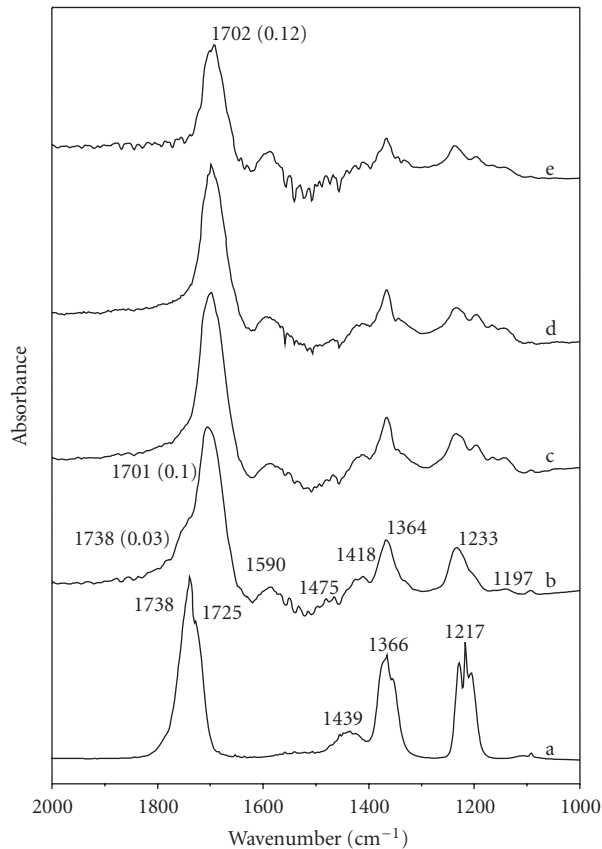


FIGURE 11: Stretching C=O, C=C, C–C, and deformation CH region vibrational bands developed on sample H3 after exposure to 0.2 μmol ($14 \mu\text{mol g}^{-1}$) of acetone vapor and recorded after a delay time of 2 minutes (curve (b)) and 15 minutes (curve (c)) and subsequent raising of sample temperature to 320 K (curve (d)) and 360 K (curve (d)). Curve (a) shows corresponding vibrational bands of acetone vapor. The numbers given in the parentheses indicate the absorbance value of the particular IR band.

Figure 11 presents corresponding plots in 2000–1000 cm^{-1} region ($\nu\text{C=O}$, $\nu\text{C=C}$, $\nu\text{C–C}$, and δCH regions). Curve (a) shows again a comparative spectrum of acetone vapor. In the CO stretching region, we observe a broad band centered at $\sim 1701 \text{ cm}^{-1}$ and a shoulder band at $\sim 1738 \text{ cm}^{-1}$ in curve (b) of Figure 11, recorded soon after adsorption of acetone over sample H3. Instead, a doublet at 1738 and 1725 cm^{-1} is observed in case of acetone vapor (curve (a)), arising due to the Fermi resonance between the fundamental CO vibration and an overtone. With an increase in contact time, the intensity of 1738 cm^{-1} band decreases further while the frequency of the new band formed at 1701 cm^{-1} shifts to a lower value of 1695 cm^{-1} (Figure 11, curve (c)). As in the case of C–H stretching bands, the $\nu(\text{CO})$ vibrational bands were found to be fairly stable on raising the sample temperature up to 470 K after acetone adsorption. Spectra (d) and (e) in Figure 11 show the representative plots obtained at sample temperatures of 320 K and 350 K, respectively.

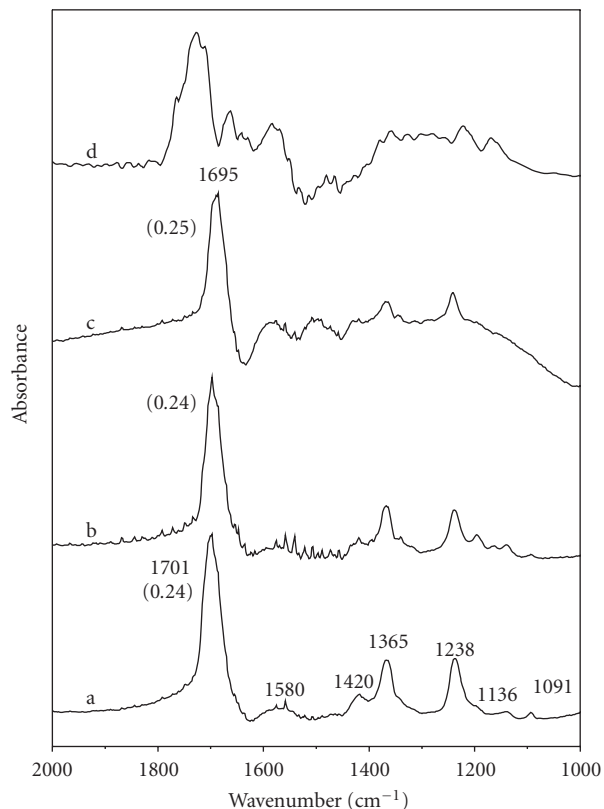


FIGURE 12: Stretching C=O, C=C, C-C, and deformation CH region vibrational bands developed on sample H3 after exposure to acetone vapor + air and recorded after a delay time of 10 minutes (curve (a)) and on subsequent raising of sample temperature to 320 K (curve (b)) and 370 K (curve (c)). Curve (d) shows comparative vibrational bands of methyl formate vapor adsorbed over H3 under nitrogen flow at room temperature. The numbers given in the parentheses indicate the absorbance value of the particular IR band.

3.6.2. Adsorption of acetone + air

The vibrational bands similar to those in Figures 10 and 11 were observed on interaction of acetone (10 mol%) + air at room temperature, the only difference being a considerable increase in the intensity of the bands. Figure 12 exhibits IR spectra of H3 sample at saturation coverage, recorded 10 minutes after exposure (curve (a)) and after subsequent rise in sample temperature to 320 (curve (b)) and 350 K (curve (c)). As seen from the absorbance values given in Figure 12, the intensity of the vibrational bands in these spectra is greater by a factor of almost 2, compared to the corresponding experiments performed using acetone alone (Figure 11). These results indicate that the presence of oxygen facilitated the reaction of acetone over catalyst surface to form certain strongly adsorbed and thermally stable species (Figures 12(curve (b)), 12(curve (C))). We may also mention that the spectral features similar to those in Figures 10, 11, and 12 were observed in the case of impregnation-prepared Au/TiO₂ samples having a different gold content.

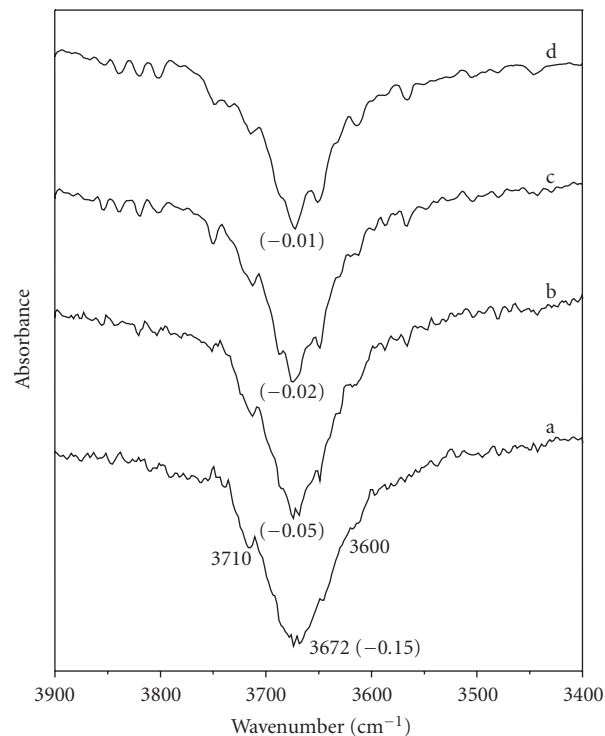


FIGURE 13: Hydroxyl region IR spectra of sample H3 after room temperature adsorption of $14 \mu\text{mol g}^{-1}$ of acetone vapor and recorded after the lapse of 15 minutes (curve (a)) and subsequent heating at 320 K (curve (b)), 350 K (curve (c)), and 380 K (curve (d)). The numbers given in the parentheses indicate the absorbance value of the particular IR band.

Adsorption of acetone over TiO₂ gave rise to the vibrational bands similar again to those shown in Figures 10 and 11, described above. The IR bands were found to be quite stable on heating of the sample up to 470 K under nitrogen flow, as in the case of results obtained using Au/TiO₂.

3.6.3. Hydroxyl region bands

Curve (a) in Figure 13 presents the hydroxyl region bands of Au/TiO₂ (sample H3), exposed to $0.2 \mu\text{mol g}^{-1}$ of acetone and recorded soon after. As seen in this figure, the spectral developments in $\nu(\text{CH})$ or $\nu(\text{CO})$ regions are accompanied with simultaneous removal of IR bands of different hydroxyl groups at titania surface, as indicated by the negative absorbance values (peaks pointing downwards) of $\nu(\text{OH})$ bands at 3710, 3672, and 3600 cm⁻¹ in Figure 13. The presence of overlapping multiple vibrational bands in 3900–3400 cm⁻¹ region, representing differently coordinated hydroxyl groups over the titania surface, has been reported earlier [31]. These results reveal a strong adsorbent-adsorbate interaction involving the hydroxyl groups, irrespective of their coordinative environment.

Based upon the above-mentioned information about the shape, width, and intensity, the IR absorption bands in Figures 10 and 11 may be attributed to an overlap of closely spaced vibrational bands, arising due to multiple adsorbed

species. In some of the previously reported studies [32, 33], acetone is found to adsorb in molecular state over TiO_2 at a lower coverage while at a higher coverage it undergoes an Aldol condensation reaction followed by dehydration to yield 4-methyl-3-penten-2-one ($(\text{CH}_3)_2\text{C}=\text{CHCOCH}_3$), commonly known as mesityl oxide (MSO). The absence of Q-branch splitting and broadening of the $\nu(\text{C}-\text{H})$ band shown in Figure 10 is in conformity with the presence of a condensed state of acetone. The IR absorption bands appearing at 2973 and 2931 cm^{-1} in Figure 10 and at 1702, 1475, and 1364 cm^{-1} in Figure 11 may be assigned to this strongly adsorbed state of acetone molecules (cf. Figures 10 and 11, curve (a)). The presence of a weak shoulder at 1738 cm^{-1} in Figure 11 (curve b) and its removal with increase in contact time (curve c) indicate that the transformation of acetone vapor to its condensed state is a slow and activated process. We, however, observe no formation of MSO, both for adsorption of acetone alone or acetone + air. As mentioned by Zaki et al. [33], the mesityl oxide is distinguishable from acetone by a $\nu\text{C}=\text{C}$ band at 1634 cm^{-1} and $\nu\text{C}-\text{C}$ band at 1294 cm^{-1} . No such bands are, however, observed in Figures 11 and 12, thus ruling out the formation of MSO under experimental conditions of this study.

The $\nu(\text{CH}_3)$ vibration at 2973 cm^{-1} (Figure 10), $\nu\text{C}=\text{O}$ vibration at 1695 cm^{-1} , and several weak absorption bands in 1900–1100 cm^{-1} region (Figure 12) may be assigned to methyl formate (methyl methanoate) in its adsorbed state, as reported in one of our earlier studies [15]. This identification is validated by a study of Ločař et al. [34] where similar bands were observed for adsorption of methyl formate over metal oxide surfaces. To further confirm the assignment of absorption bands in Figures 11 and 12, methyl formate vapor was dosed over sample H3 at room temperature and the representative spectrum thus obtained is shown in curve (d) of Figure 12, which matches well with the IR bands shown in Figures 11 and 12 (curves (a)–(c)). We may also mention that the formation of methyl formate was detected clearly in our GC-MS analysis of reaction products formed in photo-oxidation of acetone over TiO_2 . A difference in the relative intensity and the shift in frequency of some of the bands in curves (c) and (d) of Figure 12 may be attributed to the difference in the binding of methyl formate groups, formed in situ and that adsorbed in a molecular form. We may also mention that the $\nu_{\text{as}}(\text{COO}) + \delta(\text{CH})$ combination bands of adsorbed mono- and bidentate formate (HCOO^-) species give rise to absorption bands at 2970 cm^{-1} and 2936 cm^{-1} whereas corresponding $\nu(\text{CH})$ vibrations appear at 2896 cm^{-1} and 2856 cm^{-1} . Similarly, in the lower IR region, the bands at 1575 cm^{-1} and 1376 cm^{-1} are assigned to $\nu_{\text{as}}(\text{COO})$ and $\nu_{\text{s}}(\text{COO})$ vibrations of the bidentate formate species while the bands at 1542 cm^{-1} and 1363 cm^{-1} arise due to such vibrations of monodentate formate species [15, 35–38]. A considerable increase of absorbance in 2950–2850 cm^{-1} region and a large width of 2973 cm^{-1} band in Figure 10, and similarly the presence of various unresolved overlapping bands in 1800–1000 cm^{-1} region (Figures 11 and 12), help us to conclude that in addition to methyl formate, HCOO^- species may also form on interaction of acetone and subsequent thermal activation.

The active role of formate and methyl formate groups in photocatalytic reactions over titania and other oxide surfaces has been amply demonstrated by several research groups [15, 32, 33, 38, 39]. For instance, Wu et al. [39] demonstrated that the methoxy-, ethoxy-, and formate-type surface groups are photo-oxidized on TiO_2 under UV-illumination, and the rate of photo-oxidation depends on the binding mode of these species at catalyst surface, the monodentate species being more reactive as compared to their bidentate counterparts. Simultaneous FTIR and photocatalysis studies conducted in our laboratory have also exhibited the involvement of such adsorbed species in the photo-oxidation of methanol over TiO_2/MCM and UO_x/MCM catalyst surfaces [15, 38]. El-Maazawi et al. [32] proposed a reaction mechanism, where formation of O^- (ads) species from gas-phase O_2 and its reaction with adsorbed acetone are shown to play an important role.

To summarize, the results of our study reveal that the adsorption of acetone over nanostructured TiO_2 or Au/TiO_2 may occur in several modes, giving rise to a condensed and strongly adsorbed state of molecular acetone and methyl formate and formate types of surface adsorbed species. The IR results show that the host matrix and the gold particles may serve as independent adsorption and reaction sites for acetone and oxygen molecules. Since similar IR absorbance bands are observed on adsorption over TiO_2 and Au/TiO_2 and also with or without the presence of air in reaction mixture, it is apparent that the adsorption of acetone occurs primarily at titania surface. The spectral features in $\nu(\text{OH})$ region (Figure 13) reveal that the $\text{Ti}-\text{OH}$ groups may directly interact with acetone molecules. This process is reversed on thermal activation, as is apparent from the absorbance values shown in Figure 13 (curves (b)–(d)). Since acetone + air adsorption over Au/TiO_2 gave rise to higher intensity of the IR absorption bands, as described above, we may conclude that the adsorption and activation of O_2 molecules at Au sites plays an important role. This phenomenon, promoted only by nanosize Au particles, explains the high catalytic activity of sample H3 as compared to other samples having higher gold content but larger-size crystallites.

The overall photocatalytic process would therefore involve the interaction of these primary adsorbed species with the electron-hole pair generated on band gap excitation of TiO_2 , giving rise to formation of various ion-radicals, free radicals, and surface bonded transient species. Various possible photochemical steps may subsequently prevail, leading thereby to the formation of different reaction products, as has been reported widely (see, e.g., [40]).

4. CONCLUSIONS

The results of the present study demonstrate that the structural and morphological properties of Au/TiO_2 have a direct relationship with the activity of these photocatalysts. The role of a noble metal cocatalyst in semiconductor mediated photo-oxidation of organic compounds has been debated widely, and, in general, two different concepts have been accepted. According to the one theory, the enhancement of

photocatalytic activity is attributable to an increase in charge separation efficiency, and the other is that the metal particles lead to the shift in quasi-Fermi level of the semiconductor-metal composite to more negative potentials [41]. We observe no considerable shift in the UV-region absorbance band of Au/TiO₂ samples. Our IR spectroscopy results, on the other hand, suggest that the titania and gold particles serve as independent adsorption and reaction sites for acetone and oxygen molecules. Acetone molecules adsorb exclusively at TiO₂ surface, giving rise to a condensed state as well as to the formation of formate- and methyl formate-type surface species. Based on the dependence of catalytic activity on gold particle size, we may infer that the Au sites are primarily responsible for the adsorption and activation of oxygen molecules. This is in agreement with the well-reported adsorption properties of small-size (<2 nm) gold particles at Au/support interfaces, as discussed above. Since our Au/TiO₂ samples showed no activity under visible light irradiation, it is evident that the direct absorption of radiation by gold particles as seen in Figure 6 may play an insignificant role. The band gap absorbance in TiO₂ resulting in the generation of e⁻/h⁺ pair may therefore solely govern the photochemical steps. Overall, the increase in the exposed active surface sites (TiO₂ and Au) may influence both the chemisorption of the reactant molecules and the utilization efficiency of the photoinduced electron-hole pair.

ACKNOWLEDGMENTS

N. M. Gupta thanks the Council of Scientific and Industrial Research (CSIR), New Delhi, for a research grant under the Emeritus Scientist scheme. Authors thank Mr. Mahesh Kadgaonkar for help in the manuscript preparation. The help of Dr. Renu Pasricha and Dr. K. R. Patil in TEM and XPS studies is also acknowledged.

REFERENCES

- [1] Q. Sheng, S. Yuan, J. Zhang, and F. Chen, "Synthesis of mesoporous titania with high photocatalytic activity by nanocrystalline particle assembly," *Microporous and Mesoporous Materials*, vol. 87, no. 3, pp. 177–184, 2006.
- [2] J. Yu, Y. Su, B. Cheng, and M. Zhou, "Effects of p^H on the microstructures and photocatalytic activity of mesoporous nanocrystalline titania powders prepared via hydrothermal method," *Journal of Molecular Catalysis A*, vol. 258, no. 1-2, pp. 104–112, 2006.
- [3] A. J. Maira, K. L. Yeung, C. Y. Lee, P. L. Yue, and C. K. Chan, "Size effects in gas-phase photo-oxidation of trichloroethylene using nanometer-sized TiO₂ catalysts," *Journal of Catalysis*, vol. 192, no. 1, pp. 185–196, 2000.
- [4] K. L. Yeung, S. T. Yau, A. J. Maira, J. M. Coronado, J. Soria, and P. L. Yue, "The influence of surface properties on the photocatalytic activity of nanostructured TiO₂," *Journal of Catalysis*, vol. 219, no. 1, pp. 107–116, 2003.
- [5] H. Hayashi and K. Torii, "Hydrothermal synthesis of titania photocatalyst under subcritical and supercritical water conditions," *Journal of Materials Chemistry*, vol. 12, no. 12, pp. 3671–3676, 2002.
- [6] Y.-F. Chen, C.-Y. Lee, M.-Y. Yeng, and H.-T. Chiu, "Preparing titanium oxide with various morphologies," *Materials Chemistry and Physics*, vol. 81, no. 1, pp. 39–44, 2003.
- [7] J.-Y. Zheng, J.-B. Pang, K.-Y. Qiu, and Y. Wei, "Synthesis and characterization of mesoporous titania and silica-titania materials by urea templated sol-gel reactions," *Microporous and Mesoporous Materials*, vol. 49, no. 1–3, pp. 189–195, 2001.
- [8] J.-H. Lee, I.-C. Leu, M.-C. Hsu, Y.-W. Chung, and M.-H. Hon, "Fabrication of aligned TiO₂ one-dimensional nanostructured arrays using a one-step templating solution approach," *Journal of Physical Chemistry B*, vol. 109, no. 27, pp. 13056–13059, 2005.
- [9] M. Anpo, S. Dohshi, M. Kitano, Y. Hu, M. Takeuchi, and M. Matsuoka, "The preparation and characterization of highly efficient titanium oxide-based photofunctional materials," *Annual Review of Materials Research*, vol. 35, pp. 1–27, 2005.
- [10] J.-C. Xu, Y.-L. Shi, J.-E. Huang, B. Wang, and H.-L. Li, "Doping metal ions only onto the catalyst surface," *Journal of Molecular Catalysis A*, vol. 219, no. 2, pp. 351–355, 2004.
- [11] S. Karvinen, "The effects of trace elements on the crystal properties of TiO₂," *Solid State Sciences*, vol. 5, no. 5, pp. 811–819, 2003.
- [12] C.-G. Wu, C.-C. Chao, and F.-T. Kuo, "Enhancement of the photo catalytic performance of TiO₂ catalysts via transition metal modification," *Catalysis Today*, vol. 97, no. 2-3, pp. 103–112, 2004.
- [13] F. B. Li and X. Z. Li, "Photocatalytic properties of gold/gold ion-modified titanium dioxide for wastewater treatment," *Applied Catalysis A*, vol. 228, no. 1-2, pp. 15–27, 2002.
- [14] K. Bhattacharya, A. K. Tripathi, G. K. Dey, and N. M. Gupta, "Vapor-phase photo-oxidation of methanol over nanosize titanium dioxide clusters dispersed in MCM-41 host material part 1: synthesis and characterization," *Journal of Nanoscience and Nanotechnology*, vol. 5, no. 5, pp. 790–796, 2005.
- [15] K. Bhattacharyya, S. Varma, D. Kumar, A. K. Tripathi, and N. M. Gupta, "Vapor-phase photo-oxidation of methanol over nanosize titanium dioxide clusters dispersed in MCM-41 host material part 2: catalytic properties and surface transient species," *Journal of Nanoscience and Nanotechnology*, vol. 5, no. 5, pp. 797–805, 2005.
- [16] L. Davydov, E. P. Reddy, P. France, and P. G. Smirniotis, "Transition-metal-substituted titania-loaded MCM-41 as photocatalysts for the degradation of aqueous organics in visible light," *Journal of Catalysis*, vol. 203, no. 1, pp. 157–167, 2001.
- [17] Y. Xu and C. H. Langford, "Photoactivity of titanium dioxide supported on MCM41, zeolite X, and zeolite Y," *Journal of Physical Chemistry B*, vol. 101, no. 16, pp. 3115–3121, 1997.
- [18] R. Asahi, T. Morikawa, T. Ohwaki, K. Aoki, and Y. Taga, "Visible-light photocatalysis in nitrogen-doped titanium oxides," *Science*, vol. 293, no. 5528, pp. 269–271, 2001.
- [19] G. Hitoki, T. Takata, J. N. Kondo, M. Hara, H. Kobayashi, and K. Domen, "An oxynitride, TaON, as an efficient water oxidation photocatalyst under visible light irradiation ($\lambda \leq 500$ nm)," *Chemical Communications*, vol. 16, pp. 1698–1699, 2002.
- [20] C. H. Rhee, S. W. Bae, and J. S. Lee, "Template-free hydrothermal synthesis of high surface area nitrogen-doped titania photocatalyst active under visible light," *Chemistry Letters*, vol. 34, no. 5, pp. 660–661, 2005.
- [21] A. R. Gandhe, S. P. Naik, and J. B. Fernandes, "Selective synthesis of N-doped mesoporous TiO₂ phases having enhanced

- photocatalytic activity," *Microporous and Mesoporous Materials*, vol. 87, no. 2, pp. 103–109, 2005.
- [22] W. Yen and Q. Kun-Yuan, "Nonsurfactant route to nanoporous phenyl-modified hybrid silica materials," in *Nanoporous Materials: Science and Engineering*, G. Q. Lu and X. S. Zhao, Eds., vol. 4 of *Series on Chemical Engineering*, p. 873, World Scientific, Singapore, 2004.
- [23] E. L. Crepaldi, G. J. D. A. A. Soler-Illia, D. Grosso, F. Cagnol, F. Ribot, and C. Sanchez, "Controlled formation of highly organized mesoporous titania thin films: from mesostructured hybrids to mesoporous nanoanatase TiO₂," *Journal of the American Chemical Society*, vol. 125, no. 32, pp. 9770–9786, 2003.
- [24] Y. V. Kolen'ko, B. R. Churagulov, M. Kunst, L. Mazerolles, and C. Colbeau-Justin, "Photocatalytic properties of titania powders prepared by hydrothermal method," *Applied Catalysis B*, vol. 54, no. 1, pp. 51–58, 2004.
- [25] X. Z. Li and F. B. Li, "Study of Au/Au³⁺-TiO₂ photocatalysts toward visible photooxidation for water and wastewater treatment," *Environmental Science and Technology*, vol. 35, no. 11, pp. 2381–2387, 2001.
- [26] C.-M. Yang, M. Kalwei, F. Schüth, and K.-J. Chao, "Gold nanoparticles in SBA-15 showing catalytic activity in CO oxidation," *Applied Catalysis A*, vol. 254, no. 2, pp. 289–296, 2003.
- [27] M. Haruta, "Size- and support-dependency in the catalysis of gold," *Catalysis Today*, vol. 36, no. 1, pp. 153–166, 1997.
- [28] M. Valden, X. Lai, and D. W. Goodman, "Onset of catalytic activity of gold clusters on titania with the appearance of non-metallic properties," *Science*, vol. 281, no. 5383, pp. 1647–1650, 1998.
- [29] C. N. R. Rao, G. U. Kulkarni, P. John Thomas, and P. P. Edwards, "Size-dependent chemistry: properties of nanocrystals," *Chemistry: A European Journal*, vol. 8, no. 1, pp. 28–35, 2002.
- [30] N. M. Gupta and A. K. Tripathi, "The role of nanosize gold particles in adsorption and oxidation of CO over Au/Fe₂O₃ catalyst," *Gold Bulletin*, vol. 34, pp. 120–128, 2001.
- [31] G. Busca, H. Saussey, O. Saur, J. C. Lavalley, and V. Lorenzelli, "FT-IR characterization of the surface acidity of different titanium dioxide anatase preparations," *Applied Catalysis*, vol. 14, pp. 245–260, 1985.
- [32] M. El-Maazawi, A. N. Finken, A. B. Nair, and V. H. Grassian, "Adsorption and photocatalytic oxidation of acetone on TiO₂: an *in situ* transmission FT-IR study," *Journal of Catalysis*, vol. 191, no. 1, pp. 138–146, 2000.
- [33] M. I. Zaki, M. A. Hasan, and L. Pasupulety, "Surface reactions of acetone on Al₂O₃, TiO₂, ZrO₂, and CeO₂: IR spectroscopic assessment of impacts of the surface acid-base properties," *Langmuir*, vol. 17, no. 3, pp. 768–774, 2001.
- [34] V. Lochar, J. Machek, and J. Tichý, "Mechanism of selective oxidation of methanol over stannic oxide-molybdenum oxide catalyst," *Applied Catalysis A*, vol. 228, no. 1-2, pp. 95–101, 2002.
- [35] G. Busca, A. S. Elmi, and P. Forzatti, "Mechanism of selective methanol oxidation over vanadium oxide-titanium oxide catalysts: a FT-IR and flow reactor study," *Journal of Physical Chemistry*, vol. 91, no. 20, pp. 5263–5269, 1987.
- [36] I. A. Fisher and A. T. Bell, "A mechanistic study of methanol decomposition over Cu/SiO₂, ZrO₂/SiO₂, and Cu/ZrO₂/SiO₂," *Journal of Catalysis*, vol. 184, no. 2, pp. 357–376, 1999.
- [37] G. J. Millar, C. H. Rochester, and K. C. Waugh, "Infrared study of methyl formate and formaldehyde adsorption on reduced and oxidised silica-supported copper catalysts," *Journal of Chemical Society Faraday Transactions*, vol. 87, pp. 2785–2793, 1991.
- [38] D. Kumar, V. S. Kamble, and N. M. Gupta, "The role of nanosize particles of uranium oxide in the adsorption/reaction of methanol over U₃O₈/MCM-48: FTIR study," *Catalysis Letters*, vol. 88, no. 3-4, pp. 175–181, 2003.
- [39] W.-C. Wu, C.-C. Chuang, and J.-L. Lin, "Bonding geometry and reactivity of methoxy and ethoxy groups adsorbed on powdered TiO₂," *Journal of Physical Chemistry B*, vol. 104, no. 36, pp. 8719–8724, 2000.
- [40] Z. Yu and S. S. C. Chuang, "In situ IR study of adsorbed species and photogenerated electrons during photocatalytic oxidation of ethanol on TiO₂," *Journal of Catalysis*, vol. 246, no. 1, pp. 118–126, 2007.
- [41] V. Subramanian, E. Wolf, and P. V. Kamat, "Semiconductor-metal composite nanostructures. To what extent do metal nanoparticles improve the photocatalytic activity of TiO₂ films?" *Journal of Physical Chemistry B*, vol. 105, no. 46, pp. 11439–11446, 2001.

Research Article

The Effect of Transition Metal Doping on the Photooxidation Process of Titania-Clay Composites

Judit Ménesi,¹ Renáta Kékesi,¹ László Kőrösi,¹ Volker Zöllmer,² André Richardt,³ and Imre Dékány¹

¹ Department of Colloid Chemistry, Supramolecular and Nanostructured Materials Research Group of Hungarian Academy of Sciences, University of Szeged, H-6720 Szeged, Aradi Vertanuk tere 1, Hungary

² Fraunhofer Institute for Manufacturing and Advanced Materials (IFAM), Functional Structures, Wiener Strasse 12, 28359 Bremen, Germany

³ German Armed Forces Scientific Institute for Protection Technologies, NBC-Protection, 29623 Munster, Germany

Correspondence should be addressed to Imre Dékány, i.dekany@chem.u-szeged.hu

Received 8 September 2007; Accepted 23 November 2007

Recommended by M. Sabry A. Abdel-Mottaleb

Montmorillonite-TiO₂ composites containing various transition metal ions (silver, copper, or nickel) were prepared, and their photocatalytic efficiencies were tested in the degradation of ethanol vapor at 70% relative humidity. Two light sources, UV-rich ($\lambda = 254$ nm) and visible ($\lambda = 435$ nm), were used. The kinetics of degradation was monitored by gas chromatography. It was established that, in the case of each catalyst, ethanol degradation was more efficient in UV-C ($\lambda = 254$ nm) than in visible light, furthermore, these samples containing silver or copper ions were in each case about twice more efficient than P25 TiO₂ (Degussa AG.) used as a reference. In photooxidation by visible light, TiO₂/clay samples doped with silver or copper were also more efficient than the reference sample, P25 TiO₂. We show that doping metal ions can also be delivered to the surface of the support by ion exchange and significantly alters the optical characteristics of the TiO₂/clay composite.

Copyright © 2008 Judit Ménesi et al. This is an open access article distributed under the Creative Commons Attribution License, which permits unrestricted use, distribution, and reproduction in any medium, provided the original work is properly cited.

1. INTRODUCTION

The photocatalytic degradation of volatile organic compounds (VOCs) by UV light in the presence of TiO₂ catalysts has been the subject of numerous publications [1–10]. TiO₂ is one of the most efficient photocatalysts; however, since semiconductor particles are in need of the higher energy content of UV light, a mere 5% of sunlight is utilized in the course of irradiation for excitation of the catalyst. Absorption by photocatalysts in the visible range can be significantly improved by incorporation of metal ions; however, photoactivity is highly dependent on the chemical nature and the concentration of the doping ion and on the method of preparation. Dvoranová et al. [11] incorporated cobalt, chrome, and manganese ions into the crystalline structure of TiO₂ using the sol-gel method. Although the presence of the doping ions caused a significant absorption shift in the visible range relative to pure P25 titanium dioxide, the photocatalytic activity of the catalysts decreased considerably. Chiang et al. [12] prepared Degussa P25 TiO₂ doped with CuO by photodeposition for the purpose of liquid-phase degradations;

the presence of Cu²⁺ ions, however, again decreased photocatalytic efficiency. TiO₂ doped with CuO was also prepared by Slamet et al. [13], and enhanced photocatalytic effect was observed only at a single optimal Cu(II) ion content. Copper is an efficient electron trap and is therefore capable of inhibiting recombination of electron-hole pairs, thereby significantly increasing efficiency.

It has been proven by many reports that the reaction rate is dependent on how the component to be destroyed can be concentrated on the surface of TiO₂ [14, 15]. TiO₂-pillared clay minerals, these novel photocatalysts, attract attention by their ability to accelerate the photocatalytic reaction by their unique adsorption capabilities [16, 17]. This increased adsorbability is the result of the large specific surface area produced by the incorporation of TiO₂ particles among the silicate layers, creating a mesoporous structure. Liu et al. [18] obtained an Ag-TiO₂/montmorillonite composite by hydrolysis of TiCl₄ and, due to the large specific surface area and the effect of silver content to improve light absorption, they observed an increased photooxidation activity as compared to the reference material, TiO₂. Kun et al. [19] established that

TiO₂/montmorillonite nanocomposites pillared with TiO₂ nanoparticles exhibit outstanding catalytic activity in phenol degradation.

Volatile organic components are being widely utilized not only for industrial but also for household purposes, leading to water and air pollution. Photocatalytic degradation of ethanol has been discussed in detail in a number of studies [20–22]. Nimlos et al. [23] studied the mechanism of degradation and established the following sequence of products: ethanol → acetaldehyde → acetic acid → formaldehyde → formic acid → CO₂, with acetaldehyde as the main intermediate. Sauer and Ollis studied deactivation of Degussa P25 TiO₂ [24, 25]. In the presence of water vapor, intermediates and/or products may accumulate on the surface of the catalyst and deactivate it. Since water is one of the products of the reaction, the reaction rate decreases continuously due to deactivation.

Our objective was the production of catalysts also efficient in the visible range. As shown by the references above, incorporation of metal ions into TiO₂ is not always expedient; we therefore prepared composites with the transition metal ions incorporated not directly on the surface or into the crystalline structure of TiO₂, but into the clay mineral acting as support. When the photocatalyst TiO₂ is mixed to or ground with the clay mineral support, the result is a TiO₂/layer silicate composite held together by electrostatic forces [19]. We study the catalytic properties of the ion-exchanged composite, obtained in this way in ethanol degradation on the solid/gaseous interface at 70% relative humidity, to appropriately model local environmental conditions in the photocatalytic reaction.

2. EXPERIMENTAL

2.1. Materials

Starting materials for the preparation of composites were Degussa P25 TiO₂ and the fine fraction of Na-montmorillonite EXM-838 ($d < 2$ nm, Süd-Chemie AG, Munich, Germany). The following nitrates were used for ion exchange in clay minerals: nickel nitrate (Fluka Chemie GmbH, Buchs, Switzerland), copper nitrate (LightTech, Dunakeszi, Hungary), and silver nitrate (LightTech, Dunakeszi, Hungary). Vapor phase degradation was performed using 99.8% anhydrous ethanol (LightTech, Dunakeszi, Hungary).

2.2. Preparation of transition metal exchanged montmorillonite/TiO₂ composites

One gram of Na-montmorillonite (EXM838) was left to swell in 100 mL of distilled water for 1 day. The next day, 1 mmol of Ag(I) nitrate or 0.5 mmol of Ni(II) and Cu(II) nitrate were added to the montmorillonite swollen in distilled water, the volume of the medium was brought up to 500 mL by the addition of distilled water, and the suspension was left to stand in a hot air thermostat at 35°C for 2 days. The precipitate obtained was next washed 3 times in distilled water, centrifuged and dried at 65°C. The composite was prepared by grinding, for 30 minutes in an agate mortar, a powder mixture consist-

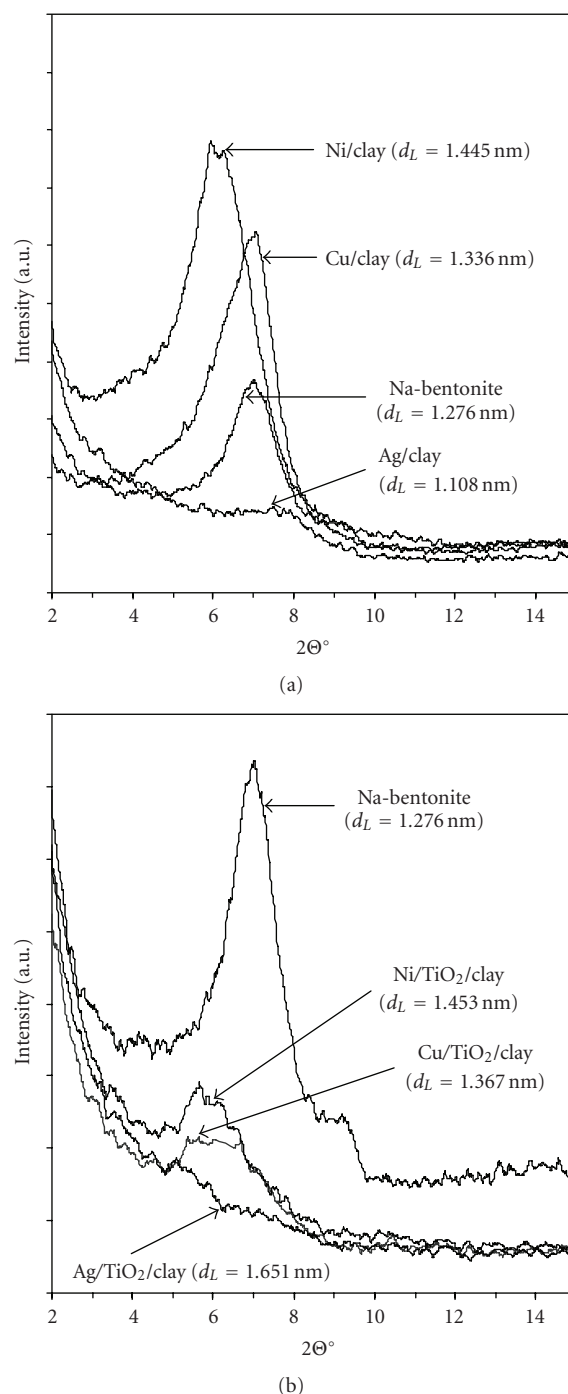


FIGURE 1: X-ray diffraction (XRD) patterns of (a) Me/clay and (b) Me/TiO₂/clay samples.

ing of 20% exchanged transition metal-montmorillonite and 80% P25 TiO₂. Metal contents relative to the total mass of the catalyst were Ag: 2.16%, Cu: 0.64%, and Ni: 0.59%.

2.3. Structure properties

The XRD experiments (Figure 1) were carried out in a Philips X-ray diffractometer (PW 1830 generator, PW 1820

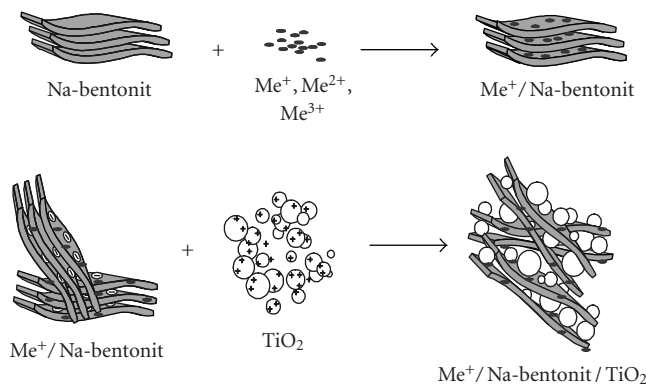


FIGURE 2: Schematic drawing of preparation of Me-ion exchanged montmorillonite/ TiO₂ composites.

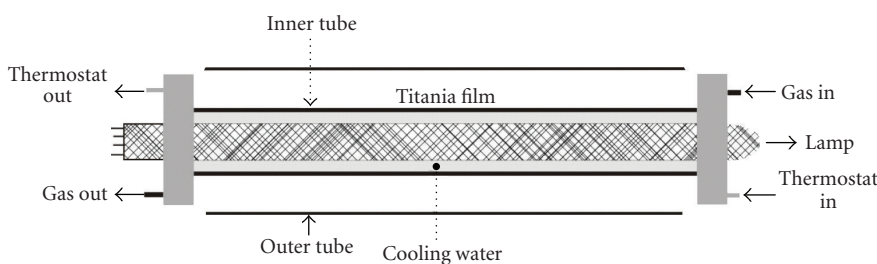


FIGURE 3: Schematic drawing of the photoreactor.

goniometer) with CuK- α radiation ($\lambda = 0.1542$ nm) 40 kV, 35 mA. The basal spacing (d_L) was calculated from the (001) reflection via the Bragg equation using the PW 1877 automated powder diffraction software. The analyses were carried out at ambient temperature in the 1–15° (2Θ) ranges. The 1–15° (2Θ) ranges are characteristic of the structure of the layer silicate.

2.4. Optical properties

A Mikropack Nanocalc 2000 spectrophotometer equipped with an integrated sphere (ISP-50-8-R-GT) was used to record the diffuse reflectance spectra of the samples. The spectra of the samples were analyzed under ambient condition in the wavelength range of 350–700 nm. The optical properties of transition metal-loaded titania/clay catalysts are listed in Table 1.

2.5. Photocatalytic reactions

Photooxidation of ethanol was performed in the reactor (volume: ca. 700 mL) at $25 \pm 0.1^\circ\text{C}$. The experimental setup is described in our previous paper [26]. The photoreactor (Figure 3) consists of two concentrically positioned tubes, namely, an inner quartz tube and an outer Pyrex glass tube. The light sources of the reactor were two types of 15 W low-pressure mercury lamp (LightTech, Dunakeszi, Hungary), namely, a GCL307T5L/CELL type (light source 1) with characteristic emission wavelength at $\lambda_{\text{max}} = 254$ nm and a GCL303T5 S#2 type (light source 2) with characteristic emission wavelength at $\lambda_{\text{max}} = 435$ nm. The catalyst was sprayed

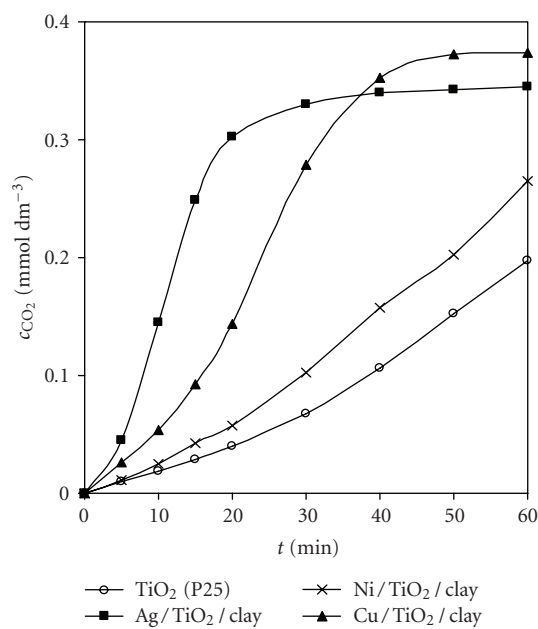
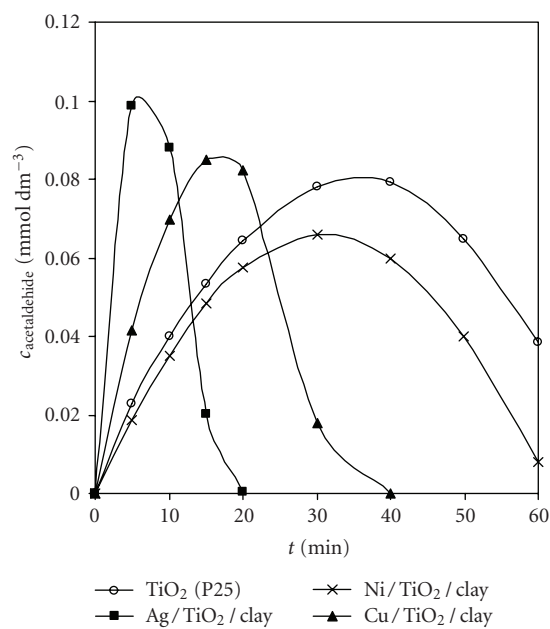
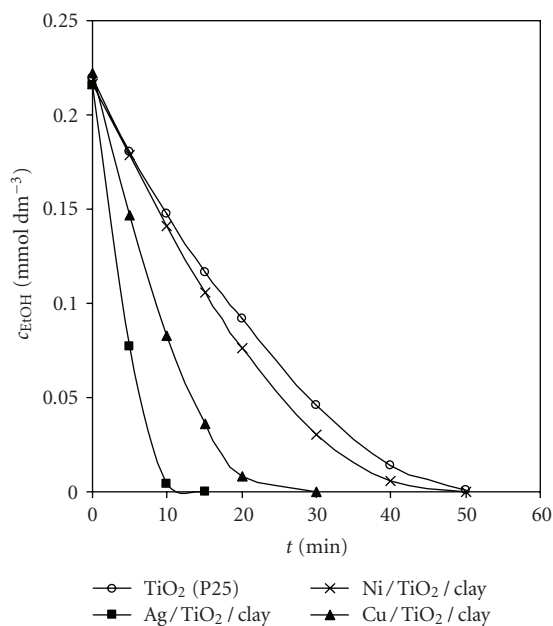
onto the outer side of the inner quartz tube from 10 to 20 (m/v)% aqueous dispersion using N₂ stream. The surface of the catalyst film was 44.8 cm², and the catalyst mass per unit surface was 0.310 ± 0.03 mg/cm². The film thickness was ca. 0.7–1.0 μm . The reactor was filled with dry synthetic air ($[\text{H}_2\text{O}] < 5$ ppm) to a final pressure of 760 Torr. After the delivery of 10 μL ethanol and 12 μL water, the system was left to stand for 30 minutes for evaporation of the components and establishment of the adsorption equilibrium. The reaction starts with switching on the lamp. Sampling from the gas phase (1 mL) was performed at selected time intervals, and the composition was analyzed in a gas chromatograph (Shimadzu GC-14B) equipped with a thermal conductivity (TCD) and a flame ionization detector (FID). The temperature of the column (HayeSep Q, length 2 m) was 140°C. A sample volume of 1 mL was introduced through a six-way valve to the online GC used for quantitative analysis of ethanol, acetaldehyde, and CO₂. A membrane pump inserted into the experimental assembly circulates the gas mixture to be degraded through the flow meter, the reactor, and the sampler of the gas chromatograph. The flow rate of the gas mixture in the measuring system was 375 mL/min. The initial concentration of ethanol was 0.25 mmol dm⁻³ at relative humidity of ~70%.

3. RESULTS

Showing the XRD pattern, we can establish that for the sodium montmorillonite, characteristic Bragg peak at $2\Theta = 7.02^\circ$ appears and the basal distance is $d_{001} = 1.276$ nm. After

TABLE 1: The composition and optical properties of the catalysts.

| | Metal content (mequ/g clay) | Metal content (wt%) | λ_g (nm) | E_g (eV) |
|---------------------------|-----------------------------|---------------------|------------------|------------|
| TiO ₂ (P25) | 0.00 | 0.00 | 390 | 3.18 |
| Ag/TiO ₂ /clay | 1.00 | 2.16 | 455 | 2.73 |
| Ni/TiO ₂ /clay | 1.00 | 0.59 | 404 | 3.07 |
| Cu/TiO ₂ /clay | 1.00 | 0.64 | 409 | 3.03 |

FIGURE 4: Ethanol concentration changes under (a) UV-Vis irradiation (light source 1), (b) kinetic curves of acetaldehyde, and (c) CO₂ formation.

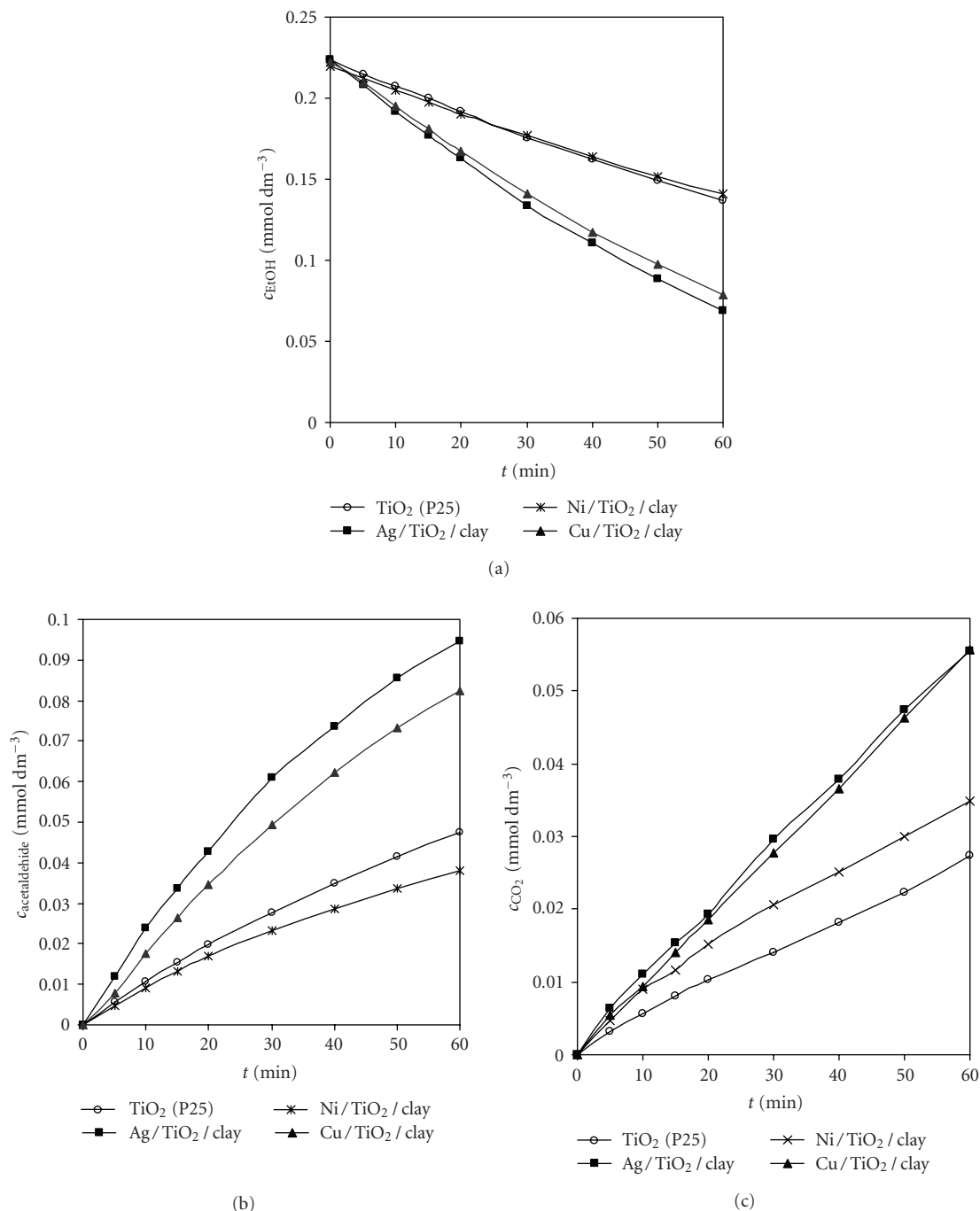


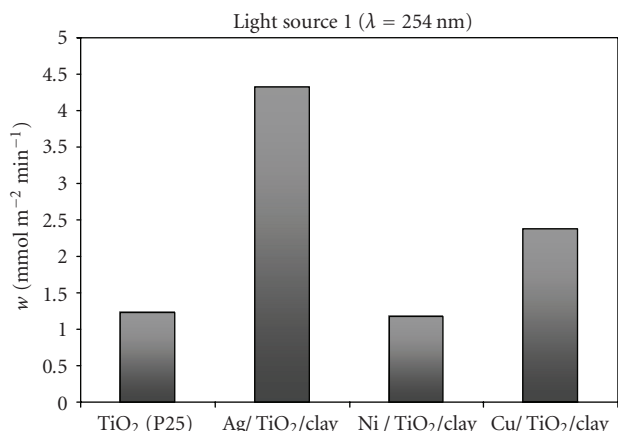
FIGURE 5: Ethanol concentration changes under (a) visible irradiation (light source 2), (b) kinetic curves of acetaldehyde, and (c) CO₂ formation.

the exchange of Ag(I) ions, the intensity of this reflection is lower and $d_{001} = 1.108$ nm because the layered structure will be partially disoriented. However, in the case of Cu(II)- and Ni(II)-ions modified montmorillonite samples, the basal distance is 1.336 nm and 1.445 nm, respectively (Figure 1(a)); that means the nickel and copper ions can be incorporated between the silicate layers, and the two valent cations can close the layers together producing well-oriented lamel-

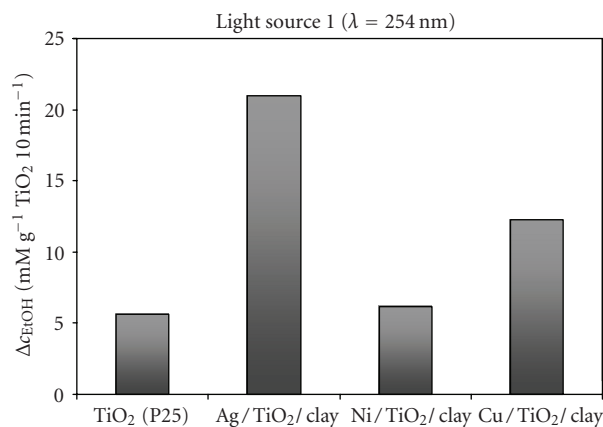
lar structures. After mixing these modified transition metal montmorillonites with TiO₂ powder, the intensity of the clay reflections will be very small, and the interlayer distance will increase to $d_{001} = 1.651$ nm (Ag/TiO₂/clay), $d_{001} = 1.453$ nm (Ni/TiO₂/clay), and $d_{001} = 1.367$ nm (Cu/TiO₂/clay), showing the possibility of the partial incorporation of any TiO₂ nanoparticles between the lamellae (Figure 1(b)). The formation of this suggested structures is presented in Figure 2.

TABLE 2: Photocatalytical characterization of the TiO₂ (P25) and the transition metal nanocomposite samples.

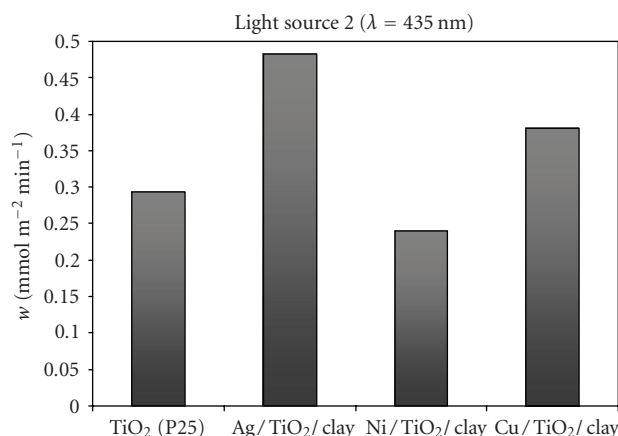
| | “Light source 1” ($\lambda = 254 \text{ nm}$) | | | “Light source 2” ($\lambda = 435 \text{ nm}$) | | |
|---------------------------|--|--|-----------------|--|--|-----------------|
| | Δc_{EtOH} (mmol dm^{-3}) 10 min | k ($\ast 10^{-4} \text{ s}^{-1}$) | efficiency % | Δc_{EtOH} (mmol dm^{-3}) 10 min | k ($\ast 10^{-4} \text{ s}^{-1}$) | efficiency % |
| TiO ₂ (P25) | 0.072 | 6.58 | 100 | 0.017 | 1.43 | 100 |
| Ag/TiO ₂ /clay | 0.211 | 34.94 | 293 | 0.032 | 2.31 | 188 |
| Ni/TiO ₂ /clay | 0.076 | 6.35 | 105 | 0.015 | 1.22 | 88 |
| Cu/TiO ₂ /clay | 0.140 | 13.96 | 194 | 0.027 | 1.88 | 159 |



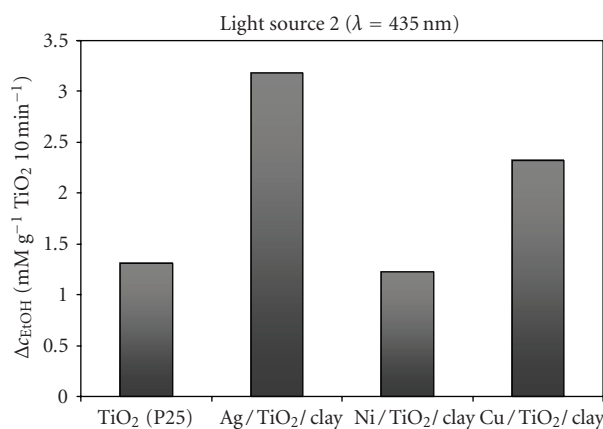
(a)



(a)



(b)



(b)

FIGURE 6: Amount of degraded ethanol in unit time (1 minute), normalized to a catalyst film surface of 1 m² (w).

The photocatalytic efficiency of montmorillonite/TiO₂ composites was tested in the degradation of ethanol vapor at 70% relative humidity. The reference catalyst was pure Degussa P25 TiO₂. The degradations were also repeated without catalyst with both light sources; it was found that ethanol concentration did not decrease in either case, indicating that self-photolysis does not take place in the vapor studied. The decrease in ethanol concentration and the formation of the main intermediate acetaldehyde were monitored in the course of the measurements (Figures 4(a), 4(b) and 5(a),

FIGURE 7: Decreasing of the ethanol concentrations is normalized to 1 g of TiO₂ in unit time (10 minutes).

5(b)). The kinetics of gaseous CO₂ formation was also studied (Figures 4(c), 5(c)). The results of the degradations are summarized in Table 2. In order to characterize catalysts, we introduced the parameter “ w ,” which means the amount of ethanol destroyed by irradiation with the given light source in unit time in a reactor volume of 1 dm³, normalized to a catalyst film surface of 1 m² (Figure 6). The parameter w is calculated by the following equation:

$$w = \frac{\text{amount of degraded EtOH (mmol/dm}^3\text{)}}{\text{time (min)} \ast \text{surface (m}^{-2}\text{)}}. \quad (1)$$

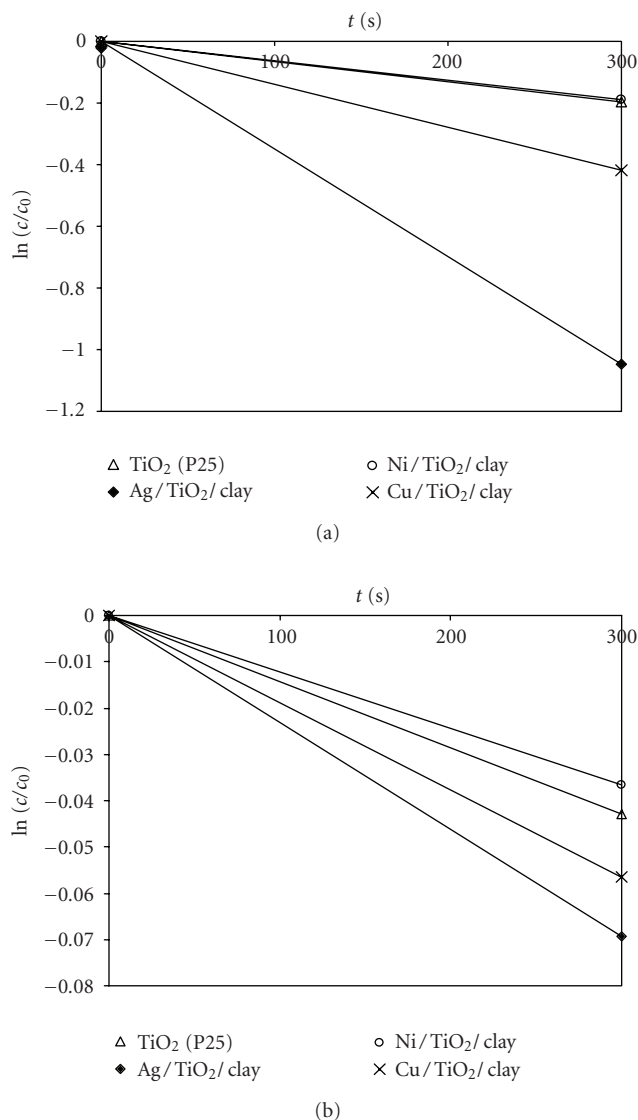


FIGURE 8: Determination of rate constants (k) with $\ln(c/c_0)$ versus t (sec) function by using (a) “light source 1” and (b) “light source 2” lamps.

The measured Δc_{EtOH} values are normalized to 1 g of TiO_2 catalyst and summarized in Figure 7. Table 2 also includes the rate constants (k) calculated from the slopes of the first-order kinetic functions $\ln(c/c_0)$ versus time. The constants unambiguously indicate that the reactions studied follow first-order kinetics (Figures 8(a), 8(b)).

All in all, it can be established that, in the case of each catalyst, ethanol is destroyed much more efficiently by irradiation with the light source rich in UV-C ($\lambda = 254$ nm) than in visible light. The reason for this is well known from the literature: the band gap energy of TiO_2 is $E_g = 3.2$ eV ($\lambda_g = 387$ nm), allowing excitation by light source 1 [27–30]. In the course of photooxidation by both light sources, samples containing silver or copper exhibit higher rates than does the reference TiO_2 sample. The composite containing nickel ions degrades ethanol at a higher rate only in the light of the

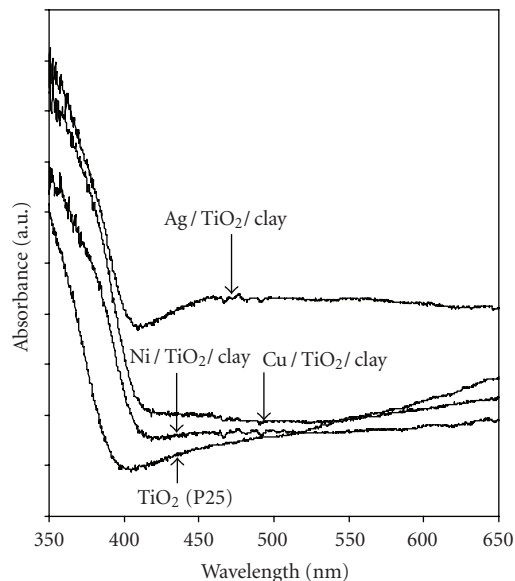


FIGURE 9: Diffuse reflectance UV-Vis spectra of exchanged Na-montmorillonite/ TiO_2 composites.

source rich in UV-C, whereas its efficiency in visible light is identical with that of the reference sample, P25 TiO_2 . Efficiencies (Table 2) are calculated from changes in concentration during a 10-minute irradiation time; ethanol degradation effected by the reference sample Degussa P25 TiO_2 is taken as 100%. The activity of the silver-containing TiO_2/clay composite during irradiation with light source 1 is threefold, and that of the copper-containing composite is twofold over P25 TiO_2 . This extraordinary effect is attributed, on the one hand, to excellent adsorption of ethanol by the layer silicate, allowing fast sorption of ethanol to the TiO_2 surface via diffusion [18]. On the other hand, the doping silver and copper, presumably present in the system in the form of silver and copper oxide nanoparticles, respectively [29, 30], significantly decrease the rate of electron-hole recombination on the TiO_2 surface, increasing catalytic activity. This outstandingly high activity, however, is somewhat decreased in visible light (light source 2), but even in this case, silver and copper degrade ethanol at rates nearly 1.5-fold faster than does P25 TiO_2 . We assume that the reason for this is an increased photon absorbance in the visible wavelength range ($\lambda = 400$ – 700 nm) on the composites prepared by us, as demonstrated by the absorbance spectra shown in Figure 9. The spectrum of $\text{Ni}/\text{TiO}_2/\text{clay}$ and Cu -loaded TiO_2/clay displays similar absorbance at wavelengths shorter than 410 nm, while $\text{Cu}/\text{TiO}_2/\text{clay}$ absorbs more photons whose wavelengths are larger than 410 nm, resulting in the color of light green. The sample of $\text{Ag}/\text{TiO}_2/\text{clay}$ possesses an additional broadened absorption peak at about 450 nm in the visible region, that indicates the brown color of the deposited silver can improve the light absorption of $\text{Ag}/\text{TiO}_2/\text{clay}$ and increase its photocatalytic activity. In other words, the efficiency of degradation in visible light can be explained by the excellent adsorption properties of the layer silicate and the red shift of photon absorbance at higher wavelengths.

4. CONCLUSIONS

Photocatalytic utilization of titanium dioxide and its composites with clay mineral support was studied in a vapor phase oxidation reaction. Since results on direct doping of TiO₂ with transient metals reported in the literature did not show an unambiguous increase in efficiency, we used 20% montmorillonite support exchanged with silver, copper, or nickel ions and mixed/ground with P25 TiO₂ in powder form. The amounts of metal normalized to the total mass of the catalyst were Ag: 2.16%, Cu: 0.64%, and Ni: 0.59%. The composite obtained was used for the preparation of films on the surface of the glass reactor, where photooxidation was carried out. The rate of photooxidation by irradiation with the light source rich in UV-C ($\lambda = 254$ nm) increased significantly as a result of the introduction of silver or copper included in the layer silicate, and the rate of the photooxidation process in visible light was also higher than that measured in the presence of the reference sample P25 TiO₂.

REFERENCES

- [1] P. Pichat, J. Disdier, C. Hoang-Van, D. Mas, G. Goutailler, and C. Gaysse, "Purification/deodorization of indoor air and gaseous effluents by TiO₂ photocatalysis," *Catalysis Today*, vol. 63, no. 2–4, pp. 363–369, 2000.
- [2] L. Zhang and J. C. Yu, "A simple approach to reactivate silver-coated titanium dioxide photocatalyst," *Catalysis Communications*, vol. 6, no. 10, pp. 684–687, 2005.
- [3] Z. Guo-Min, C. Zhen-Xing, X. Min, and Q. Xian-Qing, "Study on the gas-phase photolytic and photocatalytic oxidation of trichloroethylene," *Journal of Photochemistry and Photobiology A: Chemistry*, vol. 161, no. 1, pp. 51–56, 2003.
- [4] S. B. Kim, H. T. Hwang, and S. C. Hong, "Photocatalytic degradation of volatile organic compounds at the gas-solid interface of a TiO₂ photocatalyst," *Chemosphere*, vol. 48, no. 4, pp. 437–444, 2002.
- [5] G. Marci, M. Addamo, V. Augugliaro, et al., "Photocatalytic oxidation of toluene on irradiated TiO₂: comparison of degradation performance in humidified air, in water and in water containing a zwitterionic surfactant," *Journal of Photochemistry and Photobiology A: Chemistry*, vol. 160, no. 1–2, pp. 105–114, 2003.
- [6] Z. Pengyi, L. Fuyan, Y. Gang, C. Qing, and Z. Wanpeng, "A comparative study on decomposition of gaseous toluene by O₃/UV, TiO₂/UV and O₃/TiO₂/UV," *Journal of Photochemistry and Photobiology A: Chemistry*, vol. 156, no. 1–3, pp. 189–194, 2003.
- [7] T. Sano, N. Negishi, K. Takeuchi, and S. Matsuzawa, "Degradation of toluene and acetaldehyde with Pt-loaded TiO₂ catalyst and parabolic trough concentrator," *Solar Energy*, vol. 77, no. 5, pp. 543–552, 2004.
- [8] G.-M. Zuo, Z.-X. Cheng, H. Chen, G.-W. Li, and T. Miao, "Study on photocatalytic degradation of several volatile organic compounds," *Journal of Hazardous Materials*, vol. 128, no. 2–3, pp. 158–163, 2006.
- [9] A. Di Paola, M. Addamo, M. Bellardita, E. Cazzanelli, and L. Palmisano, "Preparation of photocatalytic brookite thin films," *Thin Solid Films*, vol. 515, no. 7–8, pp. 3527–3529, 2007.
- [10] M. Addamo, M. Bellardita, A. Di Paola, and L. Palmisano, "Preparation and photoactivity of nanostructured anatase, rutile and brookite TiO₂ thin films," *Chemical Communications*, no. 47, pp. 4943–4945, 2006.
- [11] D. Dvoranová, V. Brezová, M. Mazúr, and M. A. Malati, "Investigations of metal-doped titanium dioxide photocatalysts," *Applied Catalysis B: Environmental*, vol. 37, no. 2, pp. 91–105, 2002.
- [12] K. Chiang, R. Amal, and T. Tran, "Photocatalytic degradation of cyanide using titanium dioxide modified with copper oxide," *Advances in Environmental Research*, vol. 6, no. 4, pp. 471–485, 2002.
- [13] Slamet, H. W. Nasution, E. Purnama, S. Kosela, and J. Gunlazuardi, "Photocatalytic reduction of CO₂ on copper-doped Titania catalysts prepared by improved-impregnation method," *Catalysis Communications*, vol. 6, no. 5, pp. 313–319, 2005.
- [14] K. Mogyorósi, I. Dékány, and J. H. Fendler, "Preparation and characterization of clay mineral intercalated titanium dioxide nanoparticles," *Langmuir*, vol. 19, no. 7, pp. 2938–2946, 2003.
- [15] T. Pernyeszi and I. Dékány, "Photocatalytic degradation of hydrocarbons by bentonite and TiO₂ in aqueous suspensions containing surfactants," *Colloids and Surfaces A: Physicochemical and Engineering Aspects*, vol. 230, no. 1–3, pp. 191–199, 2004.
- [16] C. Ooka, H. Yoshida, K. Suzuki, and T. Hattori, "Effect of surface hydrophobicity of TiO₂-pillared clay on adsorption and photocatalysis of gaseous molecules in air," *Applied Catalysis A: General*, vol. 260, no. 1, pp. 47–53, 2004.
- [17] R. Kun, M. Szekeres, and I. Dékány, "Photooxidation of dichloroacetic acid controlled by pH-stat technique using TiO₂/layer silicate nanocomposites," *Applied Catalysis B: Environmental*, vol. 68, no. 1–2, pp. 49–58, 2006.
- [18] J. Liu, X. Li, S. Zuo, and Y. Yu, "Preparation and photocatalytic activity of silver and TiO₂ nanoparticles/montmorillonite composites," *Applied Clay Science*, vol. 37, no. 3–4, pp. 275–280, 2007.
- [19] R. Kun, K. Mogyorósi, and I. Dékány, "Synthesis and structural and photocatalytic properties of TiO₂/montmorillonite nanocomposites," *Applied Clay Science*, vol. 32, no. 1–2, pp. 99–110, 2006.
- [20] J. Araña, J. M. Doña-Rodríguez, O. González-Díaz, et al., "Gas-phase ethanol photocatalytic degradation study with TiO₂ doped with Fe, Pd and Cu," *Journal of Molecular Catalysis A: Chemical*, vol. 215, no. 1–2, pp. 153–160, 2004.
- [21] D. S. Muggli, J. T. McCue, and J. L. Falconer, "Mechanism of the photocatalytic oxidation of ethanol on TiO₂," *Journal of Catalysis*, vol. 173, no. 2, pp. 470–483, 1998.
- [22] E. Piera, J. A. Ayllón, X. Doménech, and J. Peral, "TiO₂ deactivation during gas-phase photocatalytic oxidation of ethanol," *Catalysis Today*, vol. 76, no. 2–4, pp. 259–270, 2002.
- [23] M. R. Nimlos, E. J. Wolfrum, M. L. Brewer, J. A. Fennell, and G. Bintner, "Gas-phase heterogeneous photocatalytic oxidation of ethanol: pathways and kinetic modelling," *Environmental Science and Technology*, vol. 30, no. 10, pp. 3102–3110, 1996.
- [24] M. L. Sauer and D. F. Ollis, "Catalyst deactivation in gas-solid photocatalysis," *Journal of Catalysis*, vol. 163, no. 1, pp. 215–217, 1996.
- [25] M. L. Sauer and D. F. Ollis, "Photocatalyzed oxidation of ethanol and acetaldehyde in humidified air," *Journal of Catalysis*, vol. 158, no. 2, pp. 570–582, 1996.

- [26] L. Kőrösi, A. Oszkó, G. Galbács, A. Richardt, V. Zöllmer, and I. Dékány, "Structural properties and photocatalytic behaviour of phosphate-modified nanocrystalline titania films," *Applied Catalysis B: Environmental*, vol. 77, no. 1-2, pp. 175–183, 2007.
- [27] H. Li, Z. Bian, J. Zhu, Y. Huo, H. Li, and Y. Lu, "Mesoporous Au/TiO₂ nanocomposites with enhanced photocatalytic activity," *Journal of the American Chemical Society*, vol. 129, no. 15, pp. 4538–4539, 2007.
- [28] C. Burda, Y. Lou, X. Chen, A. C. S. Samia, J. Stout, and J. L. Gole, "Enhanced nitrogen doping in TiO₂ nanoparticles," *Nano Letters*, vol. 3, no. 8, pp. 1049–1051, 2003.
- [29] T. Morikawa, Y. Irokawa, and T. Ohwaki, "Enhanced photocatalytic activity of TiO_{2-x}N_x loaded with copper ions under visible light irradiation," *Applied Catalysis A: General*, vol. 314, no. 1, pp. 123–127, 2006.
- [30] I. Dékány, L. Turi, and Z. Király, "CdS, TiO₂ and Pd⁰ nanoparticles growing in the interlamellar space of montmorillonite in binary liquids," *Applied Clay Science*, vol. 15, no. 1-2, pp. 221–239, 1999.

Research Article

The Effect of Sulphate Doping on Nanosized TiO₂ and MoO_x/TiO₂ Catalysts in Cyclohexane Photooxidative Dehydrogenation

P. Ciambelli, D. Sannino, V. Palma, and V. Vaiano

Dipartimento di Ingegneria Chimica e Alimentare, Università di Salerno, 84084 Fisciano (SA), Italy

Correspondence should be addressed to P. Ciambelli, pciambelli@unisa.it

Received 30 August 2007; Accepted 29 December 2007

Recommended by Leonardo Palmisano

The effect of sulphate doping of titania in promoting activity and selectivity of MoO_x/TiO₂ catalysts for the cyclohexane photooxidative dehydrogenation has been investigated in a gas-solid fluidized bed reactor. Sulphate and/or molybdate-modified titania catalysts were prepared by incipient wet impregnation of nanosized (5–10 nm crystallite size) samples. At 60% of titania surface coverage by MoO_x, sulphate surface density was obtained up to 19 μmol/m² without formation of MoO₃. The catalysts were characterized by N₂ adsorption-desorption at –196°C, micro-Raman and UV-visible reflectance spectroscopy, thermogravimetric analysis coupled with mass spectroscopy (TG-MS), and mass titration. Unsulphated and sulphated titania are both active in cyclohexane total oxidation, but sulphate doping of titania has a detrimental effect on the reaction rate. On Mo-based catalysts, polymolybdate species enabled sulphated titania to convert cyclohexane to benzene (99% selectivity) and cyclohexene, reducing at zero the formation of CO₂. Cyclohexane conversion to benzene is almost linearly dependent on sulphate surface density, resulting in enhanced yield to benzene. The enhanced photooxidative dehydrogenation activity and benzene yield by sulphate doping could be attributed to the increase of surface acidity and, as a consequence, of cyclohexane adsorption.

Copyright © 2008 P. Ciambelli et al. This is an open access article distributed under the Creative Commons Attribution License, which permits unrestricted use, distribution, and reproduction in any medium, provided the original work is properly cited.

1. INTRODUCTION

Recently, growing interest has been addressed to novel processes for the synthesis of chemicals by reversing the final goal of the photocatalytic oxidation process—enhancing the selectivity to partially oxidized products so much that the process could be used for their production. Therefore, since one of the main goals of the 21st century chemistry is to replace environmentally hazardous processes, selective photocatalytic partial oxidation can play a key role in this evolution, offering an alternative green route for the production of organics.

Titanium dioxide is the semiconductor most used in photocatalysis because of its high photocatalytic activity allowing to realize the abatement of pollutants both in liquid and gas phases [1–4]. It has been reported that the introduction of foreign species into TiO₂ leads to a dramatic change in activity of the photocatalytic process. In particular, SO₄²⁻/TiO₂ shows higher photocatalytic activity than unsulphated titania for a large variety of organic compounds [5].

Fu et al. [6] showed that the improved photoactivity of sulphated titanium dioxide was due to a greater surface area as well as a larger fraction of anatase phase which is more active than rutile for the photocatalytic application. In the presence of metal oxides such as WO₃, the surface acidity of TiO₂ was increased, resulting in enhanced photocatalytic activity [7]. The formation of acid sites increases the adsorption strength of different organics, that it is believed to contribute to enhance the photocatalytic activity.

The most of studies on photocatalytic reactions for organic synthesis deals with slurry systems. In contrast, selective oxidation in gas phase with molecular oxygen is still a real challenge to current research. Few examples of selective photocatalytic oxidative conversion of organic substrates in gas phase on modified titania-based catalysts have been reported such as alkane and cycloalkane oxidation [8–10], and olephin epoxidation [11, 12]. However, a significant enhancement of catalytic activity and energy efficiency is necessary for such application of photocatalysis. Recently, we have shown that benzene is obtained with high selectivity by

TABLE 1: List of catalysts and their characteristics.

| Catalyst | MoO ₃ wt% | SO ₃ * wt% | Surface area m ² /g | MoO ₃ density μmol/m ² | SO ₄ density μmol/m ² |
|--------------|----------------------|-----------------------|--------------------------------|--|---|
| PC500 | — | 0.55 | 345 | — | 0.17 |
| PC500S10 | — | 11 | 241 | — | 4.8 |
| PC500S18 | — | 19 | 169 | — | 11.7 |
| 24MoPC500 | 23.8 | 0.3 | 202 | 8.1 | 0.15 |
| 17MoPC500S10 | 16.6 | 10 | 144 | 8.0 | 7.3 |
| 12MoPC500S18 | 11.7 | 18 | 99 | 8.1 | 18.9 |

* Evaluated by TG-MS analysis.

photooxidative dehydrogenation of cyclohexane on MoO_x/TiO₂ catalysts in a gas-solid fixed [10] or, better, fluidized bed reactor [13, 14]. The active phases are octahedral polymolybdate species on titania surface [10]. Moreover, we found that the presence of sulphate species on the surface of different titanias (2.4 wt% maximum SO₄ content) enhances the benzene yield as more as higher is the sulphate content evidencing a synergic effect of sulphate and molybdate species [15]. It was also shown that the presence of sulphate increases surface acidity as the sulphate surface density increases. The addition of sulphate to MoO_x/γ-Al₂O₃ catalysts was found to promote the selective mono-oxidative dehydrogenation of cyclohexane to cyclohexene, demonstrating the possibility of finely tuning the process selectivity [16]. Maximum cyclohexane conversion and cyclohexene yield of 11% were obtained for SO₄ content of 2.4 wt% at 120°C. Physicochemical characterization of catalysts indicated the presence of both octahedral polymolybdate and sulphate species on alumina surface as previously found for titania. Increasing sulphate load, thermogravimetry evidenced the presence of up to three sulphate species of different thermal stability. We concluded that the lower activity observed at high sulphate content is likely due to polymolybdate decoration by sulphates [16].

In this paper, we focus the attention on the effect of sulphate doping of nanosized TiO₂ on the photocatalytic oxidative dehydrogenation of cyclohexane to cyclohexene and benzene on MoO_x/TiO₂ in a gas-solid fluidized bed reactor.

2. EXPERIMENTAL

Anatase titania with crystallites size ranging from 5 to 10 nm (PC 500 provided by Millenium Inorganic Chemicals, Stallingborough, United Kingdom) was used as catalyst support. The preparation procedure for catalyst samples (MoPCs) containing various amounts of molybdenum oxide and sulphate consisted of two steps. The first step was the impregnation of the support with an aqueous solution of ammonium sulphate. The suspension was dried under stirring at 80°C to complete removal of excess water. The sample turned into sulphate doped titania by calcination at 300°C for 3 hours. The second step was the impregnation of the sulphated sample with an aqueous solution of ammonium heptamolybdate (NH₄)₆Mo₇O₂₄·4H₂O, drying at 120°C for 12 hours and calcination in air at 400°C for 3 hours.

Photocatalysts characterization was performed by different techniques. Thermogravimetric analysis (TG-MS) of powder samples was carried out in air flow with a thermoanalyzer (Q600, TA) in the range 20–1100°C at 10°C/min heating rate. Specific surface area was evaluated by N₂ adsorption-desorption isotherms at –196°C with a Costech Sorptometer 1040. Powder samples were treated at 180°C for 2 hours in He flow (99.9990%) before testing. Laser Raman spectra of powder samples were obtained with a dispersive micro-Raman (Invia, Renishaw), equipped with 785 nm diode laser, in the range 100–2500 cm⁻¹ Raman shift. UV-Vis reflectance spectra were obtained with a Perkin Elmer Spectrometer Lambda 35 using an RSA-PE-20 reflectance spectroscopy accessory (Labsphere Inc., North Sutton, NH, USA). All spectra were performed using an 8° sample positioning holder, giving total reflectance relative to a calibrated standard SRS-010-99 (Labsphere Inc.). The reflectance data were reported as $F(R_{\infty})$ values from Kubelka-Munk theory versus the wavelength [17]. Equivalent band gap determinations were made by plotting $[F(R_{\infty}) * h\nu]^2$ versus $h\nu$ (eV) and calculating the x intercept of a line passing through $0.5 < F(R_{\infty}) < 0.8$. The zero point charge (ZPC) of supports and catalysts was determined by mass titration according to Noh and Schwarz [18].

Photocatalytic tests were carried out feeding a fluidized bed photoreactor [19] with 830 (stp) cm³/min N₂ stream containing 1000 ppm cyclohexane, 1500 ppm oxygen, and 1600 ppm water. The composition of the inlet and outlet gases was measured by an online quadrupole mass detector (TraceMS, ThermoFinnigan) and a continuous CO-CO₂ NDIR analyser (Uras 10, Hartmann & Braun). The reactor was illuminated by four UV light sources (eye mercury lamp, 125 W) in a dark box. The temperature was set at 120°C after a screening in the range 40–160°C [19]. In order to achieve fluidization conditions, 14 g of catalyst mixed with 63 g of α-Al₂O₃ (Aldrich, Milano, Italy 10 m²/g, 50 μm Sauter diameter) were loaded to the reactor. UV sources were activated after the complete adsorption of cyclohexane on catalyst surface in dark conditions.

3. RESULTS AND DISCUSSION

3.1. Catalyst characterization

The nominal MoO₃ and sulphate content together with the specific surface area (S.S.A) of the photocatalysts are reported in Table 1.

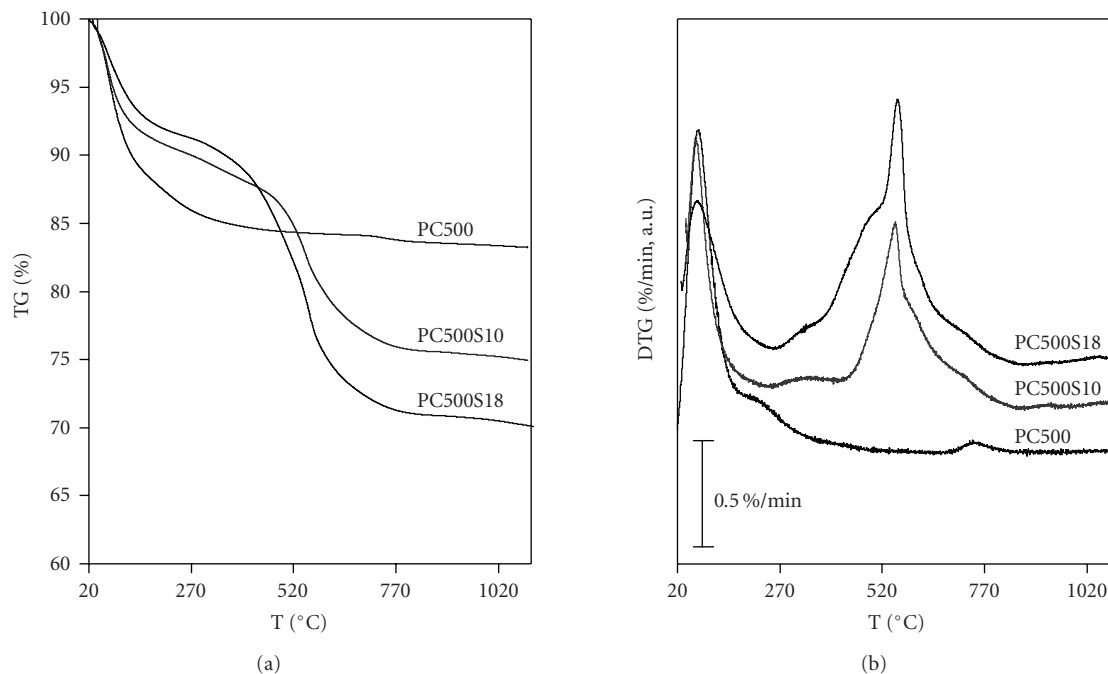


FIGURE 1: TG (a) and DTG (b) curves of PC500, PC500S10, and PC500S18 catalysts.

Both SO_4 and MoO_3 surface densities were evaluated with respect to the surface area values of the calcined catalysts. All MoPCs were designed to reach about 60% monolayer coverage of titania surface (about $8 \mu\text{mol}/\text{m}^2$).

Thermogravimetric curves of PC500, PC500S10, and PC500S18 are reported in Figure 1.

Three main steps of weight loss are recognized: (i) the first one associated with hydration water desorption, (ii) the second one related to the removal of OH^- surface groups of titania, (iii) the last one attributed to the decomposition of sulphate species giving rise to gaseous SO_3 as identified from its characteristic fragments $m/z = 48$ and 64 (not reported). The latter step ranges from 690°C to 840°C for PC500, while downshifts to $420\text{--}855^\circ\text{C}$ and $375\text{--}850^\circ\text{C}$ for PC500S10 and PC500S18, respectively. By analyzing the first derivative curves in the region of sulphate loss, only one peak centered at 741°C is observed on PC500, while PC500S10 and PC500S18 show three peaks at 552 , 599 , 717°C and at 477 , 555 , 730°C , respectively. It has been reported [20] that sulphated TiO_2 shows different regions of sulphate loss, the lowest temperature peak being attributed to a more weakly bonded sulphate species, the highest temperature peak to a more strongly bonded sulphate. The structure of metal oxide bonded sulphate is still subject of investigation in the literature. Jin et al. [20] proposed that sulphate would be coordinated to the titania surface as bidentate anion, Bensitel et al. [21] and Waqif et al. [22] described a structure in which sulphate, at lower content, would be bonded to the metal through three oxygen atoms. Moreover, the sulphate coordination to the surface depends on the dehydration state of the surface and then on the temperature. Increasing temperature and sulphate content,

polynuclear sulphates (polysulphates, S_2O_7^- , etc.) can be formed.

TG and DTG curves of 24MoPC500 , 17MoPC500S10 , and 12MoPC500S18 are displayed in Figure 2. All the samples show a decomposition step starting from about 700°C ; the onset of weight loss shifts slightly at higher temperature increasing the sulphate load. The estimated amount of weight losses of the three samples well agrees to the nominal MoO_3 content reported in Table 1, allowing the attribution of this step to Mo oxide sublimation, reported to occur in the range $800\text{--}1000^\circ\text{C}$ on $\text{MoO}_x/\text{Al}_2\text{O}_3$ catalysts [23].

The DTG curve of 24MoPC500 shows a single high temperature peak, centered at 624°C due to sulphate decomposition. We attribute the decreasing of decomposition temperature with respect to PC500 to the presence of MoO_x species, similarly as we previously found for WO_x/TiO_2 catalysts [24]. For 17MoPC500S10 , in addition to a DTG peak at about 584°C two overlapping peaks appear, with maximum at 466°C and 525°C , likely due to different surface sulphates. Similar DTG peaks, centered at 455°C , 573°C , and 630°C , are shown by 12MoPC500S18 .

UV-Vis DRS spectra of all the photocatalysts are reported in Figure 3. When supported on sulphated titania, Mo species absorption bands are difficult to distinguish, as previously reported [16]. However, the presence of MoO_3 crystallites (main band at 360 nm) on the catalysts was not detected. Sulphate doping increases the overall UV absorption of all the samples (Figure 3), correspondent to a slight increase in equivalent band gap energies, reported for MoPCs in Table 2. At similar sulphate level, the partial surface coverage with MoO_x leads to a small decrease in the equivalent band gap energies with respect to the relevant support.

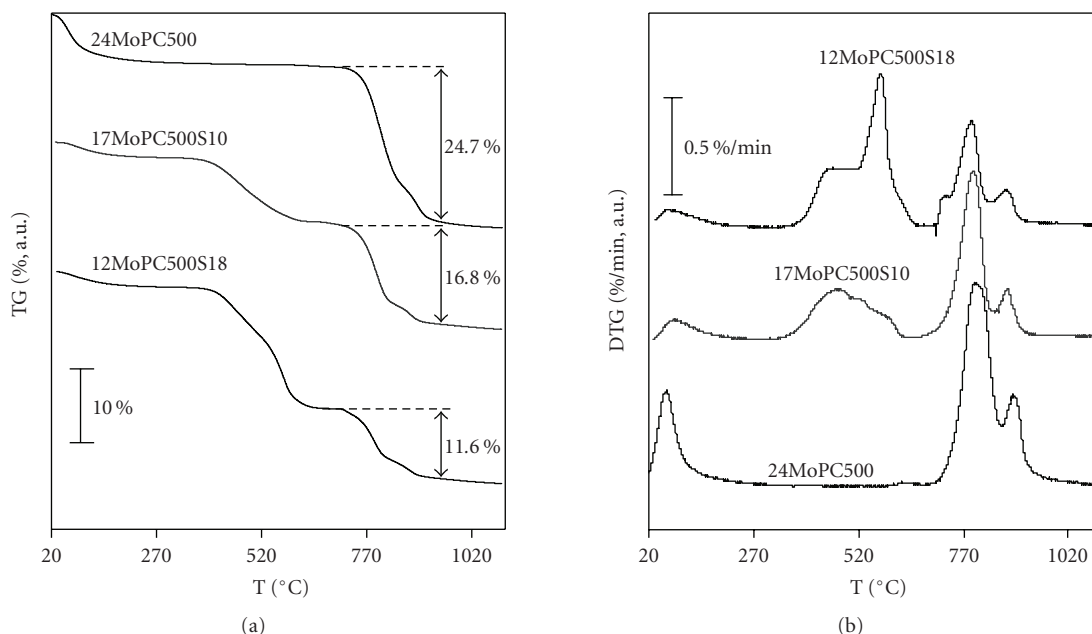


FIGURE 2: TG (a) and DTG (b) curves of 24Mo PC500, 17MoPC500S10, and 12MoPC500S18 catalysts.

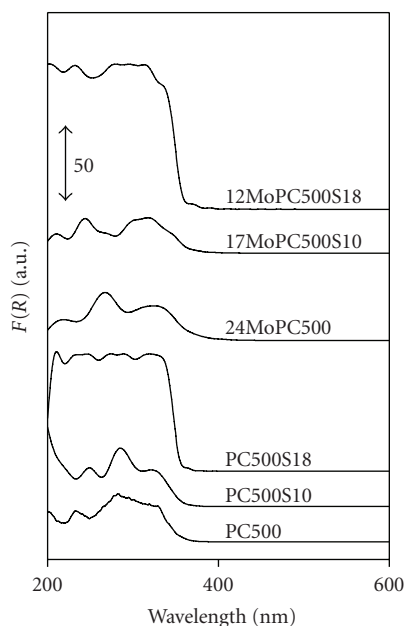


FIGURE 3: UV-Vis DRS spectra of PC500, PC500S10, PC500S18, 24MoPC500, 17MoPC500S10, and 12MoPC500S18 catalysts.

Increasing the sulphate content of titania, the values of ZPC (Table 2) decrease from 5.8 for PC500 to 2.2 for PC500S18. Also the presence of molybdenum confers, in all cases, stronger acidity, indicated by the ZPC values of MoPCs catalysts, as reported in [15].

The Raman spectra of PC and MoPC samples are reported in Figures 4(a) and 4(b), respectively. PC500S10 and PC500S18 exhibit a band around 986 cm^{-1} assigned to sym-

metric stretching mode ν_1 of sulphate belonging to point group Td [25]. The signal at about 1012 cm^{-1} for PC500S10 and at 1018 cm^{-1} for PC500S18 is due to the S=O bonds of isolated sulphates [26].

Broad bands around 1050 and 1180 cm^{-1} are due to removal of degeneration of ν_3 mode, owing the symmetry lowering with the coordination to the titania surface hydroxyl groups as bidentate anion. The upshift of S=O Raman band could indicate the strengthening of double bond due to the formation of polynuclear sulphates [25]. On MoPCs, the absence of bulk molybdena bands at 819 and 995 cm^{-1} [27] for all Mo-based catalysts confirms the absence of MoO_3 crystallites. Moreover, a complex band with several contributions in the range $940\text{--}1030\text{ cm}^{-1}$ is observed. For 24MoPC500 the maximum is at 984 cm^{-1} , with shoulders at 960 and 967 cm^{-1} . For 17MoPC500S10 the complex band is sharpened, with an additional strong signal at 992 cm^{-1} , overimposed to 970 , 980 , and 984 cm^{-1} shoulders. For 12MoPC500S18, 978 and 982 cm^{-1} signals with a maximum at 996 cm^{-1} are present, characteristic of polymolybdenyl species [28]. The Mo=O asymmetric stretching modes of hydrated octahedrally polymeric species lay in the range $940\text{--}988\text{ cm}^{-1}$ [29] with nuclearity ranging between 7 and 12. Wachs [28] reported that in hydrated conditions $\text{Mo}_8\text{O}_{26}^{4-}$ presents a Raman Mo=O band at 963 cm^{-1} on titania. The presence of polymeric octahedral species and sulphate can be thus recognised. 984 and 996 cm^{-1} signals could be ascribed to the surface sulphates, considering the absence of 820 cm^{-1} band of MoO_3 crystallites. Bands at 993 , 1009 , and 1111 cm^{-1} have been assigned to the S–O stretching vibrations of SO_4^{2-} species on CeO_2 [30]. The structure of sulphate species responsible for the band at 993 cm^{-1} cannot be definitely determined and thus requires further investigations.

TABLE 2: Equivalent band gap energy, ZPC values, and amount of adsorbed cyclohexane in dark conditions for all catalysts.

| Catalyst | Equivalent band gap energy eV | ZPC pH unit | Adsorbed cyclohexane $\mu\text{mol}/\text{m}^2$ |
|--------------|-------------------------------|-------------|---|
| PC500 | 3.3 | 5.8 | 0.048 |
| PC500S10 | 3.3 | 4.1 | 0.034 |
| PC500S18 | 3.4 | 2.2 | 0.026 |
| 24MoPC500 | 3.0 | 3.4 | 0.09 |
| 17MoPC500S10 | 3.2 | 2.2 | 0.14 |
| 12MoPC500S18 | 3.3 | 1.2 | 0.22 |

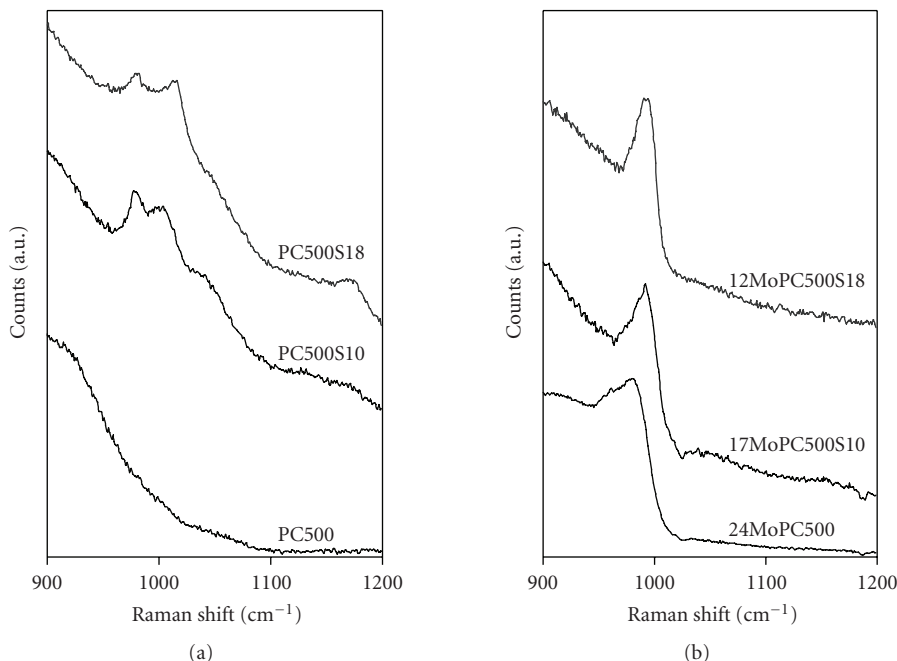


FIGURE 4: Raman spectra of PC500, PC500S10, PC500S18 (a) and of 24MoPC500, 17MoPC500S10, 12MoPC500S18 (b) catalysts.

The upshift of Mo=O band up to 980 cm^{-1} at increasing sulphate surface density indicates a progressive polymerization of MoO_x species.

3.2. Photocatalytic tests

Preliminary tests carried out in absence of UV light evidenced that no reaction occurred in dark conditions. Cyclohexane conversion and CO_2 outlet concentration on PC500, PC500S10, and PC500S18 as a function of irradiation time are reported in Figure 5. CO_2 was the only product detected in the gas phase (100% selectivity), reaching steady state values after about 30 minutes. Cyclohexane conversion to CO_2 decreases with the sulphate content.

For all titania catalysts, the total oxidation of cyclohexane to CO_2 and H_2O occurs without formation of by-products. Moreover, from Figure 6 it is evident that both cyclohexane consumption and CO_2 formation rates decreased with the sulphate surface density as previously observed in a gas-solid fixed bed photo reactor [15]. This behavior may be explained taking into account the reaction mechanism of gas-solid photocatalytic oxidation of cyclohexane to CO_2 on ti-

tania catalyst [31]. In the photocatalytic process, in fact, the surface hydroxyl groups trap the charge transfer to produce very reactive surface hydroxyl radicals. However, the presence of sulphate, grafted to the surface by reaction with hydroxyl groups, decreases their surface concentration, resulting in reduced activity. In addition, it is worthwhile to note that for total oxidation of hydrocarbons on titania the rehydroxylation of the surface is an essential step. Xie et al. [32], studying the gas-solid photocatalytic oxidation of heptane on sulphated and unsulphated titania in the presence of water, found that the presence of SO_4^{2-} was detrimental to the rehydroxylability of the catalyst.

Cyclohexane conversion and benzene outlet concentration as a function of irradiation time on MoPCS catalysts are reported in Figure 7. The analysis of outlet products disclosed the presence of benzene and cyclohexene, the absence of carbon dioxide and the stability of catalyst activity during the photocatalytic test. The trend of cyclohexene concentration (not reported) was similar to that of benzene but its concentration was very low ($<1\text{ ppm}$). It is evident that both cyclohexane total conversion and partial conversion to benzene are strongly dependent of sulphate and molybdate content.

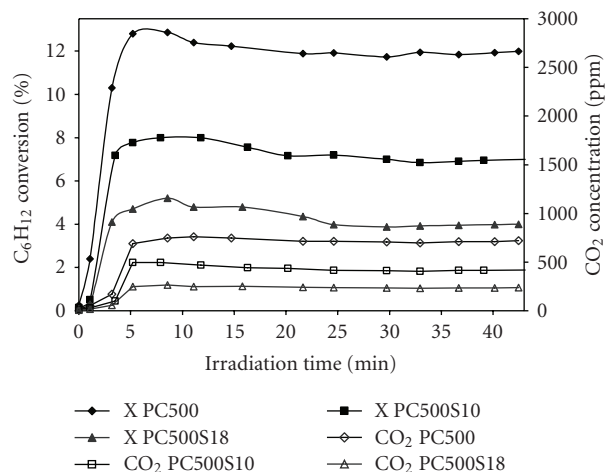


FIGURE 5: Cyclohexane conversion (X) and CO₂ outlet concentration (CO₂) as a function of irradiation time on PC500, PC500S10, and PC500S18.

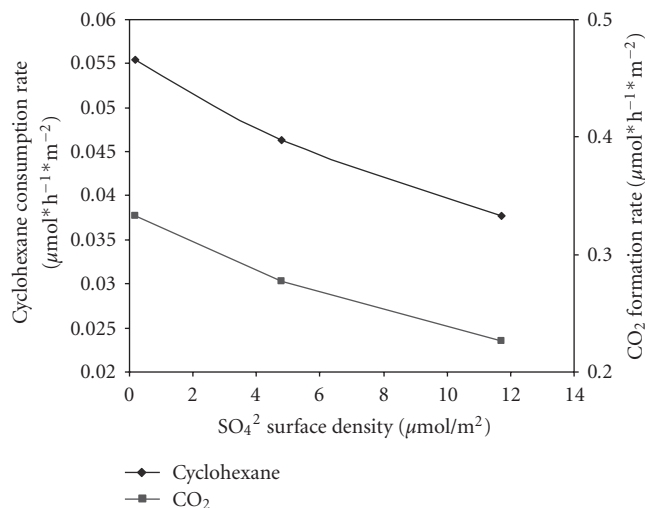


FIGURE 6: Cyclohexane consumption rate and CO₂ formation rate on PC500, PC500S10, and PC500S18 as a function of sulphate surface density.

The catalytic activity of MoPCs samples is reported in Figure 8(a) in terms of reaction rate per unit surface against sulphate surface density. Since the catalysts have the same molybdate surface density, it is evident that the catalytic activity is only dependent of the sulphate density. The values of cyclohexane consumption rate and benzene formation rate are almost coincident (about 100 % selectivity as the reaction rate to cyclohexene is two orders of magnitude lower) and linearly increase with sulphate density. We previously showed that the very high selectivity to benzene of MoO_x/TiO₂ photocatalyst is related to the coverage extent of titania surface by the polymolybdate species [10].

We retain that the mechanism for the photooxidative dehydrogenation of cyclohexane [19] involves photoexcited octahedral molybdate surface species, which are able to ini-

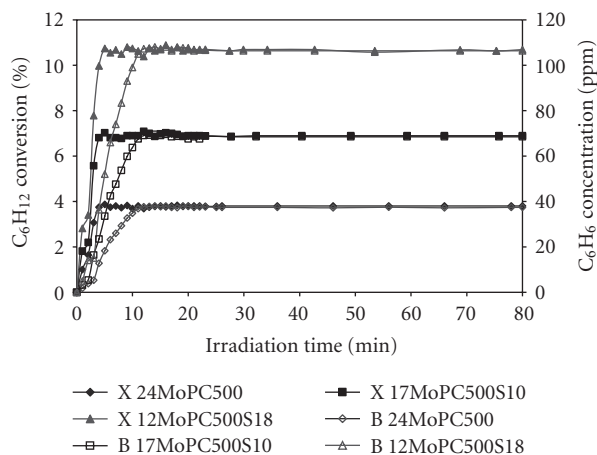


FIGURE 7: Cyclohexane conversion (X) and benzene outlet concentration (B) on 24MoPC500, 17MoPC500S10, and 12MoPC500S18 as a function of irradiation time.

tiate the oxidative dehydrogenation of adsorbed cyclohexane through hydrogen abstraction forming cyclohexene, further dehydrogenated to benzene which finally desorbs from catalyst surface. Photoreduced molybdate is then regenerated by reactive oxygen species, as O⁻ formed by the reaction between lattice oxygen and positive hole, O₂⁻ formed from gaseous oxygen and electron of the conduction band, H₂O₂ generated from OH[•] coupling. H₂O₂ is also responsible for water formation by decomposition. In summary, the formation of benzene may occur mainly according to a photocatalytic cycle that involves the molybdate both in the oxidized and in the photoreduced forms (redox mechanism) [19]. Cyclohexane may be totally oxidized into CO₂ and H₂O on unselective sites of the titania surface, according to the mechanism presented by Einaga et al. [31]. The presence of sulphate on titania is reported to give higher photoefficiency, in dependence of both energy required to excite the electrons from the valence to the conduction band (*E_g*) and limiting electron-hole pair recombination owing sulphate electron withdrawing properties. The equivalent band gap energy trend with sulphate content (Table 2) is in contrast with the first point. Further, hypotheses on the role of surface sulphate consider it to participate in the reoxidation step of the surface octahedrally coordinated polymolybdate or to promote hydrogen abstraction from adsorbed cyclohexane molecules, since its acid properties [19].

A strong indication on the main action of sulphate is suggested by Figure 8(b), where the amount of cyclohexane adsorbed in the dark on MoPCs catalysts is reported as a function of sulphate surface density. The linear raise of adsorbed amounts parallels the increase of cyclohexane reaction rate (Figure 8(a)).

The values of ZPC reported in Figure 8(b) also indicate that the adsorption of cyclohexane is correlated to the corresponding increase of catalyst acidity. These results suggest that sulphate doping facilitates hydrogen abstraction from adsorbed cyclohexane, increasing its storage.

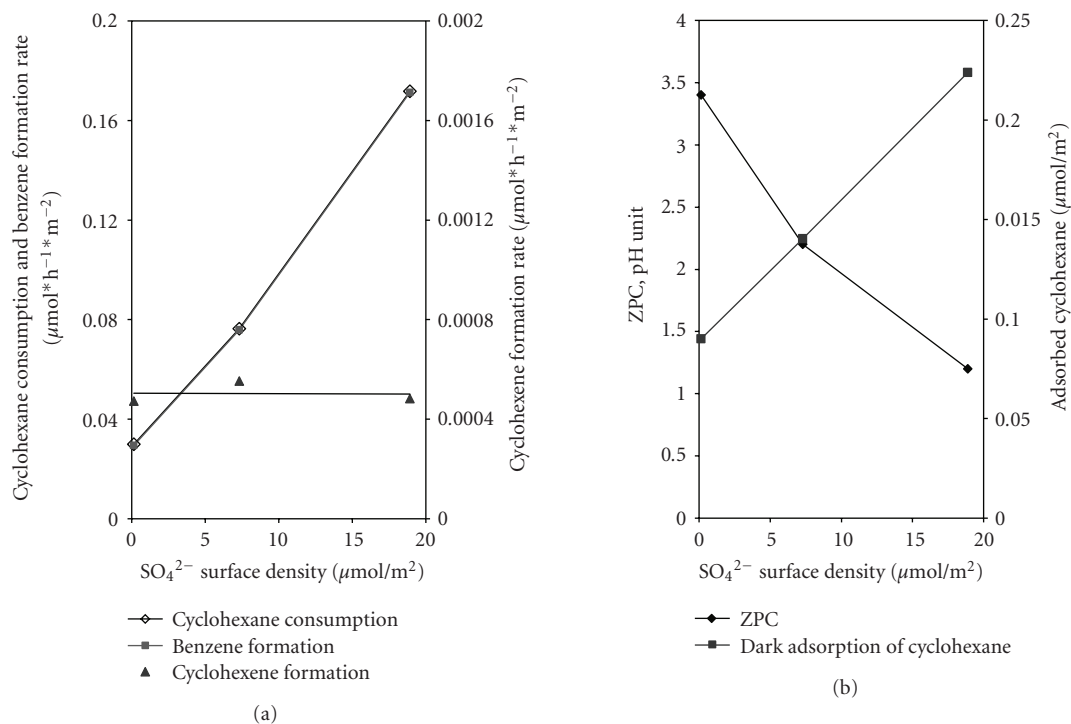


FIGURE 8: Cyclohexane consumption rate, benzene and cyclohexene formation rate (a) ZPC values and dark adsorption of cyclohexane (b) as function of sulphate surface density on 24MoPC500, 17MoPC500S10, and 12MoPC500S18.

4. CONCLUSIONS

Nanosized titania was employed to explore the effect of sulphate doping on TiO_2 and $\text{MoO}_x/\text{TiO}_2$ catalysts for the photooxidative dehydrogenation of cyclohexane in a photocatalytic gas-solid fluidized bed reactor. The high specific surface area of titania, even at 60% of MoO_x surface coverage, allowed to vary sulphate surface density up to $19 \mu\text{mol}/\text{m}^2$ without formation of segregated MoO_3 crystallites.

On nanosized titania, deep oxidation of cyclohexane only occurred. The cyclohexane consumption rate and carbon dioxide formation rate decreased as the sulphate load increases likely due to the detrimental decrease of surface free hydroxyls.

Photocatalytic selective oxidation of cyclohexane to benzene on $\text{MoO}_x/\text{nanosized titania}$ was enhanced by the sulphation. The presence of sulphate species on the surface of titania promoted benzene yield as more as higher was the sulphate content. Cyclohexene was produced in low concentration and CO_2 was not detected in gas-phase. The enhanced photooxidative dehydrogenation activity of $\text{MoO}_x/\text{TiO}_2$ catalysts is attributed to the increase of surface acidity due to sulphate doping that induces the formation of acid sites able to increase the hydrocarbon adsorption.

ACKNOWLEDGMENT

The authors thank Millenium Inorganic Chemicals for providing nanotitania samples.

REFERENCES

- [1] L. Palmisano and A. Sclafani, "Thermodynamics and kinetics for heterogeneous photocatalytic processes," in *Heterogeneous Photocatalysis*, M. Schiavello, Ed., John Wiley & Sons, West Sussex, UK, 1997.
- [2] G. Martra, S. Coluccia, L. Marchese, et al., "The role of H_2O in the photocatalytic oxidation of toluene in vapour phase on anatase TiO_2 catalyst a FTIR study," *Catalysis Today*, vol. 53, no. 4, pp. 695–702, 1999.
- [3] G. Marci, M. Addamo, V. Augugliaro, et al., "Photocatalytic oxidation of toluene on irradiated TiO_2 : comparison of degradation performance in humidified air, in water and in water containing a zwitterionic surfactant," *Journal of Photochemistry and Photobiology A: Chemistry*, vol. 160, no. 1–2, pp. 105–114, 2003.
- [4] V. Augugliaro, S. Coluccia, V. Loddo, et al., "Photocatalytic oxidation of gaseous toluene on anatase TiO_2 catalyst: mechanistic aspects and FT-IR investigation," *Applied Catalysis B: Environmental*, vol. 20, no. 1, pp. 15–27, 1999.
- [5] H. Cui, K. Dwight, S. Soled, and A. Wold, "Surface-acidity and photocatalytic activity of $\text{Nb}_2\text{O}_5/\text{TiO}_2$ photocatalysis," *Solid State Chemistry*, vol. 115, no. 1, pp. 187–191, 1995.
- [6] X. Fu, Z. Ding, and W. Su, "Structure of Titania-Based Solid Superacids and Their Properties for Photocatalytic Oxidation," *Chinese Journal of Catalysis*, vol. 20, p. 321, 1999.
- [7] D. S. Muggli and L. Ding, "Photocatalytic performance of sulfated TiO_2 and Degussa P-25 TiO_2 during oxidation of organics," *Applied Catalysis B: Environmental*, vol. 32, no. 3, pp. 181–194, 2001.

- [8] T. Tanaka, S. Takenaka, T. Funabiki, and S. Yoshida, "Selective photooxidation of propane to propanone over alkali-ion-modified silica-supported vanadium oxides," *Chemistry Letters*, vol. 23, no. 9, p. 1585, 1994.
- [9] K. Wada, H. Yamada, Y. Watanabe, and T.-A. Mitsudo, "Selective photo-assisted catalytic oxidation of methane and ethane to oxygenates using supported vanadium oxide catalysts," *Journal of the Chemical Society - Faraday Transactions*, no. 94, pp. 1771–1778, 1998.
- [10] P. Ciambelli, D. Sannino, V. Palma, and V. Vaiano, "Photocatalysed selective oxidation of cyclohexane to benzene on $\text{MoO}_x/\text{TiO}_2$," *Catalysis Today*, vol. 99, no. 1-2, pp. 143–149, 2005.
- [11] F. Amano and T. Tanaka, "Propylene oxide synthesis and selective oxidation over supported metal oxide photocatalysts with molecular oxygen," *Chemistry Letters*, vol. 35, no. 5, pp. 468–473, 2006.
- [12] X. Li and C. Kotal, "Photocatalytic selective epoxidation of styrene by molecular oxygen over highly dispersed titanium dioxide species on silica," *Journal of Materials Science Letters*, vol. 21, no. 19, pp. 1525–1527, 2002.
- [13] P. Ciambelli, D. Sannino, V. Palma, S. Vaccaro, and V. Vaiano, "Selective oxidation of cyclohexane to benzene on molybdena-titania catalysts in fluidized bed photocatalytic reactor," *Studies in Surface Science and Catalysis*, vol. 172, p. 453, 2007.
- [14] P. Ciambelli, D. Sannino, V. Vaiano, V. Palma, and S. Vaccaro, "Catalyzed photooxidative dehydrogenation of cyclohexane to benzene in a fluidized bed reactor," in *Proceedings of the 7th World Congress of Chemical Engineering*, Glasgow, UK, July 2005.
- [15] P. Ciambelli, D. Sannino, V. Palma, and V. Vaiano, "Cyclohexane photocatalytic oxidative dehydrogenation to benzene on sulphated titania supported MoO_x ," *Studies in Surface Science and Catalysis*, vol. 155, pp. 179–187, 2005.
- [16] P. Ciambelli, D. Sannino, V. Palma, et al., "Tuning the selectivity of MoO_x supported catalysts for cyclohexane photooxidation," *Catalysis Today*, vol. 128, no. 3-4, pp. 251–257, 2007.
- [17] C. Anderson and A. J. Bard, "Improved photocatalytic activity and characterization of mixed $\text{TiO}_2/\text{SiO}_2$ and $\text{TiO}_2/\text{Al}_2\text{O}_3$ materials," *Journal of Physical Chemistry B*, vol. 101, no. 14, pp. 2611–2616, 1997.
- [18] J. S. Noh and J. A. Schwarz, "Estimation of the point of zero charge of simple oxides by mass titration," *Journal of Colloid and Interface Science*, vol. 130, no. 1, pp. 157–164, 1989.
- [19] V. Vaiano, *Heterogeneous photocatalytic selective oxidation of cyclohexane*, Ph.D. thesis, 2006.
- [20] T. Jin, T. Yamaguchi, and K. Tanabe, "Mechanism of acidity generation on sulfur-promoted metal oxides," *Journal of Physical Chemistry*, vol. 90, no. 20, pp. 4794–4796, 1986.
- [21] M. Bensitel, O. Saur, J.-C. Lavalley, and B. A. Morrow, "An infrared study of sulfated zirconia," *Materials Chemistry and Physics*, vol. 19, no. 1-2, pp. 147–156, 1988.
- [22] M. Waqif, J. Bachelier, O. Saur, and J.-C. Lavalley, "Acidic properties and stability of sulfate-promoted metal oxides," *Journal of Molecular Catalysis*, vol. 72, no. 1, pp. 127–138, 1992.
- [23] H. G. El-Shobaky, M. Mokhtar, and A. S. Ahmed, "Effect of MgO-doping on solid-solid interactions in $\text{MoO}_3/\text{Al}_2\text{O}_3$ system," *Thermochimica Acta*, vol. 327, no. 1-2, pp. 39–46, 1999.
- [24] P. Ciambelli, M. E. Fortuna, D. Sannino, and A. Baldacci, "The influence of sulphate on the catalytic properties of $\text{V}_2\text{O}_5\text{-TiO}_2$ and $\text{WO}_3\text{-TiO}_2$ in the reduction of nitric oxide with ammonia," *Catalysis Today*, vol. 29, no. 1–4, pp. 161–164, 1996.
- [25] K. Nakamoto, *Infrared and Raman Spectra of Inorganic and Coordination Compounds*, John Wiley & Sons, New York, NY, USA, 4th edition, 1985.
- [26] S. M. Jung and P. Grange, "Characterization and reactivity of pure $\text{TiO}_2\text{-SO}_4$ SCR catalyst: influence of SO_4 content," *Catalysis Today*, vol. 59, no. 3, pp. 305–312, 2000.
- [27] C. Martin, M. J. Martin, and V. Rives, "Oxidation catalysts obtained by supporting molybdena on silica, alumina and titania," *Studies in Surface Science and Catalysis*, vol. 72, p. 415, 1992.
- [28] I. E. Wachs, "Raman and IR studies of surface metal oxide species on oxide supports: supported metal oxide catalysts," *Catalysis Today*, vol. 27, no. 3-4, pp. 437–455, 1996.
- [29] M. Cheng, F. Kumata, T. Saito, T. Komatsu, and T. Yashima, "Preparation and characterization of Mo catalysts over $\text{AlMCM-41}/\gamma\text{-Al}_2\text{O}_3$ extruded supports," *Applied Catalysis A: General*, vol. 183, no. 1, pp. 199–208, 1999.
- [30] J. Twu, C. J. Chuang, K. I. Chang, C. H. Yang, and K. H. Chen, "Raman spectroscopic studies on the sulfation of cerium oxide," *Applied Catalysis B: Environmental*, vol. 12, no. 4, pp. 309–324, 1997.
- [31] H. Einaga, S. Futamura, and T. Ibusuki, "Heterogeneous photocatalytic oxidation of benzene, toluene, cyclohexene and cyclohexane in humidified air: comparison of decomposition behavior on photoirradiated TiO_2 catalyst," *Applied Catalysis B: Environmental*, vol. 38, no. 3, pp. 215–225, 2002.
- [32] C. Xie, Z. Xu, Q. Yiang, et al., "Comparative studies of heterogeneous photocatalytic oxidation of heptane and toluene on pure titania, titania-silica mixed oxides and sulfated titania," *Journal of Molecular Catalysis A*, vol. 217, no. 1-2, pp. 193–201, 2004.

Research Article

Silver Doped TiO₂ Nanostructure Composite Photocatalyst Film Synthesized by Sol-Gel Spin and Dip Coating Technique on Glass

Mojtaba Nasr-Esfahani¹ and Mohammad Hossein Habibi²

¹ Department of Materials Science and Engineering, Islamic Azad University, Najafabad Branch, Najafabad 85141-43131, Iran

² Department of Chemistry, University of Isfahan, Isfahan 81746-73441, Iran

Correspondence should be addressed to Mohammad Hossein Habibi, mhhhabibi@yahoo.com

Received 26 August 2007; Revised 9 January 2008; Accepted 20 February 2008

Recommended by Leonardo Palmisano

New composite films (P25SGF-MC-Ag, MPC500SGF-MC-Ag, and ANPSGF-MC-Ag) have been synthesized by a modified sol-gel method using different particle sizes of TiO₂ powder and silver addition. Nanostructure TiO₂/Ag composite thin films were prepared by a sol-gel spin and dip coating technique. while, by introducing methyl cellulose (MC) porous, TiO₂/Ag films were obtained after calcining at a temperature of 500°C. The as-prepared TiO₂ and TiO₂/Ag films were characterized by X-ray diffractometry, and scanning electron microscopy to reveal the structural and morphological differences. In addition, the photocatalytic properties of these films were investigated by degrading methyl orange (MO) under UV irradiation. After 500°C calcination, the microstructure of MC-TiO₂ film without Ag addition exhibited a microstructure, while significant sintering effect was noticed with Ag additions and the films exhibited a porous microstructure. Nanostructure anatase-phase TiO₂ can be observed with respect to the sharpening of XRD diffraction peaks. The photodegradation of porous TiO₂ deposited with 5×10^{-4} mol Ag exhibited the best photocatalytic efficiency, where 69% methyl orange can be decomposed after UV exposure for 1 hour.

Copyright © 2008 M. Nasr-Esfahani and M. H. Habibi. This is an open access article distributed under the Creative Commons Attribution License, which permits unrestricted use, distribution, and reproduction in any medium, provided the original work is properly cited.

1. INTRODUCTION

Titanium dioxide has attracted significant attention of researchers because of many interesting physical properties that make it suitable for a variety of applications, and TiO₂ has high corrosion resistance, chemical stability, and an excellent optical transparency in the visible and near infrared regions as well as high refractive index that makes it useful for antireflection coatings in optical devices. Efforts are devoted to the development of efficient water and air purification technologies, based on TiO₂ photocatalysis. Such a treatment typically reduces toxic organic compounds to nontoxic inorganic compounds, such as carbon dioxide, water, ammonium or nitrates, and chloride ions. A number of techniques, such as spray pyrolysis [1], sol-gel method [2], sputtering [3, 4], solvothermal method [5], pulsed laser deposition [6], atomic layer deposition [7], chemical vapour deposition (CVD) [8–12] and photoassisted CVD [13] have been used to deposit TiO₂ thin films. Each of the

techniques for the TiO₂ thin film preparation has its own advantages and disadvantages, and it remains unclear at present as to which of these will eventually prove to be the most cost/quality effective. The photocatalytic activity depends strongly on the surface redox potential and the lifetime of the photogenerated electron-hole pairs. Titanium dioxide exists in three different crystalline phases: anatase, rutile, and brookite. Anatase was found to be more active photocatalytically than rutile. This enhanced photoactivity is attributed to the larger bandgap existing in this crystalline phase, which generally leads to an increase of both the surface redox potential and the charge carrier lifetime. Due to the large surface area, thin and composite coatings consisting of anatase TiO₂ nanoparticles show high photocatalytic efficiency. The photocatalytic activity of TiO₂ coatings do not depend only on the phase, but also on the crystallite size and porosity [14]. Sol-gel derived titanium dioxide composites have been also developed and investigated for the purpose of producing thin and composite films and self-supported

photocatalysts. The resulting photocatalysts exhibit relatively high surface area and enhanced mechanical stability and integrity [15].

It is well known that the initiation step of the photocatalytic process consists in the generation of electron-hole pairs upon irradiation of the material with a photon having energy at least equal to that of the bandgap of the photocatalyst. The electron-hole pairs formed can either recombine in the bulk or travel up to the surface, where they can participate in chemical reaction involving species adsorbed on the external titanol groups. The only drawback of TiO_2 is that its band gap lies in the near-UV of the electromagnetic spectrum: 3.2 eV (388 nm) and 3.0 eV (410 nm) for anatase and rutile, respectively. As a consequence, only UV light is able to create electron-hole pairs and to initiate the photocatalytic processes. It is, therefore, evident that any modification of the TiO_2 -based photocatalysts, resulting in a lowering of its bandgap [16], is representing a breakthrough in the field. This is the reason why so many scientific works have appeared during recent years. An exhaustive analysis of the different approaches used to dope TiO_2 is beyond scope of this contribution and only a selection of cases will be summarized below. (i) One case is doping TiO_2 with various transition metals such as Au, Ag, Pt, Cr, Nb, V, Mn, and Fe [17, 18]. These systems show an enhanced photoactivity in the visible with an efficiency depending highly on the preparation method. However, they are characterized by thermal instability and by a critical control of the cluster dimension and distribution [19]. (ii) Another case is represented by TiO_2 doped with nonmetal atoms such as N, S, F, C, I, Br, and Cl [20, 21]. Also in this case, the photocatalytic activity depends on the content of nonmetal atoms and on the method of preparation. (iii) A third case is a dye-sensitized TiO_2 obtained by anchoring a dye on the surface of the photocatalyst [22]. Various dyes (catechol, porphyrins, phthalocyanines, etc.) have been employed as sensitizers, but most of them are toxic and, more important, easily undergo a self-degradation process, that makes them unsuitable for durable applications in photocatalysis. (iv) As a fourth case TiO_2 doped with silver particles must be mentioned. Electrons in the valence band of TiO_2 are excited to the conduction band, with formation of holes in the valence band. At the same time electrons of Ag nanoparticles, when irradiated with the light of their plasmon resonance wavelength, are excited and transformed to adsorbed oxygen with formation of O^{2-} . The Ag nanoparticles are consequently oxidized by O^{2-} to colorless Ag^+ ions [23, 24]. In presence of TiO_2 these Ag^+ ions are reduced by the excited electrons and Ag nanoparticles are reformed. A limiting factor of the photocatalytic reaction is, therefore, recombination of the electron and hole prior to the superoxide activation step [25]. Silver has been shown to have a beneficial influence on the photoactivity of nanocrystalline semiconductor photocatalysts [26–28]. The combination of semiconductor substrate and metal cluster has been reported to give improved photocatalytic activity by trapping the photoinduced charge carriers, thereby improving the charge transfer processes [29–32].

In our previous work [33], we described a simple and repeatable approach to achieve useful materials for photocatalytic application by direct mixing of dispersed nanopowder titanium dioxide in sol-gel solution with prepolymerized material (polymer). The polymer was introduced into the sol-gel precursors in order to prevent particle aggregation, adjust the viscosity of sol, increase the strength of the unfired materials, and prevent film crack formation. In this case, it is important to avoid phase separation throughout the sol-gel reaction by a careful choice of solvents and optimized material processing conditions. Methyl cellulose (MC) is one of the ideal prepolymerized materials due to its solubility in water, which is suitable for use in sol-gel processing. Another advantage is that MC belongs to nonionic cellulose ether, which is substantially free of substances that can induce crystallization of silica or titania, and so forth during any of the coating formation and densification process steps.

For the reasons briefly mentioned above, we became interested in modifying the light absorbing property and photocatalytic activity of nanostructure composite TiO_2 films covering glass slide. Coming now to this study, it can be divided into two parts. In the first part, we illustrate a new strategy to synthesize a silver-doped titanium dioxide characterized by the presence of large surface area. In the second part, we demonstrate that the layer consists of anatase, which is efficient to remove the adsorbed molecular species from the environment via photocatalytic reaction. In this study, we have successfully synthesized three types of composite films (P25SGF-MC-Ag, MPC500SGF-MC-Ag, and ANPSGF-MC-Ag) by a modified sol-gel method using different particle size of TiO_2 powder. Methyl cellulose (MC) was added as a template to the sol for stress reduction which improved the amount of crystalline material immobilized on the support and the grain size of the films calcined at 500°C . The as-deposited TiO_2/Ag films were characterized by X-ray diffractometry, scanning electron microscopy, differential scanning calorimetry, and thermal gravimetric analysis. In addition, photocatalytic properties of these films were evaluated by degrading methyl orange under UV irradiation. The purpose of this study is to obtain insights on how the incorporation of Ag into the modified titania composite films affects the photocatalytic activity of such macroporous films, so as to design high performance TiO_2 composite films for water treatment.

2. EXPERIMENTAL

Standard ethanol solution ($M = 46.07 \text{ g/mol}$, purity $\approx 99.8\%$) was purchased from Fluka Chemical. Hydrochloric acid ($M = 36.5 \text{ g/mol}$, purity $\approx 35.5\%$) and silver nitrate (99%) were supplied from Merck. Titanium tetra isopropoxide ($\text{Ti}(\text{iOPr})_4$ or TTIP) (Sigma-Aldrich, 97%), the precursor, was used without further purification. Three types of commercial TiO_2 powders, namely, Aldrich TiO_2 powder (ANP), Degussa P-25 (P25), and Millennium PC-500 (MPC500) were used as the filler in the nanostructure composite films. Specifications of the photocatalysts filler according to the manufacturer's data are given in Table 1. Methyl cellulose (low substitution) was used as an organic binder material

TABLE 1: Properties of TiO₂ nanopowders.

| Photocatalyst | Composition | Specific BET surface area (m ² g ⁻¹) | Primary particle size (nm) |
|---------------------------------------|--------------|---|----------------------------|
| Aldrich powder TiO ₂ (ANP) | ≥97% anatase | 190–290 | 15 |
| Millennium PC-500 (MPC500) | ≥97% anatase | >250 | 5–10 |
| Degussa P25 (P25) | 70% anatase | ~50 | 20 |

[24]. Methyl orange (4-[[4-dimethylamino]phenyl]azo) benzenesulfonic acid sodium salt) analytical grade [34] was chosen as a simple model of a series of common azo dyes largely used in the industry. Methyl orange is a well-known acid-base indicator, orange in basic medium, and red in acidic medium. The preparation steps for the composite films derived from TiO₂ powder are described in detail elsewhere [35]. The sol was prepared by adding 5 mL TTIP to a 50 mL beaker containing a mixture of 10 mL ethanol and 1.8 mL HCl 35.5% that had been mixed for five minutes. Methyl cellulose 2 wt.% solution was prepared using MC and double-distilled water. These two solutions (titanium precursor and MC solution) were added dropwise and stirred overnight at room temperature. Precalcinated TiO₂ nanopowders (ANP, P25, MPC500), Degussa P25 (P25), and Millennium PC-500 (MPC500) were used as filler mixed with the sol (5% of sol). TiO₂ powder was dispersed in the sol and the prepared mixtures were deposited on the microscope glass slide (75 mm × 25 mm × 1 mm) by homemade spin coating. The dried films were heated in a muffle furnace to 500°C at a heating rate 5°C min⁻¹ and maintained at this temperature for 60 minutes and cooled at room temperature with similar rate. Three different composite (P25SGF-MC, MPC500SGF-MC, and ANPSGF-MC) films were dipped into the silver nitrate solution with various molar concentrations (5 × 10⁻⁶, 10⁻⁵, 5 × 10⁻⁵, 10⁻⁴, 5 × 10⁻⁴, 5 × 10⁻³, 10⁻³, 10⁻² M) for three seconds, washed with distilled water, dried at nitrogen atmosphere and no color change was observed. The silver-doped composite films (P25SGF-MC-Ag, MPC500SGF-MC-Ag, and ANPSGF-MC-Ag) were irradiated with two UV-C lamps (8 W) for 2 hours in air and color change was observed. These composite films were used for photocatalytic degradation; otherwise the photocatalysts were stored in the dark to avoid preactivation by room light or sunlight.

Film morphology was characterized by an environmental scanning electron microscope (ESEM, JEOL JSM-5300LV) with accelerating 10 kV. The phase composition of photocatalyst was studied by the powder and plate XRD technique. The X-ray diffraction patterns were obtained on a D8 Advanced Bruker X-ray diffractometer using Cu K α radiation at an angle of 2 θ from 15 to 60°. The scan speed was 1°/min. The strongest peaks of TiO₂ corresponding to anatase (1 0 1) and rutile (1 1 0) were selected to evaluate the crystallinity of the samples. The mean crystallite size L was determined from the broadening β of the most intense line, for each polymorph, in the X-ray diffraction pattern, based on the Scherer equation:

$$L = \frac{k\lambda}{\beta \cos\theta}, \quad (1)$$

where λ is the radiation wavelength, $k = 0.90$, and θ is the Bragg angle [36].

Evaluation of the adhesion and bonding strength between the coating and glass substrate was made by using the scratch test technique.

The photocatalytic activity of films was evaluated by degrading methyl orange solution. The distance between the UV light source and deposited films was set as 10 cm. Sol-gel derived films were prepared on microscopy glass slides. To evaluate the catalytic activity, the photodegradation of methyl orange solution was chosen as a simple model of a series of common azo dyes largely used in the industry. One TiO₂-Ag/glass with one time spin coating (75 mm × 25 mm × 1 mm) was used as photocatalyst and irradiated with two 8 W UV-A ($\lambda = 365$ nm) at a distance of 5 cm from the top of the solutions. 20 mL of the dye solutions with initial concentration of 5 ppm at pH = 4.5 was used. The solution was stirred in the dark for 90 minutes before irradiation to reach an equilibrated adsorption. Therefore, this time has been selected for the initial period to UV-irradiation to make sure that the initial degradation initiates at the equilibrium of the adsorption. The color removal of the dye solution was followed by measuring the absorbance value at $\lambda = 460$ nm, using double beam UV-visible spectrophotometer, (Varian Cary 500 Scan) initially calibrated, according to Beer-Lambert's law.

3. RESULTS AND DISCUSSION

Sol-gel derived composite film [25] can be easily employed as a fast and nonenergy consuming procedure to mass production of titania composite films (of 10 μ m in thickness) with good uniformity and reproducible properties. After dipping of the TiO₂ composite films in the silver nitrate solution and subsequent UV irradiation at 254 nm for 2 hours, the photocatalyst appears dark brown. Increasing the Ag⁺ concentration of dipping solution produces darker films at a gradient rate. Macroscopic observation of the film suggests that silver particles are widely spread on the surface without the formation of islands and that the resulting surface modified photocatalysts possess a solid structure on the glass substrate with more than satisfactory scratch resistance and adherence.

An XRD pattern of sol-gel derived TiO₂ thin film heat treated at 500°C for 1 hour shows that anatase was formed without contamination by other polymorphs: brookite or rutile (Figure 1). Nonheated thin film had an amorphous (and/or an ultra-fine crystalline) structure with a very broad peak at about 2 $\theta = 25^\circ$ (which is identified as the most intensive peak (1 0 1) for the anatase TiO₂). Diffraction peaks of anatase were observed for the coatings heat treated at

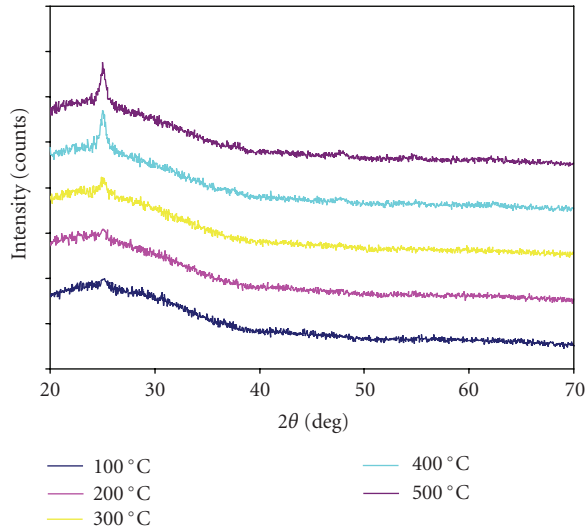


FIGURE 1: XRD patterns of TiO_2 sol-gel derived thin film by one time spin coating with heat treated at different temperatures.

temperatures higher than 300°C . Diffraction peaks of rutile were not found for the gel-derived deposited coatings heated up to 500°C .

The XRD patterns of different composite sol-gel samples (P25SGF-MC, ANPSGF-MC, and MPC500SGF-MC) before and after Ag coating are shown in Figure 2. As shown in Figure 2(a), for P25SGF-MC anatase/rutile ratio remains almost constant, as compared with the filler phase composition, after heating up to 500°C . This is because of the relatively high percentage of TiO_2 amount (the filler) compared to the amount of TiO_2 which is derived from the sol. For ANPSGF-MC and MPC500SGF-MC nanostructure composite films, which are prepared by ANP and MPC500 nanopowder, since ANP and MPC500 contain 100% anatase, diffraction peaks of rutile were not found (Figures 2(b) and 2(c)).

It can be found that films exhibited the TiO_2 composite films calcined at 500°C show relative sharp peaks indicating the coalescence of nanocrystalline anatase-phase TiO_2 . According to the Figures 2(a), 2(b), and 2(c), the intensity of the anatase and rutile main peaks in the nanostructure composite films, both before coating or after coating by Ag, are very similar. It is noticed that no additional XRD peaks corresponding to Ag additions can be revealed. This may be attributed to the well dispersion of nanocrystalline Ag particles in the TiO_2 matrix, the overlapping of Ag XRD peak or silver oxide particles are not crystallized on TiO_2 surface. On the contrary, well-organized crystal structure from titania particles is observed for the all composite films.

As shown in Table 2, for the sample sol-gel dried gel modified with MC, the crystallite size of anatase phase, which was used as a measure of TiO_2 crystallinity, increases considerably with calcinations temperature, from about 0.5 nm at room temperature to 13.4 nm at 500°C . However, for P25 and ANP, the initial anatase crystallite size increased only slightly versus temperature, from 15 nm for anatase

at room temperature to more than 16.3 nm for anatase, in ANP (at 500°C) and more than 19.2 nm for anatase, in P25 powder (at 500°C). It is suggested that the growth process of nanocrystalline anatase is mainly because of the sintering of the single crystals within the agglomerates, and finally the original agglomerate transforms to a larger single crystal [37]. However, as shown in Table 2, For MPC500 nanopowder is observed that the initial anatase crystallite size increased more significantly versus temperature, comparing other nanopowder TiO_2 .

For the heat-treated sol-gel derived composite film, the crystallite size is mainly determined by the particle size of the calcined filler powder and remains approximately constant up to 500°C . The average size of the grains in TiO_2 films prepared by P25, ANP, and MPC500 in the sol was approximately 18.6, 16.3, and 18.1 nm, respectively. The grain size of composite films, prepared with ANP which is 16.3 nm, is only a little larger than the average crystal size of ANP particles (15 nm), which demonstrates that ANP particles in the sol under these conditions cannot form much larger grains. The grain size of composite film prepared by MPC500 particles in the sol is much larger than the average crystal size of MPC500 particles (5–10 nm), which indicates that MPC500 particles in the sol can aggregate to form larger grains. It is worth to mention that the composite film with MPC500 has more scratch adhesion than other one which is confirmed by XRD and SEM images.

Because the decomposition temperature of MC as template is below 400°C , porous TiO_2 composite films can be prepared by calcining at 500°C to remove the MC microspheres. However, conventional SEM (Figure 3(a)) can only reveal a smooth surface of TiO_2 films made from the precursor sol containing no nanopowder heat treated for 1 hour at 500°C and no individual TiO_2 grain can be observed. Figure 3(b) shows the high-magnification field-emission ESEM micrograph ANPSGF-MC and Figure 3(c) shows MPC500SGF-MC after calcining where nanocrystalline TiO_2 particles can be observed. As shown in Figures 3(b) and 3(c), the diameter of the calcined TiO_2 nanoparticles was small (less than 20 nm).

In order to check the adhesion strength of these photocatalytic films on the glass substrate, scratch test technique is performed on these films. All composite films calcined at 500°C and the results are provided in Table 2, which demonstrates that 500°C is the optimum calcination temperature at or above which excellent adhesion between the nanostructure composite films and the glass substrate can be obtained. For P25, ANP, and MPC500 TiO_2 nanopowder coatings deposited from slurry (i.e., without the sol binder), the normal load needed to remove the coatings from the substrate is $\sim 0\text{ g/mm}^2$. In fact, this load is so small that can be considered as zero, especially when compared to the respective values for the nanostructure composite films, in the range of 200–350 gr/mm^2 .

The photocatalysis experiments took place in an aqueous solution of methyl orange to evaluate the composite films activity. The photocatalytic activity was evaluated as the percentage of pollutant disappearance. The photodegradation of methyl orange was followed using absorption at $\lambda_{\text{max}} 270\text{ nm}$

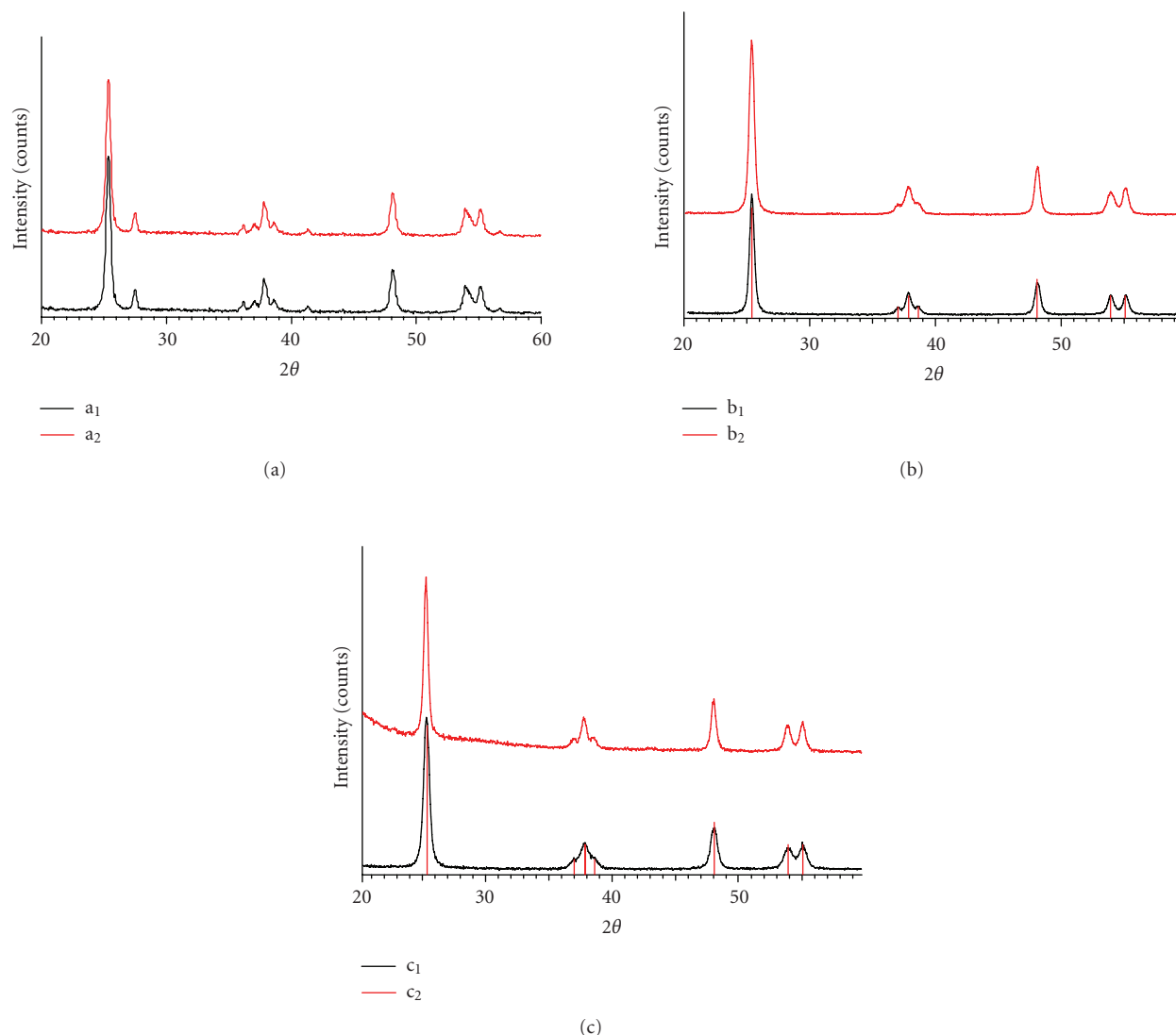


FIGURE 2: (a) XRD patterns of (a₁) sol-gel derived composite film from Degussa P25 TiO₂ with MC heat treated for 1 hour at 500°C (P25SGF-MC) and (a₂) after silver deposition (P25SGF-MC-Ag). (b) X-ray diffraction patterns of (b₁) sol-gel derived composite film from Mellenium PC 500 TiO₂ with MC heat treated for 1 hour at 500°C (MPC500SGF-MC) and (b₂) after silver deposition (MPC500SGF-MC-Ag). (c) X-ray diffraction patterns of (c₁) sol-gel derived composite film from Aldrich nanopowder TiO₂ with MC heat treated for 1 hour at 500°C (ANPSGF-MC) and (c₂) after silver deposition (ANPSGF-MC-Ag).

and 505 nm during the photodegradation reaction as a function of irradiation time. The color of methyl orange solution changes from orange to red and finally become colorless with increasing irradiation time. It should be pointed out that decomposition of methyl orange itself under UV irradiation is negligible. Each experimental set was repeated three times. The results were reproducible within narrow limits (2%) and the mean value was selected. Detailed preliminary tests were first performed in order to determine minor silver deposition parameters such as dipping duration and UV illumination time. The results with different AgNO₃ solutions have shown that the optimum conditions correspond to 3-second dipping and a 120-minute UV illumination, respectively, leading to silver-modified titania films with the best photocatalytic effect. It was also confirmed that the crucial parameter that

strongly influences the films photocatalytic activity is the concentration of the AgNO₃ dipping solution.

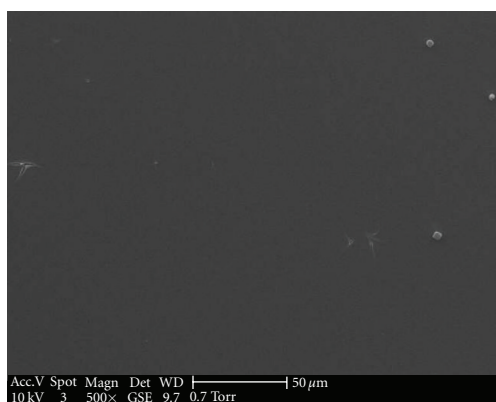
The photocatalytic efficiency (degradation percentage corresponding to 1-hour illumination) of the silver-doped titania nanostructure composite films for the MO decomposition are illustrated in Figures 4(a), 4(b), and 4(c). The corresponding performance of the original nonsupported nanostructure composite titania films is also given for comparison. The porous P25SGF-MC-Ag, MPC500SGF-MC-Ag, and ANPSGF-MC-Ag composite films exhibited 69%, 42%, and 64% degradation, respectively, after the same exposure time.

As shown in Figure 4(a), the results show that by increasing the concentration of the dipping solution, the photocatalytic efficiency of ANPSGF-MC increases. A maximum

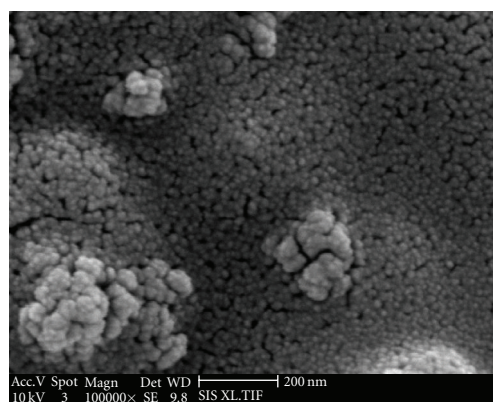
TABLE 2: Physical and chemical characteristics of different TiO₂ photocatalysts.

| Material | Heat-treatment conditions | Particle size (nm) ^(a) | Scratch adhesion (g/mm ²) |
|----------------------------------|---------------------------|-----------------------------------|---------------------------------------|
| Sol-gel derived TiO ₂ | — | — | 150 |
| modified with MC | 500°C, 1 h | 13.4 | 1500 |
| P25 | — | 18.8 | ~0 |
| | 500°C, 1 h | 19.2 | ~0 |
| ANP | — | 15 | ~0 |
| | 500°C, 1 h | 16.3 | ~0 |
| MPC500 | — | 6.6 | ~0 |
| | 500°C, 1 h | 16.7 | ~0 |
| ANPSGF-MC | — | 14.9 | 9 |
| | 500°C, 1 h | 16.3 | 200 |
| MPC500SGF-MC | — | 6.6 | 10 |
| | 500°C, 1 h | 18.1 | 350 |
| P25SGF-MC | — | 19.2 | 10 |
| | 500°C, 1 h | 18.6 | 200 |

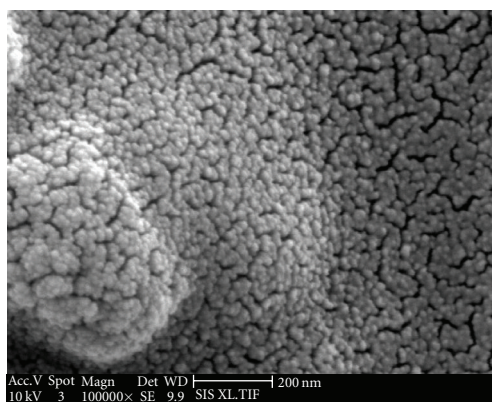
^(a)Using Scherrer equation: $D = 0.9\lambda / (B \cos \theta)$, where $\lambda = 0.15418$ nm.



(a)



(b)



(c)

FIGURE 3: Scanning electron micrographs of the surface of TiO₂ films made from the precursor sol containing (a) no nanopowder, (b) ANPSGF-MC-Ag, and (c) MPC500SGF-MC-Ag. All the samples are heat treated for 1 hour at 500°C.

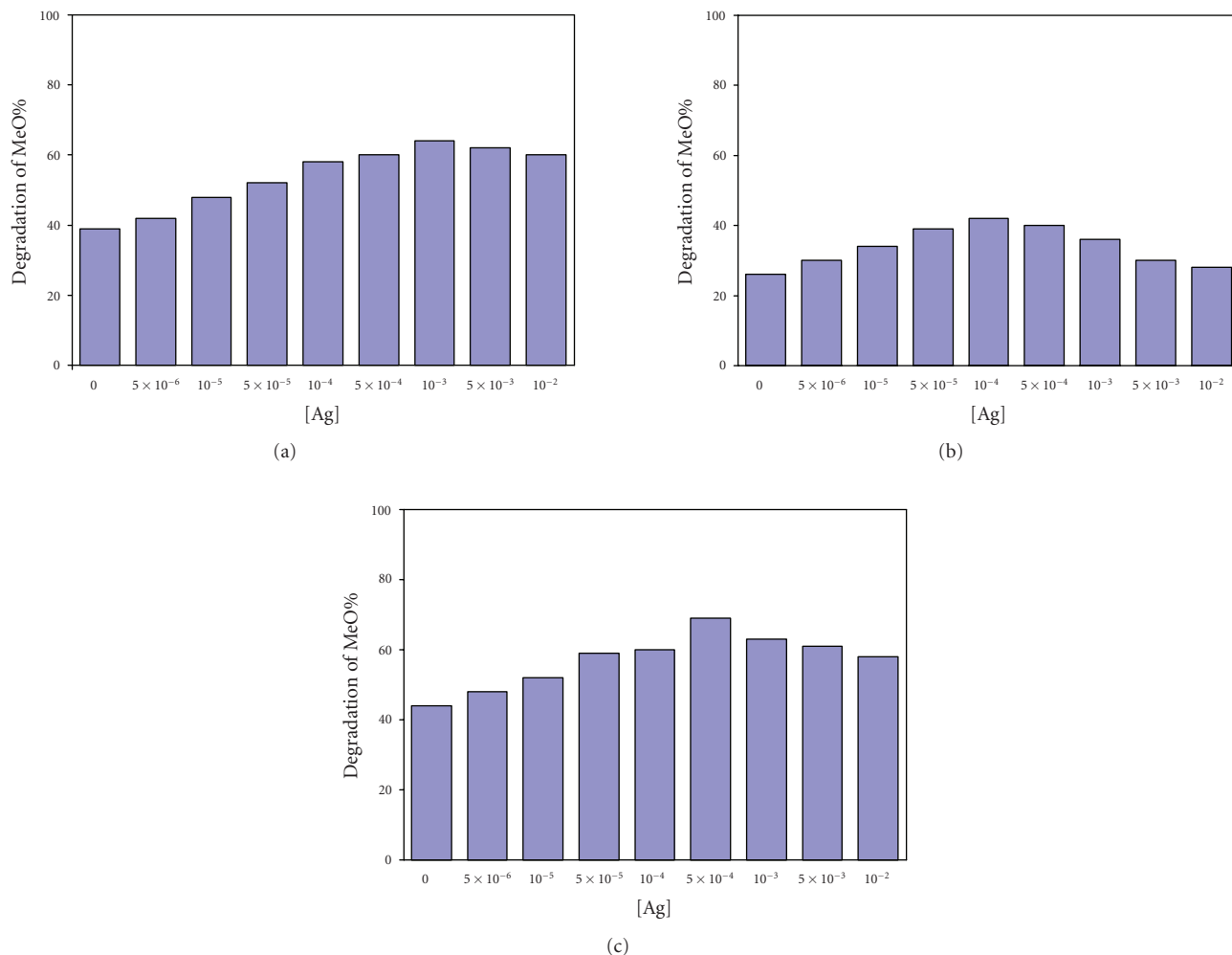


FIGURE 4: Effect of the Ag loading in the composite films on the photocatalytic activity, (a) ANPSGF-MC-Ag, (b) MPC500SGF-MC-Ag, and (c) P25SGF-MC-Ag. Conditions of the photocatalytic experiments: one-time spin coating ($75 \text{ mm} \times 25 \text{ mm} \times 1 \text{ mm}$) was used as photocatalyst and irradiated with two 8 W UV-A ($\lambda = 365 \text{ nm}$) at a distance of 5 cm from the top of the solutions. 20 mL of the dye solutions with initial concentration of 5 mg/L at pH = 4.5.

(64%) is observed for ANPSGF-MC-Ag films immersed in 10^{-3} M AgNO_3 solution. Further increase of the Ag^+ concentration results in a considerable efficiency decrease. For instance, for ANPSGF-MC films dipped in 10^{-2} M AgNO_3 solution the MO decomposition percentage goes to 58%. More spectacularly, it falls to lower decomposition percentage for more concentrated AgNO_3 , a value lower than that obtained with the nonsupported composite film. It is suspected that superfluous Ag additions reduced the surface activation sites of TiO_2 and thus the degradation efficiency decreased.

As shown in Figures 4(b) and 4(c), the similar results are obtained for other nanostructure composite films (MPC500SGF-MC-Ag and P25SGF-MC-Ag). A maximum (42%) is observed for the MPC500SGF-MC-Ag films immersed in 10^{-4} M AgNO_3 solution, while for P25SGF-MC-Ag films, maximum degradation percentage (69%) is observed after immersion in 5×10^{-4} M AgNO_3 solution. It is interesting to note that the composite film with P25 has more

photo efficiency than other one, however photoefficiency of ANPSGF-MC after coating by Ag have promoted more than other one comparing to the pure titania films. According to the results, ANPSGF-MC composite films have more ability to dope with Ag particles comparing other composite films (P25SGF-MC and MPC500SGF-MC), which is confirmed by difference in grain size of TiO_2 in these composite films.

Sol-gel derived porous and nanostructure composite film prepared by P25 (P25SGF-MC) after coating with Ag exhibited the best photocatalytic performance. It has been reported that porous TiO_2 films [4] or Ag-doped TiO_2 films [13] show an enhanced photocatalytic efficiency. In the present study, we have demonstrated the improved photocatalytic performance with both porous structure and Ag additions. Practical applications of these films are highly potential.

Figures 5(a), 5(b), and 5(c) show the photodegradation results of the TiO_2 nanostructure composite films, after deducting both the self-degradation of methyl orange under

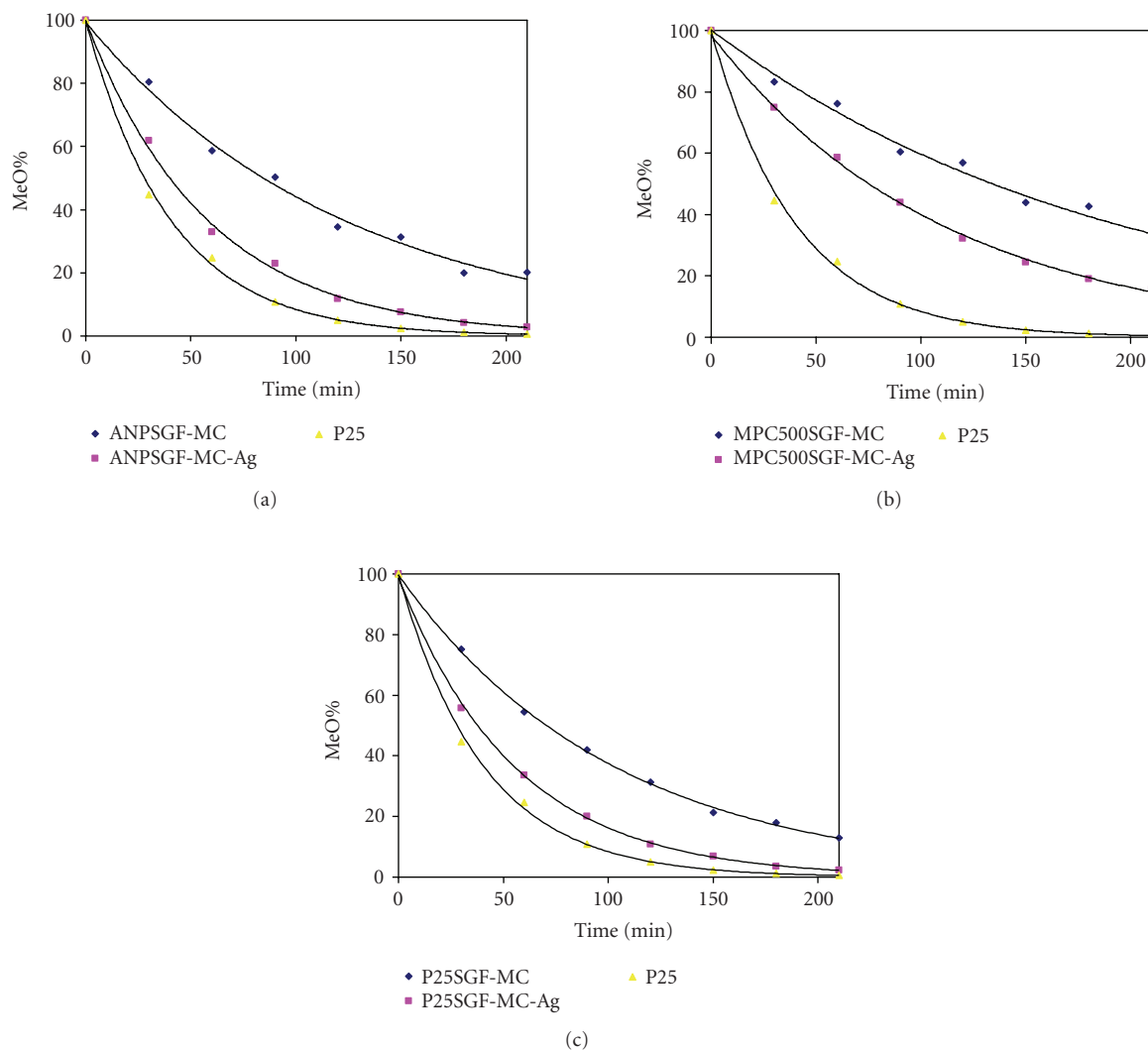


FIGURE 5: (a) Plot of the percent of MO remaining after photodegradation versus irradiation time in the presence of (a) \blacklozenge ANPSGF-MC composite film, (b) \blacksquare ANPSGF-MC-Ag composite film (immersed in 10^{-3} M AgNO_3 solution), and (c) \blacktriangle TiO_2 suspension. Conditions of the photocatalytic experiments: one-time spin coating ($75 \text{ mm} \times 25 \text{ mm} \times 1 \text{ mm}$) was used as photocatalyst and irradiated with two 8 W UV-A ($\lambda = 365 \text{ nm}$) at a distance of 5 cm from the top of the solutions. 20 mL of the dye solutions with initial concentration of 5 mg/L at pH = 4.5. (b) Plot of the percent of MO remaining after photodegradation versus irradiation time in the presence of (a) \blacklozenge MPC500SGF-MC composite film, (b) \blacksquare MPC500SGF-MC-Ag composite film (immersed in 10^{-3} M AgNO_3 solution), and (c) \blacktriangle TiO_2 suspension. Conditions of the photocatalytic experiments: one-time spin coating ($75 \text{ mm} \times 25 \text{ mm} \times 1 \text{ mm}$) was used as photocatalyst and irradiated with two 8 W UV-A ($\lambda = 365 \text{ nm}$) at a distance of 5 cm from the top of the solutions. 20 mL of the dye solutions with initial concentration of 5 mg/L at pH = 4.5. (c) Plot of the percent of MO remaining after photodegradation versus irradiation time in the presence of (a) \blacklozenge P25SGF-MC composite film, (b) \blacksquare P25SGF-MC-Ag composite film (immersed in 10^{-3} M AgNO_3 solution), and (c) \blacktriangle TiO_2 suspension. Conditions of the photocatalytic experiments: one-time spin coating ($75 \text{ mm} \times 25 \text{ mm} \times 1 \text{ mm}$) was used as photocatalyst and irradiated with two 8 W UV-A ($\lambda = 365 \text{ nm}$) at a distance of 5 cm from the top of the solutions. 20 mL of the dye solutions with initial concentration of 5 mg/L at pH = 4.5.

UV and physical adsorption. Methyl orange photodegradation kinetics permitted to directly compare the performance of the silver-modified photocatalysts to the nonsupported materials. It is clear that under the experimental conditions used, all photocatalytic curves follow first-order reaction kinetics. Initial reaction conditions provide realistic comparison of the photodegradation rates. To a reasonable approximation, the slope of the fitted lines corresponds to a relative pseudo-first-order rate constant [28]. Kinetic

parameters after 2 hours of illumination for decolorization of MO are summarized in Table 3.

It is obvious that all nanostructure composite TiO_2 films after coating by Ag are more efficient catalysts, comparing to the pure titania film. This can be explained on the basis of surface characteristics. Complete pollutant decolorization for P25SGF-MC-Ag was achieved after 120 minutes of illumination and for P25SGF-MC film after about 240 minutes, respectively. As shown in Figures 4(a) and 4(b) and Table 3,

TABLE 3: The rate constant for degradation of MO for nanostructure composite films with different mol percentages of silver.

| Concentration of AgNO ₃ dipping solution (M) | Rate constant (min ⁻¹) | | |
|---|------------------------------------|--------------|-----------|
| | ANPSGF-MC | MPC500SGF-MC | P25SGF-MC |
| 0 | 0.0081 | 0.0052 | 0.0098 |
| 5 × 10 ⁻⁶ | 0.0098 | 0.0062 | 0.0115 |
| 1 × 10 ⁻⁵ | 0.0115 | 0.0069 | 0.0132 |
| 5 × 10 ⁻⁵ | 0.0128 | 0.0081 | 0.0158 |
| 1 × 10 ⁻⁴ | 0.0151 | 0.009 | 0.0161 |
| 5 × 10 ⁻⁴ | 0.0162 | 0.0082 | 0.0181 |
| 1 × 10 ⁻³ | 0.0173 | 0.0064 | 0.0163 |
| 5 × 10 ⁻³ | 0.0166 | 0.0060 | 0.0158 |
| 1 × 10 ⁻² | 0.0153 | 0.0051 | 0.0143 |

the silver-modified composite film prepared by MPC500 (MPC500SGF-MC-Ag) showed lower photocatalytic activity than the film prepared by ANP (ANPSGF-MC-Ag). The impact of surface area on the photocatalytic activity is clearly demonstrated, where MPC500SGF-MC-Ag film shows significantly lower degradation rate than ANPSGF-MC-Ag. As a result, P25SGF-MC-Ag nanostructure composite films show more photoefficiency than other composite films, which was as expected due to presence of rutile phase in Degussa P-25 powder. We encapsulated Degussa P25 TiO₂ instead of preparing the films in order to have a combination of anatase and rutile phases in the TiO₂ films, since the presence of rutile phase enhances the activity of the anatase phase by serving as an electrons' sink. In fact, by encapsulating P25 TiO₂ within mesoporous TiO₂ film, it should be possible to optimize the two components of the composite film, for example, by incorporating more active TiO₂ particles [14]. In this work, it was found that an incorporation of commercial anatase nanoparticles into the TiO₂ thin films, then coating them by Ag provides advantages in the photodecomposition of TiO₂ by eliminating the filtration of the solutions, therefore, allowing for more efficient processes.

To evaluate the catalytic strength changes due to immobilization of the catalysts and compare the films efficiency to the Degussa P25 powder, the film weight was measured. The slurry concentration of TiO₂ was then adjusted to meet the exact quantity of TiO₂ nanostructure composite immobilized film, in order to safely compare the obtained results. Thus, a pollutant solution (20 mL) was also photolyzed in the presence of a suspension (dispersion) of Degussa P25 powder (0.0032 g = 160 ppm) and the results are represented in Figures 5(a), 5(b), and 5(c). The slope for the slurry is greater than that of the silver-modified nanostructure composite films, showing a higher efficiency as a photocatalyst. Complete depolarization of MO occurs in less than 90 minutes. It is worth mentioning that on composite film samples, only a part of the catalyst is exposed to the pollutant solution and it can, therefore, be photocatalytically active. As a result, a decrease in the overall photocatalytic performance of composite films compared to slurry solution is expected. This difference can be easily understood, if one considers that the photocatalytic process

is a surface and not a volume or mass phenomenon. The active photocatalyst is the illuminated TiO₂ material, which can be in contact with the organic pollutant. As Degussa's powder surface area is very high (50 m²g⁻¹), the slurry's surface is much higher than the film's real external surface and the silver synergetic action cannot promote such a high efficiency. However, the specific surface area of most of the composite samples, at the heat treatment (500°C), changes mostly due to the increase in the surface area of the sol-gel derived TiO₂ (titania sol), as a result of the decomposition and oxidation of the organic residues (i.e., MC), the evaporation of the solvent and excess water, and so forth.

4. CONCLUSION

In the present study, we have prepared nanostructure composite films developed on microscope glass slides by a sol-gel spin coating technique and were modified by silver deposition, characterized and successfully tested for the photocatalytic degradation of the pollutant methyl orange. TiO₂/Ag films were obtained by introducing MC microspheres and calcining at a temperature of 500°C. All the prepared composite films exhibited anatase-phase TiO₂ as determined by XRD. MC-TiO₂ films with Ag additions exhibited porous nanostructure but differed from that of porous TiO₂ film. The photocatalytic properties of the prepared thin films were evaluated by degrading methyl orange under UV. ANPSGF-MC-Ag, MPC500SGF-MC-Ag, and P25SGF-MC-Ag composite films exhibited 64%, 42%, and 69% degradation, respectively. By making the TiO₂ film porous and adding Ag element, the photocatalytic performance of the TiO₂-based composite films can be improved significantly.

ACKNOWLEDGMENTS

The authors wish to thank the Center of Excellency (Chemistry), University of Isfahan for financially supporting this work and Islamic Azad University, Najafabad Branch for their partial support.

REFERENCES

- [1] M. O. Abou-Helal and W. T. Seeber, "Preparation of TiO₂ thin films by spray pyrolysis to be used as a photocatalyst," *Applied Surface Science*, vol. 195, no. 1–4, pp. 53–62, 2002.
- [2] J. Yu, X. Zhao, and Q. Zhao, "Photocatalytic activity of nanometer TiO₂ thin films prepared by the sol-gel method," *Materials Chemistry and Physics*, vol. 69, no. 1–3, pp. 25–29, 2001.
- [3] S. K. Zheng, T. M. Wang, G. Xiang, and C. Wang, "Photocatalytic activity of nanostructured TiO₂ thin films prepared by dc magnetron sputtering method," *Vacuum*, vol. 62, no. 4, pp. 361–366, 2001.
- [4] D. Dumitriu, A. R. Bally, C. Ballif, et al., "Photocatalytic degradation of phenol by TiO₂ thin films prepared by sputtering," *Applied Catalysis B*, vol. 25, no. 2-3, pp. 83–92, 2000.
- [5] S.-H. Lee, M. Kang, S. M. Cho, et al., "Synthesis of TiO₂ photocatalyst thin film by solvothermal method with a small amount of water and its photocatalytic performance," *Journal of Photochemistry and Photobiology A*, vol. 146, no. 1-2, pp. 121–128, 2001.
- [6] R. Paily, A. DasGupta, N. DasGupta, et al., "Pulsed laser deposition of TiO₂ for MOS gate dielectric," *Applied Surface Science*, vol. 187, no. 3-4, pp. 297–304, 2002.
- [7] J. Aarik, A. Aidla, T. Uustare, et al., "Atomic layer deposition of TiO₂ thin films from TiI₄ and H₂O," *Applied Surface Science*, vol. 193, no. 1–4, pp. 277–286, 2002.
- [8] D. Byun, Y. Jin, B. Kim, J. K. Lee, and D. Park, "Photocatalytic TiO₂ deposition by chemical vapor deposition," *Journal of Hazardous Materials*, vol. 73, no. 2, pp. 199–206, 2000.
- [9] M. L. Hitchman and F. Tian, "Studies of TiO₂ thin films prepared by chemical vapour deposition for photocatalytic and photoelectrocatalytic degradation of 4-chlorophenol," *Journal of Electroanalytical Chemistry*, vol. 538–539, pp. 165–172, 2002.
- [10] A. Mills, N. Elliot, I. P. Parkin, S. A. O'Neill, and R. J. Clark, "Novel TiO₂ CVD films for semiconductor photocatalysis," *Journal of Photochemistry and Photobiology A*, vol. 151, no. 1–3, pp. 171–179, 2002.
- [11] V. G. Bessergenev, I. V. Khmelinskii, R. J. F. Pereira, V. V. Krisuk, A. E. Turgambaeva, and I. K. Igumenov, "Preparation of TiO₂ films by CVD method and its electrical, structural and optical properties," *Vacuum*, vol. 64, no. 3-4, pp. 275–279, 2002.
- [12] V. G. Bessergenev, R. J. F. Pereira, M. C. Mateus, I. V. Khmelinskii, E. Burkel, and R. C. Nicula, "TiO₂ thin film synthesis from complex precursors by CVD, its physical and photocatalytic properties," *International Journal of Photoenergy*, vol. 5, no. 2, pp. 99–105, 2003.
- [13] N. Kaliwoh, J.-Y. Zhang, and I. W. Boyd, "Characterisation of TiO₂ deposited by photo-induced chemical vapour deposition," *Applied Surface Science*, vol. 186, no. 1–4, pp. 241–245, 2002.
- [14] Y. Djaoued, S. Badilescu, P. V. Ashrit, D. Bersani, P. P. Lottici, and R. Brüning, "Low temperature sol-gel preparation of nanocrystalline TiO₂ thin films," *Journal of Sol-Gel Science and Technology*, vol. 24, no. 3, pp. 247–254, 2002.
- [15] M. Keshmiri, M. Mohseni, and T. Troczynski, "Development of novel TiO₂ sol-gel-derived composite and its photocatalytic activities for trichloroethylene oxidation," *Applied Catalysis B*, vol. 53, no. 4, pp. 209–219, 2004.
- [16] R. Isono, T. Yoshimura, and K. Esumi, "Preparation of Au/TiO₂ nanocomposites and their catalytic activity for DPPH radical scavenging reaction," *Journal of Colloid and Interface Science*, vol. 288, no. 1, pp. 177–183, 2005.
- [17] S. Rodrigues, K. T. Ranjit, S. Uma, I. N. Martyanov, and K. J. Klabunde, "Single-step synthesis of a highly active visible-light photocatalyst for oxidation of a common indoor air pollutant: acetaldehyde," *Advanced Materials*, vol. 17, no. 20, pp. 2467–2471, 2005.
- [18] P. N. Kapoor, S. Uma, S. Rodriguez, and K. J. Klabunde, "Aerogel processing of MTi₂O₅ (M = Mg, Mn, Fe, Co, Zn, Sn) compositions using single source precursors: synthesis, characterization and photocatalytic behavior," *Journal of Molecular Catalysis A*, vol. 229, no. 1-2, pp. 145–150, 2005.
- [19] W. Choi, A. Termin, and M. R. Hoffmann, "The role of metal ion dopants in quantum-sized TiO₂: correlation between photoreactivity and charge carrier recombination dynamics," *Journal of Physical Chemistry*, vol. 98, no. 51, pp. 13669–13679, 1994.
- [20] S. Usseglio, A. Damin, D. Scarano, S. Bordiga, A. Zecchina, and C. Lamberti, "(I₂)_n encapsulation inside TiO₂: a way to tune photoactivity in the visible region," *Journal of the American Chemical Society*, vol. 129, no. 10, pp. 2822–2828, 2007.
- [21] H. Luo, T. Takata, Y. Lee, J. Zhao, K. Domen, and Y. Yan, "Photocatalytic activity enhancing for titanium dioxide by co-doping with bromine and chlorine," *Chemistry of Materials*, vol. 16, no. 5, pp. 846–849, 2004.
- [22] D. Chatterjee and S. Dasgupta, "Visible light induced photocatalytic degradation of organic pollutants," *Journal of Photochemistry and Photobiology C*, vol. 6, no. 2-3, pp. 186–205, 2005.
- [23] K. Naoi, Y. Ohko, and T. Tatsuma, "TiO₂ films loaded with silver nanoparticles: control of multicolor photochromic behavior," *Journal of the American Chemical Society*, vol. 126, no. 11, pp. 3664–3668, 2004.
- [24] W. Chen, J. Zhang, Q. Fang, et al., "Sol-gel preparation of thick titania coatings aided by organic binder materials," *Sensors and Actuators B*, vol. 100, no. 1-2, pp. 195–199, 2004.
- [25] H. Gerischer and A. Heller, "The role of oxygen in photooxidation of organic molecules on semiconductor particles," *Journal of Physical Chemistry*, vol. 95, no. 13, pp. 5261–5267, 1991.
- [26] C. A. K. Gouvêa, F. Wypych, S. G. Moraes, N. Durán, and P. Peralta-Zamora, "Semiconductor-assisted photodegradation of lignin, dye, and kraft effluent by Ag-doped ZnO," *Chemosphere*, vol. 40, no. 4, pp. 427–432, 2000.
- [27] M. J. Height, S. E. Pratsinis, O. Mekasuwandumrong, and P. Praserthdam, "Ag-ZnO catalysts for UV-photodegradation of methylene blue," *Applied Catalysis B*, vol. 63, no. 3-4, pp. 305–312, 2006.
- [28] S. Chen and U. Nickel, "Controllable exciton bleaching and recovery observed in ZnO-Ag hybrid nanometre-sized particles," *Chemical Communications*, no. 2, pp. 133–134, 1996.
- [29] T. Abe, E. Suzuki, K. Nagoshi, K. Miyashita, and M. Kaneko, "Electron source in photoinduced hydrogen production on Pt-supported TiO₂ particles," *Journal of Physical Chemistry B*, vol. 103, no. 7, pp. 1119–1123, 1999.
- [30] V. Subramanian, E. E. Wolf, and P. V. Kamat, "Semiconductor-metal composite nanostructures. To what extent do metal nanoparticles improve the photocatalytic activity of TiO₂ films?" *Journal of Physical Chemistry B*, vol. 105, no. 46, pp. 11439–11446, 2001.
- [31] V. Subramanian, E. E. Wolf, and P. V. Kamat, "Green emission to probe photoinduced charging events in ZnO-Au nanoparticles. Charge distribution and Fermi-level equilibration,"

- Journal of Physical Chemistry B*, vol. 107, no. 30, pp. 7479–7485, 2003.
- [32] W. Y. Teoh, L. Mädler, D. Beydoun, S. E. Pratsinis, and R. Amal, “Direct (one-step) synthesis of TiO₂ and Pt/TiO₂ nanoparticles for photocatalytic mineralisation of sucrose,” *Chemical Engineering Science*, vol. 60, no. 21, pp. 5852–5861, 2005.
- [33] M. H. Habibi and M. Nasr-Esfahani, “Preparation, characterization and photocatalytic activity of a novel nanostructure composite film derived from nanopowder TiO₂ and sol-gel process using organic dispersant,” *Dyes and Pigments*, vol. 75, no. 3, pp. 714–722, 2007.
- [34] M. I. Cabrera, A. C. Negro, O. M. Alfano, and A. E. Cassano, “Photocatalytic reactions involving hydroxyl radical attack,” *Journal of Catalysis*, vol. 172, no. 2, pp. 380–390, 1997.
- [35] H. P. Klug and L. E. Alexander, *X-ray Diffraction Procedures*, chapter 9, John Wiley & Sons, New York, NY, USA, 1954.
- [36] D. C. Hague and M. J. Mayo, “The effect of crystallization and a phase transformation on the grain growth of nanocrystalline titania,” *Nanostructured Materials*, vol. 3, no. 1–6, pp. 61–67, 1993.
- [37] I. M. Arabatzis, S. Antonaraki, T. Stergiopoulos, et al., “Preparation, characterization and photocatalytic activity of nanocrystalline thin film TiO₂ catalysts towards 3,5-dichlorophenol degradation,” *Journal of Photochemistry and Photobiology A*, vol. 149, no. 1–3, pp. 237–245, 2002.

Research Article

Characterization and Evaluation of the Efficiency of TiO₂/Zinc Phthalocyanine Nanocomposites as Photocatalysts for Wastewater Treatment Using Solar Irradiation

Antonio E. H. Machado,¹ Marcela D. França,¹ Valdemir Velani,² Gabriel A. Magnino,¹ Hosana M. M. Velani,² Flávio S. Freitas,¹ Paulo S. Müller Jr.,² Christian Sattler,³ and Martin Schmücker⁴

¹Laboratório de Fotoquímica, Instituto de Química, Universidade Federal de Uberlândia, P.O. Box 593, 38400-902 Uberlândia, MG, Brazil

²Nanobrax, Soluções Tecnológicas e Prestação de Serviços Ltda., Avenida João Naves de Ávila 2121, Bloco 5L, Sala 05, 38408-100 Uberlândia, MG, Brazil

³German Aerospace Center, Institute of Technical Thermodynamics, Solar Research, Linder Höhe, 51147 Köln Porz, Germany

⁴German Aerospace Center, Institute of Materials Research, Linder Höhe, 51147 Köln Porz, Germany

Correspondence should be addressed to Antonio E. H. Machado, aeduardo@ufu.br

Received 28 August 2007; Revised 23 January 2008; Accepted 17 March 2008

Recommended by Leonardo Palmisano

This work reports the characterization of composites prepared by the association between zinc phthalocyanine (ZnPc) and titanium dioxide. These composites are better photocatalysts for wastewater decontamination mediated by solar radiation than pure TiO₂, performance that remains even when reused. The UV-Vis diffuse reflectance absorption spectra show for these composites two intense absorption bands. The first covers the ultraviolet and part of the visible spectrum region until 460 nm (2.7 eV), whereas the second, nonstructured, goes from 475 nm until the near infrared with an absorption peak at 683 nm attributed to the Q band of ZnPc. The production of additional e⁻/h⁺ pairs by these aggregates when photoexcited, their capability to act as charge carrier, the thickness and regularity of their distribution on the TiO₂ surface seem to be important parameters for the performance observed for these composites.

Copyright © 2008 Antonio E. H. Machado et al. This is an open access article distributed under the Creative Commons Attribution License, which permits unrestricted use, distribution, and reproduction in any medium, provided the original work is properly cited.

1. INTRODUCTION

Water recycling by destruction of the pollutant load using advanced oxidative processes (AOPs) has been suggested as an alternative for environmental remediation [1–10]. Between the AOP, heterogeneous photocatalysis can be considered as one of the new “advanced oxidation technologies” (AOTs) for air and water purification [5–7].

For many reasons, TiO₂ has been considered as the best choice among the semiconductor oxides with photocatalytic activity for wastewater treatment, aiming the elimination of organic and inorganic species [2, 3, 5–10]. However, its band-gap energy, between 3.0 and 3.2 eV [2, 3], limits its application when solar photocatalysis is desirable [3, 8, 11, 12]. To get round this problem, many research groups have proposed alternatives to amplify the photocatalytic activity

of TiO₂, improving the pickup of ultraviolet radiation and also making feasible the use of components of the visible radiation [8–20].

Electron transfer at the interface between a photoactive species and the semiconductor surface is a fundamental aspect for organic semiconductor devices [21, 22]. Certain photoactive compounds have proven to be able, when electronically excited, to inject electrons in the conduction band of semiconductors [21–33], increasing the performance of dye-sensitized solar cells. In particular, ultrafast charge separation led by electron injection from electronically excited photoactive molecules to a conduction band of a wide-gap metal oxide, and a good electronic coupling between dye molecules and surface of the substrate are key steps for improving the performance of these materials [23–25].

In this work, we report the characterization by different methodologies, such as diffuse reflectance absorption spectra, specific surface area, thickness of ZnPc coating, and their distribution on the TiO₂ particles, evaluated by transmission electron microscopy (TEM) coupled to energy disperse X-ray (EDX) of composites prepared by the association between zinc phthalocyanine (ZnPc) and titanium dioxide. Additionally, the quantum yield of hydroxyl radical production, the capacity of the studied composites to perform the degradation of organic matter present in wastewaters in reactions mediated by solar irradiation, and the possibility of reuse of such photocatalysts were also estimated.

2. EXPERIMENTAL

2.1. Chemicals

Titanium dioxide, P25, was nicely provided by Degussa Hüls. Zinc phthalocyanine (ZnPc), 98%, acetylacetone, 99%, and a sodium salt of lignosulphonic acid ((LSA), possessing a mean molecular mass of 52,000 D), were purchased from Sigma - Aldrich (São Paulo, Brasil). Methanol, UV/HPLC, dimethylformamide and dimethylsulfoxide, P.A., and ethanol, 95%, were purchased from Vetec Química Fina (Rio de Janeiro, Brasil). Ammonium phosphate buffer (pH 6.0) was prepared using a standard procedure. Potassium ferrioxalate solutions (10^{-2} mol L⁻¹) were used as chemical actinometer [34]. All chemicals were used as received.

2.2. Preparation of ZnPc/TiO₂ composites

The composites were prepared coating TiO₂ particles with zinc phthalocyanine [8, 13, 14], dissolved in a solvent mixture containing 50% dimethylsulphoxide, 20% ethanol, and 30% dimethylformamide, at 60°C. The necessary amount of TiO₂ (P25, Degussa), covering the compositions of 1.0%, 1.6%, 2.5%, 5.0%, 7.5%, and 10%, was gradually added to the dye solution, under stirring and heating, resulting in a suspension with homogeneous appearance. The suspension was maintained, stirred, and heated until almost complete solvent evaporation. The material, presenting a creamy consistency, was washed several times with distilled water, under vigorous stirring, to remove residues and remaining organic solvent. Next, the composite is dried at a temperature between 70 and 80°C, for 24 hours. After milling, the final product is a finely divided bluish powder with improved photocatalytic activity [8–14], insoluble in water, capable to give stable suspensions in this solvent.

2.3. Characterization

The diffuse reflectance absorption spectra of the composites were recorded using a Shimadzu UV-2501PC spectrophotometer equipped with an integrating sphere. Barium sulphate was used as reference in these experiments.

The specific surface area of the composites was estimated from BET (Brunauer, Emmett, and Teller) isotherms, based on the adsorption of gaseous nitrogen, using a MICROMERITICS ASAP 2000 system.

The thickness of ZnPc coating and their distribution on the TiO₂ surface was evaluated by transmission electron microscopy (TEM) coupled to energy disperse X-ray (EDX). TEM investigations were carried out using a Phillips Tecnai F30 microscope equipped with a field emission gun, a scanning transmission electron microscope (STEM) and an EDX analytical system. The specimens for TEM analysis were prepared by crushing the powder aggregates in an agate mortar, dispersing in distilled water and depositing onto a carbon film supported by a 300 mesh copper grid.

All measurements were done with unused catalyst.

2.4. Quantum yield of hydroxyl radical production ($\Phi_{HO\cdot}$)

The quantum yield of hydroxyl radicals production was estimated using a procedure proposed by Gao et al. [35], based on Nash's method [36]. It consists in the quantification of the formaldehyde concentration formed during the oxidation of methanol by the hydroxyl radicals [37], generated during the photocatalytic process. An aqueous suspension (5 mL), 0.2 mol L⁻¹ in methanol, containing TiO₂ or one of the composites (50 mg L⁻¹), placed in a closed borosilicate glass reactor with a cooling jacket, in which water was continuous circulated to minimize heating by IR irradiation, was photolysed during 30 minutes using a 400 W high-pressure mercury vapor lamp (HPL-N) positioned at 10 cm from the reactor. The suspension was mixed during 20 minutes (magnetic stirrer), prior to illumination and during it.

The radiation was filtered by the borosilicate glass (2 mm thick, cutting below 300 nm), to guarantee the excitation of the catalysts under equivalent conditions. Due to technical limitations, only the light intensity in the UV-A region was monitored during the irradiation. This was done using a solar light PMA-2100 radiometer. The illuminated area was 3.0 cm².

Formaldehyde formed due to the oxidation of methanol was determined by the Nash method [36], which is based on the Hantzsch reaction: an 1.5 mL aliquot of the photolysed sample, previously filtered using a PTFE Millipore filter (0.45 μ m of porosity), was added to 1.5 mL of 0.18 mol L⁻¹ ammonium phosphate buffer (pH = 6.0) and 15 μ L of acetylacetone. A yellow color gradually develops owing to the synthesis of diacetyl dihydrolutidine [36]. Under optimum conditions, the molecular extinction in terms of formaldehyde has a smooth maximum of $8,000$ M⁻¹ cm⁻¹ at 412 nm, regardless of dilution. The needed spectrophotometric measurements were done in a range covering this wavelength.

The photonic flux [34] of the mercury lamp was evaluated in the range between 295 and 815 nm using a radiometric/photometric setup built with components furnished by Ocean Optics, Inc. (an SD2000 UV/VIS diode array spectrometer coupled to a personal computer, a fiber optic irradiance probe with a detection head of 0.3 cm diameter, possessing a cosine corrector). These measurements were done using an integration time of 50 milliseconds. A 1 mW He-Ne laser (632.8 nm), two semiconductor lasers (650 and



FIGURE 1: Details of the CPC reactor experimental setup.

670 nm), and calibrated LEDs (380, 450, 470, and 640 nm of peak output) were used as standards for the quantification of the number of emitted photons. The radiation that can be effectively absorbed by these catalysts was considered as being in the 295 to 710 nm range, with a photonic flux of about of 3.3×10^{-6} einsteins s^{-1} .

2.5. Photodegradation essays

The capacity of the studied composites to degrade organic matter present in wastewaters, in reactions mediated by solar irradiation, and the possibility of reusing of such photocatalysts was evaluated monitoring the decrease of the organic matter content during the treatment of three 50 L batches of a model effluent (an aqueous solutions containing 160 mg L^{-1} of LSA) [8]. The reactions were done at pH 3, with the addition of 1 mL of H_2O_2 30% v/v per liter of effluent (about 9 mM), and monitored by chemical oxygen demand (COD) analysis of aliquots of effluent samples collected at different accumulated doses of UV-A radiation. (This option was due to operational limitations. The spectral pattern of the visible light does not change significantly during the execution of the experiments.) To evaluate the observed (global) reaction kinetics, the temporal variations were substituted by the UV-A accumulated dose, which warrants the reproduction of these experiments under different latitude and weather conditions.

A same sample (100 mg per liter of effluent) of the photocatalyst, containing initially 2.5% of ZnPc, was used to treat the three effluent batches. The treatment of each batch was performed using a compound parabolic concentrator (CPC) reactor, after the recovery of the photocatalyst used in the previous experiment. The CPC reactor was constructed in our laboratory [11, 12]. It was designed to process up to 150 L of effluent. This reactor consists in a module with an aperture of about 1.62 m^2 , elevation angle adjusted to the latitude of Uberlândia, Brasil (19°S), containing 10 borosilicate glass tubes (external diameter 32 mm, wall thickness of 1.4 mm, and length of 1500 mm), mounted in parallel, each on double parabolic-shaped aluminum reflector surfaces (Figure 1). The concentration ratio is about 1.0 and the reflectivity of the reflector surface within the band gap of TiO_2 (300–390 nm) is 89.5%. The flow rate is 34 L min^{-1} . The effluent was circulated in the reactor which is open to guarantee a sufficient oxygen concentration in the bulk. The fluid flow

rate in the tubing was chosen to assure a turbulent transport regimen of the effluent, warranting a better homogenization of the suspension. This and the fact that the irradiated effluent returns to the reservoir by a tubing positioned 50 cm above the surface of the remaining effluent guarantees an adequate aeration of the effluent during the photocatalytic process. The fittings and piping were made of polypropylene.

This reactor is similar to the SOLARDETOX prototypes used at the Plataforma Solar de Almería and the German Aerospace Center, Cologne [38, 39], but the mirrors were calculated exclusively for this reactor and the ratio between irradiated surface and dark tubing is higher. Since the BRITE EURAM SOLARDETOX project CPC-type reactors are known as very powerful solar reactors for water treatment up to a pilot plant scale [38, 39].

As reference, an additional effluent batch was treated under similar conditions using pure TiO_2 P25 as catalyst.

For all reactions, hydrogen peroxide (30 mg L^{-1}) was used as additional source of reactive species [8]. The incident UV-A radiation was monitored using a solar light PMA-2100 radiometer. All reactions were stopped when the accumulated dose of UV-A radiation reached 900 kJ m^{-2} .

The COD measurements were based on an Environmental Protection Agencies recommended method [40, 41], in which an aliquot of the effluent reacts under heating and closed reflux, at 423 K during 2 hours, reducing dichromate ions to chromic ions in a strongly acid medium. From absorbance measurement, done at 620 nm using a Hach DR-4000U spectrophotometer and a resident program, the COD of the samples was determined.

3. RESULTS AND DISCUSSION

3.1. Diffuse reflectance spectra

Figure 2 presents the diffuse reflectance spectra of ZnPc, TiO_2 , and some of the studied composites.

Comparison of these figures shows that the UV-Vis absorption spectrum of these composites is not simply the result of an additive effect between the absorption spectra of TiO_2 and zinc phthalocyanine (ZnPc) (compare Figures 2(a), 2(e), and 2(f)). The later figure corresponds to the diffuse reflectance spectra of pure ZnPc. The intense absorption peak at 552 nm, is due to the Q band, relative to $\pi \rightarrow \pi^*$ transitions [42, 43]. The observed blue shift for this peak can be attributed to noninteracting molecules and the absence of interaction between them and solvents [42, 44]. The Soret band is evident in the ultraviolet, with an absorption maximum at 301 nm. A low intensity and nonstructured absorption band with the absorption peak centered at 416 nm is related to an $n \rightarrow \pi^*$ transition linking the e_u azanitrogen lone pair orbital with the e_g LUMO [43, 45]. A set of three very small low-energy bands, above the Q one, can also be observed. The spectral structure of ZnPc and TiO_2 is lost in the composites. For the spectrum of the composite with 2.5% m/m of ZnPc obtained using pure TiO_2 as a reference, for example, the bands in the ultraviolet and visible are very different from that observed for pure ZnPc. In the visible, presents a large and intense three peak band

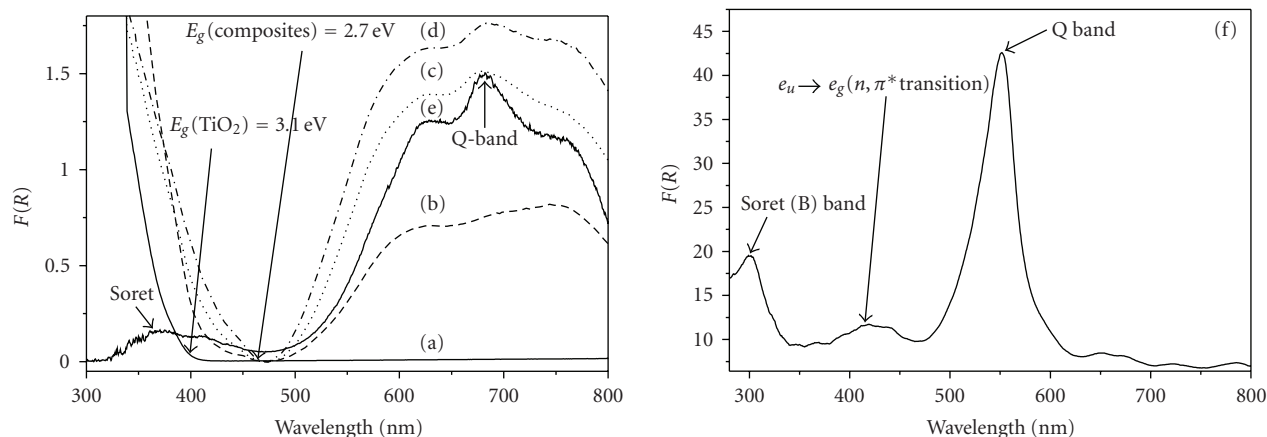


FIGURE 2: Diffuse reflectance spectra of TiO_2/ZnPC composites, prepared with different percent in mass of ZnPC: (a) TiO_2 P25. Composite containing: 1.0% of ZnPC (b); 2.5% of ZnPC (c); 5.0% of ZnPC (d); (e) composite containing 2.5% of ZnPC (TiO_2 P25 was used as reference), showing the Soret (370 nm) and Q (683 nm) bands, typical of ZnPC; (f) diffuse reflectance spectrum of pure ZnPC. Barium sulphate was used as reference for (a) to (d).

centered by a red-shifted Q band, with maximum at 683 nm [12]. The Soret (B) band presents a different shape and is red shifted when compared to its equivalent in Figure 2(f).

Thus, these absorption spectra are very different from the typical absorption profiles of TiO_2 (Figure 2(a)) and pure ZnPC in the solid state (Figure 2(f)) and in very dilute liquid solutions [44]. The absorption spectrum of these composites is characterized by an intense absorption band below 460 nm, and a large and intense absorption band, above 475 nm, most probably due to an extense superposition of the electronic states of TiO_2 and ZnPC, indicating electronic interaction between both species, resulting in several common electronic states for both species. Szaciłowski et al. [46] reported in a recent work that the diffuse reflectance spectrum of TiO_2 /prussian blue does not correspond directly to the sum of the spectra of both components, indicating electronic interaction between the particulate semiconductor and the polymeric matrix.

The spectrum shown in Figure 2(e) is very similar to the absorption spectrum for a flash-evaporated ZnPC thin film deposited on a glass substrate, as reported by Senthilarasu et al. [47], in which the two energy bands characteristic of phthalocyanines is evident, one in the region between 500 and 900 nm, with an absorption peak at 690 nm, related to the Q band, and the other, very intense, at 330 nm, attributed to Soret (B) band [48]. Mi et al. have reported a similar absorption spectrum for thin films of Magnesium Phthalocyanine [49]. The unstructured visible region band and the red shift of the Q band of these composites can be attributed to the strong intermolecular interactions due to ZnPC aggregation (ZnPC_{agg}), resulting in exciton coupling effects of the allowed transitions. This causes an important charge carrier mobility, as suggested by Hoffmann [50], or to the lift of degeneracy increasing the band splitting due to molecular distortion [49, 51, 52]. Based on the spectral characteristics of these composites, mainly in the visible, we

can conclude that the excitons formed by the aggregation of ZnPC molecules behave as Frenkel's J aggregates [53, 54].

The E_g value for ZnPC/ TiO_2 composites, estimated by diffuse reflectance, is lower (2.7 eV) than the one observed for pure TiO_2 (between 3.0 and 3.2 eV) [2, 3], and similar to the value for iron(II) phthalocyanine excitons (2.6 eV) in FePC/ TiO_2 blends [55] and other metal phthalocyanine associated to semiconductor oxides [16]. For ZnPC thin films, Senthilarasu et al. [47] have assigned an E_g of 1.97 eV, with a directly allowed optical transition, near to the value estimated by us for the peak absorption Q-band (2.25 eV) of pure ZnPC in the solid state (Figure 2(f)).

The E_g for these composites might be related to the electronic coupling between TiO_2 and ZnPC, and its positive implications. Similar to FePC/ TiO_2 blends [55] and ZnPC thin films [22, 47], the photoexcitation of ZnPC aggregates results in the formation of e^-/ZnPC^+ pairs, parallel reactions from these species and the electron injection from these ZnPC excitons to bulk TiO_2 , which explains at least in part the improved photocatalytic activity observed for some of the ZnPC/ TiO_2 composites [11, 12]. The electronic coupling strength between donor and acceptor is one of the critical factors for electron transfer to occur [22, 23, 47, 48]. Experiments based on femtosecond pump-probe laser spectroscopy have provided valuable information for understanding the electron transfer from excited dye molecules to nanocrystalline TiO_2 films or TiO_2 nanoparticles [25, 56–58]. Sharma et al. [55] observed a strong photoluminescence quenching of FePC in FePC/ TiO_2 composite film, while the photosensitivity of a device formed by FePC/ TiO_2 composite sandwiched between Al and ITO is significantly enhanced when compared to pure FePC film. The authors concluded that both effects arise from the charge transfer from FePC to TiO_2 and charge separation after photoexcitation, resulting in FePC(h^+) and $\text{TiO}_2(e^-)$. Additionally, they reported that the charge transport and the current leakage through FePC

films and the photogeneration are due to the efficient dissociation of exciton at the donor-acceptor interface of the bulk, and that the higher holes mobility in the organic material layer, combined with lower conductance leakage, leads to the more efficient collection of photogenerated carriers.

The excited-state dynamics of metal phthalocyanines in solution and thin films has been extensively studied by transient absorption spectroscopy and time-resolved photoluminescence measurements [47, 49, 59]. Despite the occurrence of several S_1 state relaxation processes in thin solid films (fluorescence, internal conversion, intersystem crossing, ultrafast exciton-exciton annihilation, exciton-phonon coupling), the nonradiative processes tend to be predominant [49, 60, 61]. The fluorescence quantum yields, for example, tend to be extremely low in thin films owing to enhanced intersystem crossing [61]. Sakakibara et al. in studies on photoluminescence properties of phthalocyanine solid films, observed that fluorescence quantum yields at room temperature were reduced to 10^{-5} – 10^{-4} , much smaller than those of the corresponding monomers (>0.5) [61]. In addition to these relaxation processes, if these films are deposited onto bulk TiO_2 , the electron transfer from metal phthalocyanine excitons has been reported [22, 55, 59].

3.2. Transmission electron microscopy

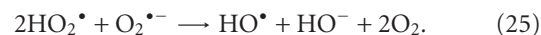
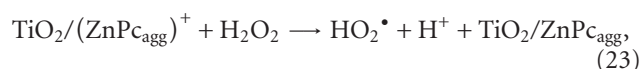
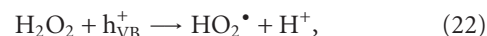
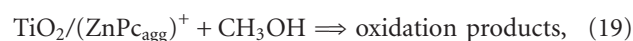
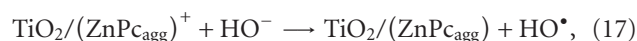
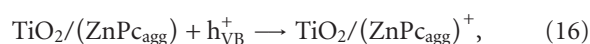
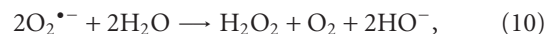
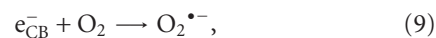
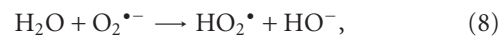
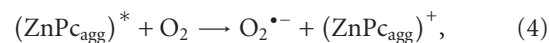
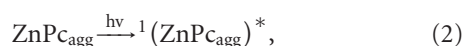
For composites containing 1%, 2.5%, and 5% m/m of ZnPc, coatings of ZnPc with irregular thickness covering the TiO_2 grains were observed (Figures 3(a)–3(c)). For the first one, the coating thickness varies between 0 and 10 nm, whereas for the composite containing 5% m/m of ZnPc, thicknesses between 0 and 25 nm were observed.

On the other hand, the composite containing 2.5% m/m of ZnPc presented the most regular coating thickness, ranging between 5 and 10 nm. Some uncoated surface areas also occur but to a much lower degree than verified for the other compositions.

ZnPc amounts exceeding about 2.5% lead to an increasingly unhomogeneous distribution. Microstructural investigations and energy dispersive X-ray (EDX) analyses of the 5% m/m coated composite (Figure 4) reveal two different regions: amorphous areas consisting of aggregates rich in carbon, zinc and sodium and crystalline regions formed by almost pure agglomerates of TiO_2 . Signals corresponding to copper, from TEM support grids, can be also observed. Sodium observed in the amorphous areas was probably incorporated during the preparation of the samples.

3.3. Quantum yield of production of hydroxyl radicals

The following set of reactions [3, 17] can be considered an approximate representation of the main reactions involved in the photocatalytic process induced by TiO_2 and composites on methanol degradation:



The methodology used to estimate the quantum yield of hydroxyl radicals production [35–37] can be considered useful and safe since the reactions related to the generation of hydroxyl radicals are sufficiently fast. For example, reaction (12) presents expressive values for the rate constant, in the range between 8.3 and 9.7×10^8 $L mol^{-1} s^{-1}$ [62, 63], whereas reaction (13), between the dehydro-methanol radical and HO^{\bullet} , the bimolecular rate constant is in the limit for diffusion-controlled reactions (10^9 – 10^{10} $L mol^{-1} s^{-1}$). On the other hand, the trapping of hydroxyl radicals by hydrogen peroxide, a possible side reaction, occurs at a considerably slower rate (2.7×10^7 $L mol^{-1} s^{-1}$) [62]. The primary steps that culminate in the formation of HO^{\bullet} are also in the limit for diffusion-controlled reactions.

Figure 5 shows the expected dependence between the quantum yield of hydroxyl radicals generation ($\Phi_{HO^{\bullet}}$) and the amount of ZnPc adsorbed on TiO_2 for experiments at the laboratory scale (Section 2.4). Initially, an increase in the $\Phi_{HO^{\bullet}}$ is observed, with a maximum value ($\Phi_{HO^{\bullet}} = 0.60$)

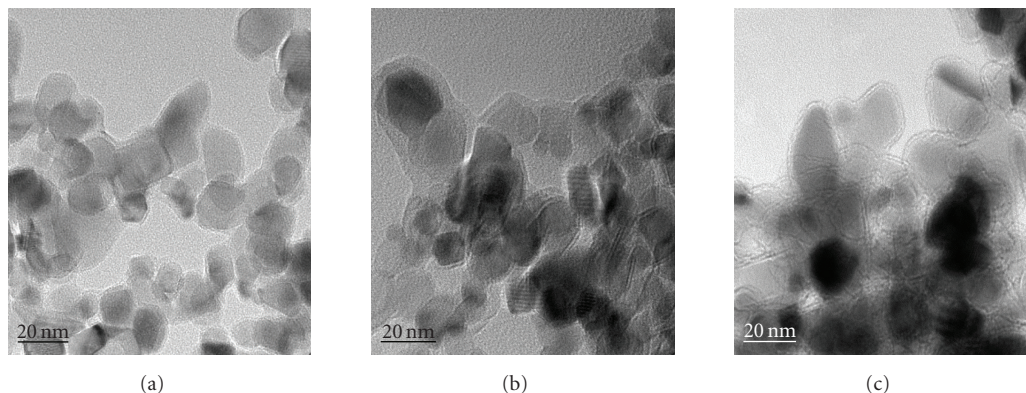


FIGURE 3: Transmission electron micrographs of granules of the different TiO_2/ZnPC composites: (a) 1% ZnPC, (b) 2.5% ZnPC, and (c) 5% ZnPC.

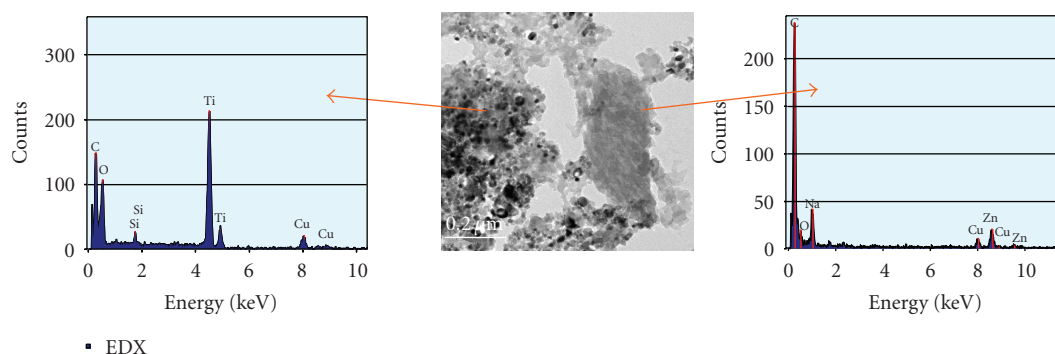


FIGURE 4: Transmission electron micrography and X-ray dispersive energy of the composite containing 5% of ZnPC.

for a ZnPC concentration equals to 2.5% m/m. For pure TiO_2 , $\Phi_{\text{HO}\cdot}$ is 0.06. A similar trend should be expected during solar photocatalysis. However, since hydrogen peroxide is involved as an additional source of hydroxyl radicals [8–12], it is expected that this must cause a significant increase in $\Phi_{\text{HO}\cdot}$. Sun and Bolton [37], investigating the generation of hydroxyl radicals by aqueous suspensions of TiO_2 (Anatase, Aldrich), reported $\Phi_{\text{HO}\cdot}$ changed from 0.04 to 0.22 with the addition of hydrogen peroxide in the reactional medium. They also observed that when the H_2O_2 concentration in the suspension is larger than 18 mM, a plateau for the $\Phi_{\text{HO}\cdot}$ values is reached. The presence of H_2O_2 in the suspension might influence the redox reactions occurring at the TiO_2 particles surface, acting as electron acceptor, competing with the O_2 , reactions (9) and (11), in the redox reactions, and also producing additional $\text{HO}\cdot$ radicals, reactions (11), (21), (22), and (23). According to the data published by Sun and Bolton [37], the H_2O_2 concentration (about 9 mM) used in our experiments under solar irradiation is capable of increasing $\Phi_{\text{HO}\cdot}$ at least 4.5 times.

In principle, the light intensity (1.1×10^{-6} einsteins $\text{s}^{-1} \text{cm}^{-2}$) in the 295 to 710 nm range, capable to trigger the photocatalytic processes mediated by the composites in the experiments at the laboratory scale, also could accelerate the e^-/h^+ recombination, impairing the production of $\text{HO}\cdot$ radicals, implying in $\Phi_{\text{HO}\cdot}$ values lower than desired [35, 37].

However, it is probable that, at this wavelength range, nor all photons are capable to generate e^-/h^+ pairs in TiO_2 , or favor the electron injection from ZnPC excitons to bulk TiO_2 . An estimate based on the spectral distribution of the mercury lamp shows that the light intensity between 295 and 390 nm, capable to photoexcite TiO_2 , generating e^-/h^+ pairs, is about 2.0×10^{-7} einsteins $\text{s}^{-1} \text{cm}^{-2}$. The light intensity between 295 and 460 nm, 3.9×10^{-7} einsteins $\text{s}^{-1} \text{cm}^{-2}$, should be capable to photoexcite TiO_2/ZnPC composites, generating e^-/h^+ pairs in both species, and consequently favoring the electron injection from ZnPC excitons to TiO_2 conduction band (Scheme 1), since in this wavelength range the superposition of the electronic states of TiO_2 and ZnPC implies in several common electronic states for both species. The rest of the emitted photons, between 460 and 710 nm (about 5.1×10^{-7} einsteins $\text{s}^{-1} \text{cm}^{-2}$), should be related to other processes directly mediated by the ZnPC excitons formed by the electronic excitation in this wavelength range. This explains the reason by which the estimated $\Phi_{\text{HO}\cdot}$ value in our measurements using pure TiO_2 (Degussa P25) is equal to 0.06, 50% higher than the value estimated by Sun and Bolton [37] for aqueous suspensions of pure TiO_2 (anatase), but equivalent to the value reported for TiO_2 Degussa P25 ($\Phi_{\text{HO}\cdot} \approx 0.06$) [64]. Several authors have shown that $\Phi_{\text{HO}\cdot}$ is inversely proportional to the square root of the incident light intensity [35, 37, 65, 66], behavior attributed to an

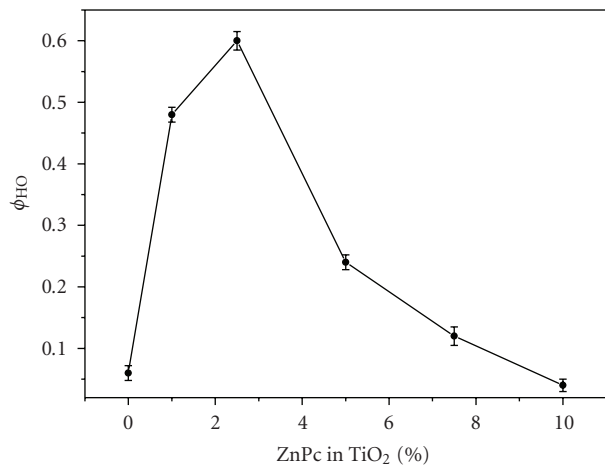


FIGURE 5: Dependence between the hydroxyl radicals quantum yield and the amount of zinc phthalocyanine adsorbed on TiO₂.

increase in the production rate of e^-/h^+ pairs, which favors the electron/hole recombination, thus decreasing the relative number of photoinduced carriers taking part in the redox reactions at the catalyst surface [35, 37]. On the other hand, as occurs in the solar photocatalytic process [8–12], the addition of H₂O₂ should contribute to reducing the recombination of photoinduced electrons and holes [37], which must increase the Φ_{HO} .

Based on these facts, considering the TiO₂/ZnPc composites, the participation of excitons formed by electronic excitation of the ZnPc aggregates is not only restricted to the electron injection into the conduction band of TiO₂, which must occur only at wavelengths lower than 460 nm. Other processes should be triggered by these charge carriers, especially after electronic excitation at wavelengths higher than 460 nm, otherwise, we should observe a strong quenching of the photocatalytic activity and not a synergic behavior involving TiO₂ and ZnPc_{agg} (observed in results to be published). This synergism explains the higher Φ_{HO} values estimated for three of the studied composites (Figure 5).

Although the values estimated by us Φ_{HO} are not definite, they suggest an important trend, since they converge to the results obtained in studies involving the photocatalytic degradation of organic matter, mediated by solar radiation, that show some TiO₂/ZnPc combinations present significant increments in their photocatalytic activity. For example, the ratio between Φ_{HO} for the composite containing 2.5% m/m of ZnPc and the estimated for pure TiO₂ shows an improvement of at least 1000% in the production of hydroxyl radicals.

The comparison of the photocatalytic degradation of the organic matter (LSA) present in a model effluent [8–10], promoted by these composites and pure TiO₂ in a solar photocatalytic process, confirms the better performance of the first ones, especially the composite containing 2.5% m/m of ZnPc, to perform wastewater treatment using photocatalytic processes mediated by solar irradiation [11, 12].

Despite the fact that part of the adsorbed ZnPc is degraded during the photocatalytic process, surprisingly, the

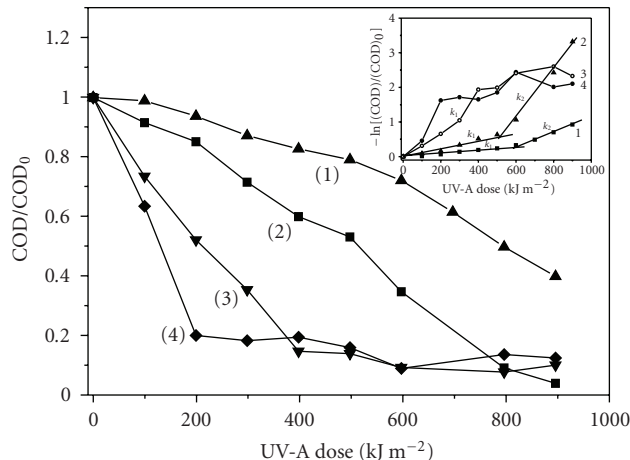
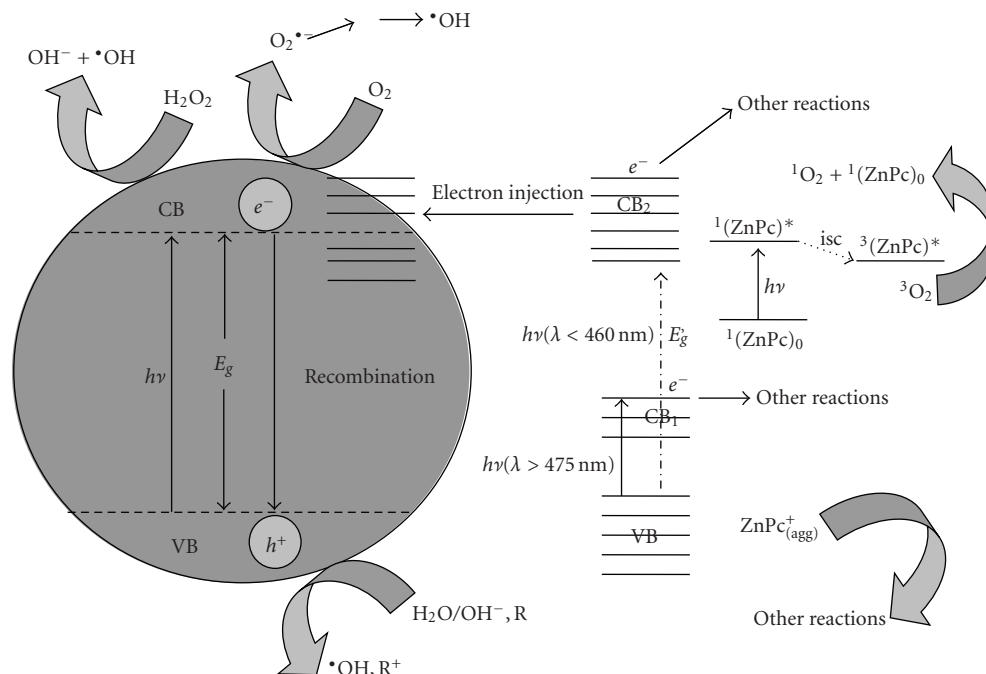


FIGURE 6: Degradation of the organic load present in 50 L of an aqueous model-effluent containing LSA (160 mg/L). Reactions done proceeded at pH 3, using 100 mg of catalyst per liter of effluent, and addition of 1.00 mL of hydrogen peroxide per liter of effluent. Effluent treated using: (1) pure TiO₂; (2) TiO₂/ZnPc 2.5% composite; (3) a recycled TiO₂/ZnPc 2.5% composite; (4) TiO₂/ZnPc 2.5% in its second recycle. *Inset*: Pseudofirst-order rate profiles for the effluent degradation under the above mentioned conditions.

photocatalytic efficiency of the recovered composite does not decrease significantly when reused. Preliminary results (not shown) suggest that a load of composite can be used at least five times before presenting photocatalytic efficiency similar to pure TiO₂. This can be due to, in great part, the gradual ZnPc degradation, which occurs during the cycles of use of the catalyst. In a minor extent, limited by its very low water solubility, ZnPc also tends to migrate to the aqueous medium.

Figure 6 shows an increase in the degradation rate, with significant changes in the degradation profile due to the use of a recovered composite. This suggests that some reactions, less probable to occur in virtue of ZnPc aggregates formation, become important for the global process. For example, the production of singlet oxygen from ³ZnPc* can be a plausible event if the level of ZnPc aggregation is drastically lowered, which is consistent with the fact that photoactive compounds like ZnPc, when aggregated, are incapable to sensitize type I and II reactions [67, 68]. This behavior is attributed to the fact that aggregates in the electronically excited state tend to be deactivated preferentially by nonradiative processes [68]. On the other hand, the better hydration of the catalyst surface, due to many cycles of use, should favor reactions involving the holes (Scheme 1).

For ZnPc concentrations above 2.5%, Φ_{HO} tends to decrease, most probably due to the occurrence of undesirable processes related to the increasing size of the ZnPc aggregates, such as exciton-exciton annihilation due to the excessive coating of the TiO₂ surface. Essays involving a ZnPc/SiO₂ composite coated with 2.5% m/m of ZnPc reinforce, as expected, that the observed process is not



SCHEME 1: Main processes involved in a photocatalytic process mediated by a TiO_2/ZnPC composites.

exclusively due to ZnPC or TiO_2 , but to a synergism between these species, indeed when the composite is excited by visible radiation (unpublished results).

It is well known that the degradation of organic matter induced by photocatalysis follows Langmuir-Hinschelwood kinetics [3, 8]. Assuming the concentration of reactive species quickly reaches a stationary state at the beginning of the photocatalytic process [8], the global rate law seems to follow pseudofirst-order behavior with respect to the organic matter (Figure 6-Inset).

The adsorption of the organic matter at the surface of the catalyst in this situation occurs at a low rate [8], since that LSA is constituted by fragments of large size and molecular mass. The formation and desorption of reactive species, derived from small molecules (water, H_2O_2 , O_2 , undegraded small fragments of LSA, etc.) should compensate the slow adsorption rate of the large fragments, reacting with them in the catalyst/solvent interface. Considering this aspect, we can consider that LSA degradation is a particular case in which at least one of the steps does not follow the Langmuir-Hinschelwood mechanism.

In the experiments using solar irradiation, to permit comparison with the results obtained under different latitude and weather conditions, it is necessary to use UV-A accumulated dose instead of the temporal variation data. Therefore, the estimated parameters refer to a constant related to the COD decrease rate relative to the variation of the accumulated dose of UV-A radiation. These constants were calculated considering an expression similar to the first-order reaction rate law in which the term $d(\text{COD})/dt$ was substituted by $d(\text{COD})/d(\text{dose})$, since $d(\text{dose}) \propto dt$. As COD is dimensionally equivalent to the concentration of organic

matter, the calculated constant (now named *degradation constant*, D) has the dimensions of the reciprocal of the radiation dose. The monitoring of only the UV-A dose was adopted exclusively due to operational limitations. However, this should have only a minor effect on the results since the spectral pattern of the visible light between a set of experiments does not vary significantly.

The *degradation constants*, D , calculated for the degradation of LSA mediated by TiO_2 and TiO_2/ZnPC 2.5% are presented in Table 1. Using pure TiO_2 or an unused sample of the composite as catalyst, the reaction seems to occur in two steps being the second faster than the first one. The observed increase in the *degradation constant* of the second step is most probably due to the increasing hydration of the surface of the catalyst and the participation of new reactive species. These results also confirm previous results which show that the apparent rate constant for reactions mediated by these composites are systematically higher than the ones using pure TiO_2 [8, 11, 12].

The *degradation constant* for the first step of the reaction mediated by the composite containing 2.5% m/m of ZnPC, (D_1), is about 130% higher than the one for pure TiO_2 , whereas the corresponding value for the second step is 3,300% higher. Although premature to present conclusions on the involved processes, a comparison between these values and the estimated increase in $\Phi_{\text{HO}\cdot}$, reinforces that the photocatalytic processes triggered by these composites is much more complex than the process catalyzed by pure TiO_2 [3], as suggests the set of reactions presented in Section 3.3.

The two steps trend is also verified in the degradation mediated by reused composite. However, in this case D_2 seems do be near zero. The estimated value for the

TABLE 1: Degradation constants (D) for LSA degradation under different conditions.

| Catalyst | D_1 (m^2J^{-1}) | D_2 (m^2J^{-1}) | $D_1(X)/D_1(A)$ | $D_2(X)/D_2(A)$ |
|-------------------------------------|-------------------------------------|-------------------------------------|-----------------|-----------------|
| Pure TiO_2 (A) | 5.6×10^{-7} | 2.0×10^{-6} | 1.0 | 1.0 |
| TiO_2/ZnPc 2.5% (B) | 1.3×10^{-6} | 6.7×10^{-6} | 2.3 | 34 |
| Composite after reuse (C) | 4.2×10^{-6} | — | 7.5 | — |

$X = A, B,$ or $C.$

TABLE 2: Specific surface area values for TiO_2 and TiO_2/ZnPc composites at different m/m ratios.

| Composition | SSA (m^2g^{-1}) |
|---------------------------------|-----------------------------------|
| P25 | 52 |
| TiO_2/FtZn 1% | 38 |
| TiO_2/FtZn 2.5% | 35 |
| TiO_2/FtZn 5% | 36 |

degradation constant of the first step (D_1) of these processes is valid until an accumulated UV-A dose of about 600 kJ m^{-2} (Figure 6-Inset) and is 650% higher than the observed value for the first step of the process mediated by pure TiO_2 , and 230% higher when compared with the first one for the composite used for the first time.

As a consequence of the reactions triggered by the composite containing 2.5% m/m of ZnPc after the first time use, the final COD of the effluent after an accumulated UV-A dose of 900 kJ m^{-2} (this value corresponds to about 3 hours of solar irradiation during a sunny day, or 5 to 6 hours during a day with moderate to high nebulosity, in Uberlândia, MG, Brasil [12]) corresponds to 4% of the initial value. For a reused composite, this value corresponds to 9%, whereas using pure TiO_2 under similar conditions, the observed reduction in COD was of 60%.

Although it is possible to perform the photocatalytic treatment until complete mineralization of the organic matter, often it is economically more suitable to use the photocatalytic process as an effluent pretreatment, completing the treatment with other more efficient processes. In a previous investigation [10], a treated lignosulphonate wastewater was tested for its biochemical oxygen demand (BOD). The results observed suggest that when a high bioavailability is reached at the point where the performance of the photocatalytic treatment decreases, its discontinuation and the beginning of a treatment based on the biological degradation technology is more favorable.

3.4. Specific surface area

Table 2 shows the specific surface area (SSA) of pure TiO_2 and of ZnPc -coated TiO_2 , at different concentrations.

The SSA of the composites is about 30% smaller than the one of pure TiO_2 , suggesting ZnPc adsorption reduces the TiO_2 porosity. The changes in the SSA of the composites do not imply in distortions of the TiO_2 crystal structure. For pure TiO_2 and composites, the peak positions and lattice parameters of the anatase and rutile phases (not shown) remain practically unchanged, supporting the structural

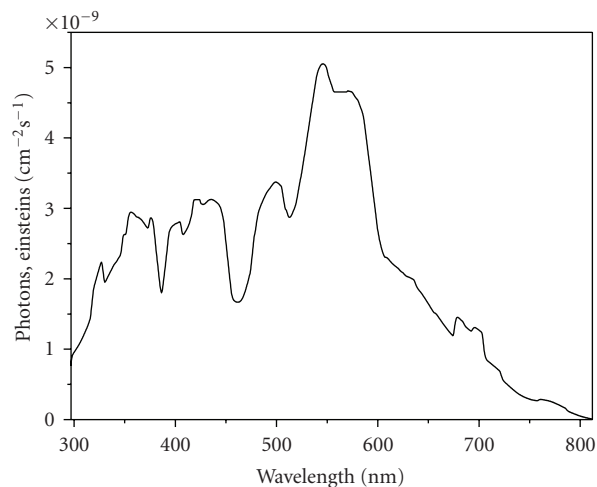


FIGURE 7: Spectral distribution of the radiation emitted by a 400 W HPL-N mercury lamp in the 295 to 815 nm spectral range.

integrity of the TiO_2 phases. The increase in the amount of dye results in a decrease of the relative intensity of the peaks, evidencing the adsorption of the dye on the semiconductor surface, and a partial absorption of the incident radiation by the dye.

X-ray powder diffraction patterns of TiO_2 and the different composites only show peaks due to the anatase and rutile phases (figure not shown), suggesting ZnPc is adsorbed on the semiconductor surface. This agrees with the results based on scanning tunneling microscopy using different metal phthalocyanines, which concluded that this class of compounds lies flat on the semiconductor surface [69].

3.5. Final remarks

The spectral distribution of a 400 W high-pressure (HP) mercury lamp, in the 295 to 815 nm range, is shown in Figure 7.

The analysis of the spectral distribution shows that the photonic flux in the 295 to 390 nm range, useful for the electronic excitation of pure TiO_2 , ZnPc , and their aggregates (Figure 2), is of 6.0×10^{-7} einsteins/s. The photonic flux of 3.3×10^{-6} einsteins/s in the 295 to 710 nm range is 5.5 times higher. Considering an ideal situation in which 100% of the incident photons furnished by HP, mercury lamps are able to trigger the photocatalytic process, the use of these composites is very advantageous, since these materials pick up 450% more photons than pure TiO_2 . This

makes these composites very attractive for use in processes induced by solar radiation, the main advantage inherent to these composites, considering that more than 90% of the incident radiation on biosphere has wavelength above 390 nm. Hence an increase in the population of excited ZnPc aggregates should imply in an electron/hole ratio higher than unity as observed for pure TiO₂ [22, 50, 70], besides the other processes triggered by ZnPc excitons.

Additional experiments using a metal vapor lamp to excite the composites exclusively with visible radiation were done and confirmed the effective participation of the visible radiation components in the photocatalytic process (not shown).

The increase in the $\Phi_{HO\bullet}$ value indicates the important role of ZnPc aggregates combined with TiO₂ on the photocatalytic processes triggered by these composites. On the other hand, the decrease of the photocatalytic efficiency observed for composites containing ZnPc amounts higher than 2.5% m/m can be attributed to an excessive ZnPc aggregation, which increases the chances of exciton-exciton annihilation affecting the charge transport.

One of the causes for the higher efficiency presented by some of these composites, mainly the one containing 2.5% m/m of ZnPc, can be attributed to the regular distribution and coating thickness of ZnPc on the TiO₂ surface. Control of the coating thickness of the photosensitizing dye can prevent/minimize the exciton-exciton annihilation, favoring electron injection in the semiconductor oxide [22, 50, 59, 70] as well as other processes directly mediated by ZnPc excitons. Besides, good electronic coupling between this one and TiO₂ is fundamental for the electron transfer process from the exciton [22]. Terasaki et al. [60] using femtosecond spectroscopy technique showed the excited-state dynamics of vanadyl phthalocyanines in various molecular arrangements to be strongly dependent on the molecular arrangements between the formed phases. The composites containing 2.5% m/m of ZnPc, who presented the best photocatalytic performance, possesses the most homogeneous coatings with an average thickness between 5 and 10 nm.

At this point, the available informations are not yet sufficient to propose a detailed mechanism involved in the enhancement of the photocatalytic activity of these composites. However, previous studies give important evidences. Based on the experimental facts reported here and the contribution of other researchers, it is reasonable to assume that the reactions triggered by these composites are based on the formation of electron/hole pairs from TiO₂ and also from ZnPc_{agg}. For these composites, the key steps which lead to the formation of active species at the solid/solution interface are (a) formation of e⁻/h⁺ pairs by the direct excitation of TiO₂ ($\lambda_{exc} \leq 390$ nm); (b) formation of e⁻/ZnPc_{agg}⁺ by the photoexcitation of ZnPc_{agg}; (c) electron transfer from ZnPc excitons to the TiO₂ conduction band; (d) charge transport by ZnPc_{agg}⁺ and its implications, and other reactions triggered by e⁻/ZnPc_{agg}⁺ pairs.

Ways to prevent/minimize the vulnerability of ZnPc during the photocatalytic process are under study, even though the results presented in this work show that, despite

ZnPc degradation, these composites are able to perform efficiently wastewater treatment using solar radiation.

ACKNOWLEDGMENTS

The authors thank the CNPq, FAPEMIG, CAPES (Brazilian agencies), and the International Bureau of the German Ministry of Education and Research for funding the project WATER BRA 00/015. They also thank Lamark de Oliveira, Edward Thomas Fleury Mendonça Duarte, Eduardo de Faria Franca, Lucas Ferreira de Paula, and Jacques Antonio de Miranda for technical assistance. A. E. H. Machado is particularly indebted to Professor Julien F. C. Boodts for the revision of the English language and valuable suggestions.

REFERENCES

- [1] O. Legrini, E. Oliveros, and A. M. Braun, "Photochemical processes for water treatment," *Chemical Reviews*, vol. 93, no. 2, pp. 671–698, 1993.
- [2] G. Palmisano, V. Augugliaro, M. Pagliaro, and L. Palmisano, "Photocatalysis: a promising route for 21st century organic chemistry," *Chemical Communications*, no. 33, pp. 3425–3437, 2007.
- [3] M. R. Hoffmann, S. T. Martin, W. Choi, and D. W. Bahnemann, "Environmental applications of semiconductor photocatalysis," *Chemical Reviews*, vol. 95, no. 1, pp. 69–96, 1995.
- [4] E. Oliveros, O. Legrini, M. Hohl, T. Müller, and A. M. Braun, "Large scale development of a light-enhanced fenton reaction by optimal experimental design," *Water Science and Technology*, vol. 35, no. 4, pp. 223–230, 1997.
- [5] R. L. Zioli and W. F. Jardim, "Mecanismo de fotodegradação de compostos orgânicos catalisada por TiO₂," *Química Nova*, vol. 21, no. 3, pp. 319–325, 1998.
- [6] D. M. Blake, "Bibliography of work on photocatalytic removal of hazardous compounds from water and air," Tech. Rep. NREL/TP-430-22197, National Renewable Energy Laboratory, Golden, Colo, USA, 1999.
- [7] R. Andreozzi, V. Caprio, A. Inola, and R. Marotta, "Advanced oxidation processes (AOP) for water purification and recovery," *Catalysis Today*, vol. 53, no. 1, pp. 51–59, 1999.
- [8] A. E. H. Machado, J. A. de Miranda, R. F. de Freitas, et al., "Destruction of the organic matter present in effluent from a cellulose and paper industry using photocatalysis," *Journal of Photochemistry and Photobiology A*, vol. 155, no. 1–3, pp. 231–241, 2003.
- [9] C. Sattler, L. de Oliveira, M. Tzschirner, and A. E. H. Machado, "Solar photocatalytic water detoxification of paper mill effluents," *Energy*, vol. 29, no. 5-6, pp. 835–843, 2004.
- [10] C. Sattler, K.-H. Funken, L. de Oliveira, M. Tzschirner, and A. E. H. Machado, "Paper mill wastewater detoxification by solar photocatalysis," *Water Science and Technology*, vol. 49, no. 4, pp. 189–193, 2004.
- [11] A. E. H. Machado, T. P. Xavier, D. R. de Souza, et al., "Solar photo-fenton treatment of chip board production waste water," *Solar Energy*, vol. 77, no. 5, pp. 583–589, 2004.
- [12] E. T. F. M. Duarte, T. P. Xavier, D. R. de Souza, et al., "Construção e estudos de performance de um reator fotoquímico tipo CPC ("Compound Parabolic Concentrator")," *Química Nova*, vol. 28, no. 5, pp. 921–926, 2005.
- [13] A. E. H. Machado, J. A. Miranda, C. Sattler, and L. Oliveira, "Compósitos de ftalocianina de zinco e óxido de titânio,

- para emprego em processos fotocatalíticos e método para sua obtenção,” Brazilian patent no. PI 03009203-3, 2005.
- [14] A. E. H. Machado, J. A. Miranda, C. Sattler, and L. Oliveira, “Zinc phthalocyanine and titanium oxide composites used as, e.g. catalyst for wastewater decontamination, prepared by combining titanium oxide and photosensitizer dye capable of potentializing photocatalytic action of titanium oxide,” European patent no. EP1646443-A2, 2006.
- [15] A. E. H. Machado and V. Velani, “Fotocatalisadores à base de óxido de titânio, dopados com íons de metais de transição, seu processo de preparação e sua aplicação em processos de descontaminação ambiental,” Brazilian patent application no. PI 0701120-2, 2007.
- [16] V. Iliev, D. Tomova, L. Bilyarska, L. Prahov, and L. Petrov, “Phthalocyanine modified TiO₂ or WO₃-catalysts for photooxidation of sulfide and thiosulfate ions upon irradiation with visible light,” *Journal of Photochemistry and Photobiology A*, vol. 159, no. 3, pp. 281–287, 2003.
- [17] G. Mele, R. Del Sole, G. Vasapollo, E. García-López, L. Palmisano, and M. Schiavello, “Photocatalytic degradation of 4-nitrophenol in aqueous suspension by using polycrystalline TiO₂ impregnated with functionalized Cu(II)-porphyrin or Cu(II)-phthalocyanine,” *Journal of Catalysis*, vol. 217, no. 2, pp. 334–342, 2003.
- [18] M. Bellardita, M. Addamo, A. Di Paola, and L. Palmisano, “Photocatalytic behaviour of metal-loaded TiO₂ aqueous dispersions and films,” *Chemical Physics*, vol. 339, no. 1–3, pp. 94–103, 2007.
- [19] C. Sattler, L. Oliveira, and C. Jung, “Volume-doped titanium dioxide composite, useful in photocatalytic procedures for decontaminating wastewater and for removing smells from environment, preferably heterogeneous photo catalysis form, comprises zinc phthalocyanine,” German patent no. DE102004053823-A1, 2006.
- [20] C. H. Langford, M. K. S. Mak, and A. M. Croch, “Photo-catalyst for refractory waste degradation esp. of PCB residues—comprises wide band semiconductor esp. titanium dioxide, coated with pyridine-contg. polymer and metal porphyrin or phthalocyanine dye,” Canadian and US patent no. US4806514-A; CA1287829-C, 1991.
- [21] M. Grätzel, “Photoelectrochemical cells,” *Nature*, vol. 414, no. 6861, pp. 338–344, 2001.
- [22] D. Ino, K. Watanabe, N. Takagi, and Y. Matsumoto, “Electron transfer dynamics from organic adsorbate to a semiconductor surface: zinc phthalocyanine on TiO₂(110),” *Journal of Physical Chemistry B*, vol. 109, no. 38, pp. 18018–18024, 2005.
- [23] J. M. Rehm, G. L. McLendon, Y. Nagasawa, K. Yoshihara, J. Moser, and M. Grätzel, “Femtosecond electron-transfer dynamics at a sensitizing dye-semiconductor (TiO₂) interface,” *Journal of Physical Chemistry*, vol. 100, no. 23, pp. 9577–9578, 1996.
- [24] M. K. Nazeeruddin, A. Kay, I. Rodicio, et al., “Conversion of light to electricity by *cis*-X₂bis(2,2′-bipyridyl)-4,4′-dicarboxylate)ruthenium(II) charge-transfer sensitizers (X = Cl⁻, Br⁻, I⁻, CN⁻, and SCN⁻) on nanocrystalline TiO₂ electrodes,” *Journal of the American Chemical Society*, vol. 115, no. 14, pp. 6382–6390, 1993.
- [25] J. B. Asbury, E. Hao, Y. Wang, H. N. Ghosh, and T. Lian, “Ultrafast electron transfer dynamics from molecular adsorbates to semiconductor nanocrystalline thin films,” *Journal of Physical Chemistry B*, vol. 105, no. 20, pp. 4545–4557, 2001.
- [26] J. Krüger, R. Plass, L. Cevey, M. Piccirelli, M. Grätzel, and U. Bach, “High efficiency solid-state photovoltaic device due to inhibition of interface charge recombination,” *Applied Physics Letters*, vol. 79, no. 13, pp. 2085–2087, 2001.
- [27] R. Argazzi, C. A. Bignozzi, G. M. Hasselmann, and G. J. Meyer, “Efficient light-to-electrical energy conversion with dithiocarbamate-ruthenium polypyridyl sensitizers,” *Inorganic Chemistry*, vol. 37, no. 18, pp. 4533–4537, 1998.
- [28] A. P. Xagas, M. C. Bernard, A. Hugot-Le Goff, N. Spyrellis, Z. Loizos, and P. Falaras, “Surface modification and photosensitisation of TiO₂ nanocrystalline films with ascorbic acid,” *Journal of Photochemistry and Photobiology A*, vol. 132, no. 1–2, pp. 115–120, 2000.
- [29] K. Tennakone, A. R. Kumarasinghe, G. R. R. A. Kumara, K. G. U. Wijayantha, and P. M. Sirimanne, “Nanoporous TiO₂ photoanode sensitized with the flower pigment cyanidin,” *Journal of Photochemistry and Photobiology A*, vol. 108, no. 2–3, pp. 193–195, 1997.
- [30] G. D. Sharma, S. C. Mathur, and D. C. Dube, “Organic photovoltaic solar cells based on some pure and sensitized dyes,” *Journal of Materials Science*, vol. 26, no. 24, pp. 6547–6552, 1991.
- [31] Y. Hao, M. Yang, C. Yu, et al., “Photoelectrochemical studies on acid-doped polyaniline as sensitizer for TiO₂ nanoporous film,” *Solar Energy Materials and Solar Cells*, vol. 56, no. 1, pp. 75–84, 1998.
- [32] C. Chen, X. Qi, and B. Zhou, “Photosensitization of colloidal TiO₂ with a cyanine dye,” *Journal of Photochemistry and Photobiology A*, vol. 109, no. 2, pp. 155–158, 1997.
- [33] T. Wu, S.-J. Xu, J.-Q. Shen, S. Chen, M.-H. Zhang, and T. Shen, “Photosensitization of TiO₂ colloid by hypocrellin B in ethanol,” *Journal of Photochemistry and Photobiology A*, vol. 137, no. 2–3, pp. 191–196, 2000.
- [34] A. M. Braun, M.-T. Maurette, and E. Oliveros, *Technologie Photochimique*, Presse Romandes, Lausanne, Switzerland, 1986.
- [35] R. Gao, J. Stark, D. W. Bahnemann, and J. Rabani, “Quantum yields of hydroxyl radicals in illuminated TiO₂ nanocrystalline layers,” *Journal of Photochemistry and Photobiology A*, vol. 148, no. 1–3, pp. 387–391, 2002.
- [36] T. Nash, “The colorimetric estimation of formaldehyde by means of the Hantzsch reaction,” *The Biochemical Journal*, vol. 55, no. 3, pp. 416–421, 1953.
- [37] L. Sun and J. R. Bolton, “Determination of the quantum yield for the photochemical generation of hydroxyl radicals in TiO₂ suspensions,” *Journal of Physical Chemistry*, vol. 100, no. 10, pp. 4127–4134, 1996.
- [38] J. Blanco, S. Malato, P. Fernández, et al., “Compound parabolic concentrator technology development to commercial solar detoxification applications,” *Solar Energy*, vol. 67, no. 4–6, pp. 317–330, 1999.
- [39] K.-H. Funken, C. Sattler, B. Milow, et al., “A comparison of prototype compound parabolic collector-reactors (CPC) on the road to SOLARDETOX technology,” *Water Science and Technology*, vol. 44, no. 5, pp. 271–278, 2001.
- [40] A. M. Jirka and M. J. Carter, “Micro semi-automated analysis of surface and wastewaters for chemical oxygen demand,” *Analytical Chemistry*, vol. 47, no. 8, pp. 1397–1402, 1975.
- [41] USEPA, “COD ranges 3–150 mg/L and 20–1500 mg/L COD are USEPA approved (5220 D) for wastewater analyses,” *Federal Register*, vol. 45, no. 78, pp. 26811–26812, 1980.
- [42] C. C. Leznoff and A. B. P. Lever, Eds., *Phthalocyanines: Properties and Applications*, vol. 1, VCH Publishers, New York, NY, USA, 1990.

- [43] C. C. Leznoff and A. B. P. Lever, Eds., *Phthalocyanines: Properties and Applications*, vol. 4, VCH Publishers, New York, NY, USA, 1996.
- [44] J. A. de Miranda, A. E. H. Machado, and C. A. de Oliveira, "Comparison of the photodynamic action of methylene blue and zinc phthalocyanine on TG-180 tumoral cells," *Journal of Porphyrins and Phthalocyanines*, vol. 6, no. 1, pp. 43–49, 2002.
- [45] G. Ricciardi, A. Rosa, and E. J. Baerends, "Ground and excited states of zinc phthalocyanine studied by density functional methods," *Journal of Physical Chemistry A*, vol. 105, no. 21, pp. 5242–5254, 2001.
- [46] K. Szaciłowski, W. Macyk, and G. Stochel, "Synthesis, structure and photoelectrochemical properties of the TiO₂-Prussian blue nanocomposite," *Journal of Materials Chemistry*, vol. 16, no. 47, pp. 4603–4611, 2006.
- [47] S. Senthilarasu, S. Velumani, R. Sathyamoorthy, et al., "Characterization of zinc phthalocyanine (ZnPc) for photovoltaic applications," *Applied Physics A*, vol. 77, no. 3-4, pp. 383–389, 2003.
- [48] D. Meissner and J. Rostalski, "Photovoltaics of interconnected networks," *Synthetic Metals*, vol. 121, no. 1–3, pp. 1551–1552, 2001.
- [49] J. Mi, L. Guo, Y. Liu, W. Liu, G. You, and S. Qian, "Excited-state dynamics of magnesium phthalocyanine thin film," *Physics Letters A*, vol. 310, no. 5-6, pp. 486–492, 2003.
- [50] M. Hoffmann, "Frenkel and charge-transfer excitons in quasi-one-dimensional molecular crystals with strong intermolecular overlap," Ph.D. thesis, Technischen Universität Dresden, Dresden, Germany, 2000.
- [51] J. Mizuguchi and S. Matsumoto, "Molecular distortion and exciton coupling effects in β metal-free phthalocyanine," *Journal of Physical Chemistry A*, vol. 103, no. 5, pp. 614–616, 1999.
- [52] A. S. Davydov, *Theory of Molecular Excitons*, McGraw-Hill, New York, NY, USA, 1962.
- [53] H. Fidler, J. Knoester, and D. A. Wiersma, "Optical properties of disordered molecular aggregates: a numerical study," *Journal of Chemical Physics*, vol. 95, no. 11, pp. 7880–7890, 1991.
- [54] O.-K. Kim, J. Je, G. Jernigan, L. Buckley, and D. Whitten, "Super-helix formation induced by cyanine J-aggregates onto random-coil carboxymethyl amylose as template," *Journal of the American Chemical Society*, vol. 128, no. 2, pp. 510–516, 2006.
- [55] G. D. Sharma, R. Kumar, and M. S. Roy, "Investigation of charge transport, photo generated electron transfer and photovoltaic response of iron phthalocyanine (FePc): TiO₂ thin films," *Solar Energy Materials and Solar Cells*, vol. 90, no. 1, pp. 32–45, 2006.
- [56] M. Hilgendorff and V. Sundström, "Ultrafast electron injection and recombination dynamics of dye sensitised TiO₂ particles," *Chemical Physics Letters*, vol. 287, no. 5-6, pp. 709–713, 1998.
- [57] J. B. Asbury, R. J. Ellingson, H. N. Ghosh, S. Ferrere, A. J. Nozik, and T. Lian, "Femtosecond IR study of excited-state relaxation and electron-injection dynamics of Ru(dcbpy)₂(NCS)₂ in solution and on nanocrystalline TiO₂ and Al₂O₃ thin films," *Journal of Physical Chemistry B*, vol. 103, no. 16, pp. 3110–3119, 1999.
- [58] S. Iwai, S. Murata, R. Katoh, M. Tachiya, K. Kikuchi, and Y. Takahashi, "Ultrafast charge separation and exciplex formation induced by strong interaction between electron donor and acceptor at short distances," *Journal of Chemical Physics*, vol. 112, no. 16, pp. 7111–7117, 2000.
- [59] V. Gulbinas, M. Chachisvilis, L. Valkunas, and V. Sundström, "Excited state dynamics of phthalocyanine films," *Journal of Physical Chemistry*, vol. 100, no. 6, pp. 2213–2219, 1996.
- [60] A. Terasaki, M. Hosoda, T. Wada, et al., "Femtosecond spectroscopy of vanadyl phthalocyanines in various molecular arrangements," *Journal of Physical Chemistry*, vol. 96, no. 25, pp. 10534–10542, 1992.
- [61] Y. Sakakibara, R. N. Bera, T. Mizutani, K. Ishida, M. Tokumoto, and T. Tani, "Photoluminescence properties of magnesium, chloroaluminum, bromoaluminum, and metal-free phthalocyanine solid films," *Journal of Physical Chemistry B*, vol. 105, no. 8, pp. 1547–1553, 2001.
- [62] G. V. Buxton, C. L. Greenstock, W. P. Helman, and A. B. Ross, "Critical review of rate constants for reactions of hydrated electrons, hydrogen atoms and hydroxyl radicals in aqueous solution," *Journal of Physical and Chemical Reference Data*, vol. 17, no. 2, pp. 513–886, 1988.
- [63] N. Motohashi and Y. Saito, "Competitive measurement of rate constants for hydroxyl radical reactions using radiolytic hydroxylation of benzoate," *Chemical and Pharmaceutical Bulletin*, vol. 41, no. 10, pp. 1842–1845, 1993.
- [64] C.-Y. Wang, J. Rabani, D. W. Bahnemann, and J. K. Dohrmann, "Photonic efficiency and quantum yield of formaldehyde formation from methanol in the presence of various TiO₂ photocatalysts," *Journal of Photochemistry and Photobiology A*, vol. 148, no. 1–3, pp. 169–176, 2002.
- [65] N. Serpone, G. Sauvé, R. Koch, et al., "Standardization protocol of process efficiencies and activation parameters in heterogeneous photocatalysis: relative photonic efficiencies ζ_r ," *Journal of Photochemistry and Photobiology A*, vol. 94, no. 2-3, pp. 191–203, 1996.
- [66] C. Kormann, D. W. Bahnemann, and M. R. Hoffmann, "Photolysis of chloroform and other organic molecules in aqueous TiO₂ suspensions," *Environmental Science and Technology*, vol. 25, no. 3, pp. 494–500, 1991.
- [67] J. R. Darwent, P. Douglas, A. Harriman, G. Porter, and M. C. Richoux, "Metal phthalocyanines and porphyrins as photosensitisers for reduction of water to hydrogen," *Coordination Chemistry Reviews*, vol. 44, no. 1, pp. 83–126, 1982.
- [68] J. G. Moser, *Photodynamic Tumor Therapy: 2nd and 3rd Generation Photosensitizers*, Harwood Academic, Amsterdam, The Netherlands, 1998.
- [69] X. H. Qiu, G. V. Nazin, and W. Ho, "Mechanisms of reversible conformational transitions in a single molecule," *Physical Review Letters*, vol. 93, no. 19, Article ID 196806, 4, 2004.
- [70] H. Donker, A. van Hoek, W. van Schaik, R. B. M. Koehorst, M. M. Yatskou, and T. J. Schaafsma, "Spectroscopy and photophysics of self-organized zinc porphyrin nanolayers. 2. Transport properties of singlet excitation," *Journal of Physical Chemistry B*, vol. 109, no. 36, pp. 17038–17046, 2005.

Research Article

The Function of TiO₂ with Respect to Sensitizer Stability in Nanocrystalline Dye Solar Cells

A. Barkschat, T. Moehl, B. Macht, and H. Tributsch

Department Solare Energetik, Hahn-Meitner-Institut, 14109 Berlin, Germany

Correspondence should be addressed to H. Tributsch, tributsch@hmi.de

Received 25 October 2007; Accepted 13 December 2007

Recommended by M. Sabry Abdel-Mottaleb

Dyes of characteristically different composition have been tested with respect to long-term stability in operating standardized dye sensitized cells during a time period of up to 3600 hours. Selective solar illumination, the use of graded filters, and imaging of photocurrents revealed that degradation is linked to the density of photocurrent passed. Photoelectrochemical degradation was observed with all sensitizers investigated. Sensitization was less efficient and sensitizers were less photostable with nanostructured ZnO compared to nanostructured TiO₂. The best performance was confirmed for cis-Ru^{II}(dcbpyH₂)₂(NCS)₂ on TiO₂. However, it was 7–10 times less stable under other identical conditions on ZnO. Stability is favored by carboxylate anchoring and metal-centred electron transfer. In presence of TiO₂, it is enhanced by formation of a stabilizing charge-transfer complex between oxidized Ru dye and back-bonding interfacial Ti³⁺ states. This is considered to be the main reason for the ongoing use of expensive Ru complexes in combination with TiO₂. The local surface chemistry of the nanocrystalline TiO₂ turned out to be a crucial factor for sensitizer stability and requires further investigation.

Copyright © 2008 A. Barkschat et al. This is an open access article distributed under the Creative Commons Attribution License, which permits unrestricted use, distribution, and reproduction in any medium, provided the original work is properly cited.

1. INTRODUCTION

The sensitization of emulsions of semiconductor particles has played a major role in the development of photography [1, 2]. Photoelectrochemical studies on the mechanisms of spectral sensitization of semiconductors were performed in the late sixties [3–5]. Shortly thereafter, it was proposed to use dye sensitization to drive a new kind of solar cell [6]. The sensitizing Chlorophyll molecules were extracted from spinach to demonstrate solar energy conversion in analogy to primary photosynthesis [5, 6] (this, and not, as later claimed [7] the so called Grätzel cell, proposed 20 years later, was the first demonstration of bioanalogue solar energy conversion using dye molecules). Although, in the subsequent years, much scientific information on the sensitization process became available and reasonably efficient dye sensitized solar cells were demonstrated [8–14] on the basis of sintered oxide ceramics, it became more and more evident that the stability of organic sensitizers in such cells was a major problem. Nevertheless, in 1980, Matsumura et al. showed that on the basis of zinc oxide ceramics made intentionally porous with addition of aluminium, an efficiency for conversion of light into electrical energy

of 2.5% could be achieved (illumination occurred only in the absorption region of the dye) [14]. Up to that time, dyes from very different groups of chemicals and many different large gap semiconductors had been tested for the sensitization phenomenon. In 1980, Dare-Edwards et al. tested Ru-based dyes by attaching them with two ester linkages to TiO₂ [15]. At that time, with respect to efficiency, no peculiar advantage of attached Ru(bipy)₂(bpca) on a TiO₂ large gap semiconductor was observed. This was probably due to the specific experimental conditions involved. Some deterioration of current efficiency after many hours of illumination of the sensitized electrode was specifically mentioned. Interestingly, it was a very similar system which became the focus of attention 10 years later when high-efficiency, long-term stable nanocrystalline dye sensitized solar cells were proposed [16]. They used nanostructured TiO₂ material sensitized via chemically attached Ru-based dyes in combination with an I⁻/I³⁻ redox electrolyte. With such systems, solar energy conversion efficiencies of 7–10% were demonstrated with at least several cm² large cells (tiny cells reached 11–12%). A reasonable short-term stability was obvious when the cells were tightly sealed but a long-term stability of 20 years was claimed on the

basis of rather complicated experimental and theoretical arguments [17]. Involvement of the excited Ru-sensitizer in photochemistry was excluded due to a fast (femtosecond) injection rate observed for the electron into TiO₂ [18].

A fast regeneration of the oxidized Ru-sensitizer, on the other hand, was deduced from the presence of a high (0.5 M) concentration of iodide in the electrolyte. Regeneration rates sufficient for stabilization of solar cells for over 10⁸ cycles corresponding to 20 years lifetime were calculated [17]. In the course of intensive research which followed in the nineties, complications with respect to electrolyte chemistry, photochemistry, purity of sensitizers, as well as with respect to sealing and iodine chemistry were noted [19]. The best performing cells saw their sensitizer change from a three nuclear Ru-complex [16] to the mononuclear cis-Ru^{II}(dcbpyH₂)₂(NCS)₂ complex (here called N3) and the electrolyte solutions were replaced by less volatile and more stable ones. But after 15 years of research on Ru-based dye solar cells, and after efforts by many groups, reasonably stable dye solar cells have still not found their way into production. In fact, several companies have failed to produce reasonably stable commercial cells, with larger panels still degrading too fast (e.g., on the main building of CSIRO-Energy in Newcastle, Australia).

Since long-term stability of dye sensitized cells is a crucial issue for economic feasibility, long-term studies of dye sensitized cells have been initiated in increasing numbers [20–27] to take advantage of the high energy-conversion efficiency observed [28, 29]. However, a major problem turned out to be the sensitivity of the cells towards electrolyte loss via evaporation and the instability of the electrolyte. The chance of a dye sensitized solar cell to break down because of secondary phenomena not related to photochemical stability was very high. To overcome this problem, photocurrent imaging techniques were applied to visualize the effect of selective illumination of dye sensitized solar cells [30]. Only part of a dye sensitized solar cell was illuminated through a mask with simulated solar light (sulphur lamp) and the development of photocurrents were followed over a longer period of time by measuring spatially resolved images of the photocurrent. In these experiments, a He/Ne-laser spot was used for scanned illumination. In this way, clear differences between illuminated and nonilluminated areas could be observed [19]. This observation confirmed previous experiments with total reflection FTIR-studies performed on working dye sensitized solar cells. They indicated photo-induced generation of oxidation products of the Ru-sensitizer [31]. Significant quantitative differences between the performances of dye sensitized solar cells from different groups were observed. However, they behaved in a similar way qualitatively with respect to photo-induced degradation relative to stability in nonilluminated areas. A theoretical analysis of these preliminary studies indicated that the branching ratio, the ratio of regeneration rate of the oxidized sensitizer to the rate of product formation, is a crucial factor for stability of dye sensitized solar cells. It was estimated that it may be one order of magnitude lower than required for 20 years stability [32].

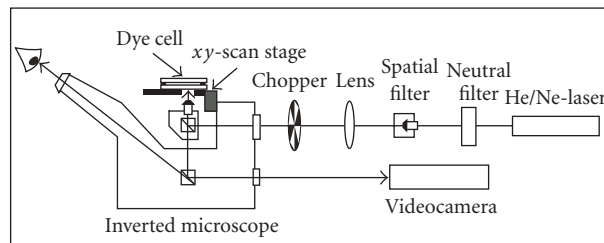


FIGURE 1: Scheme of the photoelectrochemical set up employing an optical scanning microscope (SMSC).

Some publications related the problem of dye cell degradation to the presence of water in the electrolyte [33] and other influences of the electrolyte [17, 31, 34] to higher temperatures [35] and to UV-light incidence [35]. In a more recent paper, the degradation mechanisms in a dye-sensitized solar cell were further investigated using UV/VIS- and IR-spectroscopy [36]. These results indicate a loss of the isothiocyanato-ligand of the TiO₂-adsorbed dye in the presence of air, at higher temperature or in the presence of water in the electrolyte. This effect is accelerated by illumination. It was found that this leads to a decreased, blue-shifted N3-dye absorption [36].

It is therefore necessary to investigate the problem of stability further, especially with respect to the origin of dye degradation. The question should specifically be answered is why, after so many years of intensive research on nanostructured dye solar cells, TiO₂ and expensive Ru-based sensitizers remained the by far preferred components of dye solar cells.

The aim of the present contribution is first to investigate different dyes, besides of the mainly used Ru-complex (N3), to study chemical preconditions for improved stability and, further, to find out whether the excited or the oxidized sensitizer is a key problem in inducing photochemical side-reactions. A key question will be the role which TiO₂ and its surface chemistry play for sensitizer photodegradation. For this reason, ZnO will be studied as a substrate in parallel. It should be investigated to what extent the chemical quality and surface morphology of nano-TiO₂ do have an influence on the survival of oxidized sensitizer molecules.

Photo-induced degradation, which is addressed here, is just one of several problems which can lead to degradation of dye sensitized cells. They have been discussed in a parallel publication [19] and include irreversible changes of the redox electrolyte, Li insertion into the oxide, loss of electrolyte through evaporation, and contamination from the atmosphere through the sealing material.

2. EXPERIMENTAL

The experimental strategy of this project consisted in fabrication of standard nanocrystalline dye sensitized solar cells like those now produced in many laboratories [19, 37, 38]. The cells were operated with 6 different sensitizers, which were selected as the most efficient from a larger number of dyes previously used. Both, cells made of nanocrystalline ZnO and

TiO₂ were compared, and the time-dependent performance of dye sensitized cells investigated by observing their photoelectrochemical performance and studying space resolved photocurrent images in order to distinguish the performance of illuminated and nonilluminated areas.

While screening a larger number of dyes (e.g., Ni-phthalocyanine, fluoresceine, rhodamine B, methylene blue, bromothymol blue, zinkone) for their function in standardized nanocrystalline dye sensitized cells, the work concentrated on the 6 best performing complexes. They were:

- (i) bis(tetrabutylammonium) cis-bis(isothiocyanato)bis(2,2'-bi-pyridine-4-carboxylic acid, 4'-carboxylate) ruthenium(II) or cis-Ru^{II}(dcbpyH₂)₂(NCS)₂, called N3 or Ru535 (obtained from Solaronics Inc., Aubonne, Switzerland),
- (ii) porphyrine,
- (iii) pyrogallol red,
- (iv) sodium salt of copper-chlorophylline,
- (v) di-(2,2'-dipyridylmethylene)[(2,2'-dipyridylmethylene) malonato]ruthenium(II)dihexafluorophosphate · 2HCL,
- (vi) di-(2,2'-dipyridyl)[(2,2'-dipyridylmethylene)nono-octadecyl malonato]ruthenium(II).

With the exception of porphyrine when chloroform was used, the dyes were dissolved in ethanol to give 0.3 mM stock solutions which were then applied to the nanocrystalline oxides.

2.1. Dye sensitized cells

Standard dye sensitized solar cells were prepared as described in the literature [19] and TiO₂-layers were prepared by hydrolysis of Ti(IV)isopropylate [39, 40].

For the preparation of TiO₂ layers, 1 mL 65%-HNO₃ was added to 120 mL of distilled water, and, for the next 45 minutes, a solution of 10 mL Ti(IV)isopropylate in 10 mL isopropanol was added under constant stirring in an argon atmosphere. A white colloidal precipitation was formed, and the isopropanol was removed by distillation. When the solvent left was only water, the suspension was kept under reflux for 8 hours. The suspension was then heated to 230°C while being stirred in an autoclave for 12 hours. After removing the water by vacuum distillation, 40% polyethylenglycol 20000 (40% relative to the content of TiO₂ (11–20%)) was added. This mixture was then applied onto the glass by pulling a glass rod over the surface. The thickness of the layer was kept constant by the use of a mask, which was fixed on the glass. The thickness of the TiO₂ nanolayer was adjusted to 5 μm, which is smaller than the optimum for high efficiency (10–15 μm) but adequate for 2–4% efficient experimental cells (excess dye should not be acting as a buffer). After drying for 15 minutes, the layers were tempered at 450°C for 30 minutes (cells of Figures 3(b), 3(c), 4(b), 6, 7).

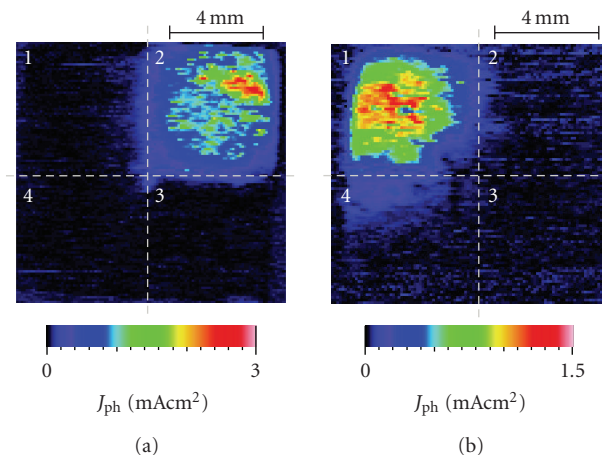


FIGURE 2: Photocurrent images of dye sensitized solar cells (nanocrystalline zinc oxide) subdivided into four sections for combinatorial testing (clock-wise from top left): (a) neutral red, N3-dye, rhodamine B, methylene blue; (b) N3-dye, neutral red, methylene blue, bromothymol blue. It is seen that only the N3 dye shows significant sensitization.

For ZnO-layers, commercial powders (Alfa, Aldrich) were used to prepare a suspension with the addition of acetyl acetone and water (1 : 10) and Triton X100 as a detergent.

The suspensions were again applied to the FTO-glass by pulling a glass rod over a mask, which was fixed on the glass. Afterwards, the samples were tempered at 450°C for 30 minutes (cells of Figures 2(a), 2(b), 3(a)).

Additionally, commercially available nanocrystalline TiO₂-layers from the Institute for Applied Photovoltaics, Gelsenkirchen (INAP) were used. (cells of Figures 4(a), 4(c), 4(d), 8).

After tempering, the layers were dipped while still hot (approx. 80°C) into a 0.2 mM or 0.3 mM solution of the dye. The second glass with the platinum back contact was fixed above the layer and the cells were sealed with Surlyn 1702 (DuPont). The whole cell was then put into electrolyte solution in an exsiccator. When vacuum was applied, the cell is filled with electrolyte. The electrolyte contained 0.5 M LiI, 50 mM I₂ and 0.2 M tert.-butylpyridine in acetonitrile.

2.2. Measurements

Dye sensitized solar cells were characterized by photocurrent voltage measurements before exposing them to solar simulated light (sulphur lamp) under short-circuit conditions. A scanning laser spot technique was used to produce images of photocurrents as described in Chaparro et al. [41]. The scanning microscope for semiconductor characterization (SMSC) (see Figure 1) is basically an inverted microscope provided with an *x-y* scan-stage. The laser spot was focussed by the microscope lens onto the dye sensitized solar cell, which was connected to a lock-in amplifier. The maximum spatial resolution of the used SMSC build up at HMI Berlin is 1 μm with a laser spot of 2 μm in diameter. In these experiments, a He/Ne-laser was used for illumination,

the light intensity was adjusted to 100 mWcm^{-2} . In order to study photodegradation, only well-defined surface areas (using masks) of the dye sensitized cell were illuminated with simulated solar light (solar simulator with sulphur lamp). The photocurrent images were recorded at intervals to investigate the development of photodegradation.

3. RESULTS

Because quantitative reproducibility of dye sensitized cells turned out to be difficult (efficiency, electrolyte stability, durability of sealing, and long-term behavior varied from cell to cell) combinatorial approaches to dye sensitized properties of different compounds seemed to be appropriate. Figure 2 shows the photocurrent images of two dye sensitized cells, each of which has been separated into four sections dyed with different sensitizers. Three of the sensitizing substances (the Ru-complex N3, neutral red and methylene blue) were identical in order to test the reproducibility. The additional sensitizers were rhodamine B in Figure 2(a) and bromothymol blue in Figure 2(b). As seen in Figures 2(a) and 2(b), only the Ru-complex N3 shows significant sensitized properties in the presence of the same iodide/triiodide-acetonitrile electrolyte. A larger number of potential candidates for sensitized were tested (e.g., Ni-phthalocyanine, fluoresceine, rhodamine B, methylene blue, bromothymol blue, zinkone) but only five additional compounds listed in the experimental section proved to be reasonably efficient for long-term testing. Among these were two additional Ru-complexes and the compounds porphyrine, pyrogallol red, and copper chlorophylline. Other compounds, such as rhodamine B or methylene blue, which had been demonstrated to sensitize ZnO reasonably well under different conditions, turned out not to be sufficiently effective in a nanocrystalline environment in the presence of an iodide/triiodide electrolyte in acetonitrile.

The six sensitizers mentioned were tested under comparable conditions in solar cells which had a nanocrystalline oxide layer of $4 \mu\text{m}$ only. This is significantly smaller than in high-efficiency dye sensitized cells ($8\text{--}16 \mu\text{m}$) so that the solar cell efficiency reached was correspondingly smaller. In the case of the N3 Ru-complex, the solar cell efficiency reached was between 2 and 3%. The same sensitized cell with ZnO yielded an efficiency between 0.3% and 0.45%. Solar cells fabricated with the above mentioned six different sensitizers were exposed to simulated solar light for periods of up to 30 days, and in the case of the Ru-N3 dye and nanocrystalline TiO_2 substrate for periods of up to 280 days. Photochemical degradation was observed in all cases. It was clearly more pronounced in the case of ZnO, even though simultaneously lower solar cell efficiencies were reached.

Figure 3(a) shows the integral photocurrent density-voltage characteristics of a nanocrystalline zinc oxide cell sensitized with the N3 ruthenium complex at the beginning of the experiment and after 20 days of continuous exposure to simulated solar light.

During this period the integral photocurrent density decreased by 35%. It is realized that basically only the photocurrent density decreased and not the photovoltage.

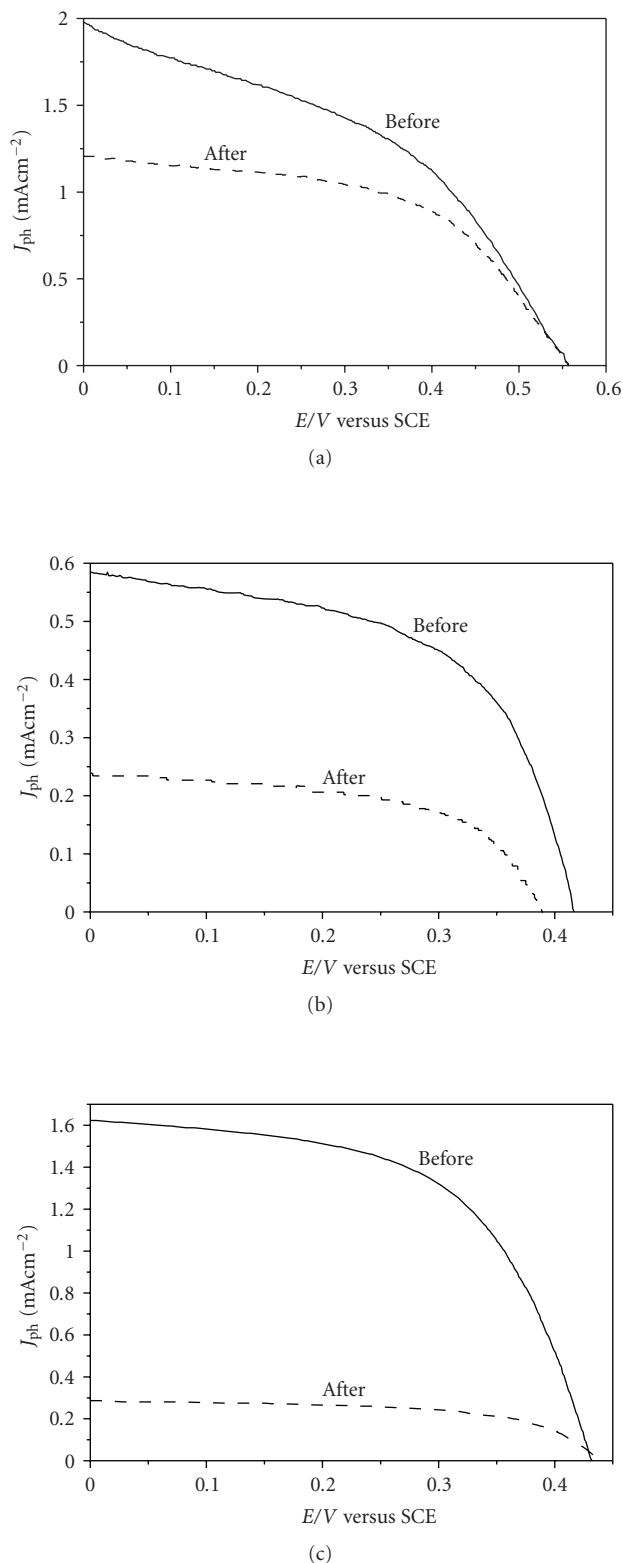


FIGURE 3: Power output characteristic (photocurrent voltage dependencies) of dye sensitized cells: (a) nanocrystalline ZnO, N3 complex before and after 20 days of simulated solar illumination; (b) nanocrystalline TiO_2 , pyrogallol red before and after 11 days of simulated solar illumination; (c) nanocrystalline TiO_2 , copper chlorophylline before and after 30 days of simulated solar illumination.

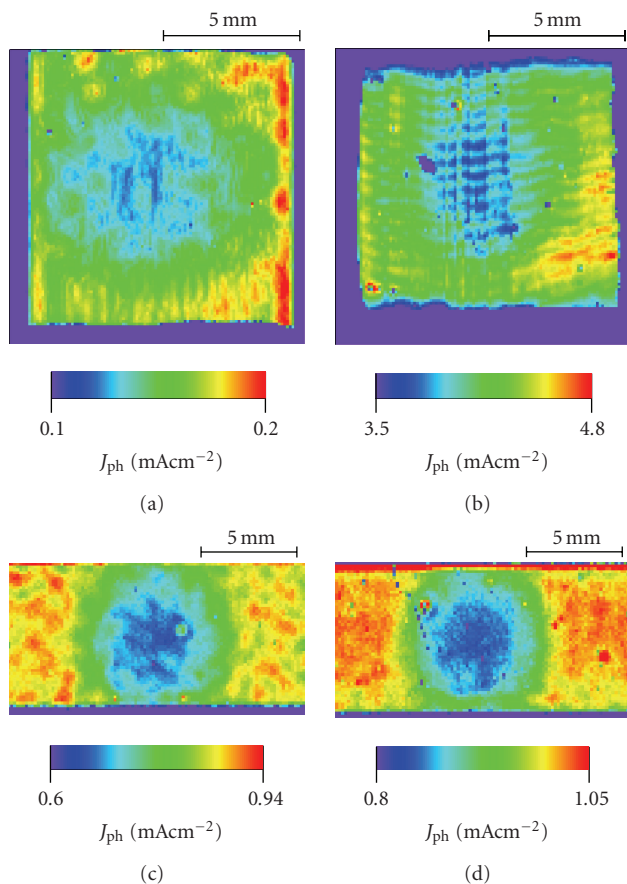


FIGURE 4: Photodegradation in photocurrent images of four regularly operating nanocrystalline TiO_2 solar cells. Sensitization with N3-dye and illumination with simulated solar light in a round central areas only. Illumination periods: (a) 1008 hours; (b) 336 hours; (c) 1248 hours; (d) 1248 hours.

Figures 3(b) and 3(c) show similar degradation curves of the power output characteristics of a nanocrystalline TiO_2 pyrogallol red cell and of a nanocrystalline TiO_2 copper chlorophylline solar cell. In the first case, Figure 3(b), the period of simulated solar light exposure was 11 days, in the second case the cell was exposed to solar light for 30 days. All investigated dyes showed a gradual photochemical degradation when exposed to simulated solar light for a prolonged period.

Among the many dyes which have been screened, only a few approach the properties of Ru-N3, as shown in Figure 2. Ru-N3 turned out to be the most favorable sensitizer, all other dyes exhibited lower efficiency and stronger degradation. Lower efficiencies and stronger degradation were also observed with nanocrystalline zinc oxide solar cells. Comparing different dyes, it was found that certain anchor groups like carboxyl or sulphone groups improve the sensitization properties of compounds. The interaction is apparently less efficient or of different nature with zinc oxide nanoparticles.

Special attention was dedicated to the degradation properties of the N3 ruthenium complex on nanocrystalline

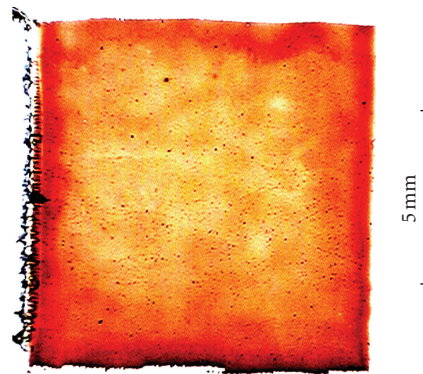


FIGURE 5: Video image of the cell in Figure 4(a), obtained under light transmission and after contrast amplification.

TiO_2 . Here, a long-term experiment, in which sensitized cells were exposed to simulated solar light during a period of 155 days, turned out to be especially informative. The cells were illuminated through a mask with a round opening in order to distinguish between illuminated and nonilluminated areas. During such long-term experiments, the instability of the iodide/triiodide electrolyte turned out to be a major problem. In some cases, depending on small variations in the preparation, the electrolyte was bleached so that the iodine largely disappeared from the electrolyte. This problem was investigated and may be understood in relation to the potential-pH diagram of iodine. Depending on traces of water which leak into the organic electrolyte through the seal from the outside, and due to the presence of tert.-butylpyridine, a slightly alkaline pH can be developed, which allows oxidation of iodide to iodate (IO_3^-). Since this iodate could not be detected spectroscopically in the electrolyte, it may have been adsorbed on the nanocrystalline TiO_2 -layer. Whatever the detailed mechanism of this process, it causes the disappearance of iodine and therefore the electron transport through the electrolyte became extremely limited.

In the above mentioned long-term experiment, four dye sensitized cells showed bleaching of the electrolyte, but were continuously operated under short-circuit conditions with a very small current flow. This means, since the photocurrent largely collapsed, that the bleached cells had a power output characteristic with low fill factor. At the end of the long-term experiment, all dye sensitized cells, both those that maintained good power output characteristics and those which were bleached and showed very unfavorable power output characteristics were investigated using the scanning laser technique to obtain photocurrent images. During these measurements, only a very small photocurrent generated by the laser spot (laser light intensity not exceeding solar light intensity) had to flow through the dye sensitized cell. Such a small current could also be maintained by those cells which had a bleached, iodine deficient electrolyte.

Figure 4 shows four dye sensitized cells (N3 ruthenium complex on nanocrystalline TiO_2) which operated with unbleached electrolyte (Figures 4(a)–4(d)). For comparison, four cells in which the electrolyte was bleached during

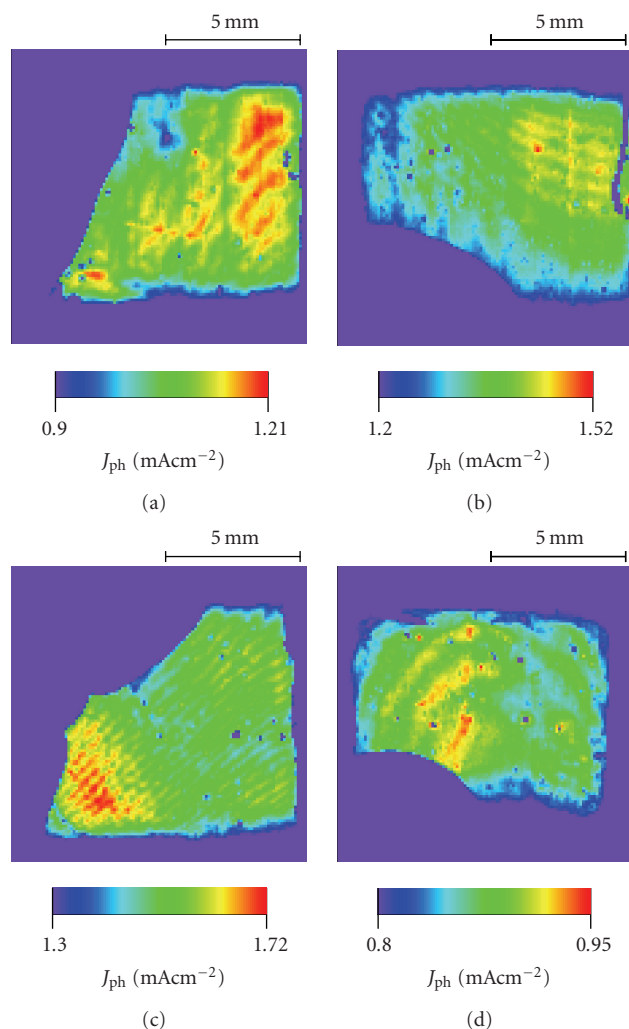


FIGURE 6: Photodegradation is not detected in photocurrent images of nanocrystalline TiO_2 solar cells with bleached electrolyte, which causes significantly decreased photocurrent densities during illumination. All cells are sensitized with N3 dye and were illuminated with simulated solar light in round central areas only. The illumination period was 150 days (3600 hours). The cells were at the end not completely wetted with electrolyte.

long-term (3600 hours) illumination are shown in Figure 6. In the first case (Figure 4), photodegradation of the ruthenium complex within the round areas illuminated with simulated solar light can clearly be recognized while in the second case there is no evidence of a difference between illuminated and nonilluminated areas of the dye sensitized solar cell. The difference between the cells in Figures 4 and 6 is simply that in the first case photocurrent could be passed in an uninhibited way, while in the second case photocurrent passage was severely hindered due to lack of iodine. This shows that photons and thermal energy alone are not the primary cause of the degradation if electrons are allowed to react back. Because the mask for forming the light patterns was black and placed directly onto the cell, thermal energy was also generated outside the circular opening. The graded

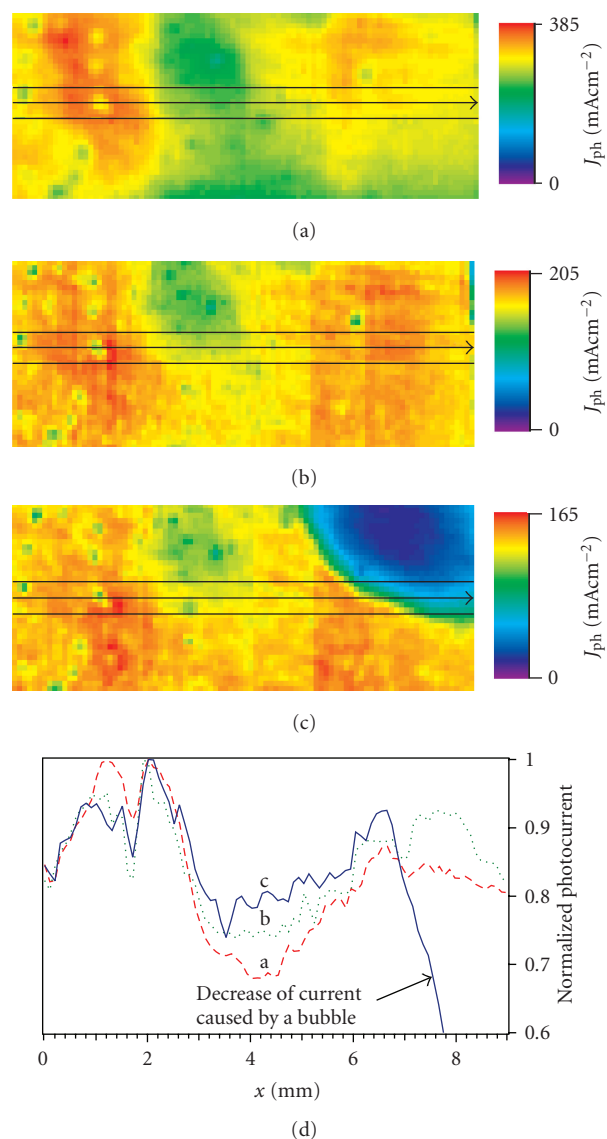


FIGURE 7: Photocurrent profiles at the same position across a dye sensitized solar cell with inhomogeneous photocurrent distribution. Measurements were done after different periods of illumination with simulated solar light. The photocurrent profiles smooth out during long-term photodegradation, because photodegradation is faster where large photocurrents are flowing. (Experiment performed with copper-chlorophylline on TiO_2): (a) before and (b) after 21 days, and (c) after another 93 days of illumination with simulated solar light.

filter also absorbed light to generate thermal energy, so that temperature gradients across nonhomogeneously illuminated solar cell surfaces were expected to be low.

The significant 15–30% photocurrent decrease observed during the long-term experiments (Figure 4) raises the question as to the optical visibility of the illuminated and degraded areas. Optical transmission was indeed changed.

As Figure 5 shows, after contrast amplification, the transmission pattern of the solar cell matches essentially the photocurrent pattern (Figure 4(a)). This video image

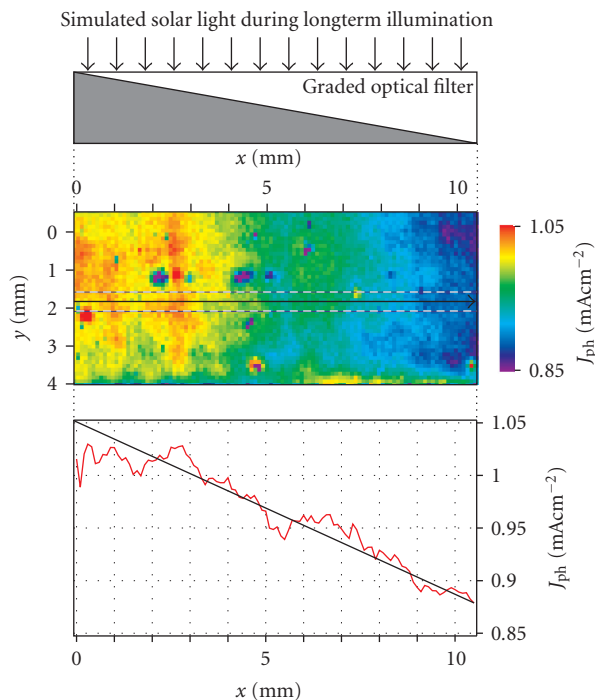


FIGURE 8: Nanocrystalline TiO_2 -N3 sensitized solar cell with graded filter placed on its surface after 1245 hours of exposure to simulated solar light. It is seen that photodegradation, measured as spatially resolved photocurrent output, is proportional to solar light intensity and thus the photocurrent passed.

(Figure 5) was obtained under light transmission, after cleaving of the cell, from only the front-half which consisted of ITO-glass and a TiO_2 -layer with adsorbed dye. An influence of the electrolyte or back-contact platinum layer is therefore excluded. However, with the naked eye the transmission change has only occasionally been observed clearly. This means it stayed within a 1-2% limit, which leads to the conclusion that the deactivated sensitizer still absorbs light in the visible spectral region. The degraded complex is still present and has only moderately changed its absorption spectrum in the visible spectral region with respect to the sensitizer.

These results show that photodegradation of the sensitizer must be related to the generation of sensitization photocurrents through the cell. In the case that these photocurrents cannot be generated, which causes the effective rapid recycling of the electrons, photodegradation is suppressed. Therefore, it can be concluded that only the oxidized state of the sensitizer is critical for photodegradation.

In order to test this interesting observation, which may also be relevant for other sensitizers, two additional experiments were performed. In the first, dye sensitized cells with very inhomogeneous photocurrent distributions were investigated. If a higher photocurrent density also means a higher rate of photodegradation, a profile through such an inhomogeneous cell should smooth out during a prolonged illumination. This means the photocurrent in high-photocurrent-density regions should decrease faster

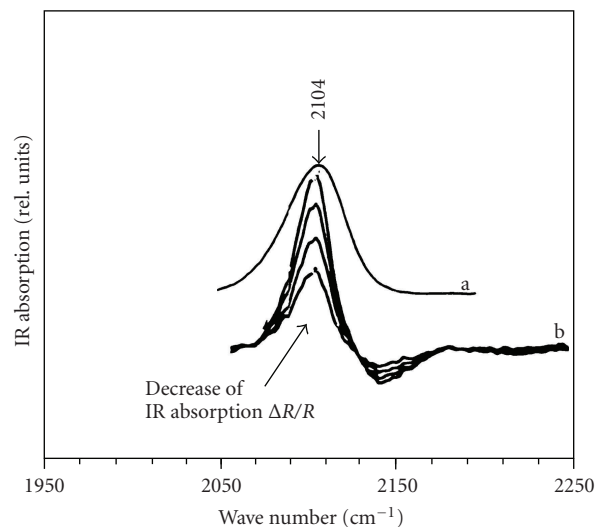


FIGURE 9: Shape of ex situ IR-CN stretch-line (2104 cm^{-1}) of N3 sensitizer (a) compared to lineshape characteristic for photodegradation loss after passage of 1.4, 5.4, 9.5, and 14 mC cm^{-2} of photoelectrical charge through the dye sensitized cell, (b) measured in total reflection FTIR-experiments.

than in lower-photocurrent-density regions. Such an experiment is demonstrated in Figure 7 showing the normalized photocurrent-profile through an inhomogeneous dye sensitized cell versus cell operation time. It is indeed recognized that the profiles smooth out with illumination time.

To confirm the conclusion that higher photocurrent flux means more degradation, a graded filter was placed onto an N3 dye sensitized cell for a long-term study. The cell with originally homogeneous photocurrent density distribution was exposed to simulated solar light attenuated by the graded optical absorption filter. Figure 8 shows that the spatially resolved photocurrent density measured after exposure of the cell to 1248 hours of simulated sunlight actually has a linear degradation profile. The laser-induced photocurrent decreases indeed proportional to the light intensity and thus to the magnitude of the photocurrent generated at the respective location. The higher the photocurrent density is, the higher the rate of degradation will be.

Total reflection infrared spectroscopy on functioning dye sensitized solar cells performed in our laboratory have demonstrated the occurrence of products parallel to photocurrent flow [31, 42]. The integrated infrared signal disappears when the current density goes to 0 and increases with increasing photocurrent density. These results confirm that the generation of oxidation products is related to the extraction of electrons from the sensitizer's environment. Depending, however, on the specific adsorption sites, sensitizer molecules may be involved in quantitatively different reaction behavior. The loss peaks in the in situ spectrum at 1988 cm^{-1} and 2104 cm^{-1} , with widths of 29 cm^{-1} and 26 cm^{-1} , respectively, showed a somewhat smaller width than in the ex-situ spectrum where the width was 33 cm^{-1} . This is shown in Figure 9 for the 2104 cm^{-1} line in the CN-vibration region. It shows the line shape from an

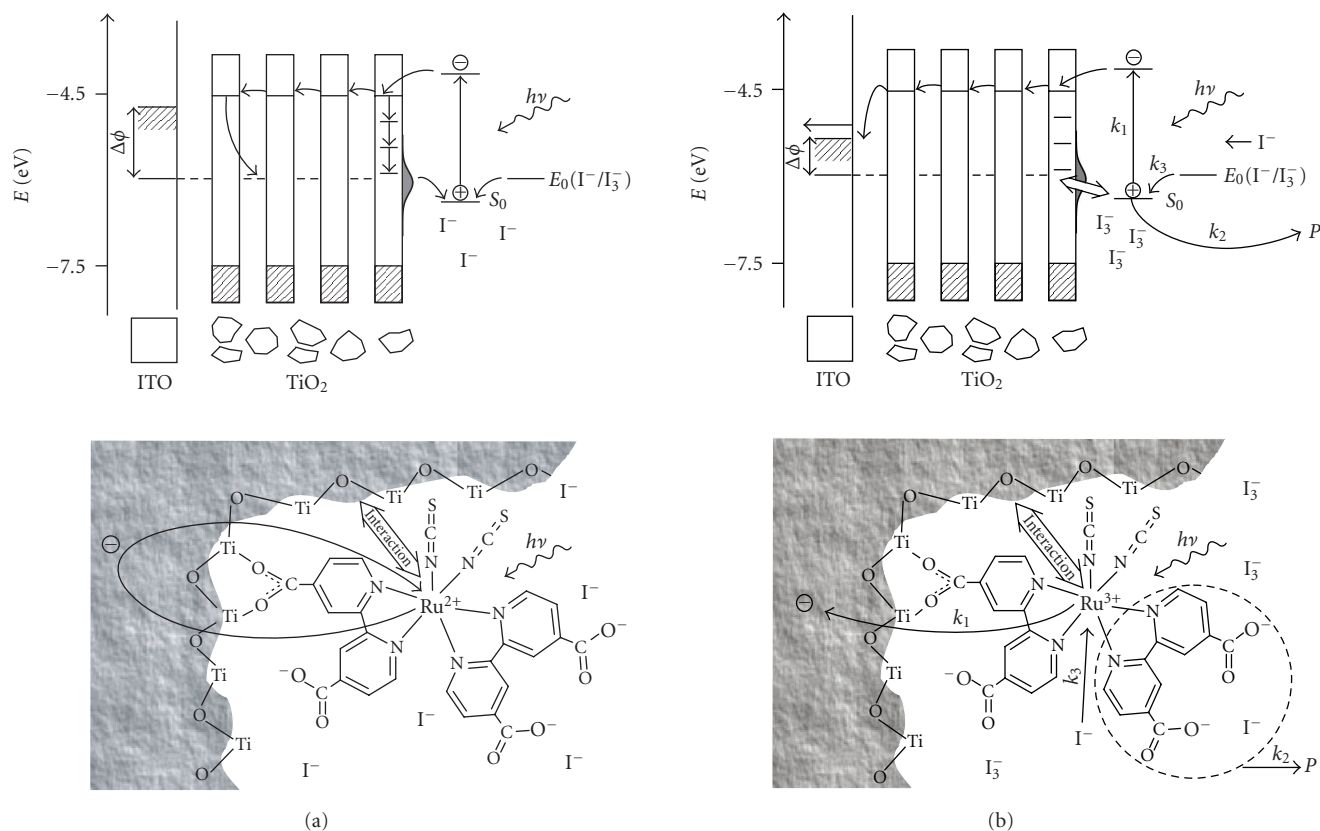


FIGURE 10: Compares the N3 ruthenium complex, both, in the state of rapid electron recovery (Figure 10(a)) and in the state of electron extraction via a reasonably high photocurrent flow (Figure 10(b)). While present in the TiO₂ interphase, the injected electron may convert Ti⁴⁺ into Ti³⁺ enabling a back bonding reaction facilitating a temporary Ti³⁺(ligand)Ru³⁺ charge transfer complex.

ex situ spectrum of cis-Ru^{II}(dcbpyH₂)₂(NCS)₂ adsorbed on nanocrystals within a 1 μm thin TiO₂ layer. It also shows the decrease of this absorption (plotted, however, in the opposite direction to permit a better comparison of line shapes) from an in situ experiment after passing the photocharge of 1.4, 5.4, 9.5, and 14 mCcm⁻² through the dye sensitized cell. A clearly narrower IR line due to the consumption of the sensitizer is realized, indicating that a limited fraction of adsorbed molecules is selectively turned over. The molecules preferentially consumed during photocurrent flow are those, which are positioned around the center of the line and not those which, due to stronger interaction with the TiO₂ substrate, are energetically positioned away from the center. This is clear evidence for the role of the TiO₂ adsorption site in determining the stability of sensitizing molecules during the photoreaction.

4. DISCUSSION

The main aim of this study was to identify physical-chemical factors relevant for long-term stability or degradation of sensitizers of nanocrystalline ZnO and TiO₂ solar cells to determine the influence of the adsorption site. The focus was on light-induced degradation. An analytical formula describing the nature of various cell parameters, and rate

constants which may influence the photocurrent voltage characteristic, had been presented in an earlier publication [32]. The photodegradation of sensitizer molecules is just one possible mechanism of degradation. Other processes involve the kinetics of the rectifying front TiO₂/fluorinated tin oxide contact (it is very critical for the performance and long-term stability of the dye sensitized solar cell), insertion of alkali atoms into TiO₂, irreversible changes of the redox electrolyte, loss of electrolyte, and contamination of the electrolyte from the atmosphere [19].

All sensitizers investigated in the present study, including the Ru-complex (N3), which presently is considered to be sufficiently stable for long-term (20 years) operation in dye sensitized cells, were found to degrade to varying extents. The N3 Ruthenium sensitizer turned out to be the most stable one, but it nevertheless photodegrades (Figure 4) and it degrades proportional to the photocurrent passed through the dye solar cell (Figure 8). This means that photodegradation will be the more pronounced the higher the cell efficiency.

Since this is a somewhat perturbing conclusion and since there have been persistent claims that the Ru-dye does not photodegrade and supports 10⁸ turnovers, let us first discuss our results in relation to other recent studies on dye solar cell performance and stability [20–29]. They, for example,

claim significant progress by using alternative electrolytes and improved sealing techniques (e.g., [20]). In this latter work, 0.6 M hexylmethyl imidazolium iodide was added to the acetonitrile electrolyte and a glass frit sealing was used. In stead of exposing the solar cell as it is to the solar simulator, the cell was first exposed to 80°C in the dark (!) for 1400 hours, and subsequently exposed to light for 1700 hours at only 25°C. The claim then was that the dye cell showed a photodegradation of less than 5% during 1700 hours. In fact, the entire procedure (thermal treatment plus subsequent illumination at 25°C) has decreased the solar cell efficiency by 20%, as seen from [20, Figure 10].

In reality, however, strong sunshine can heat a dye solar cell to 80°C, and the most damaging degradation process is the periodically daily heating and cooling of the dye solar cell under solar illumination.

For comparison, our solar cells, the selective degradation of which is depicted in Figures 4(c) and 4(d) decreased their photocurrents during 1248 hours of illumination and solar simulator determined higher temperature by approximately 10%. It has also to be considered that photodegradation was found to be proportional to its efficiency and thus to the photocurrent density passed (compare Figure 8). In addition, we are confronting these results with nearly Redox inactive solar cells, which show practically no degradation after 3600 hours (Figure 6). Our stability results therefore appear to be entirely realistic and contradict possible claims, that more recent cell configurations have solved the stability problem. Since the most stable dye cell in [20] only had an efficiency of 2%, our results also claim that a corresponding 8% solar cell will, under illumination, degrade 4 times faster, if a linear extrapolation is applicable. It will also degrade faster when illumination is not performed at 25°C, but at an illumination up to 60 degree higher temperature, which can be reached in intensive sunlight.

In our work, it could be confirmed that anchoring groups of the dye support the sensitization effect but that the nanocrystalline ZnO interface is a less favorable substrate for electron injection and long-term stability of Ru-dyes under the investigated conditions. It has, for example, been suggested [43] that the N3 ruthenium complex tends to aggregate by reacting with zinc ions dissolved from the ZnO interface. The oxide surface is electronically and chemically significantly different for TiO₂ and ZnO, the latter of which additionally exposes polar surfaces terminating with Zn and O, respectively. In our studies, degradation of this ruthenium complex is significantly faster on ZnO than on TiO₂. This degradation is faster by a factor of 7 to 10 on ZnO when the same iodide/triiodide electrolyte in acetonitrile is used.

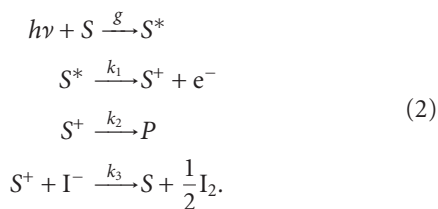
One reason why metal centered complexes (ruthenium complexes, copper chlorophylline complex) are more stable than sensitizers without transition metal centers may be due to coordination chemistry. The electron transfer occurs metal centred and involves states which are not essentially weakened by electron transfer. In addition, some coordinative interaction between iodide and oxidized metal centered sensitizers can occur. This allows a quite selective electron transfer which does not excessively weaken other

bonding states. Nevertheless, as shown in the literature [44], a ruthenium complex can undergo approximately 143 transitions involving different ligand configurations. Depending on the type of transition involved in the sensitization reaction, the oxidized product may have variable survival lifetimes because they involve different portions of the ligand environment. Figure 9 shows that not all sensitizer molecules at different adsorption sites of the TiO₂ environment are equally affected. This means that the reaction kinetics of molecules is dependent on the type of adsorption sites. Molecules which do not inject electrons or molecules which are immediately regenerated will not participate in the generation of the in situ infrared signal. Others, due to their peculiar adsorption position, may show preferred tendency towards product formation, that is, they may show a large k_2 rate constant and thus contribute to a decrease of life time (1) of dye sensitized cells, formulated below. The interface of ZnO apparently provides more unfavorable reaction possibilities. Alternatively, it may also be that the N3 dye has an especially favorable affinity to TiO₂. From Figure 9 it may be tentatively deduced that the weakly interacting N3 molecules and not the strongly interacting (large deviation from mean position of IR band) are preferentially lost to photodegradation. It may be that these molecules, after losing the injected electron, tend to irreversibly react, involving the chemistry of the interface. Recent HPLC-chromatic studies combined with UV/VIS-spectroscopy of N3-dye samples extracted from long-term illuminated solar cells have detected a variety of products which may have formed this way [45]. In this case, the interface of the substrate should be critical, which is indeed supported by the much higher degradation rate of N3 on nanocrystalline ZnO. Such an effect of the oxide interface on the rate k_2 of product formation could also explain why at the beginning of a long-term experiment the rate of photodegradation, as reflected in the branching coefficient k_{br} from relation (1), appears to be larger in some experiments before levelling off [30]. The reason may be that photo-oxidized molecules at selected surface sites, which provide an adequate surface environment, will more easily find reaction possibilities towards irreversible products.

Interestingly, however, as seen from Figure 6, degradation ceases (at least for the time window observed) when photocurrent flow through the cell is suppressed while all other parameters are maintained. This is a very important observation which has to be discussed in some detail. It explains why accelerated dye sensitized solar cell tests under high-illumination intensity, but under open-circuit conditions (no photocurrent flow), yielded no evident degradation and turnover numbers for electrons of the order of 10⁸. This would be necessary for a solar cell operation of 20 years [17]. Complementarily, experiments in Figure 4 clearly show that when photocurrent flows, the stability of the sensitizer is reduced. This is in agreement with the formula for the half-lifetime of a dye sensitized solar cell which has earlier been proposed [32]:

$$T_{1/2}^0 \sim \frac{S_0}{j_{ph0}} k_{br} \sim \frac{S_0}{j_{ph0}} \cdot \frac{k_3 I^-}{k_2} \quad (1)$$

with the branching coefficient $k_{br} = k_3[I^-]/k_2$ for the assumed simplest sensitizer reaction, S_0 = initial sensitizer concentration, j_{ph0} = initial photocurrent density, P = product for the reaction sequence



Relation (1) shows that the half lifetime of the dye sensitized cell is proportional to the initial concentration S_0 of the sensitizer in the nanostructure and inversely proportional to the initial photocurrent density. The perturbing fact is that the lifetime of the cell will be the shorter the higher its efficiency (and thus the photocurrent passing through it). This is clearly demonstrated by the graded filter experiment of Figure 8. The most successful long-term experiment of an optimized dye solar cell in [20] (1700 hours of solar illumination at only 25°C yielding less than 5% of degradation) was achieved with a cell of only 2% efficiency. A higher efficiency (photocurrent drawn) will correspondingly accelerate photodegradation. Depending on the temperature dependence of k_2 and k_3 in (2), the life time of the solar cell will be correspondingly temperature-dependent.

Additionally, it has to be considered that the rate of product formation, k_2 , will be influenced by the chemistry of the oxide/electrolyte interface (compare Figures 3(a) and 4, and 9), so that $k_2 = k_2$ (oxide interface). Considering relation (1), it has also to be pointed out that the amount S_0 of sensitizer in the nano-oxide layer may codetermine the initial degradation behavior of a cell. If the absorber layer is sufficiently thick and well be covered with dye molecules, excess sensitizer molecules may gradually and temporarily replace oxidized ones as sensitizers.

As discussed elsewhere [32], this branching coefficient may actually still be one order of magnitude too small to guarantee a 20 year lifetime of an efficient dye sensitized solar cell based on the N3 complex. But it turned out to be already surprisingly large for Ru-dyes, when compared with other sensitizers. However, the important finding that the sensitizer stability depends on the photocurrent density, and thus on the solar cell efficiency, explains, why further research on sensitizer stability is urgently needed. The instability problems are expected be the larger the higher dye solar cell efficiency, which is a critical factor for commercialization.

More recent systematic stability studies on dye sensitized cells performed [46] also show a clear dependence of degradation on the nature of the electrolyte (within 2 months approximately 40% in acetonitrile, 20% in propionitrile, 25% in methoxypropionitrile, and 75% in methoxyacetonitrile). But another study claims stability over 1000 hours at high efficiency [47] using a nonvolatile unspecified electrolyte. The experiments in this case were performed at 60°C during illumination, or at 80°C in the dark only. Real problems are to be expected and are actually found when the cell is allowed to heat to 80°C and beyond during periodic

daylight illumination, where complex instability problems arise [48]. Only one of the problems involved concerns, in this case, the dye.

If the simplified relation (1) is applied, the expected rate of dye degradation is inversely proportional to the half life time and thus

$$k_{degr}^0 \sim \frac{k_2 j_{ph0}}{S_0 k_3 [I^-]}. \quad (3)$$

This means it is determined, besides on the iodide concentration, by the reaction rates k_2 and k_3 , both of which should depend on the nature of the electrolyte as well as on the interfacial chemistry of the sensitizer adsorbed to oxide nanoparticles, and, of course, also on the temperature. It also follows that a negligible photocurrent will not induce significant degradation, as observed by comparing Figures 4 with 6. This, of course, explains why low-efficient dye solar cells yielded an apparent good long-term stability [17, 20]. But in order to understand reported good long-term stability at high current density [46], we have to assume a high rate of regeneration k_2 and a low rate of product formation k_3 . Both rates may depend on interfacial properties of the nano-oxides. In addition, a surplus of sensitizer S_0 in solar cells (S_0 in (3)) with a thick (15–20 μm) TiO₂ layer should theoretically be of advantage. However, it was found that, simultaneously, regeneration of S^+ by I^- is faced with transport problems, which lead to enhanced degradation with increasing layer TiO₂ thickness [49].

A puzzling result from our studies, apart from the fact that initial sensitizer degradation is faster than the later ongoing one, is that the same N3 dye is from 7 to 10 times less stable on ZnO compared with TiO₂ and also appears to depend on TiO₂ preparation. This means, for example, that the oxidation product of N3 generated on TiO₂ (Figure 10(b)) is different in its behavior from that formed on ZnO. This must indeed be concluded since, in both cases, electron transfer to the TiO₂ occurs in the pico to femtosecond range via the same carboxyl bridges, and since the possibly slightly different bond strength of which should only have a small influence on the life time of the large oxidized N3 molecule. Second, the initially faster degradation rate of N3 on TiO₂, and the difference in N3 degradation on differently prepared and inhomogeneous TiO₂ layers indicate that the specific surface chemistry and surface morphology of nano-TiO₂ should be critical. Therefore, it had to be investigated how the oxidized N3 species (Figure 10(b)) could differently interact with the TiO₂ and ZnO, respectively, to which an electron has previously been donated.

What this interaction could involve has been studied in a parallel paper [50]. Photocapacitive techniques (oxide layers exposed to a gas phase studied in capacitive setup) were applied to study sensitized TiO₂ and ZnO layers in contact with a controlled gas phase. When oxygen was removed from the gas phase, formation of Ti³⁺ states could be spectroscopically observed within the energy gap. When oxygen was removed in presence of the N3 sensitized TiO₂, it was found that the N3 dye forms a charge transfer complex with Ti³⁺ (generated by oxygen extraction from TiO₂ into

the gas phase) in the TiO₂ nanomaterial surface. This charge transfer complex formation is accompanied by a significant (0.4 eV) broadening of the N3 absorption band.

This phenomenon of a charge transfer complex (Figure 10(b)) turned out to be entirely reversible and disappeared when oxygen was added again to the gas phase bordering TiO₂, so that Ti³⁺ states were reconverted into Ti⁴⁺ states. This remarkable effect was only observed with the N3 dye and not observed with ZnO nor was it observed with metal cation-free dyes (Pyrogallol, Carmine) studied on the same TiO₂.

Our interpretation for the exceptional stability of N3 (and related Ru-based dyes) on TiO₂ is therefore tentatively the following: when excited N3 is transferring an electron to TiO₂ (Figure 10(b)), Ti⁴⁺ may be locally reduced to Ti³⁺, which now, via its d-state, can get involved in back bonding with the oxidized N3, so that a Ti³⁺-ligand-Ru³⁺ charge transfer complex is formed. This is a kind of microscopic feedback reaction. Macroscopically, an autocatalytic (feedback) process leads to selforganization and to a local export of entropy. This creates local order. This may also happen on a microscopic, macromolecular level. The feedback coupling (backbonding of the Ti³⁺ d-state with the oxidized N3 dye) may stabilize the oxidized N3 species, which temporarily forms a complex with (reduced) TiO₂. This could explain the longer survival of N3 sensitizer molecules on TiO₂ compared to ZnO in an entirely consistent way. As this phenomenon of a backbonding of N3 and of N3 stabilization had been predicted [51] in 2004 long before the relevant experiments were made [50], this adds credibility to the here discussed charge transfer hypothesis, which is clearly different from the traditional approach to understand electron injection from Ru(dcbpy)₂X₂ with (X₂ = 2 SCN, 2 CN or dcbpy) into TiO₂ [52]. It occurs within less than 100 femtoseconds, and sensitization efficiency was found to be dependent on the redox potential of the sensitizer. The latter observation [52] could also be consistent with the here discussed model of a charge transfer complex.

We may talk of a light-induced charge transfer complex formation of N3 on TiO₂ nanoparticles. Since TiO₂ nanomaterials require a temperature treatment for *favorable* sensitizer adsorption it may be that the TiO₂ surface has to be especially activated or optimized with respect to the charge-transfer interaction proposed. There may consequently be more favorable and less favorable nano-TiO₂ substrates.

On the basis of these new viewpoints on the stability of the dye solar cell, it is interesting to reconsider the development history of dye solar cells. The discovery of the improved efficiency and stability of dye solar cells using N3 and related Ru-based sensitizers [16] was essentially a chance discovery, based on a favorable combination of Ru sensitizer and with TiO₂. Before, dye solar cell experiments did not encourage major efforts, because the sensitizers were not sufficiently stable on sintered ZnO substrates [14] and earlier studies of Ru-dyes on TiO₂ [15] did not use the most favorable electrolytes. It also explains the comparatively flat learning curve [51] for the dye solar cell development, resulting from not recognizing the essential research targets. It equally explains why, after 15 years of

intensive research on the Grätzel cell [16], with much effort in direction of cheaper dyes, expensive ruthenium-based complexes (approx. 1000 \$ per gram) are still the preferred sensitizers.

Now the crucial role of TiO₂ chemistry should be highlighted: the most essential difference between sensitization of ZnO and of TiO₂ will be a higher life time of the oxidized N3 complex on TiO₂ due to the formation of the proposed light-induced Ti³⁺(ligand)Ru³⁺ charge transfer complex [50]. While optimizing the expensive Ru-dye further for still higher stability is a possible strategy, a preferable initiative would be to learn to get cheaper metal containing dyes reasonably charge transfer stabilized while reacting on TiO₂ surfaces. Can suitable alternative charge transfer complexes be designed to work with cheaper dyes containing more abundant transition metals?

For answering this question the here proposed mechanism will have to be studied theoretically and experimentally in greater detail. Since the nano-TiO₂ surface is critical for the formation of the charge transfer complex and for the rate of reaction (*k*₂) for formation of the oxidized sensitizer, it needs increased attention. Specifically, it should also be investigated, whether doping with transition metal ions, which can engage in d-state backbonding with the sensitizer, can increase sensitizer stability.

Interestingly, the here demonstrated influence of the nature of the absorption sites on the photochemical degradation of sensitizers has already been recognized in an early study, 35 years ago, on ZnO single crystals sensitized with chlorophyll [5]. From the degradation curve of chlorophyll sensitized electrodes, it was deduced that sensitizer molecules with widely different stabilities were active on the oxide surface.

In the future, the electronic properties of TiO₂ nanoparticle surfaces will have to be optimized for increased sensitizer stability and specific new sensitizer complexes should be tailored if advantage should be taken of the potentially low costs projected for dye solar cells.

REFERENCES

- [1] H. Meier, "Sensitization of electrical effects in solids," *Journal of Physical Chemistry*, vol. 69, no. 3, pp. 719–729, 1965.
- [2] H. Meier, *Spectral Sensitization*, The Focal Press, London, UK, 1967.
- [3] H. Gerischer, M. Michel-Beyerle, E. Rebertrost, and H. Tributsch, "Sensitization of charge injection into semiconductors with large band gap," *Electrochimica Acta*, vol. 13, no. 6, pp. 1509–1515, 1968.
- [4] H. Tributsch and H. Gerischer, "The use of semiconductor electrodes in the study of photochemical reactions," *Berichte der Bunsen-Gesellschaft für Physikalische Chemie*, vol. 73, pp. 850–854, 1969.
- [5] H. Tributsch and M. Calvin, "Electrochemistry of excited molecules: photo-electrochemical reactions of chlorophylls," *Photochemistry and Photobiology*, vol. 14, no. 2, pp. 95–112, 1971.
- [6] H. Tributsch, "Reaction of excited chlorophyll molecules at electrodes and in photosynthesis," *Photochemistry and Photobiology*, vol. 16, no. 4, pp. 261–269, 1972.

- [7] M. Grätzel, "Light and energy, dye sensitized solar cells mimic natural photosynthesis," in *Proceedings of "Solar Energy and Artificial Photosynthesis", Satellite Meeting of the SEB 14th International Congress on Photosynthesis (PS '07)*, The Royal Society, London, UK, July 2007.
- [8] H. Tsubomura, M. Matsumura, Y. Nomura, and T. Amamya, "Dye sensitized zinc oxide: aqueous electrolyte: platinum photocell," *Nature*, vol. 261, pp. 402–403, 1976.
- [9] T. Watanabe, T. Miyasaka, A. Fujishima, and K. Honda, "Photoelectrochemical study on chlorophyll monolayer electrodes," *Chemistry Letters*, vol. 7, no. 4, pp. 443–446, 1978, (Japan).
- [10] N. Alonso-Vante, M. Beley, P. Chartier, and V. Ern, "Dye sensitization of ceramic semiconducting electrodes for photoelectrochemical conversion," *Revue de Physique Appliquée*, vol. 16, pp. 5–10, 1981.
- [11] M. Nakao, K. Itoh, and K. Honda, "Effect of donor density of semiconductor on spectralsensitization photocurrent," *Denki Kagaku Oyobi Butsuri Kagaku*, vol. 52, p. 378, 1984.
- [12] M. T. Spitler and B. A. Parkinson, "Efficient infrared dye sensitization of van der Waals surfaces of semiconductor electrodes," *Langmuir*, vol. 2, no. 5, pp. 549–553, 1986.
- [13] K. Itoh, M. Nakao, and K. Honda, "Preparation of ZnO thin-film transparent electrodes and their application to electrochemical spectral sensitization," *Denki Kagaku Oyobi Butsuri Kagaku*, vol. 52, p. 382, 1984.
- [14] M. Matsumura, S. Matsudaira, H. Tsubomura, M. Takata, and H. Yanagida, "Dye sensitization and surface structures of semiconductor electrodes," *Industrial & Engineering Chemistry. Product Research and Development*, vol. 19, no. 3, pp. 4157–421, 1980.
- [15] M. P. Dare-Edwards, J. B. Goodenough, A. Andrew, K. R. Seddon, and R. D. Wright, "Sensitisation of semiconducting electrodes with ruthenium-based dyes," *Faraday Discussions of the Chemical Society*, vol. 70, pp. 285–298, 1981.
- [16] B. O'Regan and M. Grätzel, "A low-cost, high-efficiency solar cell based on dye-sensitized colloidal TiO₂ films," *Nature*, vol. 353, pp. 373–374, 1991.
- [17] O. Kohle, M. Grätzel, A. F. Meyer, and T. B. Meyer, "The photovoltaic stability of bis(isothiocyanato)ruthenium(II)-bis-2,2'-bipyridine-4,4'-dicarboxylic acid and related sensitizers," *Advanced Materials*, vol. 9, no. 11, pp. 904–906, 1997.
- [18] R. Eichberger and F. Willig, "Ultrafast electron injection from excited dye molecules into semiconductor electrodes," *Chemical Physics*, vol. 141, no. 1, pp. 159–173, 1990.
- [19] B. Macht, M. Turrion, A. Barkschat, P. Salvador, K. Ellmer, and H. Tributsch, "Patterns of efficiency and degradation in dye sensitization solar cells measured with imaging techniques," *Solar Energy Materials and Solar Cells*, vol. 73, no. 2, pp. 163–173, 2002.
- [20] J. Sastrawan, J. Beier, U. Belledin, et al., "New interdigital design for large area dye solar modules using a lead-free glass frit sealing," *Progress in Photovoltaics: Research and Applications*, vol. 14, no. 8, pp. 697–709, 2006.
- [21] T. Toyoda, T. Sano, J. Nakashima, et al., "Outdoor performance of large scale DSC modules," *Journal of Photochemistry and Photobiology A*, vol. 164, no. 1–3, pp. 203–207, 2004.
- [22] P. Wang, C. Klein, R. Humphrey-Baker, M. Zakeeruddin, and M. Grätzel, "Stable $\geq 8\%$ efficient nanocrystalline dye-sensitized solar cell based on an electrolyte of low volatility," *Applied Physics Letters*, vol. 86, no. 12, Article ID 123508, 3 pages, 2005.
- [23] P. Wang, S. M. Zakeeruddin, J. E. Moser, M. K. Nazeeruddin, T. Sekiguchi, and M. Grätzel, "A stable quasi-solid-state dye-sensitized solar cell with an amphiphilic ruthenium sensitizer and polymer gel electrolyte," *Nature Materials*, vol. 2, pp. 402–407, 2003.
- [24] G. E. Tulloch, "Light and energy—dye solar cells for the 21st century," *Journal of Photochemistry and Photobiology A*, vol. 164, no. 1–3, pp. 205–219, 2004.
- [25] K. Okada, H. Matsui, T. Kawashima, T. Ezure, and N. Tanabe, "100 mm \times 100 mm large-sized dye sensitized solar cells," *Journal of Photochemistry and Photobiology A*, vol. 164, no. 1–3, pp. 193–198, 2004.
- [26] M. Spath, P. M. Sommerling, J. A. M. van Roosmalen, et al., "Reproducible manufacturing of dye-sensitized solar cells on a semi-automated baseline," *Progress in Photovoltaics: Research and Applications*, vol. 11, no. 3, pp. 207–220, 2003.
- [27] S. Dai, K. Wang, J. Weng, et al., "Design of DSC panel with efficiency more than 6%," *Solar Energy Materials and Solar Cells*, vol. 85, no. 3, pp. 447–455, 2005.
- [28] Y. Chiba, A. Islam, R. Comiya, N. Koide, and L. Han, "Conversion efficiency of 10.8% by a dye-sensitized solar cell using a TiO₂ electrode with high haze," *Applied Physics Letters*, vol. 88, no. 22, Article ID 223505, 3 pages, 2006.
- [29] M. Wei, J. Konishi, H. Zhou, M. Janagida, H. Siguhara, and H. Arakawa, "Highly efficient dye-sensitized solar cells composed of mesoporous titanium dioxide," *Journal of Materials Chemistry*, vol. 16, pp. 1287–1293, 2006.
- [30] M. Turrion, B. Macht, P. Salvador, and H. Tributsch, "Imaging techniques for the study of photodegradation of dye sensitization cells," *Zeitschrift für Physikalische Chemie*, vol. 212, no. 1, pp. 51–57, 1999.
- [31] R. Grünwald and H. Tributsch, "Mechanisms of instability in Ru-based dye sensitization solar cells," *Journal of Physical Chemistry B*, vol. 101, no. 14, pp. 2564–2575, 1997.
- [32] H. Tributsch, "Function and analytical formula for nanocrystalline dye-sensitization solar cells," *Applied Physics A*, vol. 73, no. 3, pp. 305–316, 2001.
- [33] E. Rijnberg, J. M. Kroon, J. Wienke, et al., "More stability measurements were described," in *Proceedings of the 2nd European Photovoltaic Solar Energy Conference and Exhibition (PVSEC '98)*, p. 47, Vienna, Austria, July 1998.
- [34] S. A. Haque, Y. Tachibana, R. L. Willis, et al., "Parameters influencing charge recombination kinetics in dye-sensitized nanocrystalline titanium dioxide films," *Journal of Physical Chemistry B*, vol. 104, no. 3, pp. 538–547, 2000.
- [35] A. Hinsch, J. M. Kroon, R. Kern, et al., "Long-term stability of dye-sensitized solar cells," *Progress in Photovoltaics: Research and Applications*, vol. 9, no. 6, pp. 425–438, 2001.
- [36] H. G. Agrell, J. Lindgren, and A. Hagfeldt, "Degradation mechanisms in a dye-sensitized solar cell studied by UV-VIS and IR spectroscopy," *Solar Energy*, vol. 75, no. 2, pp. 169–180, 2003.
- [37] C. Barbé, F. Arendse, P. Comte, et al., "Nanocrystalline titanium oxide electrodes for photovoltaic applications," *Journal of the American Ceramic Society*, vol. 80, no. 12, pp. 3157–3171, 1997.
- [38] N. Papageorgiou, W. F. Maier, and M. Grätzel, "An iodine/triiodide reduction electrocatalyst for aqueous and organic media," *Journal of the Electrochemical Society*, vol. 144, no. 3, pp. 876–884, 1997.
- [39] M. A. Anderson, M. J. Giesemann, and Q. J. Xu, "Titania and alumina ceramic membranes," *Journal of Membrane Science*, vol. 39, no. 3, pp. 243–258, 1988.

- [40] B. O'Regan, J. Moser, J. Anderson, and M. Grätzel, "Vectorial electron injection into transparent semiconductor membranes and electric field effects on the dynamics of light-induced charge separation," *Journal of Physical Chemistry*, vol. 94, no. 24, pp. 8720–8726, 1990.
- [41] A. M. Chaparro, P. Salvador, and A. Mir, "Localized photoelectrochemical etching with micrometric lateral resolution on transition metal diselenide photoelectrodes," *Journal of Electroanalytical Chemistry*, vol. 422, no. 1-2, pp. 35–44, 1997.
- [42] R. Grünwald, Ph.D. thesis, Freie Universität, Berlin, Germany, 1997.
- [43] K. Keis, J. Lindgren, S. E. Lindquist, and A. Hagfeldt, "Studies of the adsorption process of Ru complexes in nanoporous ZnO electrodes," *Langmuir*, vol. 16, no. 10, pp. 4688–4694, 2000.
- [44] G. Calzaferri and R. Rytz, "Electronic transition oscillator strength by the extended Hueckel molecular orbital method," *Journal of Physical Chemistry*, vol. 99, no. 32, pp. 12141–12150, 1995.
- [45] M. Thomalla and H. Tributsch, "Chromatographic studies of photodegradation of $\text{RuL}_2(\text{SCN})_2$ in nanostructured dye-sensitization solar cells," *Comptes Rendus Chimie*, vol. 9, no. 5-6, pp. 659–666, 2006.
- [46] R. Kern, N. van der Burg, G. Chmiel, et al., "Long term stability of dye-sensitized solar cells for large area power applications," *Opto-Electronics Review*, vol. 8, no. 4, pp. 284–288, 2000.
- [47] D. Kuang, C. Klein, S. Ito, et al., "High-efficiency and stable mesoscopic dye-sensitized solar cells based on a high molar extinction coefficient ruthenium sensitizer and nonvolatile electrolyte," *Advanced Materials*, vol. 19, no. 8, pp. 1133–1137, 2007.
- [48] P. M. Sommerling, M. Späth, H. J. P. Smit, N. J. Bakker, and J. M. Kroon, "Long-term stability testing of dye-sensitized solar cells," *Photochemistry and Photobiology A*, vol. 164, no. 1–3, pp. 137–144, 2004.
- [49] M. Junghaenel and H. Tributsch, "Role of nanochemical environments in porous TiO_2 in photocurrent efficiency and degradation in dye sensitized solar cells," *Journal of Physical Chemistry B*, vol. 109, no. 48, pp. 22876–22883, 2005.
- [50] T. Dittrich, B. Neumann, and H. Tributsch, "Sensitization via reversibly inducible $\text{Ru}(\text{dcbpyH}_2)_2(\text{NCS})_2\text{-TiO}_2$ charge-transfer complex," *Journal of Physical Chemistry C*, vol. 111, no. 5, pp. 2265–2269, 2007.
- [51] H. Tributsch, "Dye sensitization solar cells: a critical assessment of the learning curve," *Coordination Chemistry Reviews*, vol. 248, no. 13-14, pp. 1511–1530, 2004.
- [52] J. B. Asbury, Y.-Q. Wang, E. Hao, H. N. Ghosh, and T. Lian, "Evidences of hot excited state electron injection from sensitizer molecules to TiO_2 nanocrystalline thin films," *Research on Chemical Intermediates*, vol. 27, no. 4-5, pp. 393–406, 2001.

Research Article

Characterization of Conjugated Polymer Poly(fluorene-co-thiophene) and Its Application as Photosensitizer of TiO₂

Rongliang Qiu,¹ Lin Song,¹ Dongdong Zhang,¹ Yueqi Mo,² Eric Brewer,³ and Xiongfei Huang¹

¹ School of Environmental Science and Engineering, Sun Yat-Sen University, Guangzhou 510275, China

² College of Material Science and Engineering, South China University of Technology, Guangzhou 510641, China

³ Viridian Environmental, LLC, Arlington, VA 22207, USA

Correspondence should be addressed to Rongliang Qiu, eesqrl@mail.sysu.edu.cn

Received 26 February 2007; Accepted 15 April 2007

Recommended by M. Sabry A. Abdel-Mottaleb

The copolymer poly(fluorene-co-thiophene) (PFT) has strong absorption in the visible light region. In this paper, PFTs with four different thiophene contents were evaluated for their suitability as photosensitizers of TiO₂. All four of the PFTs were capable of being excited by light with wavelengths above 455 nm, and all had reductive potentials more negative than the conduction band potential of TiO₂. Consequently, it was deemed that transfer of electrons from the excited PFTs to the conduction band of TiO₂ was thermodynamically possible. PFTs with higher thiophene content had more electron transitions in the excited state, resulting in increased photocatalytic activity of PFT-sensitized TiO₂. The method used to prepare the combined PFT/TiO₂ photocatalyst affected its photocatalytic activity. Best results in this study were achieved by dropwise addition of a tetrahydrofuran solution of PFT to a stirred TiO₂/ethanol suspension.

Copyright © 2008 Rongliang Qiu et al. This is an open access article distributed under the Creative Commons Attribution License, which permits unrestricted use, distribution, and reproduction in any medium, provided the original work is properly cited.

1. INTRODUCTION

Photosensitization of the semiconducting oxide TiO₂ is a method for extending its photoresponse in the visible light region by physically combining it with another semiconductor that acts as a photosensitizer. As p-type semiconductors, photosensitizers, which are commonly organic dyes, have strong absorption in the visible light region and can inject electrons into the conduction band of TiO₂ when excited by visible light, giving rise to a series of photochemical processes and allowing the photocatalytic reactions mediated by TiO₂ to operate under visible light irradiation.

Conjugated polymers composed of repeated small aryl ring molecules such as benzene, thiophene, and pyrrole are other types of organic semiconductors. Although the energy level difference between π -bonding and antibonding orbitals in a single aryl ring is large, it is found that as the number of repeated units increases, π orbitals overlap each other, causing the energy level difference between π -conjugated bonding and antibonding orbitals to decrease sharply and fall eventually to less than 4 eV. Energy level differences of this mag-

nitude make these polymers suitable for use as semiconductors. In addition, some of these polymers have a number of optical properties, such as electroluminescence and nonlinear optical behavior, that make them especially useful as photovoltaic materials. At present, conjugated polymers such as poly(3-methylthiophene) [1], poly(phenylene vinylene) [2], polyaniline [3], polypyrrole [4], poly(o-methoxy aniline) [5], poly(3-undecyl-2,2'-bithiophene) [6], and poly[2-(3-thienyl)-ethoxy-4-butylsulfonate] (PTEBs) [7] are being increasingly used in the field of photovoltaics as solid electrolytes and electrode sensitizers [8].

Methods for sensitizing semiconductors are similar to those for sensitizing electrodes of solar energy cells. However, little work has been done to date on the use of conjugated polymer-sensitized semiconductors to photocatalyze the degradation of organics under visible light irradiation, in part because of limitations of the polymers themselves. One problem is that the HOMO energy level of polymers is generally higher than those of inorganic materials and dyes, so polymers tend to be unstable and easily oxidized. In addition, the electron mobility of polymers is relatively poor. Finally,

it can be difficult to physically combine polymers and inorganic semiconductors, because most polymers are not soluble in water or ethanol. However, as research in this area continues, more and more polymers with improved characteristics are being synthesized. For example, the wide band gap polymer polyfluorene (PF) and the narrow band gap polymer polythiophene have improved antioxidative ability. Moreover, electron transfer takes place easily in thiophene-based polymers.

In this paper, a series of conjugated copolymers containing fluorene and thiophene [9] were investigated to evaluate their suitability as photosensitizers of TiO_2 .

2. EXPERIMENTAL

2.1. Materials

A series of copolymer PFTs with thiophene contents of 5%, 15%, 30%, and 50% (so called PFT5, PFT15, PFT30, and PFT50, resp.) were provided by College of Material Science and Engineering, South China University of Technology; the chemical structure is presented in Figure 1, TiO_2 (Degussa P25: 80% anatase, 20% rutile; BET $\sim 50 \text{ m}^2/\text{g}$). Purified water was obtained from a Millipore filtration system (Millipore ZLXS50020). All other chemicals were analytical grade and used without further purification.

2.2. Measurements and procedures

An HP 8453 diode array UV-Vis spectrophotometer (Agilent, USA) was used to directly record the UV-Vis spectra of the copolymer PFTs using chloroform as solvent. The electrochemical properties of PFTs were obtained with a CHI 660 A electrochemical workstation. Phenol concentration was monitored by UV-2450 spectrophotometer (Shimadzu, Japan) at a wavelength of 510 nm.

Sensitization of TiO_2 was performed according to the literature [10]. The photocatalytic degradation experiment was carried out by adding 50 mg photocatalyst into 50 mL phenol aqueous solution with 10 mg/L initial concentration. A 250 W GaI_3 lamp (DJG250, Shanghai Hualun Lighting Co. Ltd., China) with maximum radiant wavelength matched to the absorption wavelength of PFT was used as the visible light source. UV and IR cutoff filters were placed between the lamp and the glass reactor to ensure irradiation by visible light (400–700 nm) only. Light intensity was measured by a UV-A ultraviolet meter equipped with two probes with wavelengths of 420 nm and 365 nm, respectively. The glass reactor was open to air to ensure enough oxygen in the reaction solution. Prior to irradiation, the solution containing photocatalyst and phenol was magnetically stirred in darkness for 30 minutes to establish adsorption-desorption equilibrium. After a specified interval of irradiation time, a 5 mL aliquot of the reaction mixture was centrifuged and filtered through a $0.22 \mu\text{m}$ filter (Millipore), and the change in the concentration of phenol was monitored spectrophotometrically.

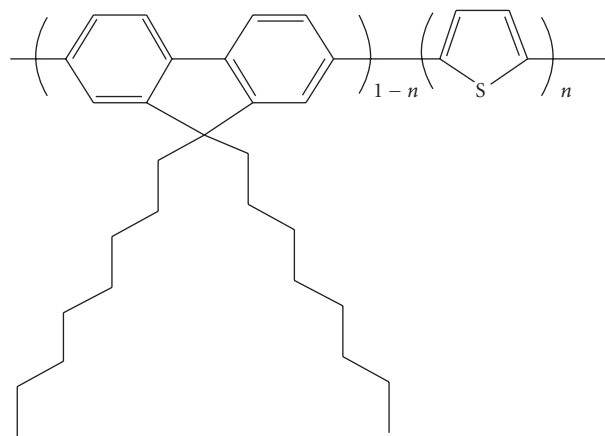


FIGURE 1: Structure of conjugated polymer poly(fluorene-co-thiophene).

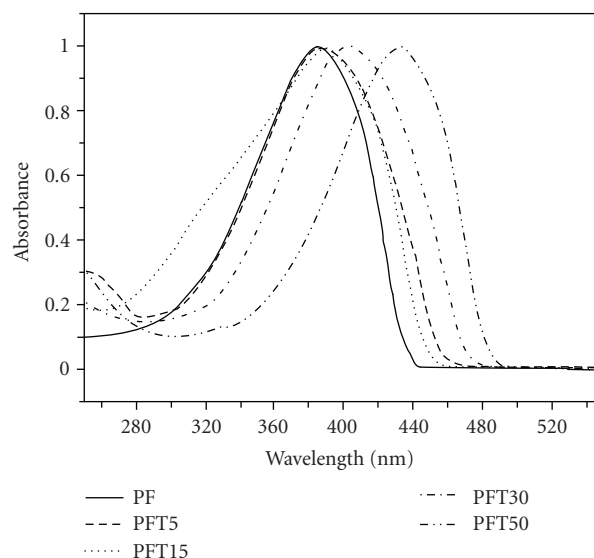


FIGURE 2: UV-Vis spectra of the different copolymers.

3. RESULTS AND DISCUSSION

3.1. Electrochemical properties of PFTs

Having strong absorption in the visible light region is the most important property of a photosensitizer. Figure 2 shows the UV-Vis spectra of the copolymers PF, PFT5, PFT15, PFT30, and PFT50 in chloroform. These polymers all have strong absorption in the visible light region. As expected, the intensity and maximum absorption peaks progressively increased and were red-shifted with increasing content of thiophene in the PFTs. The maximum absorption peaks are at 384 nm, 384 nm, 390 nm, 400 nm, and 433 nm, respectively. From Figure 2 it is observed that the absorption peaks of PFT5 and PFT15 were little changed from that of PF, while their spectra were slightly red-shifted toward the visible light region. The absorption peak of PFT30 was red-shifted from 384 nm (PF) to 400 nm, and its absorption edge

TABLE 1: Wavelength at peak absorption and electrochemical properties of PFTs.

| Copolymers | λ_{absmax} (nm) | E_{ox} (V) | E_{red} (V) | E_g (eV) | E_{HOMO} (eV) | E_{LUMO} (eV) |
|------------|-----------------------------------|------------------------|-------------------------|---------------|---------------------------|---------------------------|
| PTF5 | 455 | 1.38 | -1.35 | 2.73 | -5.78 | -3.05 |
| PTF15 | 470 | 1.31 | -1.33 | 2.64 | -5.71 | -3.07 |
| PTF30 | 480 | 1.30 | -1.28 | 2.58 | -5.70 | -3.12 |
| PTF50 | 490 | 1.22 | -1.31 | 2.53 | -5.62 | -3.09 |

was red-shifted to 480 nm. In the case of PFT50, the red shifting was more obvious; the absorption peak and edge were red-shifted to 433 nm and 490 nm, respectively. The increased red shifting that was associated with increased thiophene content of the PFTs was due to strong absorption of visible light by the thiophene units of the polymer. Compared with PF oligomers, the blocks of spatial configuration between thiophene ring and benzene ring in PFTs are smaller than those between benzene rings in PF, and twists between thiophene ring and benzene ring take place more easily, leading to higher coplanarity and a larger conjugated system in PFTs. In addition, the lone pair electrons of the sulfur atom in thiophene units increase the electron cloud density in the PFT chain, thereby increasing its ability to act as an electron donor and decreasing its band gap. Thus, higher thiophene content of a PFT is associated with higher coplanarity, lower band gap, and red shifting of its absorption spectrum.

The second most important property of a photosensitizer of TiO_2 is that its energy level matches that of TiO_2 . Only if the reductive potential of the photosensitizer is more negative than the energy level of the conduction band of TiO_2 , it is thermodynamically possible for excited electrons to be injected from the conduction band of the photosensitizer to the conduction band of TiO_2 .

Table 1 presents the wavelength at peak absorption and electrochemical properties of the PFTs used in this study. The peak and onset of absorption wavelength of PFTs were obtained from Figure 2, and the band gaps (E_g) were estimated by (1) [11]:

$$E_g = 1240/\lambda_{\text{onset}}, \quad (1)$$

$$E_{\text{red}} = (E_g E_{\text{ox}}), \quad (2)$$

$$E_{\text{HOMO}} = e(E_{\text{ox}} + 4.4), \quad (\text{eV}) \quad (3)$$

$$E_{\text{LUMO}} = e(E_{\text{red}} + 4.4), \quad (\text{eV}). \quad (4)$$

All oxidative potentials (E_{ox}) of PFTs were measured by a CHI 660 A electrochemical workstation, using a platinum electrode as working electrode, a saturated calomel electrode (SCE) as reference electrode, and a platinum wire as assistant electrode in 0.1 mol/L of tetra-*n*-butylammonium tetrafluoroborate (Bu_4NPF_6) in anhydrous acetonitrile as a supporting electrolyte with a scan rate of 50 mV/s. The reductive potentials (E_{red}), HOMO, and LUMO energy levels were calculated by empirical equations (2)–(4) [12], respectively.

The results in Table 1 indicate that the band gaps of these PFTs were less than or equal to 2.73 eV, which corresponds

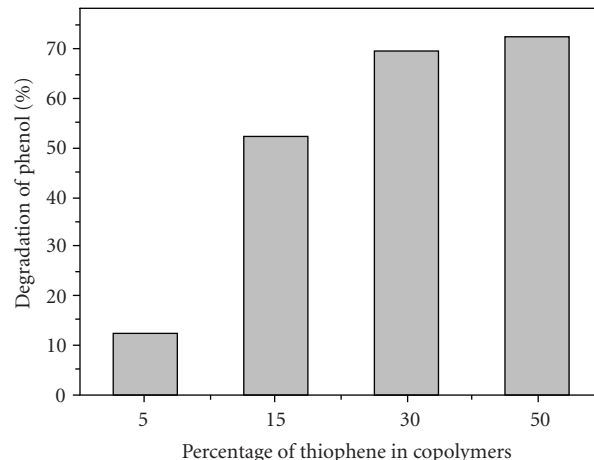


FIGURE 3: Photodegradation of phenol using PFT-sensitized TiO_2 [$\text{phenol}]_i = 10 \text{ mg/L}$, [$\text{photocatalyst}] = 1 \text{ g/L}$, irradiation time = 10 hours.

to excitation by wavelengths at or above 455 nm. The reductive potentials were approximately -1.30 V and were all more negative than the energy level of the conduction band of TiO_2 . Thus, transfer of electrons from excited PFTs to the conduction band of TiO_2 is thermodynamically possible. It was also found that with increasing thiophene content in the main chain of the polymer, the oxidative potential gradually decreased from 1.38 V (for PFT5) to 1.22 V (for PFT50). These oxidative potentials are higher than those of many polymers, and lead to stronger antioxidative ability.

3.2. Photodegradation of phenol using PFT-sensitized TiO_2

The photodegradation of phenol by PFT-sensitized TiO_2 is presented in Figure 3. During the photodegradation experiment, the light intensity was $E_{420} = 11.1 \times 100 \mu\text{W}/\text{cm}^2$ and $E_{365} = 1.4 \mu\text{W}/\text{cm}^2$. The maximum absorption wavelength of phenol is about 270 nm and phenol has no response for visible light. Our earlier experimental results showed that no phenol decomposes under visible light irradiation. From Figure 3, all of the PFTs were able to photosensitize TiO_2 . The photocatalytic activity of sensitized TiO_2 excited by visible light increased with increasing thiophene content of the PFT. The relatively small increase in catalytic activity between PFT30- and PFT50-sensitized TiO_2 was attributed to two factors. First, addition of 50% thiophene reduced the molecular weight of the PFTs from above 20000 to about 6000. As a result, there was less entwisting between PFT chains, so, the polymer film was weaker and did not adsorb as well onto the TiO_2 powder. Second, it was observed that PFT50 had lower solubility in tetrahydrofuran (THF) than the other polymers, which interfered with the physical process of combining it with the TiO_2 . Thus, we used PFT30 as sensitizer in the following experiments.

Commonly, PF has a larger band gap than PFT, with maximum absorption in the UV region [13, 14]. With increasing thiophene content in the main chain of PF, its band

gap decreases and its absorption spectrum is gradually red-shifted. It was found that PFT with a higher thiophene content had more electron transitions when excited by visible light, which resulted in greater photocatalytic activity of PFT-sensitized TiO_2 . Hara and coworkers [15] reported for the first time a new kind of sensitizers based on introducing thiophene moieties into a coumarin backbone, and then bonded it to the surface of TiO_2 with $-\text{COOH}$ bonds. Using this new compound in dye-sensitized solar cells, they achieved a remarkable solar energy-to-electricity conversion efficiencies of up to 7.7% under simulated solar irradiation ($100 \text{ mW} \cdot \text{cm}^{-2}$), which was the highest efficiency obtained among solar cells based on organic dye photosensitizers in the past decades. Luo and coworkers [16], studying the properties of oligothiophene carboxylic acid sensitized TiO_2 films, found that oligothiophene carboxylic acid could be used as a cosensitizer with N3 [Ru complex, $\text{Ru}(\text{II})\text{L}_2(\text{SCN})_2$, $\text{L} = 2,2'$ -bipyridyl-4,4'-dicarboxylate] dye, extending its spectrum and improving its photoelectric properties. Thiophene has also been used to improve the properties of porphyrin photosensitizers [17, 18]. Ha and coworkers [19] investigated singlet oxygen generation efficiencies of porphyrin and thiophene-modified porphyrin using time-resolved and steady-state spectroscopic methods. They found that the introduction of the sulfur atom from thiophene into the porphyrin core greatly increased the intersystem crossing rate due to spin-orbit coupling enhancement, resulting in enhanced triplet and singlet oxygen quantum yields. These results suggested that thiophene can improve the photophysical efficiency of photosensitizers. From the above, it is clear that addition of thiophene directly affects the properties of combinative photosensitizers.

Additionally, PFTs showed higher stability than other small molecular dyes such as rhodamine B and eosin Y under irradiation because of the higher oxidative potentials. Reused after 10 hours irradiation, PFT30 still had efficient photosensitization to TiO_2 , and the photocatalytic activity of PFT30-sensitized TiO_2 slightly decreased less than 10% under the same experiments conditions.

3.3. Effect of photosensitization method on photodegradation of phenol

In studies of organic pollution degradation using dye-sensitized TiO_2 , the primary methods used for combining dye with TiO_2 are simple adsorption [20, 21], chemical bonding [22], and LB (Langmuir-Blodgett) film technology [23]. The combining of TiO_2 with polymers depends primarily on adsorption and wrapping by polymer long chains. The conjugated polymer PFTs used in this paper have high solubility in aromatic solvents, begin to precipitate in ethanol, and have very low solubility in water. Thus, in the combining method that we designed, PFTs were first dissolved in THF, a good solvent, and then the solution was added to ethanol, a worse solvent, in order to initiate a gradual precipitation of PFT via wrapping of long chains. Finally, the solvents were removed by a rotary evaporator (RE-100, QUICKFIT, England), leaving the PFT coated on the surface of the TiO_2 . The precipitation of PFT and its bonding to TiO_2 are af-

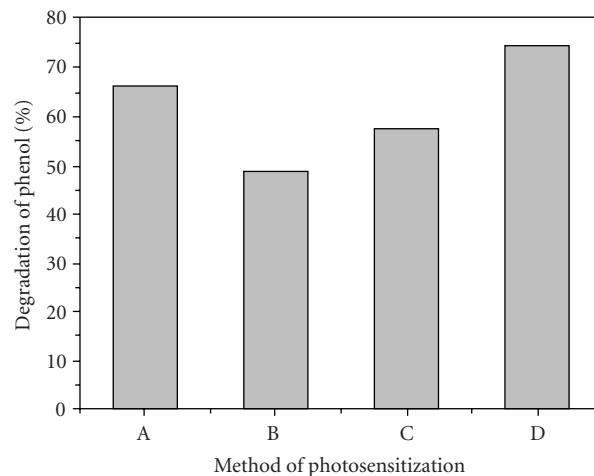


FIGURE 4: Photodegradation of phenol using PFT30-sensitized TiO_2 with different methods of photosensitization. A: PFT30/THF solution added to TiO_2 /ethanol suspension quickly. B: TiO_2 /ethanol suspension added to PFT30/THF solution quickly. C: PFT30/THF solution added to TiO_2 /ethanol suspension in two parts. D: PFT30/THF solution added dropwise to TiO_2 /ethanol suspension.

ected by the physical parameters of the combining process, including the method of mixing the solvents, the mixing time, and the method of adding the TiO_2 powder. These parameters must be optimized in order to avoid uneven deposition of PFT or premature agglomeration of TiO_2 , both of which can adversely affect configuration and separateness of the combinative photocatalyst and impair its photocatalytic activity. Figure 4 shows the results of an experiment in which the photodegradation of phenol was catalyzed by PFT30-sensitized TiO_2 prepared using four different methods. The photodegradation experiments conditions were the same with Section 3.2 in this paper.

Figure 4 indicates that addition of PFT30/THF solution to a TiO_2 /ethanol suspension produced a more active photocatalyst than addition of TiO_2 /ethanol suspension to the PFT30/THF solution. The best results were obtained by dropwise addition of PFT30/THF solution to the TiO_2 /ethanol suspension, which ensured that the PFT precipitated slowly enough to evenly coat the surface of the TiO_2 .

4. CONCLUSION

Four copolymers, consisting of poly(fluorene-co-thiophene) (PFT) with a range of thiophene content, were evaluated as photosensitizers of TiO_2 . All of the PFTs had strong absorption in the visible light region and had band gaps less than or equal to 2.73 eV, which corresponds to excitation by wavelengths above 455 nm. The reductive potentials of the PFT copolymers were approximately -1.30 V , which was more negative than the energy level of the TiO_2 conduction band. Thus, transfer of electrons from the excited PFTs to the conduction band of TiO_2 is thermodynamically possible. All of the PFTs were capable of photosensitizing TiO_2 . Photocatalytic activity of PFT-sensitized TiO_2 increased with

increasing thiophene content of the PFT. The method of preparation of the combined PFT/TiO₂ photocatalyst affected its photocatalytic activity. The best method of photocatalyst preparation in our study was dropwise addition of a solution of PFT in tetrahydrofuran to a stirred suspension of TiO₂ in ethanol.

ACKNOWLEDGMENT

This work was financed by the New Century Excellent Talent Program of MOE (NCET-04-0790), China.

REFERENCES

- [1] A. F. Nogueira, L. Micaroni, W. A. Gazotti, and M.-A. de Paoli, "Enhanced photoresponse of poly(3-methylthiophene) supported on TiO₂," *Electrochemistry Communications*, vol. 1, no. 7, pp. 262–265, 1999.
- [2] T. J. Savenije, J. M. Warman, and A. Goossens, "Visible light sensitization of titanium dioxide using a phenylene vinylene polymer," *Chemical Physics Letters*, vol. 287, no. 1-2, pp. 148–153, 1998.
- [3] M. S. Liu, Y. Z. Hao, X. B. Qiao, M. Z. Yang, M. S. Cai, and Y. F. Li, "Photoelectrochemical studies on nanoporous TiO₂/Pan film electrode," *Electrochemistry*, vol. 4, no. 3, pp. 246–251, 1998.
- [4] M. Martini and M.-A. de Paoli, "Effect of the electrolyte cations and anions on the photocurrent of dodecylsulphate doped polypyrrole films," *Solar Energy Materials and Solar Cells*, vol. 73, no. 3, pp. 235–247, 2002.
- [5] A. F. Nogueira, N. Alonso-Vante, and M.-A. de Paoli, "Solid-state photoelectrochemical device using poly(*o*-methoxy aniline) as sensitizer and an ionic conductive elastomer as electrolyte," *Synthetic Metals*, vol. 105, no. 1, pp. 23–27, 1999.
- [6] C. D. Grant, A. M. Schwartzberg, G. P. Smestad, J. Kowalik, L. M. Tolbert, and J. Z. Zhang, "Characterization of nanocrystalline and thin film TiO₂ solar cells with poly(3-undecyl-2,2'-bithiophene) as a sensitizer and hole conductor," *Journal of Electroanalytical Chemistry*, vol. 522, no. 1, pp. 40–48, 2002.
- [7] J. T. McLeskey Jr. and Q. Qiao, "Hybrid solar cells from water-soluble polymers," *International Journal of Photoenergy*, vol. 2006, Article ID 20951, 6 pages, 2006.
- [8] J. N. de Freitas, V. C. Nogueira, B. I. Ito, et al., "Dye-sensitized solar cells and solar module using polymer electrolytes: stability and performance investigations," *International Journal of Photoenergy*, vol. 2006, Article ID 75483, 6 pages, 2006.
- [9] Q. Hou, Y. Niu, W. Yang, R. Yang, M. Yuan, and Y. Cao, "Synthesis and electroluminescent properties of copolymer of fluorene and thiophene," *Acta Polymerica Sinica*, no. 2, pp. 161–165, 2003.
- [10] L. Song, R. Qiu, Y. Mo, D. Zhang, H. Wei, and Y. Xiong, "Photodegradation of phenol in a polymer-modified TiO₂ semiconductor particulate system under the irradiation of visible light," *Catalysis Communications*, vol. 8, no. 3, pp. 429–433, 2007.
- [11] T. Sasaki, N. Koshizaki, J.-W. Yoon, and K. M. Beck, "Preparation of Pt/TiO₂ nanocomposite thin films by pulsed laser deposition and their photoelectrochemical behaviors," *Journal of Photochemistry and Photobiology A: Chemistry*, vol. 145, no. 1-2, pp. 11–16, 2001.
- [12] D. M. de Leeuw, M. M. J. Simenon, A. R. Brown, and R. E. F. Einerhand, "Stability of n-type doped conducting polymers and consequences for polymeric microelectronic devices," *Synthetic Metals*, vol. 87, no. 1, pp. 53–59, 1997.
- [13] Q. Pei and Y. Yang, "Efficient photoluminescence and electroluminescence from a soluble polyfluorene," *Journal of the American Chemical Society*, vol. 118, no. 31, pp. 7416–7417, 1996.
- [14] Y. W. Di, X. W. Ba, D. M. Xie, and R. S. Wang, "The novel functional materials polyalkylfluorene derivatives and their applications," *Journal of Functional Materials*, vol. 28, no. 4, pp. 346–349, 1997.
- [15] K. Hara, M. Kurashige, Y. Dan-Oh, et al., "Design of new coumarin dyes having thiophene moieties for highly efficient organic-dye-sensitized solar cells," *New Journal of Chemistry*, vol. 27, no. 5, pp. 783–785, 2003.
- [16] Z. Luo, S.-X. Tan, J. Zhai, et al., "Photo-electric conversion properties of oligo-thiophene carboxylic acid sensitized porous TiO₂ films," *Chemical Journal of Chinese Universities*, vol. 25, no. 1, pp. 154–156, 2004.
- [17] C.-H. Hung, C.-K. Ou, G.-L. Lee, and S.-M. Peng, "Structure and characterization of the first metal complex of dithiaporphyrin: Ru(S₂TTP)Cl₂," *Inorganic Chemistry*, vol. 40, no. 26, pp. 6845–6847, 2001.
- [18] L. Latos-Grazyński, J. Lisowski, M. M. Olmstead, and A. L. Balch, "21-Thiatetra-*p*-tolylporphyrin and its copper(II) bicarbonate complex. Structural effects of copper-thiophene binding," *Journal of the American Chemical Society*, vol. 109, no. 14, pp. 4428–4429, 1987.
- [19] J.-H. Ha, S. Ko, C.-H. Lee, W.-Y. Lee, and Y.-R. Kim, "Effect of core atom modification on photophysical properties and singlet oxygen generation efficiencies: tetraphenylporphyrin analogues core-modified by oxygen and/or sulfur," *Chemical Physics Letters*, vol. 349, no. 3-4, pp. 271–278, 2001.
- [20] D. Chatterjee and A. Mahata, "Demineralization of organic pollutants on the dye modified TiO₂ semiconductor particulate system using visible light," *Applied Catalysis B: Environmental*, vol. 33, no. 2, pp. 119–125, 2001.
- [21] D. Chatterjee and A. Mahata, "Visible light induced photodegradation of organic pollutants on dye adsorbed TiO₂ surface," *Journal of Photochemistry and Photobiology A: Chemistry*, vol. 153, no. 1–3, pp. 199–204, 2002.
- [22] X. Li, W. Zhao, and J. Zhao, "Visible light-sensitized semiconductor photocatalytic degradation of 2, 4-dichlorophenol," *Science in China, Series B: Chemistry*, vol. 45, no. 4, pp. 421–425, 2002.
- [23] X.-S. Feng, S.-Z. Kang, H.-G. Liu, and J. Mu, "Study of the photophysical properties of composite film assembled of porphyrin and TiO₂ nanoparticles," *Thin Solid Films*, vol. 352, no. 1-2, pp. 223–227, 1999.

Research Article

Influence of Irradiance, Flow Rate, Reactor Geometry, and Photopromoter Concentration in Mineralization Kinetics of Methane in Air and in Aqueous Solutions by Photocatalytic Membranes Immobilizing Titanium Dioxide

Ignazio Renato Bellobono,¹ Mauro Rossi,¹ Andrea Testino,² Franca Morazzoni,² Riccardo Bianchi,³ Giulia de Martini,⁴ Paola Maria Tozzi,⁴ Rodica Stanescu,⁵ Cristina Costache,⁵ Liliana Bobirica,⁵ Mauro Luigi Bonardi,⁶ and Flavia Groppi⁶

¹ Environmental Research Centre, University of Milan, Camillo Golgi 19 Street, 20133 Milan, Italy

² Department of Materials Science, University of Milano Bicocca, Cozzi 43 Street, 20126 Milan, Italy

³ ISTM, Institute of Molecular Sciences and Technologies, National Research Council (CNR), 20133 Milan, Italy

⁴ R&D Group, BIT srl, 20121 Milan, Italy

⁵ Department of Inorganic Technology and Environmental Protection, Polytechnic University of Bucharest, 011061 Bucharest, Romania

⁶ LASA, Department of Physics, University of Milan and National Institute of Nuclear Physics (INFN), 20133 Milan, Italy

Correspondence should be addressed to Ignazio Renato Bellobono, ignazio.bellobono@unimi.it

Received 19 September 2007; Accepted 13 December 2007

Recommended by M. Sabry Abdel-Mottaleb

Photomineralization of methane in air (10.0–1000 ppm (mass/volume) of C) at 100% relative humidity (dioxygen as oxygen donor) was systematically studied at 318 ± 3 K in an annular laboratory-scale reactor by photocatalytic membranes immobilizing titanium dioxide as a function of substrate concentration, absorbed power per unit length of membrane, reactor geometry, and concentration of a proprietary vanadium alkoxide as photopromoter. Kinetics of both substrate disappearance, to yield intermediates, and total organic carbon (TOC) disappearance, to yield carbon dioxide, were followed. At a fixed value of irradiance ($0.30 \text{ W} \cdot \text{cm}^{-1}$), the mineralization experiments in gaseous phase were repeated as a function of flow rate ($4\text{--}400 \text{ m}^3 \cdot \text{h}^{-1}$). Moreover, at a standard flow rate of $300 \text{ m}^3 \cdot \text{h}^{-1}$, the ratio between the overall reaction volume and the length of the membrane was varied, substantially by varying the volume of reservoir, from and to which circulation of gaseous stream took place. Photomineralization of methane in aqueous solutions was also studied, in the same annular reactor and in the same conditions, but in a concentration range of 0.8–2.0 ppm of C, and by using stoichiometric hydrogen peroxide as an oxygen donor. A kinetic model was employed, from which, by a set of differential equations, four final optimised parameters, k_1 and K_1 , k_2 and K_2 , were calculated, which is able to fit the whole kinetic profile adequately. The influence of irradiance on k_1 and k_2 , as well as of flow rate on K_1 and K_2 , is rationalized. The influence of reactor geometry on k values is discussed in view of standardization procedures of photocatalytic experiments. Modeling of quantum yields, as a function of substrate concentration and irradiance, as well as of concentration of photopromoter, was carried out very satisfactorily. Kinetics of hydroxyl radicals reacting between themselves, leading to hydrogen peroxide, other than with substrate or intermediates leading to mineralization, were considered, and it is paralleled by a second competition kinetics involving superoxide radical anion.

Copyright © 2008 Ignazio Renato Bellobono et al. This is an open access article distributed under the Creative Commons Attribution License, which permits unrestricted use, distribution, and reproduction in any medium, provided the original work is properly cited.

1. INTRODUCTION

Air and water pollution is notoriously a serious problem facing all anthropic activities throughout the world. To reduce this problem, many physical, chemical, and biological technologies are available [1]. Conventional methods based

on stripping, such as adsorption by activated carbon, result only in transfer of pollutants from one phase to another, and not to integral destruction. On another side, thermal oxidation techniques may be valuable but surely not cost effective, particularly at low contamination values, due to the added fuel consumption; furthermore these methods contribute to

massive carbon dioxide production. Photocatalytic processes on semiconductors, on the contrary, are one of the newer advanced oxidation processes (AOP) techniques. They were developed during the last twenty five years [1–9], in the presence of catalysts, such as titanium dioxide, with UV radiation. If the UV radiation is from the sun, the treatment costs are reduced drastically by transforming photocatalysis in one of the most appealing and environmentally friendly processes for complete mineralization of organic pollutants. Furthermore, photocatalytic processes may be used as a pretreatment of toxic chemicals, in order to convert them into fully biodegradable compounds to be finally processed by the most economical technology presently available, that of active sludge [10]. Combination of photocatalysis with active sludge techniques is undoubtedly one of the most promising technologies to degrade and mineralize, efficiently and inexpensively, wastes containing toxic compounds.

The major problem in photocatalysis, from the point of view of industrial applicability, is given by the necessity of immobilizing the semiconductor photocatalyst, by firmly anchoring it to a suitably reacting structure, and of reaching the highest performance as possible in photocatalytic reactors, in continuous mode [11]. These two aspects (kind of immobilization, as linked to kinetic modeling of the whole course of the photomineralization process, and quantum yields) need therefore to be considered as priority options for engineering applications. In all preceding papers of this series (see, e.g., among the most recent ones [12–14]), the main concern has been devoted to these topics, and immobilization of semiconductor photocatalyst and its photopromoting agents in a membrane structure has been the choice, in order to manufacture modular membrane reactors, the performance of which has been effectively estimated as one of the highest for energy efficiency [11].

From the point of view of mechanisms of surface photochemical reactions that take place in heterogeneous systems, a recent article [15] has criticized the a priori assumed validity of the Langmuir-Hinshelwood kinetic model to interpret the experimental observations, as well as the assertion that the kinetics of a heterogeneous photoreaction are either first-order or half-order dependent on photon flow. Such a criticism has already been emphasized in the literature also from the point of view of engineering applications, and dates back to earlier pilot plant studies [16], which have shown, for example, the influence of flow rate on apparent thermodynamic constant of adsorption/desorption, relative to the Langmuir-Hinshelwood model, as well as the inadequacy of this model to fit kinetics of mineralization, other than in the segment of the initial rate [12–14], particularly when using immobilized photocatalysts, so that this pseudothermodynamic parameter of the Langmuir-Hinshelwood model should have a, partly at least, kinetic character.

It is well known that, in carefully deaerated water, and in the absence of any kind of oxygen donors, following radiation absorption by the semiconductor, photogenerated holes react with hydroxyl groups of water to give hydroxyl radicals $\cdot\text{OH}$, while photogenerated electrons reduce hydroxonium ions and cause hydrogen evolution. On the contrary, in aerated water, the photogenerated conduction-band electrons

reduce dissolved oxygen or other oxygen donors added to this purpose to yield $\text{O}_2^{\cdot-}$ in acid-base equilibrium with HO_2^{\cdot} . The possibility of the latter reaction to take place quantitatively is of uttermost importance in environmental applications of photocatalysis, because, in the last case, oxidation of organic compounds may be carried out by HO_2^{\cdot} together with $\cdot\text{OH}$ radicals. This allows to obtain a fourfold maximum quantum yield with respect to that permissible if each absorbed photon would be able to produce a single hydroxyl radical only. This occurrence has been shown as effective [12, 16, 17] when using, for example, ozone as oxygen donor and when promoting the activity of the immobilized semiconductor by suitable doping agents, such as Co(III) or V(V), coimmobilized with the semiconductor itself in a membrane structure and acting as scavengers of generated photoelectrons.

Comparison of efficiency of different kinds of supported or immobilized photocatalysts, and objective, quantitative characterization of their photocatalytic power are thus the major problems to define kinetic reactivity. In most of literature works, this kind of assessment is often made simply by matching qualitatively concentration profiles of degraded species. In addition, in many cases described in the literature, no regard is made to total organic carbon (TOC) mineralization, but merely to the transformation of substrate into some intermediate compound, as the first step of the complicated reaction mechanism leading finally to carbon dioxide. Moreover, it is a common practice, even when quantitative evaluations are made, to consider the photocatalytic process as a first-order reaction, while it has been definitely ascertained that apparent reaction order varies with the concentration of substrate [13, 16]. With an evident transition from a limiting zero-order, at high concentrations, to a limiting first-order at low concentrations. Modeling of photocatalytic reactions, on the contrary, in a wide range of concentrations, and over all the kinetic concentration profile of TOC, leading to full mineralization, has been approached systematically in previous papers of this series [12–14, 18], mostly for processes carried out in aqueous solutions. This has been done also from the standpoint of quantum yields and energy efficiencies, a very important aspect, which is often neglected in the literature pertinent to photocatalysis.

In the present paper, modeling will be extended to photocatalytic kinetic runs in gaseous phase, by using methane in air as a model molecule, both to apply the four-parameter kinetic model used successfully in preceding studies [12–14, 18] for fitting the whole kinetic profile, and to broaden the application of this model, as a function of all variables which show an influence on the photocatalytic kinetics, and consequently play a primary role in all trustworthy characterization procedures of immobilized materials. The dependence of the four parameters of the kinetic model cited above [12–14, 18] on flow rate, on reactor geometry, on radiation flow, and on the concentration of a proprietary photopromoter coimmobilized with the semiconductor in the photocatalytic membranes will be first examined. By this way, information, preliminarily investigated in a previous work [19] on methane in air, will be implemented and get deeper. Secondly, the influence of these variables on the same parameters above [12–14], relatively to experiments carried

out in aqueous solutions, will be checked in order to systematically compare reactivity in liquid and gaseous phases. Finally, the dependence of quantum yields on the concentration of substrate and on photon flow will be considered and analyzed, with the goal of attaining, by all these variables expressed in the most convenient ways, a complete rationalization of the photocatalytic process, both in liquid and gaseous phases, from the engineering point of view, as well from the perspective of establishing a reliable standardization method of the photocatalytic performance of materials.

2. EXPERIMENTAL

2.1. Materials

Methane was obtained from Fluka (GC purity greater than 99.8%). It was used as received with no further purification. Ultra pure water, to be used for preparation of methane solutions, or to be aerosolized in the reactor, when performing kinetic runs of methane in air, to maintain a 100% relative humidity at the operating temperature of the photoreactor (maximum contents of Na^+ and heavy metal ions 0.02 and 0.004 mg Kg^{-1} , resp.), was obtained by cross-flow ultrafiltration on composite membranes immobilizing active carbon and nuclear grade ion exchange resins, as described [20]. Concentration of substrate in the gas phase was 10.0–1000 ppm (mass expressed as carbon/volume), while in aqueous solution it could be varied, for solubility reasons, only between 0.80 and 2.00 ppm.

2.2. Photocatalytic membranes

The photocatalytic membranes (*PHOTOPERM BIT/313*), kindly supplied by B.I.T. srl, Milan, I, were standard photocatalytic membranes, immobilizing 30 ± 3 wt.% of titanium dioxide (P25 by Degussa, Germany) in the absence and in the presence of a photocatalytic promoter, as cocatalyst. In the latter case, a proprietary synergic mixture of tri-(*t*-butyl)- and tri-(*i*-propyl)vanadate(V) [10] was used, by varying the vanadium concentration in the range 0.1–10 mol/mol % with respect to that of titanium. Photocatalytic membranes [16, 21], and more generally membranes, prepared by photografting, to immobilize reagents, catalysts, and sorbents [22–24], were described and characterized in previous studies. These membranes were prepared (patents pending) by grafting and graft-polymerizing, onto a non-woven microporous polypropylene tissue, $250 \pm 9 \text{ g}\cdot\text{m}^{-2}$ of a prepolymeric blend containing 30 ± 3 wt.% of titanium dioxide (P25 by Degussa, Germany), under rheological control, in the presence of proprietary photoinitiating and photosensitizing systems.

2.3. Apparatus and procedures

The laboratory-scale photoreactor was substantially the same as that already described [25], with some differences in the materials and operating procedures, as it will be specified later on, and the change is that it was made gas tight to avoid any leakage of substrate and/or intermediates through the

vapour phase, both when operating with gaseous methane in air or with its aqueous solutions. Contrarily to procedure of previous work [19], in which, when operating in the gaseous phase, an aqueous solution of hydrogen peroxide was aerosolized continuously into the reactor, in order to supply the stoichiometric amount of this oxygen donor, in the present work, only ultra pure water was aerosolized in the photoreactor, just to maintain a 100% relative humidity at $318 \pm 3 \text{ K}$, which was the operating temperature of the reactor. This was made, to check the influence on the rate of the oxygen content of air, instead of using hydrogen peroxide. Stoichiometric hydrogen peroxide, on the contrary, was always used when operating with aqueous solutions of methane. Overall volume of gaseous or liquid phase being treated was $4.000 \pm 0.005 \text{ L}$, in standard experiments; the ratio between the overall reacting volume and the length of the lamp, corresponding to the length of the irradiated side of the membrane, was $160 \pm 6 \text{ cm}^3/\text{cm}$. A high-pressure mercury arc lamp with a nominal power of 1.00 KW was employed, kindly supplied by Chimia Prodotti e Processi (Muggiò, Milan, Italy): it was further provided with a step-by-step power regulation device, so that power absorbed by the membrane, as determined actinometrically, could be varied between 0.10 and $4.0 \text{ W}\cdot\text{cm}^{-1}$. The membrane being concentric to the lamp in the photoreactor used, absorbed power per unit length of lamp was also the same, if referred to unit length of membrane. At $0.30 \text{ W}\cdot\text{cm}^{-1}$, the overall power absorbed by the membrane, within the absorption range of immobilized semiconductor, in the experimental conditions of the present work, was 30 W, corresponding to $4.45 \times 10^{-5} \text{ Einstein s}^{-1}$. In this paper, as well as in all preceding papers of this series, when concerning laboratory-scale experiments carried out in the presence of hydrogen peroxide as an oxygen donor, the radiating flow, unless otherwise stated, being filtered by a suitable borosilicate glass, corresponded to a radiation wavelength range from the band gap of TiO_2 downwards to 315 nm, so that direct photolysis of hydrogen peroxide to give hydroxyl radicals was inhibited. Owing to the refrigeration system of the lamp, by means of water circulating in the lamp sheath, made of quartz, mean temperature, during the runs, was $318 \pm 3 \text{ K}$.

In the present, as well as in previous papers of this series, membranes were placed and fixed coaxially with the lamp, in such a way that the flow was perpendicular to the membrane. Owing to the microporous structure of the membrane, the pressure drop was very modest: it corresponded to 0.9–1.6 mm Hg, when the flow rate of the liquid system was $4 \text{ m}^3/\text{h}$ in the laboratory-scale photoreactor.

During some of the gaseous phase experiments, the flow rate was varied between 4 and $400 \text{ m}^3/\text{h}$. In these experiments, in order to examine the influence of flow rate on parameters of kinetic model used, irradiance was fixed at a value corresponding to $0.30 \text{ W}\cdot\text{cm}^{-1}$.

The standard flow rate in gaseous phase kinetic runs, to study the influence of irradiance on parameters above, was $300 \text{ m}^3/\text{h}$. In this latter experimental condition of flow rate, the ratio between the overall reaction volume and the length of the membrane was varied substantially by varying the volume of reservoir, from and to which circulation of

gaseous stream took place. This was carried out to study the influence of reactor geometry on kinetic parameters above, and by operating at a constant irradiance, corresponding to $0.30 \text{ W} \cdot \text{cm}^{-1}$

The disappearance of methane, as such, was followed by GC-MS quantitative analysis into the injection port of a GC-MS system. A Varian 3400 with a septum-equipped programmable injector was used. In the GC oven, a $30 \text{ m} \times 0.53 \text{ mm}$ DB5MS megabore column was installed with the following temperature programme: 20°C for 1 minute followed by a temperature raise of $5^\circ\text{C}/\text{min}$ to 240°C , which was held for 4 minutes.

As a carrier gas, He was used at a flow rate of $25 \text{ mL}/\text{min}$. The GC was interfaced via jet separator (0.3 mm Hg in the separator and 0.03 mm Hg in the analyser) and a transfer line (270°C) to an ITS40 ion trap mass-spectrometer (ITMS). The ion trap was operated at 300°C in the electron impact mode, scanning from $35 \text{ M}/\text{Z}$ to $550 \text{ M}/\text{Z}$ in 1.5 second. The GC-ITMS data were acquired on a 386/387 Compaq personal computer with Saturn I software (Varian). Methane was identified by its mass spectrum and standard samples. Quantification was based on seven-point calibration curves using, as internal standard, a standard sample containing perdeuterated methane.

In order to study the relationship between the rate of methane disappearance, as such, and the overall rate of organic carbon disappearance, this latter was also followed by total organic carbon (TOC) analysis. To this purpose, a Shimadzu TOC-V instrument was used, by which the contribution of inorganic carbon present was always evaluated, in order to obtain TOC by difference from total carbon and inorganic carbon determinations. Determinations were accurate within 20 ppb C .

During all the duration of the runs, no sensible decrease of activity of the immobilized photocatalyst was observed, as checked both by random repetition of experiments at various initial concentrations of the hydrocarbons, both in the liquid and in the gaseous phase, and by reiteration of whole series of tests at the beginning and at the end of the prolonged period, throughout which experimentation has been carried out.

2.4. Kinetic modeling

Kinetic modeling was carried out by generalizing procedures followed in preceding papers [12, 13, 26]. These procedures have not the goal of proposing and checking photochemical mechanisms, but simply its goal is to reproduce closely experimental data, for engineering purposes, without any strict implication on the true mechanisms.

If mineralization of substrate **S** to CO_2 is supposed to occur through one single intermediate **I**, following scheme (1)



and if both **S** and **I** show a competitive apparent adsorption onto the immobilized semiconductor surface, as expressed by apparent adsorption constants K_1 and K_2 , respectively, models for experimental data, used in nonlinear regression anal-

ysis, are not expressed in a closed-form equation

$$y_{(\text{calc})} = f(x), \quad (2)$$

but as the following system of first-order ordinary differential equations in the dependent variables C_S , C_I , and C_{CO_2} :

$$\left(\frac{dC_S}{dt}\right) = \frac{-k_1 \cdot K_1 \cdot C_S}{1 + K_1 \cdot C_S + K_2 \cdot C_I}, \quad (3)$$

$$\left(\frac{dC_I}{dt}\right) = \frac{k_1 \cdot K_1 \cdot C_S \cdot k_2 \cdot K_2 \cdot C_I}{1 + K_1 \cdot C_S + K_2 \cdot C_I}, \quad (4)$$

$$\left(\frac{dC_{\text{CO}_2}}{dt}\right) = \frac{k_1 \cdot K_1 \cdot C_I}{1 + K_1 \cdot C_S + K_2 \cdot C_I}, \quad (5)$$

where C denotes concentrations of species to which the pertinent suffix refer, t time; k_1 and k_2 the kinetic constants relative to degradation of **S** and **I**, respectively. Intermediate **I** is supposed to simulate the behavior of all the often uncountable, numerous intermediates, which are on the route from the substrate **S** to CO_2 . Experimentally speaking, only kinetic profiles of **S** and CO_2 may be easily followed. Even if, for the molecule chosen in the present investigation, a limited number of intermediates may be reasonably envisaged from the substrate to CO_2 , the same is not true [12, 13, 26] for aromatic and/or heterocyclic compounds, or still for long-chain aliphatics, which have been the object of previous investigations.

Random errors in t can be neglected, and only the random errors in the dependent variables are considered.

The error sum, $G(k_1, k_2, K_1, K_2) = \sum_{i=1}^n w_i [C_{\text{S}(\text{exp})}^i - C_{\text{S}(\text{calc})}^i]^2$, is minimized to obtain the best values of the k_1 , k_2 , K_1 , K_2 parameters; $C_{\text{S}(\text{exp})}^i$ and $C_{\text{S}(\text{calc})}^i$ represent the n measured and calculated substrate concentration values, respectively, and $w_i = 1/\sigma^2(C_{\text{S}(\text{exp})}^i)$ is the weighting factor.

Furthermore the conservative balance of carbon has to be accounted for and verified experimentally, all concentrations of substrate and intermediate being expressed in terms of carbon content, as obtained from TOC analysis

$$\begin{aligned} C_c \text{ (at time } t) & \\ &= C_{\text{TOC}} \text{ (at time 0)} \\ &= C_S \text{ (at time } t) + C_I \text{ (at time } t) + C_{\text{CO}_2} \text{ (at time } t) \end{aligned} \quad (6)$$

where C_c represents the total carbon, both organic and inorganic, carbon dioxide representing the final product of the mineralization process

$$C_{\text{TOC}}(\text{at time 0}) \text{ being equal to } C_S \text{ (at time 0)}, \quad (6a)$$

$$C_{\text{TOC}}(\text{at time } t) \text{ being equal to } C_S \text{ (at time } t) + C_I(\text{at time } t). \quad (6b)$$

The major limitation of (6) is to regard only intermediates containing carbon, which is, anyway, the most common

condition in degradation of organics. If this should not be the case, (6) should be substituted by

$$C_c \text{ (at time } t) = C_{\text{TOC}} \text{ (at time } t) = C_S \text{ (at time } t) = C_{\text{CO}_2} \text{ (at time } t) \quad (7)$$

and substitute (5) by

$$\left(\frac{dC_{\text{CO}_2}}{dt}\right) = -\left(\frac{dC_S}{dt}\right). \quad (8)$$

Equations (3)–(6) constitute a suitable model for temporal disappearance of TOC, which is a relevant analytical parameter to follow environmental pollution problems.

When $t = 0$ (beginning of photodegradation), C_I is completely negligible with respect to C_S . Furthermore, the hypotheses that $k_1 \sim k_2$ and symmetrically that $K_1 \sim K_2$, even if this is not always true, may be used, in some cases, simply as a starting approximation. With this approximation, (3) can be simplified to

$$r_0 = \frac{k_1 \cdot K_1 \cdot C_0}{1 + K_1 \cdot C_0}, \quad (9)$$

where r_0 is the initial rate, and C_0 represents the initial concentration of substrate **S**. The reciprocal of (9) has exactly the same form of the Langmuir-Hinshelwood model (13). Moreover, being initially $C_I = 0$, from (5) and (6) one obtains, at $t = 0$,

$$\left(\frac{dC_{\text{CO}_2}}{dt}\right) = \left(\frac{dC_{\text{TOC}}}{dt}\right) = 0. \quad (10)$$

In other words, the formation of carbon-containing intermediates, if the latter are not photodegraded yielding CO_2 at a higher rate than that of the substrate, gives rise to a characteristic plateau in the curve of TOC content versus time. This trend is only approximated experimentally, both because there is often a preferential, even if not prevailing, route to rapid CO_2 formation from **S**, and because intermediates are often more reactive than the substrate itself towards photodegradation, so that TOC disappearance is initially low, particularly in aromatic compounds, usually around one order of magnitude lower than that of the substrates, but is still measurable.

Now, let us suppose that a time t^* exists, such as that for $t > t^*$, $C_S \ll C_I$. At time t^* , (4) becomes

$$\frac{dC_I}{dt} \sim -\frac{k_2 \cdot K_2 \cdot C_I}{1 + K_2 \cdot C_I}, \quad (11)$$

and as for (6) in these conditions $C_{\text{TOC}} \sim C_I$, (11) becomes

$$\frac{dC_{\text{TOC}}}{dt} \sim -\frac{k_2 \cdot K_2 \cdot C_{\text{TOC}}}{1 + K_2 \cdot C_{\text{TOC}}}. \quad (12)$$

An important experimental result is thus substantiated and rationalized in these cases, where the rate of mineralization of intermediates is much lower than that of transformation of substrate into an intermediate (the cases of aromatic compounds particularly): the curve C_{TOC} versus time explicitly

follows a Langmuirian-type rate law (13), by which k and K parameters acquire the physical significance of k_2 and K_2 , as stated above.

That time t^* effectively exists, as a time at which the substrate is completely converted into intermediates, even with a modest decrease of TOC content and nearly complete mineralization of eventual heteroatoms present in the substrate, is experimentally recognized by both literature data [27] and by results of our preceding work [26].

In most cases, both k and K couples are accessible experimentally, as starting values from initial-rate data, relative to substrate, and TOC as well, using the Langmuirian equation (13)

$$\frac{1}{r_0} = \frac{1}{k} + \frac{1}{k K C_0}, \quad (13)$$

where r_0 is the initial rate of substrate disappearance, whether measured by direct analysis of substrate itself (to obtain the k_1 and K_1 couple) or by the rate of decrease of total organic carbon (TOC) as a function of time (to obtain the k_2 and K_2 couple). The values drawn from (13) may be used as starting values to find the absolute minimum in the error sum, G , with respect to k_1 , K_1 , k_2 and K_2 kinetic parameters. In particular cases, as stated before, when only k_2 and K_2 values are available experimentally by TOC measurements, the approximation $k_1 \sim k_2$ and $K_1 \sim K_2$ can be used as a starting point in the minimization algorithm as has been suggested on a theoretical basis [28]. Variation of kinetic parameters, in order to optimize the fitting, may additionally be restricted within the expected range of experimental uncertainty, but also chemical considerations may be of great help, as well as simultaneous consideration of k and K parameters for other chemically related substrates and/or intermediates, which may be studied by the same methodology.

2.5. Modeling of quantum yields as a function of irradiance and of substrate concentration

By using the optimized parameters of the section above, the rates of photomineralization were evaluated as a function of initial concentration, C_0 , and consequently, by operating at a certain value of the photon flow, the corresponding quantum yields Φ_0 were obtained.

Quantum yields Φ_0 , calculated from rates, followed an apparently Langmuirian function of initial concentration of substrate C_0 , by which Φ_∞ values at *infinite* concentration could be obtained as

$$\frac{1}{\Phi_0} = \frac{1}{\Phi_\infty} + \frac{1}{\Phi_\infty C_0 K}, \quad (14)$$

where the K value substantially coincided with the lowest between the two K_1 and K_2 constants above, for many molecules being $K_1 \sim K_2$.

Finally, by repeating all sets of experiments, at different values of the absorbed radiant power per unit length of photocatalytic membrane, which was varied in the range 0.10 – $4.0 \text{ W} \cdot \text{cm}^{-1}$, and by applying (14) to each set of these experiments, the Φ_∞ values, as a function of the absorbed radiant power, per unit length of photocatalytic membrane, were obtained.

TABLE 1: Parameters*, k_1 and K_1 , k_2 and K_2 , able to fit the whole photomineralization curve, following Scheme (2), at various values of absorbed power per unit length of membrane expressed in $W \cdot cm^{-1}$. They were obtained by the optimization of kinetic curves, by using the set of differential equations corresponding to kinetic model of Scheme (2). All the parameters are expressed in ppm of carbon (mass of C/volume, mg/L) and refer to the photodegradation of methane in gaseous phase, and in aqueous solutions, in the presence of stoichiometric hydrogen peroxide (for the aqueous solutions) or of dioxygen of air (for the gas-phase experiments), as oxygen donors (treated volume of the gas phase or of the aqueous solutions 4.00 L; membrane length 100.0 ± 0.5 cm; ratio between overall reaction volume and membrane length 160 ± 6 cm^3/cm^2 ; PHOTOPERM®BIT/313 membranes immobilizing 30 ± 3 wt.% TiO_2 , in the absence of any photopromoter).

| Aqueous solutions | | | | |
|--|-------------------|-------------------|-----------------------------|-----------------------------|
| Absorbed power per unit length of membrane ($W \cdot cm^{-1}$) | k_1 (ppm C/min) | k_2 (ppm C/min) | K_1 (ppm C) ⁻¹ | K_2 (ppm C) ⁻¹ |
| 0.15 | 0.111(3) | 0.293(3) | 0.0124(3) | 0.0086(3) |
| 0.30** | 0.224(1) | 0.584(2) | 0.0126(3) | 0.0089(3) |
| 0.70 | 0.494(2) | 1.23(4) | 0.0130(3) | 0.0091(3) |
| 0.90 | 0.589(3) | 1.45(4) | 0.0131(4) | 0.0090(3) |
| 1.50 | 0.802(4) | 1.95(4) | 0.0125(3) | 0.0086(4) |
| 2.00 | 0.890(3) | 2.24(3) | 0.0133(6) | 0.0090(2) |
| 3.00 | 0.896(4) | 2.39(6) | 0.0128(3) | 0.0088(2) |
| 4.00 | 0.894(5) | 2.28(7) | 0.0127(2) | 0.0086(3) |
| Gas phase | | | | |
| Absorbed power per unit membrane length ($W \cdot cm^{-1}$) | k_1 (ppm C/min) | k_2 (ppm C/min) | K_1 (ppm C) ⁻¹ | K_2 (ppm C) ⁻¹ |
| 0.15 | 0.115(6) | 0.288(7) | 0.0127(7) | 0.0085(7) |
| 0.30 | 0.223(5) | 0.581(5) | 0.0131(9) | 0.0082(6) |
| 0.90 | 0.586(3) | 1.57(4) | 0.0131(4) | 0.0091(3) |
| 1.50 | 0.805(4) | 1.92(4) | 0.0125(3) | 0.0087(2) |
| 2.00 | 0.891(3) | 2.33(3) | 0.0130(3) | 0.0090(2) |
| 3.00 | 0.892(4) | 2.37(5) | 0.0127(3) | 0.0088(2) |
| 4.00 | 0.889(5) | 2.32(6) | 0.0129(4) | 0.0091(2) |

*Uncertainties are indicated between parentheses and expressed, relatively to the last digits, as probable errors of the means of optimized values from 9 sets of runs in the range of concentrations tested.

**Data relative to these experiments were taken from [14].

2.6. Modeling of quantum yields as a function of photopromoter concentration

For experiments in which the photopromoter was added, the same procedure described in the preceding paragraph was adopted, and the Φ_∞ values obtained at a high value of absorbed irradiance, typically Φ_∞ values at $4 W \cdot cm^{-1}$, much smaller than the maximum allowable Φ_∞ values corresponding to irradiances tending to zero, were plotted as a function of concentration of photopromoter in the photocatalytic membrane.

3. RESULTS AND DISCUSSION

Photomineralization of methane in air at 100% relative humidity, and in a concentration range corresponding to 10.0–1000 ppm (mass/volume) of carbon, was studied at 318 ± 3 K, in a laboratory-scale reactor, by using dioxygen of air as an oxygen donor, and by photocatalytic membranes immobilizing $30 \pm 3\%$ of titanium dioxide, as a function of absorbed power per unit length of membrane, expressed in $W \cdot cm^{-1}$. The latter was varied in the range 0.15–4.0 $W \cdot cm^{-1}$. This is a convenient measure of power absorbed per unit apparent geometrical membrane surface, since, owing to the annular geometry of photoreactor, absorbed power per unit length, divided by membrane circumference, yields exactly that value. Kinetics of both substrate disappearance,

to yield intermediates, and total organic carbon (TOC) disappearance, to yield carbon dioxide, were followed.

At a fixed value of irradiance, corresponding to 0.30 $W \cdot cm^{-1}$, the mineralization experiments in gaseous phase were repeated as a function of flow rate, which was varied between 4 and 400 $m^3 \cdot h^{-1}$. Moreover, at a standard flow rate of 300 $m^3 \cdot h^{-1}$, the ratio between the overall reaction volume and the length of the membrane was varied, substantially by varying the volume of reservoir, from and to which circulation of gaseous stream took place.

Photomineralization of methane in aqueous solutions was also studied, in the same reactor and in the same conditions, but in a concentration range of 0.8–2.0 ppm of carbon, and by using stoichiometric hydrogen peroxide as an oxygen donor.

3.1. Parameters of kinetic model as a function of absorbed power per unit length of membrane

Treating of experimental data by the kinetic model above (see Experimental) allowed to obtain, for all sets of kinetic runs, performed as a function of concentration, two couples of parameters, k_1 and K_1 , k_2 and K_2 , which fitted the whole photomineralization curve, and not only its initial segment, as the Langmuirian parameters generally do. These parameters, as a function of absorbed power per unit membrane length, are reported in Table 1, both for experiments carried

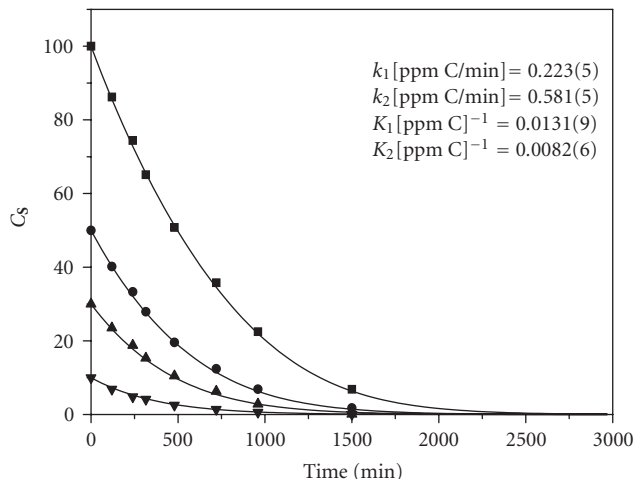


FIGURE 1: Kinetics of disappearance of methane, as substrate, from the gas phase, with $0.30 \text{ W}\cdot\text{cm}^{-1}$ of absorbed radiation power per unit membrane length. Concentrations, C_s in mg/L, for methane, are expressed as carbon, which was not transformed into intermediates, as a function of time, expressed in minutes, as time necessary to treat 1 L of gas phase. Photocatalytic membranes used in these experiments did not contain any photopromoting agent.

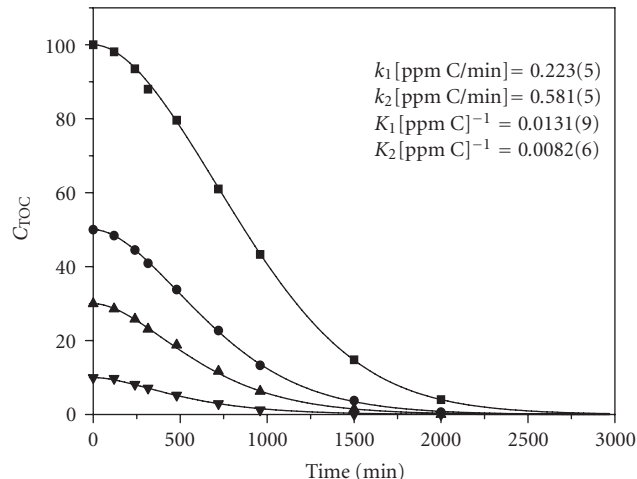


FIGURE 2: Kinetics of disappearance of total organic carbon (TOC) from gaseous methane in the laboratory-scale photoreactor (see Experimental), expressed as concentrations, C_{TOC} in mg/L of carbon, which was not mineralized, as a function of time, expressed in minutes, as time necessary to treat 1 L of gas phase. Absorbed radiation power per unit membrane length was $0.30 \text{ W}\cdot\text{cm}^{-1}$ during these runs. Photocatalytic membranes used in these experiments did not contain any photopromoting agent.

out on methane in aqueous solutions, with hydrogen peroxide as an oxygen donor, as well as in the gaseous phase, with dioxygen of air as oxygen donor. In this same Table, the values measured in aqueous solutions, at $0.30 \text{ W}\cdot\text{cm}^{-1}$, in a preceding work [14], are also reported. The very satisfactory fitting of experimental kinetic data by this model, notwithstanding its extreme simplicity, is shown, as an example, in Figures 1 and 2 for the kinetic curves of disappearance of methane in air as such, and of its TOC disappearance, respectively, at the various initial concentrations specified for this substrate, and at $0.30 \text{ W}\cdot\text{cm}^{-1}$ of absorbed power per unit length of membrane.

From the observation of the values of kinetic parameters reported in Table 1, some interesting considerations may be immediately drawn.

(i) First of all, the four parameters above, obtained from data of the present paper, relatively to photodegradation and photomineralization of methane in the gas phase, substantially coincide, within the limits of experimental uncertainty, with those measured during experiments carried out in aqueous solution, both kind of experiments being performed in conditions of turbulent flow, at every value of absorbed radiation power per unit length of membrane. Furthermore, the kinetic parameters obtained in previous work [14], at a fixed value of irradiance, are in a perfect agreement with the present ones. At least, this behavior is surely shown by TiO_2 immobilized in photocatalytic membranes tested.

(ii) Given the coincidence of kinetic parameters of Table 1, remarked in point (i) above, between experiments carried out in liquid and gaseous phase, Table 1 points out that, while k_1 and k_2 appear to be a clear function of irradiance, showing a saturation behavior at absorbed powers per unit membrane length greater than about $2 \text{ W}\cdot\text{cm}^{-1}$,

K_1 and K_2 parameters show an evident independency on irradiance.

(iii) By operating in a gaseous phase saturated by water vapour, as has been done in the present paper, mineralization proceeds smoothly and completely, as it occurs in the liquid phase, and as may be observed in Figures 1 and 2. On the contrary, if relative humidity is much less than 100%, and particularly when using chlorinated hydrocarbons as substrates [29], the formation of some amounts of relatively photostable intermediates, such as carbon monoxide and phosgene, has been detected. Complete mineralization was thus sensibly retarded. This inconvenience, however, may be completely obviated, other than maintaining a high humidity in the reaction medium, also by adding suitable photopromoting agents to the membrane [29]. For methane, evidently, only the first of these two experimental conditions is already able to assure complete mineralization.

(iv) Another aspect stems out from data of Table 1. In experiments of preceding work [19], carried out on gaseous methane at a fixed irradiance corresponding to $0.30 \text{ W}\cdot\text{cm}^{-1}$, hydrogen peroxide was aerosolized in the reactor in order to be able to compare results with those of methane solutions [14], in which hydrogen peroxide was the oxygen donor. Anyway, the two kinds of experiments gave substantially equal results. In experiments of this paper, on the contrary, the addition of hydrogen peroxide was omitted during gas-phase experiments, thus giving to dioxygen of air the role of oxygen donor in these experiments. In fact k and K parameters, as may be checked from results at $0.30 \text{ W}\cdot\text{cm}^{-1}$, are the same, in gaseous phase experiments, independently on whether hydrogen peroxide is present or not, and furthermore coincide with those of liquid phase runs. This should mean that the scavenging ability of hydrogen peroxide in

aqueous solutions is comparable, or at least undistinguishable from that of dioxygen in air, with the photocatalytic membranes yielding substantially equal rates, in the two series of kinetic runs. On the contrary, dissolved dioxygen in water gives photomineralization rates about ten times lower than those measurable in the presence of hydrogen peroxide [16, 21]. This marked that the difference of behavior may be reasonably attributed to the great difference between chemical potential of dioxygen in air and that of aqueous solutions, even if saturated with air, also on the light of considerations expounded in the following point (v).

(v) By employing the same line of thoughts, as that deriving from (i) above, we may guess that, onto photocatalytic membranes, reactions at the interface control the process. In transport phenomena through the gaseous phase onto polymers, the sorption and permeation of gases and vapours in polymers have been shown to be well described over widely varying conditions by the dualmode sorption theory [30–33], in which sorption by dissolution (Henry's law) and sorption in microvoids (Langmuir isotherm) play a significant role. Factors which relate to the molecular structure of the polymer, such as polarity, hydrogen bonding, cohesive energy density, chain flexibility, steric hindrance, and crystallinity, will, among others, all have an influence on transport properties. When dealing with sorbents or reagents or catalysts immobilized onto a membrane structure, such as in the photocatalytic membranes of the present work, thermodynamics of sorption and reaction control appear to be among the most important factors in determining transport processes [34]. These reactions are ruled kinetically, and also thermodynamically, by concentration gradients, independently on diffusion and other phenomena in the bulk, either if the latter is constituted by a liquid or by a gas phase. The presence of a sorbent in a membrane structure, such as the structure which has been obtained by the photografting method used to manufacture the photocatalytic membranes employed in the present work, affords an alternative concept in membrane science and technology [22], since the endothermic step of creating a molecular-size cavity in the polymer for the reacting species, either if arriving from the gas or from the liquid phase, is virtually eliminated. At the same time, the thinnest of all conceivable membranes may be realized, consisting in a monolayer where the adsorbed molecules may interact with its surroundings. Consequently, as it has been shown [22], surface diffusion and surface reactivity must be the prevailing mechanism for transport and reaction in these membranes, since a mobile adsorption layer results, which is able to contribute efficiently to both diffusion and reactivity [22]. This surface diffusion has been inferred by the activation energy for solubility of species, either from the gas or from the liquid phase, which nearly equals the desorption enthalpy [22]. Mass transfer, in the presence of irradiation, is accompanied by the photocatalytic reactions across these photocatalytic membranes, manufactured by the photografting nanotechnology, or by similar nanotechnologies, as those used for the preparation of photocatalytic membrane structures. As a consequence, this may occur either by an activated process, most seemingly involving migration of an adsorbed unimolecular layer across the

surface, or by Knudsen diffusion. The first kind of mechanism should prevail, as has been found [23, 24], when relatively strong adsorption interactions with active sites arise. This is in fact the case for photocatalytic membranes.

(vi) The similarity of behavior, and the coincidence of the k and K parameters (see Table 1), between experiments in the gas and in the liquid phase, is thus fully compatible with, and clearly interpreted by, the general mechanisms outlined in (v) above, as deduced and commented in previous studies concerning reactive membranes.

(vii) It should be also underlined that consideration on rates, based exclusively on k values, following a Langmuir-Hinshelwood model, should not be regarded as fully and absolutely reliable. In fact, it has been shown, since long time and unequivocally [16, 21], that also K parameters have a kinetic significance, so that these latter are integral part of a convenient and fitting model, rather than attributing to them a truly and purely physical meaning in the sense of adsorption. This notwithstanding, a rough indication based on k values can be considered, at high concentrations of substrate, as complementary to the use of the rate equation, the latter being anyway the most reliable method to treat experimental data, as has been done, for example in kinetic modeling of data reported in Table 1, in which the kK factor may play the most relevant role. This behavior may be tentatively attributed to the fact that k parameters rule the photochemical reactivity properly, while K parameters reflect, partly at least, kinetic aspects tied to flow rates, and possibly other engineering features of the photoreactors, as it will be discussed later.

3.2. Parameters of kinetic model as a function of flow rate in the photoreactor and of reactor geometry

Maximum photomineralization rates, as shown by the variation of K values with flow rates [16], could be attained, when operating in aqueous solutions, only if the flow rate exceeded about $3 \text{ m}^3/\text{h}$, corresponding to a Reynolds regime, in the operating conditions of the plant.

Consequently, it has been deemed useful, in the present work, to perform a similar investigation in the gas phase, by operating at a fixed value of irradiance (corresponding to $0.30 \text{ W} \cdot \text{cm}^{-1}$) and by varying the flow rate in the range $4\text{--}400 \text{ m}^3 \cdot \text{h}^{-1}$. Results are shown graphically in Figure 3. It readily emerges that, while no influence on k_1 and k_2 values could be detected, outside the limits of experimental uncertainty, a variation of both K_1 and K_2 values with flow rate was operative, similar to that evidenced in liquid phase [16], so that all experimental runs for mineralization of methane in air were standardized at a flow rate of $300 \text{ m}^3 \cdot \text{h}^{-1}$, in order to explore the influence of other variables, such as that of irradiance itself. This again is a clear indication of the fact that the K parameters contain a kinetic contribution due to diffusion of species towards the interface of the photocatalytic membrane.

To examine further the possible influence of reactor geometry, and given that in the laboratory-scale apparatus, as well as in all the pilot plant-scale modules, the optical path was already optimized [12, 16], the ratio α between the

overall reaction volume and the length of the membrane was varied, at the standard flow rate of $300 \text{ m}^3 \cdot \text{h}^{-1}$, and at a fixed value of irradiance corresponding to $0.30 \text{ W} \cdot \text{cm}^{-1}$. In an annular laboratory-scale apparatus, suitable to carry out characterization or standardization procedures, such as that employed in present as well as in preceding studies, and in which batch operation is the rule, the best way to vary reactor geometry consists in varying the volume of reservoir, from and to which circulation of the reacting stream takes place. Consequently, ratio α above is the most suitable parameter to define reactor geometry, when reactor diameter, and optical path maximizing photochemical yields have been chosen and fixed at the most convenient values. By varying this α ratio from 80 to $450 \text{ cm}^3 \cdot \text{cm}^{-1}$, it was confirmed that k values varied accordingly, with respect to those relating to the standard value of $\alpha = 160 \text{ cm}^3 \cdot \text{cm}^{-1}$ used, while the K values remained substantially unaffected. Consequently, k values, reflecting the influence of concentrations, and expressed, for example, in $(\text{mg/L}) \cdot \text{min}^{-1}$, were transformed into mass reacted per unit time and per unit apparent surface of membrane (e.g., by expressing them in $\text{mg} \cdot \text{min}^{-1} \cdot \text{m}^{-2}$), by taking into account the variable α above, following the relation $\kappa = k \cdot 10 \alpha / \beta$, where β is the circumference of the membrane, expressed in cm. Then all these k parameters gave a common κ value, independent on reactor geometry, if expressed in the $\text{mg} \cdot \text{min}^{-1} \cdot \text{m}^{-2}$ units above, or in any other related unit, which may be preferred. As a result, by this way, data may be standardized and compared quite easily, even in different experimental conditions.

3.3. Modeling of quantum yields as a function of absorbed power per unit length of membrane and of substrate concentration

By (14), in which the K values substantially coincided with K_2 of Table 1, and by applying the procedure described above (see Experimental), the Φ_∞ values as a function of the absorbed radiant power per unit length of photocatalytic membrane, expressed in $\text{W} \cdot \text{cm}^{-1}$, were obtained and reported in Figure 4, both for experiments carried out in the gas phase (red symbols) and for experiments performed in aqueous solutions (blue symbols). The practical coincidence between these two sets of values, as discussed above, readily appears. The mean values of Φ_∞ between these two sets of experiments are reported in Figure 5.

To explain the behavior of sigmoid curves, such as that of Figures 4 or 5, a competition kinetics of the reaction of hydroxyl radicals with themselves to give hydrogen peroxide, accompanied by the reaction of these radicals, as well as of superoxide anion radical and/or its conjugate acid, with the substrate and intermediates, leading to mineralization, may be envisaged, such as given by reaction (a) on one side and reactions (b) and (b') on the other.

Reaction (a) corresponds to the formation of hydrogen peroxide by recombination of hydroxyl radicals, $dC_{\text{H}_2\text{O}_2}/dt$, where t is time,

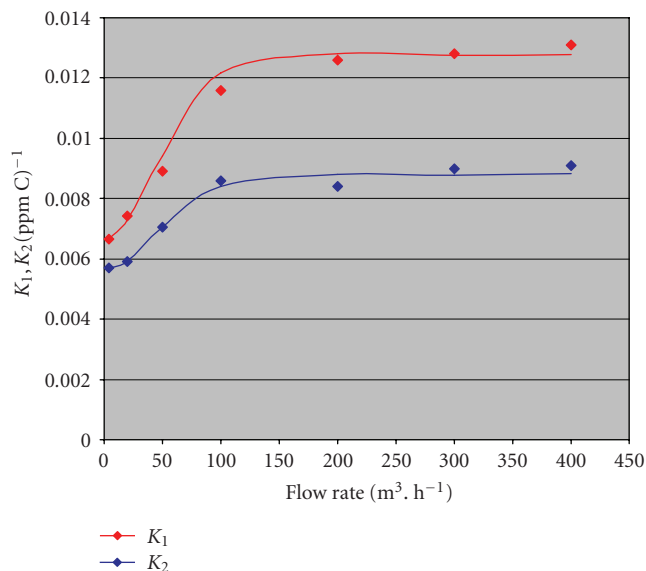


FIGURE 3: Variation of K_1 and K_2 parameters, expressed in $(\text{ppm C})^{-1}$ (see kinetic modeling in Experimental), as a function of flow rate ($\text{m}^3 \cdot \text{h}^{-1}$), for photomineralization of methane in air, and experiments carried out at a fixed irradiance corresponding to $0.30 \text{ W} \cdot \text{cm}^{-1}$. The mean values of k_1 and k_2 parameters, resulting from modeling of these same experiments, were sensibly constant ($k_1 = 0.225 \pm 0.005 \text{ ppm C} \cdot \text{min}^{-1}$; $k_2 = 0.578 \pm 0.007 \text{ ppm C} \cdot \text{min}^{-1}$), independently on values of flow rates. Photocatalytic membranes used in the relative experiments did not contain any photopromoting agent.

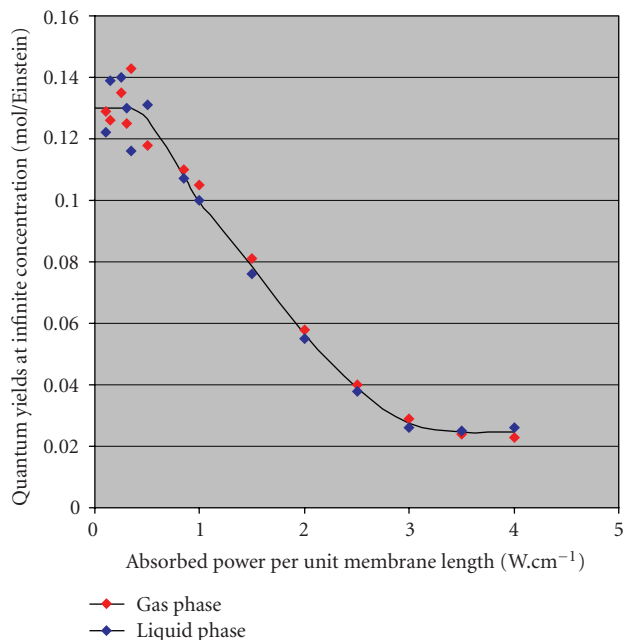


FIGURE 4: Quantum efficiencies Φ_∞ (mol/Einstein), extrapolated by (14) (see Experimental), at *infinite* concentration of substrate, for methane in air (red dots) and in aqueous solution (blue dots), as a function of absorbed power per unit length of irradiated photocatalytic membrane, expressed as $\text{W} \cdot \text{cm}^{-1}$. Photocatalytic membranes used in the relative experiments did not contain any photopromoting agent.

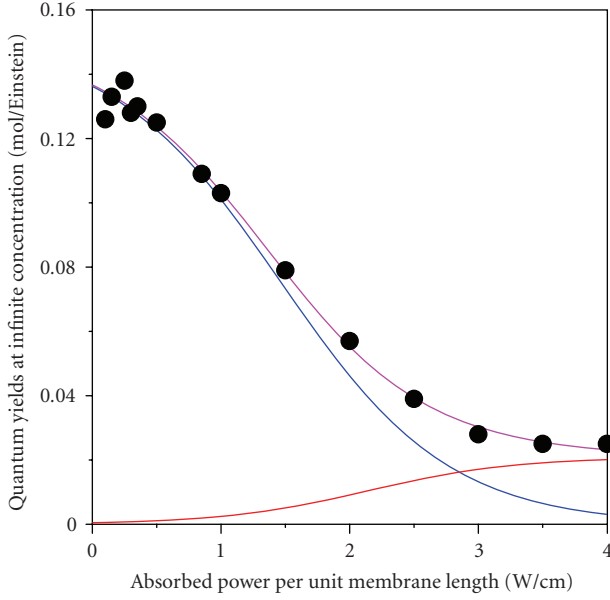


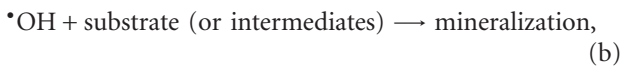
FIGURE 5: Quantum efficiencies Φ_{∞} (mol/Einstein) of methane, extrapolated by (17), at *infinite* concentration of substrate, evaluated as mean values (black dots) relative to measurements in aqueous solution and in the gaseous phase, reported in Figure 4, as a function of absorbed power per unit length of irradiated photocatalytic membrane, expressed as $W \cdot cm^{-1}$. The blue curve represents the calculated contribution of reaction (b), as modeled in the present work, decreasing with increasing power. The red curve represents the calculated contribution of reaction (b'), as modeled in the present work, increasing with increasing power. The mauve curve represents equation modeled in the present work, as a sum of both these contributions. Photocatalytic membranes used in the relative experiments did not contain any photopromoting agent.

and its rate r_a may be written as

$$r_a = k_a \cdot C_{\cdot OH^2}, \quad (15)$$

where k_a is the rate constant of reaction (a), and $C_{\cdot OH}$ is the concentration of hydroxyl radicals.

Reaction (b) is given by



and its rate r_b may be written as

$$r_b = k_b \cdot C_S \cdot C_{\cdot OH}, \quad (16)$$

where k_b is the rate constant of reaction (b), and C_S is the concentration of substrate or intermediates, on the surface of the photocatalytic membrane on to which mineralization takes place.

Reaction (b') by the $O_2^{\cdot-}/HO_2^{\cdot}$ superoxide radical couple is given by

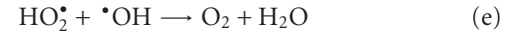
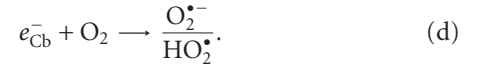
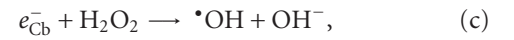


and its rate $r_{b'}$ may be written as

$$r_{b'} = k_{b'} \cdot C_S \cdot C_{O_2^{\cdot-}/HO_2^{\cdot}}, \quad (17)$$

where $k_{b'}$ is the rate constant of reaction (b').

At very low photon flows, corresponding to the upper plateau of curve of Figure 4, at which the concentration of hydroxyl radicals formed by irradiation onto the semiconductor surface is relatively low, reaction (a) is certainly negligible, with respect to reaction (b). Furthermore, in these circumstances, and particularly when operating in the presence of hydrogen peroxide as an oxygen donor, scavenging of photogenerated electrons of the conduction band e_{Cb}^- should be quantitative and compatible with reactions (c) and (d) occurring at comparable rates, and followed by reaction (e) as



If these conditions are working, a quantum efficiency equal or very near to the maximum one allowable may be attained. This hypothesis obviously corresponds to stating that each absorbed photon, in the optimal conditions of a membrane photoreactor, should give rise to a hydroxyl radical, at every C_0 value of (14) C_0 values being the corresponding C_S values of (16) and (17), for each initial concentration of substrate. Following this same hypothesis, reactivity of conduction-band electrons, in the presence of hydrogen peroxide as an oxygen donor, should give rise, almost quantitatively, to molecular oxygen, or, alternatively to reactions (c)–(e), to reduced species, in the semiconductor lattice or at the interface, by reaction with donors (water itself included). If these reactions take place quantitatively, also the contribution of $r_{b'}$ to the overall rate r given by

$$r = r_a + r_b + r_{b'} \quad (18)$$

will be negligible. Radical reactivity leading to integral mineralization of substrate should be controlled by (18), with both r_a and $r_{b'}$ much lower than r_b and consequently the r_b/r factor should reach the maximum value permissible (approaching the unity). This situation is surely achieved at very low values of the photon flow, since effectively, in these conditions, in Figure 4 the maximum allowable quantum yields for methane mineralization are operative, corresponding to reactivity of hydroxyl radicals alone, as shown by the apparent upper plateau of this curve. These values are very near to 0.125 mol/Einstein, which corresponds to the mineralization of methane by 8 hydroxyl radicals, as required by stoichiometry. Typically, as stated above (see Experimental), at 0.30 W/cm (a representative value in the range of 0–0.5 W/cm, where maximum quantum yields of Figure 4 are operative, and consequently the r_b/r ratio is unitary) this photon flow amounted to 4.45×10^{-5} Einstein s^{-1} . This means that, for each cm of membrane length, and consequently for each cm of length of the photoreactor, photogeneration of

4.45×10^{-5} moles (of hydroxyl radicals) $s^{-1}cm^{-1}$ took place. To transform this value in amount of hydroxyl radicals generated per unit time and per unit reactor volume, one should consider that in the laboratory scale module, given its overall volume in standard conditions, and owing to engineering design, the volume corresponding to each cm of membrane length was $160 \pm 6 cm^3/cm$ (see Experimental). As a consequence, the production rate of $\bullet OH$ radicals, always at the given absorbed power per unit length of $0.30 W/cm$, was calculated as $1.11 \times 10^{-3} mol s^{-1} L^{-1}$. This linear relationship allows to evaluate the production rate of hydroxyl radicals in the upper apparent plateau of curves such as that of Figure 4, at each value of W/cm .

This mechanism, however could not rule also at high photon flows, when the quantum yields of Figure 5 from the upper apparent plateau begin to decrease with increasing photon flow, and finally reach an apparent lower second plateau. This may be due, on one side, the fact that the production rate of hydroxyl radicals, at W/cm values higher than about 0.5, should vary with photon flow by a nonlinear relationship, and their evaluation is possible, by supposing that $C_{\bullet OH}$ decreases exponentially with increasing W/cm values

$$C_{\bullet OH} = f \cdot e^{-g(W/cm)}, \quad (19)$$

with f and g positive constants.

On the other side, with increasing photon flow, and with decreasing rate of hydroxyl radicals production, the rate of the generation of superoxide radical couples, $O_2^{\bullet -}/HO_2^{\bullet}$, increases. The $C_{O_2^{\bullet -}/HO_2^{\bullet}}$, as a function of absorbed power per unit length of membrane, may be assumed to vary according an equation of the same kind as (19), but with a negative g constant, as the production of these radicals should increase with increasing irradiance, in a complementary way by which hydroxyl radicals decrease.

Reaction (b') thus yields a supplementary contribution to mineralization, besides that due to the photocatalytic reactivity of holes onto the semiconductor surface. In other words, to the r_b contribution to mineralization, a further contribution $r_{b'}$ should be added, deriving from the concentration of superoxide radical anion and/or its conjugate acid generated by reaction (d). The overall contribution to mineralization, $(r_b + r_{b'})/r$, can be approximated by a weighted sum of the two contributions (b) and (b') as

$$\begin{aligned} & \frac{r_b + r_{b'}}{r} \\ & \cong y_{(calc)} = \frac{f_1}{[1 + e^{-g_1(W-W_1)/cm}]} + \frac{f_2}{[1 + e^{-g_2(W-W_2)/cm}]} \end{aligned} \quad (20)$$

The error sum, $G(f_1, g_1, W_1, f_2, g_2, W_2) = \sum_{i=1}^n w_i [y_{(exp)}^i - y_{(calc)}^i]^2$, is minimized with respect to $f_1, g_1, W_1, f_2, g_2,$ and W_2 parameters, to find the best model (20) that fits the data. As shown in Figure 5 for methane, the calculated curve (red curve) perfectly fits experimental data, and gives rise to a sigmoid curve, with two apparent plateaux values, as found experimentally.

In Figure 5, the contributions to quantum yields given by these two processes have been plotted as a function of W/cm .

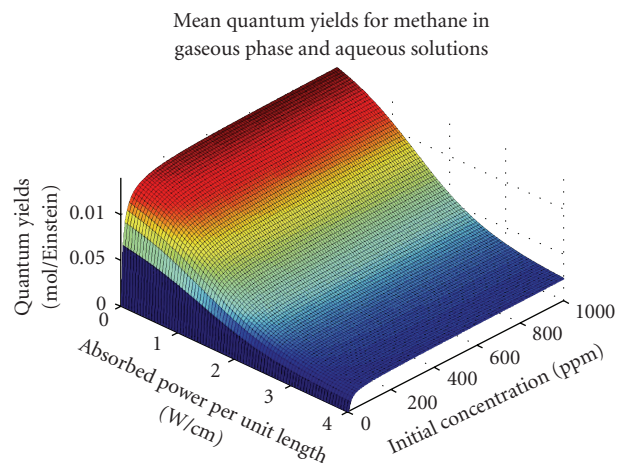


FIGURE 6: Quantum yields Φ_0 (mol of methane/Einstein) for photomineralization of methane, as a function of initial concentration C_0 , expressed as mg/L of carbon, and of absorbed power per unit length of lamp (and membrane), expressed as $W \cdot cm^{-1}$. Quantum yields are expressed as means of values, from experiments in gaseous phase and in aqueous solutions. Photocatalytic membranes used in these experiments did not contain any photopromoting agent.

It clearly appears that the contribution (blue curve) of hydroxyl radicals to mineralization decreases with irradiance, while the contribution (mauve curve) of superoxide anion radical and its conjugate acid increases.

Finally, if the best curve

$$y_{(calc)} = \frac{0.15088}{[1 + e^{1.5246(w-1.4629)/cm}]} + \frac{0.020853}{[1 + e^{-1.7655(w-2.1448)/cm}]}, \quad (21)$$

calculated for methane, is coupled with (14), a three-dimensional graph results (see Figure 6), in which quantum yields Φ_0 may be plotted and rationalized as a function of initial concentration, C_0 , and of irradiance, in the form of the absorbed power per unit length of photocatalytic membrane, W/cm , which has been defined and used in the present paper.

To sum up, only the model given by both reactions (b) and (b'), in competition with (a), is completely compatible with experimental data, and able to represent, fully satisfactorily, the dependence of quantum yields on irradiance values.

3.4. Modeling of quantum yields, at high irradiance values, as a function of photopromoter concentration

For the experiments carried out by photocatalytic membranes coimmobilizing the photopromoter together with titanium dioxide, the sigmoid shape of curves such as that of Figure 5 changed with increasing concentration of photopromoter, and the curves were flattened, as reported in the example of Figure 7, at a concentration of photopromoter corresponding to 3.0 mol/mol % of photopromoter vanadium with respect to titanium. This effect may be correlated to the kinetic influence of the photopromoter, reflected in the

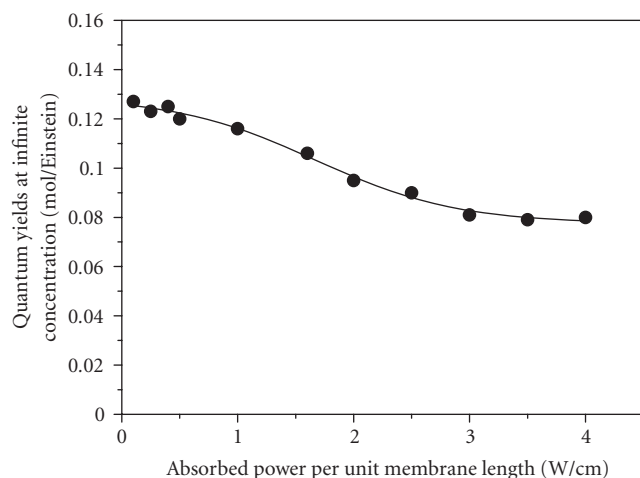


FIGURE 7: Quantum efficiencies Φ_{∞} (mol/Einstein) of methane, extrapolated by (17), at *infinite* concentration of substrate, relative to measurements carried out in the gaseous phase, as a function of absorbed power per unit length of irradiated photocatalytic membrane, expressed as $\text{W}\cdot\text{cm}^{-1}$. Photocatalytic membranes used in the relative experiments contained the photopromoter (see Experimental) at a concentration corresponding to 3.0 mol/mol % of vanadium with respect to titanium present as main photocatalyst.

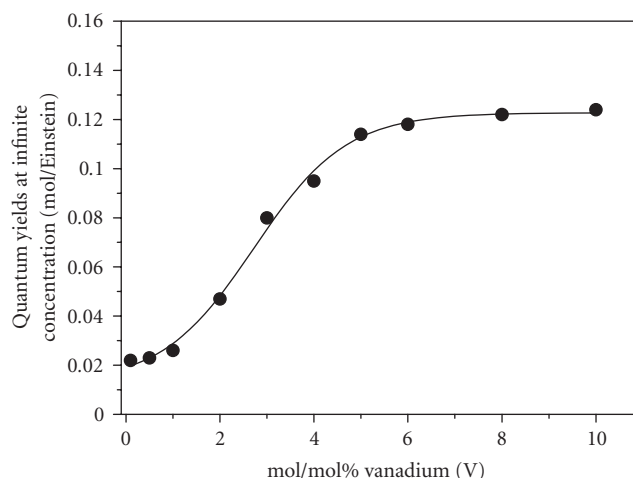


FIGURE 8: Quantum efficiencies Φ_{∞} (mol/Einstein) of methane, extrapolated by (17), at *infinite* concentration of substrate, relative to measurements carried out in the gaseous phase, and corresponding to an absorbed power per unit length of irradiated photocatalytic membrane, expressed of $4.0\text{ W}\cdot\text{cm}^{-1}$, as a function of mol/mol % of vanadium, used as photopromoter in the photocatalytic membranes, with respect to titanium present as main photocatalyst.

relationship between quantum yields and kinetic parameters. When the Φ_{∞} values corresponding to the highest irradiances, typically at $4\text{ W}\cdot\text{cm}^{-1}$, were plotted as a function of % molar concentration of photopromoter, Figure 8 was obtained. This behavior shows that at low values of the % mol/mol concentration of photopromoter vanadium, up to about 0.5, the same Φ_{∞} values measured in the absence of any photopromoting agent (see Figure 5) were obtained. When increasing photopromoter concentration, on the contrary, above this threshold value, Φ_{∞} values increase considerably and approach the maximum allowable for methane (0.125 mol/Einstein), starting from about 5% on of photopromoter vanadium. This should mean that the decrease of quantum yield brought about by the increase of irradiance, and interpreted (see preceding paragraph) by a recombination mechanism of hydroxyl radicals may be fully compensated by the addition of appropriate photopromoters at suitable concentration. By this way, operation at high irradiance values is possible, without losing any efficiency for the mineralization process.

4. STANDARDIZATION OF IMMOBILIZED PHOTOCATALYTIC MATERIALS

As recalled in Introduction, comparison of photocatalytic properties of immobilized materials, between different laboratories, is very difficult, if not impossible, owing to the variety of procedures employed in the literature. By examining kinetic curves, such as those of Figures 1 and 2, it becomes readily apparent that if criteria based on rates, either maximum or medium, are adopted, these will depend on concentration, besides the influence of reactor geometry, such as overall volume, or ratio between volume and geometri-

cal surface of immobilized material. The same applies also to criteria based on isotransformation times, owing to the influence of concentration on reaction order, and obviously also on criteria based on first-order kinetic constants. Their possible meaning as internal matching tools apart, these criteria, consequently, should be judged as inadequate to compare results obtained in different conditions and/or by different experimental devices, as has been thoroughly discussed in this work. In the present paper too, the influence of photochemical parameters, such as irradiance, and of engineering parameters, such as flow rate, has been clearly evidenced.

In order to reach order and rationalization, first of all a reliable kinetic model should be employed to modeling of data, such as that based on four-kinetic parameters, which has been used in the present as well as in previous work, able to fit the whole mineralization kinetic profile. This model, together with the knowledge of the influence of all variables outlined, allows to operate in quite reproducible conditions, both from the point of view of photochemistry (irradiance, possibility of isolating truly photocatalytic effects from photolysis of substrate or from photolysis of oxygen donors, influence of substrate concentration on quantum yields) and from the point of view of more strictly geometrical or engineering factors (possibility of transforming k into κ values, these latter taking into account geometrical aspects of the photoreactor used for standardization or characterization procedures, as well of the immobilized material, such as its geometrical surface). Secondly, rationalization of quantum yields, as a function of substrate concentration and irradiance allows not only to shed light onto the general photocatalytic mechanisms, at least from the perspective of modeling, but also to achieve a fully consistent and trustworthy design of industrial photoreactors.

5. CONCLUSIONS

A kinetic model was employed to study photocatalytic mineralization of methane, both in air and in aqueous solutions, by an annular laboratory-scale membrane reactor, fitted with photocatalytic membranes immobilizing titanium dioxide. By a set of differential equations, four final optimized parameters, k_1 and K_1 , k_2 and K_2 , were calculated, able to fit the whole kinetic profile satisfactorily. The influence of irradiance on k_1 and k_2 , as well as of flow rate on K_1 and K_2 , could be rationalized by this model. The influence of reactor geometry on k values could also be considered, in view of standardization procedures of photocatalytic experiments, or of characterization of immobilized photocatalytic materials.

The similarity of behavior, and the coincidence of the k and K parameters, between experiments in the gas and in the liquid phase, is fully compatible with, and clearly interpreted by, reactions control at the interface. These reactions are ruled kinetically, and also thermodynamically, by concentration gradients, independently on diffusion and other phenomena in the bulk, either if the latter is constituted by a liquid or by a gas phase, provided conditions of turbulent flow are assured. The presence of a sorbent in a membrane structure, such as the structure which has been obtained by the photografting method used to manufacture the photocatalytic membranes employed in the present work, affords an alternative concept in membrane science and technology, since the endothermic step of creating a molecular-size cavity in the polymer for the reacting species, either if arriving from the gas or from the liquid phase, is virtually eliminated. At the same time, the thinnest of all conceivable membranes may be realized, consisting in a monolayer where the adsorbed molecules may interact with its surroundings.

Quantum yields of mineralization of substrates in annular photoreactors immobilizing the photocatalyst in a membrane structure show a Langmuirian-type dependency on initial concentration of substrates themselves, by which limiting quantum yields, corresponding to *infinite* concentration may be calculated, together with an apparent thermodynamic constant, coinciding with the lowest between K_1 and K_2 values, very often being $K_1 \sim K_2$.

These limiting quantum yields depend on radiant power absorbed per unit membrane length, in the cylindrical geometry of photoreactors. In the low radiant power range, they take the shape of a plateau corresponding to the maximum allowable quantum yields, evaluated on the basis of a single hydroxyl radical produced per each absorbed photon, thus showing the excellent performance of the photocatalytic membrane reactors. On the contrary, at high radiant power values, another apparent plateau is evident, at a value of about 1/5 (for the experimental case of methane) with respect to the maximum value. This was interpreted on the basis of the competition kinetics of hydroxyl radicals with themselves, leading to hydrogen peroxide formation, other than with substrate or intermediates molecules leading to mineralization. In this model, the contribution of hydroxyl radicals to mineralization decreases with irradiance, while the contribution of superoxide anion radical and its conju-

gate acid increases. Two radical reactions thus appear to be responsible for mineralization, that of $\cdot\text{OH}$ radicals, and that of the $\text{O}_2^{\cdot-}/\text{H}_2\text{O}_2$ radical couple, the last of which acquiring importance only in the experimental conditions of high radiating power. If these contributions are considered together, in a weighted form, the calculated equation perfectly fits experimental data, and gives rise to a sigmoid curve, with two apparent plateau values, as found experimentally.

Finally, the action of a photopromoting agent may be easily quantified and rationalized by measuring quantum yields at infinite concentration, at high irradiance values, as a function of concentration of photopromoting agent coimmobilized in the photocatalytic membrane. When increasing photopromoter concentration above an apparent threshold value, for which no effect could be observed, Φ_∞ values increase considerably and approach the maximum allowable for the investigated molecule. This should mean that the decrease of quantum yield brought about by the increase of irradiance, and interpreted by a recombination mechanism of hydroxyl radicals, may be fully compensated by the addition of appropriate photopromoters at suitable concentration. By this way, operation at high irradiance values is possible, without losing any efficiency for the mineralization process.

ACKNOWLEDGMENTS

The present paper is the 81st in a series of papers authored by Ignazio Renato Bellobono and his collaborators over the past 21 years which are collectively referred to as the *Photosynthetic Membranes* series. Some of us (R. Stanesco, C. Costache, and L. Bobirica) gratefully acknowledge B.I.T. srl (Milan, Italy), in the work of a permanent agreement with the Polytechnic University of Bucharest, concerning research on B.I.T. patented membranes and processes. Financial contribution by *Fondazione Cariplo* is also gratefully acknowledged.

REFERENCES

- [1] A. L. Linsebigler, G. Lu, and J. T. Yates Jr., "Photocatalysis on TiO_2 surfaces: principles, mechanisms, and selected results," *Chemical Reviews*, vol. 95, no. 3, pp. 735–758, 1995.
- [2] M. R. Hoffmann, S. T. Martin, W. Choi, and D. W. Bahnemann, "Environmental applications of semiconductor photocatalysis," *Chemical Reviews*, vol. 95, no. 1, pp. 69–96, 1995.
- [3] O. Legrini, E. Oliveros, and A. M. Braun, "Photochemical processes for water treatment," *Chemical Reviews*, vol. 93, no. 2, pp. 671–698, 1993.
- [4] J. Cunningham, G. Al-Sayyed, and S. Srijaranai, "Adsorption of micropollutants onto TiO_2 particles in relation to photoremediation of contaminated water, chapter 22," in *Aquatic and Surface Photochemistry*, G. R. Zepp and D. G. Crosby, Eds., pp. 317–348, CRC Press, Boca Raton, Fla, USA, 1994.
- [5] R. W. Matthews, "Photooxidation of organic impurities in water using thin films of titanium dioxide," *Journal of Physical Chemistry*, vol. 91, no. 12, pp. 3328–3333, 1987.
- [6] A. Mills, R. H. Davies, and D. Worsley, "Water purification by semiconductor photocatalysis," *Chemical Society Reviews*, vol. 22, no. 6, pp. 417–425, 1993.

- [7] M. R. Prairie, L. R. Evans, B. M. Stange, and S. L. Martinez, "An investigation of TiO_2 photocatalysis for the treatment of water contaminated with metals and organic chemicals," *Environmental Science & Technology*, vol. 27, no. 9, pp. 1776–1782, 1993.
- [8] M. Schiavello, *Photocatalysis and Environment: Trends and Applications*, vol. 238 of *NATO ASI Series C*, Kluwer, London, UK, 1987.
- [9] D. Bahnemann, "Photocatalytic detoxification of polluted waters," in *The Handbook of Environmental Chemistry*, P. Boule, Ed., vol. 2, part 1, pp. 185–212, Springer, Berlin, Germany, 1999.
- [10] I. R. Bellobono, B. Barni, and F. Gianturco, "Pre-industrial experience in advanced oxidation and integral photodegradation of organics in potable waters and waste waters by PHOTOPERMTM membranes immobilizing titanium dioxide and promoting photocatalysts," *Journal of Membrane Science*, vol. 102, pp. 139–147, 1995.
- [11] M. F. J. Dijkstra, E. C. B. Koerts, A. A. C. M. Beenackers, and J. A. Wesselingh, "Performance of immobilized photocatalytic reactors in continuous mode," *AIChE Journal*, vol. 49, no. 3, pp. 734–744, 2003.
- [12] F. Ascari, I. R. Bellobono, and P. M. Tozzi, "Kinetic modelling of pilot plant photomineralization of aqueous cibacron CR as model molecule of industrial azo dyes on titanium dioxide-immobilizing membranes," *Fresenius Environmental Bulletin*, vol. 12, no. 10, pp. 1195–1201, 2003.
- [13] I. R. Bellobono, F. Ascari, C. Lagrasta, et al., "Kinetic modelling of photomineralization of phenol, as model molecule of aromatic micropollutants, and validation of a photochemical reactor based on photocatalytic membranes immobilizing titanium dioxide and promoting photocatalysts," *Fresenius Environmental Bulletin*, vol. 12, no. 12, pp. 1536–1544, 2003.
- [14] I. R. Bellobono, F. Morazzoni, R. Bianchi, et al., "Laboratory-scale photomineralisation of n-alkanes in aqueous solution, by photocatalytic membranes immobilising titanium dioxide," *International Journal of Photoenergy*, vol. 7, no. 2, pp. 79–85, 2005.
- [15] A. V. Emeline, V. K. Ryabchuk, and N. Serpone, "Dogmas and misconceptions in heterogeneous photocatalysis. Some enlightened reflections," *Journal of Physical Chemistry B*, vol. 109, no. 39, pp. 18515–18521, 2005.
- [16] B. Barni, A. Cavicchioli, E. Riva, et al., "Pilot-plant-scale photodegradation of phenol in aqueous solution by photocatalytic membranes immobilizing titanium dioxide (PHOTOPERM[®] process)," *Chemosphere*, vol. 30, no. 10, pp. 1861–1874, 1995.
- [17] F. Gianturco, C. M. Chiodaroli, I. R. Bellobono, M. L. Raimondi, A. Moroni, and B. Gawlik, "Pilot-plant photomineralization of atrazine in aqueous solution, by photocatalytic membranes immobilizing titanium dioxide and promoting photocatalysts," *Fresenius Environment Bulletin*, vol. 6, pp. 461–468, 1995.
- [18] I. R. Bellobono, G. de Martini, P. M. Tozzi, et al., "Modelling of quantum yields in photocatalytic membrane reactors immobilising titanium dioxide," *International Journal of Photoenergy*, vol. 2006, Article ID 26870, 8 pages, 2006.
- [19] I. R. Bellobono, R. Stanesco, C. Costache, et al., "Laboratory-scale photomineralisation of n-alkanes in gaseous phase, by photocatalytic membranes immobilising titanium dioxide," *International Journal of Photoenergy*, vol. 2006, Article ID 73167, 8 pages, 2006.
- [20] I. R. Bellobono, R. Tacchi, E. Selli, and F. Muffato, "Photosynthetic membranes for pure and ultra pure water production," in *Membrane Separation Processes*, A. Green, Ed., pp. 187–193, BHRA, Cranfield, UK, 1989.
- [21] B. Barni, A. Cavicchioli, E. Riva, et al., "Laboratory-scale photodegradation of phenol in aqueous solution by photocatalytic membranes immobilizing titanium dioxide," *Chemosphere*, vol. 30, no. 10, pp. 1847–1860, 1995.
- [22] I. R. Bellobono, F. Muffato, C. Ermondi, E. Selli, and L. Righetto, "Gas separation membranes containing carbon immobilized by photochemical grafting onto polymers," *Journal of Membrane Science*, vol. 55, no. 3, pp. 273–281, 1991.
- [23] I. R. Bellobono, F. Muffato, C. Ermondi, E. Selli, L. Righetto, and M. Zeni, "Thermodynamic study of sorption of n-alkanes onto 5A zeolites immobilized in photosynthetic membranes," *Journal of Membrane Science*, vol. 55, no. 3, pp. 263–272, 1991.
- [24] I. R. Bellobono, E. Selli, L. Righetto, F. Muffato, and C. Ermondi, "Thermodynamic study of sorption of linear aliphatic monohydric alcohols and monocarboxylic acids from n-heptane and n-decane solution onto α -iron(III) oxide immobilized in photosynthetic membranes," *Materials Chemistry and Physics*, vol. 21, no. 2, pp. 155–167, 1989.
- [25] I. R. Bellobono, A. Carrara, B. Barni, and A. Gazzotti, "Laboratory- and pilot-plant-scale photodegradation of chloroaliphatics in aqueous solution by photocatalytic membranes immobilizing titanium dioxide," *Journal of Photochemistry and Photobiology A*, vol. 84, no. 1, pp. 83–90, 1994.
- [26] F. Rota, M. Cavassi, D. Niego, et al., "Mathematical modelling of photomineralization of phenols in aqueous solution, by photocatalytic membranes immobilizing titanium dioxide," *Chemosphere*, vol. 33, no. 11, pp. 2159–2173, 1996.
- [27] N. Serpone, E. Pelizzetti, and K. Hidaka, "Identifying primary events and the nature of intermediates formed during the photocatalyzed oxidation of organics mediated by irradiated semiconductor," in *Photocatalytic Purification and Treatment of Water and Air*, D.F. Ollis and H. Al-Ekabi H, Eds., pp. 225–250, Elsevier, Amsterdam, The Netherlands, 1993.
- [28] C. S. Turchi and D. F. Ollis, "Mixed reactant photocatalysis: intermediates and mutual rate inhibition," *Journal of Catalysis*, vol. 119, no. 2, pp. 483–496, 1989.
- [29] I. R. Bellobono, "Advanced oxidation and integral degradation of trichloroethene in air by photocatalytic membranes immobilizing titanium dioxide and promoting photocatalysts," *Life Chemistry Reports*, vol. 13, pp. 63–70, 1995.
- [30] W. R. Vieth, J. M. Howell, and J. H. Hsieh, "Dual sorption theory," *Journal of Membrane Science*, vol. 1, pp. 177–220, 1976.
- [31] R. T. Chern, W. J. Koros, H. B. Hopfenberg, and V. T. Stannett, "Material selection for membrane-based gas separations," *Polymeric Materials Science and Engineering*, vol. 50, pp. 88–92, 1984.
- [32] W. J. Koros, "Simplified analysis of gas/polymer selective solubility behaviour," *Journal of Polymer Science*, vol. 23, no. 8, pp. 1611–1628, 1985.
- [33] A. S. Sangani, "An application of an homogenization method to a model of diffusion in glassy polymers," *Journal of Polymer Science B*, vol. 24, no. 3, pp. 563–575, 1986.
- [34] I. R. Bellobono, F. Muffato, E. Selli, L. Righetto, and R. Tacchi, "Transport of oxygen facilitated by peroxy-bis[*N,N'*-ethylene bis-(salicylideneiminato)-dimethylformamide-cobalt(III)] embedded in liquid membranes immobilized by photografting onto cellulose," *Gas Separation & Purification*, vol. 1, no. 2, pp. 103–106, 1987.